ACTA PHYSICA

ACADEMIAE SCIENTIARUM HUNGARICAE

VOLUME 52 No. 1

AKADÉMIAI KIADÓ, BUDAPEST
1982

ACTA PHYS. HUNG. APAHAQ 52 (1) 1—116 (1982)

ACTA PHYSICA

A JOURNAL OF THE HUNGARIAN ACADEMY OF SCIENCES

EDITED BY

I. KOVÁCS

Acta Physica publishes original papers on subjects in physics. Papers are accepted in English, French, German and Russian.

Acta Physica is published in two yearly volumes (4 issues each) by

AKADÉMIAI KIADÓ
Publishing House of the Hungarian Academy of Sciences
H-1054 Budapest, Alkotmány u. 21

Subscription information

Orders should be addressed to

KULTURA Foreign Trading Company
1389 Budapest P.O. Box 149

or to its representatives abroad.

ACTA PHYSICA

ACADEMIAE SCIENTIARUM HUNGARICAE

VOLUME 52

AKADÉMIAI KIADÓ, BUDAPEST
1982

ACTA PHYS. HUNG.

CONTENTS

Volume 52

CONDENSED MATTER

CROSS-DISCIPLINARY PHYSICS

ACTA PHYSICA
ACADEMIAE SCIENTIARUM HUNGARICAE

VOLUME 52 No. 1

AKADÉMIAI KIADÓ, BUDAPEST
1982

ACTA PHYS. HUNG.

CONTENTS

Acta Physica Academiae Scientiarum Hungaricae, 52 (1), pp. 3—13 (1982)

ELECTRICAL TRANSPORT AND STRUCTURAL PROPERTIES OF Se—Te SEMICONDUCTORS*

M. F. KOTKATA**
INTERNATIONAL CENTRE FOR THEORETICAL PHYSICS, TRIESTE, ITALY

A. A. EL-ELA, E. A. MAHMOUD and M. K. EL-MOUSLY
PHYSICS DEPARTMENT, FACULTY OF SCIENECE, AIN SHAMS UNIVERSITY, CAIRO, EGYPT

(Received 10. III. 1981)

dc conductivity of different $TeSe_x$ semiconducting alloys, with $x = 50$, 30, 20, 15, 10 and 5, are studied in both the liquid and the crystallized phases. The composition dependence of σ_0 (temperature independent pre-exponent) and E_σ (activation energy of conduction) in liquid Se-Te mixtures has been correlated with the electronic features and ability of the Te atoms to dissociate the Se chains. The conductivity dependence on time (t) in supercooled liquid Te-Se alloys is investigated in the temperature range of 90—180 °C. The data obtained are used to calculate the crystallization kinetic parameters K and n of an AVRAMI equation in the form, $\alpha(t) = 1 - \mathrm{Exp}(-Kt^n)$. The activation energy of the crystallization process shows a certain compositional dependence with a minimum value 0.37 eV at the composition of $TeSe_{30}$.

I. Introduction

According to the phase diagram of the selenium—tellurium system, solid solutions are formed from the two elements in all atomic proportions and the variation of the lattice parameters with concentration shows little deviation from VEGARD's law [1—3]. The liquid Te—Se alloy system spans a wide range of electronic behaviour between metals and insulators. Liquid Se is a fairly wide gap semiconductor which displays activated electrical conductivity [4]. In liquid Te, experimental evidence suggests that the Fermi energy E_F is within the valence band [5] and that the density of states at the Fermi energy $N(E_F)$ is temperature-dependent. X-ray and neutron diffraction experiments [6—10] indicate that the co-ordination number of liquid Te is about three at the melting point T_M and increases rapidly with temperature, while that of liquid Se is about two and weakly temperature-dependent. In liquid Se—Te mixtures the average co-ordination number remains nearly two, irrespective of composition in the Se-rich region and it increases with the Te concentration in the Te-rich region. These evidences led to suggest that a change from Se-like to Te-like structure may occur at some intermediate concentration region in Se—Te mixtures [11].

* Published in ICTP Preprints, Miramare-Trieste, IC/80/70, 1980.

** Permanent address: Physics Department, Faculty of Science, Ain Shams University, Cairo, Egypt.

Recently, KOTKATA et al [3] have constructed an equilibrium phase diagram of the Se–Te system from DTA thermograms considering both the endothermic effect on heating and the exothermic effect on cooling. An eutectic point has been proved to exist at the composition of $TeSe_{30}$ and 180 °C during the supercooling processes. This paper presents results of dc conductivity measurements on some Se-Te alloys, including $TeSe_{30}$, in both liquid and crystallized states. Also, the crystallizing kinetic parameters of supercooled liquid Se—Te alloys are studied in detail. This has been done by considering the dc conductivity at any intermediate point during the liquid—crystalline transition as a structural characteristic quantity for a material containing two phases, liquid and crystalline [12].

II. Samples, preparation and experimental details

Six alloys of the general formula $TeSe_x$, with $x = 50$, 30, 20, 15, 10 and 5, were prepared from high purity (99.999%) elemental selenium and tellurium. The exact proportions required to prepare 6 g of each composition (see Table I) were enclosed in a vacuum-sealed ($\sim 10^{-2}$ Pa) quartz ampoule (0.012 m in diameter). The tubes were heated at 800 °C for eight hours in an electric oven and shaken several times during the course of synthesis to ensure complete mixing. The molten materials were then quenched in icy water. This method of preparation leads to the formation of the considered compositions in the amorphous state as confirmed by the presence of halo patterns in the X-ray diffraction [13] as well as strong exothermic peaks in the DTA thermograms [3].

In order to apply electrical measurements, about 2 g from the bulk amorphous sample (6 g), which had been obtained by the quenching technique, was sealed ($\sim 10^{-2}$ Pa) in a pyrex ampoule (0.01 m in diameter) provided with two tungsten electrodes. Measurements of dc conductivity were carried out

Table I

Summary of dc conductivity measurements of liquid and crystalline Se-Te alloys

Sample	Te content (%)	Liquid samples		Samples as-crystallized at 130 °C	
		E_σ (eV)	$\ln \sigma_0 (\Omega^{-1} \mathrm{cm}^{-1})$	E_σ(eV)	$-\ln \sigma_{20} (\Omega^{-1} \mathrm{cm}^{-1})$
$TeSe_{50}$	1.96	1.60	0.8	1.23	11.0
$TeSe_{30}$	3.23	1.44	−0.1	0.90	7.9
$TeSe_{20}$	4.76	1.28	−0.3	1.05	8.4
$TeSe_{15}$	6.25	1.72	1.9		
$TeSe_{10}$	9.09	1.90	2.8	0.73	6.1
$TeSe_5$	16.67	2.20	4.1	0.40	5.4

using an electrometer of the type VAJ-52 (error less than 2.5%) and applying low stable voltage (<5 V). Three sets of measurements were considered:

i) Study of the function $\sigma = f(T)$ in the liquid state, i.e. at temperatures T higher than T_M which had been previously determined [3].

ii) Study of the function $\sigma = f(t)$ during the crystal growth in the supercooled liquid phases. This had been done by heating the as-prepared quenched sample for one hour at 300 °C, then rapidly transferring it into a preheated oven adjusted to a required temperature in the range of 90—180 °C. The latter was kept constant during the disorder—order transition period using an automatic control system with temperature variation less than 0.5 °C.

iii) Study of the function $\sigma = f(T)$ for samples crystallized at different isothermal temperatures, i.e. after the end of each transitional step in set ii).

III. Results

The results of *dc* conductivity measurements are given in Figs. 1 to 3. Fig. 1 shows the plot of $\ln \sigma$ versus $1/T$ for the investigated liquid alloys, where the relationship is linear in the measured temperature range. Table I gives E_σ, the activation energy of conduction as a function of composition, calculated from the slopes of the curves $\ln \sigma$ versus $1/T$, and $\ln \sigma_0$, the intercept of the ordinate for $1/T = 0$. Values of E_σ vary from 1.28 to 2.20 eV, while those of $-\ln \sigma_0$ lie in the region of $+0.3$ to -4.1 (σ is measured in $\mathrm{Ohm^{-1}\,cm^{-1}}$), and none of the two functions varies in a monotonic way. The respective values for the composition of $TeSe_{30}$ are 1.44 eV and 0.1.

The change of the electrical conductivity σ during the disorder—order phase transitions of the supercooled liquid Se—Te alloys has been recorded continuously as a function of time t. In Figs. 2a and 2b, the variations of $\ln \sigma$

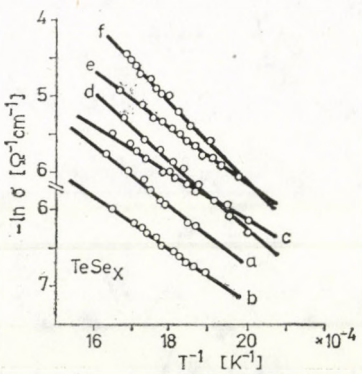

Fig. 1. Temperature-dependence of electrical conductivity of $TeSe_x$ liquid alloys; $x = 50$ (a), 30 (b), 20 (c), 15 (d), 10 (e) and 5 (f).

with the annealing time during transitions carried out at different annealing temperatures are given for the compositions of $TeSe_{50}$ and $TeSe_{10}$, respectively. The small difference between the initial values of σ, the points A in Fig. 2a or Fig. 2b, is related with the moment at which the measurements started to record. Fig. 2c shows the variation of $\ln \sigma$ versus t for different compositions crystallized at 130 °C. In Fig. 2, it is obvious to see that two processes combine

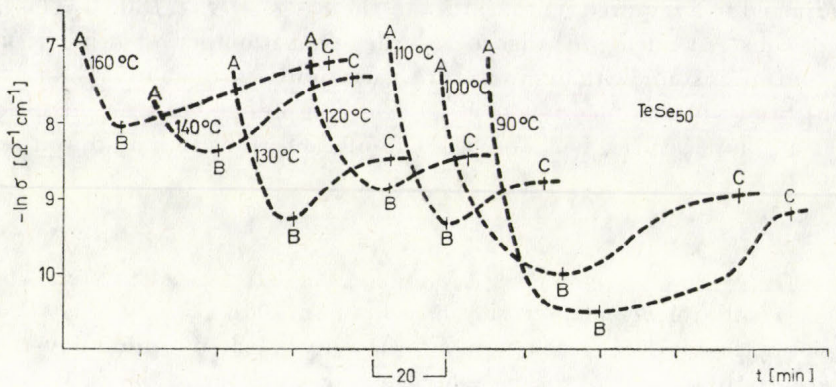

Fig. 2a

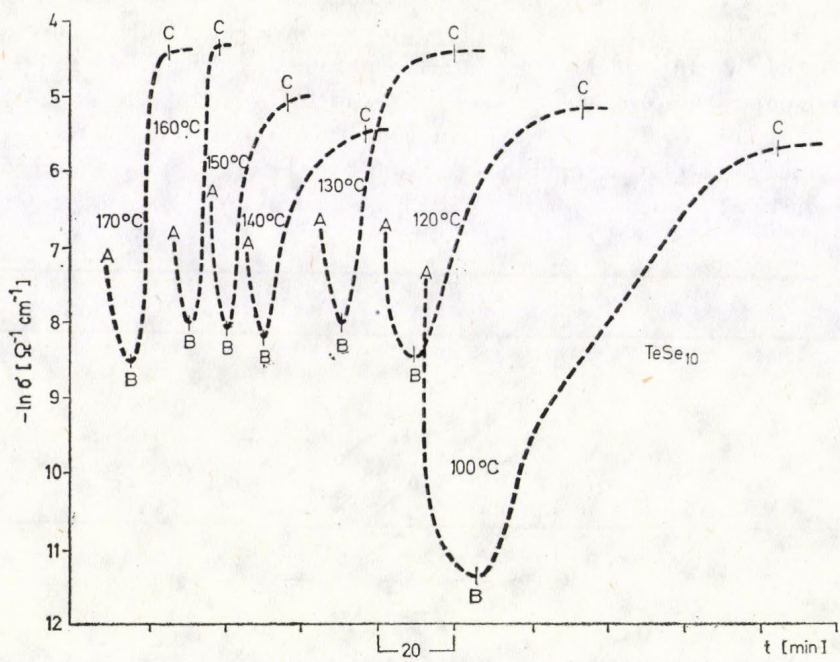

Fig. 2b

at each annealing temperature. The first causes a gradual decrease of the conductivity σ due to the normal cooling of the liquid sample from 300 °C (path AB). This process terminates when the temperature of the sample drops to the temperature of the oven (point B). The second process could be identified with the structural ordering occurring during the isothermal heat treatment and, as a consequence, the growth of the new phase in the supercooled liquid matrix (path BC). X-ray analysis has proved that the crystallization process in the supercooled samples does not start before the point B [13].

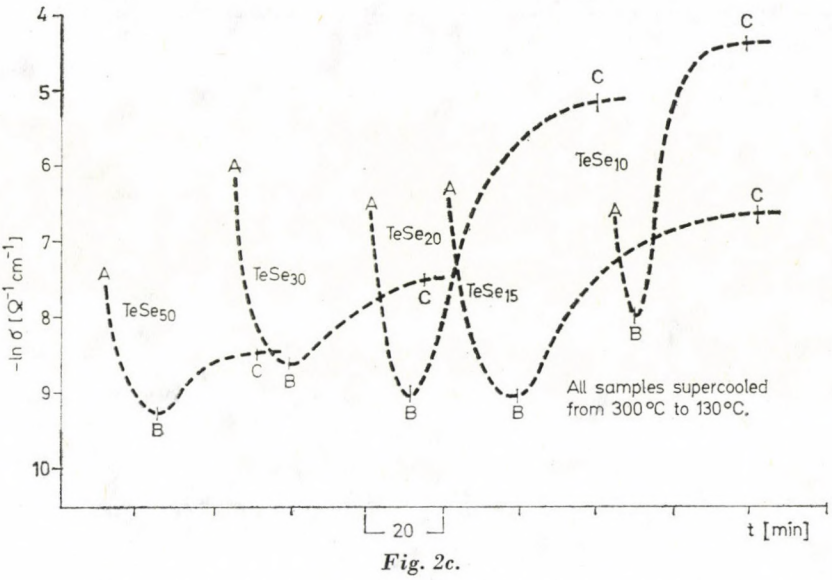

Fig. 2c.

Fig. 2. Time-dependence of electrical conductivity during the liquid-crystalline transformations of (a) $TeSe_{50}$, (b) $TeSe_{10}$ and (c) for different compositions crystallized at 130 °C

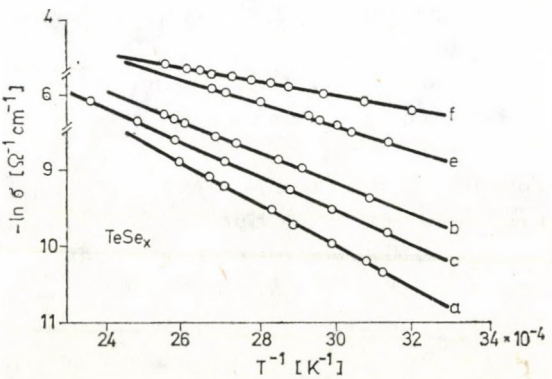

Fig. 3. Temperature-dependence of electrical conductivity of $TeSe_x$ alloys as-crystallized at 130 °C; $x = 50$ (a), 30 (b), 20 (c), 10 (e), 5 (f)

In the case of $TeSe_{50}$, the time τ necessary for the completion of the transition process decreases with decreasing $\Delta T = T_1 - T_c$ (the difference between the liquid temperatures and that at which the growth takes place) up to $\Delta T = 190$ °C, and then increases. For $TeSe_{10}$, τ decreases with ΔT up to 140 °C and then increases. The general behaviour of the function $\sigma = f(t)$ during the

Table II

Duration of the two processes AB and BC (Fig. 2) in $l-c$ transformations of $TeSe_x$ at different temperatures of crystallization

Temp. (°C)	Time (min)									
	$TeSe_{50}$		$TeSe_{30}$		$TeSe_{20}$		$TeSe_{15}$		$TeSe_{10}$	
	AB	BC	AB	BC	AB	BC	AB	BC	AB	BC
90	30	50	20	45						
100	30	46	15	44	18	62			15	65
110	15	18								
120	20	20	28	42	10	58			8	44
130	15	25	15	35	9	50	18	60	5	30
140	15	35	10	30	6	42	22	34	5	26
150			7	16	5	7	7	24	4	16
160	10	60			7	11	5	20	4	8
170							8	17	6	10
180			36	22	15	13	13	15		

liquid—crystalline transition in the other investigated compositions is similar to those shown in Figs. 2. However, a simple time-dependence of ΔT as a result of the increase of Te-content in the $TeSe_x$ investigated alloys was not detected. Table II gives this dependence during the individual processes AB and BC of the transitions.

A plot of the function $\ln \sigma = f(1/T)$ for samples crystallized at different conditions, where the conductivity measurements were carried out after attaining the stabilization period of each transition (path AC), gave a straight line relationship. For the composition of $TeSe_{30}$, the obtained lines were parallel and correspond to $E_\sigma = 0.9 \pm 0.05$ eV. But, this is not exactly the case which was found for the other Se—Te compositions investigated. Fig. 3 shows $\ln \sigma$ versus $1/T$ for different Se—Te alloys where the measurements are carried out on samples crystallized at 130 °C. The corresponding values of E_σ and $\ln \sigma_{20}$ are given in Table I. It shows that σ_{20}, the conductivity at 20 °C as obtained from extrapolation of plots of Fig. 3, varies over five orders of magnitude for the compositional range studied, 2—17 at % Te.

IV. Discussion

IV.1. Temperature-dependence of conductivity

As stated earlier, the plots of $\ln \sigma$ versus $1/T$ may be represented by a straight line over the whole of the temperature range investigated. It follows the activated relation:

$$\sigma = \sigma_0 \operatorname{Exp}(-E_\sigma/2\, K_B\, T),$$

where K_B is the Boltzmann constant, T is the Kelvin temperature, σ_0 is temperature-independent, and E_σ may be temperature-dependent. Such a behaviour has been found in a large number of amorphous materials (solid and liquid) and resembles that found in intrinsic semiconducting crystals. It should, however, not be concluded from the intrinsic-like behaviour in the considered amorphous liquid alloys and in other amorphous materials that amorphous materials are intrinsic. In intrinsic crystalline semiconductors all electrons in the conduction band come from the valence band so that $n = p$. In amorphous semiconductors $n \neq p$ because of the much larger number of electrons and holes in localized tail states and gap states, see e.g. FRITZSCHE [14]. However, published values of σ_0, derived from experimental data, often lie in the range of 10^3—10^4 $\mathrm{Ohm^{-1}\,cm^{-1}}$. It has been argued that conduction takes place due to carriers excited beyond the mobility shoulders into non-localized states. Exceptions with lower values of σ_0 ($\sim 10^{-2}$ $\mathrm{Ohm^{-1}\,cm^{-1}}$) had been found (see e.g. ALLGAIER [15] and BHAT et al [16]). This attributed to a wide range of localized states at the valence band edge. In Table I, σ_0 shows a dependence on composition in a certain manner. This refers to a presence of different electronic features between the alloys. The low values of σ_0 for at % Te $\lesssim 5$ compositions indicate that the low density of the electron state nay be localized in the quasi-gap. The degree of localization is affected by the addition of Te and at about 17 at % Te ($TeSe_5$), $\sigma_0 \simeq 10^4$ $\mathrm{Ohm^{-1}\,cm^{-1}}$.

ABDINOV et al [17] have studied the electrical conductivity and thermo emf of the system Se—Te in the liquid state. These authors reported that the addition of Te to Se dissociates the long Se chains and this dissociation begins immediately after melting. The compositional dependence of E_σ (liquid) in the present study is in agreement with that of ABDINOV et al [17]. At low Te-content in the Se—Te alloy, being distributed uniformly over the Se chains, the Te atoms facilitate their dissociation. This leads to the observed decrease of E_σ (liquid) upto about 5 at % Te ($TeSe_{20}$). In the composition range of Te $\simeq 5$—17 at %, the molecular size of the liquid system Se—Te decreases so markedly that their dissociation energy becomes dependent on the molecular weight and therefore E_σ increases with the Te-content. In other words, it is due to the decrease of the molecular weight of the chains in this region of concentration.

IV.2. Time-dependence of conductivity

In the function plots of $\sigma = f(t)$ in Figs. 2, the process path BC proceeds smoothly and covers a relatively large increase of σ (2—4 orders of magnitude) and indicates subsequent growth of a new phase until complete transition of the supercooled sample volume is attained. This increase of σ is associated with the possibility of binding the nuclei during the growth of the new phase and finally producing non-isolated crystallites extended through the crystallized sample. To study the kinetics of this liquid—crystalline (or disorder—order) transition of $TeSe_x$ alloys, an AVRAMI equation [18] in the form:

$$\alpha(t) = 1 - \mathrm{Exp}\,(-Kt^n)$$

is applied. In this equation $\alpha(t)$ is the fraction transformed in time t, K is a temperature-dependent rate constant and defines the crystallization rate, and n is an exponent which need not be an integer [19, 20]. The two kinetic parameters K and n have been calculated using the authors' previous procedure described elsewhere [12].

The calculated values of $\ln \ln [1/(1-\alpha)]$ were plotted versus $\ln (t)$ for all compositions at the different supercoolings. Such a function is shown in Fig. 4 for the composition of $TeSe_{30}$, which represents a series of straight lines each of which corresponds to a certain temperature. Values of the kinetic parameter n, as calculated from the line slopes of $\ln \ln [1/(1-\alpha)]$ versus $\ln (t)$, are given in Table III at the different temperatures of crystallization. The drastic changes of n indicate that different crystallization geometry is dominant in various ranges of temperature. However, the approximate constant value of

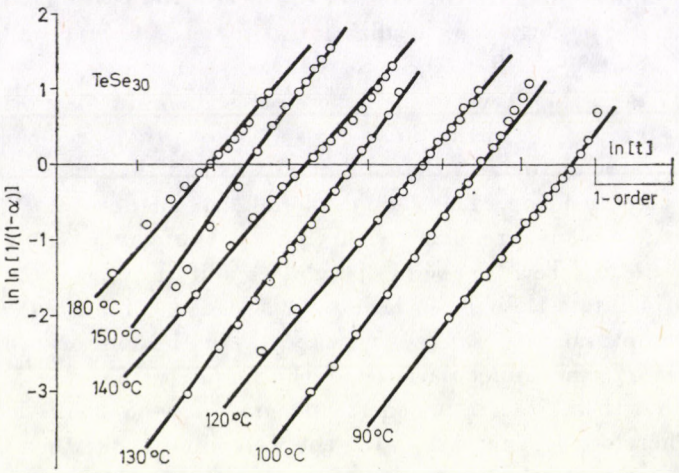

Fig. 4. AVRAMI plots of the crystallization of the supercooled matrix of $TeSe_{30}$ at different isotherms

$n = 1.3 \pm 0.1$ for the compositions of $TeSe_{30}$ and $TeSe_{15}$ refers to unique growth geometry.

The rate constant K is given the by Arrhenius equation as: $K = K_0 \text{ Exp } (-E/RT)$, where K_0 is the constant and R is the gas constant. For each

Table III

Values of the AVRAMI kinetic parameter n calculated at different temperatures of crystallization

Temp. (°C)	n				
	$TeSe_{50}$	$TeSe_{30}$	$TeSe_{20}$	$TeSe_{15}$	$TeSe_{10}$
90	1.7	1.3			
100	2.0	1.3	1.5		1.3
110	2.1				
120	2.0	1.3	1.8		1.3
130	1.9	1.4	1.4	1.3	1.4
140	1.6	1.2	1.1	1.2	1.2
150		1.45	3.2	1.2	1.2
160	1.6		2.8	1.3	3.4
170				1.4	2.7
180		1.3	2.5	1.4	

Table IV

Crystallization activation energy of the supercooled $TeSe_x$ liquid alloys

Sample	E (eV)	Range of (°C) temperature
$TeSe_{50}$	0.76	90—130
$TeSe_{30}$	0.37	90—180
$TeSe_{20}$	0.50	100—150
$TeSe_{15}$	0.60	130—160
$TeSe_{10}$	0.70	100—150

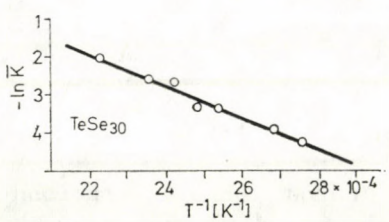

Fig. 5. Dependence of ln K on reciprocal of absolute temperature T for the composition of $TeSe_{30}$

$TeSe_x$ composition, a plot of $\ln K = f(1/T)$ could be fitted over a certain temperature range, with a straight line whose slope defines the activation energy of the process E. Here, the average values of K over the range of $\alpha \simeq 10\%$—90% are considered. Fig. 5 shows the plot of $\ln K$ versus $1/T$ for the composi-

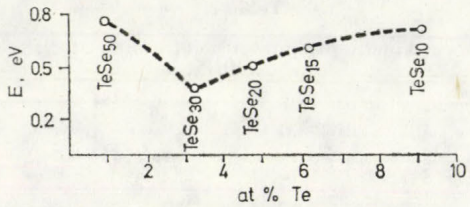

Fig. 6. Crystallization activation energy as a function of atomic percent tellurium in the Se-Te compositions

tion of $TeSe_{30}$. The solid line is a least square fit to the experimental points. Table IV gives the calculated values of E with their corresponding valid ranges of temperature. It shows that the crystallization activation energy of the supercooled $TeSe_x$ alloys decreases from 0.76 eV for the composition of $TeSe_{50}$ to 0.37 eV for $TeSe_{30}$, and then E increases with the Te concentration up to 0.7 eV for the rich Te composition $TeSe_{10}$, (Fig. 6).

V. Conclusion

In conclusion, the following points can be mentioned:

1) In liquid state, the variation behaviour of σ_0 with the amount of Te content is accompanied by different electronic features among the Se—Te materials. On the other hand, the concentration of Te atoms and consequently the molecular weight of the liquid Se—Te mixtures greatly affects the facilitation of the dissociation energy as appeared from the change of E_σ.

2) The non-systematic variation of the AVRAMI kinetic parameter n with the supercooling (Table III) for the compositions of $TeSe_{50}$, $TeSe_{20}$ and $TeSe_{10}$ seems to be a temperature-dependent function. This gives evidence for different growth geometry in different temperature ranges. The constant value of $n = 1.3 \pm 0.1$ for the compositions of $TeSe_{30}$ and $TeSe_{15}$ indicates unique growth geometry. The latter is not a purely one-dimensional process.

3) The calculated activation energies for the crystallization in supercooled $TeSe_x$ samples are significantly less than those for amorphous-crystalline transformations determined from electrical conductivity data [21, 22] and from other techniques (e.g. DTA, [23]). In the amorphous-crystalline transformation of $TeSe_x$ for the present composition range, E has been found to

be >2 eV. This is likely to be due to the difference in viscosities of the supercooled liquid and of the vitreous state. Such a decrease might make the diffusion, self-diffusion, and switching of the chemical bonds easier.

Acknowledgement

One of us (M.F.K.) would like to thank Professor ABDUS SALAM, the Internati ona Centre for Theoretical Physics, Trieste, for hospitality.

REFERENCES

1. E. GRISON, J. Chem. Phys., **19**, 1109, 1951.
2. P. M. HANSEN and K. ANDERKO, Construction of Binary Alloys, 2nd Edition, McGraw-Hill, New York, 1958, pp. 1188—1189.
3. M. F. KOTKATA, E. A. MAHMOUD and M. K. EL-MOUSLY, Acta Phys. Hung., **50**, 61, 1981.
4. H. GOBRECHT, D. GAWLIK and E. MAHJURI, Phys. Condens. Mater., **13**, 156, 1971.
5. M. CUTLER, Phil. Mag., **33**, 559, 1976.
6. G. TOURAND, B. CABANE and M. BREUIL, J. Non-Cryst. Solids, **8—10**, 676, 1972.
7. G. TOURAND, J. Phys. (France), **34**, 937, 1973.
8. W. HOYER, E. THOMAS and M. WOBST, Z. Naturforsch., **30**a, 1633, 1975.
9. M. MISAWA and K. SUZUKI, Trans. JIM., **18**, 427, 1977.
10. R. BELLISSENT and G. TOURAND, J. Non-Cryst. Solids, **36**, 1221, 1980.
11. M. YAO, M. MISONOU, K. TAMURA, K. ISHIDA and J. ENDO, J. Phys., Soc. (Japan) **48**, 109, 1980.
12. M. K. EL-MOUSLY, M. F. KOTKATA and S. A. SALAM, J. Phys. C., **11**, 1077, 1978.
13. M. F. KOTKATA, E. A. MAHMOUD and M. K. EL-MOUSLY, to be published.
14. H. FRITZSCHE, Amorphous and Liquid Semiconductors, Ed. J. Tauc, Plenum Press, London, 1974, Chap. 5.
15. R. S. ALLGAIR, J. Vac. Sci. Technol., **8**, 113, 1971.
16. P. K. BHAT, K. L. BHATIA and S. C. KATYAL, J. Non-Cryst. Solids, **27**, 399, 1978.
17. D. SH. ABDINOV, V. R. NAMAZOV and G. M. ALIEV, Inorgan. Mater., **10**, 1960, 1974.
18. M. AVRAMI, J. Chem. Phys., **8**, 212, 1940.
19. U. R. EVANS, Trans. Faraday Soc., **41**, 365, 1945.
20. N. HAY, Br. Polym. J., **3**, 74, 1971.
21. L. N. SUVOROVA and E. V. SHKOLNIKOV, Inorgan. Mater., **12**, 610, 1976.
22. M. K. EL-MOUSLY and M. M. EL-ZAIDIA, J. Non-Cryst. Solids, **27**, 265, 1978.
23. M. F. KOTKATA and E. A. MAHMOUD, Mat. Sci. and Engng., **54**, 165, 1982.

Acta Physica Academiae Scientiarum Hungaricae, 52 (1), pp. 15—18 (1982)

THE ELECTRONIC PRESSURE IN DENSE PLASMAS

A. E. Pozwolski
UNIVERSITY OF PARIS, 75020 PARIS, FRANCE*

(Received 12. V. 1981)

A thermodynamic calculation of the electronic pressure in a dense plasma is given. Approximations involved by the use of the Debye length are avoided, so the above theory remains valid even if the Debye length is smaller than the interionic distance.

I. Introduction

The Coulomb interaction between charged particles lowers the pressure and it was shown that for electrons such pressure can even become negative [1]. For strongly correlated electrons ($e^2 n^{1/3} > kT$, n: electronic density) the correlation function oscillates as in liquids [2] and even crystallization appears possible at low temperature.

Recently, the author has shown [3] that at moderate density the ionic pressure is strongly reduced. For low density but high ionization number the possibility of self confinement [4] was shown assuming an electron—ion interaction on the basis of a Yukawa potential, implying

$$e^2 n^{1/3}/kT \ll 1 . \tag{1}$$

Now such restriction will be removed, in order to find the pressure for plasmas where the Debye length is comparable or even smaller than the interionic distance.

II. Equilibrium of a dense plasma

When the inequality defined by Eq. (1) is reversed the Coulomb energy becomes larger than the average translational kinetic energy and then a quasi lattice structure of the plasma is to be expected, as was shown by Cook [5]. Spectroscopic observation of dense plasmas is in good agreement with such structure [6].

So a completely ionized plasma (ion charge number Z) is considered; the interionic distance is $d = n_i^{-1/3} = Z^{-1/3} n^{-1/3}$. Now, ions are assumed to be evenly distributed in planes with a reticular density $1/d^2$, the spacing of the

* Address: 4 et 6 rue de la Plaine, 75020 Paris, France

planes being d. The superficial charge density is Ze/d^2 and each plane is surrounded by two electron sheath of thickness $d/2$. The origin 0 for distance x is taken in the middle of two adjacent reticular planes and the potential V between these planes checks:

$$\begin{aligned} &dV/dx = 0 \quad \text{for} \quad x = 0\,; \qquad dV/dx = 2\pi\,\bar{n}ed \quad \text{for} \quad x = d/2\,, \\ &V = 0 \qquad \text{for} \quad x = 0\,; \qquad V = V_0 \qquad\quad \text{for} \quad x = d/2\,; \end{aligned} \tag{2}$$

Furthermore it is assumed that the electronic density n (average value $\bar{n}$) follows Boltzmann equation $n = n_0 \exp(eV/kT)$ where n_0 is the value of n when $x = 0$. For convenience the following parameters are introduced: $E_T = kT/e = T/11{,}600$ the electron volt equivalent of temperature, $u = V/E_T$, the reduced potential, and the characteristic lengths h and H defined by $h^2 = kT/4\pi n_0 e^2$, $H^2 = kT/4\pi\bar{n}e^2$.

Combining Poisson and Boltzmann relations the following equation results

$$d^2u/dx^2 = \exp(u)/h^2\,, \tag{3}$$

In view of the last remark in the introduction any series development of the exponential term is now precluded. Eq. (3) integrates to

$$du/dx = (2^{1/2}/h)(\exp u - 1)^{1/2} \tag{4}$$

after using conditions (2).

Integrating again it is found that the potential changes according to

$$\mathrm{tg}^{-1}(\exp u - 1)^{1/2} = x/2^{1/2}h\,. \tag{5}$$

Since $u = u_0$ for $x = d/2$:

$$\exp u_0 - 1 = h^2 d^2/8H^4 \tag{6}$$

and

$$\mathrm{tg}\, d/2 \times 2^{1/2}h = dh/2 \times 2^{1/2} H^2. \tag{7}$$

Solving this equation gives h and the reduced potential drop is:

$$u_0 = \mathrm{Log}\,(1 + h^2 d^2/8H^4)\,. \tag{8}$$

Relationship between the densities n_0 and $\bar{n}$

$$\bar{n} = 2/d \int_0^{d/2} n_0 \exp(u)\; dx = 2/d \int_0^{u_0} n_0 \exp(u)/(du/dx)\, du =$$

$$= 2^{d/2}\, n_0\, h/d \int_0^{u_0} \exp(u)/(\exp u - 1)^{1/2}\; du = 2^{3/2}\, n_0\, h/d(\exp u_0 - 1)^{1/2}.$$

Using Eq. (6) it is found that $\bar{n} = n_0\, h^2/H^2$.

Potential energy of the electrons

The energy per unit area of the two sheath surrounding a reticular plane is given by

$$dW = -2n\,dx\,eu\,E_T \text{ so } W = -2eE_T \int_0^{d/2} nu\,dx\,.$$

Using Eq. (5) with $n = n_0 \exp(u)$ the equation for energy becomes

$$W = 2n_0\,eE_T \int_0^{d/2} \frac{\text{Log } \cos^2 x/2^{1/2}h}{\cos^2 x/2^{1/2}h}\,dx\,.$$

Let $t = \text{tg}\, x/2^{1/2}h$, then

$$W = -2^{3/2}\,eE_T\,n_0\,h \int_0^{hd/2^{3/2}H^2} \text{Log}\,(1 + t^2)\,dt$$

which it is easy to integrate by part, the result is

$$W = -\bar{n}kTd\,[u_0 - 2(1 - H^2/h^2)]\,. \tag{9}$$

III. Derivation of the pressure and critical ionization number for self confinement

For a plasma volume v including N electrons ($\bar{n} = N/v$) the potential energy can be rewritten, making* the further approximation $h \simeq H$, and using Eq. (8)

$$U = -NkT\,\text{Log}\,(1 + d^2/8H^2)$$

or

$$U = -NkT\,\text{Log}\,(1 + \pi d^2 e^2 N/2kTv)\,. \tag{10}$$

It is useful to introduce the parameter $\beta = 1/kT$ so the free energy is

$$F = \beta^{-1} \int U d\beta = -\beta^{-1} \int (N/\beta)\,\text{Log}\,(1 + \pi d^2 e^2 N\beta/2v)\,d\beta\,. \tag{11}$$

Now the pressure due to the electron—ion interaction is

$$p_1 = -\partial F/\partial v = N\beta^{-1} \int \frac{\partial}{\partial v}\,[\text{Log}\,(1 + \pi d^2 e^2 N\beta/2v)]\,d\beta =$$

$$= -\frac{\pi d^2 e^2 N^2}{2\beta v^2} \int \left(1 + \frac{\pi d^2 e^2 N}{2v}\beta\right)^{-1} d\beta = -\frac{N}{v\beta}\,\log\left(1 + \frac{\pi d^2 e^2 N\beta}{2v}\right),$$

* Dropping the $(1 - H^2/h^2)$ term in Eq. (9) is not restrictive since $H^2/h^2 = n_0/\bar{n}$ and so is independent of β and v; its contribution to the free energy disappears by differentiation.

which can be rewritten as

$$p_1 = -\bar{n}kT \operatorname{Log}(1 + \pi d^2 e^2 \bar{n}/2kT) . \tag{12}$$

Adding the kinetic pressure of the free non interacting electron gas, the total pressure is found to be:

$$p = \bar{n}\, kT\, [1 - \operatorname{Log}(1 + \pi d^2 e^2 \bar{n}/2kT)] . \tag{13}$$

The total presssure vanishes and the plasma is self contained when the logarithmic term is equal to unity so:

$$\pi d^2 e^2 \bar{n}/2kT = \epsilon - 1 \qquad (\epsilon = 2.71) . \tag{14}$$

Noting that $\bar{n}d^2 = Z/d$ it is found that the critical ionization number Z_c is

$$Z_c = 2(\epsilon - 1)kTd/\pi e^2 = 653\, Td , \tag{15}$$

where T is in K and d in cm.

It is interesting to note that considering the interaction of charges according a Yukawa potential, DRUMMOND [7] found:

$$Z_c = 350\, Td.$$

As an example take $n_i = 5 \times 10^{22}$ cm^{-3}, $d = 0.27$ nm, $H = 0.08$ nm, then for $Z = 16$ self confinement is possible according to (15), if the temperature does not exceed 0.91×10^6 K.

REFERENCES

1. R. ABE, Progr. Theor. Phys., **22**, 213, 1959.
2. J. H. MALMBERG and T. M. O'NEIL, Phys. Rev. Lett., **39**, 1333, 1977.
3. A. E. POZWOLSKI, The Ionic Pressure in Dense Plasmas, International Conf. on Statistical Phys., Budapest, Aug. 25—29, p. 212, 1975.
4. A. E. POZWOLSKI, Acta Phys. Hung., **41**, 29, 1976.
5. MELVIN A. COOK, The Science of High Explosives, Reinhold, p. 420, 1968.
6. N. V. JHERMOKHIN, B. M. KOVALIOV, P. P. KULIK, V. A. RIYABI and I. S. SOKOLOWSKY, 9th International Conf. on Phen. in Ion. Gases, Sept. 1—6, Bucarest, 410, 1968.
7. J. E. DRUMMOND, Editor, Power Conversion Technology, P.O. Box 2607, La Jolla, CA 92038, USA, private communication, 1975.

Acta Physica Academiae Scientiarum Hungaricae, 52 (1), pp. 19–23 (1982)

BAND INTENSITY PARAMETERS AND GROUND STATE DISSOCIATION ENERGY OF CS RADICAL

M. RAMJEE, M. L. P. RAO, D. V. K. RAO and P. T. RAO
DEPARTMENT OF PHYSICS, ANDHRA UNIVERSITY, WALTAIR — 530 003, INDIA

(Received 15. VI. 1981)

The band intensity parameters, the Franck—Condon factors and *r*-centroids have been evaluated for the $a^3\Pi - X^1\Sigma^+$ system of the astrophysically important CS radical. The ground state dissociation energy has been estimated by fitting the Hulbert—Hirschfelder potential curve to the true potential curve.

1. Introduction

Accurate knowledge of Franck—Condon factors, *r*-centroids and dissociation energies is of great importance in astrophysics and in the study of chemical physics. It has been pointed out [1] that an uncertainty of 0.3 eV in the dissociation energy leads to an uncertainty by a factor of two in the molecular solar abundance and a still higher factor for cooler stars. As the bands of CS radical are observed in interstellar spectra [2], it is thought worthwhile to calculate the Franck—Condon factors, *r*-centroids for the $a^3\Pi - X^1\Sigma^+$ system of CS radical and its ground state dissociation energy. The band intensity parameters are evalutaed using "TRAPRB" program of JARMAIN [3] and the ground state dissociation energy has been estimated by fitting the HUBERT—HIRSCHFELDER [4] potential energy curve to the true potential curve using the data of TALL [5] and COSSART et al [6].

2. r-centroids and Franck—Condon factors

Band strength factors without vibration—rotation interaction are given by

$$P_{v',v''} = |\int \psi_{v'} R_e(r) \psi_{v''} dr|^2 \ldots \quad (1)$$

where $\psi_{v'}$ and $\psi_{v''}$ are the vibrational wave functions of upper and lower states and $R_e(r)$ is the electronic transition moment. The *r*-centroid ($\bar{r}_{v',v''}$) approximation used in the analysis of intensity measurements of band spectra, allows a separation of band strength into a pure vibratioanl term (the FCf, $q_{v',v''}$) and an electronic term (the electronic transition moment). Hence $P_{v',v''}$ can be

Table I

$q_{v',v''}$ and $r_{v',v''}$ for a-X system of CS

v' \ v''	0	1	2	3	4
0	0.825	0.158	0.015	0.001	0.000
	1.556	1.652	1.735	1.811	1.884
1	0.157	0.528	0.267	0.043	0.004
	1.469	1.564	1.661	1.742	1.817
2	0.016	0.262	0.301	0.328	0.051
	1.375	1.482	1.571	1.669	1.750
3	0.001	0.046	0.317	0.142	0.346
	1.265	1.390	1.493	1.577	1.678
4	0.000	0.005	0.085	0.328	0.046
	1.134	1.286	1.406	1.505	1.586

1st row: $q_{v',v''}$
2nd row: $r_{v',v''}$

written as

$$P_{v',v''} = R_e^2\,(\bar{r}_{v',v''})\;|\int \psi_{v'}\psi_{v''}\,dr\,|^2 = R_e^2(\bar{r}_{v'.v''})\;q_{v',v''}\,, \tag{2}$$

where r-centroid $(\bar{r}_{v',v''})$ is defined as the average internuclear separation of a $v' - v''$ transition and is given by

$$\bar{r}_{v',v''} = \int \psi_{v'}\, r\psi_{v''}\,dr / \int \psi_{v'}\psi_{v''}\,dr\,. \tag{3}$$

The r-centroids and Franck—Condon factors for a — X system of CS radical have been calculated using the program of "TRAPRB" of JARMAIN and the results are presented in Table I. From the magnitude of FCf's it can be concluded that a narrow Condon parabola is expected in consistency with the experimental observation.

The sequence differences in r-centroids have been found to be constant in accordance with the observation of NICHOLLS and JARMAIN [7]. The value of $\bar{r}_{0,0}$ is slightly greater than $(r_{e1} + r_{e2})/2$ value, suggesting that the potentials are not very anharmonic.

3. Dissociation energy

The ground state dissociation energy of CS radical has been evaluated by fitting the H—H function to the true potential (RKRV) curve. HULBERT and HIRSCHFELDER modified the three parameter Morse function by introducing

Table II
Potential energy curves of $X^1\Sigma^+$ state of CS

r nm	U_{RKRV} 10^{-19} J	U_{HH} 10^{-19} J	$100\frac{(U_{RKRV}-U_{HH})}{D_e}$
0.1483	0.1273	1.1272	0.00
0.1593	0.1273	0.1274	0.00
0.1448	0.3799	0.3797	0.00
0.1639	0.3799	0.3801	0.00
0.1421	0.6300	0.6295	0.00
0.1674	0.6300	0.6303	0.00
0.1408	0.8775	0.8766	0.00
0.1703	0.8775	0.8779	0.00
0.1394	1.1224	1.1209	0.01
0.1729	1.1224	1.1229	0.00
0.1382	1.3648	1.3624	0.01
0.1754	1.3648	1.3653	0.00
0.1371	1.6046	1.6011	0.02
0.1777	1.6046	1.6050	0.00
0.1361	1.8418	1.8369	0.04
0.1800	1.8418	1.8421	0.00
0.1352	2.0764	2.0699	0.05
0.1821	2.0764	2.0766	0.00
0.1344	2.3084	2.3000	0.07
0.1842	2.3084	2.3083	0.00
0.1337	2.5379	2.5273	0.08
0.1863	2.5379	2.5374	0.00
0.1330	2.7648	2.7516	0.11
0.1883	2.7648	2.7637	0.00
0.1323	2.9891	2.9731	0.13
0.1903	2.9891	2.9873	0.01
0.1317	3.2108	3.1917	0.16
0.1922	3.2108	3.2082	0.02
0.1311	3.4300	3.4075	0.19
0.1941	3.4300	3.4262	0.03

two additional spectroscopic constants $\omega_e x_e$ and α_e. The H—H function is then given by

$$U(r) = D_e\big((1 - \exp(-x))^2 + cx^3(1 + x)\exp\big(-(3 - b)x\big)\big) \qquad (4)$$

where

$$x = \frac{\omega_e}{2(B_e D_e)^{1/2}} \frac{r - r_e}{r_e} . \qquad (5)$$

Table III

Ground state dissociation energy values of CS radical

Method	D_0 10^{-19} J
Photoionization of CS_2 [11]	11.86 ± 0.05
$O + CS \rightarrow CO + S$ [12]	$\leqslant 12.16$
$CS_2 + S \rightleftarrows CS + S_2$ [13]	11.55 ± 0.16
By mass spectroscopy	
$CS(A'^1\Sigma^+ - X^1\Sigma^+)$ [7]	11.78 ± 0.02
High resolution spectroscopy	
Fluorescence from CS_2 [14]	11.84 ± 0.05
Photodissociation	
GAYDON [15]	12.16
Present study	11.82

The constants b and c are determined by the relations

$$c = 1 + a_1 (D_e/a_0)^{1/2}, \tag{6}$$

$$b = 2 - (7/12 - D_e a_2/a_0)/c, \tag{7}$$

where a_0, a_1 and a_2 are DUNHAM [8] coefficients given by

$$a_0 = \frac{\omega_e^2}{4B_e}, \quad a_1 = -1 + \frac{\omega_e \alpha_e}{6 B_e^2}$$

and

$$a_2 = \frac{5 a_1^2}{4} - \frac{2\omega_e x_e}{3B_e}.$$

By using the RKR method as modified by VANDERSLICE et al [9] the turning points corresponding to each vibrational level have been computed. The U values corresponding to $r_{\min}$ and $r_{\max}$ are evaluated for all vibrational levels at different values of D_e from Eq. (4) and the average percentage deviation $(100(U_{RKRV} - U_{HH})/D_e)$ has been evaluated. The particular value of D_e corresponding to minimum percentage deviation is regarded as the true dissociation energy. The values obtained for RKRV turning point and the HH potential energy values obtained for the estimated D_e value are shown in Table II. It can be seen from Table II that the average discrepancy between

the potential curve as evlauated by RKRV method and H—H method is only 0.04 percent of D_e throughout the useful range of f values. This small value for the average percentage deviation for all r values shows that this empirical function is a quite suitable one for this molecule [10].

The value of D_e which is measured from the minimum of the curve is slightly greater than the true dissociation energy measured from the lowest vibrational level. The value D_0^0 ($11.82\ 10^{-19}$ J) is calculated in order to make a comparison with the existing values by using the equation

$$D_e = D_0^0 + \frac{1}{2}\omega_e - \frac{1}{4}\omega_e x_e \,.$$

The values of D_0^0 for the ground state of CS radical as reported by various investigators are given for comparison with the present value in Table III. The present value is in good agreement with those obtained from fluorescence, high resolution spectroscopy and photoionization methods. Since this empirical H—H potential is quite a suitable one for this molecule the present value of D_0^0 cited above is claimed as a sufficiently accurate value for the dissociation energy of the ground state of CS radical.

Acknowledgements

The authors are thankful to Prof. W. R. JARMAIN for sending the TRAPRB and to the UGC and CSIR (New Delhi) for financial assistance.

REFERENCES

1. N. GREVESSE and A. J. SAUVAL, Proc. 21st Astrophys. Colloq. Liège, Belgium Paper II, 1, 1977.
2. T. TAM, Astrophys. J. **202**, L83, 1975.
3. W. R. JARMAIN, J. Quant. Spectrosc. Radiat. Transfer., **11**, 421, 1971.
4. H. M. HULBERT and J. O. HIRSCHFELDER, J. Chem. Phys., **9**, 61, 1941.
5. N. TALL, J. Mol. Spectrosc., **74**, 190, 1979.
6. D. COSSART, M. HORANI and J. ROSTAR, J Mol. Spectrosc., **67**, 283, 1977.
7. W. R. NICHOLLS and W. R. JARMAIN, Proc. Phys. Soc., **69A**, 253, 1956.
8. J. L. DUNHAM, Phys. Rev., **41**, 713 and 721, 1932.
9. J. T. VANDERSLICE, E. A. MAISON, W. G. MAISCH and E. R. LIPPINCOTT, J. Mol. Spectrosc., **3**, 17, 1969.
10. D. STEELE, E. R. LIPPINCOTT and J. T. VANDERSLICE, Rev. Mod. Phys., **34**, 239, 1962.
11. V. H. DIBELER and J. A. WALKER, J. Opt. Soc. Amer., **57**, 1007, 1967.
12. G. HANCOCK, C. MORLEY and I. W. W. SMITH, Chem. Phys. Letters., **12**, 193, 1971.
13. D. L. HILDERBRAND, Chem. Phys. Letters., **15**, 379, 1977.
14. H. OKABE, J. Chem. Phys., **56**, 4381, 1972.
15. A. G. GAYDON, Dissociation Energies and Spectra of Diatomic Molecules, Chapman and Hall Ltd., London, 1953.

Acta Physica Academiae Scientiarum Hungaricae, 52 (1), pp. 25—30 (1982)

POTENTIAL ENERGY CURVES AND DISSOCIATION ENERGY OF DIATOMIC ALUMINIUM MOLECULE

P. SAMBASIVA RAO* and T. V. RAMAKRISHNA RAO**

SPECTROSCOPIC LABORATORIES, PHYSICS DEPARTMENT
S.V.U.A. POST-GRADUATE CENTRE, ANANTAPUR-515003, INDIA

* PHYSICS DEPARTMENT, J. N. TECHNOLOGICAL UNIVERSITY
COLLEGE OF ENGINEERING, ANANTAPUR-515002, INDIA

** INSTITUT DES SCIENCES EXACTES
UNIVERSITE DE CONSTANTINE, CONSTANTINE, ALGERIA

(Received 9. VII. 1981)

The experimental potential energy curves for $X^3\Sigma_g^-$ and $A^3\Sigma_u^-$ states of the diatomic aluminium molecule have been constructed by the RYDBERG—KLEIN—REES method. The dissociation energy for the ground state of the molecule has been estimated to be 1.42 $\pm$ $\pm$ 0.11 eV by the method of curve fitting using the electronegativity potential function of SZŐKE and BAITZ. The estimated value of D_0 is in good agreement with the thermochemical value of 1.55 eV recommended by HUBER and HERZBERG.

Introduction

The construction of experimental potential energy curves for atomic interactions is of fundamental importance in chemical physics for the understanding of various physical problems arising in astrophysics, gas kinetics and molecular spectra. Also a knowledge of the exact values of the dissociation energies (D_0) of the diatomic molecules is necessary in thermochemistry. The D_0 of the diatomic aluminium molecule has been estimated by various investigators [1—4] by different methods. But the values reported show disagreement with one another. Also no attempt had been made so far to evaluate theoretically the D_0 of the Al_2 molecule. As such the present work is undertaken to estimate D_0 from the experimental potential energy curve for the ground state of the Al_2 molecule. The molecular constants required for the present work have been taken from HUBER and HERZBERG [4].

Potential energy curves

The wide spread applicability of the knowledge of the potential energy curves has resulted in a very extensive program of obtaining reliable potential energy curves for different electronic states of the diatomic molecules. One of

Table I

RKR turning points
for the $X^3\Sigma_g^-$ state of Al_2

v	U (cm^{-1})	$U + T_e$ (cm^{-1})	r_{min} (nm)	r_{max} (nm)
	$T_e = 0$		$r_e = 0.2466$	
0	174.5	174.5	0.2386	0.2555
1	520.4	520.4	0.2331	0.2626
2	862.2	862.2	0.2295	0.2677
3	1199.8	1199.8	0.2266	0.2721
4	1533.1	1533.1	0.2243	0.2761
5	1862.1	1862.1	0.2222	0.2798
6	2186.8	2186.8	0.2204	0.2833
7	2506.9	2506.9	0.2187	0.2866
8	2822.5	2822.5	0.2171	0.2898
9	3133.6	3133.6	0.2157	0.2929
10	3440.0	3440.0	0.2144	0.2959
11	3741.7	3741.7	0.2131	0.2989
12	4038.7	4038.7	0.2119	0.3018
13	4330.8	4330.8	0.2108	0.3046
14	4618.0	4618.0	0.2097	0.3074
15	4900.3	4900.3	0.2087	0.3102
16	5177.5	5177.5	0.2077	0.3130
17	5449.7	5449.7	0.2067	0.3157
18	5716.7	5716.7	0.2058	0.3184

the most widely employed and reliable procedure is to make use of the observed energy levels to obtain the classical turning points by a procedure first developed by RYDBERG [5] and KLEIN [6]. Their graphical procedure was changed into an analytical procedure by REES [7]. VANDERSLICE et al [8] had also made a valuable contribution on the use of the RYDBERG—KLEIN method [5, 6].

The experimental potential energy curves for $X^3\Sigma_g^-$ and $A^3\Sigma_u^-$ states of Al_2 molecule have been constructed using the RYDBERG—KLEIN—REES (RKR) method [7] which is in reality a Wentzel—Kramers—Brillouin procedure where one starts with the known energy levels and finds out the classical turning points. As the details of the method [7] have been thoroughly discussed in literature [5—8] only the results of the present work are given in Table I and Table II.

Table II

RKR turning points
for the $A^3\Sigma_u^-$ state of Al_2

v	U (cm^{-1})	$U + T_e$ (cm^{-1})	r_{min} (nm)	r_{max} (nm)
	$T_e = 17269.4$		$r_e = 0.2560$	
0	139.2	17408.6	0.2470	0.2659
1	416.3	17685.7	0.2409	0.2738
2	691.6	17961.0	0.2370	0.2796
3	965.2	18234.6	0.2340	0.2845
4	1236.8	18506.2	0.2315	0.2889
5	1506.5	18775.9	0.2294	0.2930
6	1774.2	19043.6	0.2275	0.2968
7	2039.9	19309.3	0.2258	0.3004
8	2303.4	19572.8	0.2243	0.3039
9	2564.7	19834.1	0.2229	0.3073
10	2823.7	20093.1	0.2216	0.3105
11	3080.5	20349.9	0.2204	0.3137
12	3334.8	20604.2	0.2193	0.3167
13	3586.8	20856.2	0.2183	0.3197
14	3836.2	21105.6	0.2173	0.3227
15	4083.0	21352.4	0.2164	0.3256

Dissociation energy

An accurate estimation of the dissociation energy (D_e) requires an empirical potential function which gives the best reproduction of the experimental potential energy (RKRV) curve. Various attempts to get such empirical functions have been reported in the literature. A critical evaluation of the more important of these functions was given by STEELE et al [9] and they have shown that the potential function of HULBURT and HIRSCHFELDER [10] and the LIPPINCOTT potential function [11] fit well with the RKRV curves of a large number of diatomic molecules. In the present investigation, the electronegativity potential function proposed by SZŐKE and BAITZ [12] has been used to estimate D_0 of Al_2.

The proposed function is of the form:

$$U(r) = D_e\left[1 - \exp\left(-\frac{\gamma \Delta r^2}{2r}\right)\right] \times$$

$$\times\left[1 - a\left(\frac{b^2\gamma}{2r}\right)^{1/2} \Delta r \exp\left\{-\left(\frac{b^2\gamma}{2r_e}\right)^{1/2} \Delta r\right\}\right],$$

where $\gamma = de/D_e^{1/2}$. d is obtained from the expression $k_e = d(e_1 e_2 D_e)^{1/2} r_e^{-1}$, b is considered a constant ($\sim$1.065) and $a = 0.35\sqrt{e}$ where $e = (e_1 e_2)^{1/2}$, e_1 and e_2 being the electronegativities of the atoms constituting the molecules. This potential function has been found to give quite a good fit to the experimental potential curve as measured by $(U - U_{\mathrm{RKRV}})/D_e$ throughout the useful range of r values. It has been observed by SINGH et al [13] that the average error is only 1 to 2%.

The turning points of the ground state of Al_2 are used in the SZŐKE and BAITZ potential function and for a particular value of D_e the observed energy values of U are compared with the calculated energy values $[U(r)]$. This procedure is repeated for different values of D_e and the D_e value (1.44 eV) for which the best fit of the energy values $[U(r)]$ is observed is taken as the dissociation energy (D_e) of the molecule.

Results and discussion

The turning points obtained for nineteen vibrational levels of the ground state and sixteen vibrational levels of the excited state of Al_2 molecule are presented in Table I and Table II.

It is obvious from Table III that the best fitting of the energy values is achieved for $D_e = 1.44$ eV since the average percentage deviation in this case is minimum. Hence the dissociation energy for the ground state of Al_2 is 1.44 ± 0.11 eV and the value as measured from the lowest vibrational level is $D_0 = 1.42 \pm 0.11$ eV. This estimated value is in good agreement with the value of 1.55 eV recommended by HUBER and HERZBERG [4]. The other values of D_0 determined by various investigators are given in Table IV for comparison purpose.

In the estimation of D_e, it is observed that the HULBURT and HIRSCHFELDER function is not very sensitive to the variation in the value of D_e. Whereas, in the case of the LIPPINCOTT function the average deviation for the best fit of the calculated energy values, at $D_0 = 1.99$ eV, is about 4.5%. The considerable divergence of the D_0 values observed in the present study supports the view of STEELE et al [9] expressed in their review article that no single function is best fit for all molecular states considered, nor can we predict a suitable function which will give an ideal potential for a restricted range of r. The same kind of divergence in the values of dissociaton energies for various molecules determined by different methods has been noticed also by LAKSHMAN and RAMANAIAH [14].

Table III

Estimation of dissociation energy of Al_2
Comparison of the observed and calculated energy values

r (nm)	U (cm^{-1})	$D_e = 1.50$ eV		$D_e = 1.44$ eV		$D_e = 1.37$ eV	
		$U(r)$ (cm^{-1})	% deviation	$U(r)$ (cm^{-1})	% deviation	$U(r)$ (cm^{-1})	% deviation
0.2386	174.5	172.1	1.35	172.3	1.25	172.5	1.14
0.2555	174.5	176.7	1.28	176.5	1.15	176.3	1.01
0.2295	862.2	860.3	0.22	862.2	0.00	864.2	0.23
0.2677	862.2	872.9	1.24	870.0	0.90	866.9	0.54
0.2243	1533.1	1541.9	0.57	1546.1	0.85	1550.6	1.14
0.2761	1533.1	1555.9	1.49	1548.3	0.99	1540.2	0.46
0.2204	2186.8	2217.6	1.41	2224.5	1.73	2224.0	1.70
0.2833	2186.8	2223.1	1.66	2209.1	1.02	2194.0	0.33
0.2171	2822.5	2887.8	2.31	2897.6	2.66	2907.9	3.03
0.2898	2822.5	2872.0	1.75	2850.0	0.96	2826.0	0.12
0.2144	3440.0	3553.4	3.30	3566.2	3.67	3579.7	4.06
0.2959	3440.0	3500.0	1.74	3468.0	0.81	3433.7	0.18
0.2119	4038.7	4214.6	4.36	4230.5	4.75	4247.5	5.17
0.3018	4038.7	4104.8	1.64	4061.5	0.56	4015.3	0.58
0.2097	4618.0	4871.9	5.50	4890.8	5.91	4911.0	6.34
0.3074	4618.0	4684.7	1.44	4628.6	0.23	4568.9	1.06
0.2077	5177.5	5525.6	6.72	5547.6	7.15	5571.1	7.60
0.3130	5177.5	5237.8	1.16	5167.6	0.19	5093.0	1.63
0.2058	5716.7	6175.6	8.03	6200.8	8.47	6227.5	8.94
0.3184	5716.7	5762.7	0.81	5677.4	0.69	5586.7	2.27
		Average	2.40		2.20		2.38

Table IV

Estimated values of D_0 of Al_2

Author and method	D_0 (eV)
Linear Birge-Sponer extrapolation	1.88
Graphical Birge-Sponer extrapolation	1.50 ± 0.20
CHUPKA et al [1] (Mass Spectrometric)	2.00 ± 0.40
STEARNS and KOHL [2] (Knudsen Cell)	1.55 ± 0.15
GAYDON [3]	1.60 ± 0.30
HUBER and HERZBERG [4]	1.55
Present authors (SZŐKE and BAITZ)	1.42 ± 0.11
Present authors (LIPPINCOTT)	1.99

Acknowledgements

The authors wish to express their thanks to Professors S. V. J. LAKSHMAN and S. V. SUBRAHMANYAM for their interest in the present work

REFERENCES

1. W. A. CHUPKA, J. BERKOWITZ, C. F. GIESE and M. G. INGHRAM, J. Phys. Chem., **62**, 611, 1958.
2. C. A. STEARNS and F. J. KOHL, High Temp. Sci., **5**, 113, 1973.
3. A. G. GAYDON, Dissociation Energies and Spectra of Diatomic Molecules, Chapman and Hall Ltd., London, 1968.
4. K. P. HUBER and G. HERZBERG, Molecular Spectra and Molecular Structure. IV. Constants of Diatomic Molecules, Van Nostrand Reinhold Co., New York, 1979.
5. R. RYDBERG, Z. Phys., **73**, 376, 1931; ibid. **80**, 514, 1933.
6. O. KLEIN, Z. Phys., **76**, 226, 1932.
7. A. G. L. REES, Proc. Phys. Soc., **59**, 998, 1947.
8. J. T. VANDERSLICE, E. A. MASAN, W. G. MAISCH and E. R. LIPPINCOTT, J. Mol. Spectrosc., **3**, 17, 1959; ibid. **5**, 83, 1960.
9. D. STEELE, E. R. LIPPINCOTT and J. T. VANDERSLICE, Rev. Mod. Phys., **34**, 239, 1962.
10. H. M. HULBURT and J. O. HIRSCHFELDER, J. Chem. Phys., **9**, 61, 1941; ibid. **35**, 1901, 1961.
11. D. STEELE and E. R. LIPPINCOTT, J. Chem. Phys., **35**, 2065, 1961.
12. S. SZÖKE and E. BAITZ, Can. J. Phys., **46**, 2563, 1968.
13. J. SINGH, K. P. R. NAIR and D. K. RAI, J. Mol. Structure, **5**, 492, 1970.
14. S. V. J. LAKSHMAN and N. VENKATARAMANAIAH, Curr. Sci., **49**, 579, 1980.

Acta Physica Academiae Scientiarum Hungaricae, 52 (1), pp. 31—37 (1982)

THERMAL EXPANSION COEFFICIENT OF IONIC CRYSTALS — AN INTERATOMIC POTENTIAL APPROACH*

S. P. SRIVASTAVA
INDIAN INSTITUTE OF PETROLEUM, DEHRADUN-248005, INDIA

(Received 9. VII. 1981)

Considering contributions of the cubic and other higher order anharmonic terms in the potential energy function, a new equation for the thermal expansion coefficient, α, for ionic solids has been derived. It has been shown that all the equations derived by earlier workers are either one or the other special case of this equation. The present equation has been applied to some face-centred cubic, body-centred cubic and zinc-blende structure types of ionic crystals to compute the values of α on the basis of Born—Mayer interaction potential function and on comparison with the experimental values of α a satisfactory agreement has been found.

Introduction

A number of attempts have been made to correlate the thermal expansion of solids with other properties such as melting point, specific heat and coordination number [1]. SMYTH [2] derived an equation correlating the thermal expansion coefficient, α, and vibration characteristics of vitreous silica. Following him, KUMAR [3] derived an approximate thermodynamic equation for nonmetallic crystals following the interaction potential approach and tested this equation by calculating the values of α in case of alkali halide and other ionic crystals on the basis of a simple inverse power law for the repulsive term in the interaction potential representation [4]. These equations for α have recently been tested by BOWMAN [5] in his studies on isotopic lithium hydride crystals and have been shown to be applicable only approximately.

In what follows in the present investigation, we have rederived SMYTH's [2] equation for α by taking into account the cubic and other higher-order anharmonicity terms of the potential energy function. Using this equation the values of α in cases of a few ionic crystals belonging to the face-centred cubic, body-centred cubic and the zinc-blende structures have been calculated. The results have been compared with those obtained experimentally and discussed.

* The work was done at the Indian Institute of Technology, Kanpur, India.

Equation for α

The Helmholtz free energy of a solid system consists of two parts: the first representing the potential energy of a non-vibrating lattice and the second owing its origin to the presence of thermal vibrations. The determinations of both parts require a knowledge of the configuration of interacting particles, the law of force and the vibrational spectrum. For a mole of a crystal the free energy, F, is given by the expression

$$F = N\psi - NkT \log Z \,, \tag{1}$$

where N is the Avogadro's number, ψ is the potential energy function of the static lattice including the zero-point vibrational energy, k is the Boltzmann constant and T is the absolute temperature. $kT \log Z$ is the contribution of the lattice vibrations to the free energy in which Z is the partition function, which by considering the potential energy function as [6]

$$V = \frac{p^2}{2m} + ar^2 + br^3 + cr^4 + dr^5 + \ldots \,, \tag{2}$$

(where p is the momentum and m is the mass of the vibrating atom, r is the displacement from the equilibrium position and a, b, c, d, etc. are the coefficients determined by the shape of the interatomic potential) and following WILSON [6] can be derived as

$$Z = \frac{2\pi}{h}(m/a)^{1/2}\, kT \left(1 - \frac{3}{4}\,\frac{ckT}{a^2} + \frac{15}{16}\,\frac{b^2}{a^3}\,kT\right) \tag{3}$$

in which h is Planck's constant. The higher-order terms in Eq. (3) have been neglected since b/a and c/a are small.

Thus, the temperature dependent term $kT \log Z$ includes the contributions of cubic and other higher-order anharmonic terms of the potential energy function.

The coefficient of linear thermal expansion is defined as

$$\alpha = \left(\frac{1}{r_0}\right) \frac{\partial(\Delta r)}{\partial T} \,, \tag{4}$$

where r_0 is the value of r at equilibrium and Δr is the change in r due to thermal expansion. Following SMYTH [2], as the main contribution is due to the frequency term, we have

$$\Delta r = B/2a \,, \tag{5}$$

where

$$B = \frac{d}{dr}(kT \log Z) \,. \tag{6}$$

On the basis of Eq. (3), the Eq. (6) can be written as

$$B = \frac{\left(-\frac{kT}{2a}\frac{da}{dr}\right)\left[1-\frac{35}{4}\frac{c}{a^2}kT+\frac{105}{16}\frac{b^2}{a^3}kT+\frac{5}{2}\frac{d}{ab}kT\right]}{\left[1-\frac{3}{4}\frac{c}{a^2}kT+\frac{15}{16}\frac{b^2}{a^3}kT\right]}. \tag{7}$$

Hence

$$\alpha = \left(\frac{1}{2ar_0}\right)\left(\frac{\partial B}{\partial T}\right). \tag{8}$$

Since $\left(\frac{\partial B}{\partial T}\right)$ can be obtained from Eq. (7), after neglecting terms containing k^2T^3 and other higher-orders, as

$$\left(\frac{\partial B}{\partial T}\right) = \left(-\frac{k}{2a}\frac{da}{dr}\right)\left[1-16\frac{c}{a^2}kT+\frac{45}{4}\frac{b^2}{a^3}kT+\frac{5d}{ab}kT\right] \tag{9}$$

the equation for the thermal expansion coefficient, α, can be finally derived as

$$\alpha = \left[-\frac{C_v}{2r_0}\frac{3b}{2a^2}\right]-\left(\frac{1}{r_0}\right)\frac{6k^2T}{(2a)^5}\left[225\,b^3-348\,abc+120\,a^2d\right]. \tag{10}$$

In Eq. (10) C_v is the specific heat at constant volume which at high temperature can be evaluated from the equation

$$C_v = 6k\left[1+\left(\frac{15}{8}\frac{b^2}{a^3}-\frac{3}{2}\frac{c}{a^2}\right)kT\right], \tag{11}$$

which includes the anharmonic contributions.

The Eq. (11) in conjunction with Eq. (10) may thus be expected to explain the variation of α at high temperatures, particularly above the Debye temperature of solids.

Eq. (10) is thus an improvement over the equations of α derived by SMYTH [2] and KUMAR [3] in that its second term on the right hand side contains contributions due to cubic and higher-order terms of anharmonicity of the potential energy function, which were neglected in these earlier treatments.

On neglecting terms involving higher-order derivatives like $\left(\frac{dc}{dr}\right)_{r=r_e}$, $\left(\frac{db}{dr}\right)_{r=r_e}$ etc while deriving Eq. (7), we obtain our earlier derived equation [7] for α.

Table I

Calculated values of $\alpha(10^{-6}/\text{deg})$ of some ionic crystals at room temperature belonging to face-centred cubic, body-centred cubic and zinc-blende structures

Crystal	α_{qh}	α_{anh}	$\alpha_{\text{calc.}}$ (Eq. 10)	$^{*}\alpha_{\text{exptl.}}$
1	2	3	4	5
Face-centred cubic				
LiF	29.98	0.47	30.45	34.0
LiCl	39.38	0.59	39.97	44.0
LiBr	45.05	0.69	45.74	50.0
LiI	52.07	0.78	52.85	59.0
NaF	37.14	0.49	37.63	36.0
NaCl	40.12	0.76	50.48	40.0
NaBr	43.44	0.80	44.24	43.0
NaI	45.19	0.94	46.13	48.3
KCl	42.14	0.87	43.01	38.3
KBr	47.86	0.94	48.80	40.0
KI	51.10	1.10	52.20	45.0
RbCl	47.27	0.92	48.19	36.0
RbBr	48.69	1.04	49.73	38.0
RbI	49.31	1.17	50.48	43.0
MgO	7.86	0.54	8.40	10.2 [13]
CaO	10.55	0.62	11.17	12.5
SrO	11.15	0.42	11.57	13.72
CuBr	21.23	0.67	21.90	20.7
Body-centred cubic				
CsCl	47.33	1.09	48.42	56.0
CsBr	49.46	1.19	50.65	47.51
CsI	52.88	1.36	54.24	47.54
TlCl	49.25	1.87	51.12	56.0
NH_4Cl	47.89	0.96	48.85	47.3 [14]
NH_4Br	48.30	1.07	49.37	53.9 [14]
Zinc-blende structure				
CuCl	20.26	0.58	20.84	21.8 [14]
ZnS	6.92	0.05	6.97	6.3
SiC	4.67	0.02	4.69	4.0—4.3

* $\alpha_{\text{exptl.}}$, where the references are not cited, are taken from the compilation of KUMAR [3].

Applications to ionic crystals

Using the quantum-mechanically favoured exponential form of the interatomic potential due to BORN and MAYER [4] viz.,

$$\psi = -\frac{AZ'e^2}{r} + \lambda \exp(-r/\varrho), \tag{12}$$

where A is Madelung's constant, Z' is the valency, e is the electronic charge and λ and ϱ are the potential parameters, in conjunction with Eq. (10) and using the experimental values of C_v [3, 8, 9] the values of α of a few ionic solids belonging to face-centred cubic, body-centred cubic and zinc-blende structures including alkali, ammonium, copper and thallium halides, metal oxides, zinc-sulfide and silicon carbide have been calculated at room temperature and are reported in Table I. In this Table α_{qh} is the contribution due to the first term at the right hand side of Eq. (10) and is representing the contribution under the quasi-harmonic approximation. α_{anh} is the contribution due to the cubic and other higher-order terms of the potential energy function representing the second-term of Eq. (10). The potential parameter λ and ϱ for these solids have been calculated by following the usual procedure [7, 10] to compute the values of the coefficients a, b, c and d.

Discussion of the results

On a comparison of the calculated and experimental values of α in Table I, it can be seen that for almost all the three structures, the Eq. (10) for α yields satisfactory results. It can be noted that the contributions due to the anharmonicity terms of Eq. (10) are quite substantial even at room temperature. A careful analysis of Table I suggests that these anharmonic contributions appear to be dependent upon stability, the nature of the ions and the reduced mass of the crystal.

However, on a close observation, it can be noted that there is larger deviation of the theoretical values of α from their experimental counterpart in cases of rubidium and cesium halides. There are many possible explanations for this discrepancy. Firstly, the interionic potential adopted is only an approximate one where contributions of dipole—dipole and dipole—quadrupole interactions between the ion pairs have been neglected to avoid mathematical complexities. It has been shown in a number of investigations [11] that these contributions are substantial in many cases including rubidium and cesium

Table II

Values of $\alpha(10^{-6}/\text{deg})$ for KCl crystal at high temperatures on the basis of Eq. (10)

°C	α_{qh}		α_{anh}	$\alpha_{\text{calc. (Eq. 10)}}$		$\alpha_{\text{exptl [12]}}$
	C_v [12] (exptl)	C_v (Eq. 11)		C_v (exptl)	C_v (Eq. 11)	
300	43.30	44.41	1.66	44.96	46.07	44.44
350	43.50	44.79	1.81	45.31	46.60	46.14
400	43.55	45.15	1.94	45.49	47.09	47.82
450	43.73	46.00	2.10	45.83	48.10	49.49
500	44.05	46.86	2.24	46.29	49.10	51.14

halides. Another reason for this discrepancy might be the inaccuracy in the experimental C_v values which are quite old and since then no redetermination has been made. A third reason, though of minor consequence, is that a contribution beyond nearest neighbours has not been considered in Eq. (12).

Our Eq. (10) for the thermal expansion coefficient α has been derived under the classical oscillator model approximation and as such is expected to be more applicable at high temperatures, particularly above the Debye temperature of solids. From Table I it can be seen that for many solids this is not the case. A better picture of the behaviour of Eq. (10) for explaining the temperature-dependence of α at high temperatures can be obtained from Table II, where we have computed the values of α at different temperatures above the Debye temperature for KCl crystal [12]. From this Table it can be seen that the agreement between the calculated and experimental values [12] of α is satisfactory particularly between those values which have been obtained using Eq. (11) for C_v.

For alkali halides and some metal oxides, the values of α have also been calculated by KUMAR [3]. He derived his equation for α under the quasi-harmonic approximation, by considering only the quadratic term of Eq. (2) and allowing this term to depend upon volume, in conjunction with the inverse power law for the repulsive force representation in the potential energy function. He has also made some arbitrary modifications in the final form of his equation to account for the polarizability of ions, the contributions due to dipole—dipole and dipole—quadrupole interactions, etc. However, these modifications did not have any theoretical justification and the use of C_p values in place of C_v as has been done by KUMAR [3] must yield high values for α. This has been perhaps compensated by choosing the inverse power law for the repulsive forces which has invariably been found to be inferior in comparison to the BORN—MAYER exponential function [11].

Conclusions

The present investigation thus presents a clearer picture on the study of α for ionic solids in which anharmonic effects have been explicity considered and all the limitations and arbitrary modifications of earlier workers [2, 3] are removed. The present equation for α is quite general and can be used with any form of the interatomic potential.

On the basis of the present equation, the study of the temperature-dependence of α is also possible in conjunction with Eq. (11) for C_v, which has hitherto been a major limitation of the equations developed by earlier workers [2, 3] and the results obtained in the case of KCl crystal clearly demonstrated its applicability.

REFERENCES

1. F. A. HUMMEL, J. Amer. Ceram. Soc., **33,** 102, 1950; J.R. PARTINGTON, An Advance Treatise on Physical Chemistry, Vol. 3, Longman and Green Co. Ltd., London, 1952; J. B. AUSTIN, J. Amer. Ceram. Soc., **35,** 243, 1952.
2. H. T. AMYTH, J. Amer. Ceram. Soc., **38,** 140, 1955.
3. S. KUMAR, Central Glass Ceram. Res. Inst. Bull. Calcutta, **7,** 58, 1960; Proc. Nat. Inst. Sci. India, **25A,** 364, 1959.
4. S. P. SRIVASTAVA, S. KUMAR and M. P. MADAN, Indian J. Phys., **41,** 833, 1967; S. P. SRIVASTAVA and M. P. MADAN, J. Phys. Soc. Japan, **23,** 1433, 1967; S. P. SRIVASTAVA, Phys. Status Solidi (b) **50,** k 123, 1973; J. N. PLENDL, S. S. MITRA and P. J. GIELISSEE, Phys. Status Solidi, (b), **12,** 367, 1965.
5. R. C. BOWMAN, Jr., Phys. Chem. Solids, **34,** 1754, 1973.
6. A. H. WILSON, Thermodynamics and Statistical Mechanics, Univ. Press, Cambridge, 1957.
7. S. P. SRIVASTAVA and R. S. SARASWAT, J. Phys. Chem. Solids, **36,** 351, 1975.
8. W. E. BLEICK, J. Chem. Phys., **2,** 160, 1934.
9. J. E. MAYER, J. Chem. Phys., **1,** 330, 1933; J. E. MAYER and B. B. LEVY, J. Chem. Phys., **1,** 647, 1933.
10. S. P. SRIVASTAVA and K. C. LAL, Zeit. f. physik. Chemie, New Folge, **91,** 153, 1974; S. P. SRIVASTAVA and K. C. LAL, J. Phys. Soc. Japan, **28,** 525, 1970.
11. S. P. SRIVASTAVA, S. KUMAR and M. P. MADAN, Indian J. Phys., **41,** 833, 1967; M. L. HUGGINS and J. E. MAYER, J. Chem. Phys., **5,** 143, 1937; G. C. BENSON and E. DEMPSEY, Proc. Roy. Soc., **A266,** 344, 1962.
12. S. HART, Brit. J. Appl. Phys. (J. Phys. D) **1,** 1285, 1968; F. D. ENCK, Phys. Rev., **119,** 1977, 1960.
13. "American Institute of Physics Handbook" (McGraw Hill Book Co. Inc., N. Y.) 4—73, 1963.
14. J. E. MAYER, J. Chem. Phys., **1,** 330, 1933; W. E. BLEICK, J. Chem. Phys., **2,** 160, 1934; J. E. MAYER and B. B. LEVY, J. Chem. Phys., **1,** 647, 1933.

Acta Physica Academiae Scientiarum Hungaricae, 52 (1), pp. 39—46 (1982)

SIMPLIFIED FORMS OF THE FIELEK MODEL FOR bcc TRANSITION METALS

R. N. KHANNA* and R. P. S. RATHORE
DEPARTMENT OF PHYSICS, R.B.S. COLLEGE, AGRA-282 003, INDIA

(Received in revised form 17. VII. 1981)

Two simple forms of the FIELEK [1] model are developed to infer about the nature of the interactions among neighbouring *d*-shells, characterising the transition metals. The first model expresses this interaction as the sum of first two terms of the Taylor's expansion for energy, while the second model describes this interaction to be three body (angular or unpaired) type. Both of these models obey the equilibrium condition and represent core-core interactions to be central pairwise extending to immediate neighbours only. Volume interactions among core and conduction electrons and also among *d*-shells and conduction electrons follow the modified BHATIA Scheme [5].

The theoretical findings given by these models on phonon dispersion in bcc zirconium and niobium are compared with the experimental data. Further these findings are also compared with those of the original FIELEK model which is simplified by substituting the said BHATIA scheme for that due to KREBS [3].

Introduction

Passage of thermal wave through lattice causes changes in coupling energy of the various constituents of a transition metal. According to FIELEK [1] this change is expressed as a sum of the second order changes in the potential energy coupling the constituents. First order changes, which are responsible for inequality [2] between the statical and dynamical elastic constants, are completely ignored while developing the FIELEK model. Moreover, this omission leaves the crystal in a state of inequilibrium. The FIELEK model [1] assumes the second order changes in the coupling energy of the system comprising core and conduction electrons to be negligibly small. This drawback poses difficulties regarding the cohesion and the stability of the lattice. Further the FIELEK Model [1] describes the volume interactions among *d*-shells and conduction electrons on the lines of KREBS scheme [3] which (a) depicts the perfectly free picture of the electron gas, (b) does not include the condition for crystal equilibrium and (c) involves enormous computational efforts.

Presently we have developed two different models. The first model expresses the core—core and the *d* shell — *d* shell interactions separately as the

* Department of Physics, R.E.I. College, Dayalbagh, Agra-5, India.

sum of first and second term of the respective Taylor's expansions. In our second model the core—core interactions remain the same but the mutual interactions among the *d*-shells are considered to be unpaired and described within the framework of the angular scheme due to CLARK et al [4].

The effect of core—*d* shell energy in both models is considered on the lines of the FIELEK model. The volume interactions are included on the lines of BHATIA [5] scheme which is modified (a) to incorporate the crystal anisotropy by using an inference factor G^2 which distributes the total force over the polyhedron-shaped atomic cell as a whole and (b) to account for the exchange and correlation effects associated with the conduction electrons by employing a proper dielectric function ($\mathbf{q}$). Equilibrium conditions for both models are derived in a physically consistent and simple manner. The FIELEK model is thus made physically sound and computationally less intricate as far as the description of the equilibrium condition [6] and the volume interactions are concerned.

The two models are employed to derive the dispersion relations in bcc zirconium and niobium. To show the relative merits of the model, the results on phonon dispersion are compared (a) with the experimental data on the said metals and (b) with the theoretical findings of the original Fielek model, which is simplified by using the said BHATIA scheme to take care of the volume interactions.

Theory

The frequencies (ν) of the normal modes are obtained by solving the following secular determinant

$$| D(\mathbf{q}) - 4\pi^2 m\nu^2 I | = 0 , \tag{1}$$

where m is the mass of the core and I is the unit matrix of the order three. The elements of the dynamical matrix $D(\mathbf{q})$ may be written in terms of the first (α_1) and the second (β_1) derivatives of the central pairwise energy coupling the immediate neighbours, i.e.

$$\begin{aligned} D_{\alpha\alpha}(\mathbf{q}) &= -\frac{8}{3}(\beta_1 + 2\alpha_1)(1 - C_\alpha C_\beta C_\gamma) + K + AG_{\alpha\alpha}(\mathbf{q}) + \frac{K^2}{N} , \\ D_{\alpha\beta}(\mathbf{q}) &= -\frac{8}{3}(\beta_1 - \alpha_1)\, S_\alpha S_\beta C_\gamma , \end{aligned} \tag{2}$$

where $S_\alpha = \sin(1/2\, aq_\alpha)$, and $C_\alpha = \cos(1/2\, aq_\alpha)$, a is the lattice constant and q_α is the α-component of the phonon wave vector ($\mathbf{q}$). K is a parameter appearing due to the interaction among the cores and the *d*-shells. The term N is evaluated

from the determinant

$$| D'(\mathbf{q}) - NI | = 0 , \tag{3}$$

where the elements of $D'(\mathbf{q})$ in our first model may be written in terms of the first (α_1) and the second (β_1) derivatives of the pairwise energy coupling the immediate neighbours, i.e.

$$\begin{aligned} D'_{\alpha\alpha}(\mathbf{q}) &= \frac{8}{3}(\beta'_1 + 2\alpha'_1)(1 - C_\alpha C_\beta C_\gamma) + K - A' G_{\alpha\alpha}(\mathbf{q}) , \\ D'_{\alpha\beta}(\mathbf{q}) &= \frac{8}{3}(\beta'_1 - \alpha'_1) S_\alpha S_\beta C_\gamma . \end{aligned} \tag{4}$$

For the second model, we have

$$\begin{aligned} D'_{\alpha\alpha}(\mathbf{q}) &= 16\gamma_1(1 - C_\alpha C_\beta C_\gamma) - 2\gamma_1(4C_{2\alpha} - C_{2\beta} - C_{2\gamma} - 2) + K - A' G_{\alpha\alpha}(\mathbf{q}), \\ D'_{\alpha\beta}(\mathbf{q}) &= -8\gamma_1 S_\alpha S_\beta C_\gamma , \end{aligned} \tag{5}$$

where $C_{2\alpha} = \cos(aq_\alpha)$ and γ_1 is the angular force constant for the immediate neighbours. The parameters A and A' appearing in Eqs. (2) and (4) are the deformation parameters associated with perturbation of volume energy associated with the conduction electrons due to the displacement of cores and d-shells, respectively. The term $G_{\alpha\alpha}(\mathbf{q})$ may be expressed on the lines of the BHATIA scheme, i.e.

$$G_{\alpha\alpha}(\mathbf{q}) = \frac{q_\alpha^2 \, \Omega g^2 (q r_s)}{a + \dfrac{aq^2}{K_C^2 \, \epsilon(\mathbf{q})}} , \tag{6}$$

where Ω is the atomic volume, g^2 is the inference factor and r_s is the inter-electronic separation. K_C, the screening parameter, is evaluated in the BOHM—PINES [7] limit. The factor g^2 is evaluated by the more realistic expressions first given by BARDEEN [8] and recently reported by RAMAMURTHY [9]. These expressions, account (a) for the crystal anisotropy and (b) for the Umklapp-process to some extent as is evident from the studies of TOYA [10] and DAYAL and SRIVASTAVA [11]. The dielectric function $(\mathbf{q})$ may be written as

$$\epsilon(\mathbf{q}) = \epsilon_H(\mathbf{q}) [1 - S(\mathbf{q})] . \tag{7}$$

where $\epsilon_H(\mathbf{q})$ is the usual Hartree function and the correction term $S(\mathbf{q})$, arising out of the exchange and correlation effects of the conduction electrons, may be written within the frame of the recent scheme due to SINGWI et al [12], i.e.

$$S(\mathbf{q}) = A_1 \left[1 - \exp\left(\frac{-B_1 q^2}{K_F^2} \right) \right] . \tag{8}$$

where K_F is the Fermi wave vector and the constants A_1 and B_1 are taken from [12] quoted above.

For considering the equilibrium of the whole lattice its energy (V) can be written as

$$V = V_{cc} + V_{dd} + V_{ce}\left(\frac{1}{\epsilon(\mathbf{q})} - 1\right) + V_{de}\left(\frac{1}{\epsilon(\mathbf{q})} - 1\right), \tag{9}$$

where V_{cc} and V_{dd} are the mutual coupling energies for the cores and d-shells, respectively. V_{ce} and V_{de} are the interaction energies for the system comprising (a) cores and conduction electrons and (b) d-shells and conduction electrons, respectively. For the equilibrium $\frac{\partial V}{\partial \Omega}$ should vanish, i.e.

$$\frac{\partial}{\partial \Omega}(V_{cc} + V_{dd}) = -\frac{\partial}{\partial \Omega}(V_{ce} + V_{de})\left(\frac{1}{\epsilon(\mathbf{q})} - 1\right). \tag{10}$$

Assuming $\epsilon(\mathbf{q})$ independent of volume, we have for our first model

$$\alpha_1 + \alpha_1' = -\frac{a}{2}(P_e + p_d)\left(\frac{1}{\epsilon(\mathbf{q})} - 1\right) \tag{11}$$

and for the second model,

$$\alpha_1 = -\frac{a}{2}(P_e + P_d)\left(\frac{1}{\epsilon(\mathbf{q})} - 1\right), \tag{12}$$

where P_e and P_d are the pressures associated with the conduction and the d-shell electrons. Moreover

$$A = -a\Omega\frac{\partial P_e}{\partial \Omega}. \tag{13}$$

The value of P_e and A are evaluated considering the usual volume-dependent energies, i.e. Fermi, exchange and correlation ones associated with the conduction electrons. The scheme due to WIGNER and SEITZ [13] is employed to obtain the correlation part of the energy. The quantitative values of P_e and A are taken from [14] which duly explain cohesion and stability of the lattice. The obscure nature of V_{de} and the transitions (inter and intra band) make it impossible to evaluate the quantitative contribution of V_{de} in the equilibrium conditions given by Eqs. (11) and (12).

Calculations

Our first model comprises seven parameters, i.e. α_1, β_1, α_1', β_1', K, A and A'. Two of these parameters are calculated by the help of the Eqs. (11) and (13). Three of the model parameters are obtained by the knowledge of the elastic constants. The remaining two parameters are obtained in terms of the zone boundary frequencies ν_T [$\zeta 00$] and ν_{T_1} [$\zeta\zeta 0$] for which the required relations may be written as

$$\delta\pi^2 m\nu_T^2[\zeta 00] = -\frac{16}{3}(\beta_1 + 2\alpha_1) - K + \frac{K^2}{K + \frac{16}{3}(\beta_1' + 2\alpha_1')} \times$$
$$\times 4\pi^2 m\nu_{T_1}^2[\zeta\zeta 0] = -8\alpha_1 - K + \frac{K^2}{K + 8\alpha_1'}. \tag{14}$$

The six model parameters, α_1, β_1, γ_1, K, A and A_2, appearing in our second model are evaluated by employing Eqs. (12) and (13), three elastic relations and the following expression for the zone boundary frequency

$$4\pi^2 m\nu_T^2[\zeta 00] = -\frac{16}{3}(\beta_1 + 2\alpha_1) - K + \frac{K^2}{K + 32\gamma_1}. \tag{15}$$

Results and discussion

The input data for the bcc zirconium and niobium are shown in Table I. Table II lists the calculated model parameters for the said metals. The theoretical dispersion curves, given by the models reported are depicted in Figs. 1 and 2 for zirconium and niobium, respectively. These curves are compared

Table I

Input data for bcc zirconium and niobium

Input data	bcc zirconium	Ref.	Niobium	Ref.
C_{11}	0.783		2.46	
C_{12}	0.503 $\}$ 10^{11} Pa	[17]	1.34 $\}$ 10^{11} Pa	[18]
C_{44}	0.29		0.287	
a	3.64×10^{-10} m		3.300×10^{-10} m	
ν_{T_1} [SOO]	4.69 $\}$ 10^{12} Hz	[15]	6.49 $\}$ 10^{12} Hz	[16]
ν_{T_1} [SSO]	3.64		5,07	

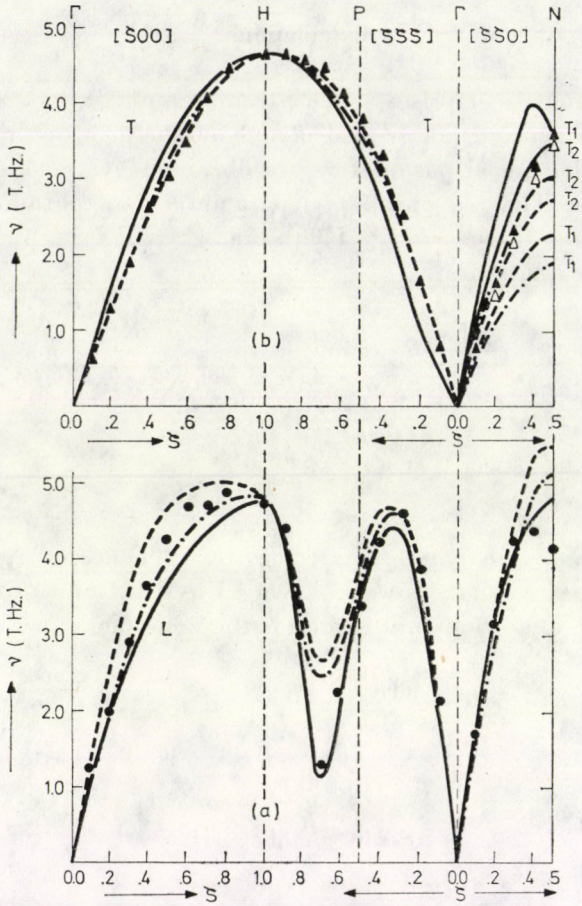

Fig. 1. Dispersion curves for bcc zirconium (a) longitudinal (b) transverse. Experimental points (●, ▲, △) due to STASSIS et al [15]. Theoretical curves (———) model 1 (-------) model 2 and (—.—.—.—) original FIELEK model.

Table II

Calculated model parameters (10 N/m)

Model 1			Model 2			Original FIELEK Model		
Parameter	bcc zirconium	Niobium	Parameter	bcc zirconium	Niobium	Parameter	bcc zirconium	Niobium
α_1	0.0612	−0.2482	α_1	0.8401	1.4528	β_1	−4.551	−10.5159
β_1	−2.3545	−3.735	β_1	−2.5336	−2.7416	β_2	−0.5096	− 1.8484
α_1'	0.3159	0.6755	γ_1	−0.2433	−0.5282	β_1'	2.9676	9.0949
β_1'	−1.2807	−4.1628	K	82.4077	46.6092	K	37.4216	81.73
K	−1.9432	−3.8725	A	0.2606	0.2954	A'	0.7753	3.4757
A	0.2606	0.2954	A'	0.899	1.5954			
A'	1.5338	6.8774						

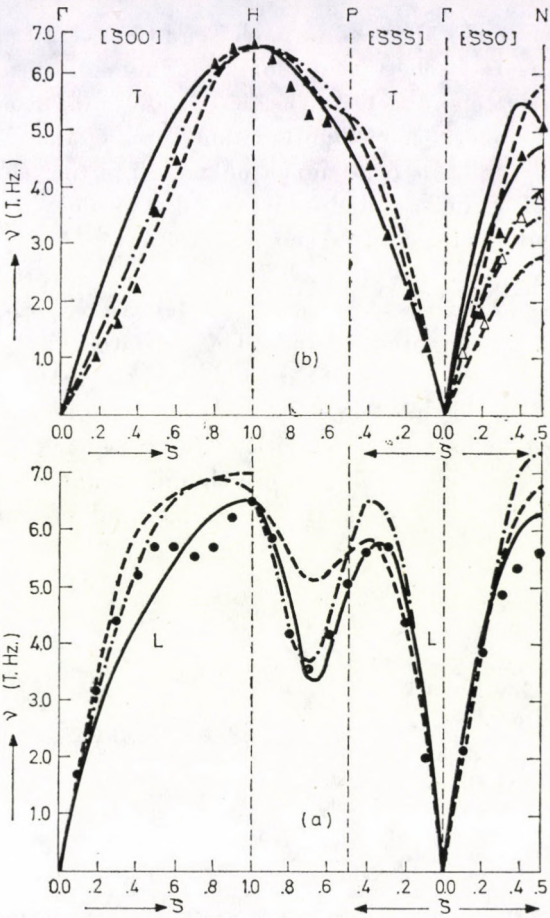

Fig. 2. Dispersion curves for niobium (a) longitudinal (b) transverse. Experimental points (●, ▲, △) due to POWELL et al [16]. Theoretical curves (———) model 1 (--------) model 2 and (—.—.—.—) original FIELEK model

with those given by the said original FIELEK model and also with the experimental data reported by STASSIS et al [15] and POWELL et al [16] for bcc zirconium and niobium, respectively.

Conclusions

Fig. 1 reveals that the theoretical predictions on phonon dispersion in bcc zirconium are very well reproduced by the first model. The second model seems to be relatively better with transverse modes. Fig. 2 clearly shows that none of the present models could explain the peculiar feature associated with $[\zeta 00]L$ branch at higher wave vectors. However, the essential feature of $[\zeta\zeta\zeta]T$

mode is very well given by the second model and the overall agreement of the second model seems to be better in niobium. Phonon excitations of $[\zeta\zeta\zeta]L$ modes are excellently reproduced by the first model in both metals. It is thus apparent that in L-modes, paired interactions among the d-shells are more effective whereas T-modes depend much on unpaired (i.e. three body) interaction. The original FIELEK model simplified by us does reproduce phonon excitations quite satisfactorily. It seems that the interactions associated with the second neighbours in the original FIELEK model are responsible for its success. The success of our first and second model can be largely attributed to the equilibrium conditions used therein. The deviations at zone boundaries are dominantly attributed to the inherent drawback of the BHATIA scheme.

It can be concluded that the short ranged paired and unpaired interactions among the d-shells govern significantly the L and the T-vibrations, respectively, in complicated metals like bcc zirconium and niobium. Moreover, the equilibrium condition incorporated with the said interactions enhances their efficacy.

REFERENCES

1. B. L. FIELEK, J. Phys., F-**5**, 17, 1975.
2. J. W. MARTIN, J. Phys., C-**8**, 2837, 1975.
3. K. KREBS, Phys. Rev., **138**, 143, 1965.
4. B. C. CLARK, D. C. GAZIS and R. F. WALLIS, Phys. Rev., **134A**, 1486, 1964.
5. A. B. BHATIA, Phys. Rev., **97**, 363, 1955.
6. B. L. FIELEK, J. Phys., F-**8**, 577, 1978.
7. D. BOHM and D. PINES, Phys. Rev., **92**, 609, 1953.
8. J. BARDEEN, Phys. Rev., **52**, 688, 1937.
9. V. RAMAMURTHY, Pramana, **11**, 233, 1978.
10. T. TOYA, J. Res. Inst. Catal., Hokkaido Univ., **6**, 161, 1958; ibid, **6**, 183, 1958.
11. B. DAYAL and P. L. SRIVASTVA, Proc. Roy. Soc., **A 277**, 183, 1964.
12. K. S. SINGWI, M. P. TOSI, R. H. LAND and A. SJO LANDER, Phys. Rev., **175**, 589, 1968.
13. E. WIGNER and F. SEITZ, Phys. Rev., **43**, 804, 1933.
14. R. P. S. RATHORE and M. R. AGRAWAL, Phys. Stat. Sol., (b) **97**, 597, 1980.
15. C. STASSIS, J. ZERESTKEY and N. WAKABAYASHI, Phys. Rev., Lett., **41**, 1726, 1978.
16. B. M. POWELL, P. MARTEL and A. D. B. WOODS, Can. J. Phys., **50**, 1101, 1977.
17. J. ASHKENARI, M. DACORAGNA, M. PETER, V. TALMOR, E. WALKER and S. STEINMANN, Phys. Rev., **B-18**, 4120, 1978.
18. I. D. BOLEF, J. Appl. Phys., **32**, 100, 1961.

Acta Physica Academiae Scientiarum Hungaricae, 52 (1), pp. 47—57 (1982)

SUR L'ALGEBRE DE HEISENBERG DE LA THEORIE DE CHAMPS ET DES ESPACES FIBRES TYPE VECTORIEL

J. D. M. VIANNA

DEPARTAMENTO DE FISICA, INSTITUTO DE CIENCIAS EXATAS, UNIVERSIDADE DE BRASILIA
70.910 — BRASILIA — DF — BRAZIL

(Reçu 17. VII. 1981)

On présente une généralisation des relations de commutation entre les éléments de l'algèbre de Lie du groupe inhomogène de Lorentz et les opérateurs de champs de bosons. On considère une variété différentiable Σ, l'ensemble de hyperplans du genre espace de l'espace de Minkowski. Les éléments de l'algèbre de Heisenberg de la théorie de champs sont définis comme des êtres géométriques sur Σ, ce qui permet d'obtenir les relations de commutation en employant des espaces fibrés et certaines constructions à eux se rapportant.

1. Introduction

La catégorie des espaces fibrés est forte utile dans l'étude de représentations de groupes de LIE [1] et dans la discussion des transformations de jauge [2, 3, 4]. Le présent article a pour but de montrer, en employant des relations qui sont à la base de la théorie quantique de champs une façon d'introduire la catégorie des espaces fibrés dans l'étude de champs. En effet, nous présentons une application de fibrés vectoriels en théorie de champs en développant les relations de commutation entre les éléments de l'algèbre de Lie du groupe de Poincaré et les variables de champs. Le résultat est une généralisation de la formulation usuelle du problème [5], et les relations obtenues peuvent être considérées comme des définitions des opérateurs moment et énergie-impulsion $M_{\mu\nu}$ et P_μ, respectivement, dans le formalisme mathématique présenté. Notre développement est formulé en représentation de Heisenberg et traite des champs de bosons. Nous désignerons l'espace de Minkowski par M et ses éléments par $x = (\mathbf{x}, x^0)$, $\mathbf{x} \in R^3$. Notre $g^{\mu\nu}$, $\mu, \nu = 0, 1, 2, 3$, est tel que $g^{11} = g^{22} = g^{33} = -g^{00} = 1$, $g^{\mu\nu} = 0$ si $\mu \neq \nu$, et nous ferons usage dans les sommations de la convention d'Einstein.

Après la section 2 où nous suivons la référence [6] pour présenter les relations qui seront généralisées, et la section 3 où nous présentons l'algèbre de Heisenberg avec la construction due à HERMANN [3], nous définissons dans la section 4 la variété Σ et considérons les élements de l'algèbre de Heisenberg

comme des êtres géométriques définis sur Σ. Dans la section 5 il y a quelques définitions et résultats mathématiques, et dans la section 6 nous présentons la généralisation obtenue. La section 7 contient quelques remarques finales.

2. L'algèbre de Lie du groupe de Poincaré

Soient $\Phi_r(x)$, avec l'indice de spin r variant de 1 a m, les variables de champs et $\Pi_r(x)$ leurs variables canoniquement conjuguées. Elles sont dans le formalisme hamiltonien les solutions du problème de Pauli—Heisenberg dont la première partie consiste à trouver des opérateurs linéaires $\Pi_s(x)$ et $\Phi_s(x)$ qui opèrent dans un espace de Hilbert et satisfont aux relations de commutation:

$$[\Phi_s(\mathbf{x}, x^0), \Phi_r(\mathbf{x}', x^0)] = 0, \quad \mathbf{x} \in R^3, \tag{1}$$

$$[\Phi_s(\mathbf{x}, x^0), \Pi_r(\mathbf{x}', x^0)] = i\delta_{sr}\,\delta(\mathbf{x} - \mathbf{x}'), \tag{2}$$

$$[\Pi_s(\mathbf{x}, x^0), \Pi_r(\mathbf{x}', x^0)] = 0; \; r, s = 1, 2, \ldots, m. \tag{3}$$

Soit $\mathsf{P} = \{L \equiv (a, \Lambda)/(a, \Lambda)x = \Lambda x + a; \; x, a \in M\}$ le groupe de Poincaré, et $U(a, \Lambda)$ une représentation de P dans un espace de Hilbert. $U(a, \Lambda)$ sera un opérateur unitaire si $\Lambda \in L\uparrow$ ($L\uparrow$ est la partie orthochrone du groupe homogène de Lorentz) et un opérateur antiunitaire si $\Lambda \in L\downarrow$ ($L\downarrow$ est la partie antichrone).

Considérons des transformations infinitésimales de P. Alors, nous avons:

$$U(\alpha^\mu, g^{\mu\nu} + \alpha^{\mu\nu}) = 1 + \frac{i}{2} M_{\mu\nu}\,\alpha^{\mu\nu} + iP_\mu\,\alpha^\mu; \; \alpha^{\mu\nu} = -\alpha^{\nu\mu},$$

où $\alpha^{\mu\nu}$ et α^μ sont des infinitésimaux de première ordre, et les dix opérateurs $M_{\mu\nu} = M_{\nu\mu}$ et P_μ sont les éléments d'algèbre de Lie (ou de sa représentation) de P. Ils satisfont aux relations

$$[P_\mu, P_\nu] = 0,$$

$$i[M_{\mu\nu}, P_\lambda] = g_{\mu\lambda} P_\nu - g_{\nu\lambda} P_\mu,$$

$$i[M_{\mu\nu}, M_{\varrho\sigma}] = g_{\mu\varrho} M_{\nu\sigma} - g_{\mu\sigma} M_{\nu\varrho} + g_{\nu\sigma} M_{\mu\varrho} - g_{\nu\varrho} M_{\mu\sigma},$$

et avec les opérateurs $\Phi_s(x)$ et $\Pi_s(x)$, que nous désignerons indistinctement par $\psi_s(x)$ ($\psi_s(x) = \Phi_s(x)$, $\psi_{s+m}(x) = \Pi_s(x)$; $s = 1, 2, \ldots, m$), nous avons les relations

$$[\psi_s(x), P_\mu] = -i\partial_\mu \psi_s(x); \; \partial_\mu = \frac{\partial}{\partial x^\mu}, \; s = 1, 2, \ldots, 2m, \tag{4}$$

$$[\psi_s(x), M_{\mu\nu}] = i(x_\mu\,\partial_\nu - x_\nu\,\partial_\mu)\,\psi_s(x) + iI^r_{s\mu\nu}\,\psi_r(x). \tag{5}$$

Comme on sait, les relations (4) et (5) suivent de la condition d'invariance relativiste de la théorie et sont obtenues de

$$\psi'_s(x) = U(a, \Lambda)\,\psi_s(x)\,U^{-1}(a, \Lambda)\,,$$

où

$$\psi'_s(Lx) = S^r_s\,\psi_r(x)\,,$$

avec $L = (a, \Lambda)$ un élément infinitesimal de P et

$$S^r_s = \delta^r_s + \frac{1}{2}\,I^r_{s\mu\nu}\,\alpha^{\mu\nu}. \tag{6}$$

Les coefficients $I^r_{s\mu\nu}$ dans les relations (5) et (6) sont antisymétriques en les indices μ et ν.

Dans cet article nous obtenons des relations qui remplaceront (4) et (5) si on utilise des espaces fibrés dans l'étude de champs.

3. L'algèbre de Heisenberg de la théorie de champs

Soint N l'hyperplan $x^0 = t =$ constant et $F_0(N)$ l'algèbre des fonctions infiniment dérivables et à support compact sur N.

Considérons les intégrales formelles [7]

$$\Phi_s(f, x^0) = \int \Phi_s(\mathbf{x}, x^0)\,f(\mathbf{x})\,d\mathbf{x}\,; \quad s = 1, 2, \ldots, m\,, \tag{7}$$

$$\Pi_s(f, x^0) = \int \Pi_s(\mathbf{x}, x^0)\,f(\mathbf{x})\,d\mathbf{x}\,;\ f \in F_0(N) \tag{8}$$

pour lesquelles nous trouvons grâce à (1), (2) et (3) que

$$[\Phi_s(f_1, x^0)\,,\ \ \Phi_r(f_2, x^0)] = 0\,,$$
$$[\Phi_s(f_1, x^0)\,,\ \ \Pi_r(f_2, x^0)] = i\delta_{sr}\int (f_1 f_2)(\mathbf{x}, x^0)\,d\mathbf{x}\,,$$
$$[\Pi_s(f_1, x^0)\,,\ \ \Pi_r(f_2, x^0)] = 0\,;\ \ f_1, f_2 \in F_0(N)\,.$$

Ces résultats peuvent être interprétés comme les images homomorphiques des relations correspondantes entre les éléments d'une algèbre de Lie. Pour arriver à cette formulation algèbrique, considérons un espace vectoriel Γ' [3] engendré par les éléments $\{\Pi_s(f), \Phi_s(f)\}$ où $f \in F(N)$ ($F(N)$ est l'ensemble de fonctions C^∞ sur N). Avec les définitions

$$g\Phi_s(f, x^0) = \Phi_s(gf, x^0)\,,$$
$$g\Pi_s(f, x^0) = \Pi_s(gf, x^0), \quad (g, f \in F(N))\,,$$

Γ' a la structure de module.

Γ' est un module libre. En effet , on peut prendre l'ensemble de $2m$ éléments $\{\Phi_s(1), \Pi_s(1)\}$ comme une base de Γ'. La base $\{\Phi_s(1), \Pi_s(1)\}$ engendre un espace vectoriel V' et nous pouvons considérer d'une façon naturelle Γ' comme l'ensemble $\Gamma'(\mathsf{F})$ des sections du fibré du type vectoriel (voir la partie 5) (F, N, p) où $\mathsf{F} = N \otimes V'$ $\otimes$ étant le produit cartésien.

Définissons sur V' une forme bilinéaire w, antisymétrique, telle que

$$w\left(\Pi_s(1)\,,\ \Phi_r(1)\right) = \delta_{rs}\,,$$
$$w\left(\Pi_s(1)\,,\ \Pi_r(1)\right) = 0\,,$$
$$w\left(\Phi_s(1)\,,\ \Phi_r(1)\right) = 0\,.$$

et soit $\Gamma = \Gamma' \oplus 1$ l'ensemble somme directe de Γ' et 1.

En considérant l'extension de la forme bilinéaire w,

$$w : \Gamma' \otimes \Gamma' \to F(N)\,,$$

nous pouvons définir une structure d'algèbre de Lie sur Γ avec la seconde loi de composition interne donnée par le commutateur, c'est-à-dire,

$$[\psi_0, \psi_\alpha] = 0\,, \qquad \psi_0 \equiv 1\,,$$
$$[\psi_\alpha, \psi_\beta] = \int w(\psi_\alpha, \psi_\beta)\,(\mathbf{x}, x^0)\,d\mathbf{x} = w^{\gamma'}_{\alpha\beta}\,\psi_{\gamma'},$$

où nous avons désigné indistinctement les élements de Γ par ψ_α, $\alpha = 0, 1, 2, \ldots, 2m$.

L'algèbre de Lie Γ a dans la théorie quantique de champs un role analogue au role de l'algèbre de Lie des P_i et Q_i's de la mécanique quantique. Γ est l'algèbre de Heisenberg de la théorie de champs.

4. La variété différentiable Σ

Dans le paragraphe précédent nous avons présenté la construction de l'algèbre de Heisenberg à l'aide de l'hyperplan N de l'espace de Minkowski. Une construction analogue peut être réalisée en termes d'une hypersurface générale du genre espace, c'est-à-dire, une hypersurface $\sigma(n, \tau)$ caracterisée par un vecteur normal $n \equiv (n^\mu)$ du genre temps et un paramètre instant τ tels que:

$$\sigma(n, \tau) : n \cdot x + \tau = 0\,, \quad n \cdot n = -1\,, \quad n, x \in M,$$

où $n \cdot x = n^\mu x_\mu$ est le produit scalaire de n et x.

Une modification dans ce cas est que dans les commutateurs (2) apparaîtra une fonction delta, $\delta^\mu(x, y)$, définie par rapport à l'hypersurface $\sigma(n, \tau)$

et telle que

$$\int \delta^{\mu}(x, y) f(y) n_{\mu} d\sigma = f(x),$$

où f est une fonction définie sur M.

On sait que [6]:

— les variables de champs ne sont pas nécessairement des observables, mais la description du champ est complète seulement s'il est possible d'obtenir un ensemble d'observables qui commutent entre eux,

— les observables sont formés, entre autres, à l'aide de formes quadratiques dans les variables de champ,

— dans la représentation de Heisenberg, les vecteurs d'état sont fixes et la dépendance du temps est portée par les observables. Ainsi, les propriétés dynamiques du système physique sont caractérisées par les relations entre les observables,

— les observables en vertu de la condition de commutabilité (microcausalité) sont associées aux hypersurfaces $\sigma(n, \tau)$.

Donc, l'ensemble des hypersurfaces $\sigma(n, \tau)$ joue un rôle remarquable dans la théorie, ce qui nous permet de considérer la variété différentiable

$$\Sigma = \{\sigma(n, \tau)/n \cdot x + \tau = 0, \quad n \cdot n = -1\}$$

et les éléments $\psi \in \Gamma$ comme des êtres geométriques définis sur Σ (une généralisation des intégrales (7) et (8)).

Pour obtenir avec cette formulation les relations, correspondantes à (1)—(3), considérons Σ plongé dans E, E étant un espace euclidien de dimension cinq [8].

Soit $k = (k^i) = (k^0, k^1, k^2, k^3, k^4)$ les coordonnées du point $k \in E$, $i = 0, 1, 2, 3, 4$.

Avec la correspondance

$$(k^0, k^1, k^2, k^3, k^4) \longleftrightarrow (n^0, n^1, n^2, n^3, \tau), \tag{9}$$

Σ est le sous-espace de E caractérisé par

$$-(k^0)^2 + (k^1)^2 + (k^2)^2 + (k^3)^2 + 1 = 0, \; k^0 > 0.$$

Soit $L = (a, \Lambda) \in \mathsf{P}$. Alors, d'après

$$L : (n^{\mu}, \tau) \to (\Lambda^{\mu}_{\nu} n^{\nu}, \tau + a \cdot n),$$

$$L : k^i \to L^i_j k^j, \quad i, j = 0, 1, 2, 3, 4,$$

et (9), il suit que

$$L^{\mu}_{\nu} = \Lambda^{\mu}_{\nu}, \; L^{\mu}_4 = 0, \quad L^4_{\nu} = a, \quad L^4_4 = 1, \; \mu, \nu = 0, 1, 2, 3.$$

Comme les ψ_α, ($\psi_0 = 1$), sont des êtres mathématiques définis sur Σ, en considérant les élements infinitesimaux de P, aux relations (4) et (5) correspondent les relations suivantes:

$$[\psi_s(k), P_\mu] = -ik_\mu \partial_4 \psi_s(k)\,, \tag{10}$$

$$[\psi_s(k), M_{\mu\nu}] = i(k_\mu \partial_\nu - k_\nu \partial_\mu)\psi_s(k) + iI^r_{s\mu\nu}\psi_r(k), \tag{11}$$

où $\partial_i = \dfrac{\partial}{\partial k^i}$, $i = 0, 1, 2, 3, 4$; $\mu, \nu = 0, 1, 2, 3$; $s, r = 1, 2, \ldots, 2\mathrm{m}$.

D'après (10), (11) et grâce à (9), il résulte que

$$[\psi_s(n, \tau), P_\mu] = i\, n_\mu\, \partial_\tau \psi_s(n, \tau)\,; \quad \partial_\tau = \frac{\partial}{\partial \tau}\,, \tag{12}$$

$$[\psi_s(n, \tau), M_{\mu\nu}] = i\,(n_\mu\, \partial_\nu - n_\nu\, \partial_\mu)\,\psi_s(n, \tau) + iI^r_{s\mu\nu}\psi_r(n, \tau), \tag{13}$$

où $$\partial_\mu = \frac{\partial}{\partial n^\mu}\,.$$

Les relations (12) et (13) sont les relations correspondantes à (4) et (5) en considérant ψ comme des êtres géométriques définis sur Σ. Elles constituent une des étapes par lesquelles nous parviendrons à généralisation de (4) et (5).

5. Les espaces fibrés

Cette section est consacrée à un exposé rapide des résultats mathématiques [9] et la nomenclature qui seront utilisés dans la section 6.

Définition 1:

Supposons que F et m soient des C^k-variétés et que p: F $\to$ m soit une surjection de classe C^k.

On dit que le triplet (F, m, p) est une fibration différentiable si:

(C.1) pour tout $y \in$ m ils existent un voisinage ouvert U de y dans m, une C^k-variété V et un C^k-difféomorphisme $\mathfrak{a}$,

$$\mathfrak{a} : p^{-1}(U) \to U \otimes V,$$

tel que

$$p|_p - 1_{(U)} = pr \cdot \alpha,$$

où pr: $U \otimes V \to U$ est la première projection.

On dit aussi que F est un fibré de base m et de projection p. $\mathsf{F}(y) = p^{-1}(y)$ est appelée la fibre au-dessus de $y \in \mathsf{m}$.

La condition (C.1) s'exprime aussi en disant que F est localement trivial.

Un ouvert U tel que $U \subset M$ est dit trivialisant, et on montre [1] que toutes les fibres au-dessus des points d'un ouvert trivialisant U sont difféomorphes à une varieté V. Si toutes les fibres sont difféomorphes à une même variété V, on dit que F est un espace fibré de fibre type V, et si V a une structure d'espace vectoriel, $(\mathsf{F}, \mathsf{m}, \mathsf{p})$ est dit un fibré du type vectoriel.

On appelle section d'une fibration $(\mathsf{F}, \mathsf{m}, p)$ toute l'application $\Psi : \mathsf{m} \to \mathsf{F}$ telle que $p \cdot \Psi = I$ (donc pour $y \in \mathsf{m}$, $\Psi(y) \in \mathsf{F}(y)$).

Définition 2:

Soient $(\mathsf{F}, \mathsf{m}, p)$ un fibré du type vectoriel, $V(\mathsf{m})$ l'algèbre de Lie de champs de vecteurs sur m (c'est-à-dire, l'espace des opérateurs différentiels de première ordre), $\Gamma(\mathsf{F})$ l'ensemble de sections de F, et $F(\mathsf{m})$ l'algèbre de fonctions C^∞ sur m. On appelle connexion linéaire du fibré $(\mathsf{F}, \mathsf{m}, p)$ une application bilinéaire:

$$\nabla : V(\mathsf{m}) \otimes \Gamma(\mathsf{F}) \to \Gamma(\mathsf{F})$$

telle que, si on donne $X \in V(\mathsf{m})$ et $\Psi \in \Gamma(\mathsf{F})$, $\nabla(X, \Psi) = \nabla_X(\Psi)$ satisfait aux conditions:

$$\text{i)}\ \nabla_{fX}(\Psi) = f \nabla_X \Psi,$$
$$\text{ii)}\ \nabla_X(f\Psi) = X(f)\Psi + f\nabla_X(\Psi), \quad f \in F(\mathsf{m}).$$

Une connexion est complètement déterminée si on donne ses composantes par rapport à un système $\{\Psi_\beta, X_i\}$ où $\{\Psi_\beta\}$ est une base de $\Gamma(\mathsf{F})$ et $\{X_i\}$ une base de $V(\mathsf{m})$.

La connexion linéaire n'est pas un tenseur. On peut cependant associer à ∇, un tenseur appelé tenseur de courbure, entre autres.

Définition 3:

On appelle tenseur de courbure associé à la connexion ∇, l'application trilinéaire:

$$R_\nabla : V(\mathsf{m}) \otimes V(\mathsf{m}) \otimes \Gamma(\mathsf{F}) \to \Gamma(\mathsf{F}),$$

telle que, si $X, Y \in V(\mathsf{m})$ et $\Psi \in \Gamma(\mathsf{F})$,

$$R_\nabla(X, Y)(\Psi) = \nabla_X \nabla_Y \Psi - \nabla_Y \nabla_X(\Psi) - \nabla_{[X,Y]}(\Psi).$$

On vérifie facilement que si $f \in F(\mathsf{m})$,

$$R_\nabla(fX, Y)(\Psi) = fR_\nabla(X, Y)(\Psi) = R_\nabla(X, fY)(\Psi) = R_\nabla(X, Y)(f\Psi)$$

ce qui garantit le caractère tensoriel de R_∇.

D'après les définitions 2 et 3, on voit que, s'il existe une base $\{\Psi_\beta\}$ de $\Gamma(\mathsf{F})$ telle que

$$\nabla_X(\Psi_\beta) = 0\,, \quad X \in V(\mathsf{m})$$

alors,

$$R_\nabla = 0\,.$$

Si le tenseur de courbure est nul, le processus connu sous le nom la translation parallèle est indépendant du chemin choisi en m.

6. Le fibré (F, E, p)

Dans cette section, E est l'espace euclidien introduit dans la section 4 et ψ_α ($\alpha = 0, 1, 2, \ldots$) sont les éléments de l'algèbre de Heisenberg $\Gamma = \Gamma' \oplus 1$.

Soit $\Gamma(\mathsf{F}) = \{\psi_\alpha\}$ l'ensemble de sections du fibré (F, E, p) avec F isomorphe a $E \otimes H$, où H est un espace vectoriel, l'espace de réalizations de $\Gamma = \Gamma' \oplus 1$. H est la fibre type de F.

Si k et k' sont deux points en E, l'espace euclidien de dimension cinq, et compte tenu de l'isomorphisme existant entre les fibres $\mathsf{F}(k)$, nous avons:

$$\varrho_{kk'} : \mathsf{F}(k) \to \mathsf{F}(k')\,,$$

où $\varrho_{kk'}$ est l'isomorphisme différentiable tel que:

$$\varrho_{kk'}\varrho_{k'k''} = \varrho_{kk''}\,.$$

Donc, si $k = (k^i) \equiv (k^0, k^i, k^2, k^3, k^4)$ sont les coordonnées du point k, nous pouvons écrire

$$\psi_\alpha(k) = T(k, k')\, \varrho(k, k')\, \psi_\beta(k')\, \varrho(k, k')^{-1}, \tag{14}$$

où $\varrho\,(k, k')$ est un opérateur sur H et $T^\beta_\alpha(k, k')$ sont des numéros-c qui satisfont aux relations obtenues de

$$[\psi_\alpha(k), \psi_\beta(k)] = w^\gamma_{\alpha\beta}\, \psi_\gamma\,(k)\,, \tag{15}$$

c'est-à-dire,

$$T^\gamma_\alpha\, T^\varepsilon_\beta\, w^\delta_{\gamma\varepsilon} = w^\gamma_{\alpha\beta}\, T^\delta_\gamma\,, \quad \alpha, \beta, \gamma, \delta, \varepsilon = 1, 2, \ldots .$$

Supposons que k et k' sont tels que $k' = k + dk$. La relation (14) nous permet de définir les coefficients nommés coefficients de la connexion,

$$t^{\beta}_{\alpha i} = \partial_i T^{\beta}_{\alpha}(k, k')|_{k=k'},$$

$$\varrho_i = \partial_i \varrho(k, k')|_{k=k'}$$

et de former les combinaisons:

$$a\partial_i \psi_\alpha + b\,[\varrho_i, \psi_\alpha] + ct^{\beta}_{\alpha i}\psi_\beta, \tag{16}$$

où

$$a, b, c = \pm 1.$$

La combinaison (16) satisfait aux conditions de la définition 2, c'est-à-dire, $\left(\text{avec } X_i = \dfrac{\partial}{\partial k^i} = \partial_i;\ a, b, c = \pm 1\right)$

$$\nabla(X_i, \psi_\alpha) = a\partial_i \psi_\alpha + b\,[\varrho_i, \psi_\alpha] + ct^{\beta}_{\alpha i}\psi_\beta\,, \tag{17}$$

est une connexion linéaire de (F, E, p).

Le tenseur de courbure associé à la connexion ∇ est obtenu facilement de la définition 3. On obtient

$$\begin{aligned} R_\nabla(X_i\, X_j)(\psi_\alpha) = ac\,(\partial_j t^{\beta}_{\alpha i} - \partial_i t^{\beta}_{\alpha j})\psi_\beta + (t^{\gamma}_{\alpha j} t^{\beta}_{\gamma i} - \\ - t^{\gamma}_{\alpha i} t^{\beta}_{\gamma j})\psi_\beta + ab\,[\partial_j \varrho_i - \partial_i, \varrho_j, \psi_\alpha] + [[\varrho_j, \varrho_i], \psi_\alpha]\,. \end{aligned} \tag{18}$$

Si nous désirons que le processus de translation parallèle soit indépendant des chemins parcourus en E, c'est-à-dire, que la connaissance d'une fibre au-dessus d'un point $k \in E$ détermine par l'intermède de ϱ une fibre au dessus du point k' indépendamment de chemin choisi en E, le tenseur du courbure doit être nul, condition qu'on obtient si $\nabla = 0$. D'après (14) et (17), la connexion qui satisfait cette condition est:

$$\nabla_{X_i}(\psi_\alpha) = \partial_i \psi_a - [\varrho_i, \psi_\alpha] - t^{\beta}_{\alpha i}\psi_\beta\,. \tag{19}$$

D'autre part, il résulte de (18), avec $a = 1$, $b = -1$ et $c = -1$, que

$$\begin{aligned} R_\nabla(X_i, X_j)(\psi_\alpha) = -(\partial_j t^{\beta}_{\alpha i} - \partial_i t^{\beta}_{\alpha j})\psi_\beta + (t^{\gamma}_{\alpha j} t^{\beta}_{\gamma i} - \\ - t^{\gamma}_{\alpha i} t^{\beta}_{\gamma j})\psi_\beta - [\partial_j \varrho_i - \partial_i \varrho_j, \psi_\alpha] + [[\varrho_j, \varrho_i], \psi_\alpha]\,. \end{aligned} \tag{20}$$

La connexion (19) avec la formule (20) nous permet d'obtenir une généralisation de (4) et (5). En effet, il suit de $\nabla_{X_i}(\psi_\alpha) = 0$ que

$$\partial_i \psi_\alpha = [\varrho_i, \psi_\alpha] + t^\beta_{\alpha i} \psi_\beta, \qquad \partial_i = \frac{\partial}{\partial k^i} \tag{21}$$

et grâce à la correspondance (9), nous pouvons écrire (12) et (13) comme:

$$[\psi_\alpha(n, \tau), P_\mu] = -in_\mu \left(t^\beta_{\alpha 4} \psi_\beta(n, \tau) - [\varrho_4(n, \tau), \psi_\alpha(n, \tau)]\right) \tag{22}$$

$$\begin{aligned}[\psi_\alpha(n, \tau), M_{\mu\nu}] = {} & in_\mu \left(t^\beta_{\alpha\nu}(n, \tau) \psi_\beta(n, \tau) - [\varrho_\nu(n, \tau), \psi_\alpha(n, \tau)]\right) - \\ & - in_\nu \left(t^\beta_{\alpha\mu}(n, \tau) \psi_\beta(n, \tau) - [\varrho_\mu(n, \tau), \psi_\alpha(n, \tau)]\right) + \\ & + I^\beta_{\alpha\mu\nu} \psi_\beta(n, \tau)\end{aligned} \tag{23}$$

qui remplaceront les relations (4) et (5) dans cette formulation de la théorie de champs.

7. Conclusions

Nous avons présenté une façon d'obtenir les relations de commutation entre les éléments de l'algèbre de Lie de groupe de Poincaré et les variables de champ de bosons en employant les objects connus sous le nom d'espaces fibrés et certaines constructions se rapportant à eux.

Les résultats ont été obtenus en partant de la considération que les éléments de l'algèbre de Heisenberg peuvent être définis comme des êtres géométriques sur la variété différentiable Σ (voir la section 4) et que le groupe de Poincaré agit transitivement sur Σ. Yodzis [8] en considérant les générateurs de groupes de symétries "internes" et l'algèbre de Lie correspondante a utilisé un développement mathématique semblable dans l'étude de la géométrie de rupture de symétries. C'est le travail très interessant de Yodzis qu' a été l'origine du sujet de cet article. Notre intention a été d'explorer le fait que des champs de bosons constituent une algèbre, pour introduire la catégorie d'espaces fibrés dans la formulation de la théorie quantique de champs.

Des développements comme ce que nous avons employé dans cet article peuvent être utiles pour exprimer des idées physiques indépendamment de la représentation des algèbres par des opérateurs dans l'espace de Hilbert. Les relations (22) et (23) peuvent être considérées comme des définitions pour les êtres $M_{\mu\nu}$ et P_μ dans ce formalisme mathématique. La construction explicite de $M_{\mu\nu}$ et P_μ en termes des variables de champ va dépendre des caractéristiques dynamiques du champ considéré, et cet aspect du problème nous n'avons pas discuté dans ce travail.

BIBLIOGRAPHIE

1. A. TRAUTMAN, Preprint no. 47 Dep. of Theor. Phys. N. Copernicus University, Cracow, Poland, 1968.
2. R. HERMANN, Phys. Rev., **177**, 2449, 1969.
3. R. HERMANN, Vector Bundles in Mathematical Physics, Vol. I, W. A. Benjamin, New York, 1970, pp. 184—90.
4. M. DANIEL et C. M. VIALLET, Rev. of Mod. Phys., **52**, 175, 1980.
5. J. D. BJORKEN et S. D. DRELL, Relativistic Quantum Fields, Mc. Graw-Hill Book Company, New York, 1965, chap. 11.
6. J. M. JAUCH et F. ROHRLICH, Theory of Photons and Electrons, Addision-Wesley Publishing Co., New York, 1959, pp. 7—14.
7. A. S. WIGHTMAN et L. GARDING, Arkiv för Fysik, **28**, 129, 1964.
8. P. YODZIS, N. Cimento, **68B**, 153, 1970.
9. S. LANG, Introduction aux Variétés Différentiables, Dunod, Paris, 1967; la référence [3], pp. 88—94.

Acta Physica Academiae Scientiarum Hungaricae, 52 (1), pp. 59—76 (1982)

SOME REMARKS ON THE ORIGIN OF X-RAY DIFFRACTION PHENOMENA

(CONTRADICTIONS IN THEIR USUAL TREATMENT) PART I

F. HAJDU

CENTRAL RESEARCH INSTITUTE FOR CHEMISTRY OF THE HUNGARIAN ACADEMY OF SCIENCES
1525 BUDAPEST, HUNGARY

(Received in revised form 4. VIII. 1981)

The adequacy of the classical Thomson theory on coherent X-ray scattering of the atoms is disputed because of its inconsistency with well known quantised properties of (electro-magnetic) radiations and the atoms as well. The assumption on secondary dipole radiation by the atomic electrons involves numerous contradictory hypotheses as e.g. the usual derivation of the angular dependence of Compton scattering of the atoms, that for the coherent scattering of the hydrogen atom, etc. The theoretical problems seem to be due to rather arbitrary alternations of the corpuscular (quantum-mechanical) and undulatory (classical) treatments of radiation.

1. Introduction

The results of fine structure studies carried out since LAUE's discovery in 1912 on all types of materials by X-ray diffraction are well known. The importance of these studies in all branches of science from petrology to molecular biology and in technology is also apparent. Some of the outstanding results (as, e.g., the double helix of DNS) have even been given wide publicity.

The early development of X-ray diffraction methods has greatly facilitated the spread of more recent diffraction procedures, namely that of electron and neutron diffraction, soon after discovering the wave-like properties of these radiations. The wave-like behaviour is the common basis of the three wide-spread methods resulting in many identical and analogous features of processing and interpreting measured diffraction data.

Being aware of the results and uninterrupted progress of X-ray diffraction, the reader will certainly feel our statement provocative that the usual treatment of X-ray diffraction phenomena if derived from the so-called "coherent" scattering by electrons is not consistent with some important principles and results of classical and quantum physics.

Nevertheless, one encounters contradictory statements, usually in the introductory chapters of textbooks and manuals on X-ray diffraction. The statements contradict partly each other, partly generally accepted theses of other sections of physics.

As to terminology, below we shall use instead of "coherent" scattering

by matter (atom, electron), rather the term "unmodified" scattering or, when speaking of the interpretation just criticised by us, the term "Thomson" scattering. The essence of our standpoint is namely that the X-ray scattering theory of J. J. THOMSON is so completely out-of-date that its application even as a first, rough approximation to real facts, is inexpedient.

Although the figure given by Thomson for the scattering cross-section of the electron, and the factor $(1 + \cos^2 2\theta)/2$ for its angular dependence (where 2θ is the scattering angle) are consistent with diffraction experiments, we mean that Thomson's theory gives no adequate description of a real physical phenomenon, neither in its original formulation, nor in a modernized form in terms of quantum mechanics. But there is a general opinion that the unquestionable existence of X-ray diffraction would be a positive proof of the reality of Thomson scattering. This vie wis found throughout the literature, some items of which of different type and origin might be referred to quite arbitrarily to give some examples ([1] to [5]).

A more profound explanation for the maintenance of Thomson's theory would need an absorbing study in the history of physics. Let us mention the persistent and often sharp discussion on the nature and scattering of X-rays among scientists defending the classical electromagnetic theory (as e.g. THOMSON) on the one hand, and those pioneering in quantum physics (as e.g. COMPTON), on the other [6].

The controversies discussed below are somehow connected with those between the electromagnetic and quantum-mechanical theories of light which reflect the contradictions between the wave-like and particle-like properties of radiations. We do not intend to involve ourselves into ultimate questions of natural philosophy, but we propose to find a satisfactory solution at the level of the present state of physical optics [7].

As to the dualism of corpuscle and wave, it causes no conflicts in practice, neither in research, nor in application and teaching, if the processes of emission and absorption of radiations are treated in terms of a discontinuous quantum model while their propagation, bending, interference and diffraction are dealt with on the basis of the wave model.

It appears to us as if the scattering of radiations (and especially of X-rays) by small obstacles formed a peculiar group of optical phenomena where the interpretation would hesitate between the two models and there would be a possibility (rather danger) for mixing them up. The question could namely be put that on impact of a "pencil" of light (X-ray) on an atom, whether the light observed behind it is the continuation of the incident beam with an inflexion and with either unmodified or modified (i.e. reduced) energy, or is it rather a "new" ray emitted by the atom at the cost of an absorbed photon. We do not decide this question of principle, instead we propose to treat X-ray scattering in the following way.

Let us divide scattering phenomena into two groups, modified and unmodified scattering, and apply to them the quantum model and the wave model, respectively, so that the essential differences as well as the correlation between them should be kept in view. Such a distinction in treatment seems to be especially important for X-rays because in dealing with the scattering of very soft and very hard electromagnetic radiations (visible light, γ-rays), emphasis can be put on the wave model and the quantum model, respectively, neglecting the other aspect as a first approximation. The scattering of medium energy X-rays (and similarly that of fast electrons and thermal neutrons) falls in a range of interactions between radiation and matter where both apparently opposing aspects must be equally emphasized. So, we propose that Compton modified scattering, fluorescence, Auger and Raman effect of X-rays should be treated in the usual way as interactions between photons and atoms (electrons); but, at the same time, the unmodified scattering and diffraction of X-rays should be dealt with as the result of perturbed wave propagation. The logical and physical relationship between the two groups consists in that the processes mentioned first cause themselves the perturbations for the waves mentioned secondly.

2. Remarks on the coherent and incoherent scattering of X-rays

The interaction of X-rays with matter gives rise, beside ejected electrons and ionized atoms, to several kinds of secondary X-rays. These are fluorescent radiation with a line spectrum characteristic of the excited atom; Compton modified scattering, the wavelength shift of which depends primarily on the scattering angle, not on the type of the scattering atom and on the energy of the incident photon: in the literature on X-ray diffraction the term "incoherent scattering" is often used as the synonym for Compton scattering; and last but not least the unmodified scattered radiation, mostly called "coherent scattering", the frequency of which is exactly equal to that of the primary beam and their phases are in a well defined relation to one another. This unmodified type of scattered radiation is generally explained — following J. J. THOMSON — as the classical electromagnetic dipole radiation of the electrons oscillating harmonically under the influence of the alternating electric field of the incoming waves. The literature unanimously states that this Thomson scattering is the only coherent one which is alone capable of forming a diffraction pattern of the fine structure of a specimen. In this sense, all other types of secondary rays mentioned above are incoherent, giving no diffraction image of the interior of matter. Compton scattering and fluorescence play the undesired role of parasitic r ys in all diffraction experiments. X-ray diffrac-

tion literature suggests such a picture that the electrons of an atom emit under the influence of an arbitrary primary X-ray beam several kinds of incoherent and one kind of coherent secondary radiation. One gets the impression that coherency and incoherency are innate features of this or that type of secondary radiations. This picture is, however, misleading and its inadequacy can be shown by the everyday practice of X-ray laboratories. As opposed to optics of visible light where diffraction experiments need sophisticated devices, X-ray diffraction patterns of very good quality can be obtained by utilizing emitted rays from an area of about 1 mm^2 and collimating the beam with simple slits to a divergence angle of 1—2°. The beam may be either monochromatic when using BRAGG's method on a rotating single crystal or the usual angle-dispersive diffractometers for studying crystal powders, glasses, or liquids or polychromatic when the Laue method is used or, recently, the energy-dispersive diffractometry. The whole emission spectrum of an X-ray tube is efficient including sharp spectral lines and the continuous "bremsstrahlung". The spectrum can be made visible and analysable by the aid of a rotating single crystal called the analyzer in X-ray spectrometry. If, on the other hand, the primary beam falls on a sample of arbitrary chemical composition and physical condition and the analyzer crystal cannot "see" the primary beam but only the secondary one emerging from the irradiated sample, the observed spectrum will be much different from that of the X-ray source. The spectrum of the tube appears again with much lower intensity which is determined by the coherent scattering power of the sample but in addition there appear secondary spectra due to Compton effect and fluorescence. Each wavelength of the primary beam gives rise to a relatively broad band, called Compton profile; eventual fluorescence produces sharp peaks. This experiment shows that all components of the secondary beam, Compton modified radiation and fluorescence included, are reflected by the analyzer crystal in the same manner, and obeying Bragg's law, as do the primary beam of the X-ray tube and the unmodified coherent secondary beam of the sample. This means that at an additional diffracting object behind the first one there are no obvious differences between the diffracting abilities of various types of secondary X-rays and the primary ray.

Considering the stochastic character of excitation processes and the macroscopic dimensions of the irradiated sample, Compton scattered and fluorescent radiations ought to be incoherent and the same holds for the emitted beam of the X-ray tube excited by accelerated thermal electrons of a hot wire. Nevertheless, at a certain distance from the source and constrained to a low divergence angle, all of them are capable of interference and diffraction. For analogies one may refer to astronomy and radioastronomy where stellar interferometers are used for measuring the angular dimensions of sources; the coherence of light, and of radio waves, respectively, depend on

the ratio of distances between independent sources to the distance between the sources and the observer.

Another example for the exploitation of uniform behaviour of secondary X-rays on a crystal is the application of a crystal monochromator in the diffracted beam of an X-ray diffractometer. In this case the reflecting angle of the crystal is fixed as the Bragg angle for the primary wavelength used for diffraction. Thus the crystal transmits (i.e. reflects) the unmodified secondary waves of the sample with maximum intensity whereas the modified components are not reflected at this angle. The application of a Bragg reflecting crystal as a very selective filter is based upon the uniformly coherent behaviour of all components because being reflected or not being reflected by a crystal at a given Bragg angle means nothing else but interference among waves being in phase or in opposite phase, respectively.

There is no doubt, of course, that the diffraction image of a structure is formed by the waves scattered unmodified and all other components of the scattered beam form a more or less uniform background reducing the contrast of the diffraction pattern. But the real reason why these radiations seem to be absolutely incoherent is that they are emitted by the atoms of the sample and are really incoherent on the spot and at the moment of their start. Yet, a narrow beam of them at a certain distance from the source can produce interference patterns. But in this respect modified secondary beams do not differ from the so-called primary beam of an X-ray tube which is also incoherent at the spot of the origin: this beam contains no pieces of information on the fine structure of the metal plate where it has started from, but a narrow pencil of it at a certain distance from the tube can be utilized for fine structure determination on an arbitrary target. Usual X-ray diffraction patterns can be evaluated according to the rules of Fraunhofer diffraction patterns in visible optics. The first condition for Fraunhofer diffraction is that the distance between the pointlike source and the diffracting object be sufficiently large.

As to the mechanism of unmodified scattering, Thomson's hypothesis claims it to be the dipole radiation of the electrons induced by the incident wave. However, Fraunhofer diffraction (or other types of diffraction) in optics do not require that the diffracting object be composed of active luminous spots which themselves emit induced radiation coherently with each other under the influence of an incident primary wave. On the contrary, diffracting objects in optics mostly consist of passive components (like screens with slits or holes, transparent or reflective plates with grooves, etc.), i.e. distinct spots differ from their surroundings by their response (transmittivity, reflectivity, etc.) to an incident light beam.

The intention of the present paper is to point out some inconsistent features of the Thomson theory and also to show a possible way of explaining X-ray diffraction without the intervention of this theory, by following more

closely the path already beaten by physical optics of visible light. Before doing so, a brief summary of Thomson's X-ray scattering theory should be given in the next paragraph.

3. The X-ray scattering theory of J. J. Thomson and some of its consequences

The summary given below contains no statement which could not be found in different textbooks on X-ray diffraction (see e.g. [1] to [5]).

A free electron when hit by an X-ray beam, begins to vibrate under the influence of the alternating electric field of the incident wave and is therefore acting as an oscillating dipole source of secondary spherical waves with the same wavelength and frequency as the primary planar wave. The cross-section of this process has been determined numerically by THOMSON from which a universal length constant, called the "classical radius of the electron" can be derived: $r_e = 2.8 \times 10^{-15}$ m. The formula of the differential cross-section contains beside the constant σ_e, an angle-dependent factor, $(1 + \cos^2 2\theta)/2$ where 2θ denotes the angle of scattering. The angular variation is due to partial polarization of an unpolarized incident beam being scattered. Accordingly, the scattered intensity exhibits two equal maxima at angles $2\theta = 0°$ and 180° and a minimum at 90° which has half of the value of the maxima.

The polar intensity diagram is circularly symmetric around the propagation direction as axis and mirror-symmetric to the plane perpendicular to it. The accuracy of the angle-dependent factor is confirmed by the practice of diffraction measurements. Integration over the sphere surrounding the electron yields the total scattering cross-section Q_e which is the ratio of scattered energy to the incident one. Its value is $Q_e = (8\pi/3)\sigma_e = 66.6 \times 10^{-30}$ m^2. The orders of magnitude of figures given by THOMSON are in all probability correct, but their accuracy has not been checked by direct measurements for lack of scattering objects consisting of free electrons.

When, however, A. H. COMPTON began to study thoroughly the scattering by light elements with the consideration in mind that they contain weakly bound electrons, he was not able to verify Thomson's formula, but he did discover a type of scattering unknown before, i.e. he found the Compton effect. Concerning the free electron, Compton's discovery has fully disproved the Thomson hypothesis since it is the unanimous view of physics that a free electron is capable only of Compton scattering, not at all of Thomson scattering. Despite this, Thomson's concept has kept a firm position in literature explaining the coherent, unmodified scattering of atoms. It is namely a widely accepted hypothesis that the electrons of an atom do scatter in two different ways according to Thomson and Compton. The first is called coherent, the

second incoherent scattering, their sum is the total scattering of the atom. The notion of total scattering power has been introduced by RAMAN (1928) and COMPTON (1930) [4]. According to generally accepted views, the total scattering of an atom is the sum of the total scattering powers of all of its electrons which are uniformly equal to the Thomson cross-section σ_e. Within this sum, the incoherent scattering is also a simple sum of the contributions by the individual electrons, but the coherently scattered intensity is the square of the resultant coherent amplitude which, in turn, is composed of elementary amplitudes with regard to their phases. Accordingly, the coherently scattered amplitude at zero angle is maximal because all elementary waves are in phase, its magnitude is Z electron units (e.u.) where Z is the atomic number; with increasing scattering angle, the resultant amplitude rapidly decreases due to the phase shifts among the elementary waves. In accordance with this, the coherently scattered intensity of the atom starts from Z^2 e.u. at angle 0 and also falls rapidly with increasing angle. The phase shifts depend on the mutual positions of the electrons within the atom. The coherently scattered amplitude of a free atom is given by a function $f = f(\theta)$ taking the amplitude of a hypothetical Thomson-scattering free electron as unity. Instead of the angle, the scattering variable $q = (4\pi/\lambda) \cdot \sin\theta$ is chosen as independent variable which renders the function f independent of the wavelength λ. $f(q)$ is called atomic amplitude or atomic form factor. Variable q is the module of a vector obtained as the difference between the Poynting vectors of the incident and scattered waves, respectively (their module taken as $2\pi/\lambda$ unit) and, strictly speaking, f is a function of vector $\mathbf{q}$. The vector can be replaced by its module if the electronic cloud of the atom is spherically symmetric.

It follows from Thomson's hypothesis that the intensity of coherent scattering is inversely proportional to the square of the mass of the vibrating charged particle. For this reason, the Thomson scattering of atomic nuclei must be by several orders weaker than that of an electron, thus being negligible.

As already seen, the classical Thomson theory had to make a compromise with quantum theory by sharing the intensity with Compton scattering. Another important step towards quantum mechanics is made in calculating the atomic amplitudes $f(q)$, because initial calculations with classical point-like electrons gave wrong results. Now, the electrons are treated as electronic clouds characterized in the atom by the radial charge density function $\varrho(\mathbf{r})$ and obtained, in turn, from the atomic wave function as its squared module. $f(\mathbf{q})$ is the Fourier transform of $4\pi r \cdot \varrho(\mathbf{r})$. For spherically symmetric atoms, $\mathbf{r}$ is replaced by $r = |\mathbf{r}|$. In this case, the atomic amplitude is

$$f(q) = 4\pi \int_0^\infty r^2 \varrho(r) \cdot \frac{\sin(qr)}{qr} dr = 4\pi \int_0^\infty r^2 \sum_{j=1}^{Z} \varrho_j(r) \cdot \frac{\sin(qr)}{qr} dr \qquad (1)$$

and the coherent intensity is

$$I(q) = f^2(q) \,. \tag{1a}$$

As seen from Eq. (1), the total charge density can be composed additively from the contributions $\varrho_j(r)$ $(j = 1, \ldots, Z)$ of the electrons. Owing to the relationships between $f(q)$, $\varrho(r)$ and the eigenfunctions Ψ, calculated atomic and molecular amplitudes have become more and more accurate following the improvements on the quantum mechanical atomic and molecular models.

As known, detection techniques for X-rays cannot measure amplitudes but only the intensities. The unmodified intensity scattered by N pieces of free atoms (realizable in practice by a sample of low-pressured inert gas) is equal to $N \cdot f^2(q)$. In all other cases, i.e. for free molecules and for any kinds of condensed matter, the unmodified scattering is the square of a resultant amplitude composed of the atomic amplitudes. In calculating the resultant amplitude for a bulk specimen, Fourier transformation plays a similar role as in calculating the atomic amplitude from the radial charge density of the atom. The simple spatial densities (measured as number of electrons or atoms in unit volume vs co-ordinates in space) yield through Fourier transformation the scattered amplitudes in the q-space (= reciprocal space) and vice versa. The amplitudes are not measurable quantities. The measurable intensities can be obtained theoretically as the Fourier transform of certain auto-correlation functions of the simple density functions. Such functions are known in practice of crystal structure analysis as the Patterson functions and in studies on liquid and amorphous structures as the radial distribution function of atoms (eventually of electrons). The relationships are mutual and so, measured intensities can be transformed into Patterson functions and radial distribution functions, respectively. This means also a possibility for checking the correctness of theoretical atomic amplitude functions and the atomic models as well. There is generally a good agreement between experimental and theoretical data, thus verifying the adequacy of fundamental formulas utilized in data processing and in theoretical calculations. Despite all positive experiences, the philosophy behind the formulas as coming from the Thomson theory is not necessarily as correct as the formulas themselves. Below, we try to point out that insistence on any form of Thomson's model necessarily leads to statements contradicting several laws and facts accepted by quantum mechanics and physical optics to-day. Before dealing with these contradictions, the anomalous scattering or dispersion of atoms as interpreted by the Thomson model should be mentioned.

Following the terminology of Thomson scattering, the simple formula (1) for calculating $f(q)$ — even for spherically symmetric atoms — yields accurate results only when all electrons of the atom are "almost free" for the vibrating

effect of the incident wave, viz. if the "own frequency" of all electrons is far enough from that of the incident wave. But when the incoming wave frequency lies in the neighbourhood of an X-ray absorption edge of the atom, then the electron responsible for this edge is no more free and its vibration excited by the incident wave must be some kind of forced oscillation near to its point of resonance. The contributions of the electrons in question — primarily those in the K-shell — will differ from the others in amplitude and phase. The amplitude of the whole atom becomes a complex expression obtained from Eq. (1) by adding to it two correction terms, namely a real f' and an imaginary f'', as follows:

$$f(q) = f_0(q) + f' + if'' \tag{2}$$

and

$$I(q) = f(q) \cdot f(q)^* = [f_0(q) + f']^2 + f''^2, \tag{2a}$$

where $f_0(q)$ stands for $f(q)$ of Eq. (1); f' and f'' are practically independent of q, but they strongly depend on the atomic species and the wavelength. As f' can be $\lesseqgtr 0$, it either reduces or increases the atomic intensity while the imaginary term f'' always increases it. Numerically, f' and f'' have been determined by several authors on quantum mechanical basis and their accuracy could be improved from time to time, similarly to the $f_0(q)$ functions (see e.g. [4], Vol. IV).

They play an important role not only in simply processing experimental data, but also in planning new experiments applying the "heavy atom method". But again, we must make a distinction between good formulas and accurate numerical calculations on the one hand, and the dubious philosophy of Thomson scattering on the other.

4. Contradictions resulting from Thomson scattering

The modified scattering of X-rays discovered by A. H. COMPTON [6] had not been predicted and could not be explained by the classical electromagnetic theory. We must note, however, that Maxwell's equations imply the notion of the momentum of a propagating electromagnetic field and so they predict radiation pressure. Thus, it would have been possible to foresee the elastic collision of an electron with light instead of its harmonic vibration as claimed by the Thomson theory but, of course, without predicting the energy loss and wavelength shift of radiation after collision. Well known is Compton's idea by which he succeeded to obtain the wavelength shift from the principles of conservation of energy and of momenta applied to the photon-electron collision within the frames of special relativity.

Beside verifying the reduced hardness of scattered rays by their increased absorption, Compton was arguing for the novelty of this type of scattering that its angular distribution had been found by him strongly asymmetric in favour of the forward direction as opposed to the forward-backward symmetry of Thomson scattering [6]. A paradoxical feature of this science-historical fact is that regarding the X-ray scattering of free atoms, it is the coherent part — i.e. the Thomson scattering — whose amplitude and intensity exhibits maximum value at zero angle and decreases drastically with increasing angle while the Compton modified intensity of the atoms starts from zero in forward direction and, increasing monotonously, tends to its maximum in backward direction (owing to the recoil factor of Breit—Dirac, it passes through a very flat maximum below the angle 180°). To clear this paradox, let us first remember that both the symmetrical Thomson intensity, and Compton's equation for the wavelength shift together with the Klein—Nishina formula for the Compton intensity are valid for a hypothetical free electron. But all real scattering measurements are performed on atomic systems, not on free electrons and so the scattering properties of the atoms with bonded electrons and also the energy range of the applied radiation must be taken into account [4]. The Klein—Nishina formula yields an asymmetric intensity distribution characteristic of primary radiations above 1 MeV but it yields a fully symmetrical one quite similar to the Thomson intensity distribution for radiations below 0.1 MeV which is just the range of X-rays used for diffraction work. In addition, the bonding energy of the electrons necessarily defines a lower angle limit below which Compton effect is not possible (see also Part II [8] Section 5).

Despite the known deficiencies of electromagnetic light theory, the Thomson cross-section is generally accepted for the atomic electrons with the only change that it should pertain to the total scattering power (coherent + incoherent). We dare not state that this usage would not be consistent with the X-ray diffraction work of nearly 70 years. Yet, we must ask the question, what is the ratio of unmodified to modified intensities within their sum and on what parameters does it depend.

We have already referred to the general view that a really free electron exhibits only Compton scattering. Nevertheless, the lack of "coherent" scattering has not been verified by a crucial experiment on free electrons. It is a fact, however, that the scattered radiation of all atomic systems consists of unmodified (interfering) and modified (not interfering) components. Any progress in atomic models involves the improvement of not only the $f(q)$ atomic scattering factors, but also that of Compton atomic cross-sections (intensities). Computed and measured Compton profiles have already been utilized for molecular structure studies. The formulas and numerical tables are again consistent with measuring practice, but we find some illogical

moments in the way in which the two types of scattering are related to each other in terms of the Thomson theory.

As already mentioned, the total scattering of the electrons in an atom is now taken as the fundamental property (I_{tot}) composed of a coherent (I_{coh}) and an incoherent (I_{inc}) part:

$$I_{tot}(q) = I_0 \cdot \sigma_e \cdot \frac{1 + \cos^2 2\theta}{2} = I_{coh}(q) + I_{inc}(q) \tag{3}$$

for each electron. The total scattering of an atom with atomic number Z, integrated over the whole sphere around the atom, is therefore

$$2\pi Z \int_0^{\pi} I_{tot}(\varphi) \cdot \sin \varphi \, d\varphi = Z \cdot Q_e \,, \tag{4}$$

where φ is the scattering angle (2θ elsewhere) and Q_e is the integrated intensity of an electron, i.e.

$$Q_e = I_e \cdot 2\pi \int_{-1}^{+1} \frac{1 + \cos^2 \varphi}{2} \, d(\cos \varphi) = \frac{8\pi}{3} \cdot I_e = \frac{8\pi}{3} \cdot \sigma_e I_0. \tag{4a}$$

On the other hand, we know that the amplitude of the wave scattered coherently is given by the Fourier transform of the radial electron density of the atom and the coherent intensity is the square of this expression. Thus, I_{tot} and I_{coh} are known and I_{inc} must be defined as the difference $I_{tot} - I_{inc}$. Here, we feel a deficiency in the chain of ideas.

The way of calculating the coherent amplitude scattered by the atom unambiguously shows that this is composed of contributions of all electrons without distinction but taking into account their cloud-like distribution around the nucleus. The Fourier transform of the density comprises the interferences among the waves scattered by the individual electrons. These result in a perfect amplification at $q = 0$ and a perfect extinction for $q = \infty$. The amplitude and the intensity are monotonously decreasing between $q = 0$ and the physically existing upper limit $q = 4\pi/\lambda$ ($2\theta = 180°$, $\sin \theta = 1$). The over-all monotonous decrease is the sum of contributions of different shapes. The amplitude curves of electrons in different shells are different; for the K-electrons of most of the atoms it is constantly 2 e.u. in the whole q-range; that of the outer (valence) electrons is rapidly decreasing like e^{-aq} or e^{-aq^2}; those of the medium shells show strongly damped oscillations. The total amplitude at $q = 0$ is Z e.u., the intensity is thus Z^2 e.u. of intensity (unit is the Thomson cross-section of the electron). Within the finite range of q, the coherent intensity decreases from Z^2 to a low level but not zero [1], [4]. We must here realize that inter-

ferences among waves of definite intensities cannot change the total scattered energy of the sum of these waves, only their intensity distribution in space. So, the integrated intensity of the atom is not higher and not lower than Z e.u. because each electron contributes to it by 1 e.u. But then Eq. (3) would yield $I_{\text{tot}} = I_{\text{coh}}$ and consequently, $I_{\text{inc}} = 0$ which is an absurd result.

True, one never finds Eq. (3) in integrated form in the literature. The incoherent intensity function is given vs q, as the difference between the constant Z and a q-dependent term:

$$I_{\text{inc}}(q) = I_e \cdot \sum_1^Z [1 - f_{e,m}^2(q)] = I_e \cdot \left[Z - \sum_1^Z f_{e,m}^2(q) \right], \tag{5}$$

where $f_{e,m}$'s are new functions not to be confused with the atomic amplitude $f(q)$. Each of the $f_{e,m} (m = 1, 2, \ldots, Z)$ is the sine Fourier transform of the charge density contribution of the m'th electron of the atom. The charge density can really be regarded as superimposed of contributing single electron densities, and so, the terms $f_{e,m}$ can be the components of the atomic scattered amplitude. The square of their sum yields the coherently scattered intensity of the atom, because then the amplitudes are additive (vectorially). But the sum of the squares, $\sum_1^Z f_{e,m}^2$ or the single terms $f_{e,m}^2$ do not correspond to any measurable intensity. We must accept the fact that the sum of the complements $[1 - f_{e,m}^2(q)]$ yields a useful expression for the Compton modified scattering of the atom. Eq. (5) of Waller and Hartree has been completed with the cross-terms $-\sum_m^Z \sum_k^Z f_{e,mn}$ by WENTZEL [1], [4] to account for the Pauli exclusion principle. The completed Eq. (5) has to be multiplied by the polarization factor of Thomson and the recoil factor of Breit—Dirac in order to obtain the accurate Compton intensity as a function of q. Some important features of $I_{\text{inc}}(q)$ can be inferred also from Eq. (5). For $q = 0$, all $f_{e,m} = 1$, consequently, $I_{\text{inc}}(0) = 0$ for all types of atoms. Beginning from the third row of the periodic system, the two electrons of the K-shell give $f_{e,1} = f_{e,2} = 1$ constantly, thus, these electrons do not contribute to $I_{\text{inc}}(q)$ at all; the contributions of all others are monotonously increasing from 0 towards 1; accordingly the Compton intensities of light atoms approach Z, those of heavier atoms $Z - 2$ e.u. at high q.

The physical contents of Eqs. (3) and (5) is explained very often in the literature so that the coherent scattering of the atom is furnished mainly by its strongly bound inner electrons while the incoherent scattering must be ascribed to the weakly bound outer ones [1], [2]. The latter part of the statement is certainly correct, but the first one can easily be disproved. In the lower part of the q-range, evidently all electrons contribute to $f(q)$ in equal

manner, since $f(0) = Z$, and $I_{coh}(0) = Z^2$. It is true that $I_{coh}(q)$ decreases quite rapidly with increasing q while $I_{inc}(q)$ gradually increases, nevertheless the relationship between the two changes cannot be as simple as suggested by Eqs. (3) and (5). The decrease of $I_{coh}(q)$ does not need the explanation by the increases of I_{inc} but rather the rules of the addition of coherent waves. According to this, a range of constructive interference must necessarily be accompanied by a range of destructive one, otherwise the energy conservation law would be violated. The q-dependence of I_{inc} must be deduced from first principles.

Another problematic feature of this view is that the coherent intensity of the free atom is almost never observed (except measurements on a diluted noble gas) because the additivity of coherent amplitudes extends to the atoms of a molecule and to other atoms or molecules in a condensed system. The coherently scattered intensity at a certain point q is, quite naturally, a function of the atomic structure of the sample. At the same time, the Compton intensity is composed nearly additively of the atomic intensities, hardly influenced by the structure of the bulk sample. In terms of Eq. (3), this would mean that by extending the validity of this Equation to an N-atom system, its left-hand side and the second term on the right-hand side would simply be multiplied by N whereas the first term of the r.h.s. would be completely redistributed, so that its value could vary between zero and $N^2 \cdot I_{coh}(q)$. Our question is, why should the Compton scattering "remember" a fictitious atomic coherent scattering power and produce somehow its complementary scattering when, at the same time, the coherent intensity has "forgotten" its own value in the independent atomic state. We are sceptical about such an ability. A possible answer would be that the l.h.s. of Eq. (3) should be not simply $N \cdot I_{tot}(q)$ but it should vary together with $I_{coh,N}(q) + N \cdot I_{inc}(q)$. Then Eq. (3) loses its physical significance and means only an extra notation for the sum of scattered intensities. In such a role, it is really utilized in practice as the base for normalizing the experimental intensity function before submitting it to Fourier transformation.

The comment frequently made on Eqs. (3) and (5) about the different roles of inner and outer electrons in the coherent scattering can be objected also by the fundamental requirement of the Thomson theory concerning the "almost free" state of the electrons. We see, indeed, that the simple expression for the coherent amplitude, i.e. the Fourier transform of the radial electron density, needs special corrections just for strongly bound inner electrons. Attention must be paid to the fact that the innermost electrons (K-shell) take no part in Compton scattering but exhibit a great cross-section for "true" absorption (fluorescence excitation) and simultaneously for coherent scattering. Later we shall return to these facts.

Here, we emphasize the opinion that the Compton scattering power of atoms and of bulk samples has to be treated as the sum of elementary colli-

sions between electrons and photons, though influenced by the structure of materials, but by no means determined by the coherent unmodified intensity of either free atoms, or the sample as a whole.

Admitting that Eqs. (1) through (5) have been very useful in evaluating diffraction measurements, the use of physical pictures and explanations usually added to them, including Thomson's picture about the oscillating electrons, seems very much doubtful. It is hardly understandable that Thomson's classical electrodynamical model — yet without accounting for radiation pressure — which had been meant originally for free electrons but proved to be inadequate for them, should be suitable to explain the "total" scattering of the electrons in the atom. The notion of total scattering amalgamates the classical Thomson scattering with the quantic Compton effect (but does not include "true" absorption, i.e. one of the most important interactions between atoms and X-ray photons). Apart from Eq. (3), the treatments of Thomson and Compton scattering, respectively, reflect two opposite views of the nature of X-radiation.

Compton scattering is described as due to the elastic collision of a photon of energy $h\nu_0$ and momentum $\mathbf{K}_0$, with an electron (at rest or with its momentum in the atom) after which the photon will exhibit less energy, $h\nu_1 < h\nu_0$, and a changed momentum $\mathbf{K}_1 \neq \mathbf{K}_0$; $|\mathbf{K}_1| < |\mathbf{K}_0|$, the differences being transferred to the electron. The scattered intensity in this terminology is the flux of photons proportional to the squared amplitude of the wave associated to them; the amplitude itself plays no role. The number of photons is invariable, so, each impact contributes to the scattered intensity by one photon the energy loss of which depends on the scattering angle.

On the other hand, descriptions of Thomson scattering represent the primary beam as a planar wave with wave vector $\mathbf{K}_0$, the amplitude given by the electric field strength $\mathbf{E}_0$, the intensity by E_0^2. The wave passing by the electron (at rest) makes it vibrate harmonically by which it becomes the source of secondary electro-magnetic spherical waves, the scattered waves having in all directions the amplitude E_1 (where $E_1 \ll E_0$) and the intensity $I_1 = E_1^2$ modulated with the polarization factor $(1 + \cos^2 2\theta)/2$. The ratio $I_1/I_0 = (E_1/E_0)^2$ is the Thomson differential cross-section. The scattered amplitude of a macroscopic sample containing $N \cdot \bar{Z}$ electrons (N is of the order of 10^{20}, $\bar{Z}$ the mean atomic number) is obtained as the vectorial sum of amplitudes (but not necessarily all elementary amplitudes in one sum) and the intensity as the square of the resultant amplitude(s). The energy states of the scattering atoms are claimed to be invariant while emitting coherent secondary radiation in a finite, continuous wavelength range. The quantised behaviour of the atoms and radiations is ignored by this theory. Unquestionable is the fact that the coherent intensity scattered by a macroscopic sample depends directly on the configuration of all electrons, it cannot be composed additively of contribu-

tions by the electrons and in the majority of cases, not of atomic contributions either.

The concept of "total" scattering thus amalgamates not only two types of scattering, but also two deviating theories of radiation. As seen above, it may have two different meanings: i) a simple comprehensive name for the sum of two intensities; in this meaning, it can be well utilized for practical calculations; ii) fixing the total scattering power of the electron, it suggests that Compton scattering must be the result of a subtraction $(I_{\text{tot}} - I_{\text{coh}})$. It is the validity this of meaning that is challenged in the present paper.

The inconsistencies manifest themselves very markedly in the usual treatment of the hydrogen atom. As mentioned above, the strong decrease of unmodified atomic scattering with increasing q is generally ascribed to destructive interferences among coherent elementary waves but without participation of the atomic nuclei. One might expect therefore that the unmodified scattering of a single-electron system, the hydrogen atom, has no q-dependence (except polarization) and accordingly, this atom does not participate in Compton scattering. Contrary to this expectation, we find (in theory as well as in practice) that the coherent scattering of H-atom decreases rather abruptly from 1 to 0 and simultaneously, its Compton scattering changes in the opposite way. Eq. (3) seems to be valid without modification (because $Z = 1$), i.e.,

$$I^H_{\text{tot}}(q) = I^H_{\text{coh}}(q) + I^H_{\text{inc}}(q) = I_e(q) \,, \tag{3a}$$

where I_e is the Thomson scattering of the electron (polarization factor included). In e.u., the amplitude and the intensity of the unmodified scattering at $q = 0$ are both $= 1$. At every q, the Compton scattering is

$$I^H_{\text{inc}}(q) = 1 - [f^H(q)]^2 \,.$$

What is surprising there is the formulation of $I^H_{\text{coh}}(q)$ and its square root, $f^H(q)$; the latter is namely the sine Fourier transform of the electron density caused by the only electron of the H-atom, it is thus identical with the form factor of this electron, $f^H_{e,1}(q)$.

The Fourier transform of the radial electron density of an atom is nothing else but the operation of summing up elementary amplitudes with regard to their phase differences which derive from the path differences of coherent incident waves and scattered waves travelling from the primary source towards the detector and changing direction at the scattering centres of the object. The Thomson theory of one hydrogen atom tells us that the electronic cloud of a single electron must be divided into infinitesimally small volume elements dV and similar charge "elements" ϱdV each of which oscillate independently,

under the influence of infinitesimally weak partial waves of the incident beam; the emerging secondary waves which must be still weaker (by 10^{26}) interfere with each other, resulting finally in the abrupt fall of coherent intensity; a similar description must hold for the complementary Compton scattering. The absurdity of this idea — eight decades after PLANCK's and EINSTEIN's theories — may be evident, nevertheless, a similar description of the scattering of the H-atom can be found in all X-ray diffraction textbooks with the only difference that no stress is laid on the word "infinitesimal" [1, 2, 3].

A further question arising from the Thomson theory of atomic scattering concerns the role of the atomic centres. It is obvious that the radial electron density function $\varrho(\mathbf{r})$ is related to the atomic centre. But remembering again the meaning of the Fourier integral, one must see that the atomic centre is also a scattering point whose fictitious waves interfere with those of the electronic clouds and just these interferences have the main role in determining the amplitude factor of the atom and that of the separate shells as well. But again, it is the Thomson theory itself which contradicts this idea by demonstrating the negligible scattering power of atomic nuclei. In spite of this inconsistency, experience shows that the characteristic shape of atomic scattering curves can really be derived from the mean radii of electron shells as follows from Eq. (1). We must return to this problem in the second part of this paper.

It is well known that X-rays and atomic materials exert still other types of interaction on each other besides modified and unmodified scattering. First of all, "true" absorption comprising photo-electric effect, ionization, and fluorescence; also the Auger effect. All interactions are strongly correlated with one another; a distinction between some of them is only expressing the existence of different measuring techniques and possibilities as e.g. absorption-, photo-electron and fluorescence spectroscopy. We must pay some attention to X-ray absorption. The so-called total absorption cross-section of materials is composed of three main components: 1) "true" absorption appearing also as photo-effect and fluorescence; 2) modified scattering; 3) unmodified scattering. (An alternative terminology is "extinction" instead of "total absorption" and "absorption" for "true absorption".) Thanks to new, powerful X-ray sources (e.g. synchrotron) and sensitive measuring devices, measuring of the fine structure and the extended fine structure of absorption, photo-electron and fluorescence spectra, Compton profiles, Auger electron spectra, etc. offers new pieces of information on the structure of matter interacting with X-rays. But all measuring techniques, older and newer, require an adequate theory for setting clear objects to measurements. This holds also for X-ray diffraction which belongs, in a sense, to another category of measuring methods.

The most important common feature of interactions mentioned above is their primary dependence on energy conditions, i.e. on the incident photon energy and the energy states of the target atoms; all other conditions like

chemical bonding, physical state, crystal structure, etc. affect these phenomena by modulating the energy levels. It follows from this that they cannot be treated, explained and predicted in terms of classical theories, being subjected to the laws of quantum mechanics.

On the contrary, the unmodified scattering of atoms, and diffraction patterns of any forms of matter are primarily determined by the geometrical configuration of electrons within the atom, and the spatial arrangement of the atoms in the sample, respectively. Energy conditions exert secondary effects on diffraction as e.g. the anomalous scattering in the vicinity of an absorption edge. The wavelength of the incident beam is also taken in the geometrical sense as a unit length of periodic repetitions and not as a measure of photon energy. For this reason, diffraction phenomena can be interpreted in terms of classical optics and wave theories without the explicit use of quantum mechanics. However, the object of this paper is to show that Thomson's scattering theory or model does not belong to the group of adequate classical theories.

The separate use of a quantum-mechanical model and a classical model for the two groups of interactions, respectively, can be reconciled. Their inconsistency becomes evident only when they are applied simultaneously to one and the same physical process. The difficulties get even more serious if an inadequate model is chosen either in classical or in quantum-mechanical terms. In order to separate the two groups of physical processes, we must also see the relationship between them.

As to the inadequacy of the Thomson scattering model, it should be emphasized that treating the atoms as arbitrarily and continuously tunable oscillators is not justifiable; such a model is even less permissible for X-rays than for visible light regarding the energy ratios between X-quanta and the bonding of (inner) electrons.

How is it possible that e.g. the loosely bonded electrons of H-atoms — if present in a diffracting sample — could emit X-rays as hard as those emitted by much heavier atoms of the anode of the X-ray tube? How could one understand that the atoms of a sample are able to reproduce all frequencies which are present in the primary beam supposing that the sample is used as a diffracting object, but the radiation of the same atoms is strictly determined by quantum-mechanical rules if the sample serves for fluorescence analysis, or is used as anode material in an X-ray tube?

We shall endeavour to propose an interpretation of unmodified scattering and diffraction, different in principle from the dipole radiation of Thomson. We shall try to find a possible solution for our problem among existing and living physical theories and to avoid creating new hypotheses.

REFERENCES

1. A. GUINIER, X-Ray Diffraction in Crystals, Imperfect Crystals, and Amorphous Bodies' W. H. Freeman and Company, San Francisco and London, 1963, Chapters 1, 2, 3.
2. M. A. BLOCHIN, Physik der Röntgenstrahlen, (Redakteur Dr. H. Rother. Übersetzung der 2. Ausgabe) VEB Verlag Technik, Berlin, 1957, 7. Kapitel.
3. L. V. AZÁROFF, Elements of X-Ray Crystallography, McGraw-Hill Book Co., New York, Sidney, 1968, Chapters 5, 6, 8, 9.
4. International Tables for X-Ray Crystallography, edited by The International Union of Crystallography, The Kynoch Press, Birmingham, England, Volume III, 1962, Chapter 3, Volume IV, 1974, Chapters 1, 2.
5. W. HEITLER, A sugárzás kvantumelmélete (Quantum Theory of Radiation) Hungarian translation of the 3rd ed. Akadémiai Kiadó, Budapest, 1959, Chapter 5, Paragraphs 19, 22, 25.
6. R. H. STUEWER, The Compton Effect — Turning Point in Physics, Science History Publications, New York, 1975.
7. M. BORN and E. WOLF, Principles of Optics, Pergamon Press, London, New York, Paris, Los Angeles 1959, Chapters VIII, XI, XIII.
8. F. HAJDU, Acta Phys. Hung., **52**, 77, 1982.

Acta Physica Academiae Scientiarum Hungaricae, 52 (1), pp. 77—87 (1982)

SOME REMARKS ON THE ORIGIN OF X-RAY DIFFRACTION PHENOMENA

(CONTRADICTIONS IN THEIR USUAL TREATMENT) PART II

F. HAJDU

CENTRAL RESEARCH INSTITUTE OF CHEMISTRY OF THE HUNGARIAN ACADEMY OF SCIENCES
1525 BUDAPEST, HUNGARY

(Received in revised form 4. VIII. 1981)

Contradictions are pointed out between Thomson's theory on coherent X-ray scattering of the atoms and well tried principles of physical optics such as those of HUYGENS, FRESNEL, KIRCHHOFF, FRAUNHOFER, BABINET, MIE, and others. It is proposed by the present author that all types of modified scattering, i.e. Compton effect, fluorescence, and Auger effect should be regarded as the primary products of X-photon — atom collisions, the probabilities of which should be derived from quantum-mechanical principles. On the other hand, coherent scattering is claimed to be a secondary phenomenon accompanying the effects mentioned first and owing to the perturbations of the homogeneous incident wave front. This means that diffraction patterns are formed by photons of the primary beam which themselves have not collided with electrons but rather have passed round them. Accordingly, Thomson's hypothesis can be dropped as being physically inconsistent and logically redundant as well.

1. Introduction

In the first part of this paper [1] contradictions within the usual treatment of X-ray scattering and diffraction have been dealt with. The contradictions are ascribed to the mixing of quantum mechanical and classical physical aspects and to the use of an apparently inadequate model of scattering, the Thomson model. In the present second part we point to further inconsistent statements contradicting well-proved principles of physical optics. Although optics is mostly dealing with visible light, there is no serious reason for sharply separating X-rays from it, because diffraction phenomena seem to obey physical laws common for all types of waves, especially for those belonging to the family of electromagnetic radiations.

In the present part we give some proposals to replace Thomson scattering by a more up-to-date treatment of X-ray scattering and diffraction but without aiming at a final and mathematically exact solution of the problems brought up in both parts of the paper.

2. Thomson scattering and some principles of physical optics

Physical optics is based upon the Maxwell equations of electrodynamics. The Thomson theory of X-ray scattering claims the same. Yet, surprisingly, we find several important statements of the latter theory not being in accordance with the principles of optics.

Physical optics deals among others with the interference, scattering and diffraction of electromagnetic waves [2], most often neglecting the quantum properties of radiations. It can interpret light diffraction patterns both qualitatively and quantitatively by the aid of the HUYGENS principle perfected by YOUNG, FRESNEL, KIRCHHOFF, FRAUNHOFER, and others. According to this, each point in space attained by a wave becomes itself the source of new spherical waves; superimposition of these from all points of a homogeneous field yields simply the linear propagation of the whole wave front (planar or spherical). In the presence of inhomogeneities, the resultant wave front declines from the linear direction whereby a situation for the appearance of interference or diffraction patterns is created.

Practically important forms of diffraction are obtained when Fraunhofer conditions are met, which holds for usual X-ray diffraction measurements. Under these conditions the incident beam is represented by a planar wave and when the target contains inhomogeneities commeasurable with the wavelength, then diffraction takes place in ther surroundings and interference patterns appear on the screen. The phenomena can be interpreted with the aid of the Huygens—Fresnel principle. The arrangement of spots of inhomogeneity in the diffracting object and that of spots of maximum intensities on the screen are interconnected by Fourier transformation. The physical properties of diffracting spots may be very different as e.g. openings cut into an opaque diaphragm, opaque spots on a transparent plate, scratches in an optically smooth surface (glass or metal), floating particles in a homogeneous medium (gas or liquid), and so forth. The main features of their diffraction pattern are determined by geometrical characteristics: dimensions, shapes and mutual positions; other physical properties of the spots, like refraction index, absorption, etc. affect some secondary features of the picture (intensity, contrast).

There is a second important "principle" valid for diffraction pictures, known as BABINET's principle. According to this, the members of a complementary pair of diffracting objects yield the same diffraction pattern, apart from the central illuminated spot. Thus a diffraction image behind of a system of transparent and opaque areas of required dimensions will not essentially change, if the diffracting system is replaced by its complementary system where opaque and transparent areas are just oppositely fashioned.

Let us now examine, how the two principles of Huygens—Fresnel, and of Babinet, respectively, can be applied to a common X-ray diffraction experi-

ment. The Fraunhofer conditions are met since both distances (X-ray source to sample, and sample to detector) are about 10 cm or more. The primary beam is collimated in order to have a low angle of divergence, so that its trace in the plane of detector is confined to a small spot (or, eventually, to a narrow rectangle of $\sim$1 cm length) if no diffracting object is present. In the presence of a sample of whatever composition and physical state, there appears a pattern of dark and light areas (distinct spots, sharp or diffuse circles) around the central spot. What is the cause of this well-known result? Is there indeed no other explanation than the harmonic oscillation of electrons at no matter what frequency or frequencies within the entire X-range and the secondary dipole radiation as the consequence of their oscillations? We feel that a physically consistent explanation must be more simple and ought to be found among the recognized laws of the competent discipline.

In [1] we alluded to the fact that X-rays — owing to their photon energy range — inevitably interact with the electrons of whichever atomic species whenever they meet, having chances of several types of interaction: modified scattering, absorption or Auger effect. The effect that each of them has on the primary beam is to remove from it every time one photon either by absorbing it or by pushing it aside. This being so, each electron of the target represents a singular spot in the field of radiation, i.e. an obstacle perturbing the incident wave front. One would say that every electron is an opaque particle for the X-ray, similar to dust grains in the atmosphere which are opaque for and scatter sunlight. It is this effect of the electrons that compels the remaining waves of the primary beam to bend round the electrons following the Huygens—Fresnel principle. That means that the unmodified scattered radiation which forms the diffraction pattern is itself not the product of a photon—electron interaction, but is rather a part of the original beam passing through the space between the electrons. From this standpoint it becomes obvious that beside the existence of several types of photon—atom and photon—electron interactions, which all need rigorous quantum-mechanical treatment, there exists only one type of unmodified coherent radiation which can be, in addition, quite well described in terms of classical wave theory. Since there is no doubt that one part of the incident radiation is absorbed, a second part is scattered by collisions, and a third part can pass — though not undisturbed — without colliding with electrons, we may state that this is sufficient reason for producing unmodified scattering and diffraction. Accordingly, the assumption of a secondary dipole radiation of electrons is logically redundant, not to speak about the physical arguments against its reality.

Now, let us turn to Babinet's principle. It follows from the foregoing that a diffracting object is considered as an ordered (crystals) or partially ordered (atomic or molecular glasses, liquids, or gases) system of electrons floating in vacuum and being opaque for X-rays. Such a system must

produce a diffraction pattern. In the sense of the Babinet principle, the complementary object ought to be built up of X-ray transparent electrons and impenetrable vacuum which is nonsense. Even if assuming the reality of Thomson scattering, this would manifest itself in the transmitted beam as an absorbing effect because the energy bundle coming in at a narrow steric angle, would be dispersed in all directions at steric angle 4π. So, this would not make a system complementary to that of "opaque" electrons and its diffraction power would be only a fraction of that of absorbing and Compton-scattering electrons. Babinet's principle excludes the co-existence of absorbing and incoherently scattering electrons with those radiating coherently.

In the literature we often find a quantum-mechanical interpretation of Thomson scattering stating that in this type of scattering process the final and the initial states of the atom are equal. From this assumption we really obtain a Schrödinger equation which yields the (stationary) electron density of the atom. As seen before, the Fourier transform of this density results in accurate atomic amplitudes. But in our way of thinking, there is a very simple explanation why this form of the Schrödinger equation holds for coherent scattering. The constancy of state suggests the absence of any physical interaction between the atom and the incident as well as the scattered photons during unmodified scattering. For this reason the unmodified scattering is not sensitive for small variations of the energy states and depends primarily on the mean charge distribution in space. The name of the atomic amplitudes used earlier, namely the "atomic form factor" is quite correct.

It is invariably correct to compose the extinction cross-section of three terms, namely the absorption (photo effect), the modified (Compton), and the unmodified scattering, since all the three cause a certain attenuation in the flux of photons penetrating a sample. The use of the notion "total" scattering in the sense that it would express an inherent scattering power of electrons or atoms, can be criticized; instead of this, the analogies between absorption and Compton scattering ought to be better emphasized under a collective term, since both of them are consuming — totally or partially — the energy of the impacting photons. These processes together determine the attenuation of incident beam by collisions which is, so to say, copied or doubled by the unmodified scattering or, in other terms, by the Huygens principle. A similar phenomenon in the scattering of visible light is known and called the "extinction paradox" [3]. Accepting such a "cause and effect" relationship between modified and unmodified scattering, respectively, it is easier to understand the applicability of a common scattering cross-section and polarization factor for both types. It must be elucidated, however, in what manner the absorption cross-section could be added to that of Compton scattering in order to yield the accurate intensity of unmodified scattering (with or without correction for anomalous scattering).

An optical analogy should be given in order to verify the lack of any sophistication in the proposed model of unmodified X-ray scattering. This analogy should especially demonstrate that modified scattering, in spite of its irregular statistical character, can be the cause which gives rise to coherent scattering and diffraction phenomena. When preparing an optical grating by scratching parallel grooves in the smooth surface of a glass or metal plate, we spoil intentionally the homogeneous refractivity or reflectivity of the surface and create there new, irregular surfaces which scatter light irregularly, so to say, incoherently. One certainly could detect the distribution and intensity of this scattered light by the aid of a suitably situated and moved photometer. However, for the user of a grating spectrograph these data are quite irrelevant, important is for him the spectrum alone formed by Fraunhofer diffraction of the light which passes the undisturbed parts of the glass or metal plate. Nevertheless without the grooves scattering irregularly, Fraunhofer diffraction would not take place at all.

There is, however, a section within the discipline of X-rays where the treatment of scattering is similar to that proposed above, from the very beginning of studies and this is the small-angle scattering of X-rays (SAXS). In all papers and textbooks dealing with SAXS, we find that the intensity of small-angle scattering caused by colloidal particles of mean electron density ϱ_1 and floating in a solvent of electron density ϱ_0 is proportional to the difference $(\varrho_1 - \varrho_0)^2$. This means that the intensity is independent of the sign of the electron density difference. To explain this independence, all authors refer to Babinet's principle (see e.g. [4]).

In spite of existing analogies, our allusions to optical gratings and to Huygens's principle are not sufficient to interpret X-ray diffraction. We find some more results in optics offering further analogies with X-rays and a deeper understanding of their unmodified scattering.

3. The light scattering theory of three-dimensional particles

Devices used for producing diffraction with visible light are mostly two-dimensional which means that their thickness can be neglected in comparison with the two other dimensions. The intensity of light diffracted by them vanishes at the limiting angle $\pi/2$, i.e. there is no amplitude and intensity "backwards". This behaviour has been explained theoretically by KIRCHHOFF [2]. On the other hand, scattered and diffracted X-rays can be observed in the whole space around the scattering object, the limiting angle for them is π. One can understand this difference in behaviour considering that X-ray diffraction rests on scattering by single electrons which by no means can be regarded as two-dimensional obstacles for X-photons.

Fortunately, the scattering of visible light by small, three-dimensional particles is also an important phenomenon of nature (dust and water droplets in the atmosphere, cosmic dust in space, colloidal sols, etc.), its theory has therefore been developed, too. Because of mathematical problems, exact theories could be worked out only for some idealized limiting cases. Prominent among them is Mie's theory on scattering by small, spherical, conducting particles of infinitely high electric conductance, and dielectric particles of similar shape and infinitely high relative permittivity. It has also been known from experience that the average intensity and its distribution in space very strongly depend on the ratio of the radius of (spherical) particle to the wavelength of radiation. On this basis several types and ranges of light scattering by small particles are distinguished and named after their discoverers: RAYLEIGH, MIE and TYNDALL.

The important paper of MIE published in 1908 (see [2]) gives exact solutions for the intensities, polarization state, and angular distribution of scattered light as functions of the ratio sphere radius/wavelength. Mie's theory has been based upon the Maxwell field equations and starts from the transition conditions of electric and magnetic field vector components at the boundary surfaces between vacuum and the conductive (isolating) particle. The solutions of field equations with the proper limiting conditions yield, without any assumptions in addition, the accurate description of scattering. It is a very important fact from the point of view of our subject that Mie's final formulas proved to be identical with those describing the emitted radiation of an oscillating electric dipole. The identical formulas reflect, however, two very different physical processes. Two of the results of Mie's theory shall be emphasized.

i) The spatial intensity distribution and polarization of light scattered by very small spheres ($R/\lambda \sim 10^{-3}$) are exactly equal to those given by Thomson for the X-ray scattering of the free electron. This type of scattering is characteristic for the Rayleigh range which means that Mie's theory contains the Rayleigh scattering as a marginal case but without assuming vibrating dipoles.

ii) With increasing radius of the sphere, the forward—backward symmetry of intensity distribution is gradually distorted in favour of the forward direction. This type of scattering is characteristic for spheres whose diameter is commeasurable with the wavelength. The asymmetry of intensity is called, in a narrow sense, the Mie effect. The intensity vs angle curves of spheres in the Mie range exhibit striking likeness to those of the coherent scattering of the hydrogen atom and all the other atoms. The analogy can be continued with the optical scattering of still larger spheres and SAXS by dilute solutions of macromolecules.

We must note on this analogy that according to the Mie theory, the total amount of scattered light very strongly increases with the diameter of

sphere. On the other hand, the X-ray scattering power of the atoms varies with the atomic number, i.e. each electron contributes to it equally (1 e.u.), independently of the dimensions of its cloud. This difference seems to upset the analogy between the two processes. However, one must take into account that in the Mie theory, the spheres are naturally thought of as uniformly filled with the scattering material; the scattering mass increases therefore as the third power of the radius. The electronic clouds in the atoms, however, represent always one unity of charge obtained as the volume integral of each separate cloud independently of its radius. That means that the difference lies in the preconditions, not in the scattering mechanism.

Generally speaking, the analogies cannot be dealt with as identities between light scattering caused by small, though finite spheres of well-conducting metal and X-ray scattering caused by an elementary particle. However, we feel that these analogies can turn out to be more far-reaching and more productive than those with oscillating dipoles. A successful adaptation of the Mie theory to the unmodified X-ray scattering would mean at the same time that the formal principle of Huygens could be replaced by the principles of electrodynamics.

4. Interpretation of the anomalous scattering

In Section 3 of [1] we alluded to anomalous scattering (in other terms: dispersion) treated by the Thomson theory as forced vibrations of strongly bonded electrons in the vicinity of points of resonance. But if one rejects the fundamental assumption on harmonically oscillating, "almost free" electrons, then its extension to bonded ones must be discarded too.

We propose again to follow the line of thought: Compton scattering and "true" absorption → Huygens's principle → Babinet's principle → unmodified scattering and diffraction. According to Section 2, one can consider in general the unmodified atomic scattering as a peculiar "shadow" effect caused by the two main types of photon — electron collisions, namely Compton scattering and true absorption of average probability. In the simple case each electron exhibits practically the same collision cross-section for the incident photons. If, however, the photon energy falls in the vicinity of a K, L, or M excitation potential of the atom, then the absorption cross-section of the excitable electrons increases by some orders of magnitude. So long as the increments are not very big, these electrons will simply add an increased contribution to the mean amplitude and intensity. But if the "opacity" of such electrons exceeds very much the average value, the effect must change sign, so that the amplitude scattered by them is being subtracted from the sum of the others (Babinet's principle); in this case the anomalous intensity will be lower

than the normal one. Thus, we can understand at least qualitatively both positive and negative amplitude corrections. Deduction of quantitative formulas, and explanation of the imaginary, phase-correction term may be a future task.

5. Compton scattering of the atoms and the Klein—Nishina formula

In Section 4, [1] we have criticized the procedure by which Compton scattered intensities of the atoms are obtained as the difference of "total" scattering and unmodified scattering. Our suggestion is to derive the atomic modified intensities directly from the states of the electrons without the use of the ambiguous notion of "total" scattering power.

The formulas of KLEIN and NISHINA (1928) [5], [6], [7], accurately giving the Compton cross-sections of electrons as functions of the scattering angle 2θ, and the photon energy $h\nu_0$, respectively, are well known in quantum mechanics and quantum electrodynamics. The initial value of all these functions for $2\theta = 0$ is given as exactly equal to the Thomson cross-section 7.94×10^{-30} m^2/steradian. With increasing angle, the runs of the curves are very much different depending on the photon energy as parameter. For those above 1 MeV, the scattering cross-section decreases monotonously with increasing angle towards a minimum value at $2\theta = 180°$, the minimum being the lower, the higher is the photon energy. The curves pertaining to photon energies below 1 MeV all exhibit a shallow minimum at $2\theta = 90°$ tending to a second maximum at $2\theta = 180°$. Finally, in the energy range of $\sim$0.01 MeV, the second maximum becomes equal to the initial value, the minimum is equal to their half value and the curves get a symmetrical shape around the minimum. X-rays used for diffraction purposes belong to this range and the shape of their Klein—Nishina curves looks similar to the intensity curve of the free electron according to Thomson: it is given by $(1 + \cos^2 2\theta)/2$. This fact is usually commented on so that for soft X-rays the Klein—Nishina theory reproduces Thomson's theory.

In the opinion of the present author, this comment is erroneous and prepossessed in favour of the Thomson theory, considering that Thomson scattering is perfectly unmodified while the results of Klein and Nishina are valid jointly with those of Compton on modified energy and momentum. The coincidence between the two curves reflects, however, the parallelism of two types of scattering, at least for the case of the free electron where the unmodified cross-section is a "copy" of the modified one as stated above. But according to Section 4 [1] the notion of Thomson scattering has to be replaced by the scattering of Rayleigh—Mie.

The Klein—Nishina formulas apply to scattering by free electrons, there-

fore the modified scattering functions of atoms do not obey them. As already seen, all of them have the initial value zero for $2\theta = 0$ and, gradually increasing, they tend towards Z e.u. without actually reaching it. In other terms, the electrons — those in the K-shell excepted — have the tendency to contribute to Compton scattering by 1 unit but cannot reach this limit below certain values of the scattering angle. This fact can easily be understood from the bound state of the electrons. In contrast to free electrons, there must be a minimum amount of kinetic energy for each atomic electron to be ejected from its orbit. The amount is given by the ionization energy for that orbit or the excitation potential for one of the spectral lines. The necessary energy transfer together with momentum transfer define a minimum Compton scattering angle for each orbit below which the energy transfer by the Compton mechanism would be too low. The total Compton cross-section of an atom of number Z is composed of Z terms which begin to rise from zero at different scattering angles depending on the potential energies of the electrons which they belong to. The superimposition of such terms must result in a gradual rise of the Compton intensity curve in accordance with experience. We have seen that the Compton scattering curve of the H-atom grows abruptly from 0 to 1, also affirming our assumption.

The interaction between an electron and a photon not meeting the condition for Compton scattering, can follow one of two other ways. i) The photon is either totally absorbed by inelastic collision (photoelectric effect, fluorescence excitation), or, ii) scattered without appreciable energy transfer and loss of momentum by an elastic collision with the atom as a whole. We should not call it simply the elastic collision as opposed to the "inelastic" Compton effect as they are sometimes referred to, because both of them are elastic in the sense of the analogous collisions in mechanics with conservation of kinetic energy and momenta. The difference between them consists in the relative masses of the partners colliding with the photon. The assumption of the eventual existence of elastically scattered unmodified photons does not mean that they would be thought of as the components of unmodified scattering and diffraction by the macroscopic sample. This would contradict the argumentation of this paper.

6. Conclusions

6.1. All interactions (collisions) between the photons of an incident X-ray beam and the atoms viz. electrons of a material sample are governed by the laws of quantum mechanics. The energy and the direction of emitted or scattered secondary X-rays cannot be independent of the energy states of the atoms and of the incident radiation. On the other hand, they can be neither influenced, nor determined by the intensity of the unmodified scattering of the

sample which, on its part, obeys very well the laws of classical electromagnetic wave theory.

6.2. X-rays produced by traditional methods in common diffraction and spectroscopic laboratories are, by nature, neither definitely coherent, nor incoherent. All available primary and secondary X-rays are capable of producing diffraction on a sample if the latter is separated by a certain distance from the source of rays and the conditions for Fraunhofer diffraction are fulfilled in the measuring equipment.

6.3. The atoms and/or electrons do not emit classical electromagnetic dipole radiation under the influence of incident waves. Their ability to scatter unmodified X-rays can be explained by the analogy with optical Rayleigh scattering of small particles in the interpretation of Mie. The final equations of Mie are formally identical with those of an oscillating dipole but their physical content is different; they describe the intensity distribution of waves not penetrating into the particle, yet forced to change direction.

6.4. In general, the production of unmodified scattering and diffraction patterns by single atoms or bulk specimens is explained by the Huygens—Fresnel principle applied to a perturbed coherent X-ray beam, the perturbations being caused by the electrons opaque for the X-rays. The opacity of electrons follows from their Compton scattering and absorbing property. Thus, the two latter processes can be considered as the cause, and unmodified scattering and diffraction as effects, but not the other way round.

6.5. The "total" scattering power of the electron cannot be accepted as an inherent capability of the electron. This notion amalgamates two types of scattering whose physical origin is very different. The Compton scattering cross-sections of the atoms ought to be deduced independently, by the use of the Klein—Nishina formulas and the energy levels of the atoms. This, together with the "true" absorption cross-section makes a "total" consisting of the effects of elastic and inelastic photon—electron collisions. This kind of total colliding cross-section can be thought of as doubled by unmodified scattering (via Huygens's principle). The opacity of electrons being an unquestionable fact, the Babinet principle of optics makes the assumption on their simultaneous radiating property redundant and impossible as well.

6.6. In spite of all the above criticism, neither the results of X-ray diffraction studies, nor the experimental and mathematical methods leading to them, are disputed by the present author. The intention of this paper is to start a process of collective thinking over the theoretical foundations of this very important and productive discipline.

The ideas set forth in this paper might appear primarily in teaching. In certain details, however, they may lead to practical consequences. Certainly there are some statements, mathematical derivations, and practical recommendations in the literature on X-rays which have been generally accepted

but not really verified by experiments and which had been inferred from the Thomson model taken too literally.

6.7. The suggested change of attitude to X-ray diffraction should be followed by a critical survey of theoretical functions and equations utilized in everyday X-ray studies. Such a work could clear up which of the equations and functions should remain unvariable, changing only the verbal explication of their contents, and which of them should be subjected to some alterations in the qualitative or quantitative sense of the word.

Acknowledgements

The author wishes to express his gratitude to Prof. F. KÁROLYHÁZY for revising and discussing two versions of the paper in an instructive and encouraging manner, and to Dr. J. BERGOU for similar help, and for his detailed remarks on the first version initiating essential changes and improvements in the argumentation. Prof. G. SCHAY is gratefully thanked for reading and correcting the manuscript and Dr. G. JALSOVSZKY for revising the English of the text. Thanks are due also to Dr. G. HERMS (Rostock, GDR) for his advice on the final improvements to the text.

REFERENCES

1. F. HAJDU, Acta Phys. Hung., **52**, 59, 1982.
2. M. BORN and E. WOLF: Principles of Optics Pergamon Press, London, New York, Paris, Los Angeles 1959, Chapter XIII.
3. H. C. VAN DE HULST, Light Scattering by Small Particles, John Wiley and Sons, Inc., New York, Chapman and Hall, Ltd., London, 1957, Chapter 8.
4. A. GUINIER, X-Ray Diffraction in Crystals, Imperfect Crystals, and Amorphous Bodies, W. H. Freeman and Company, San Francisco and London, 1963, Chapter 10.
5. International Tables for X-Ray Crystallography, edited by The International Union of Crystallography, The Kynoch Press, Birmingham, England, Volume IV, 1974, pp. 48.
6. W. HEITLER, A sugárzás kvantumelmélete (Quantum Theory of Radiation), Hungarian translation of the 3rd ed. Akadémiai Kiadó, Budapest, 1959, Chapter 5.
7. R. H. STUEWER, The Compton Effect — Turning Point in Physics, Science History Publications, New York, 1975.

Acta Physica Academiae Scientiarum Hungaricae, 52 (1), pp. 89—98 (1982)

THE WATANABE MODEL FOR ^{6}LI-NUCLEUS OPTICAL POTENTIAL

A. RABIE,* M. A. EL-GAZZAR**
INTERNATIONAL CENTRE FOR TEHORETICAL PHYSICS, TRIESTE, ITALY
and
A. Y. ABUL-MAGD
PHYSICS DEPARTMENT, FACULTY OF MEDICINE, ABDULAZIZ UNIVERSITY, JEDDAH, SAUDI ARABIA

(Received in revised form 6. VIII. 1981)

Optical potentials for the scattering of ^{6}Li projectiles are calculated using the Watanabe model and an $\alpha + d$ cluster model wave function for ^{6}Li. Reasonable fits to the elastic differential cross section and vector polarization are obtained.

1. Introduction

Considering ^{6}Li as an alpha particle and a deuteron in S-state motion and each in its ground state, (WATSON [1]) modified the (WATANABE [2]) deuteron optical potential to give the central part of ^{6}Li optical potential in the form

$$V_{^6\mathrm{Li}}(r) = \int d\mathbf{R}\, |\psi(R)|^2 \left[V_\alpha \left(\left| \mathbf{r} - \frac{1}{3}\mathbf{R} \right| \right) + V_d \left(\left| \mathbf{r} + \frac{2}{3}\mathbf{R} \right| \right) \right], \qquad (1.1)$$

where V_α and V_d are the α- and deuteron-nucleus optical potentials, $\mathbf{R} = \mathbf{r}_d - \mathbf{r}$ and $\mathbf{r} = \frac{1}{3}\mathbf{r}_d = \frac{2}{2}\mathbf{r}_\alpha$ are the relative and centre of mass coordinates of ^{6}Li and $\psi(R)$ is the wave function of the internal motion of ^{6}Li which is taken as the wave function for the bound state at -1.47 MeV of the following potential,

$$\begin{aligned} V(R) &= V_0 \left[1 + \exp\left(\frac{R - R_0}{a} \right) \right]^{-1} + V_c(R), \quad R \geqslant R_{\mathrm{core}}\,, \\ V(R) &= \infty\,, \qquad\qquad\qquad\qquad\qquad\quad R < R_{\mathrm{core}}\,, \end{aligned} \qquad (1.2)$$

with the parameters $V_0 = -45.25$ MeV, $R_0 = 2.0$ fm, $R_{\mathrm{core}} = 1.25$ fm and $a = 0.7$ fm, WATSON [1] evaluated the integral (1.1) numerically. He used the calculated potential to generate satisfactorily the existing differential cross section of ^{6}Li elastically scattered by different targets.

* Permanent address: Physics Department, Faculty of Science, Mansoura University, Mansoura, Egypt
** Permanent address: Mathematics and Theoretical Physics Department, Atomic Energy Establishment, Cairo, Egypt

Then after existing data on the vector polarization **P** (WEISS et al [3]), a spin-orbit part is required in addition to the central part, given by (1.1). We have evaluated both the central part and the spin-orbit part using instead a simple harmonic oscillator wave function which has resulted in a single integral other than time consuming double integral. Moreover, the choice of this simple wave function proved to be quite reasonable. The potentials calculated were used to generate both the differential cross section and vector polarization of the elastically scattered ^{6}Li projectiles showing a satisfactory fitting.

2. Potential calculation

a) *The central part*

Using the normalized ground state harmonic oscillator wave function

$$\psi(R) = \left(\frac{2\alpha}{\pi}\right)^{3/4} \exp\left(-\alpha R^2\right), \tag{2.1}$$

the potential, given by Eq. (1.1) becomes, after integrating over the angular dimensions and changing the variables,

$$V_{\mathrm{Li}}(r) = \frac{3}{r}\sqrt{\frac{2\alpha}{\pi}}\left[2\int_0^\infty \exp\left\{-18\alpha(\varrho^2+r^2)\right\} Sh(36\alpha\varrho r)\, V_\alpha(\varrho)\,\varrho\, d\varrho + \right.$$
$$\left. + \int_0^\infty \exp\left\{-9\alpha(\varrho^2+r^2)/2\right\} Sh(9\alpha\varrho r)\, V_d(\varrho)\varrho d\varrho\right]. \tag{2.2}$$

Using the oscillator cluster-model wave function:

$$\psi(R) = \frac{4\alpha}{\sqrt{15}}\left(\frac{2\alpha}{\pi}\right)^{3/4} R^2 \exp\left(-\alpha R^2\right) \tag{2.3}$$

the potential, given by Eq. (1.1), becomes:

$$V_{\mathrm{Li}}(r) = \frac{16a^2}{5r}\sqrt{\frac{2\alpha}{\pi}}\int_0^\infty \varrho\, d\varrho \left[V_\alpha(\varrho)\left\{\left[\left(81\,(r-\varrho)\right)^4 + \frac{1}{\alpha}\left(9(r-\varrho)\right)^2 + \frac{1}{2\alpha}\right)\right] \times \right.$$
$$\times \exp\left[-18\alpha(r-\varrho)^2\right] -$$
$$- \left[81(r+\varrho)^4 + \frac{1}{\alpha}\left(9\,(r+\varrho)^2 + \frac{1}{2\alpha}\right)\right] \exp\left[-18\alpha\,(r+\varrho)^2\right]\Big\} +$$
$$+ \frac{1}{2}V_d(\varrho)\left\{\left[\frac{81}{16}(r-\varrho)^4 + \frac{1}{\alpha}\left(\frac{q}{4}(r-\varrho)^2 + \frac{1}{2\alpha}\right)\right] \times \right. \tag{2.4}$$
$$\times \exp\left[-\frac{9\alpha}{2}(r-\varrho)^2\right] - \left(\frac{81}{16}(r+\varrho)^4 + \frac{1}{\alpha}\left(\frac{9}{4}(r-\varrho)^2 + \frac{1}{2\alpha}\right)\right) \times$$
$$\left.\left. \times \exp\left[-\frac{9\alpha}{2}(r+\varrho)^2\right]\right\}\right].$$

b) *The spin-orbit part*

Due to the lack of experimental data on the tensor polarization, we shall not consider the spin tensor components of the ^{6}Li optical potential. In this case, the nuclear potential will take the form:

$$V_{\mathrm{Li}}(r) = V_{\mathrm{Li}}(r) = V_{\mathrm{SO}}(r)(\mathbf{l} \cdot \mathbf{S}) \,. \tag{2.5}$$

Using the WATANABE [2] model, we have estimated the spin-orbit part, $V_{\mathrm{SO}}(r)$, averaging the d-spin-orbit interaction, $V_{\mathrm{SO}-d}(r_d)$, over the relative motion of the d- and α-clusters; i.e.

$$V_{\mathrm{SO}}(r) = \int |\psi(R)|^2 V_{\mathrm{SO}-d}(r_d)\, d\,\mathbf{R} \,. \tag{2.6}$$

Using the harmonic oscillator wave function (2.1) or (2.3) and using the approximate relation:

$$\int \psi(R, r)\mathbf{R}\, d\mathbf{R} \simeq \frac{\mathbf{r}}{r^2} \int \psi(R, r)\, \mathbf{r} \cdot \mathbf{R}\, d\mathbf{R} \tag{2.7}$$

we get

$$\mathbf{l} \cdot \mathbf{S}\, V_{\mathrm{SO}}(r) = \frac{1}{3} \int d\mathbf{R}\ |\psi(R)|^2 V_{\mathrm{SO}+d} \left(\left| \mathbf{r} + \frac{2}{3}\mathbf{R} \right| \right) \left(1 + \frac{2}{3} \frac{\mathbf{R} \cdot \mathbf{r}}{r^2} \right) \mathbf{L} \cdot \mathbf{S}_d, \tag{2.8}$$

where

$$L = -i\hbar\, (\mathbf{R}\, \Lambda\, \nabla_R) \,.$$

Taking $V_{\mathrm{SO}-d}$ in the Thomas form; i.e.

$$V_{\mathrm{SO}-d}(r) = U_{\mathrm{sdo}} \frac{1}{r} \frac{d}{dr} f_d(r) \,, \tag{2.9}$$

we get

$$\mathbf{l} \cdot \mathbf{S}\, V_{\mathrm{SO}}(r) = \frac{1}{3} U_{\mathrm{sdo}} \frac{1}{r} \frac{d}{dr} f_{\mathrm{Li}}(r)\, \mathbf{L} \cdot \mathbf{S}_d \,, \tag{2.10}$$

where

$$f_{\mathrm{Li}}(r) = \int |\psi(R)|^2 f_d(r_d)\, d\mathbf{R} \tag{2.11}$$

and f_a is the real part of the deuteron nuclear potential. Eq. (2.10) means that if the deuteron spin-orbit potential is of a Thomas form with strength U_{sdo}. the ^{6}Li spin-orbit potential will also take the Thomas form but with a strength reduced to 1/3 U_{sdo} a result supporting the frequently expected smaller spin-orbit potential the heavier the projectile is. The projectile mass number (A) dependence of the spin-orbit potential was investigated (AMAKAWA and KUBO [4]) with the result that the spin-orbit potential is almost proportional to A^{-2}.

Inserting, for $\psi(R)$, the form (2. 1) into Eq. (2.10) and changing the variables, we get

$$(\mathbf{l}\cdot\mathbf{S})V_{\mathrm{SO}}(r)=\sqrt{\frac{\alpha}{2\pi}}\,\frac{U_{\mathrm{sdo}}}{r^3}(\mathbf{L}\cdot\mathbf{S}_d)\left[\int_0^\infty \varrho d\varrho f_d(\varrho)\{(9\alpha r(\varrho-r)-1)+\right.$$
$$\left.+(9\alpha r(\varrho+r)+1)\exp(-18\alpha r\varrho)\}\exp[9\alpha(\varrho-r)^2/2]\right]. \tag{2.12}$$

Inserting, for $\psi(R)$, the form (2.3) into Eq. (2.10) and changing the variables, we get

$$(\mathbf{l}\cdot\mathbf{S})V_{\mathrm{SO}}(r)=\frac{16\alpha^{5/2}}{5r^3}(\mathbf{L}\cdot\mathbf{S}_d)\sqrt{\frac{2}{\pi}}\int_0^\infty \varrho d\varrho f_d(\varrho)\left[F_1(r-\varrho)+F_2(r+\varrho)\right], \tag{2.13}$$

where

$$F_1(r-\varrho)=r\left\{\left(\frac{81}{4}(r-\varrho)^3+\frac{9}{2\alpha}(r-\varrho)\right)-9\alpha(r-\varrho)\times\right.$$
$$\times\left(\frac{81}{16}(r-\varrho)^4+\frac{1}{\alpha}\left(\frac{9}{4}(r-\varrho)^2+\frac{1}{2\alpha}\right)\right)-(81(r-\varrho)^4+$$
$$\left.+\frac{1}{\alpha}\left(9(r-\varrho)^2+\frac{1}{2\alpha}\right)\right)\Big\}\exp[-9\alpha(r-\varrho)^2]$$

and

$$F_2(r+\varrho)=\left\{\frac{81}{16}(r+\varrho)^4+\frac{1}{\alpha}\left(\frac{9}{4}(r+\varrho)^2+\frac{1}{2\alpha}\right)-r\left(\frac{81}{4}(r+\varrho)^3+\right.\right.$$
$$+\frac{9}{2\alpha}(r+\varrho)\Big)+9\alpha r(r+\varrho)\left(\frac{81}{16}(r+\varrho)^4+\right.$$
$$\left.\left.+\frac{1}{\alpha}\left(\frac{9}{4}(r+\varrho)^2+\frac{1}{2\alpha}\right)\right)\right\}\exp[-9\alpha(r+\varrho)^2].$$

3. Results and discussion

We have calculated the integral in Eqs. (2.4) and (2.12) for a number of targets with the value $\alpha=0.096$ fm^{-2} which gives a root mean square (rms) for ^{6}Li equal to that given by the electron scattering data $\langle r^2\rangle_{\mathrm{Li}}^{1/2}=$ $=2.3$ fm. (Burleson and Hofstadter [5], Jackson [6]). Using for the potentials V_α, V_d and V_{sod}, the phenomenological α- and d-nucleus optical potentials at $E_d=\frac{2}{3}E_{\mathrm{Li}}$ and $E_d=\frac{1}{3}E_{\mathrm{Li}}$.

For the optical potentials, we have used Woods—Saxon parametrization of the form

$$V(r) = -V_0 f(X_0) + \lambda_\pi^2 U_{SO} \mathbf{l}\cdot\mathbf{S} \frac{1}{r}\frac{d}{dr} f(X_{SO}) - i\left(Wf(X_w) 4 W_D \frac{d}{dx_D} f(\bar{X}_D)\right), \tag{3.11}$$

where

$$f(x_i) = [1 + \exp(X_i)]^{-1}, \quad x_i = (r - r_i A^{1/3})/a_i$$

and

$$\lambda_\pi^2 = 2.0 \text{ fm}.$$

As an example, we present here the potential for the elastic scattering ^{6}Li + ^{58}Ni at $E_{Li} = 22.8$ MeV. The potential parameters used are listed in Table I.

For the parameters of the spin-orbit potential, the geometrical parameters are taken to be the same as those of the central real part of the d-^{58}Ni scattering potential while the strength is taken as a free parameter.

To see the effect of different forms of $\psi(R)$ on the folding procedure, we have plotted the folded potential for the form (2.1) with $\alpha = 0.096$ fm^{-2} and for the form (2.3) with $\alpha = 0.11$ fm^{-2}. Fig. 1 shows the folded potentials for ^{6}Li compared with the Woods—Saxon potentials used to fit the same data (WEISS [3]) from which the former is seen deeper than the latter. This makes one expect a deeper potential for averaging over the internal motion of individual nucleons than the α-p-n than the α-d folded potential. Different internal wave functions have the result of approximate coincidence until $r = 5.5$ fm, then deviate more and more at larger distances. It is then expected that different wave functions will affect the elastic scattering differential cross section.

The potentials calculated for ^{6}Li-nucleus scattering have been used to produce the elastic scattering cross section and the vector polarization p of ^{6}Li projectiles. The results of the ratio σ/σ_R and $\mathbf{P}$ are compared with the experimental data (WEISS [3]) for $E_{Li} = 22.8$ MeV incident on ^{12}C, ^{16}O, ^{28}Si and ^{58}Ni in addition to the results for ^{12}C at $E_{Li} = 20$ MeV.

Table I

Optical potential parameter sets for $\alpha(d)$—^{53}Ni scattering*

	E_{lab} (MeV)	V	r_0	a_0	W	W_D	r_w	a_w
α + ^{58}Ni	21	180.7	1.37	0.56	21.9	0.0	1.37	0.56
α + ^{58}Ni	11.8	106.1	1.07	0.81	0.0	16.6	1.36	0.63

* The data are from PEREY and PEREY [7].

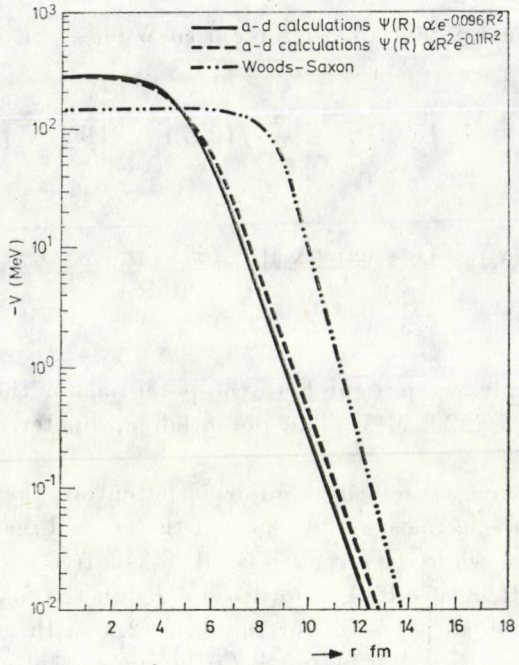
a-d calculations Ψ(R) ∝e^-0.096R^2
a-d calculations Ψ(R) ∝R^2e^-0.11R^2
Woods-Saxon
-V (MeV)
r fm

Fig. 1a

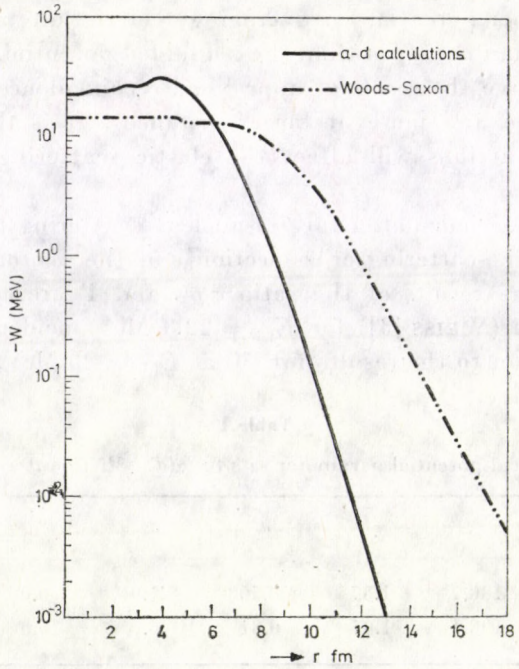
a-d calculations
Woods-Saxon
-W (MeV)
r fm

Fig. 1b

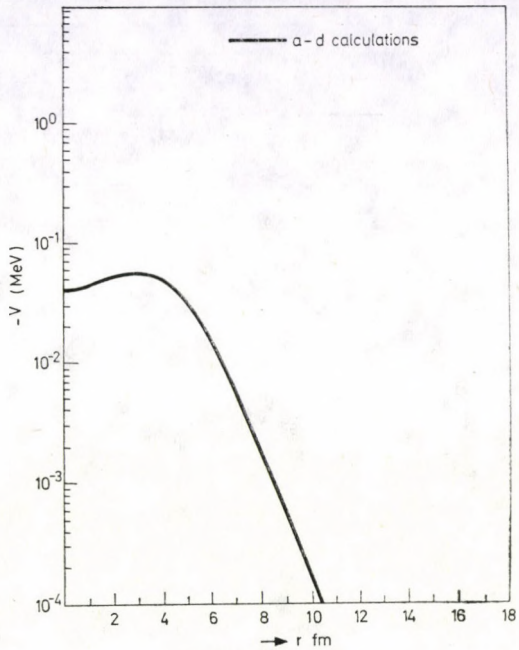

Fig. 1c

Fig. 1. The radial dependence of the calculated ^{6}Li—^{58}Ni folded optical potential. a) The real part calculated with two different wave functions and compared with the Woods—Saxon potential used to fit the same scattering data. b) The imaginary part compared with the Woods—Saxon and c) The spin-orbit potential part

Figs. 2 and 3 show the results of calculations with two different internal wave functions for ^{6}Li given by Eqs. (2.1) and (2.3). The gross structure, in the sense that the diffraction feature which tends to a structureless limit as the target nucleus gets heavier, is reasonably produced. However, it is to be noted that the results of calculations with the wave function (2.1) describe better the experimental data, especially the polarization p, than do the results of calculations with the wave function (2.3).

One must, however, take caution. If we remember that the wave function parameter defines a rms radius, one may attribute the difference in results to different rms radii of one form or to different forms with one rms radius. To avoid this puzzle, we present the results of calculation with the two forms of $\psi(R)$ given by Eqs. (2.1) and (2.3) having the same rms radius (2.8 fm) and the results of calculation with the form given by Eq. (2.3) having two different rms radii (2.8 and 3.99 fm). The results are shown for both the angular distribution of the ratio σ/σ_R and the vector polarization p for ^{6}Li—^{12}C and ^{6}Li—^{58}Ni scattering. Figs. 4 and 5 display the result which say that: while the differential cross section of elastic scattering cannot produce a definite answer, the vector polarization P is able to say that the difference in results is due to different

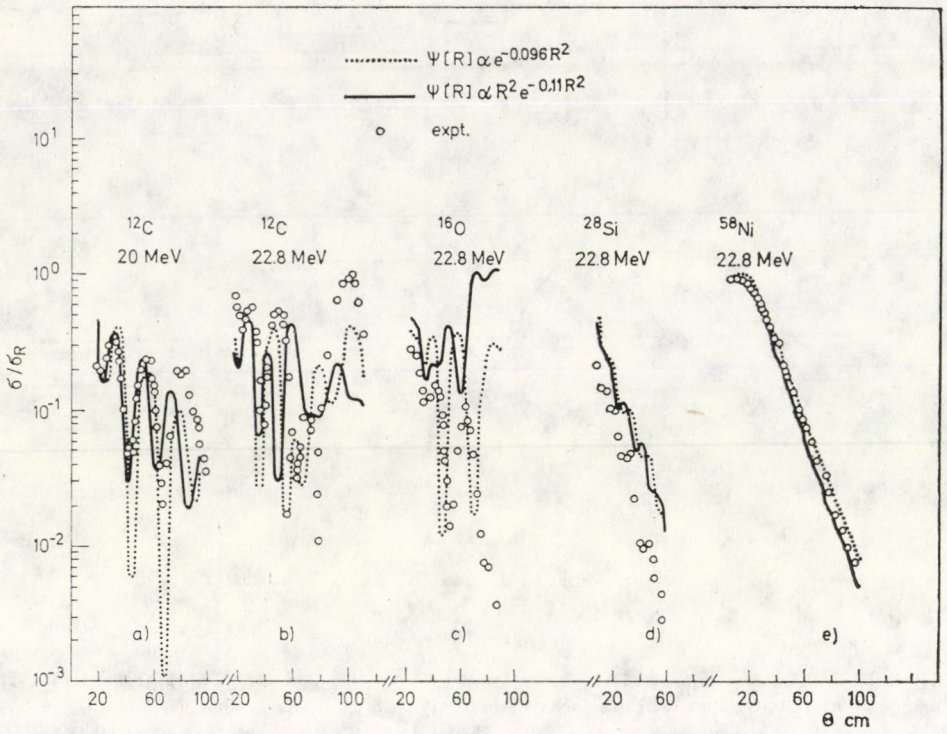

Fig. 2. The angular distributions of the ratio σ/σ_R calculated with two different wave functions for different targets and compared with the experimental data of WEISS [3]

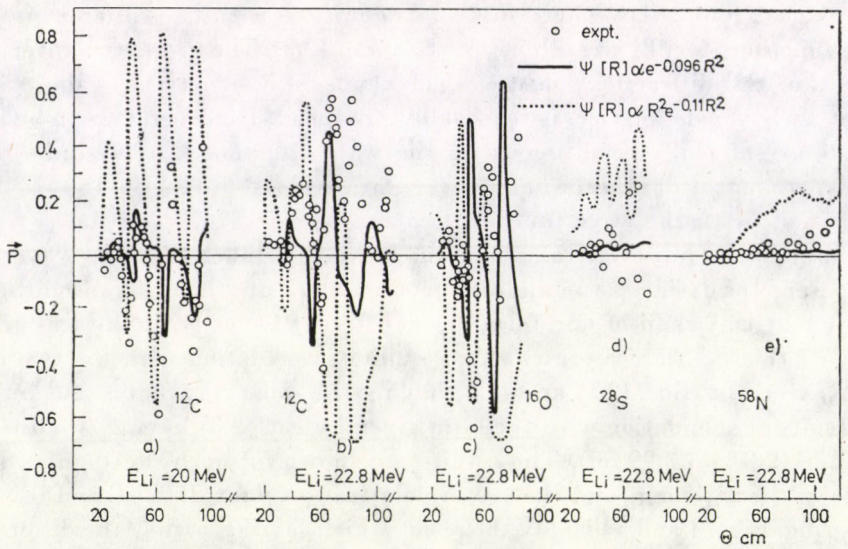

Fig. 3. The angular distributions or the vector polarization calculated with two different wave functions for different targets and compared with the experimental data

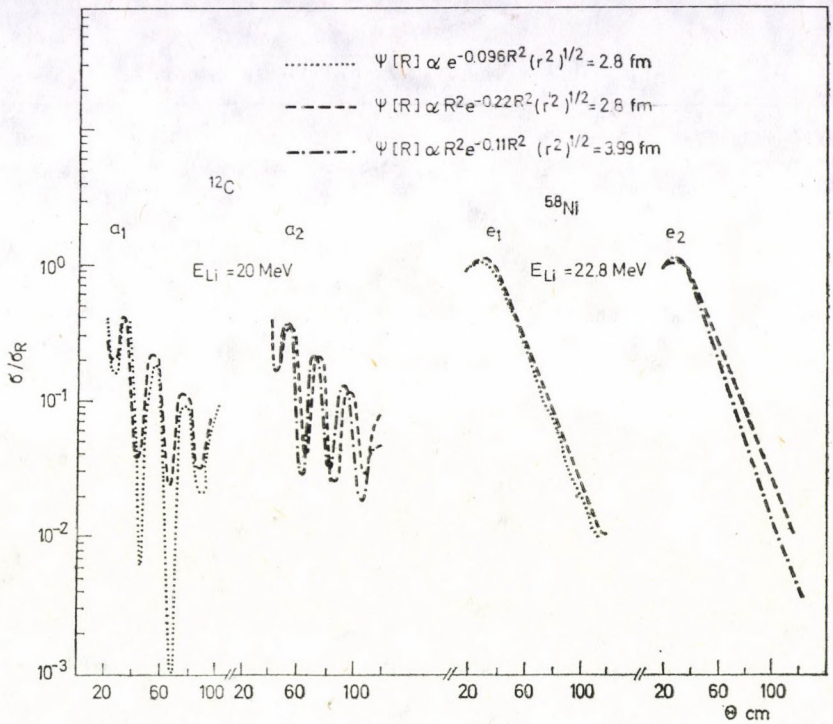

Fig. 4. The angular distributions of the ratio σ/σ_R for ^{6}Li—^{12}C and ^{6}Li—^{58}Ni scattering. Different wave functions with the same rms and the same wave function with different rms radii are compared

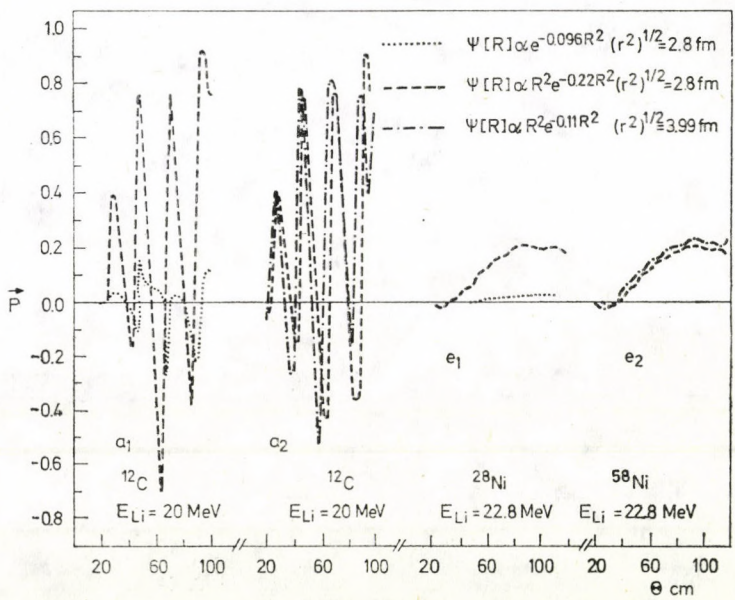

Fig. 5. The angular distributions of the vector polarization of ^{6}Li—^{12}C and ^{6}Li—^{58}Ni scattering. Different wave functions with the same rms radius and the same wave function with different rms radii are compared

Table II

Optical potential parameters for $\alpha(d)$-nucleus scattering*

E_{Li} (MeV) Target E_α (MeV)	20.0 ^{12}C		22.8 ^{12}C		22.8 ^{16}O		22.8 ^{28}Si		22.8 ^{58}Ni	
	23.0	6.67	16.0	7.0	17.2	7.8	18.7	8.0	11.8	21.0
V	185	103.2	125	130.1	150	118	121	117.4	180.7	106.1
r_0	1.4	1.05	1.97	0.9	1.93	1.0	1.55	1.05	1.37	1.07
a_0	0.52	0.8	0.5	0.9	0.5	0.6	0.52	0.912	0.56	0.807
W	25.0	9.58	0.0	11.0	0.0	0.0	17.5	0.0	21.9	0.0
W_D	0.0	0.0	1.5	0.0	7.5	4.9	0.0	19.7	0.0	16.6
r_W	1.4	1.28	1.97	2.1	1.93	1.9	1.55	1.69	1.37	1.35
a_W	0.52	0.755	0.5	0.6	0.5	0.6	0.52	0.46	0.56	0.629

* The date are from PEREY and PEREY [7].

forms of wave functions irrespective of their rms radii. For this reason it is unquestionable to compare the results of two forms with two different rms radii. Moreover, it is seen that the results of the form (2.1) are better than those given by the form (2.3). For this it is enough to use the form (2.1) in our calculations. The optical parameters used are listed in Table II.

We may conclude that:

1. Generally speaking, the WATANABE potential is affected by the choice of the form of the internal wave function of the projectile.

2. The differential cross section and vector polarization are not sensitive to the change in the value of the rms radius of the projectile but to the form of the internal wave function.

3. The vector polarization is more sensitive to the form of the wave function than is the differential cross section.

Acknowledgements

Two of the authors (A.R.) and (M. A. E-G.) would like to thank Professor ABDUS SALAM, the International Atomic Energy Agency and UNESCO for hospitality at the International Centre for Theoretical Physics, Trieste. The authors would like to thank Professor L. FONDA for reading the manuscript.

REFERENCES

1. J. W. WATSON, Nucl. Phys., **A198,** 129, 1972.
2. S. WATANABE, Nucl. Phys. **8,** 484, 1958.
3. W. WEISS et al, Phys. Letters, **61B,** 237, 1976.
4. H. AMAKAWA and K. I. KUBO, Nucl. Phys., **A226,** 521, 1976.
5. G. R. PURLESON and R. HOFSTADTER, Phys. Rev., **112,** 1182, 1958.
6. D. F. JACKSON, Proc. Phys. Soc., London, **76,** 949, 1960.
7. C. M. PEREY and F. G. PEREY, Atomic data and Nucl. data tables **17,** 1, 1976.

Acta Physica Academiae Scientiarum Hungaricae, 52 (1), pp. 99—111 (1982)

A CORRECTION TO ^{6}Li-WATANABE POTENTIAL

A. RABIE,* M. A. EL-GAZZAR**
INTERNATIONAL CENTRE FOR THEORETICAL PHYICS, TRIESTE, ITALY
and
A. Y. ABUL-MAGD
PHYSICS DEPARTMENT, FACULTY OF MEDICINE, ABDULAZIZ UNIVERSITY
JEDDAH, SAUDI ARABIA

(Received in revised form 6. VIII. 1981)

Using the adiabatic approximation, an analytic expression for the correction to ^{6}Li Watanabe potential is obtained. In addition, we have corrected this potential through a proper choice of the energy at which the potential parameters of the constituents of ^{6}Li, alpha and deuteron, should be taken. The elastic scattering differential cross section and vector polarization of ^{6}Li on ^{12}C, ^{16}O, ^{28}Si and ^{58}Ni are calculated with a corrected Watanabe potential. The results are compared with both experimental data and the calculated one with uncorrected Watanabe potential.

1. Introduction

Using the Watanabe folding model, one cannot intend to obtain a good fit to the elastic scattering data since no account for absorption modes is included in its formulation. WATSON [1] has improved the fit through the modification of the imaginary well. Using GLAUBER's [2] multiple-scattering theory, the correction to the Watanabe potential was calculated analytically for deuterons [3] and tritons [4]. We extended this method to the case of ^{6}Li with the result of the necessity to modify both the real and imaginary wells to improve the fitting of the calculated elastic scattering differential cross section of ^{6}Li on ^{12}C, ^{16}O, ^{28}Si and ^{58}Ni with the experimental data.

In addition, an analytic expression relating the proper energies of both the α- and d-clusters which are no longer 2/3 E_{Li} and 1/3 E_{Li}, respectively, was obtained. Taking the optical parameters of both the α- and d-nucleus scattering at the proper energies made some improvement in the fitting.

2. The analytical evaluation of the correction

In GLAUBER's theory, the scattering amplitude for a ^{6}Li projectile is given by.

$$F(\theta) = -iK \int \exp(i\mathbf{q} \cdot \mathbf{b}) \left[\langle \exp\{i(\mathbf{b}, \mathbf{s})\}\rangle - 1\right] d\mathbf{b}\,, \qquad (2.1)$$

* Permanent address: Physics Department, Faculty of Science, Mansoura University, Mansoura, Egypt

** Permanent address: Mathematical and Theoretical Physics Department, Atomic Energy Establishment, Cairo, Egypt

where the bracket $\langle\ \rangle$ denotes the average over the internal coordinates of ^{6}Li neglecting the internal motion of both the α- and d-clusters, $\mathbf{b}$ is the ^{6}Li impact parameter and $\mathbf{s}$ is the projection of the vector $\mathbf{r}_d$ in the plane perpendicular to the direction of incidence. The phase function is given by [2]

$$\chi(\mathbf{b}, \mathbf{s}) = \chi_\alpha\left(\mathbf{b} - \frac{1}{3}\mathbf{s}\right) + \chi_d\left(\mathbf{b} + \frac{2}{3}\mathbf{s}\right), \tag{2.2}$$

where

$$\chi_{\alpha(d)}(\mathbf{b}) = \frac{1}{\hbar v}\int_{-\infty}^{\infty} V_{\alpha(d)}\left(\{b^2 + Z^2\}^{1/2}\right) dZ \tag{2.3}$$

and v is the velocity of ^{6}Li projectiles. Let us define the ^{6}Li optical potential $V_{^6\mathrm{Li}}$ as the effective potential yielding a scattering amplitude identical with that given by Eq. (2.1), i.e.

$$\chi_{^6\mathrm{Li}}(\mathbf{b}) = -\frac{1}{\hbar v}\int_{-\infty}^{\infty} V_{^6\mathrm{Li}}\left([b^2 + Z^2]^{1/2}\right) dZ, \tag{2.4}$$

where

$$\exp\left\{i\chi_{^6\mathrm{Li}}(\mathbf{b})\right\} = \langle \exp\left\{i\chi(\mathrm{b}, \mathrm{s})\right\}\rangle. \tag{2.5}$$

GLAUBER [2] has used a similar definition for the optical-model phase shifts in his study of hadron-nucleus scattering.

Following GLAUBER, the solution of (2.5) is given by

$$i\chi_{^6\mathrm{Li}}(\mathbf{b}) = \sum_{n=1}^{\infty} \frac{i^n}{n!} K_n(\mathbf{b}), \tag{2.6}$$

where

$$\begin{aligned} K_1(\mathbf{b}) &= \langle\chi(\mathbf{b}, \mathbf{s})\rangle, \\ K_2(\mathbf{b}) &= \langle[\chi(\mathbf{b}, \mathbf{s}) - \langle\chi(\mathbf{b}, \mathbf{s})\rangle]^2\rangle, \\ K_3(\mathbf{b}) &= \langle[\chi(\mathbf{b}, \mathbf{s}) - \langle\chi(\mathbf{b}, \mathbf{s})\rangle]^3\rangle, \\ K_4(\mathbf{b}) &= \langle[\chi(\mathbf{b}, \mathbf{s}) - \langle\chi(\mathbf{b}, \mathbf{s})\rangle]^4\rangle - 3K_2^2(\mathbf{b}). \end{aligned} \tag{2.7}$$

If we ignore the distortion of ^{6}Li during scattering, we are left with the expansion (2.6) and $\chi_{^6\mathrm{Li}}$ will reduce to

$$\begin{aligned} \chi_{^6\mathrm{Li}}(\mathbf{b}) = \frac{-1}{\hbar v}\int |\psi(R)|^2 d\mathbf{R}\Bigg[\int_{-\infty}^{\infty} V_\alpha\left(\left\{\left(\mathbf{b} - \frac{1}{3}\mathbf{S}\right)^2 + Z_\alpha^2\right\}^{1/2}\right) dZ_\alpha + \\ + \int_{-\infty}^{\infty} V_\alpha\left(\left\{\left(\mathbf{b} + \frac{1}{3}\mathbf{S}\right)^2 + Z_d^2\right\}^{1/2}\right) dZ_d\Bigg]. \end{aligned} \tag{2.8}$$

Changing the variable z_α in the first integral inside the square bracket by $z' = z_\alpha + 1/3\, z$ and the variable z_d in the second integral by $z' = z_{d\alpha} + 2/3\, z$ and comparing with Eq. (2.4) we get

$$V^{(0)}_{^6\mathrm{Li}}(r) = \int |\psi(R)|^2\left[V_\alpha\left(\left|\mathbf{r} - \frac{1}{3}\mathbf{R}\right|\right) + V_d\left(\left|\mathbf{r} + \frac{2}{3}\mathbf{R}\right|\right)\right] d\mathbf{R}, \tag{2.9}$$

which is exactly equal to the Watanabe potential. If we express the ^{6}Li optical potential as

$$V_{^6\mathrm{Li}}(r) = V^{(0)}_{^6\mathrm{Li}}(r) + \delta V(r)\,, \tag{2.10}$$

then $\delta V(v)$ characterizes the contribution from the distortion and virtual disintegration of the ^{6}Li in the process of scattering.

Numerical studies with the Watanabe model [6, 7] concluded that corrections to the real part for deuterons are of the order of the leading term. Since the correction to the imaginary part is not expected to exceed the real Watanabe potential, we can safely assume the series (2.6) to converge so rapidly that the second term is sufficient for estimating the correction. In this case we have

$$-\frac{1}{hv}\int_{-\infty}^{\infty} \delta V\left([b^2+Z^2]^{1/2}\right)\,dZ \approx \frac{i}{2}\left\langle\left[\chi(\mathbf{b},\mathbf{s}) - \langle\chi(\mathbf{b},\mathbf{s})\rangle\right]^2\right\rangle. \tag{2.11}$$

To obtain an analytic expression for Eq. (2.11), we shall take both the α- and d-nucleus optical potentials of the Gaussian form

$$V_{\alpha(d)}(\mathbf{r}) = -(V_{0\alpha(d)} + iW_{0\alpha(d)})\exp\left(-r^2/r^2_{0\alpha(d)}\right). \tag{2.12}$$

Substituting Eqs. (2.12) and (2.3) into (2.6), we can, in principle, calculate $\chi_{^6\mathrm{Li}}(\mathbf{b})$ up to any order. The expression found in this way will consist of a superposition of Gaussian functions, and the corresponding Gaussian potential can be immediataly found due to the linearity of Eq. (2.4). If we restrict ourselves to the first two terms in Eq. (2.6), we find the following expressions for the Watanabe potential $V^{(0)}_{^6\mathrm{Li}}(r)$ and its correction $\delta V_{^6\mathrm{Li}}(r)$

$$V^{(0)}_{^6\mathrm{Li}}(r) = -U_{0\alpha}\left(\frac{r_{0\alpha}}{R_\alpha}\right)^3 \exp\left(-\frac{r^2}{R^2_\alpha}\right) - U_{0d}\left(\frac{r_{0d}}{R_d}\right)^3 \exp\left(-\frac{r^2}{R^2_d}\right), \tag{2.13}$$

where

$$R^2_\alpha = r^2_{0\alpha} + \frac{9}{2\alpha}, \quad R^2_d = r^2_{0d} + \frac{2}{9\alpha} \tag{2.14}$$

$$U_{0\alpha(d)} = V_{0\alpha(d)} + iW_{0\alpha(d)}$$

and

$$\begin{aligned}\delta V_{^6\mathrm{Li}}(r) = -i\sqrt{\frac{\pi}{2}}\,\frac{1}{\hbar v}\Bigg[&\frac{U^2_{0\alpha}\,r^4_{0\alpha}}{R'^3_\alpha}\exp\left(-2r^2/R^2_\alpha\right) + \\ &+ \frac{U^2_{0d}\,r^4_{0d}}{R'^3_\alpha}\exp\left(-2r^2/R'^2_d\right) + \frac{4r^2_{0\alpha}\,r^2_{0d}\,U_{9\alpha}\,U_{0\alpha}\,(r^2_{0\alpha}r^2_{0d}+1/2\alpha)^{1/2}}{(r^2_{0d}\,R'^2_\alpha + r^2_{0\alpha}\,R'^2_d)^{3/2}}\times \\ &\times\exp\left(-\frac{2(r^2_{0\alpha}+r'_{0d}+1/2\alpha)}{r^2_{0d}\,R'^2_\alpha + r^2_{0\alpha}\,R'^2_d}\,r^2\right) - (U^2_{0\alpha}r^6_{0\alpha}/R^5_\alpha)\exp\left(-2r^2/R^2_\alpha\right) - \\ &- (Ur^6_{0d}\,r^6_{0d}/R^5_{0d})\exp\left(-2\,r^2/R^2_d\right) - \frac{\sqrt{2}\,U_{0\alpha}\,U_{0d}\,r^3_{0\alpha}r^3_{0d}\,(R^2_\alpha+R^2_d)^{1/2}}{R^3_\alpha\,R^3_d}\times \\ &\times\exp\left\{-\left(\frac{1}{R^2_\alpha}+\frac{1}{R^2_d}\right)r^2\right\}\Bigg],\end{aligned} \tag{2.15}$$

where

$$R_\alpha'^2 = r_{0\alpha}^2 + 1/9\alpha \quad \text{and} \quad R_d'^2 = r_{0d}^2 + 4/9\alpha\,. \tag{2.16}$$

Using the expressions $J_{\alpha(d)} = \Pi^{3/2} r_{0\alpha(d)}^3\, U_{0\alpha(d)}$ and $\langle r^2\rangle_{\alpha(d)} = 3/2\; r_{0\alpha(d)}^2$ for the volume integral and mean square radius of the Gaussian potential (2.12) the volume integral and the mean square radius of the potential $V_{^6\mathrm{Li}}^{(0)}(r)$ and its correction $\delta V_{^6\mathrm{Li}}(r)$ are given by

$$J_{R\mathrm{Li}} = J_{R\mathrm{Li}}^W\big(1 - \alpha(E)\big),\quad J_{I\mathrm{Li}} = J_{I\mathrm{Li}}^W\big(1 + \beta(E)\big),$$

where

$$J_{R\mathrm{Li}}^W = J_{R\alpha} + J_{Rd}\,,\quad J_{I\mathrm{Li}}^W = J_{I\alpha} + J_{Id}\,,$$

$$\alpha(E) = \frac{3\langle r_{\alpha d}^2\rangle}{4\pi\hbar v J_{R\mathrm{Li}}^W}\left[\frac{J_{I\alpha}J_{R\alpha}}{9\langle r^2\rangle_\alpha\left(\langle r^2{}_\alpha\rangle + (1/9)\langle r_{\alpha d}^2\rangle\right)} + \right.$$
$$+ \frac{4\,J_{Rd}J_I}{9\langle r^2\rangle_d\langle r^2\rangle_d + (4/9)\,\langle r_{\alpha d}^2\rangle} -$$
$$\left. - \frac{8(J_{R\alpha}J_{Id} + J_{Rd}\,J_{I\alpha}}{9(\langle r^2\rangle_\alpha + \langle r^2\rangle_d + \langle r_{\alpha d}^2\rangle)\,(\langle r^2\rangle_\alpha + \langle r^2\rangle_d + \langle r_{\alpha d}^2\rangle)}\right] \tag{2.17}$$

and

$$\beta(E) = \frac{3\langle r_{\alpha d}^2\rangle}{8\,\pi\hbar v\, J_{I\mathrm{Li}}^W}\left[\frac{J_{R\alpha}^2 - J_{I\alpha}^2}{9\,\langle r^2\rangle_\alpha\big(\langle r^2\rangle_\alpha + (1/9)\,\langle r_{\alpha d}^2\rangle\big)} + \right.$$
$$+ \frac{4(J_{Rd}^2 - J_{Id}^2)}{9(\langle r^2\rangle_d + (4/9)\,\langle r_{\alpha d}^2\rangle)\,\langle r^2\rangle_d} -$$
$$\left. - \frac{8J_{R\alpha}J_{Rd} - J_{I\alpha}J_{Id})}{9(\langle r^2\rangle_\alpha + \langle r^2{}_d\rangle + \langle r_{\alpha d}^2\rangle)\,\big(\langle r^2\rangle_\alpha + \langle r^2\rangle_d + (5/9)\,\langle r_{\alpha d}^2\rangle\big)}\right], \tag{2.18}$$

$$\langle r_R^2\rangle_{\mathrm{Li}} = \langle r_R^2\rangle_{\mathrm{Li}}^W\big(1 - \gamma(E)\big),$$

where

$$\langle r_R^2\rangle_{\mathrm{Li}}^W = \frac{1}{J_{R\mathrm{Li}}}\left[J_{R\alpha}\langle r^2\rangle_\alpha + J_{Rd}\langle r^2\rangle_d + (1/9)\,(J_{R\alpha} + 4J_{Rd})\langle r_{\alpha d}^2\rangle\right],$$

$$\gamma(E) = \frac{3}{8\pi\hbar v\, J_{R\mathrm{Li}}\langle r_R^2\rangle_{\mathrm{Li}}^W}\left[\frac{2J_{R\alpha}J_{I\alpha}\langle r_{\alpha d}^2\rangle}{9\langle r^2\rangle_\alpha} + \frac{8J_{Rd}J_{Id}\langle r_{\alpha d}^2\rangle}{9\langle r^2\rangle_d} + \right.$$
$$+ \frac{4(J_{R\alpha}J_{Id} + J_{I\alpha}J_{Rd})\big[\langle r^2\rangle_\alpha\langle r^2\rangle_d + (1/9)\,\langle r_{\alpha d}^2\rangle\,(\langle r^2\rangle_d + (4\langle r^2\rangle_\alpha)\big]}{(\langle r^2\rangle_\alpha + \langle r^2\rangle_d + \langle r_{\alpha d}^2\rangle)^2}\Big] -$$
$$\left. - \frac{4\,(J_{R\alpha}J_{Id} + J_{I\alpha}J_{Rd})\big[\langle r^2\rangle_\alpha + (1/9)\,\langle r_{\alpha d}^2\rangle\big]\big(\langle r^2\rangle_d + (4/9)\,\langle r_{\alpha d}^2\rangle\big)}{\big[\langle r^2\rangle_\alpha + \langle r^2\rangle_d + (5/9)\langle r_{\alpha d}^2\rangle\big)^2}\right], \tag{2.19}$$

Also

$$\langle r_I^2\rangle_{\mathrm{Li}} = \langle r_I^2\rangle_{\mathrm{Li}}^{W}\left(1-\delta(E)\right),$$

where

$$\langle r_I^2\rangle_{\mathrm{Li}}^{W} = \frac{1}{J_{I\mathrm{Li}}}\left[J_{Ia}\langle r^2\rangle_\alpha + J_{Id}\langle r^2\rangle_d + (1/9)\left(J_{I\alpha}+4J_{Id}\right)\langle r_{\alpha d}^2\rangle\right],$$

and

$$\delta(E) = \frac{3}{16\,\hbar\pi v\, J_{I\mathrm{Li}}\langle r_I^2\rangle^{W}}\left[\frac{2\langle r_{\alpha d}^2\rangle\left(J_{R\alpha}^2 - J_{I\alpha}^2\right)}{9\langle r^2\rangle_\alpha} - \frac{8\langle r_{\alpha d}^2\rangle\left(J_{Ra}-J_{Id}^2\right)}{9\langle r^2\rangle_d} + \right.$$

$$+\frac{8\left(J_{R\alpha}J_{Rd}-J_{I\alpha}J_{Id}\right)\left[\langle r^2\rangle_d\langle r^2\rangle_\alpha + (1/9)\langle r_{\alpha d}^2\rangle\left(\langle r^2\rangle_d + 4\langle r_\alpha^2\rangle\right)\right]}{\left(\langle r^2\rangle_\alpha + \langle r^2\rangle_d + \langle r_{\alpha d}^2\rangle\right)^2} -$$

$$\left. -\frac{8\left(J_{R\alpha}J_{Rd}-J_{I\alpha}J_{Id}\right)\left(\langle r^2\rangle_\alpha + (1/9)\langle r_{\alpha d}^2\rangle\right)\left(\langle r^2\rangle_d + (4/9)\langle r_{\alpha d}^2\rangle\right)}{\left(\langle r^2\rangle_\alpha + \langle r^2\rangle_d + (5/9)\langle r^2\rangle_{\alpha d}\right)^2}\right], \quad (2.20)$$

where

$$\langle r_{\alpha d}^2\rangle = \int |\psi(R)|^2\, R^2\, d\mathbf{R}\,. \quad (2.21)$$

To calculate these expressions we assume that different potentials yielding equal values of the volume integrals J and the mean square radii $\langle r^2\rangle$ give an equivalent degree of fitting. Hence we can use the optical potential parameters to calculate the expressions (2.17)—(2.20).

3. Empirical evaluation of the correction

The optical model analysis of proton and neutron scattering indicates that the depth of the real part of the optical potential and hence its volume integral is linearly decreasing with energy, i.e.

$$J_{Rn}/A = C_n - B_n E_n\,, \quad (3.1)$$

where C_n and B_n are parameters depending on the target mass number. The same can be fairly expected for deuterons and alpha particles, i.e.

$$J_{Rd}/A = C_d - B_d E_d\,, \quad (3.2)$$

and

$$J_{R\alpha}/A = C_\alpha - B_\alpha E_\alpha\,. \quad (3.3)$$

According to Eq. (2.17), the volume integral per nucleon of the real part of ^{6}Li optical potential is

$$J_{R^6\mathrm{Li}}/A = \left(C_d - \frac{1}{3}B_d E_{\mathrm{Li}} + C_\alpha - \frac{2}{3}B_\alpha E_{\mathrm{Li}}\right)\left(1-\alpha(E_{\mathrm{Li}})\right). \quad (3.4)$$

But the volume integral per nucleon of the Watanabe potential is given by

$$J_{R^6\mathrm{Li}}/A = C_d - B_d E_d + C_\alpha - B_\alpha E_\alpha . \tag{3.5}$$

Comparing Eqs. (3.4) and (3.5), one easily observes that it is possible to make the volume integral of the Watanabe potential equal to the volume integral of the potential, given by Eq. (3.4) which takes into account the disintegration of the ^{6}Li by taking the deuteron and the α-particle energies not at $1/3\, E_{\mathrm{Li}}$ and $2/3\, E_{\mathrm{Li}}$, respectively, but at energies related by

$$B_\alpha E_\alpha + B_d E_d = \left(\frac{2}{3} B_\alpha + \frac{1}{3} B_d\right) E_{\mathrm{Li}} + (C_\alpha + C_d)\, \alpha(E_{\mathrm{Li}}). \tag{3.6}$$

This is a straightforward extension of a method used by M. H. SIMBEL for deuterons and tritons [8].

4. Results and discussion

Expressions (2.17) and (2.18) suggest that we can improve the fitting by varying the depths of the real and imaginary parts of the potential. Moreover, it was found that the correction to the mean square radius, which contains all the geometrical parameters, is negligible. So, if the Watanabe potential is expressed as

$$V(r) = Uf(r) + iwg(r) + V_{\mathrm{SO}}\, h(r)(\mathbf{l} \cdot \mathbf{s}), \tag{4.1}$$

the potential expected to improve the fitting will take the form

$$V'(r) = aUf(r) + ibwg(r) + cV_{\mathrm{SO}}\, h(r)\, \mathbf{l} \cdot \mathbf{s}, \tag{4.2}$$

where a, b and c are fitting parameters. Figs. 1 and 2 represent the results of the ratio σ/σ_R and the vector polarization **P** induced by the potential (4.1) [12], whereas Figs. 3 and 4 display the results induced by the potential (4.2) which show an improvement in fitting especially for the vector polarization **P**. The optical potential parameters used are listed in Table I.

Choosing the suitable values of a and b, the location of maxima and minima is reasonably fitted for both the ratio σ/σ_R and **P** as shown in Figs. 3 and 4. It seems that the parameter b is not sufficient to predict correctly the amplitude of the oscillation. For the sake of comparison, we have calculated the correction factors a and b according to expressions (2.17) and (2.18) using the parameters of Table I. The calculated and fitting values are listed in Table II.

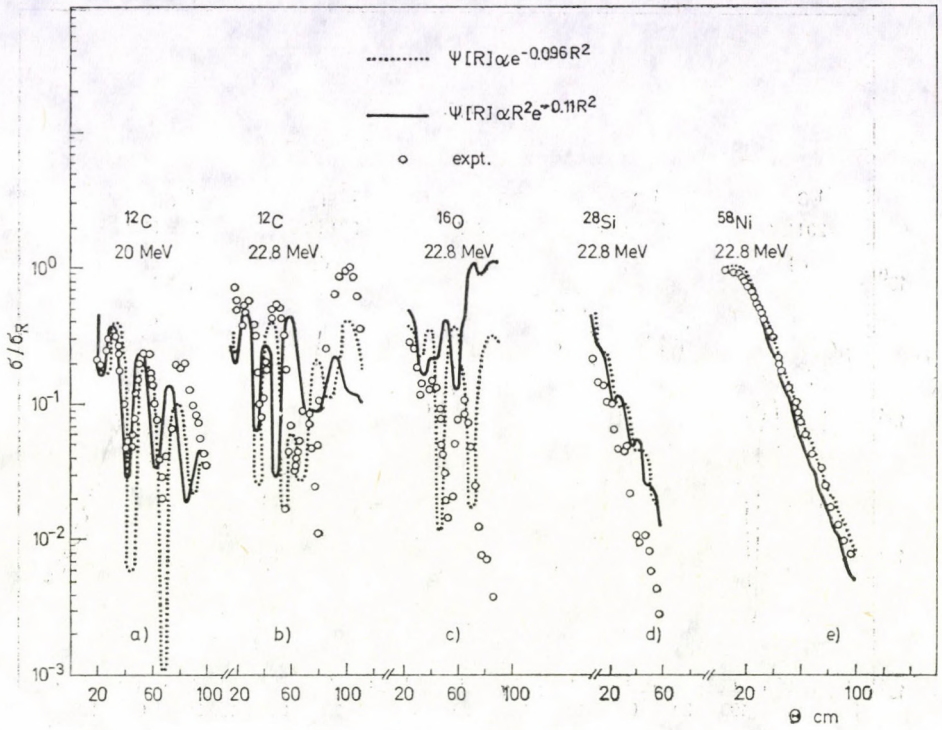

Fig. 1. The angular distributions of the ratio σ/σ_R calculated according to the α-d cluster model of ^{6}Li. The experimental data are taken from [11]

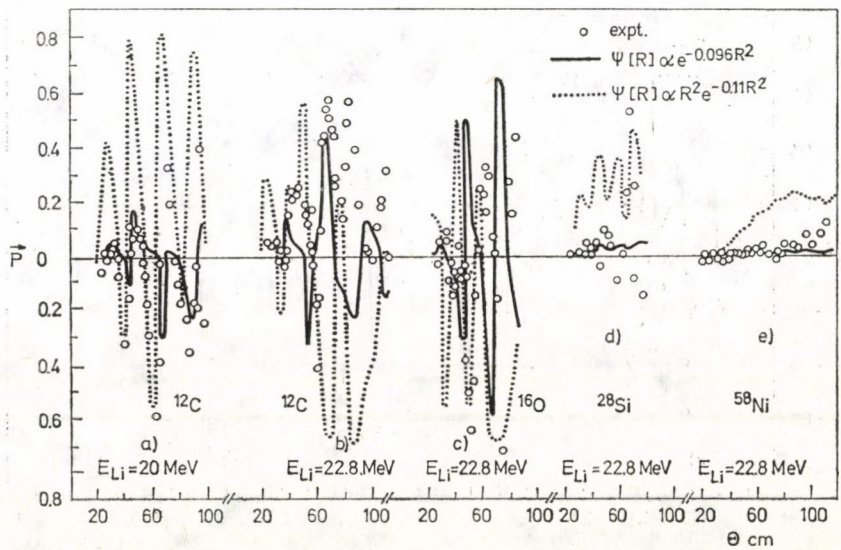

Fig. 2. The angular distributions of the vector polarization **P** calculated according to the α-d cluster model of ^{6}Li

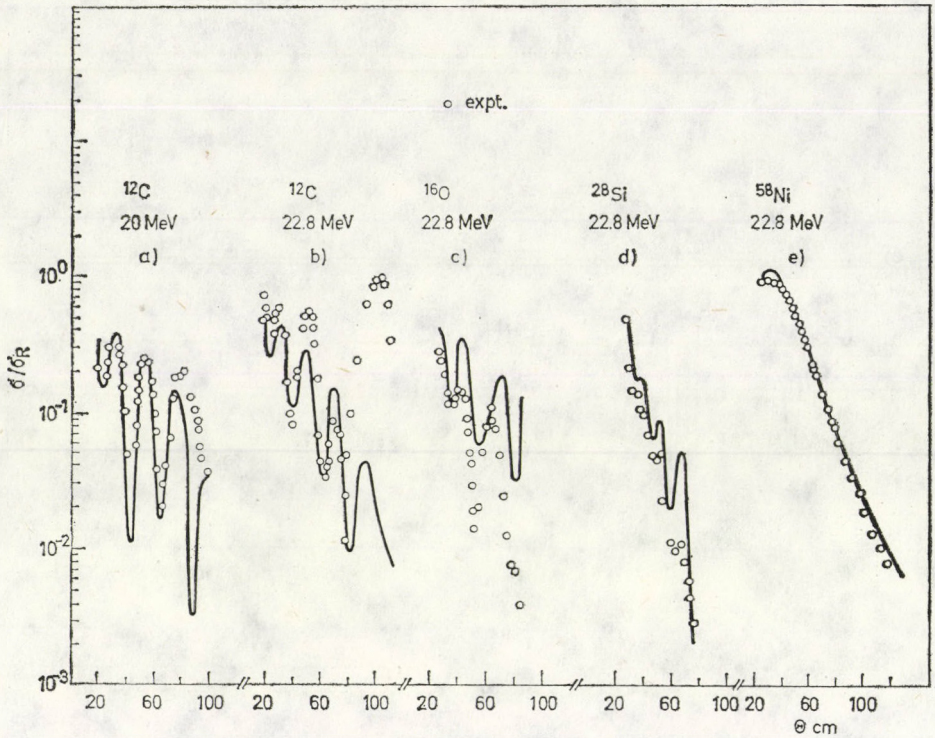

Fig. 3. The angular distributions of the ratio σ/σ_R calculated through the corrected Watanabe potential

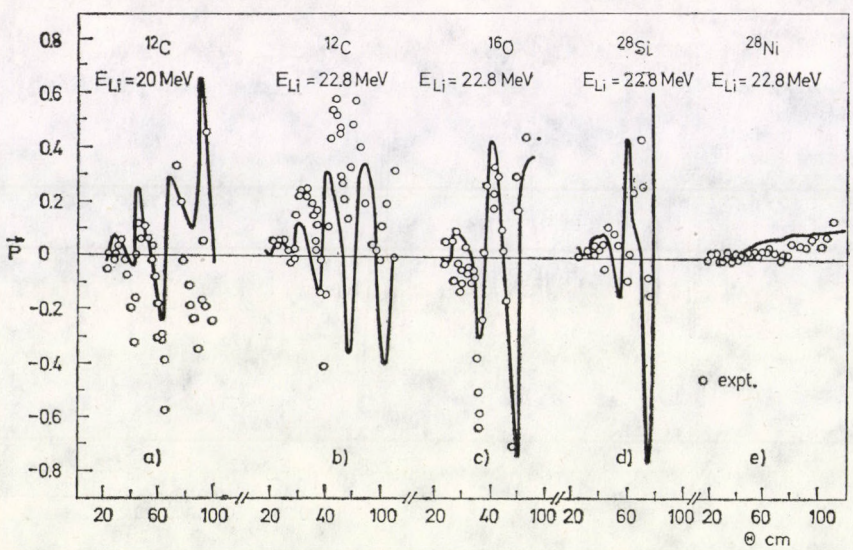

Fig. 4. The angular distributions of the vector polarization P calculated through the corrected Watanabe potential

Table I

Optical potential parameters for α (d)-nucleus scattering [10]

E_{Li} (MeV)	20.0		22.8		22.8		22.8		22.8	
Target	^{12}C		^{12}C		^{16}O		^{28}Si		^{58}Ni	
$E_{\alpha(d)}$ (MeV)	23.0	6.67	16.0	7.0	17.2	7.8	15.7	8.0	21.0	11.8
V	185	103.2	125	130.1	150	118	121	117.4	180.7	106.1
r_0	1.4	1.05	1.97	0.9	1.93	1.0	1.55	1.05	1.37	1.07
a_0	0.52	0 .8	0.5	0.9	0.5	0.6	0.52	0.912	0.56	0.807
W	25.0	9.58	0.0	11.0	0.0	0.0	17.5	0.0	21.9	0.0
W_D	0.0	0.0	1.5	0.0	7.5	4.9	0.0	19.7	0.0	1.66
r_W	1.4	1.28	1.97	2.1	1.93	1.9	1.55	1.69	1.37	1.35
a	0.52	0.755	0.5	0.6	0.5	0.6	0.52	0.46	0.56	0.629

Table II

Fitting parameters

E_{Li} (MeV) Target	20.0 ^{12}C		22.8 ^{12}C		22.8 ^{16}O		22.8 ^{28}Si		22.8 ^{58}Ni	
	a	b	a	b	a	b	a	b	a	b
Calculated	0.98	1.47	1.01	1.32	0.98	1.44	1.0	1.03	1.0	1.03
Fitting	1.4	1.1	0.3	1.0	0.6	1.0	1.3	0.52	1.0	1.0

Changing the depths only and neglecting the geometry change may be a reason for the missed optimum coincidence. Really, we have not this choice of varying the geometrical parameters otherwise we have to vary 9 parameters for the α- and d-optical potentials. This is large enough to hide any physical meaning even when an optimum fit is attained.

To determine the constants B_α, B_d, C_d and C_α of Eqs. (3.2) and (3.3), the volume integral of the real part of both the deuteron and the alpha particle optical potential was calculated according to the approximate formulae [9]

$$J_R = \frac{4}{3}\pi R_R^3 V_0 \left(1 + \frac{\pi^2 a_R}{R_R^2}\right),$$
$$r_R^2 = \frac{3}{5} R_R^2 \left(1 + \frac{7\pi^2 a_R^2}{3R_R^2}\right) \tag{4.3}$$

for different energies. Then, by the least square method, the best values of the constants that give the best linear dependence of Eqs. (3.2) and (3.3) are

found. The optimum forms are found to be

$$J_{Rd}/A = 973 - 7.6\,E_d$$
$$\text{and} \qquad J_{R\alpha}/A = 3826 - 17.74\,E\,. \tag{4.4}$$

Substituting these C and B values and the values of the correction parameters $a(a = 1 - \alpha(E))$ in the expression (3.6), we have found the relations

$$\begin{aligned} 17.74\,E_\alpha + 7.6\,E_d &= 3230 \text{ for } E_{^6\mathrm{Li}} = 24.5 \text{ MeV} \\ &= 2923 \text{ for } E_{^6\mathrm{Li}} = 36.6 \text{ MeV} \\ &= 2643 \text{ for } E_{^6\mathrm{Li}} = 50.6 \text{ MeV} \\ &= 1669 \text{ for } E_{^6\mathrm{Li}} = 63.0 \text{ MeV} \end{aligned} \tag{4.5}$$

for the ^{6}Li—^{12}C scattering data [10].

In principle, any two values of E_α and E_d satisfying any of the relations (4.5) are expected to give a fitting of the same quality as that given by cor-

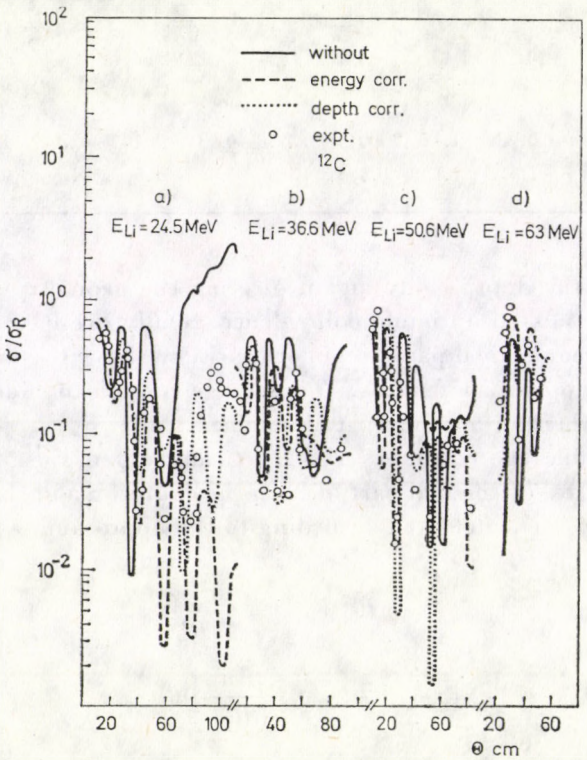

Fig. 5. The angular distributions of the ratio σ/σ_R for ^{6}Li—^{12}C scattering at different E_{Li} calculated through the depth corrected and the energy corrected Watanabe potential compared with the noncorrected Watanabe potential. The experimental data are taken from [9]

Table III

Optical potential parameter sets for $\alpha(d)$—^{12}C scattering [10]

E_{Li} (MeV)	24.5		36.6		50.6		63.0	
$E_{\alpha(d)}$ (MeV)	α 16.0	d 8.0	α 27.2	d 12.1	α 32.0	d 15.9	α 32.0	d 20.5
V	125.0	132.0	52.5	118.0	71.87	111.7	24.0	108.4
r_0	1.97	0.9	1.9	0.97	1.89	0.9	1.99	0.9
a_0	0.5	0.9	0.6	0.93	0.45	0.9	0.42	0.84
W	0.0	0.0	6.0	0.0	12.23	0.0	13.0	0.0
W_D	1.5	7.73	0.0	9.44	0.0	11.2	0.0	7.46
r_W	1.97	1.665	1.9	1.83	1.89	1.92	1.99	1.74
a_W	0.5	0.569	0.6	0.47	0.446	0.449	0.42	0.624

Table IV

Fitting parameters

E_{Li} (MeV)	24.5		36.6		50.6		63.0	
	a	b	a	b	a	b	a	b
Calculated	1.0	1.53	0.99	1.06	1.0	1.04	0.98	1.03
Fitting	0.4	1.5	0.52	1.2	0.6	0.9	0.94	0.87

rection through the depths. Due to the lack of data, we tried one set for each of the four cases. The results are shown in Fig. 5 for the two corrections compared with the case of no correction. The parameters used in fitting the data are given in Table III.

From these parameters we have calculated a and b according to expressions (2.17) and (2.18). The calculated and the fitting values are listed in Table IV.

The fitting parameters used in the case of correction by energy choice are listed in Table V.

The ratio E_α/E_{Li} and E_d/E_{Li} were plotted against E_{Li} for this data. Fig. 6 shows that both ratios begin with a large value at small E_{Li} then decrease till it reaches the value 2/3 at $E_{Li} \approx 220$ MeV for E_α/E_{Li} and the value 1/3 at $E_{Li} \approx 124$ MeV for the ratio E_d/E_{Li}.

From the expressions (2.17) and (2.18) it is clear that the corrections to the volume integral per nucleon of the real and imaginary parts of the Watanabe potential are inversely proportional to E_{Li} and to the target mass

Table V

Optical potential parameter sets for $\alpha(d)-{}^{12}C$ scattering [10]

E_{Li} (MeV)	24.5		36.6		50.6		63.0	
$E_{\alpha(d)}$ (MeV)	α 166.0	d 34.4	α 139.0	d 52.0	α 139.0	d 25.2	α 56.0	d 80.0
V	85.0	91.41	108.1	71.8	108.1	109.0	115.8	60.67
r_0	1.34	1.038	1.22	1.25	1.22	0.9	1.5	1.25
a_0	0.7	0.788	0.76	0.7	0.76	0.822	0.555	0.666
W	17.7	0.0	16.9	0.0	16.9	0.0	24.0	0.0
W_D	0.0	9.75	0.0	11.0	0.0	8.39	0.0	10.06
r_W	1.77	1.426	1.85	1.25	1.85	1.545	1.5	1.157
a_W	0.52	0.693	0.47	0.7	0.47	0.729	0.4	0.808

number A_2. These systematics are seen in Table IV for the parameter b. With respect to the mass number variation these systematics are missed both with respect to energy and mass number variation. The brave adoption that expressions (2.17) and (2.18) are independent of the form of the potential needs justification. The ambiguities in the optical potential parameters used in calculations may be a reason. The non-equality of the quality of fitting for different targets and different energies and also the ambiguity in the parameter may be a reason for the missed systematics.

From Table II and IV, one notices a difference between the calculated values of a and b and that obtained by the fitting process, which may be due to the use of the adiabatic approximation in the calculations of the correction.

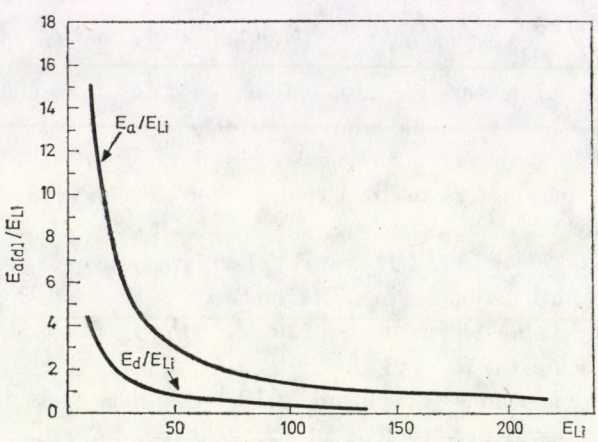

Fig. 6. The ratios E_α/E_{Li} and E_d/E_{Li} against E_{Li}

Acknowledgements

The authors would like to thank Professor L. FONDA for reading the manuscript. Two of them (I.R.) and (M.A. E-G.) would like to thank Professor ABDUS SALAM, the International Atomic Energy Agency and UNESCO for hospitality at the International Centre for Theoretical Physics, Trieste.

REFERENCES

1. J. W. WATSON, Nucl. Phys. A, **198**, 129, 1972.
2. R. J. GLAUBER, Lectures in Theoretical Physics, Vol. **I**, p. 315, Interscience, New York, 1958.
3. M. H. SIMBEL and A. Y. ABUL-MAGD, Nucl. Phys., **A177**, 322, 1971.
4. M. H. SIMBEL, Phys. Rev. C **10**, 1083, 1974.
5. M. H. SIMBEL, Phys. Rev., C **8**, 85, 1973.
6. A. Y. ABUL-MAGD and M. EL-NADI, Prog. Theor. Phys., **35**, 798, 1966.
7. E. COFFOU and D. J. B. GOLDFARB, Nucl. Phys., **A94**, 241, 1967.
8. G. W. GREENLEES et al, Phys. Rev., **171**, III5, 1968.
9. P. K. BINDAL et al., Phys. Rev., C**9**, 2154, 1974.
10. C. M. PEREY and F. G. PEREY, Atomic data and Nucl. data tables, **17**, 1, 1976.
11. W. WEISS et al, Phys. Lett., **61B**, 237, 1976.
12. A. RABIE ,M. A. EL-GAZZAR and A. Y. ABUL-MAGD, Preprint IC/80/159 (to be published).

BOOK REVIEWS

Phonon Scattering in Condensed Matter

Edited by Humphrey J. Maris, Plenum Press, New York and London 1980

This book is the Proceedings of the Third International Conference on Phonon Scattering in Condensed Matter, held at Brown University, Providence, Rhode Island (USA), August 28—31, 1979.

Recent developments, like the application of the heat pulse method and the new "monochromatic" phonon generators and detectors allowed to carry out in the past years a detailed study of the propagation of phonons and their interaction with other excitations and defects. The works presented at the Conference show that our understanding of the basic interaction processes has been greatly improved due to these new developments.

The choice of the invited talks indicates that the most active area in the study of phonon propagation is the phonon transmission across interfaces (Kapitza resistance) and the phonon propagation in elastically anisotropic materials (phonon focusing). As for the scattering processes, particular attention was paid to the study of phonon scattering in amorphous materials (the interaction of phonons and the tunneling states) and to the phonon scattering by electrons in semiconductors. Related topics include spin-phonon and phonon-phonon interactions, the study of the role of phonons in phase transition problems and in helium and the new techniques for generating and detecting phonons.

The book gives an up-to-date account of the research done in the field of phonons.

J. Sólyom

Statistical Physics, Part 2 (Theory of the Condensed State)

E. M. Lifshitz and L. P. Pitaevskii
Pergamon Press, Oxford 1980, 387 pages

Written about the quantum theory of the condensed state of matter, this book constitutes Volume 9 of the famous "Course of Theoretical Physics" by L. D. Landau and E. M. Lifshitz.

Though not among the authors, Landau's creative genius is clearly felt throughout the volume. His original works form the basis of several Chapters like the one on Fermi liquid theory, superfluidity, etc. At the same time, however, the most important results relevant to the topics included in this book as produced by the rapid development of the field in the past 20 years are also adequately accounted for by the authors.

Chapter I deals with the theory of normal Fermi liquid. In Chapter II the most important mathematical method of present-day statistical physics, the Green's function formalism is introduced and discussed in detail for Fermi systems at zero temperature. Superfluidity is the subject matter of Chapter III. The main characteristics of quantum Bose liquids are treated here as well as their Green's functions and the diagram technique applicable to their approximate calculation. Chapter IV contains details of the Green's function technique at non-zero temperature. Chapter V is devoted to superconductivity. Description of the microscopic theory of a superfluid Fermi gas is followed by the Ginzburg—Landau theory of superconductivity in metals. Chapter VI has the title: "Electrons in the crystal lattice". After

introducing the concept of Bloch electrons the effect of magnetic field on the electrons in the lattice is given detailed treatment. Chapter VII, written about magnetism starts with deriving the classical equation of motion of the magnetic moment in a ferromagnet. Magnons are dealt with subsequently. Microscopic theory is based on the Heisenberg Hamiltonian. The last two Chapters are about electromagnetic and hydrodynamic fluctuations. Previously electromagnetic fluctuations in material media were the subject of Volume 8 of the Course. The reason for the change has been that using the Green's function formalism the theory could be presented in a much simpler manner.

This book has been intended for postgraduate students in theoretical physics. By virtue of its clear style and the easily comprehensible way of presenting the main physical ideas, however, it can be recommended to a much wider audience: to last-year undergraduates in physics as well as to chemists and non-theorist physicists.

P. SZÉPFALUSY

Manuscript received by Akadémiai Kiadó: 18 Sept. 1981
Manuscript received by the Printers: 29 Sept. 1981
Date of publication: 23 Aug. 1982

PRINTED IN HUNGARY

Akadémiai Nyomda, Budapest

NOTES TO CONTRIBUTORS

I. PAPERS will be considered for publication in Acta Physica Hungarica only if they have not previously been published or submitted for publication elsewhere. They may be written in English, French, German or Russian.

Papers should be submitted to

Prof. I. Kovács, Editor
Department of Atomic Physics, Technical University
1521 Budapest, Budafoki út 8, Hungary

Papers may be either articles with abstracts or short communications. Both should be as concise as possible, articles in general not exceeding 25 typed pages, short communications 8 typed pages.

II. MANUSCRIPTS

1. Papers should be submitted in three copies.

2. The text of papers must be of high stylistic standard, requiring minor corrections only.

3. Manuscripts should be typed in double spacing on good quality paper, with generous margins.

4. The name of the author(s) and of the institutes where the work was carried out should appear on the first page of the manuscript.

5. Particular care should be taken with mathematical expressions. The following should be clearly distinguished, e.g. by underlining in different colours: special founts (italics, script, bold type, Greek, Gothic, etc.); capital and small letters; subscripts and superscripts, e.g. x^2, x_3; small *l* and 1; zero and capital O; in expressions written by hand: *e* and *l*, *n* and *u*, *v* and *v*, etc.

6. References should be numbered serially and listed at the end of the paper in the following form: J. Ise and W. D. Fretter, Phys. Rev., **76**, 933, 1949.

For books, please give the initials and family name of the author(s), title, name of publisher, place and year of publication, e.g.: J. C. Slater, Quantum Theory of Atomic Structures, I. McGraw-Hill Book Company, Inc., New York, 1960.

References should be given in the text in the following forms: Heisenberg [5] or [5].

7. Captions to illustrations should be listed on a separate sheet, not inserted in the text.

8. In papers submitted to Acta Physica all measures should be expressed in SI units.

III. ILLUSTRATIONS AND TABLES

1. Each paper should be accompanied by three sets of illustrations, one of which must be ready for the blockmaker. The other sets attached to the copies of the manuscript may be rough drawings in pencil or photocopies.

2. Illustrations must not be inserted in the text.

3. All illustrations should be identified in blue pencil by the author's name, abbreviated title of the paper and figure number.

4. Tables should be typed on separate pages and have captions describing their content. Clear wording of column heads is advisable. Tables should be numbered in Roman numerals (I, II, III, etc.).

IV. RETURN OF MATERIAL

Owing to high postage costs, the Editorial Office cannot undertake to return *all* material not accepted for any reason for publication. Of papers to be revised (for not being in conformity with the above Notes or other reasons) only *one* copy will be returned. Material rejected for lack of space or on account of the Referees' opinion will not be returned to authors outside Europe.

Periodicals of the Hungarian Academy of Sciences are obtainable at the following addresses:

AUSTRALIA
C.B.D. LIBRARY AND SUBSCRIPTION SERVICE
Box 4886, G.P.O., *Sydney N.S.W. 2001*
COSMOS BOOKSHOP, 145 Ackland Street
St. Kilda (Melbourne), Victoria 3182

AUSTRIA
GLOBUS, Höchstädtplatz 3, *1206 Wien XX*

BELGIUM
OFFICE INTERNATIONAL DE LIBRAIRIE
30 Avenue Marnix, *1050 Bruxelles*
LIBRAIRIE DU MONDE ENTIER
162 rue du Midi, *1000 Bruxelles*

BULGARIA
HEMUS, Bulvar Ruszki 6, *Sofia*

CANADA
PANNONIA BOOKS, P.O. Box 1017
Postal Station "B", *Toronto, Ontario M5T 2T8*

CHINA
CNPICOR, Periodical Department, P.O. Box 50
Peking

CZECHOSLOVAKIA
MAD'ARSKÁ KULTURA, Národní třida 22
115 66 Praha
PNS DOVOZ TISKU, Vinohradská 46, *Praha 2*
PNS DOVOZ TLAČE, *Bratislava 2*

DENMARK
EJNAR MUNKSGAARD, Norregade 6
1165 Copenhagen K

FEDERAL REPUBLIC OF GERMANY
KUNST UND WISSEN ERICH BIEBER
Postfach 46, *7000 Stuttgart 1*

FINLAND
AKATEEMINEN KIRJAKAUPPA, P.O. Box 128
SF-00101 Helsinki 10

FRANCE
DAWSON-FRANCE S. A., B. P. 40, *91121 Palaiseau*
EUROPÉRIODIQUES S. A., 31 Avenue de Versailles, *78170 La Celle St. Cloud*
OFFICE INTERNATIONAL DE DOCUMENTATION ET LIBRAIRIE, 48 rue Gay-Lussac
75240 Paris Cedex 05

GERMAN DEMOCRATIC REPUBLIC
HAUS DER UNGARISCHEN KULTUR
Karl Liebknecht-Straße 9, *DDR-102 Berlin*
DEUTSCHE POST ZEITUNGSVERTRIEBSAMT
Sraße der Pariser Kommüne 3–4, *DDR-104 Berlin*

GREAT BRITAIN
BLACKWELL'S PERIODICALS DIVISION
Hythe Bridge Street, *Oxford OX1 2ET*
BUMPUS, HALDANE AND MAXWELL LTD.
Cowper Works, *Olney, Bucks MK46 4BN*
COLLET'S HOLDINGS LTD., Denington Estate
Wellingborough, Northants NN8 2QT
WM. DAWSON AND SONS LTD., Cannon House
Folkstone, Kent CT19 5EE
H. K. LEWIS AND CO., 136 Gower Street
London WC1E 6BS

GREECE
KOSTARAKIS BROTHERS INTERNATIONAL BOOKSELLERS, 2 Hippokratous Street, *Athens-143*

HOLLAND
MEULENHOFF-BRUNA B.V., Beulingstraat 2,
Amsterdam
MARTINUS NIJHOFF B.V.
Lange Voorhout 9–11, *Den Haag*
SWETS SUBSCRIPTION SERVICE
347b Heereweg, *Lisse*

INDIA
ALLIED PUBLISHING PRIVATE LTD., 13/14 Asaf Ali Road, *New Delhi 110001*
150 B-6 Mount Road, *Madras 600002*
INTERNATIONAL BOOK HOUSE PVT. LTD.
Madame Cama Road, *Bombay 400039*
THE STATE TRADING CORPORATION OF INDIA LTD., Books Import Division, Chandralok 36 Janpath, *New Delhi 110001*

ITALY
INTERSCIENTIA, Via Mazzé 28, *10149 Torino*
LIBRERIA COMMISSIONARIA SANSONI, Via Lamarmora 45, *50121 Firenze*
SANTO VANASIA, Via M. Macchi 58
20124 Milano
D. E. A., Via Lima 28, *00198 Roma*

JAPAN
KINOKUNIYA BOOK-STORE CO. LTD.
17-7 Shinjuku 3 chome, Shinjuku-ku, *Tokyo 160-91*
MARUZEN COMPANY LTD., Book Department, P.O. Box 5050 Tokyo International, *Tokyo 100-31*
NAUKA LTD. IMPORT DEPARTMENT
2-30-19 Minami Ikebukuro, Toshima-ku, *Tokyo 171*

KOREA
CHULPANMUL, *Phenjan*

NORWAY
TANUM-TIDSKRIFT-SENTRALEN A.S., Karl Johansgatan 41–43, *1000 Oslo*

POLAND
WĘGIERSKI INSTYTUT KULTURY, Marszałkowska 80, *00-517 Warszawa*
CKP I W, ul. Towarowa 28, *00-958 Warszawa*

ROUMANIA
D. E. P., *Bucureşti*
ILEXIM, Calea Grivitei 64–66, *Bucureşti*

SOVIET UNION
SOJUZPECHAT — IMPORT, *Moscow*
and the post offices in each town
MEZHDUNARODNAYA KNIGA, *Moscow G-200*

SPAIN
DIAZ DE SANTOS, Lagasca 95, *Madrid 6*

SWEDEN
ALMQVIST AND WIKSELL, Gamla Brogatan 26
101 20 Stockholm
GUMPERTS UNIVERSITETSBOKHANDEL AB
Box 346, *401 25 Göteborg 1*

SWITZERLAND
KARGER LIBRI AG, Petersgraben 31, *4011 Basel*

USA
EBSCO SUBSCRIPTION SERVICES
P.O. Box 1943, *Birmingham, Alabama 35201*
F. W. FAXON COMPANY, INC.
15 Southwest Park, *Westwood Mass. 02090*
THE MOORE-COTTRELL SUBSCRIPTION AGENCIES, *North Cohocton, N. Y. 14868*
READ-MORE PUBLICATIONS, INC.
140 Cedar Street, *New York, N. Y. 10006*
STECHERT-MACMILLAN, INC.
7250 Westfield Avenue, *Pennsauken N. J. 08110*

YUGOSLAVIA
JUGOSLOVENSKA KNJIGA, Terazije 27, *Beograd*
FORUM, Vojvode Mišića 1, *21000 Novi Sad*

HU-ISSN 0001-6705

Index: 26.022

ACTA PHYSICA

ACADEMIAE SCIENTIARUM HUNGARICAE

VOLUME 52 NUMBER 2

AKADÉMIAI KIADÓ, BUDAPEST
1982

ACTA PHYS. HUNG. APAHAQ 52 (2) 117—254 (1982)

ACTA PHYSICA

A JOURNAL OF THE HUNGARIAN ACADEMY OF SCIENCES

EDITED BY

I. KOVÁCS

Acta Physica publishes original papers on subjects in physics. Papers are accepted in English, French, German and Russian.

Acta Physica is published in two yearly volumes (4 issues each) by

AKADÉMIAI KIADÓ

Publishing House of the Hungarian Academy of Sciences

H-1054 Budapest, Alkotmány u. 21

Subscription information

Orders should be addressed to

KULTURA Foreign Trading Company

1389 Budapest P.O. Box 149

or to its representatives abroad.

ACTA PHYSICA

ACADEMIAE SCIENTIARUM HUNGARICAE

VOLUME 52 NUMBER 2

AKADÉMIAI KIADÓ, BUDAPEST
1982

ACTA PHYS. HUNG.

CONTENTS

Acta Physica Academiae Scientiarum Hungaricae, 52 (2), pp. 117—122 (1982)

ABSORPTION SPECTRA OF Mn^{2+} IN MANGANOAN CLINOZOISITE

B. J. REDDY and K. B. N. SARMA

SPECTROSCOPIC LABORATORIES, S. V. UNIVERSITY, TIRUPATI — 517502, INDIA

(Received 19. V. 1981)

EPR and optical absorption studies are reported on manganoan clinozoisite for the first time. The ESR spectrum shows a six-line transition due to Mn^{2+} ion and gives $g \approx 2.00$ and $A \approx 84 \times 10^{-4}$ cm^{-1}. An intense resonance line at $g = 4.7$ is identified as due to Fe^{3+}. The optical absorption spectrum of clinozoisite mainly consists of six bands, located at 15380, 18510, 20400, 23520, 25180 and 34470 cm^{-1}. The bands at 20400 and 25180 cm^{-1} are assigned to $^4A_1$, $^4E(G)$ and $^4E(D)$ states, respectively, since they are sharp and do not show any shifts on cooling to 80 K. The other bands at 15380, 18510, 23520 and 34470 cm^{-1} are assigned to $^4T_1(G)$, $^4T_2(G)$, $^4T_2(D)$ and $^4A_2(F)$ states, respectively, due to spin-forbidden transitions of Mn^{2+} sited in a distorted octahedron of oxygen atoms. The crystal field parameters which gave a good fit to the observed band positions are $B = 683$ cm^{-1}, $C = 2714$ cm^{-1} and $Dq = 683$ cm^{-1}.

1. Introduction

DOLLASE [1] refined the crystal structure of clinozoisite, $Ca_2Al_3Si_3O_{12}(OH)$. LANGER and RAITH [2] studied the infrared spectra of Al—Fe III clinozoisites. TSANG and GHOSE [3] reported the EPR and optical spectra of a blue zoisite whereas SCHMETZER [4] studied the absorption of a chromian zoisite. As neither optical nor ESR spectrum of manganoan clinozoisite is reported, the authors took up the present investigation.

TSANG and GHOSE [3] suggest that Mn^{2+} ions in zoisite occupy one of the Ca sites preferably Ca (I) position in agreement with ionic radius and charge considerations. A similar situation exists in clinozoisite in which Mn^{2+} might be sited in Ca (1) position with oxygen atoms as ligands in a slightly distorted octahedral symmetry (Ca—O = 0.242 nm).

2. Experimental

Pink coloured clinozoisite collected from a open-cast mica mine in Rapur taluk of Nellore district, A. P., India, was used in the present work. Its absorption spectrum was recorded in the mull form at room temperature in the range 200—2000 nm on a Cary — 17D spectrophotometer and on a DMR — 21 spectrophotometer. Room and low temperature spectra of the crystal

(0.7 mm thick) were also recorded in the wavelength region 300—950 nm on a medium quartz spectrograph on ORWO film (27 Din) and Kodak IN plates for 5 to 80 minutes. From the microphotometric profiles of the bands and iron spectrum, the wavelengths and oscillator strengths of the bands were determined. The band positions of the sample observed by different devices are found to agree very closely. EPR spectra of the sample were recorded at room and low temperatures on a Jeol X-band ESR spectrometer. Manganese and iron were determined quantitatively on a Varian Techtron AA-6 Atomic Absorption spectrometer. The clinozoisite sample is found to contain 0.38% of Mn and 0.045% of Fe by weight. So the observed absorption spectrum might be attributed to Mn in the sample.

3. Theory

The Mn^{2+} ion has the electronic configuration $A(3d^5)$ where A stands for the closed argon shell. This configuration gives rise to the free ion terms ^6S and ^4G and several other quartet and doublet states of which ^6S is the ground state. In an octahedral crystal field ^6S transforms as $^6A_{1g}(S)$ whereas ^4G splits into $^4A_{1g}(G) + {}^4E_g(G) + {}^4T_{2g}(G) + {}^4T_{1g}(G)$. Of these, the $^6A_{1g}(G)$ lies lowest according to Hund's rule. Thus all the absorption bands of Mn^{2+} result from the spin-forbidden transitions.

4. Results and analysis

4.1. *EPR measurements*

The EPR spectrum of manganoan clinozoisite in powder form was observed at 300 K (shown in Fig. 1) at 9.287 GHz. No significant changes were observed in the spectrum at 80 K. The EPR spectrum of clinozoisite has a six-line Mn^{2+} central transition broadened and gives $g = 2.002 \pm 0.005$ and $A = (84 \pm 4) \times 10^{-4}$ cm^{-1}. The experimental values of g and A are in general agreement with Mn^{2+} values for zoisites [3] and for other oxides [5]. The intense resonance line on the left was identified as Fe^{3+} because of the lack of hyperfine splitting. This peak at $g = 4.7$ at 1400 G in the figure must be due to an ion with $S = 5/2$ in a strongly asymmetric potential as was first demonstrated by CASTNER et al [6].

4.2. *Optical absorption studies*

The optical absorption spectrum of clinozoisite at 300 K recorded on Cary-17D spectrophotometer for nujol mull of the sample is shown in Fig. 2. The room temperature spectrum consists of broad bands at 15 380, 18 510 and

23 520 cm^{-1} and sharp bands at 20 400 (ν_1), 25 180 (ν_2) and 34 470 cm^{-1}. Optical studies at low temperature on medium quartz spectrograph for crystal form (Fig. 3) indicate that the first two sharp bands (ν_1 and ν_2) do not show any shifts whereas the first two broad bands show redshift. Therefore, the two sharp bands are assigned to transitions from $^6A_1(S)$ to $^4A_1$, $^4E(G)$ and

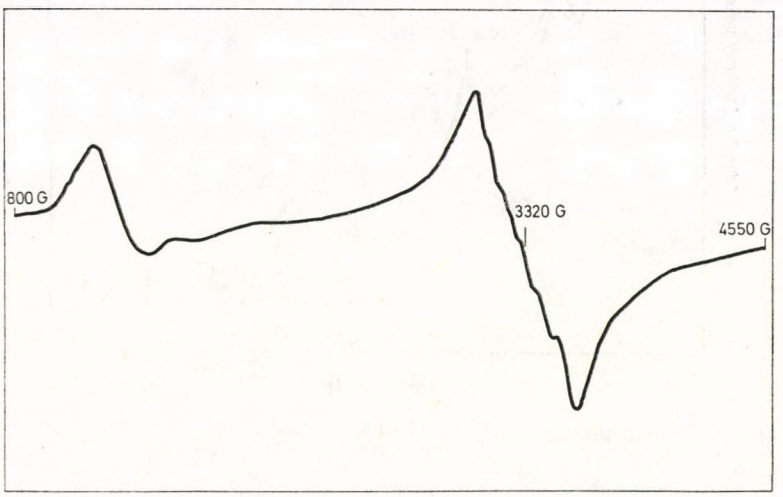

Fig. 1. EPR spectrum of clinozoisite powder at 300 K.

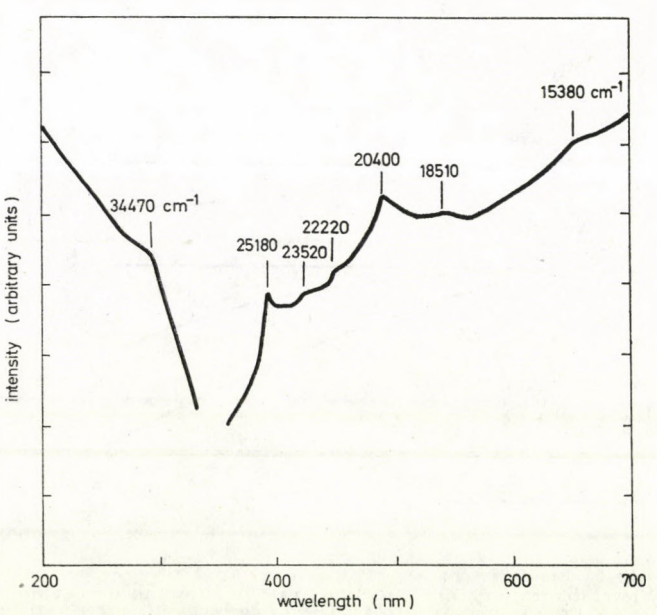

Fig. 2. Trace of the spectrophotometric record of clinozoisite in mull form at 300 K.

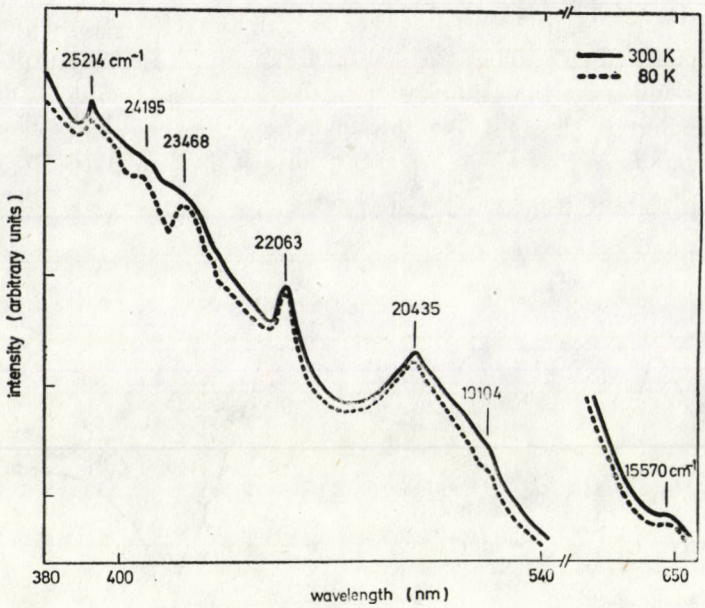

Fig. 3. Trace of the microphotometric profiles of absorption spectrum of clinozoisite at 300 K and 80 K.

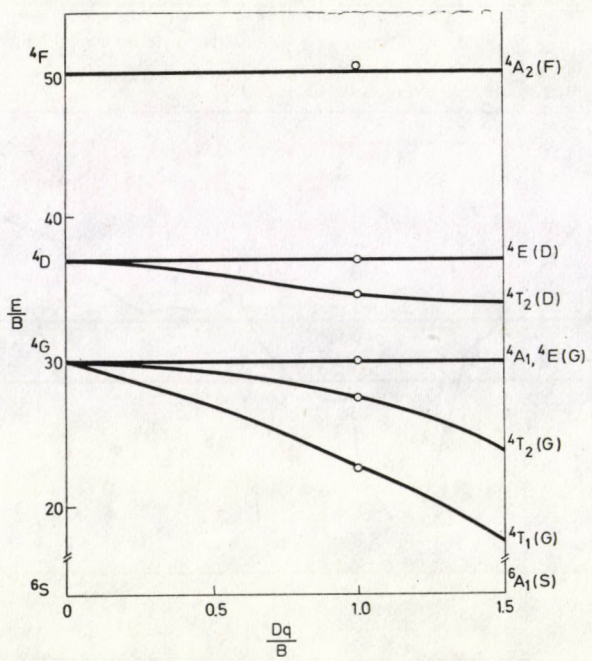

Fig. 4. Energy level diagram of Mn^{2+} in clinozoisite in an octahedral symmetry plotted as a function of the crystal field parameter Dq with $B = 683$ cm^{-1} and $C = 4B$. The solid circles show the experimental energies at 300 K.

$^4E(D)$, respectively (suffix g is omitted). The crystal field dependent bands which show red shifts are assigned accordingly to $^4T_1(G)$ and $^4T_2(G)$ states.

The values of B and C are calculated from the solutions of Tanabe—Sugano equations from the expressions [7]

$$\nu_1 = E(^4A_1, {}^4E(G) - E(^6A_1(S)) = 10B + 5C,$$
$$\nu_2 = E(^4E(D) - E(^6A_1(S)) \quad = 17B + 5C$$

and found to be $B = 683\ cm^{-1}$, $C = 2714\ cm^{-1}$ and C/B is nearly 4.0. Energy matrices for d^5 configuration in octahedral field are solved on an IBM computer for different Dq values and graph drawn between E/B and Dq/B (shown in Fig. 4). From energy-level diagram the bands at 22 220 and 23 520 cm^{-1} are assigned to $^4T_2(D)$ state and the band at 34 470 cm^{-1} to $^4A_2(F)$ state. A good fit of the experimentally observed band positions is obtained for $Dq/B = 1$.

5. Discussion

An interesting feature was observed for the band at 20 435 cm^{-1} when studied with incident polarized light in two mutually perpendicular directions. For one of the planes of vibration, the band was observed to split into two (20 164 and 19 788 cm^{-1}). It has been suggested by KOIDE and PRYCE [8] that $^4A_1(G)$ state lies lower than $^4E(G)$ state by about 100 cm^{-1}. The bands at 20 164 and 19 788 cm^{-1} are, therefore, attributed to $^4A_1(G)$ and $^4E(G)$ states, respectively. The measured oscillator strengths (Table I) for some of the bands

Table I

Observed wavelengths, wavenumbers and oscillator strengths, calculated energies and assignment of bands for Mn^{2+} in clinozoisite ($Dq = 683\ cm^{-1}$, $B = 683\ cm^{-1}$ and $C = 4B$)

Observed band positions						Cary — 17D Spectrophotometer At 300 K		Calculated band positions (cm^{-1})	Assignment w.r.t. the ground state $^6A_1(S)$
Recorded on medium quartz spectrograph									
at 300 K			at 80 K						
Wavelength (nm)	Wave number (cm^{-1})	Oscillator strength ($f \times 10^6$)	Wavelength (nm)	Wave number (cm^{-1})	Oscillator strength ($f \times 10^{-6}$)	Wave length (nm)	Wave number (cm^{-1})		
642.1	15 570	5.1	643.1	15 545	4.0	650	15 380	15 531	$^4T_1(G)$
523.3	19 104		536.5	18 634	3.0	540	18 510	18 728	$^4T_2(G)$
489.2	20 435	19.5	489.2	20 435	13.0	490	20 400	20 490	$^4A_1, {}^4E(G)$
453.12	22 063	4.3	453.12	22 063	3.8	450	22 220		
426.0	23 468		427.2	23 402	7.8	425	23 520	23 680	$^4T_2(D)$
413.2	24 195		413.2	24 195					
396.6	25 214	0.3	396.6	25 214	0.2	397	25 180	25 271	$^4E(D)$
						290	34 470	34 150	$^4A_2(F)$

are low as expected for spin-forbidden transitions [9] and are of the same order as reported for Mn^{2+} in a silicate [10]. The values of B and C for Mn^{2+} in the clinozoisite are similar to those observed for silicates by MANNING [11]. The observed absorption spectrum does not possess the features of Mn^{3+} spectrum in epidote [12] which has a similar structure as clinozoisite. The good agreement between experimental and theoretical studies justifies the assignment of clinozoisite bands to Mn^{2+}. Further, the observed EPR spectrum has similar features as observed by SARASWAT and UPRETI [13] and UPRETI [14] for Mn^{2+}. For the pink coloured sample, the ESR and optical absorption studies indicate the presence of Mn^{2+} in clinozoisite sited in a slightly distorted octahedron.

Acknowledgement

The authors are thankful to Prof. S. V. J. LAKSHMAN for his keen interest in this field of work. They are thankful to Dr. R. J. RAO, Professor of Geology, Special Officer, S. V. University P. G. Centre, for identifying and providing the sample. They acknowledge the help rendered by the authorities of the CIL, Central University, Hyderabad for providing the facilities to record the spectra on Cary-17D spectrophotometer and Jeol ESR spectrometer. One of the authors (KBNS) is grateful to UGC, New Delhi, for the award of teacher fellowship under FIP.

REFERENCES

1. W. A. DOLLASE, Am. Mineral., **53**, 1882, 1968.
2. K. LANGER and M. RAITH, Am. Mineral., **59**, 1249, 1974.
3. T. TSANG and S. GHOSE, J. Chem. Phys., **54**, 856, 1971.
4. K. SCHMETZER, News. Jahab. Min., **5**, 197, 1978.
5. J. W. ROBINSON, Handbook of Spectroscopy, Vol II, CRC Press, Cleveland, 1974.
6. T. CHASTNER, Jr., G. S. NEWELL, W. C. HOLTON and C. P. SLITCHTER, J. Chem. Phys., **32**, 668, 1960.
7. K. L. KEESTER and W. B. WHITE, Proc., 5th Int. Mineral. Assoc. Meeting, Cambridge, 1966.
8. S. KOIDE and M. H. L. PRYCE, Phil. Mag., **8**, 607, 1958.
9. C. J. BALLHAUSEN, Introduction to Ligand Field Theory, McGraw Hill Book Co., Inc. New York, 1962.
10. S. V. J. LAKSHMAN and B. J. REDDY, Physica, **71**, 197, 1974.
11. P. G. MANNING, Can. Mineral., **10**, 677, 1970.
12. R. G. BURNS and R. G. J. STRENS, Mineral. Mag., **36**, 204, 1967.
13. R. S. SARASWAT and G. C. UPRETI, J. Chem. Phys., **67**, 5428, 1977.
14. J. C. UPRETI, J. Mag. Reso., **14**, 274, 1974.

Acta Physica Academiae Scientiarum Hungaricae, 52 (2), pp. 123—128 (1982)

ELECTRICAL PROPERTIES OF $AgTlSe_2$ SEMICONDUCTOR IN THE LIQUID STATE

A. H. ABOU EL ELA and N. ABDELMOHSEN

PHYSICS DEPARTMENT, ISLAMIC GIRLS COLLEGE, NASR CITY, CAIRO, EGYPT

(Received in revised form 24. VII. 1981)

The electrical conductivity and thermoelectric power of $AgTlSe_2$ have been investigated as a function of temperature from 390 °C up to 508 °C. The experimental data are analyzed in terms of a model developed for the density of states and electrical transport in solid amorphous semiconductors (MOTT [12]). Positive thermoelectric power suggests a large predominance of holes in electrical conduction. It appears that the conduction is due to holes in localized states near the band edge.

1. Introduction

Much time and research have been devoted to understand the properties of liquid semiconductors. The physical character of liquid semiconductors puts them in an intermediate position between several other classes of materials: liquid metals, molten salts and amorphous solids. Various models were suggested for liquid semiconductors [1—8], and the most comprehensive attack on the theoretical problems posed by the existence of liquid semiconductors has been made by MOTT [1, 2]. MOTT [2] and CUTLER [5] have shown that liquid semiconductors have a special relationship to solid amorphous semiconductors, the fact that there is a liquid rather than a solid has no significance in many aspects of electronic behaviour, since the time scale for many types of electronic motion is much faster than for atomic motion, and the same concepts or theories are applicable.

Of all the physical properties, the electronic transport parameters are the most distinctive ones for liquid semiconductors. The aim of the present contribution is to investigate the electrical conductivity and thermoelectric power of $AgTlSe_2$ ternary semiconductor in the liquid state. $AgTlSe_2$ possesses a chalcopyrite structure [9, 10], and its melting point is 328 °C. Recently ternary chalcopyrite semiconductors have attracted a great deal of attention because of their possible applications in electro-optical devices [11] and infrared detection and generation.

2. Experimental techniques

$AgTlSe_2$ samples were prepared by melting the proper amounts of highly pure component elements (99.999%) obtained from Goodfellow Metals Co. The material was sealed in evacuated quartz tubes at 10^{-3} Pa and heated at 1200 °C for 12 hours with frequent rocking to ensure homogenization of the melt. Then the tubes were quenched in ice to obtain the sample in the amorphous state. The solid material is then heated in inert atmosphere until it melts and then is transferred to the measuring cell.

The measuring cell was made from a ceramic material and was fitted with graphite electrodes, heater and thermocouples for accurate measurements of temperature. The working space between the electrodes was made highly homogeneous and the spacing between the electrodes was 10^{-4} m. Measurements of the electrical conductivity were carried out using a highly stabilized power supply, a sensitive voltmeter and a sensitive galvanometer capable of measuring currents as low as 10^{-9} A.

3. Results and discussion

Figs. 1 and 2 show the temperature dependence of the electrical conductivity and thermoelectric power in the liquid state from 390 °C up to 508 °C. $\ln \sigma$ and S are found to be linear with $1/T$ only at low temperatures, and the activation energy determined from the slope of $\ln \sigma$ versus $1/T$ in the low temperature region is found to be $E_\sigma = 0.54$ eV. For higher temperatures the activation energy becomes temperature dependent and decreases with temperature. The temperature dependence of the thermopower which is positive yields a slightly lower value for the activation energy $E_S = 0.5$ eV. Positive values of thermoelectric power indicate a large predominance of holes in electrical transport.

The measured transport data can be interpreted in terms of the model developed by MOTT [12] and DAVIS and MOTT [13] for a solid amorphous semiconductor. According to this model, the electronic structure of energy bands is not significantly different from that in the corresponding crystal. The main difference is that the electronic states at the band edges are tailed in the forbidden gap and become localized. Therefore, the conduction mechanism changes radically from crystalline to amorphous structure. To explain the positive sign of the thermoelectric power usually observed, it is supposed that the range of localized states in the conduction band is wider than in the valence band.

Two conduction processes may occur: (a) conduction due to holes excited in extended states at E_v; (b) conduction due to holes excited in localized states

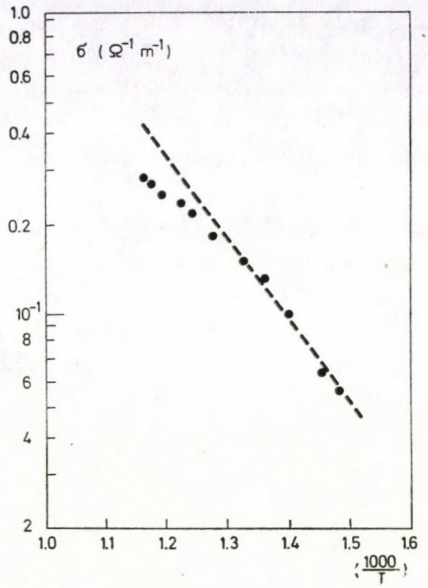

Fig. 1. Temperature dependence of the electrical conductivity for $AgTlSe_2$ in the liquid state.

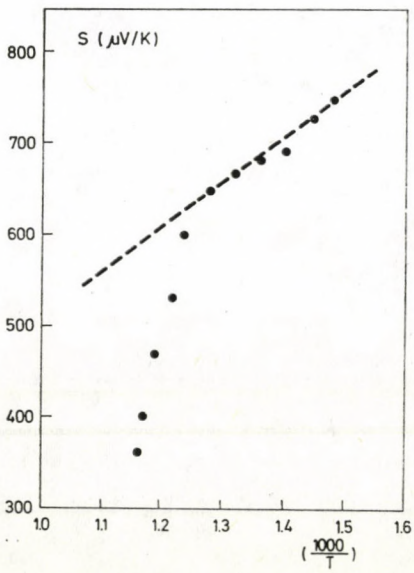

Fig. 2. Temperature dependence of the thermoelectric power for $AgTlSe_2$ in the liquid state.

near the band edges with an activated mobility, in the latter case the activation energy of the electrical conductivity (E_σ) must be slightly higher than that of the thermopower (E_S). Indeed, the activation energy of the conductivity is composed of two terms: the activation energy for carrier creation and for carrier hopping, while the activation energy of thermopower only includes the one for carrier creation [14].

The present results show that $E_\sigma = 0.54$ eV is slightly higher than $E_S = 0.5$ eV, therefore, the conduction mechanism may be attributed to holes excited in localized states near the band edges with an activated mobility. MOTT [12] and CUTLER [15] have shown that when the activation energy for the hole mobility is small compared with the energy gap, the electrical conductivity may be expressed as

$$\sigma = \sigma_0 \exp\left(-\frac{E_F - E_v}{kT}\right), \tag{1}$$

where the value of σ_0 varies strongly with the conduction process and can be determined from the intercept of $\log \sigma$ curve at $1/T =$ zero, and is equal to 130 ($\Omega^{-1} \cdot \mathrm{m}^{-1}$). Moreover, $(E_F - E_v)$ depends on the temperature and is given by

$$E_F - E_v = E(0) - \gamma T\,. \tag{2}$$

From Eqs. (1) and (2) one obtains

$$\sigma = \sigma_0 \exp(\gamma/k) \exp(-E(0)/kT) \tag{3}$$

with $E_\sigma \simeq E_S$, the temperature coefficient γ, which gives the temperature dependence of the energy gap, may be calculated directly from the thermopower which is given by

$$S = \frac{k}{e}\left(\frac{E_F - E_v}{kT} + A\right) = \frac{k}{e}\left(\frac{E(0)}{kT} - \frac{\gamma}{k} + A\right), \tag{4}$$

where the average energy of the transported hole is kTA measured with respect to E_v and the value of A depends on the nature of the scattering process. If A is known, γ can be determined from the intercept on the $1/T =$ zero axis of a plot of S versus $1/T$. From Eqs. (1) and (4) one obtains the relation between σ and S

$$\sigma = \sigma_0 \exp\left(-\frac{eS}{k} + A\right). \tag{5}$$

It is clear from Figs. 1 and 2 that $\log \sigma$ and S vary linearly with $1/T$, in the low temperature range, in accordance with Eqs. (3) and (4). The straight line extrapolated to $1/T =$ zero yields $S_0 = (-\gamma + kA)/e$. MOTT and DAVIS [14] and CUTLER and MOTT [15] have shown that the kinetic term A is of the order of unity for disordered structures. In the present discussion, we assume

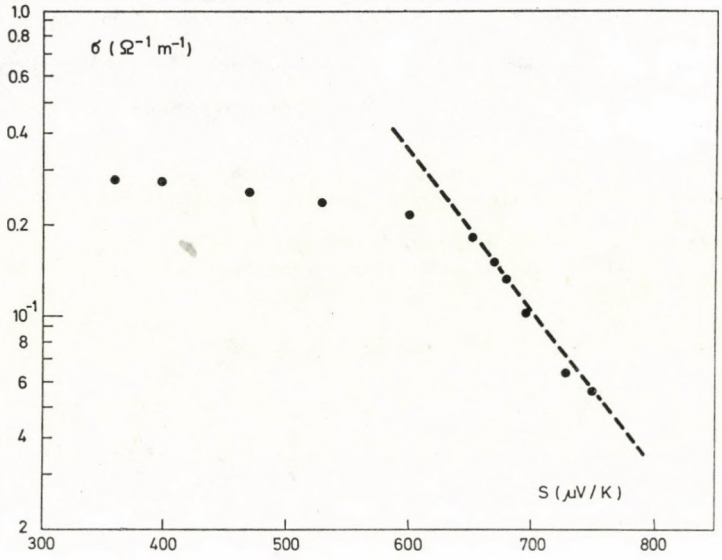

Fig. 3. log (electrical conductivity) versus thermoelectric power for liquid $AgTlSe_2$.

$A = 1$, then the value of γ for liquid $AgTlSe_2$ is found to be 0.56×10^{-4} eV/K. MOTT [14] has attributed the linear decrease of the gap with increasing temperature to the fact that the difference between the distance from one atom to nearest and next nearest neighbour decreases.

Fig. 3 shows that the dependence of $\log \sigma$ versus S is linear in the low temperature range, in accordance with Eq. (5). The behaviour of Figs. 1, 2 and 3 at high temperatures may be attributed to the effect of the temperature on the energy gap. The linear decrease of the gap may give rise to the transition from semiconducting to metallic behaviour expected at higher temperatures [14, 16]. As the gap contracts with increasing temperature, the tails of the conduction and valence bands become more pronounced and the activation energy is lowered. At sufficiently high temperatures, these tails overlap leading to a filling in of the gap and the disappearance of localization. Consequently, the electrical conductivity shows a weak temperature dependence and the thermoelectric power should approach zero.

REFERENCES

1. N. F. Mott, Phil. Mag., L3, 1966, ibid., **24**, 1, 1971.
2. N. F. Mott, Adv. Phys., **16**, 49, 1967.
3. M. Cutler and C. E. Mallon, J. Appl. Phys., **36**, 201, 1965.
4. M. Cutler and R. L. Paterson, Phil. Mag., **21**, 1033, 1970.
5. M. Cutler, Liquid Semiconductors, Academic Press, New York, 1977.
6. J. E. Enderby and L. Walsh, Phil. Mag., **14**, 991, 1966.
7. J. E. Enderby and C. J. Simmons, Phil. Mag., **20**, 125, 1969.
8. J. E. Enderby and E. W. Collings, J. Non-Crystalline Solids, **4**, 161, 1970.
9. V. P. Zhuze, V. M. Sergeeva and E. L. Shtrum, Sov. Phys. Tech. Phys. Vol. **3**, No. 10, 1925, 1958.
10. J. L. Shay and J. M. Wernick, Ternary Chalcopyrite Semiconductors, Pergamon Press, Oxford, 1975.
11. M. J. Thwaites, R. D. Tomlinson and M. J. Hampshire, Solid State Commun., **23**, 905, 1977.
12. N. F. Mott, Phil. Mag., **22**, 7, 1970.
13. E. A. Davis and N. F. Mott, Phil. Mag., **22**, 903, 1970.
14. N. F. Mott and E. A. Davis, Electronic Processes in Non-Crystalline Materials, Oxford, Second Edition, 1979.
15. M. Cutler and N. F. Mott, Phys. Rev., **181**, 1336, 1969.
16. N. F. Mott, Metal-Insulator Transition, Taylor and Francis Ltd. London, 1974.

Acta Physica Academiae Scientiarum Hungaricae, 52 (2), pp. 129—135 (1982)

GAIN MEASUREMENTS IN THE He—I^+ LASER

A. TASZNER and J. WOJTKOWIAK

INSTITUTE OF PHYSICS, UNIVERSITY OF GDANSK, 80—952 GDANSK, POLAND

(Received in revised form 22. VIII. 1981)

The gain of some visible transitions of the excited iodine ion was examined using frequency selective absorption technique. This method can be used to find optimum discharge parameters in the lasing medium. As an example the positive column He—I^+ system was studied. The results were compared with a simple theory of discharge radiation propagating along the axis of the discharge tube.

Introduction

Absorption methods are convenient to determine many parameters of gas lasers, such as the population densities, atomic temperature, absorption coefficient at the centre of line and the other parameters. Using as an example the positive column He—I^+ laser, the method presented here offers a simple way to search for new laser transitions and confirms the presumable excitation mechanisms of the lasing levels.

The He—I^+ laser system is a well known mixture, in which laser oscillation was obtained using both the hollow-cathode discharge [1—4] and the positive column discharge [5—7]. FOWLES and JENSEN [6] and SHAY et al. [8] have suggested that the thermal — energy charge transfer reaction between the helium ion state $^2S_{1/2}$ and iodine atom ground state $^2P_{3/2}$ is the dominant process for the population of some excited iodine ion states belonging to the $5s^2\,5p^3\,(^2D^0)\,6p$ configuration (shortly $6p'$) [9]:

$$\mathrm{He}^+ + \mathrm{I}_{(\text{ground state})} \rightarrow \mathrm{He} + \mathrm{I}^+ + \Delta E\,. \tag{1}$$

ΔE is the energy defect between laser levels $^1P_1$, $^3D_{1/2}$ and $^3F_{2/3}$ and the helium ion ground state, respectively. PIPER and WEBB [2] found laser oscillation from the $6p\ ^1D_2$ level which has a negative energy defect for process (1). They proposed a new charge transfer process for the levels lying above the ion ground state as is shown below

$$\mathrm{He}^+ + I^*_{(\text{metastable})} \rightarrow \mathrm{He} + \mathrm{I}^{+*} - \Delta E\,, \tag{2}$$

where I^* denotes metastable excited state $5p^5\,^2P_{1/2}$.

For this reaction ΔE is positive. For the effective ionization of He fast electrons are desired. This condition is easily available in a hollow-cathode discharge in which no saturation of the laser power vs discharge current was observed [2]. This is contrary to the behaviour of the laser power in positive column discharge. In this report the laser line intensities vs discharge current for various helium pressures and the gain of the three strongest laser lines have been determined experimentally. The gain of all measured lines was compared with our calculations, using a simple model of positive-column discharge radiation.

Principle of measurement

Fig. 1 shows the experimental set-up. The laser tube was similar to a conventional $He-I^+$ positive column laser [7]. The tube was 1.5 m long and 3.5 mm bore. The molecular sieves 5A (Union Carbide) were used for absorbing molecular iodine in the oven and in the front of the cathode. The reservoir of molecular sieves located in front of the cathode was cooled by liquid nitrogen. The temperature of the oven with molecular iodine was measured by a thermocouple and was carefully controlled. The laser tube was placed in a copper tube to eliminate external thermal fluctuations. Cold aluminium cathode of high purity was used. Broad band mirrors of 2 m radius of curvature and reflectivities of 100% and 98% were placed at a distance of 180 cm while measuring the laser power. For the gain measurements a flat mirror of ~100% reflectivity was used. A Carl Zeiss Jena SPM-2 grating monochromator was used.

For the observation of the intensity of laser lines and the gain of lines the frequency selective technique was employed. Choppers 1 and 2 (Fig. 1) at a frequency $f = 270$ Hz and a selective nanovoltmeter model "Unipan" type 237 were used. The signal from the FEU-38 photomultiplier was set at the selective nanovoltmeter. For these measurements a time constant of 10 s was used. The intensity of 540.7 nm, 576.0 nm and 612.7 nm laser oscillations was recorded when chopper 1 was switched on. It allowed to measure the laser oscillations without any noise.

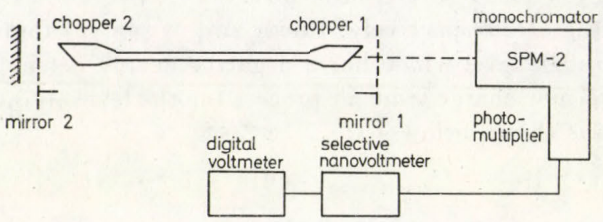

Fig. 1. Experimental set-up.

Gain study of different I^+ lines

Measurements of gain as a function of discharge current for the cw laser transition of I^+ at 540.7, 567.8, 576.0 and 612.7 nm and for the 524.6 and 533.8 nm non-lasing transitions were performed. The measurements were carried out using the differential method of light intensity recording. In the lasing system each fragment of the active discharge is assumed to be a source of light. Such a situation with non-thermal distribution was previously discussed by ALLEN and PETERS [10]. They measured the gain of the He—Ne plasma using several tubes of different length. SILFVAST and DEECH [11] and FOWLES and SILFVAST [12] measured the gain coefficient of the He-metal vapour pulsed laser in small discharge tubes by means of amplified stimulated emission (ASE) measurement. In our case one long discharge tube was used. To calculate the total gain coefficient one can use a simple model which takes into account the divergence of the ASE light at the distance "z".

The coefficient k of the four lasing lines and two non-lasing lines is defined as

$$k = \Delta I / I_0, \tag{3}$$

where I_0 denotes the intensity of selected line when chopper 1 is switched on (see Fig. 1) and the mirror is removed. ΔI denotes the intensity of respective line with chopper 2 switched on. For this case a flat mirror with a reflectivity $R = 100\%$ was used.

The light intensity observed from the element $dV = S \cdot \mathrm{d}x$, where S is the tube area, after covering distance x can be taken as

$$dI_0 = k' + (L_0 + h - x)^{-2} \cdot \exp\left[\alpha(L_0 - x)\right] \cdot \mathrm{d}x\,, \tag{4}$$

where k' is the constant proportional to the light intensity radiated from the element $S \cdot \mathrm{d}x$ of the discharge column, L_0 is the laser tube length, h is the distance between the tube end and the entrance slit of the monochromator and α is the total average gain coefficient. Substituting $z = L_0 + h - x$ into (4), the integration of the formula gives the total intensity of ASE

$$I_0 = k' \exp(-\alpha h) \cdot \int_L^{h+L_0} \exp(\alpha z) \cdot z^{-2} \cdot \mathrm{d}z\,. \tag{5}$$

When the flat mirror is used, the total active length is equal to $2L_0$ The intensity difference can be easily calculated from Eq. (6)

$$\Delta I = k' \exp(-\alpha h) \int_{L_0+h}^{2L_0+h} \exp(\alpha z) \cdot z^{-2}\, \mathrm{d}z. \tag{6}$$

ΔI is the intensity of the measured light, when the chopper placed in front of the flat mirror of reflectivity $R = 100\%$ was switched on. For this case

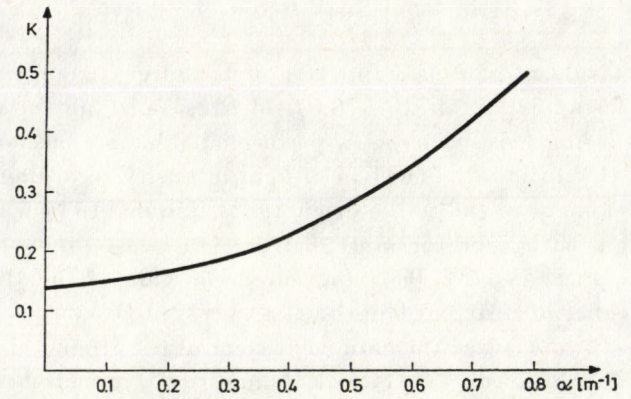

Fig. 2. Graphical transformation of the $k(\alpha)$ coefficient.

the intensity I_0 is not modulated so it is not measured in the value of ASE. Substituting Eqs. (5) and (6) into Eq. (3), after simple calculations, one can obtain coefficient k as given in (7)

$$k = \int_{L_0+h}^{2L_0+h} \exp(\alpha \cdot z) \cdot z^{-2}\,\mathrm{d}z \Big/ \int_{h}^{L_0+h} \exp(\alpha \cdot z) \cdot z^{-2}\,\mathrm{d}z. \tag{7}$$

The coefficient $k(\alpha)$ for $L_0 = 1.4$ m and $h = 0.4$ m was numerically calculated and is shown in Fig. 2.

Results and discussion

All measurements were made for one iodine pressure. Fig. 3 shows the intensity of laser lines as a function of discharge current for various helium pressures. The intensity of laser lines in the current characteristic shows a saturation character and the maximum of intensity decreases with increasing helium pressure. In the He—I^+ discharge the laser levels population depends on electron energy. Due to the increase of the buffer gas pressure both the electron kinetic energy and the rate of the charge-transfer excitation decrease. It is in accordance with the result of MORI et al [12], i.e. the electron temperature decreases with the increase of helium pressure in positive column He-metal vapour laser discharge.

Fig. 4 presents the partial diagram of I^+ energy levels with the studied transitions. Fig. 5 shows the coefficient α for lasing and non-lasing lines (dash curves). The values of α were obtained using the $k(\alpha)$ transformation shown in Fig. 2 and from the experimental dependence of the k value as a function of discharge current.

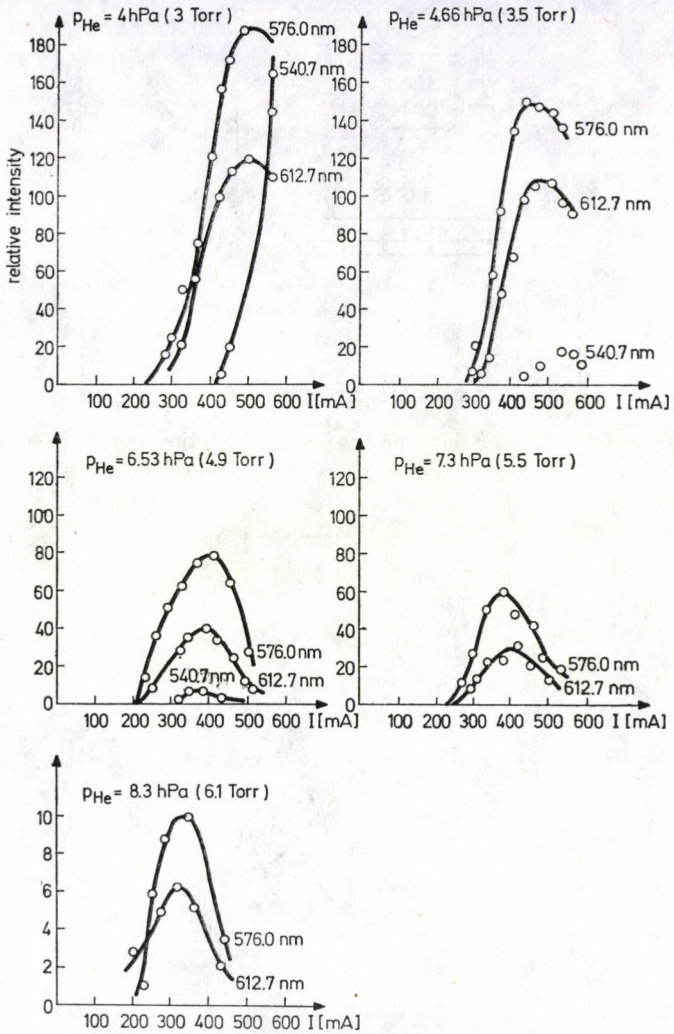

Fig. 3. Laser line intensity as a function of discharge current.

As can be seen from Fig. 5 the coefficient α shows a typical saturation for the current range 300—400 mA. The coefficient α for non-lasing lines, particularly for 524.6 nm, shows an inverted behaviour.

The resonance shape of the coefficient for 524.6 nm line is caused probably by helium ion collisions with metastable iodine atoms, which populate the $^3P_2$ state. The antisymmetrical shape of the α coefficient for the 524.6 nm line, together with the comparison of the α variation for the laser lines, suggests the influence of the $^3P_2$ state on the laser levels via inelastic collisions.

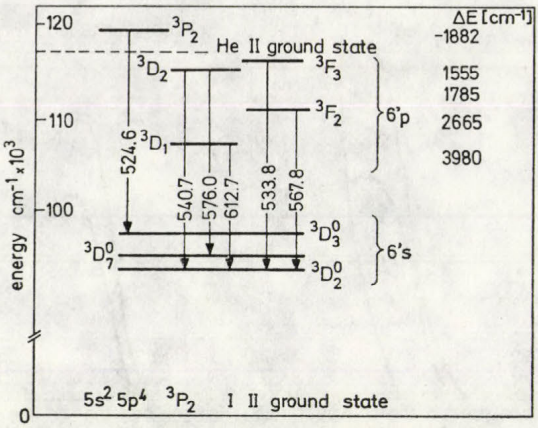

Fig. 4. Partial energy-level diagram of I^+ with the transitions studied.

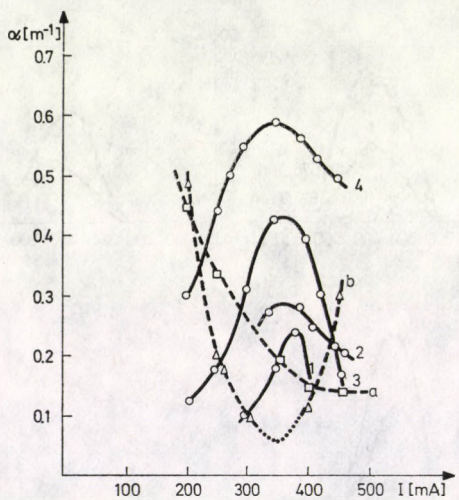

Fig. 5. The gain coefficient as a function of discharge current. Solid curves: 1 — 540.7 nm; 2 — 576.0 nm; 3 — 567.8 nm; 4 — 612.7 nm (lasing transitions). Dash curves: a — 533.8 nm; b — 524.6 nm (non-lasing transitions).

The absorption method described allows to estimate the magnitude of the average gain coefficient. This method is similar to the self-absorption method developed by HARRISON [14], in which one discharge tube and a reflective mirror were used. BROWN and DUNN [15] employed this method to determine the population densities of the metastable helium atoms. In this method the self-absorption in small length discharge tubes (a few centimeters) was considered. GOTO et al introduced the modified absorption method to determine atom or ion densities in cataphoretic type positive column gas discharges [16]. This method was applied in some further experiments [17], [18] as well.

In the experiments referred to above small discharge tubes had to be used and it was attempted to create the same conditions of discharge parameters as in real laser tubes. As our aim was to study spectral lines where no considerable absorption is expected we could use a real laser tube.

The method allows to select the optimum value of the mirror transmission for a given laser tube. It can help to find the best discharge conditions for different transitions which are expected to be laser lines. It also allows to calculate the average gain coefficient in any laser tube.

Finally, knowing the value of the α coefficient, it can help search for new laser oscillations in the laser tubes usually employed. The apparent drawback of the method is that the coefficient α is calculated indirectly from the results of measurements. However, it allows to trace qualitative changes of the coefficient in various conditions.

REFERENCES

1. J. A. Piper, J. Phys. D, **7**, 323, 1974.
2. J. A. Piper and C. Webb, IEEE J. Quantum Electron, QE — **12**, 21, 1976.
3. J. A. Piper, Opt. Commun., **19**, 189, 1976.
4. K. Rozsa, M. Janossy, J. Bergou and L. Csillag, Opt. Commun., **23**, 15, 1977.
5. S. Hattori, H. Kano, H. Tokutome, G. J. Collins and T. Goto, IEEE J. Quantum Electron., QE-**10**, 530, 1974.
6. G. R. Fowles and R. C. Jensen, Appl. Opt., **3**, 1191, 1964.
7. T. Goto, H. Kano, N. Koshino, J. K. Mizeraczyk and S. Hattori, J. Phys. E., **10**, 292, 1977.
8. T. Shay, H. Kano and G. J. Collins, Appl. Phys. Lett., **26**, 9, 1975.
9. Ch. M. Moore, Atomic Energy Levels (National Bureau of Standards, Washington, 1952) **3**, 109, 1972.
10. L. Allen and G. I. Peters, J. Phys., **4**, 564, 1971.
11. W. T. Silfvast and J. S. Deech, Appl. Phys. Lett., **11**, 97, 1967.
12. G. R. Fowles and W. T. Silfvast, Appl. Phys. Lett., **6**, 236, 1967.
13. M. Mori, T. Goto and S. Hattori, J. Phys. Soc. Japan, **43**, 662, 1976.
14. J. A. Harrison, Proc. Phys. Soc. London, **73**, 841, 1959.
15. P. G. Browne and M. H. Dunn, J. Phys. B **6**, 1103, 1973.
16. T. Goto, M. Mori and S. Hattori, Appl. Phys. Lett., **29**, 358, 1976.
17. T. Arai, T. Yabumoto and T. Goto, IEEE J. Quantum Electron., QE—**14**, 374, 1978.
18. K. Takasu, T. Goto and S. Hattori, Physica, **98B**, 125, 1979.

Acta Physica Academiae Scientiarum Hungaricae, 52 (2), pp. 137—142 (1982)

STRUCTURAL STUDIES ON A HUMAN BLADDER STONE — PMR AND IR STUDIES

B. KRISHNAN and A. SRINIVASA RAO

DEPARTMENT OF PHYSICS, JAWAHARLAL INSTITUTE OF POST-GRADUATE MEDICAL EDUCATION AND RESEARCH, PONDICHERRY, 605006 — INDIA

(Received 10. IX. 1981)

Wide line Proton Magnetic Resonance spectra of a human urinary bladder stone powder at several temperatures (in the range 77 K to 298 K) and its IR spectra (at 77 K and 298 K) were recorded and analysed. The PMR spectrum at 77 K was a broad signal and at 143 K it exhibited two signals, one broad and one narrow superimposed on each other. The line width of the broad signal and its second moment value remained constant up to 298 K and this signal was identified as due to the protons of water molecules in the sample. The narrow signal was attributed to the protons of NH_4 group in the sample and reduction in the value of its second moment at higher temperatures has been interpreted as due to the hindered rotation of NH_4 group. The IR spectrum at 77 K has shown the presence of O—H...O bonds in the sample.

Introduction

The importance of the studies on the structural aspects of the biological materials is stressed by many workers [1—5]. The study of molecular arrangements and phase transitions in urinary bladder stone and the effect of various physical factors on these solid deposits can be of great value in understanding the formation of the stone and probably help in their prevention and elimination. In the present investigation, infrared (IR) and proton magnetic resonance (PMR) spectroscopy techniques were employed in the analysis of a bladder stone with the following objectives: (i) IR studies were undertaken to identify the chemical nature of the stone and assess the strength of any possible hydrogen bonds since hydrogen bonds are known to play a significant role in determining the group structure and shape of the biomolecules. (ii) Wide line PMR studies have been undertaken with a view to determine the relative position of the hydrogen atoms and also to identify the nature and type of water, if any, so that the structural features of the stone are more clearly understood.

Experimental

A sample of urinary bladder stone was obtained from this Institute Hospital. The stone was dried under vacuum at room temperature and powdered finely. The sample powder was mixed with KBr and pressed into a thin disc under pressure and its IR spectrum was recorded at 298 K in the range 650—4000 ($\times 10^2$ m^{-1}) with a Perkin—Elmer model 257 spectrophotometer.

The IR spectrum of the sample was also recorded at 77 K by keeping the sample with a cold finger which was kept in liquid nitrogen. For this purpose the spectrum was taken of nujol mulled paste sandwiched between two KBr plates. The KBr pellet method does not give a good spectrum at low temperature because of large scattering and poor thermal contact.

The PMR spectrum of the sample was recorded using Varian wide line spectrometer operating at an R. F. frequency of 6.95 MHz. The modulation frequency employed in the experiment was 80 Hz. The signals were recorded using continuous averaging technique on a small computer having 1024 channels. Accumulated data were transferred to an X—Y recorder. The first derivatives of the PMR absorption spectra of the bladder stone powder were recorded at various temperatures, i.e. from 77 K to 298 K. The line width of the resonance absorption signal (defined as the interval between the maximum and minimum slopes of the absorption curve) was determined from the first derivative curve. Whenever two signals are superimposed on each other, they are separated out by extrapolation [6] and the second moment of each curve was calculated by graphical integration [7] and corrected for the error due to modulation amplitude. This method would not affect the value of the second moment significantly even though the line shape is uncertain at or near the centre of the resonance line where the contribution to the second moment is small.

Results and discussion

IR studies

The bands observed in the IR spectrum of the stone powder were superimposable on the bands found in the IR spectrum of pure magnesium ammonium phosphate [8]. In the sample powder there is a broad band in the region 2900—3500 ($\times 10^2$ m^{-1}) and its centre is around 3200 ($\times 10^2$ m^{-1}). A comparison of the IR spectrum of the sample with the standard IR spectrum of magnesium ammonium phosphate and the observation of a broad and diffused band in the region 2900—3500 ($\times 10^2$ m^{-1}) suggests that the present sample is magnesium ammonium phosphate hexahydrate as this is the commonly occurring hydrated form of this compound. As this is identified as an hydrated one, the band centered around 3200 ($\times 10^2$ m^{-1}) may be attributed to the presence of (O—H . . . O) bonds as well as (N—H . . . O) bonds.

PMR studies

The first derivative of the PMR absorption spectrum of the sample recorded at 77 K and at room temperature (298 K) are shown in Figs. 1 and 2. At 77 K, the PMR spectrum shows a very broad signal of line width 18.66

$\times 10^{-4}$ tesla. An additional narrow line observed in this spectrum is an artifact and found to be due to the protons of condensed water on the probe assembly. As the temperature is increased, the line width remained constant up to 143 K. At 143 K, two signals, one broad (14.00×10^{-4} tesla), the other narrow (4.77

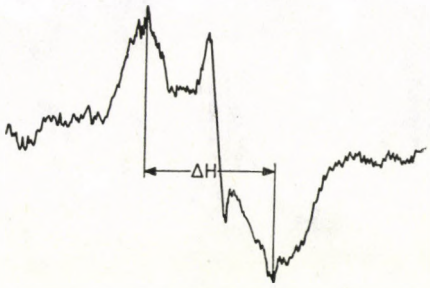

Fig. 1. First derivative tracing of the PMR absorption line of the sample powder at 77 K.

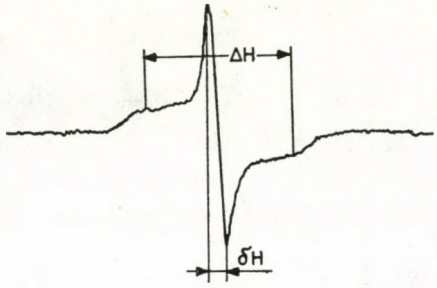

Fig. 2. First derivative tracing of the PMR absorption line of the sample powder at 298 K.

$\times 10^{-4}$ tesla) were observed. On further increase of temperature, the value of narrow signal line width was found to be decreased (from 4.77×10^{-4} tesla at 143 K to 2.39×10^{-4} tesla at 298 K) while there was no appreciable change in the line width of broad signal.

The appearance of two signals at 143 K, one broad and the other narrow, shows that there are two kinds of protons in the sample. As the sample is a hydrated one, one signal must be from the protons of water of hydration and the other from the protons of NH_4 group. The second moment value of the broad signal at 143 K is calculated to be 29.16 ± 2.20 ($\times 10^{-8}$ tesla^2) and this value remains more or less constant in the temperature range 143K to 298K. The second moment value of the broad signal in the present sample agrees fairly well with the second moment value of compounds having only water of hydration [9]. Hence it may be concluded that the broad signal may be due to the protons of water of crystallisation in the sample. To obtain further

confirmation on this conclusion, the sample powder was deuterated and its PMR spectrum at 298 K was recorded (Fig. 3). The complete absence of broad signal in the deuterated sample confirms the above conclusion. As there is no appreciable variation in the second moment of the broad line with temperature, the water molecules may be assumed to be rigid in the lattice without

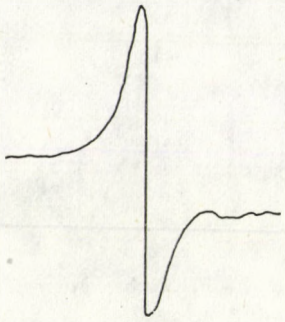

Fig. 3. First derivative tracing of the PMR absorption line of the deuterated sample powder at 298 K.

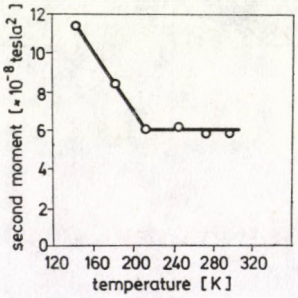

Fig. 4. Variation of second moment with temperature of the narrow signal.

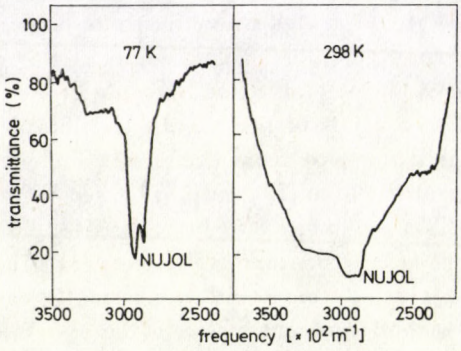

Fig. 5. Infrared spectra of the sample (in Nujol) at 77 K and 298 K in the range 2500 to 4000 ($X10^2\ m^{-1}$).

any significant molecular motion. Using the experimental value of the second moment and the VAN VLECK's second moment formula [10] for rigid lattice configuration, the nearest proton-proton distance is calculated to be 0.153 nm which compares reasonably well with the H—H distances observed in similar compounds [11].

As the broad signal is attributed to the protons from water molecules, it may be concluded that the narrow signal is due to the protons of NH_4 group in the sample. The value of the second moment of the observed narrow signal drops from a value of 11.50×10^{-8} tesla^2 at 143 K to 6.20×10^{-8} tesla^2 at 213 K and then remains reasonably constant upto 298 K (Fig. 4). The changes in the value of the second moment indicate that there is some kind of reorientation of the protons of NH_4 group. Such type of rotation of NH_4 group is known to exist in the case of ammonium chloride [12]. From the present measurements, it is not possible to fix up the temperature at which the transition begins but it is clear that the transition is complete at 213 K. The experimental value of the second moment of the narrow signal observed in the present sample (about 6×10^{-8} tesla^2 at 213 K) agrees fairly well with the value obtained for ammonium chloride above the transition temperature of 180 K [12]. This agreement suggests that the protons contributing to the narrow signal in the present bladder stone sample is due to the NH_4 group. It is clear that the protons which give rise to the narrow signal are undergoing hindered rotation of a type similar to the one observed in ammonium chloride.

The value of the second moment of the curve at 77 K is calculated to be $43.57 \pm 4.70\times10^{-8}$ tesla^2. This value compares with the dominant contribution of 45.30×10^{-8} tesla^2 coming from more closely spaced interionic proton pairs of ammonium chloride [13]. This suggests that the nuclear dipole-dipole interaction in the protons of NH_4 group of the sample dominates over the protons in the water molecules.

The hindered rotation of the NH_4 group should have some effect on the hydrogen bond system at room temperature. The rotation of NH_4 group is likely to weaken the (N—H . . . O) bonds. To study the effect of hindered rotation on the hydrogen bond system, the IR spectrum of the present sample was recorded in Nujol mull at 77 K and 298 K. Fig. 5 shows the IR spectra in the wave number region 2500—4000 ($\times10^2$ m^{-1}) as this is the region where the absorption due to hydrogen bonded N—H and O—H groups is likely to occur. The IR spectra at 77 K and 298 K appear to be the same in the wave number region 650—2000 ($\times10^2$ m^{-1}). From Fig. 5, it can be seen that two relatively weak bands are observed at 3200 and 3460 ($\times10^2$ m^{-1}) which may be identified as the O—H stretching vibrations of (O—H . . . O) bonds. It is known that such a splitting occurs in the IR spectra at low temperatures [14, 15]. At 77 K, it should be expected that the (N—H . . . O) bonds should be strong as compared to the bonds at room temperature. It is not possible to

estimate the strength of (N—H . . . O) bonds in the present studies due to the interference of the absorption by Nujol in the range 2800—2900 ($\times 10^2$ m^{-1}) even though some splitting of bands is observable in the Figure at 77 K in the region 2800—2900 ($\times 10^2$ m^{-1}). From the criterion of LIPPINCOTT et al [16], the (O—H . . . O) bond lengths at 77 K are estimated to be 0.276 nm and 0.29 nm and they agree fairly well with the hydrogen bonds formed in similar hydrated salts [4, 5].

Our earlier studies [4, 5] on two different types of urinary bladder stones have revealed the existence of the tumbling of protons of water molecules. But the present investigation on the third type of stone has shown that protons of NH_4 group are undergoing some kind of hindered rotation. These studies suggest that the rotation of one group or other exists in the urinary bladder stones and this may probably make the stones softer.

Acknowledgements

The authors wish to thank the Director of this Institute for encouragement, Prof. R. VIJAYARAGHAVAN, Tata Institute of Fundamental Research, Bombay, for facilities provided to record PMR spectra and Prof. RAJ KHANNA of the University of Maryland, U.S.A. for arranging to get IR spectrum at 77 K.

REFERENCES

1. H. M. MYERS, Nature, **206,** 713, 1965.
2. H. M. MYERS, Exptl. Cell Res., **38,** 686, 1965.
3. M. F. LITTLE and F. S. SCIANI, Arch. Oral Biol., **11,** 565, 1966.
4. B. KRISHNAN and A. SRINIVASA RAO, Curr. Sci., **48,** 1026, 1979.
5. B. KRISHNAN and A. SRINIVASA RAO, Indian J. Pure Appl. Phys., **11,** 780, 1979.
6. I. M. WARD, Trans. Faraday Soc., **56,** 648, 1960.
7. G. E. PAKE and E. M. PURCELL, Phys. Rev., **74,** 1184, 1948.
8. G. T. BENDER, Chemical Instrumentation: A laboratory manual based on Clinical Chemistry, W. B. Saunders Company, Philadelphia, 1972.
9. K. MUTHUKRISHNAN nad J. RAMAKRISHNAN, Curr. Sci., **41,** 769, 1972.
10. J. H. VAN VLECK, Phys. Rev., 74, 1168, 1948.
11. P. J. WHEATLEY, The Determination of Molecular Structure, 2nd Edn., The Clarendon Press, Oxford, p. 248, 1968.
12. R. BERSOHN and H. S. GUTOWSKY, J. Chem. Phys., **22,** 651, 1954.
13. E. R. ANDREW, Nuclear Magnetic Resonance, The University Press, Cambridge, p. 162, 1958.
14. S. BRATOZ, J. Chem. Phys., **27,** 997, 1957.
15. J. E. KATON, J. T. MILLER Jr. and F. F. BENTLAY, Arch. Biochem. Biophys., **121,** 798, 1967.
16. E. R. LIPPINCOTT and A. SRINIVASA RAO, J. Chem. Phys., **41,** 3006, 1964.

Acta Physica Academiae Scientiarum Hungaricae, 52 (2), pp. 143—151 (1982)

ELECTRICAL CONDUCTION OF THIN BISMUTH FILMS

A. H. ABOU EL ELA, S. MAHMOUD* and M. A. MAHMOUD

PHYSICS DEPARTMENT, ISLAMIC GIRLS COLLEGE, NASR CITY, CAIRO, EGYPT
AND PHYSICS DEPARTMENT*, NATIONAL RESEARCH CENTRE, CAIRO, EGYPT

(Received 10. IX. 1981)

The electrical resistivity of thin bismuth films, thermally evaporated onto freshly cleaved mica and glass substrates has been studied. Measurements were carried out in a wide range of temperatures and thicknesses. The data measured for thicker films were fitted to a FUCHS—SONDHEIMER model with $p = 0$, while the abrupt rise of resistivity for very thin films is described assuming a tunnelling mechanism for island film.

1. Introduction

The behaviour of electrical conductivity and galvanomagnetic coefficients of thin metal films has been the subject of many theoretical [1, 2] and experimental investigations. Information regarding the nature of electron scattering from film surface can be obtained from measurements of the electrical conductivity as a function of the film thickness. Data analysis for such measurements is generally carried our using the well-known FUCHS size effect theory [1], or FUCHS—SONDHEIMER model [2, 3]. MAYADAS [4] and MAYADAS and SHATZKES [5] had reconsidered these models to include the reflection of the charge carriers at the grain boundary specially when the grain size is of the order of the mean free path of the carriers.

The study of size effect in bismuth films is of importance due to the possible existence of classical as well as quantum size effects. In bismuth the mean free path of electrons at room temperature is of the order 2000 nm, also, the Fermi energy of electrons is about 25 meV and the effective masses along some crystal orientations are two or three orders of magnitude smaller than the free-electron mass. Quite a large number of measurements [6—10] on size effect were reported with a number of contradictions.

The aim of the present contribution is to investigate the electrical conduction in thin bismuth films of different thicknesses (20—400 nm) at different temperatures. In this work the tunnelling through vacuum between islands and through the supporting substrate were taken in consideration.

2. Experimental

Thin bismuth films of different thicknesses (20—400 nm) were prepared by thermal evaporation of highly pure bismuth (99.999%), using a helical tungsten wire as a filament for evaporation, in a vacuum of $\sim 10^{-4}$ Pa at an evaporation rate of about 2 nm/s, onto freshly cleaved surface of mica and smooth glass on which evaporated gold electrodes were previously prepared. The film thickness was measured by the TOLANSKY interference method [11]. The resistivity was measured using the potentiometric technique.

a) *Temperature dependence of the resistivity*

The experimental dependence of the electrical resistivity on temperature for bismuth films of different thicknesses evaporated onto smooth glass and mica substrates is shown in Figs. 1 and 2. It is seen that with an increase in

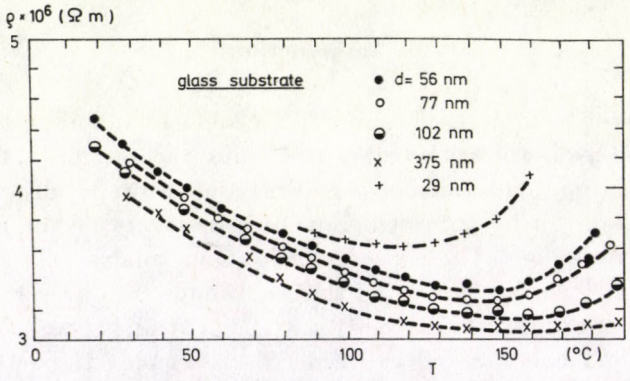

Fig. 1. Temperature dependence of the resistivity for bismuth films thermally evaporated at 10^{-4} Pa on smooth glass substrate.

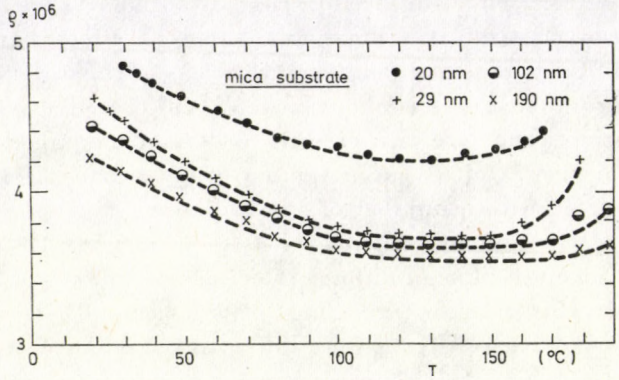

Fig. 2. Temperature dependence of the resistivity for bismuth films thermally evaporated at 10^{-4} Pa on mica substrate.

temperature ϱ decreases, reaching its lowest value at different temperatures depending on the film thickness. A further increase in the temperature leads to an increase in resistivity. This behaviour can be explained taking in consideration that the electrical resistivity of a bismuth layer is given by

$$\frac{2}{\varrho} = \sigma = en(\mu_e + \mu_h),$$

where n is the number of charge carriers and μ is their mobility. As the temperature rises the mobility decreases which is attributed to the decrease of the mean free path, because of the scattering of electrons and holes at the outer surface of the film and at the boundaries of its crystallites. On the other hand, the charge carrier density unlike their mobilities, increase noticeably faster. An analysis of the data on the temperature dependence of the density of charge carriers and their mobilities [12—15] shows that with an increase in the temperature, the increase in carrier density leads the fall-off in their mobilities, which leads, on the whole, to a decrease in electrical resistivity. With a further increase in temperature, however, the reverse situation is observed, and the electrical resistivity increases. This behaviour leads to a negative temperature coefficient of resistance below about 120 °C and positive TCR above 140 °C. Fig. 3 shows the variation of TCR with thickness for 45 °C. TCR has large negative values for very thin films and decreases with thickness.

b) *Thickness dependence of the resistivity*

Fig. 4 shows a representative example for the variation of the electrical resistivity with thickness up to 400 nm at 40 °C and 100 °C. The resistivity values are very large for thin films and decrease strongly with thickness. The electrical resistivity of a continuous film could be the described by the LUCAS equation [16]

$$\frac{\varrho_f}{\varrho_0} = \Phi'(p, q, k) = 1 - \frac{3}{4k}\int_1^\infty \left(\frac{1}{t^3} - \frac{1}{t^5}\right) \frac{1 - e^{-kt}}{1 - pqe^{-2kt}} \cdot \\ \cdot [2 - p - q + (p + q - 2pq)\, e^{-kt}]\, dt, \tag{1}$$

where ϱ_0 is the resistivity of the bulk material and $k = d/l_0$, d is the film thickness, l_0 is the bulk mean free path, $t = 1/\cos\theta$, (the electron mean free path subtends an angle θ with the normal to the film), and p, q are the specularity parameters for the two surfaces of the film.

For a polycrystalline film the background scattering may be different from bulk which implies the replacement of ϱ_0 and l_0 by their intrinsic values

ϱ_i and l_i and a thin polycrystalline film approximation is

$$\frac{\varrho_f}{\varrho_0} = 1 + \frac{3l_i(2-p-q)}{16\,d} \qquad \text{for } d < l_i\,. \tag{2}$$

The results for a series of films were fitted to Eq. (2), with $p = q = 0$. A representative example is shown in Fig. 5, where $\varrho\, d$ is plotted versus d.

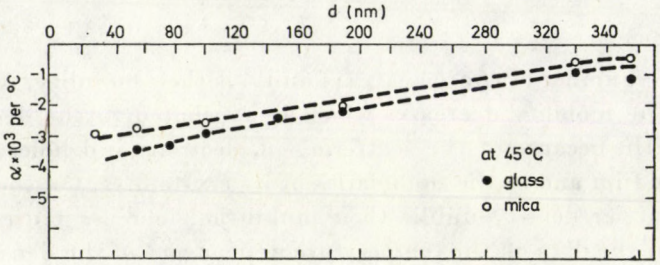

Fig. 3. TCR vs thickness for bismuth films at 45 °C.

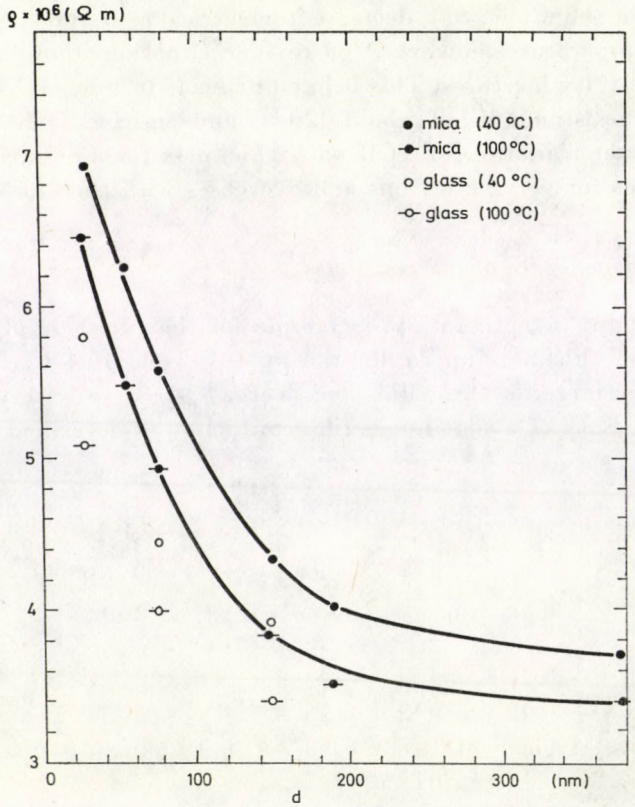

Fig. 4. The dependence of the resistivity on thickness for bismuth films evaporated onto glass and mica substrates and annealed at 40 °C and 100 °C.

The values of ϱ_i and l_i obtained by least square fitting of data are $\varrho_i = 3.6 \times \times 10^{-6}\ \Omega \cdot$ m and $l_i = 1824$ nm for mica substrate and $\varrho_i = 3.65 \times 10^{-6}\ \Omega \cdot$ m and $l_i = 1875$ nm for glass substrate annealed at 100 °C. The calculated value of l_i is in good agreement with that for bulk bismuth crystal [17], where $l = 2000$ nm, however ϱ_i is higher than the corresponding value of bulk bismuth. The possible gas adsorption, aggregation of bismuth crystallites and

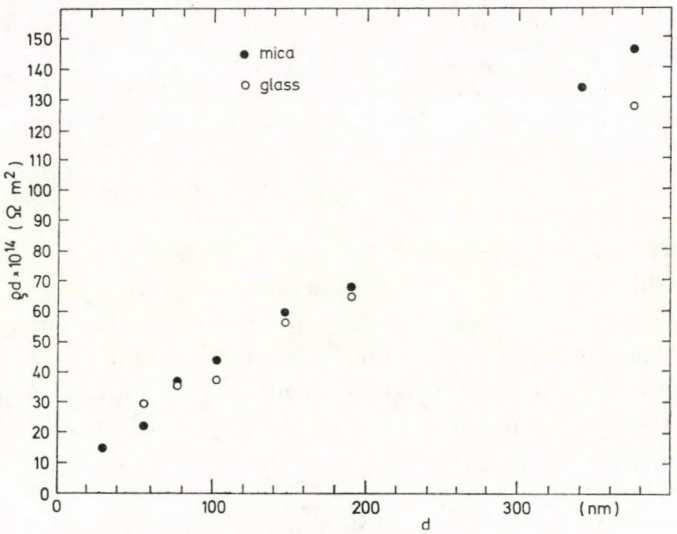

Fig. 5. The dependence of the product of resistivity times thickness on the thickness for bismuth films at 100 °C.

the limitations imposed by boundary conditions on the electron momentum perpendicular to the plane of the film may explain the high value of ϱ_i.

Using the experimental values of ϱ_i and l_i, the Fermi surface area of bismuth was calculated from the relation

$$\frac{1}{\varrho_i l_i} = \frac{e^2 A_F}{12 \pi^2 \hbar},$$

a value $A_F = 7 \times 10^{-20}$ m^2.

The abrupt increase in resistivity of films thinner than 40 nm could not be explained in terms of either LUCAS [16] or FUCHS—SONDHEIMER [1, 2] models. Such films, condense with a discontinuous structure subdivided into islands. Therefore, the conduction electrons must move by means of a tunnelling mechanism [18, 19]. MAYADAS and SHATZKES [5] have calculated the resistivity of a polycrystalline film in which three types of scattering mechanisms are simultaneously operative: an isotropic background scattering (due to phonons and point defects), scattering due to grain boundaries, and scattering

due to external surfaces. The total film resistivity is given by

$$\frac{\varrho_f}{\varrho_i} = \frac{\Phi'(p = q, k)}{f(\gamma)}, \tag{3}$$

where

$$f(\gamma) = \frac{\varrho_i}{\varrho_g} = 3\left[\frac{1}{3} - \frac{1}{2}\gamma + \gamma^2 - \gamma^3 \ln\left(1 + \frac{1}{\gamma}\right)\right], \tag{4}$$

$$\gamma = 2\frac{l_i}{D}\frac{S^2}{\hbar^2 v_F^2} = \frac{l_i}{D}\frac{R}{1-R},$$

where D is the grain size,

$$k_i = \frac{d}{l_i f(\gamma)},$$

R is the coefficient of reflection at grain boundaries, l_i is the intrinsic MFP of electrons within the grains, ϱ_f is the intrinsic resistivity due to background scatterers only, ϱ_g is the grain resistivity and S is the grain boundary strength. The above equations could be applied for island boundaries scattering [20], instead of grain boundaries, where the boundary strength S is given by the product of the barrier potential V and the gap width a, and the reflection coefficient R is

$$R = \frac{2S^2}{2S^2 + \hbar^2 v_F^2},$$

where for too weak boundary $S \ll \hbar v_F$ and R approach zero, while for too strong boundary $S \gg \hbar v_F$ and R approach 1. For vacuum tunnelling as the charge transfer mechanism the process is an activated one and the energy W needed for the removal of a charge from an initially neutral island to another is given by

$$W \simeq \frac{e^2}{\varepsilon D} - \frac{e^2}{\varepsilon(D + a)}$$

and

$$S = \frac{e^2}{\varepsilon}\frac{a^2}{D(D + a)}, \tag{5}$$

where ε is the dielectric constant of the interposed medium. In terms of D and a estimated by electron microscopy the resistivity of films between 25 nm and 370 nm was fitted to Eq. (3) with $p = 0$.

The electrical resistivity of thinner films of island structure ($d < 25$ nm) is ruled by scattering due to grain boundaries, scattering due to external surfaces and scattering due to island boundaries. For island film it is reasonable to add the effect of grain boundaries and it is reasonable practical approxi-

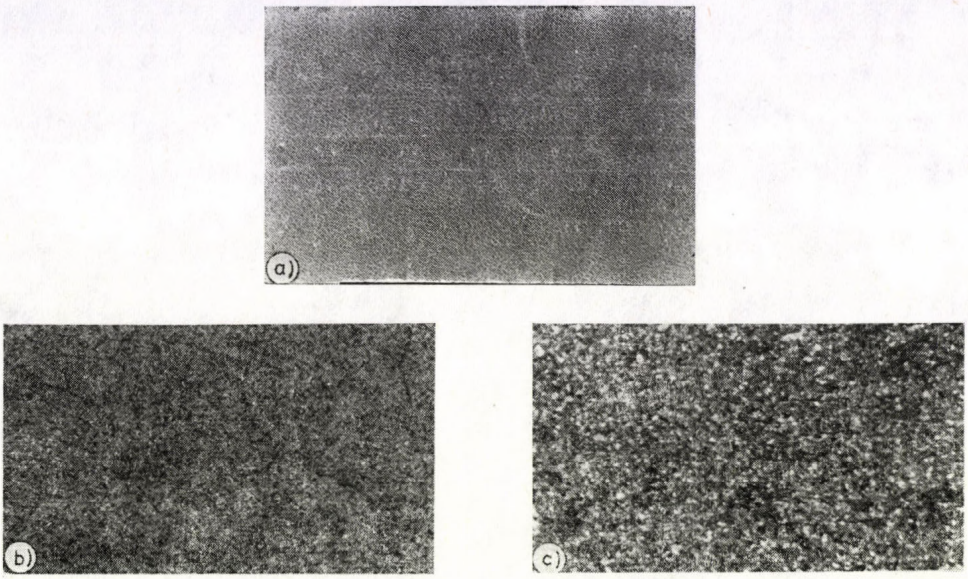

Fig. 6. Electron microscopy micrographs for thin bismuth films evaporated onto amorphous carbon substrate: a) 12 nm, 8000 X; b) 18 nm, 6000 X; c) 22 nm, 6000 X.

mation to attribute the abrupt change in resistivity of thinner films to the variation of island size and separations and to neglect the external surface effect. The total resistivity of the island film is given by

$$\frac{\varrho_f}{\varrho_i} = [f(\gamma)]^{-1}, \tag{6}$$

where $f(\gamma)$ is given by Eq. (4) and takes the limits [5]

$$\frac{\varrho_f}{\varrho_i} = 1 + \frac{3}{2} - \gamma, \quad \gamma \ll 1, \tag{7a}$$

$$\frac{\varrho_f}{\varrho_i} = -\frac{4}{3} - \gamma, \quad \gamma \gg 1. \tag{7b}$$

Using the values of D and a estimated from the electron micrographs (Figs. 6 and 7) and Eqs. (5) and (7) the ratio (ϱ_f/ϱ_i) can be calculated. Full display of the estimated values is shown in Tables I and II.

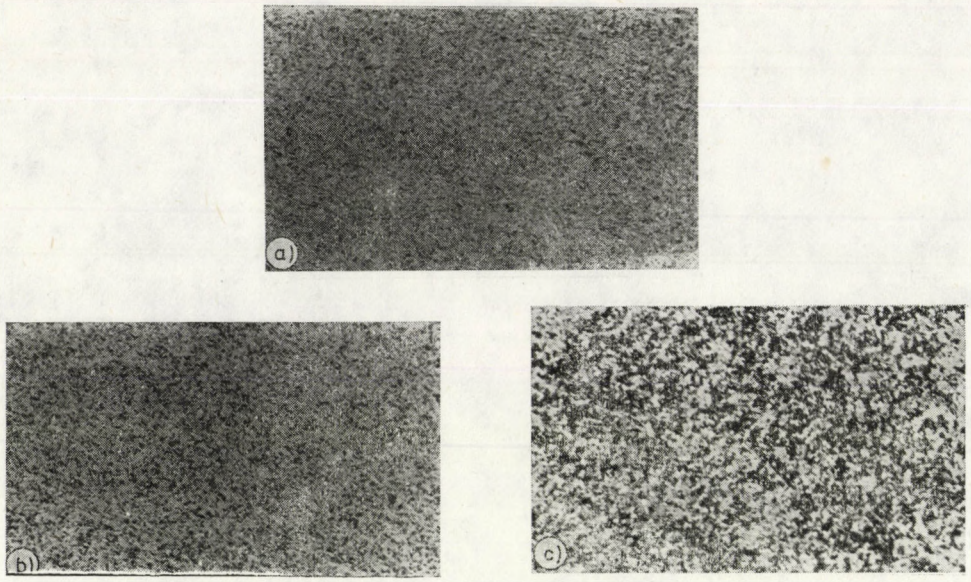

Fig. 7. Electron microscopy micrographs for thin bismuth films evaporated onto mica substrate: a) 12 nm, 6000 X; b) 17 nm, 6000 X; c) 22 nm, 6000 X.

Table I

Estimated values used to calculate ϱ_f/ϱ_i for thin bismuth films on glass under a vacuum of 10^{-4} Pa with $\varepsilon = 1$

d(nm)	D(nm)	a(nm)	V(eV)	S(eV · m)	R	γ	ϱ_f/ϱ_i
12	27	122.5	0.0436	0.53×10^{-8}	0.997	42.2×10^{3}	56.3×10^{3}
18	45	61	0.018	0.11×10^{-8}	0.93	1.07×10^{3}	1.43×10^{3}
22	57.5	27	0.008	0.022×10^{-8}	0.34	32.73	43.64

Table II

Estimated values used to calculate ϱ_f/ϱ_i for thin bismuth films deposited on mica under a vacuum of 10^{-4} Pa with $\varepsilon = 1$

d(nm)	D(nm)	a(nm)	V(eV)	S(eV · m)	R	γ	ϱ_f/ϱ_i
12	37.5	147	0.031	0.456×10^{-8}	0.996	22.34×10^{3}	29.78×10^{3}
17	58	69	0.014	0.093×10^{-8}	0.906	0.6×10^{3}	0.8×10^{3}
22	78.6	41	0.006	0.026×10^{-8}	0.43	34.96	36.6

REFERENCES

1. K. Fuchs, Proc. Cambridge Phil. Soc. **34**, 100, 1938.
2. E. H. Sondheimer, Adv. in Phys., **1**, 1, 1952.
3. D. S. Campell, in The Use of Thin Films in Physical Investigations (Academic Press Inc. New York 1966) p. 315.
4. A. F. Mayadas, J. Appl. Phys., **39**, 4241, 1968.
5. A. F. Mayadas and M. Shatzkes, Phys. Rev. B, **1**, 1382, 1970.
6. E. C. Crittenden Jr. and R. W. Hoffman, Rev. Mod. Phys., **25**, 310, 1953.
7. V. P. Duggal and Raj Rup, J. Appl. Phys., **40**, 492, 1969.
8. R. A. Hoffman and D. R. Frankel, Phys. Rev. B, **3**, 1825, 1971.
9. N. Garcia, Y. H. Kao and M. Strongin, Phys. Rev. B, **5**, 2029, 1972.
10. L. S. Hsu and Y. Y. Chang, J. Appl. Phys., **47**, 2359, 1976.
11. S. Tolansky, Introduction to Interferometry, Longman Group, 1955.
12. Yu. Komnik, Ye. I. Bukhshtab and Yu. V. Nikitin, Fiz. Tverd. Tela, **13**, 793, 1970.
13. G. A. Ivanov and Yu. T. Levitskii, Fiz. Metallov. Metallovedenyia, **24**, 253, 1967.
14. G. F. Callo, B. S. Chadrasekhar and P. H. Sutter, J. Appl. Phys. **35**, No. 1, 1963. 144.
15. V. M. Abrosimov, B. N. Yegorov and M. A. Krykin, Soviet Physics JETP, **64**, 217, 1973.
16. M. S. Lucas, J. Appl. Phys., **36**, 1682, 1965.
17. V. I. Kaidanov and A. R. Regel, Sov. Phys. Tech. Phys., **3**, 376, 1958.
18. K. L. Chopra, Thin Film Phenomena, McGraw Hill 1969.
19. C. A. Neugbaur and M. B. Webb, J. Appl. Phys., **33**, 74, 1962.
20. A. V. Joglekar, J. Phys. D. (Appl. Phys.) **7**, 1270, 1974.

Acta Physica Academiae Scientiarum Hungaricae, 52 (2), pp. 153—163 (1982)

AN APPROXIMATE VARIATIONAL SOLUTION OF BOUNDARY LAYER FLOW WHEN FREE STREAM VARIES AS POWER FUNCTION

P. SINGH and S. ANTONY RAJ

DEPARTMENT OF MATHEMATICS, INDIAN INSTITUTE OF TECHNOLOGY
KANPUR—208016, INDIA

(Received 17. IX. 1981)

A variational method is developed to solve the boundary layer equations when the free stream velocity varies as a power function ($U_\infty = ax^m$). The method is based on the governing principle of dissipative processes (GPDP). The Lagrangian density is obtained in the energy picture of GPDP and the partial differential equations of motion are reduced to ordinary differential equations in terms of boundary layer thickness. The velocity profile and the skin friction are calculated for various values of m. It is found that the present results are quite close to the exact ones and are better than those of known approximate methods.

1. Introduction

The study of the flow characteristics of the laminar boundary layer with arbitrary distribution of main flow velocity is very difficult even for the constant property flow because the system is governed by a set of non-linear partial differential equations. But it was shown by FALKNER and SKAN [1] that the system of governing equations can be reduced to that of ordinary differential equations if the free stream velocity is assumed to vary as power function of distance from the start of the boundary layer. FALKNER and SKAN also obtained an approximate solution for this type of flow. Later HARTREE [2] studied the problem in detail and found more accurate numerical solutions. He also proved that the solution was unique if $m > 0$. STEWARTSON [3] showed that in the range of unfavourable pressure gradient ($-0.091 < m < 0$) the solutions were not unique. In view of the considerable amount of labour involved in the numerical computations many approximate methods were suggested to study the flow characteristics. The well-known method is of Karman—Pohlhausen. According to the boundary layer theory in flows around bodies the irreversible processes of momentum transfer occur inside a thin layer near the surface. Therefore the natural way to study this non-equilibrium phenomenon is to use the theory of irreversible processes. In the present study we develop an approximate variational formulation which reduces the partial differential equations into an ordinary differential equation which can be solved for any value of m in the range $0 \leq m < \infty$. This equation further reduces to an algebraic polynomial equation if similarity considerations are taken into account.

In the sixties, GYARMATI [4, 5] proposed a variational principle by means of which evolution of dissipative transport processes can be described in space and time. The principle based on ONSAGER's linear theory [6, 7] and reciprocal relations is called the 'Governing Principle of Dissipative Processes' (GPDP). The most general form of the principle is given by [4]

$$\delta \int_V [\sigma - \Psi - \Phi] \, dV - 0 \tag{1}$$

for any instant of time under the constraints that the balance equations

$$\dot{\varrho}_i + \nabla \cdot \mathbf{J}_i = \sigma_i \quad (i = 1, 2, \ldots, f) \tag{2}$$

are satisfied. Here V denotes the entire volume of the thermodynamic system. σ, the entropy production per unit time and volume, is expressed as a bilinear function of thermodynamic forces and currents. That is,

$$\sigma = \sum_{i=1}^{f} \mathbf{J}_i \cdot \mathbf{X}_i \geq 0 \, . \tag{3}$$

This is a positive definite quantity according to the second law of thermodynamics. f is the number of independent fluxes $\mathbf{J}_i$ and thermodynamic forces $\mathbf{X}_i$. In the linear Onsager theory, the fluxes $\mathbf{J}_i$ and the forces $\mathbf{X}_i$ are related by the linear constitutive equations

$$\mathbf{J}_i = \sum_{k=1}^{f} L_{ik} \mathbf{X}_k \, ; \; \mathbf{X}_i = \sum_{k=1}^{f} R_{ik} \mathbf{J}_k \, , \tag{4}$$

where R_{ik} and L_{ik} satisfy the relations

$$\sum_{e=1}^{f} L_{ie} R_{ek} = \sum_{e=1}^{f} R_{ie} L_{ek} \quad (i, k = 1, 2, \ldots, f) \tag{5}$$

and

$$L_{ik} = L_{ki} \, ; \; R_{ik} = R_{ki} \, . \tag{6}$$

Using (4) σ can be expressed as

$$\sigma \equiv \sum_{i,k=1}^{f} L_{ik} \mathbf{X}_i \mathbf{X}_k \equiv \sum_{i,k=1} R_{ik} \mathbf{J}_i \mathbf{J}_k \geq 0 \, . \tag{7}$$

The above two forms of σ are called force and flux representations of the entropy production. The non-equilibrium local potentials [4] Ψ and Φ which are equal

to half of the entropy production are given by

$$\Psi(\mathbf{X}, \mathbf{X}) \equiv \frac{1}{2} \sum_{i,k=1}^{f} L_{ik} \mathbf{X}_i \cdot \mathbf{X}_k \geq 0\,, \tag{8}$$

$$\Phi(\mathbf{J}, \mathbf{J}) \equiv \frac{1}{2} \sum_{i,k=1}^{i} R_{ik} \mathbf{J}_i \cdot \mathbf{J}_k \geq 0\,. \tag{9}$$

Ψ and Φ are also the local measures of irreversibility. The potential character of Ψ and Φ can be seen from the relations

$$\mathbf{J}_i = \frac{\partial \Psi}{\partial \mathbf{X}_i} = \sum_{k=1}^{f} L_{ik} \mathbf{X}_k \quad (i = 1, 2, \ldots, f)\,, \tag{10}$$

$$\mathbf{X}_i = \frac{\partial \Phi}{\partial \mathbf{J}_i} = \sum_{k=1}^{f} R_{ik} \mathbf{J}_k \quad (i = 1, 2, \ldots, f) \tag{11}$$

which are the linear constitutive equations (4). Using the expressions of σ, Ψ and Φ in principle (1) we get

$$\delta \int_V \left[\sum_{i=1}^{f} \mathbf{J}_i \cdot \nabla \Gamma_i - \frac{1}{2} \sum_{i,k=1}^{f} L_{ik} \nabla \Gamma_i \cdot \nabla \Gamma_k - \frac{1}{2} \sum_{i,k=1}^{f} R_{ik} \mathbf{J}_i \cdot \mathbf{J}_k \right] \mathrm{d}V = 0, \tag{12}$$

where the dissipative forces $\mathbf{X}_i$ can be generated as the gradients of certain Γ variables which are state parameters and simultaneously internal parameters with respect to forces [4]:

$$\mathbf{X}_i = \nabla \Gamma_i. \tag{13}$$

The principle (12) is operative if and only if the balance equations (2) are treated as auxiliary conditions for whose variations the restrictions

$$\delta(\dot{\varrho}_i - \sigma_i) = -\delta(\nabla \cdot \mathbf{J}_i) = -\nabla \cdot (\delta \mathbf{J}_i) \quad (i = 1, 2, \ldots, f) \tag{14}$$

are valid. This principle has already been used to derive the equations of thermo-hydrodynamics by VINCZE [8].

2. Formulation of GPDP

Prandtl's boundary layer equations for two-dimensional incompressible steady fluid flow are

$$\frac{\partial u}{\partial x} + \frac{\partial v}{\partial y} = 0\,, \tag{15}$$

$$\varrho \left(u \frac{\partial u}{\partial x} + v \frac{\partial u}{\partial y} \right) = -\frac{\partial p}{\partial x} + \mu \frac{\partial^2 u}{\partial y^2} = \varrho U_\infty \frac{\mathrm{d}U_\infty}{\mathrm{d}x} + \mu \frac{\partial^2 u}{\partial y^2}\,, \tag{16}$$

where u, v are the velocity components along x and y directions, respectively, ϱ the density and μ the coefficient of shear viscosity. The boundary conditions of the problem are

$$y = 0 \ : u = 0, \qquad v = 0, \tag{17}$$
$$y \to \infty : u \to U_\infty .$$

It is well-known that in the formulation of GYARMATI's principle the balance equations play the basic role which in this case are

$$\nabla \cdot \mathbf{V} = 0 , \tag{18}$$
$$\varrho (\mathbf{V} \cdot \nabla) \mathbf{V} + \nabla \cdot \boldsymbol{P} = 0 . \tag{19}$$

These equations represent the mass and the momentum balance, respectively. $\boldsymbol{P}$ denotes the pressure tensor and it takes the form for the present problem [9]

$$\boldsymbol{P} = p\delta + \overset{\circ}{\boldsymbol{P}}{}^{vs}, \tag{20}$$

where p is the hydrostatic pressure and $\overset{\circ}{\boldsymbol{P}}{}^{vs}$ is the symmetrical part of the viscous pressure tensor, the trace of which is zero. $\mathbf{V}$ is the velocity vector

$$\mathbf{V} = \mathbf{i}u + \mathbf{j}v . \tag{21}$$

In the study of fluid flow problems, the energy picture of GYARMATI's principle is preferable over entropy picture. We shall, therefore, use the energy dissipation $T\sigma$ instead of entropy production σ. The energy dissipation for the problem is [5]

$$T\sigma = - \overset{\circ}{\boldsymbol{P}}{}^{vs} : (\nabla \overset{\circ}{\mathbf{V}})^s = - P_{12} \frac{\partial u}{\partial y} \geq 0 , \tag{22}$$

where $(\nabla \overset{\circ}{\mathbf{V}})^s$ is the symmetrical part of the velocity gradient tensor and its trace is zero. In this case it has only one component $(\nabla \overset{\circ}{\mathbf{V}})^s_{12} = \dfrac{\partial u}{\partial y}$. The viscous pressure tensor $\overset{\circ}{\boldsymbol{P}}{}^{vs}$ also has only one component P_{12}. The double dots represent the scalar product of two tensors. The linear constitutive relation for the present case is

$$P_{12} = - \mu \frac{\partial u}{\partial y} . \tag{23}$$

The dissipation potentials Ψ and Φ in the energy picture are

$$T\Psi \equiv \frac{\mu}{2} \left(\frac{\partial u}{\partial y} \right)^2 \geq 0 ,$$
$$T\Phi \equiv \frac{1}{2\mu} P_{12}^2 \geq 0 . \tag{24}$$

Using (22) and (24) the energy picture of principle (1) assumes the form

$$\delta \int_0^L \int_0^\infty \left[- P_{12} \frac{\partial u}{\partial y} - \frac{\mu}{2} \left(\frac{\partial u}{\partial y} \right)^2 - \frac{1}{2\mu} P_{12}^2 \right] dy\, dx = 0 , \tag{25}$$

where L is the characteristic length of the body. Following the dual field method [10], we introduce a new velocity field u^* through the approximate constitutive equation

$$P_{12} = - \mu \frac{\partial u^*}{\partial y} . \tag{26}$$

It is assumed that u^* satisfies the same boundary conditions as u. The momentum balance (16) and the principle (25) now become

$$\varrho \left(u \frac{\partial u}{\partial y} + v \frac{\partial u}{\partial y} \right) = - \frac{\partial p}{\partial x} + \mu \frac{\partial^2 u^*}{\partial y^2} , \tag{27}$$

$$\delta \int_0^L \int_0^\infty \left[\frac{\partial u}{\partial y} \frac{\partial u^*}{\partial y} - \frac{1}{2} \left(\frac{\partial u^*}{\partial y} \right)^2 - \frac{1}{2} \left(\frac{\partial u^*}{\partial y} \right)^2 \right] dy\, dx = 0 . \tag{28}$$

3. Method of solution

We consider the two-dimensional inviscid potential flow past an unlimited wedge placed symmetrically in a stream with apex at the orgin and the centre line on the positive x-axis. The flow creates along the surface a velocity variation like

$$U_\infty(x) = a x^m, \tag{29}$$

where a is a constant and the exponent m is connected with the apex-angle $\pi\beta$ by the relation

$$m = \beta/(2 - \beta). \tag{30}$$

We confine our analysis to realistic flows only, that is, when $0 \leq m < \infty (0 \leq \leq \beta < 2)$.

We assume a third degree trial function for longitudinal velocity u as

$$\frac{u}{U_\infty} = \frac{3y}{\alpha} - \frac{3y^2}{\alpha^2} + \frac{y^3}{\alpha^3} \, (0 \leq y \leq \alpha) , \tag{31}$$

where α is the boundary layer thickness. When $y > \alpha$, $u = U_\infty$. The profile (31) satisfies the boundary conditions

$$y = 0 : u = 0 ,$$

$$y = \alpha : u = U_\infty , \frac{\partial u}{\partial y} = 0 , \frac{\partial^2 u}{\partial y^2} = 0 . \tag{32}$$

Equation of continuity (15) yields the transverse velocity component v as follows

$$\frac{v}{U_\infty} = \frac{m}{x}\left(-\frac{3y^2}{2\alpha} + \frac{y^3}{\alpha^2} - \frac{y^4}{4\alpha^3}\right) + \alpha'\left(\frac{3y^2}{2\alpha^2} - \frac{2y^3}{2\alpha^3} + \frac{3y^4}{4\alpha^4}\right), \tag{33}$$

where prime indicates differentiation with respect to x. From momentum balance (27) we obtain

$$\begin{aligned} \nu u^* = {} & \frac{mU_\infty^2}{x}\left[\frac{53\alpha y}{160} - \frac{y^2}{2} + \frac{3y^4}{8\alpha^2} - \frac{3y^5}{10\alpha^3} + \frac{y^6}{8\alpha^4} - \frac{y^7}{28\alpha^5} + \frac{y^8}{224\alpha^6}\right] + \\ & + U_\infty^2\,\alpha'\left[\frac{9y}{160} - \frac{3y^4}{8\alpha^3} + \frac{3y^5}{5\alpha^4} - \frac{3y^6}{8\alpha^5} + \frac{3y^7}{28\alpha^6} - \frac{3y^8}{224\alpha^7}\right] + \frac{\nu U_\infty\, y}{\alpha}, \end{aligned} \tag{34}$$

when Eqs. (27), (31) and (33) are used.

Using (31) and (34) in principle (28) and integrating it with respect to y, we get

$$\begin{aligned} \delta\int_0^L \Bigg[& (0.1241071)\frac{m\,U_\infty^3\,\alpha}{\nu x} + (0.03482143)\frac{U_\infty^3\,\alpha'}{\nu} - (0.4)\frac{U_\infty^2}{\alpha} - \\ & - \frac{1}{2\nu^2}\left\{(0.01943109)\frac{m^2\,U_\infty^4\,x^3}{x^2} + (0.001624899)\,U_\infty^4\,\alpha'^2\alpha + \right. \\ & \left. + (0.01056987)\frac{mU_\infty^4\alpha'\alpha^2}{x}\right\}\Bigg]\mathrm{d}x = 0\,. \end{aligned} \tag{35}$$

Here the boundary-layer thickness α is substituted for the limit of integration ∞.

The concise formulation of the principle (35) is given with the help of Lagrangian density $\mathfrak{L}$ as $\delta\int_0^L \mathfrak{L}\,dx = 0$. The Euler-Lagrange equation

$$\frac{\partial\mathfrak{L}}{\partial\alpha} - \frac{\mathrm{d}}{\mathrm{d}x}\left(\frac{\partial\mathfrak{L}}{\partial\alpha}\right) = 0 \tag{36}$$

becomes in the present case

$$\begin{aligned} & (16.24899)\,U_\infty^4 x^2(\alpha''\alpha + \alpha'^2)\alpha^2 - (8.12449)\,U_\infty^4\alpha'^2\alpha^2x^2 \\ & + (64.99596)\,mU_\infty^4\alpha'\alpha^3x - (80.069)\,m^2U_\infty^4\alpha^4 \\ & - (52.8494)\,U_\infty^4 m\alpha^4 + (196.428)\,mU_\infty^3\alpha^2\nu x \\ & + 4000\,U_\infty^2\nu^2x^2 = 0, \end{aligned} \tag{37}$$

which is an ordinary differential equation in boundary layer thickness α. α can be given in terms of dimensionless boundary layer thickness α^* as

$$\alpha = \alpha^* \sqrt{\nu x / U_\infty}. \tag{38}$$

The relation (38) and its derivatives transform the ordinary differential equation (37) to an algebraic polynomial equation

$$\alpha^{*4}[m^2(106.4736) + m(24.41362) + 2.031124] - \\ - \alpha^{*2} m(196.4281) - 4000 = 0, \tag{39}$$

which is a simple relation between dimensionless boundary layer thickness α^* and m. The only positive root of the equation (39) is the boundary layer thickness α^*.

Eq. (34) is employed to calculate the velocity distributions at various points inside the boundary layer. The results for the cases $m = 1/3$ and $m = 1$ are quite comparable with Hartree's numerical solutions as can be seen in Table I.

The trial function for velocity (31) is not valid for the case $m = 0$ (flow over flat plate) because it fails to satisfy the compatibility condition $\dfrac{\partial^2 u}{\partial y^2} = 0$ at $y = 0$. Hence for this case we choose the longitudinal velocity as a polynomial of fourth degree

$$\frac{u}{U_\infty} = \frac{2y}{\alpha} - \frac{2y^3}{\alpha^3} + \frac{y^4}{\alpha^4} \tag{40}$$

satisfying the conditions

$$y = 0 : u = 0, \quad \frac{\partial^2 u}{\partial y^2} = 0, \\ y = \alpha : u = U_\infty, \quad \frac{\partial u}{\partial y} = 0, \quad \frac{\partial^2 u}{\partial y^2} = 0. \tag{41}$$

As in the previous analysis we obtain v and the approximate velocity u^* as given below

$$\frac{v}{U_\infty} = \alpha' \left(\frac{y^2}{\alpha^2} - \frac{3y^4}{2\alpha^4} + \frac{4y^5}{5\alpha^5} \right), \tag{42}$$

$$\gamma u^* = U_\infty^2 \alpha' \left[(0.05611111)\, y - \frac{y^4}{6\alpha^3} + \frac{7y^6}{30\alpha^5} - \frac{11y^7}{105\alpha^6} - \right. \\ \left. - \frac{3y^8}{56\alpha^7} + \frac{2y^9}{54\alpha^8} - \frac{4y^{10}}{450\alpha^9} \right] + \frac{\nu U_\infty y}{\alpha}. \tag{43}$$

Table I

Comparison between the present approximate results and HARTREE's velocity profiles

β	0		0.5		1	
$\eta = y\sqrt{\frac{(m+1)U_\infty}{2\nu x}}$	HARTREE	Present results	HARTREE	Present results	HARTREE	Present results
0.2	0.0939	0.0949	0.1756	0.1758	0.2266	0.2267
0.4	0.1876	0.1896	0.3311	0.3318	0.4144	0.4146
0.6	0.2806	0.2835	0.4670	0.4680	0.5662	0.5662
0.8	0.3720	0.3757	0.5834	0.5848	0.6859	0.6853
1.0	0.4606	0.4649	0.6811	0.6830	0.7778	0.7761
1.2	0.5453	0.5500	0.7615	0.7638	0.8467	0.8433
1.4	0.6244	0.6296	0.8258	0.8284	0.8968	0.8916
1.6	0.6967	0.7025	0.8760	0.8786	0.9324	0.9257
1.8	0.7610	0.7675	0.9141	0.9164	0.9569	0.9495
2.0	0.8167	0.8240	0.9421	0.9437	0.9732	0.9667
2.2	0.8633	0.8715	0.9621	0.9629	0.9841	0.9803
2.4	0.9011	0.9099	0.9760	0.9761	0.9905	0.9923
2.6	0.9306	0.9398	0.9852	0.9852	0.9946	1.0000
2.8	0.9529	0.9618	0.9913	0.9921	—	—
3.0	0.9691	0.9769	0.9952	0.9983	—	—
3.2	0.9804	0.9867	0.9974	1.0000	—	—
3.6	0.9929	0.9961	—	—	—	—
4.0	0.9978	1.0000	—	—	—	—

Principle (28) for the case under consideration reduces to

$$\delta\int_0^L \left[(0.03092519)\,\frac{U_\infty^3\,\alpha'}{\gamma} - (0.242857)\,\frac{U_\infty^2}{\alpha} - \right.$$

$$\left. - (0.000992228)\,\frac{U_\infty^4\,\alpha'^2\alpha}{\nu^2}\right]dx = 0\,. \tag{44}$$

The Euler-Lagrange equation is obtained again as an ordinary differential equation

$$(19.82456)\,U_\infty^4\alpha^2(\alpha''\alpha + \alpha'^2) - (9.91228)\,U_\infty^4\alpha'^2\alpha^2 + (2428.57)\,\nu^2U_\infty^2 = 0. \tag{45}$$

As before this equation ultimately reduces to the following simple form

$$\alpha^{*4} - 980.0253 = 0. \tag{46}$$

Table II

Velocity profiles for various β

η \ β	0.4	0.8	1.2	1.6
0.2	0.1634	0.2078	0.2421	0.2706
0.4	0.3107	0.3843	0.4381	0.4807
0.6	0.4419	0.5308	0.5919	0.6376
0.8	0.5567	0.6497	0.7089	0.7505
1.0	0.6555	0.7437	0.7953	0.8293
1.2	0.7388	0.8161	0.8574	0.8833
1.4	0.8072	0.8702	0.9011	0.9207
1.6	0.8620	0.9095	0.9319	0.9479
1.8	0.9044	0.9375	0.9543	0.9695
2.0	0.9361	0.9573	0.9719	0.9882
2.2	0.9588	0.9718	0.9871	1.0000
2.4	0.9744	0.9834	1.0000	—
2.6	0.9847	0.9936	—	—
2.8	0.9916	1.0000	—	—
3.0	0.9967	—	—	—
3.2	1.0000	—	—	—

Solving the above equation we obtain the positive root

$$\alpha^* = 5.595119. \tag{47}$$

The velocity distribution given in Table I for this case is also found in good agreement with HARTREE's results. Fig. 1 indicates the velocity profiles for the cases $m = 0$, 1/3 and 1 while Table II gives the velocity distribu-

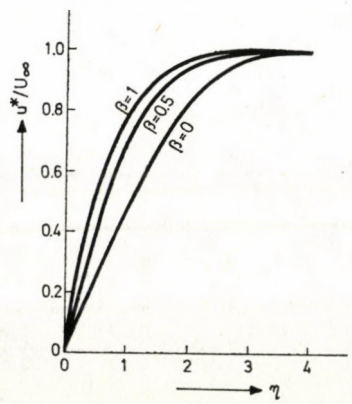

Fig. 1. Velocity distribution u^*/U_∞ vs dimensionless ordinate η for various β.

Table III

Comparison between the present approximate results and SMITH's exact values of skin friction

β	SMITH	Present results	β	SMITH	Present results
0.0	0.4696	0.4737	0.50	0.9277	0.9294
0.05	0.5311	0.5369	0.60	0.9958	0.9965
0.10	0.5870	0.5919	0.80	1.1203	1.1188
0.20	0.6867	0.6909	1.00	1.2326	1.2333
0.30	0.7748	0.7782	1.20	1.3357	1.3300
0.40	0.8544	0.8571	1.60	1.5215	1.5118

tion $\frac{u^*}{U_\infty}$ at various points inside the boundary layer for various values of m.

The skin friction at the surface of the wall is calculated with the help of the formula

$$\tau_w^* = \left(\frac{\partial u}{\partial y}\right)_{y=0}. \tag{48}$$

The non-dimensional skin friction τ_w^* is given by the following relation

$$\tau_w^* = \sqrt{\frac{2\nu x}{(m+1)\, U_\infty^3}} \left(\frac{\partial u^*}{\partial y}\right)_{y=0}. \tag{49}$$

In Table III we have compared the skin friction obtained from the present analysis with SMITH's results [11] for $0 \leq \beta < 2$. It is found that the approximate results differ by less than 2 percent from numerical values. We

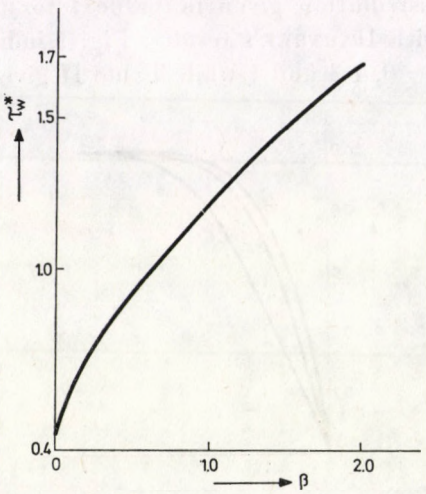

Fig. 2. Dimensionless skin friction τ_w^* vs the Falkner—Skan parameter β.

also compare our results with those of Karman—Pohlhausen in order to assess the power of the present method. The skin friction calculated with the help of Karman--Pohlhausen technique for the cases $m = 0$ and 1 are 0.485 and 1.19, respectively. It can be easily observed that the results of the present method are better. Fig. 2 shows the skin friction τ_w^* for various values of β.

4. Concluding remarks

The main objective of this paper is to introduce the variational principle based on sound physical reasoning as a powerful tool for solving boundary layer problems. The exact theory of irreversible processes is used to get the analytical solution of the boundary layer flow when the free stream velocity varies as power function of x. The non-linear partial differential equations are reduced to algebraic equations (39) and (46) which can be solved very easily for any positive value of m. The skin friction and velocity profile are compared with known numerical solutions for some values of m. For the required value of m the boundary layer thickness can be calculated easily and thus study can be made with the help of profile (34).

It is interesting to note that this approximate variational procedure yields results which are analytical and almost exact. The great advantage of this analysis is that the amount of calculation is considerably less. It can be suggested that the results of this method can be used as initial guesses for obtaining numerical solutions of the boundary layer differential equations for various values of β.

Acknowledgement

The co-author (S. A.) acknowledges the FIP Fellowship of University Grants Commission, New Delhi.

REFERENCES

1. V. M. Falkner and S. W. Skan, Phil. Mag., **12**, 865, 1931.
2. D. R. Hartree, Proc. Camb. Phil. Soc., **33**, 223, 1937.
3. K. Stewartson, Proc. Camb. Phil. Soc., **50**, 454, 1954.
4. I. Gyarmati, Ann. Phys., **23**, 353, 1969.
5. I. Gyarmati, Non-equilibrium Thermodynamics, Field Theory and Variational Principles, Springer Verlag, Berlin, 1970.
6. L. Onsager, Phys. Rev., **37**, 405, 1931.
7. L. Onsager, Phys. Rev., **38**, 2265, 1931.
8. Gy. Vincze, Ann. Phys., **27**, 225, 1971.
9. S. R. De Groot and P. Mazur, Non-equilibrium Thermodynamics, North Holland, Amsterdam, 1969.
10. P. Singh, Int. J. Heat Mass Transfer, **19**, 581, 1976.
11. A. M. O. Smith, Inst. Aero. Sci. S. M. F. Fund Paper FF-10, 1954.

Acta Physica Academiae Scientiarum Hungaricae, 52 (2), pp. 165—169 (1982)

A NEARLY EXACT HELICAL-WAVE SOLUTION TO THE EQUATIONS OF SLIGHTLY DISSIPATIVE MAGNETOHYDRODYNAMICS

BHIMSEN K. SHIVAMOGGI

DEPARTMENT OF THEORETICAL PHYSICS, RESEARCH SCHOOL OF PHYSICAL SCIENCES
THE AUSTRALIAN NATIONAL UNIVERSITY, CANBERRA, A.C.T., 2600 AUSTRALIA

(Received 17. IX. 1981)

A nearly exact solution to the magnetohydrodynamic equations of a fluid of small resistivity describing the propagation of a helical magnetosonic wave parallel to the direction of a uniform magnetic field is given. Departures from an ideal magnetohydrodynamic situation in the context of the earth's magnetosphere seem to lead to a loss of charged particles from a given region.

It is well known that difficulties arise in obtaining exact solutions to the equations of magnetohydrodynamics. One way to make progress is to make some symmetry postulates or prescribe a priori the dependence of the solution on space and time (LIN [1], UBEROI [2], WOOLLEY [3], SHIVAMOGGI and UBEROI [4]). WOOLLEY [3] gave an exact solution to the magnetohydrodynamic equations of an infinitely-conducting fluid which describes the propagation of a helical magnetosonic wave parallel to the direction of a uniform magnetic field. This solution is of relevance in the propagation of waves in the earth's magnetosphere.

Since a real plasma always has a finite resistivity, the purpose of this paper is to extend WOOLLEY's [3] treatment to the case of a fluid with finite resistivity. However, it then turns out that an exact solution is no longer possible, but a nearly exact solution may be obtained by assuming the resistivity of the fluid to be small. Besides, it turns out that, physically, departures from an ideal magnetohydrodynamic situation in the context of the earth's magnetosphere may lead to a loss of charged particles from a given region.

The magnetohydrodynamic equations of a conducting fluid are (FERRARO and PLUMPTON [5])

$$\varrho \frac{d\mathbf{V}}{dt} = = \nabla p + \frac{1}{4\pi}(\nabla \times \mathbf{H}) \times \mathbf{H}\,, \tag{1}$$

$$\frac{d\varrho}{dt} = -\varrho \nabla \cdot \mathbf{V}\,, \tag{2}$$

$$p = k\varrho^{\gamma}\,, \tag{3}$$

$$\frac{\partial \mathbf{H}}{\partial t} = \nabla \times (\mathbf{V} \times \mathbf{H}) + \eta \nabla^2 \mathbf{H}\,, \tag{4}$$

$$\nabla \cdot \mathbf{H} = 0\,, \tag{5}$$

where **V** is the fluid velocity, p the pressure, ϱ the mass density, η the resistivity, γ the ratio of specific heats of the fluid, **H** the magnetic field.

Use a system of rectangular coordinates (x, y, z), and look for a solution that depends only on x, and time t. Eqs. (1)–(5), then become

$$\varrho\left(\frac{\partial V_x}{\partial t}+V_x\frac{\partial V_x}{\partial t}\right)=-\frac{\partial p}{\partial x}-\frac{1}{8\pi}\frac{\partial}{\partial x}(H_y^2+H_z^2)\,, \tag{6}$$

$$\varrho\left(\frac{\partial V_y}{\partial t}+V_x\frac{\partial V_y}{\partial x}\right)=\frac{1}{4\pi}H_x\frac{\partial H_y}{\partial x}\,, \tag{7}$$

$$\varrho\left(\frac{\partial V_z}{\partial t}+V_x\frac{\partial V_z}{\partial x}\right)=\frac{1}{4\pi}H_x\frac{\partial H_z}{\partial x}\,, \tag{8}$$

$$\frac{\partial\varrho}{\partial t}+V_x\frac{\partial\varrho}{\partial x}=-\varrho\frac{\partial V_x}{\partial x}\,, \tag{9}$$

$$p=k\varrho^{\gamma}\,, \tag{10}$$

$$\frac{\partial H_x}{\partial t}=\eta\frac{\partial^2 H_x}{\partial x^2}\,, \tag{11}$$

$$\frac{\partial H_y}{\partial t}=-\frac{\partial}{\partial x}(V_xH_y-V_yH_x)+\eta\frac{\partial^2 H_y}{\partial x^2}\,, \tag{12}$$

$$\frac{\partial H_z}{\partial t}=\frac{\partial}{\partial x}(V_zH_x-V_xH_z)+\eta\frac{\partial^2 H_z}{\partial x^2}\,, \tag{13}$$

$$\frac{\partial H_x}{\partial x}=0\,. \tag{14}$$

One obtains from Eqs. (14) and (11)

$$H_x=\text{const.} \tag{15}$$

Putting

$$\varrho=\frac{\partial\lambda}{\partial x} \tag{16}$$

Eq. (9) gives

$$\frac{d\lambda}{dt}\equiv\left(\frac{\partial}{\partial t}+V_z\frac{\partial}{\partial x}\right)\lambda=0\,. \tag{17}$$

Putting

$$H_y=\frac{\partial\xi}{\partial z}\,,\quad H_z=\frac{\partial\zeta}{\partial x} \tag{18}$$

and using (15), Eqs. (12) and (13) give

$$\frac{d\xi}{dt}=H_xV_y+\eta\frac{\partial^2\xi}{\partial x^2}\,, \tag{19}$$

$$\frac{d\zeta}{dt}=H_xV_z+\eta\frac{\partial^2\zeta}{\partial x^2}\,. \tag{20}$$

Using (15)—(20), Eqs. (6)—(8) become

$$\frac{\partial\lambda}{\partial x}\frac{dV_x}{\partial t} = -k\frac{\partial}{\partial x}\left[\left(\frac{\partial\lambda}{\partial x}\right)^{\gamma}\right] - \frac{1}{8\pi}\frac{\partial}{\partial x}\left[\left(\frac{\partial\xi}{\partial x}\right)^2 + \left(\frac{\partial\zeta}{\partial x}\right)^2\right], \tag{21}$$

$$\frac{\partial\lambda}{\partial x}\frac{d^2\xi}{dt^2} = \left(\frac{H_x^2}{4\pi} + \eta\frac{\partial\lambda}{\partial x}\frac{d}{dt}\right)\frac{\partial^2\xi}{\partial x^2}, \tag{22}$$

$$\frac{\partial\lambda}{\partial x}\frac{d^2\zeta}{dt^2} = \left(\frac{H_x^2}{4\pi} + \eta\frac{\partial\lambda}{\partial x}\frac{d}{dt}\right)\frac{\partial^2\zeta}{\partial x^2}. \tag{23}$$

If ξ, ζ, and ϱ are regarded as functions of λ and t, Eqs. (21)—(23) may be written as

$$\frac{\partial V_x}{dt} = -\frac{d}{d\lambda}(k\varrho^{\gamma}) - \frac{1}{8\pi}\frac{d}{d\lambda}\left[\varrho^2\left\{\left(\frac{\partial\xi}{\partial x}\right)^2 + \left(\frac{\partial\zeta}{\partial x}\right)^2\right\}\right], \tag{24}$$

$$\frac{\partial^2\xi}{\partial t^2} = \left(\frac{H_x^2}{4\pi} + \eta\varrho\frac{\partial}{\partial t}\right)\left[\frac{\partial}{\partial\lambda}\left(\varrho\frac{\partial\xi}{\partial\lambda}\right)\right], \tag{25}$$

$$\frac{\partial^2\zeta}{\partial t^2} = \left(\frac{H_x^2}{4\pi} + \eta\varrho\frac{\partial}{\partial t}\right)\left[\frac{\partial}{\partial t}\left(\varrho\frac{\partial\zeta}{\partial\lambda}\right)\right]. \tag{26}$$

Following WOOLLEY [3], let us look for a helical motion of the fluid and assume

$$\left.\begin{aligned}\xi &= f(\lambda)\cos\omega t + h(\lambda)\sin\omega t\\ \zeta &= h(\lambda)\cos\omega t - f(\lambda)\sin\omega t\end{aligned}\right\} \tag{27}$$

which implies that the component of the magnetic field perpendicular to the direction of the uniform field H_x rotates uniformly about the latter direction.

Using (27), Eqs. (25) and (26) become

$$-\omega^2 f = \frac{H_x^2}{4\pi}\frac{\partial}{\partial\lambda}\left(\varrho\frac{\partial f}{\partial\lambda}\right) + \eta\varrho\omega\frac{\partial}{\partial\lambda}\left(\varrho\frac{\partial h}{\partial\lambda}\right), \tag{28}$$

$$-\omega^2 h = \frac{H_x^2}{4\pi}\frac{\partial}{\partial\lambda}\left(\varrho\frac{\partial h}{\partial\lambda}\right) = \eta\varrho\omega\frac{\partial}{\partial\lambda}\varrho\left(\frac{\partial f}{\partial\lambda}\right). \tag{29}$$

Now, Eq. (24) gives

$$V_x = ut + v, \tag{30}$$

where u and V are two constants. The motion of the fluid may thus be described in term of the variable φ where

$$\varphi = x - \frac{ut^2}{2} - vt + w, \tag{31}$$

where w is another constant. Eqs. (24), (28) and (29) then give

$$u\lambda = I_0 - k\left(\frac{d\lambda}{d\varphi}\right)^{\gamma} - \frac{1}{8\pi}\left[\left(\frac{df}{d\varphi}\right)^2 + \left(\frac{dh}{d\varphi}\right)^2\right], \tag{32}$$

$$\frac{d^2 f}{d\varphi^2} = -\frac{4\pi\omega^2}{H_x^2} f\frac{d\lambda}{d\varphi} - \frac{4\pi\omega}{H_x^2}\eta\frac{d^2 h}{d\varphi^2}\frac{d\lambda}{d\varphi}, \tag{33}$$

$$\frac{d^2 h}{d\varphi^2} = -\frac{4\pi\omega^2}{H_x^2} h\frac{d\lambda}{d\varphi} + \frac{4\pi\omega}{H_x^2}\eta\frac{d^2 f}{d\varphi^2}\frac{d\lambda}{d\varphi}, \tag{34}$$

where I_0 is a constant of integration. Assuming that η is small, Eqs. (32)—(34) have two integrals L_0 and I_1 given by

$$f\frac{dh}{d\varphi} - h\frac{df}{d\varphi} \approx \begin{cases} L_0 + \dfrac{4\pi\omega}{H_x^2}\eta\int\left(f\dfrac{d^2 f}{d\varphi^2} + h\dfrac{d^2 h}{d\varphi^2}\right)\times \\ \quad \times\left\{\left[\dfrac{\omega^2}{2H_x^2}(f^2+h^2) - I_1 - u\varphi\right]\dfrac{\gamma-1}{k\gamma}\right\}^{\frac{1}{\gamma-1}} d\varphi\,, \quad \gamma \neq 1 \\ L_0 + \dfrac{4\pi\omega}{H_x^2}\eta\int\left(f\dfrac{d^2 f}{d\varphi^2} + h\dfrac{d^2 h}{d\varphi^2}\right)\times \\ \quad \times\left(\exp\left\{\left[\dfrac{\omega^2}{2H_x^2}(f^2+h^2) - I_1 - u\varphi\right]\dfrac{1}{k}\right\}\right) d\varphi\,, \quad \gamma = 1 \end{cases} \tag{35}$$

$$\frac{\omega^2}{2H_x^2}(f^2+h^2) \approx \begin{cases} I_1 + \dfrac{k\gamma}{\gamma-1}\left(\dfrac{d\lambda}{d\varphi}\right)^{\gamma-1} + u\varphi - \dfrac{\omega}{H_x^2}\eta L_0\,, & \gamma \neq 1\,, \\ I_1 + k\ln\left(\dfrac{d\lambda}{d\varphi}\right) + u\varphi - \dfrac{\omega}{H_x^2}\eta L_0\,, & \gamma = 1\,. \end{cases} \tag{36}$$

Now, noting that

$$V_y H_y + V_z H_z = \frac{\omega}{H_z}\left(h\frac{df}{d\varphi} - f\frac{dh}{d\varphi}\right) \tag{37}$$

one observes, on using (35), that in the presence of a small resistivity in the fluid, the magnetic-field lines no longer move with the fluid.

Putting

$$f = r\cos\theta, \qquad h = r\sin\theta, \tag{38}$$

Eqs. (32), (36) and (35) give

$$\left(\frac{dr}{d\varphi}\right)^2 + r^2\left(\frac{d\Theta}{d\varphi}\right)^2 = 8\pi\left[I_0 - k\left(\frac{d\lambda}{d\varphi}\right)^{\gamma} - u\lambda\right], \tag{39}$$

$$\frac{d\lambda}{d\varphi} = \begin{cases} \left(\frac{\gamma-1}{k\gamma}\right)^{\frac{1}{\gamma-1}} \left(\frac{\omega^2 r^2}{2H_x^2} - u\varphi - I_1 - \frac{\omega}{H_x^2}\eta L_0\right)^{\frac{1}{\gamma-1}}, & \gamma \neq 1 \\ \exp\left[\frac{1}{k\gamma}\left(\frac{\omega^2 r^2}{2H_x^2} - u\varphi - I_1 - \frac{\omega}{H_x^2}\eta L_0\right)^{\frac{1}{\gamma-1}}\right], & \gamma = 1 \end{cases} \tag{40}$$

$$\frac{d\theta}{d\varphi} = \frac{L_0}{r^2} + \\ + \frac{4\pi\omega}{rH_x^2}\eta \int \frac{4\pi\left[k\gamma\left(\frac{d\lambda}{d\varphi}\right)^{\gamma-1}\frac{d^2\lambda}{d\varphi^2} - u\frac{d\lambda}{d\varphi}\right]}{\left[8\pi\left\{I_0 - k\left(\frac{d\lambda}{d\varphi}\right)^{\gamma} - u\lambda\right\} - \frac{L_0^2}{r^2}\right]^{1/2}} \cdot \frac{d\lambda}{d\varphi}\, d\varphi . \tag{41}$$

It is clear that the system (39)—(41), in general, has to be integrated numerically. For the case $u = 0$, one may write the system (39)—(41) in the form

$$\left(\frac{dr}{d\varphi}\right)^2 = \Phi(r) . \tag{42}$$

In the absence of a resistivity in the fluid (i.e. $\eta = 0$) (42) shows that $r(\varphi)$ will be a periodic motion which represents a helical magnetosonic wave and corresponds to the fact that a charged particle in an electromagnetic wave propagating parallel to a uniform magnetic field moves in a region between concentric cylinders which have their axes in the direction of the uniform magnetic field, (WOOLLEY [6]). (42) shows that the effect of the presence of a small resistivity is to introduce a slight aperiodicity in the fluid motion. In the context of the earth's magnetosphere (wherein the local magnetic field of the earth may be taken to be uniform as a first approximation, and the gravitational forces may be thought to produce electromagnetic waves propagating along the earth's magnetic field lines), the implication of this result may be a loss of charged particles from a given region due to departures from an ideal magnetohydrodynamic situation.

REFERENCES

1. C. C. LIN, Arch. Rat. Mech. Anal., **1**, 391, 1958.
2. M. S. UBEROI, Phys. Fluids, **6**, 1379, 1963.
3. M. L. WOOLLEY, Plasma Phys., **15**, 89, 1973.
4. B. K. SHIVAMOGGI and M. S. UBEROI, Phys. Fluids, **22**, 2247, 1979.
5. V. C. A. FERRARO and C. PLUMPTON, Introduction to Magnetofluid Mechanics, Clarendon Press, Oxford, 1966.
6. M. L. WOOLLEY, Plasma Phys., **12**, 779, 1970.

Acta Physica Academiae Scientiarum Hungaricae, 52 (2), pp. 171—173 (1982)

ESTIMATION OF DISSOCIATION ENERGIES OF WEAKLY BOUND MOLECULES

A. M. GHODGAONKAR and K. RAMANI

WESTERN REGIONAL INSTRUMENTATION CENTRE, UNIVERSITY OF BOMBAY, BOMBAY 400 098, INDIA

(Received 6. X. 1981)

The applicability of ENGELKE Potential to determine the dissociation energy of weakly bound molecules in terms of Dunham, Morse and Lennard-Jones potentials is examined. A simple expression for dissociation energy of weakly bound molecules is derived and the predicted values are in accordance with the available experimental data.

Power series expansion of the vibrational number or the inter-nuclear distance is one of the most important methods of relating spectra of diatomic molecules to their molecular structure. The utility of such expansions largely depends upon the radius of convergence. In the case of the DUNHAM series [1], it is severely restricted. The non-analytic behaviour of the potential at zero inter-nuclear distance is one of the possible sources of this shortcoming. Various methods have been suggested [2—6] to overcome this difficulty, however, all the terms in these series are not available to improve the range of utility. The solution to this problem has recently been provided by ENGELKE [7] by generalising the OGILVIE—TIPPING and THAKKAR series and is referred to as the (β, q) representation.

In this communication we relate the ENGELKE Potential to the Dunham, Morse and Lennard-Jones Potentials and obtain a simple expression for the dissociation energy of weakly bound molecules.

The ENGELKE potential $V(R)$ is represented by a series in λ of the form,

$$V(\lambda) = V_e + c_0 \lambda^2 \left[1 + \sum_{n=1}^{\infty} c_n \lambda^n \right], \tag{1}$$

where

$$\lambda = \mathrm{sgn}(p) \left[1 - \left\{ \frac{(\beta + 1) R_e}{R + \beta R_e} \right\}^p \right], \tag{2}$$

β, p are the free parameters and sgn (p) is the sign of p.

The transformation given in Eq. (2) maps the positive real R axis into the interval $[\{1 - (1 + \beta^{-1})^p, 1]$ of the λ axis, if β and $p > 0$; if $\beta > 0$ and $p < 0$, the interval is $[\{\beta/(\beta + 1)\}^{[p]} - 1, \infty]$. The advantage of this expansion is that for $p > 0$, λ has no singularities on $0 < R < \infty$, provided $\beta > 0$.

Table I

Comparison of the predicted and experimental values of ground state dissociation energies (D_e) of some weakly bound molecules

Molecule	n	D_e calc (Eq. 13) (cm^{-1})	D_e exp(cm^{-1})
NaNe	3	150	149.7
NaAr	4	440	492
Ca_2	3	1330	1079
Mg_2	3	443.6	429.9

Another salient feature of this series is that $\lambda(R)$ is finite as $R \to 0$ and as $R \to \infty$, $\lambda(R) \to 1$, indicating thereby, the dissociation can be determined.

The expansion coefficient c_0 is related to the Dunham coefficient by the relation

$$c_0 = a_0(1+\beta)^2 p^{-2}, \tag{3}$$

where

$$(1+\beta) = -(1+p)\, a_1 \tag{4}$$

and

$$p = \left(\frac{12\, a_2 - 11\, a_1^2}{12\, a_2 - 7\, a_1^2} \right). \tag{5}$$

Further it can be easily seen that

$$\frac{c_0 p^2}{(1+\beta)^2} = D_e\, \omega_e\, x_e / B_e = D_e\, \alpha_e^2\, R_e^2, \tag{6}$$

where D_e, α_e are the dissociation energy and Morse parameter, respectively. Rearranging Eq. (6), one obtains

$$D_e = c_0 [p^2/(1+\beta)^2]\, \alpha_e^2\, R_e^2. \tag{7}$$

Applying VARSHNI's condition [8] for Morse and Dunham potential curves, we get

$$\begin{aligned} \alpha_e &= (6\, B_e^2/\omega_e) \cdot (1 + a_1) \\ &= (6\, B_e^2/\omega_e) \cdot F, \end{aligned} \tag{8}$$

where

$$F = \left\{ 1 + \frac{1}{3} \frac{U'''(R_e)}{U''(R_e)} \right\}. \tag{9}$$

Following Eqs. (8) and (9) we get

$$D_e = c_0\, p^2/(1+\beta)^2\, a_1^2 = a_0/a_1^2 . \tag{10}$$

The above expression, however, does not lead to a correct value of the dissociation energy of weakly bound molecules, due to the inability of the Morse function to express itself as an inverse long range expansion dominated by leading terms $(R)^{-6}$.

We next consider the Lennard-Jones potential and apply as usual VARSHNI's conditions. The Lennard-Jones potential is given by

$$V(r) = D_e\left[1 + \left(\frac{R_e}{R}\right)^{2n} - 2\left(\frac{R_e}{R}\right)^{n}\right]. \tag{11}$$

Application of VARSHNI's criteria leads to

$$a_1 = (n+1) \tag{12}$$

and

$$D_e = \frac{a_0}{(n+1)^2}, \tag{13}$$

where

$$a_0 = \omega_e^2/4\,B_e.$$

Eq. (13) has been used to compute the dissociation energies of weakly bound molecules.

Table I compares the calculated values of dissociation energies with the experimental values [9]. The agreement with experimental data is satisfactory except in the case of Ca_2.

REFERENCES

1. J. L. DUNHAM, Phys. Rev., **41,** 713, 1932.
2. I. SANDEMAN, Proc. Roy. Soc., **60,** 210, 1940.
3. C. L. BECKEL and R. ENGELKE, J. Chem. Phys., **49,** 5199, 1968.
4. J. F. OGILVIE, Canadian Spectroscopy Symposium, Ottawa, Canada, Oct. 1974.
5. G. SIMONS, R. G. PARR and J. M. FINLAN, J. Chem. Phys., **59,** 3229, 1973.
6. A. J. THAKKAR, J. Chem. Phys., **62,** 1693, 1975.
7. R. ENGELKE, J. Chem. Phys., **68,** 3514, 1978.
8. Y. P. VARSHNI and R. C. SHUKLA, Rev. Mod. Phys., **35,** 130, 1963.
9. K. P. HUBER and G. HERZBERG, in 'Constants of Diatomic Molecules', Van Nostrand Reinhold Co., New York, 1979.

Acta Physica Academiae Scientiarum Hungaricae, 52 (2), pp. 175—187 (1982)

AN X-RAY STUDY OF THE Se—Te SYSTEM

M. F. KOTKATA, E. A. MAHMOUD and M. K. EL-MOUSLY

PHYSICS DEPARTMENT, FACULTY OF SCIENCE, AIN SHAMS UNIVERSITY, CAIRO, EGYPT

(Received 16. X. 1981)

For various Se—Te compositions, quenched from 800 °C (8 h) at room temperature, the diffraction pattern of the vitreous phases is characterized by two broad maxima. With CuKα radiation the low-angle halo extends from 16 to 40° in 2θ values, covering the range of Bragg angles corresponding to the crystal planes reflecting with the highest intensities. The second maximum is flatter and broader with increasing Te-content, hardly discernible from the background, and extends up to an angle of 62° in the 2θ scale. The effect of heat on structure is briefly discussed. For the crystallized samples changes with composition and structural features are considered. The interplanar spacings (d_{hkl}) and their relative intensities for all forms of the component elements are reported. The phase diagram of the whole system shows the presence of three distinguishable substitutional solid solution phases; called: A, $A + B$, and B phases; the compositions of these three phases are given.

Introduction

Series of Se—Te alloys ranging in chemical composition from pure Se to pure Te have been prepared [1]. The molten mass is quenched and the structural nature of the produced ingots is examined by X-ray diffraction technique. Differential thermal analysis (DTA) was carried out for the different compositions [1, 2]. X-ray diffraction and DTA thermograms of the quenched massive alloys have indicated that samples of $\geq$50 at% Te are completely crystalline. The ability to form crystalline solids decreases with increasing Se-content. The compositions from 0.0 to 30 at% Te tend to supercool strongly and solidify in the vitreous rather than in the crystalline state.

An investigation of the structure of the crystalline state of the same compositions as the vitreous state offers valuable means to explain the properties and structural peculiarities of glasses, and the changes in these properties during transition from the vitreous to the crystalline state.

In the present work results obtained from X-ray diffraction patterns, the effect of heat and the change in composition of the glass structure are discussed. The corresponding polycrystalline forms were effected by annealing the vitreous samples in the range of their softening and crystallization temperatures, $T_g - T_c$ [2].

X-ray diffraction patterns for the different forms have been automatically recorded using a modern Philips diffractometer. The general operating

conditions were kept constant all over the work and were: CuKα radiation 50 KV, 25 mA; slits: 1°, 2×10^{-4} m, 1°; proportional counter; scanning velocity: 2°(2θ)/min.; L. L.: 3.50; W.: 3.50; ratemeter: 1×10^{3} counts/s.

Significance of the diffraction patterns of the quenched samples

The diffraction patterns of the Se—Te quenched compositions having <50 at% Te are shown in Fig. 1. All patterns are characterized by the absence of any diffraction peaks indicating the amorphous nature of these materials.

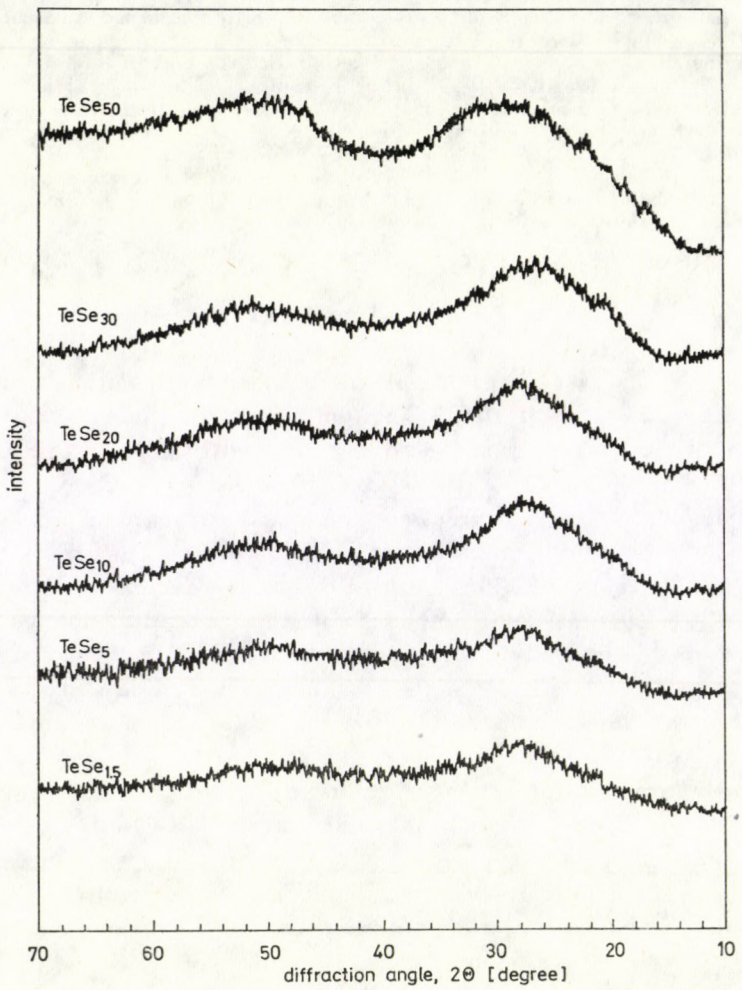

Fig. 1. X-ray diffraction patterns of Te—Se quenched samples having at % Te < 50%.

Samples having at% Te $\geq 50\%$ are characterized by the appearance of diffraction lines due to the formation of a crystalline state.

The amorphous patterns in Fig. 1 may be described as "stepped-humps". The low-angle halo extends from 16° to 40° in 2θ angular units. These broad maxima have the highest intensity in all patterns. The second step is flatter and broader, hardly discernible from the background with increasing Te-content, and extends up to an angle of 62° in 2θ values.

The scattering of X-ray by amorphous matter, the main contribution to the intensity arriving at the point of observation, is due to one single scattering of the primary beam by each volume element V_1. It may be also due to successive secondary scattering from different volume elements V_x present in the amorphous matrix. These volumes are distributed at random and the area under the respective hump should be proportional to their scattering-power contribution [3]. For the glasses depicted in Fig. 1 the hump is divided into two angular ranges, which may be due to a certain degree of directional scattering by these volumes. In other words, these angular ranges correspond to numerous lattice directions or atomic planes of high scattering power in the corresponding crystalline forms.

Effect of heat treatment

When a supercooled Se—Te sample is subjected to an isothermal treatment between its T_g and T_c temperatures, a defined time period is required to complete the crystallization process [4]. The latter, of course, depends on the temperature at which the crystal growth takes places.

The composition $TeSe_{20}$ [5] is selected, as an example, to study the rate of crystal growth. For this purpose, five dry-clean pyrex tubes each containing about 0.5 g of amorphous $TeSe_{20}$ were sealed under vacuum ($\sim 10^{-2}$ Pa) and heated at 300 °C for 1 h. Then, the tubes were quickly transferred to another preheated oven kept at 130 °C and sintered for 10, 12, 20, 30 and 45 min. After the required time, each tube was quenched in icy water to prevent any possible phase transition. After the heat treatment an X-ray scanning covering the angular range of the two broad maxima has been recorded. Fig. 2 shows the diffraction scans for the different soaking times. The intensity I and the interplanar spacings d have been measured for all patterns and are given in Table I along with the results for a completely crystallized $TeSe_{20}$ sample.

Fig. 2 shows clearly that the X-ray diffraction spectrum of the sample annealed for 10 min does not differ from that of the amorphous quenched one, in Fig. 1, revealing no evidence of any crystallization. After annealing for 12 min, the low-angle diffuse hump is slightly sharpened and a line at $d = 0.302$ nm appeared, apparently reflecting some minor structure adjustments within

the amorphous matrix. Annealing for 20 min shows that six new lines began to appear at $d = 0.3792$, 0.219, 0.208, 0.2001, 0.1774 and 0.1649 nm. The intensity of the lines increased and the relative half width of the peaks decreased with increasing annealing time. In the sample annealed for 30 min a new line appeared at $d = 0.1436$ nm. Another line started to appear at $d = 0.1374$ nm after annealing for 45 min. The rest of the characteristic diffraction lines of the composition $TeSe_{20}$ appeared in the complete crystallized sample as given

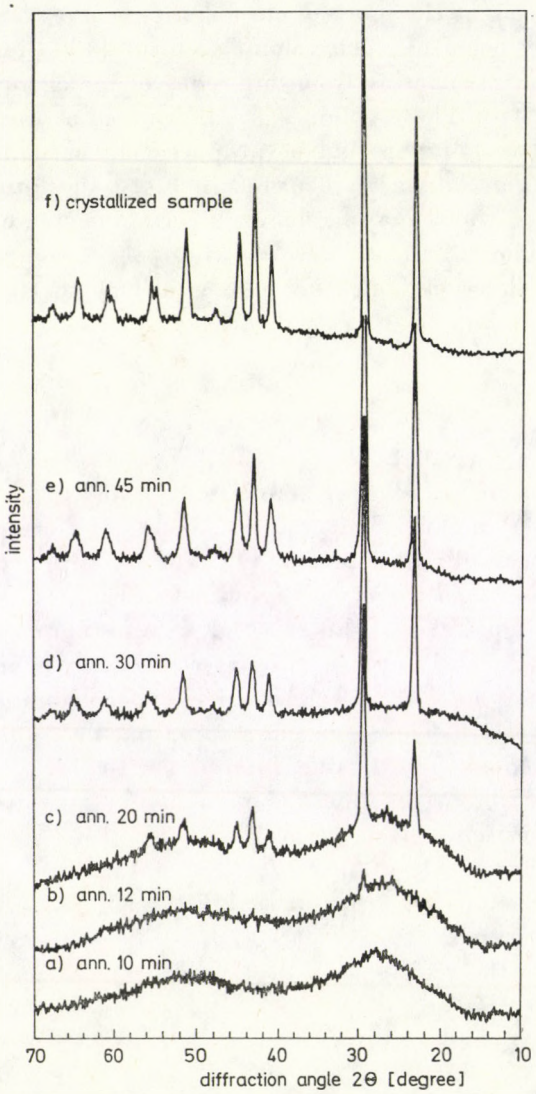

Fig. 2. X-ray diffraction patterns of the sample $TeSe_{20}$ annealed at 130 °C for different times.

Table I

X-ray intensity I (arbitrary units) and interplanar spacing d(nm) for different isothermal crystallization of supercooled liquid $TeSe_{20}$ at 130 °C

Soaking time in minutes									
12		20		30		45		Complete cryst.	
d	*I*	*d*	*I*	*d*	*I*	*d*	*I*	*d*	*I*
—	—	0.3792	11	0.3784	45	0.380	53	0.3815	53
0.302	6	0.3016	26	0.3016	86	0.3011	96	0.3303	100
—	—	0.219	3	0.2186	10	0.219	14	0.2191	19
—	—	0.2084	6	0.2084	13	0.2084	25	0.2094	32
—	—	0.2001	4	0.2006	10	0.201	16	0.2014	21
—	—	—	—	—	—	—	—	0.1879	4
—	—	0.1774	4	0.1775	9	0.1772	15	0.1779	21
—	—	0.1649	3	0.1647	6	0.1655	7	0.1668	8
—	—	—	—	—	—	—	—	0.1652	10
—	—	—	—	—	—	—	—	0.1515	9
—	—	—	—	—	—	—	—	0.1504	4
—	—	—	—	0.143	6	0.1436	7	0.1435	11
—	—	—	—	—	—	0.1374	4	0.1379	4

in Table I. From Fig. 2, one may also infer that the low-angle halo is still visible in the range of the Bragg angles of the crystal planes reflecting at highest intensities.

Structural changes with composition

In this Section, the changes in the structural features of the polycrystalline forms of composite samples of the system Se—Te are discussed. The materials which had been found to be in the amorphous phase by the quenching technique were subjected to an annealing process at 160 °C for 12 h, and then allowed to cool slowly in the oven. The samples were prepared in powder form for X-ray analysis.

The two component elements of the system

The diffraction patterns of the two pure elements Se and Te are given in Fig. 3. The calculated d values of both elements are found to be close to those given in the Diffraction Data File Index [6]. Both Se and Te have a hexagonal structure [7]; Table III gives their unit cell dimensions. The higher increase of the lattice parameters "a" and "c" for Te than those for Se is mainly

Table

Interplanar spacings and relative intensities

	Se		$TeSe_{50}$		$TeSe_{30}$		$TeSe_{20}$		$TeSe_{10}$	
hkl	*d*, nm	I/I_0	*d*, nm	I/I_0	*d*, nm	I/I_0	*d*, nm	I/I_0	*d*, nm	I/I_0
—	—	—	—	—	—	—	—	—	—	—
100	0.3783	85	0.380	92	0.3815	33	0.815	53	0.380	91
—	—	—	—	—	—	—	—	—	—	—
—	—	—	—	—	—	—	—	—	—	—
—	—	—	—	—	—	—	—	—	—	—
101	0.301	100	0.3012	100	0.3036	100	0.303	100	0.302	100
—	—	—	—	—	—	—	—	—	—	—
—	—	—	—	—	—	—	—	—	—	—
—	—	—	—	—	—	—	—	—	—	—
110	0.2181	32	0.2188	25	0.2193	14	0.2191	19	0.2191	28
—	—	—	—	—	—	—	—	—	—	—
102	0.2076	50	0.2081	53	0.2084	27	0.2094	32	0.2094	39
111	0.1995	34	0.2004	33	0.2007	17	0.2014	21	0.20065	28
—	—	—	—	—	—	—	0.1907	4	0.1901	7
—	—	—	—	—	—	—	—	—	—	—
200	0.1809	8	0.1898	7	0.1898	6	0.1897	4	0.1892	7
201	0.1766	29	0.1788	28	0.1774	15	0.1779	21	0.1775	28
—	—	—	—	—	—	—	—	—	—	—
003	0.1654	12	0.1661	12	0.1661	5	0.1668	8	0.1669	10
112	0.1640	16	0.1646	17	0.1652	12	0.1652	10	0.1648	13
—	—	—	—	—	—	—	—	—	—	—
—	—	—	0.1520	11	0.1524	8	0.1523	7	0.1525	7
103	0.1513	10	0.1510	15	0.1510	10	0.1515	9	0.1513	12
202	0.1506	15	0.1509	14	0.1508	8	0.1504	4	0.1510	12
—	—	—	—	—	—	—	—	—	—	—
210	0.143	17	0.1434	14	0.1441	8	0.1435	11	0.1435	16
—	—	—	—	—	—	—	—	—	—	—
211	0.1373	7	0.1373	7	0.1405	3	0.1379	4	0.1387	3

due to the larger diameter of Te-atom (0.143 nm) compared to that of Se (0.116 nm).

The calculated interplanar spacings (d_{hkl}) of the observed reflections and their corresponding relative intensities (I/I_0) are listed in Table II for all examined alloys together with those of Se and Te. Investigation of the X-ray data justify the following classification of the materials of the Se—Te system.

II

of the examined polycrystalline Te—Se samples

$TeSe_5$		$TeSe_{2.5}$		$TeSe_{1.5}$		TeSe		Te_2Se		Te		
d, nm	I/I_0	*d*, nm	I/I_0	*d*, nm	I/I_0	*d*, nm	I/I_0	*d*, nm	I/I_0	*d*, nm	I/I_0	*hkl*
—	—	—	—	—	—	—	—	0.3862	51	0.3848	25	100
0.3816	33	0.3815	89	0.3815	67	0.3818	100	—	—	—	—	—
0.340	5	0.3398	10	0.339	11	—	—	—	—	—	—	—
—	—	0.3225	10	0.321	5	0.3234	4	—	—	—	—	—
—	—	—	—	—	—	—	—	0.3198	100	0.3245	100	101
0.3062	100	0.309	100	0.31	100	0.3135	94	—	—	—	—	—
0.299	8	0.298	15	0.298	16	—	—	—	—	—	—	—
—	—	—	—	—	—	—	—	0.2318	18	0.2347	35	102
0.2206	11	0.2206	51	0.2206	39	0.2211	79	0.2229	54	0.2221	29	110
—	—	—	—	0.2183	24	—	—	—	—	—	—	—
0.2118	24	0.2161	19	0.2158	9	0.2163	7	—	—	—	—	—
0.2027	13	0.2027	25	0.203	19	0.2048	20	0.2081	15	0.2081	9	111
0.2002	5	0.2006	8	0.1971	4	0.1985	4	—	—	0.1972	12	003
0.1911	4	0.1909	13	0.1903	10	0.1911	15	0.19295	12	0.1924	5	200
—	—	—	—	—	—	0.1810	24	0.1831	25	0.1835	16	201
0.1877	4	0.1895	6	0.1870	7	—	—	—	—	—	—	—
0.1791	12	0.1794	29	0.1798	22	0.1794	10	0.1766	6	0.1774	5	112
0.1692	5	0.1692	11	0.1698	9	0.1718	7	—	—	—	—	—
0.1664	7	0.1661	10	0.1658	6	0.1680	4	—	—	—	—	—
—	—	—	—	—	—	—	—	—	—	—	—	—
—	—	—	—	—	—	—	—	0.1589	10	0.1616	8	202
0.1547	5	0.1549	10	0.1551	10	0.1560	7	—	—	—	—	—
0.1527	7	0.1528	10	—	—	—	—	—	—	—	—	—
—	—	—	—	—	—	—	—	—	—	—	—	—
—	—	—	—	—	—	—	—	0.1458	21	0.1478	8	113
0.1442	6	0.1442	25	0.1445	15	0.1449	30	0.1445	10	0.1456	8	210
0.1402	3	0.1393	11	0.1393	7	0.1402	13	0.1412	13	0.1417	6	211
0.1387	3	0.1384	8	0.1382	7	0.1396	11	0.1396	6	0.1382	7	203

Samples Se, $TeSe_{50}$, $TeSe_{30}$, $TeSe_{20}$ and $TeSe_{10}$; the A-phase

The *A*-phase is represented by the five mentioned samples, their corresponding diffraction patterns are given in Fig. 4. They represent pure Se, and a Te-content of 1.96, 3.23, 4.76 and 9.1 at%, respectively. One may see that any composition of this phase is characterized by a clear and limited num-

ber of diffraction peaks. Table II shows that the relative order of the six peaks of Se having the maximum intensities is nearly the same as that of the compositions of this phase. Besides, the d values are within the same range, i.e. the deviation in d with regard to any hkl-plane does not exceed 0.0002 nm. It is worth noting that there is no obvious trend in the variation of both in

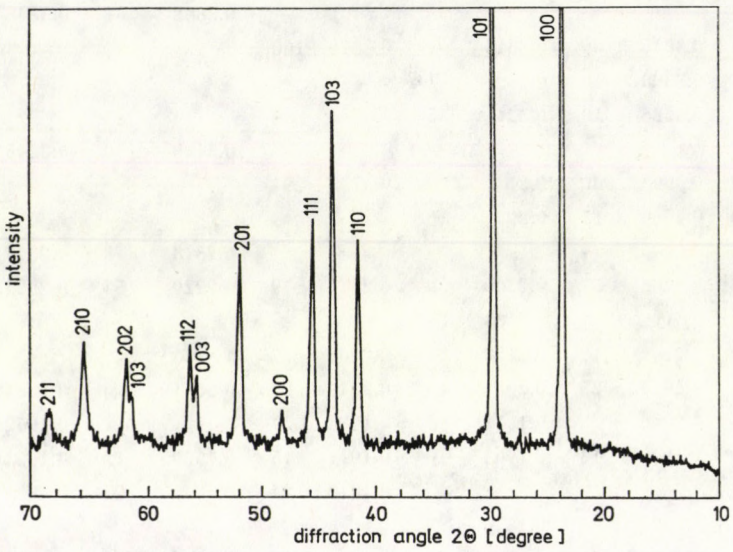

Fig. 3a. X-ray diffraction pattern of crystalline Se.

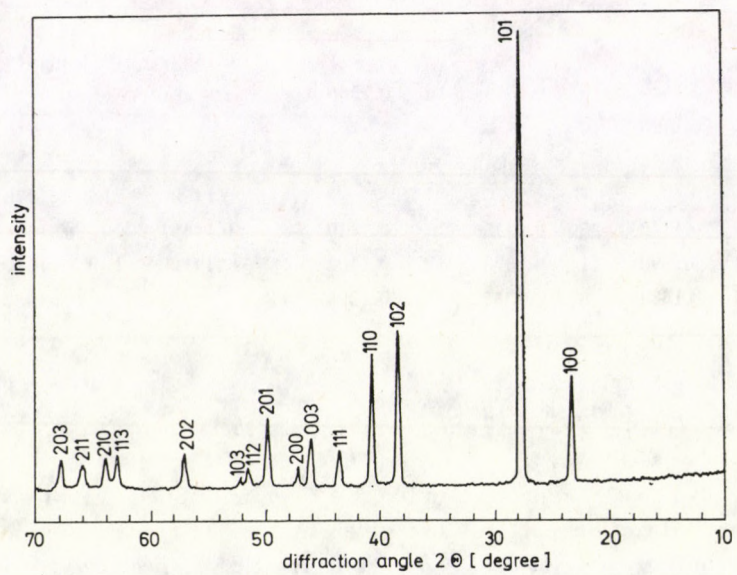

Fig. 3b. X-ray diffraction pattern of crystalline Te.

the intensity (I) or in the relative intensity (I/I_0) of the corresponding diffraction lines of the compositions of this phase. The range of composition is essentially represented by substitutional solid solution of mainly Se-like structure. This agrees with the obtained slight variation in the lattice parameters of the materials in the compositional range of this phase [1].

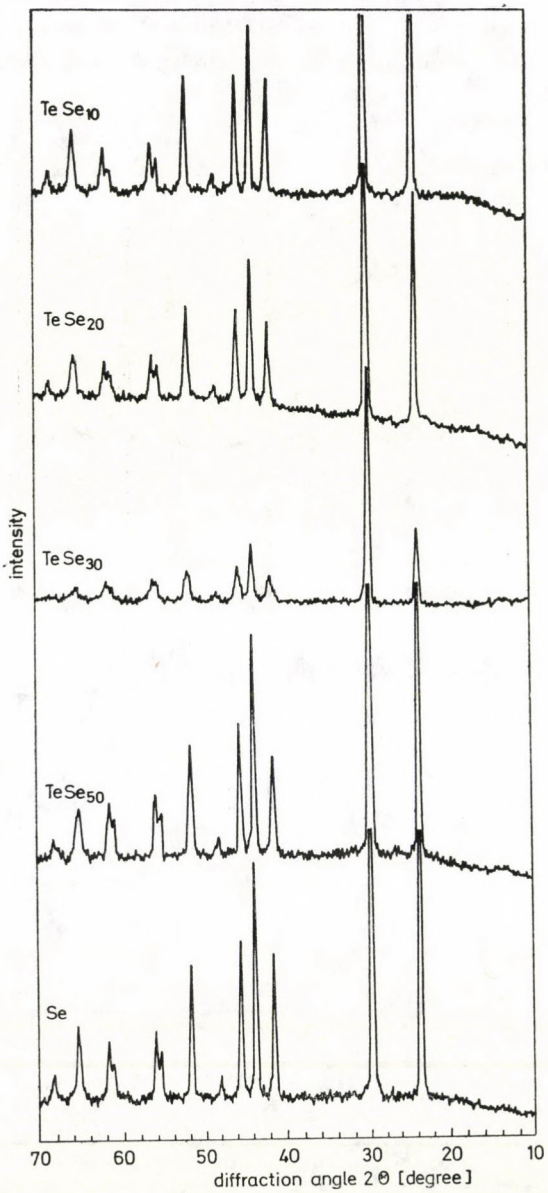

Fig. 4. X-ray diffraction patterns for the crystallized samples of Se, $TeSe_{50}$, $TeSe_{30}$, $TeSe_{20}$ and $TeSe_{10}$.

Samples Te and Te_3Se; the B-phase

The phase is represented by the pure Te and that with a Se-content of 25 at%. The diffraction pattern is shown in Fig. 5. The pattern of Te_3Se is a simple one and has mainly the diffraction lines appearing in pure Te. Table II shows that the *d* values are nearly the same for both compositions of this phase. The structure of Te_3Se is characterized by the presence of some Te-lines which are manifested in the other compositions, such as those of 0.2318, 0.1598 and

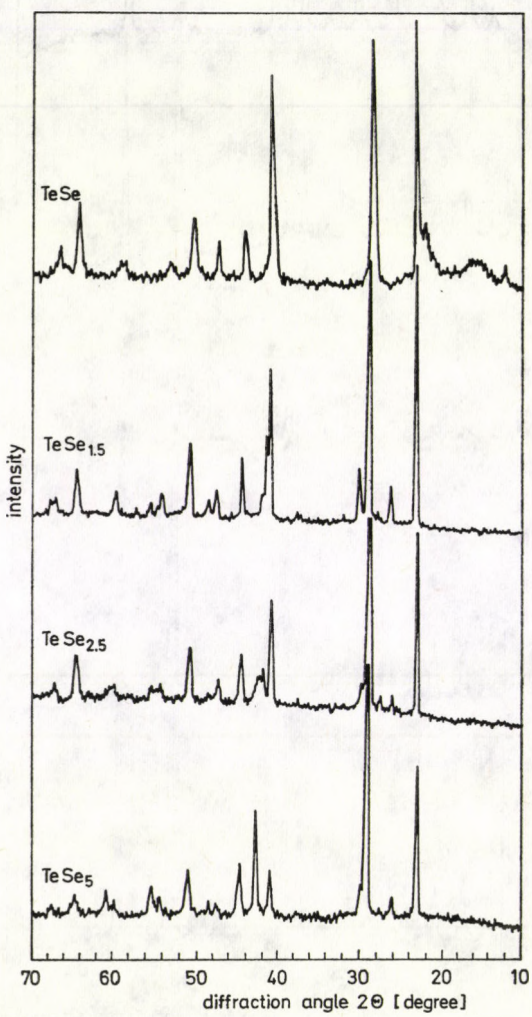

Fig. 5. X-ray diffraction patterns for the crystallized samples of $TeSe_5$, $TeSe_{2.5}$, $TeSe_{1.5}$ and TeSe.

0.1458 nm. Materials of Te levels in the region of 0.0—25 at% Se represent a substitutional solid solution of the Te-like structure.

A detectable change has been observed in the d values and/or in the relative intensity of Te_3Se compared to those of elemental Se. These lines with regard to Se are at $d = 0.3783$ and 0.301 nm.

Samples $TeSe_5$, $TeSe_{2.5}$, $TeSe_{1.5}$ and TeSe; the (A + B)-phase

Samples of this phase represent compositions having a Te component of 16.67, 28.6, 40 and 50 at%, respectively. The corresponding diffraction patterns are given in Fig. 6. This group of compositions is characterized by the presence of some new and sharp diffraction lines. The intensities of these lines

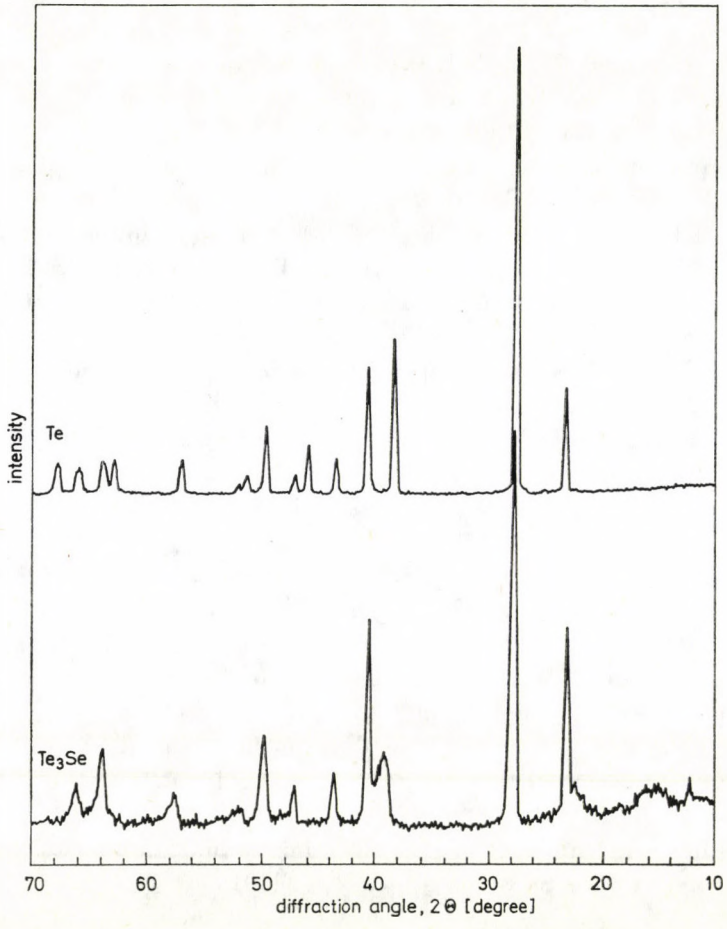

Fig. 6. X-ray diffraction patterns for the crystallized samples of Te_3Se and Te.

Table

Structural changes of the Se—Te system with composition

Composition	Classification				
	A-phase				
	Se	$TeSe_{50}$	$TeSe_{30}$	$TeSe_{20}$	$TeSe_{10}$
Te-content	From 0.0 to ~15 at % Te				
Deduced structure	Hexagonal: $a = 0.43662$ nm $c = 0.49536$ nm	Substitutional solid solution of Se-like structure			

are relatively small. The new lines for the sample $TeSe_5$ are those at $d = 0.340$, 0.299, 0.1692, and 0.1402 nm. Those of $TeSe_{2.5}$ and $TeSe_{1.5}$ appeared at about $d = 0.3398$, 0.3225, 0.298, 0.2161, 0.1692 and 0.1393 nm, where the actual d values are given in Table II. For TeSe, the new peaks correspond to $d = 0.3234$, 0.2163, 0.181, 0.1718 and 0.1402 nm.

Starting from pure Se, some few lines disappeared in this phase. For instance, the lines corresponding to $d = 0.164$ and 0.1506 nm for pure Se, and the line at 0.1513 nm (Se) disappeared with the composition of $TeSe_{2.5}$.

On the other hand, some characteristic lines of pure Se are still present in the compositions of this phase, proving the continuous effect of Te till the composition of $TeSe_5$, 16.67 at% Te. This may be related to the detectable variation in the unit cell dimension "*c*" found in the the composition of $TeSe_5$ [1]. However, the composition structure of $TeSe_5$ is closer to the first phase (*A*-phase), and that of TeSe is nearer to the *B*-phase.

The structure proposed for this range of the composition: ~15—50 at% Te, represents two intermediate solid solutions based on the structures of the *A* and *B* phases, respectively.

However, there are some peaks which appear with the different compositions containing Se and Te. From the Se side, these lines correspond to $d = 0.2076$, 0.1766 and 0.1373 nm. Although the variation in the d values for each line is small or monotonic with the addition of Te, the *hkl* reflection is not the same. For example, d is 0.2076 nm for Se of (102) and it is (111) for Te (0.2081 nm). The diffraction line due to the plane (210) corresponds to 0.144 ± 0.0017 nm for all the compositions considered. For the composition TeSe where the percentage of Se: Te is 1 : 1, the line of 100% intensity at $d = 0.3818$ nm is neither that of the 100% for Te (0.3245 nm) nor that of the 100% line intensity for Se which appears at 0.301 nm.

Table III summarizes the deduced structural changes of the Se—Te system as obtained from the X-ray powder analysis considered.

III

as deduced from X-ray diffraction investigation

(A + B)-phase				B-phase	
$TeSe_8$	$TeSe_{2.5}$	$TeSe_{1.5}$	TeSe	Te_3Se	Te
From >15 to ~50 at % Te				From >50 to 100 at % Te	
Two substitutional solid solutions having structure based on A and B phases				Substitutional solid solution of Te-like structure	Hexagonal: $a = 0.44572$ nm $c = 0.59290$ nm

REFERENCES

1. M. F. Kotkata, E. A. Mahmoud and M. K. El-Mously, Acta Phys. Hung., **50,** 61, 1981.
2. M. F. Kotkata and E. A. Mahmoud, Materials Sci. and Eng., **54,** 163, 1982.
3. B. E. Warren and R. L. Mozzi, Act. Cryst., **21,** 459, 1966.
4. M. F. Kotkata, A. A. El-Ela, E. A. Mahmoud and M. K. El-Mously, ICTP Preprints, Trieste (1980), IC/80/70.
5. M. F. Kotkata, E. A. Mahmoud and M. K. El-Mously, Acta Phys. Hung., **47,** 345, 1979.
6. Index to the Powder Diffraction File, A.S.T.M. Publication, Philadephia, U.S.A. (1968), Nos. 6—0362 and 4—0554.
7. E. Grison, J. Chem. Phys., **19,** 1109, 1951.

Acta Physica Academiae Scientiarum Hungaricae, 52 (2), pp. 189—198 (1982)

SOLUTIONS OF WAVE EQUATION FOR THE SUPERPOSED POTENTIAL WITH APPLICATION TO CHARMONIUM SPECTROSCOPY

A. P. KAJWADKAR and L. K. SHARMA

DEPARTMENT OF APPLIED PHYSICS, GOVT. ENGINEERING COLLEGE, JABALPUR—482 011, INDIA

(Received 16. X. 1981)

Using perturbation theory, asymptotic expansions are derived for the eigenenergies and eigenfunctions of the wave equation for a superposed potential. These expansions have been applied to study the behaviour of Regge trajectories and in determining the bound quark-antiquark mass and decay widths.

Introduction

Recently much interest has been shown by high energy physicists in productively employing nonrelativistic methods in the discovery of the ψ (3 GeV/c^2) and y (10 GeV/c^2) families of heavy neutral mesons [1—5]. Actually the possibility that heavy mesons can be identified as eigenstates of the Schrödinger equation has stimulated considerable attempts directed towards the achievement of a predictive spectroscopy of hadrons. In these attempts the relevant wave equation for the bound state is given prime consideration while for spin, tensor forces and hyperfine structure considerations [6] this equation is modified accordingly. The charmonium model [4, 7] has been successful in interpreting ψ and ψ' as charmed quark-antiquark ($c\,\bar{c}$) bound states and other subsequently observed phenomena. However, many things still remain to be unveiled in relation to level spacing and decay rates etc. for want of correct theoretical potential models.

For interpreting various observations, therefore, different models have been developed. EICHTEN et al [5] proposed the long range binding between quarks by the relation $V(r) = ar$. KRAMER et al. [8] used harmonic oscillator potential. MÜLLER-KIRSTEN et al [6, 9] have considered in details the superposition of arbitrary power quark confining potential with a short range gluon exchange coulomb component and the logarithmic potential. After the discovery of y states [10] certain doubts were raised on the suitability of linear potential as a phenomenological ansatz for the quark confining interaction. QUIGG et al [11] and ROSNER et al [12] made thorough investigation of charmonium spectroscopy for the logarithmic and power potentials, respectively, but so far no suitable potential form has been approximated. Motivated by

the above consderations SHARMA et al [13] have recently investigated the ollowing three potentials which are the superposition of

(i) a quark confining linear potential and short range modified coulomb potential $\left(-g_2/r \log\left(\frac{r}{r_0}\right)\right)$,

(ii) a logarithmic potential and the short range coulomb potential similar to that considered in (i) and

(iii) an arbitrary power quark confining potential and a short range centrifugal potential.

We now undertake the study of charmonium spectroscopy for a potential which is the superposition of a quark confining linear potential, a loga-

Table I

The lowest S and P states of charmonium obtained for the potential (3). The input value is underlined. The quark mass has been chosen to be equal to 1.65 GeV and 1.56 GeV.

States	Mass calculated (GeV) for the potential (3) (a)	Mass calculated (GeV) for the potential (3) (b)	Mass (GeV) calculated for linear potential (c)	Mass (GeV) calculated for logarithmic potential (d)	Mass (GeV) observed (e)
1^3S_1	3.096	3.096	3.096	3.095	3.096
1^3P	3.24	3.416	3.469	—	—
2^3S_1	3.684	3.682	3.684	3.685	3.684
2^3P	3.792	4.14	3.952	—	—
3^3S_1	4.156	4.16	4.173	4.163	4.16
3^3P	4.308	5.20	—	—	—

(a) Input values used for calculation are $\beta = 0.3$ GeV^3, $\eta = 0.001$ GeV^2, $\delta = 0.0001$ GeV and $r_0 = 1$ (GeV)$^{-1}$, $m = 1.65$ GeV.
(b) Input values used for calculation are $\beta = 1$ GeV^3, $\eta = 0.887$ GeV^2, $\delta = 0$ and $r_0 = 5$(GeV)$^{-1}$, $m = 1.56$ GeV.
(c) See reference [6].
(d) See reference [9].
(e) See reference [6].

Table II

Leptonic decay rates in KeV with $M_\psi = 1.65$ GeV for the potential (3). All the parameters are the same as given in Table I

States	Mass in GeV	Decay width in KeV for the potential (3)	Decay width in KeV for linear potential (b)	Observed values (a)
1^3S_1	3.096	4.784	4.80	4.8 ± 0.6
2^3S_1	3.684	3.103	2.10	2.1 ± 0.3
3^3S_1	4.156	2.48	3.01	—

(a) See reference [6].
(b) See reference [9].

rithmic potential and a weak short-range gluon exchange coulomb potential. We have obtained the asymptotic expansions for energy eigenvalues and Regge trajectories. We have also evaluated quark masses in S and P states along with the leptonic decay rates. The results obtained are shown in Tables I and II. In these Tables the results of earlier workers are also referred to for comparison. Finally we give a brief discussion of our results.

General solution

We consider the Schrödinger equation in the radial form for relative motion of the two particles of masses m_1 and m_2, i.e.

$$\frac{d^2\psi}{dr^2} + \frac{2\mu}{\hbar^2}\left[E - \frac{l(l+1)\hbar^2}{2\mu r^2} - V(r)\right]\psi = 0\,, \tag{1}$$

where as usual

$$\Psi = \left(\frac{1}{r}\right)\psi(r)\, P_l^m(\cos\vartheta)\, e^{im\Phi}\,, \tag{2}$$

$\mu = m_1 m_2/m_1 + m_2$, μ is the reduced mass of the two particles and r their separation. The potential considered by us has the form

$$V(r) = \left[g_1 r - g_2 \log\frac{r}{r_0} - \frac{g_3}{r} - V_0\right], \tag{3}$$

where $g_1 > g_2 > g_3$ and V_0 is the scaling parameter.

Substituting (3) in Eq. (1) and setting

$$\left.\begin{aligned} &\alpha = 2\mu(E + V_0)/\hbar^2\,, && \beta = 2\mu g_1/\hbar_2 \\ &\eta = 2\mu g_2/\hbar^2\,, && \delta = 2\mu g_3/\hbar^2 \\ &\gamma = l(l+1) && c = \log r_0 \end{aligned}\right\} \tag{4}$$

yields

$$\frac{d^2\psi}{dr^2} + \left[\alpha - \beta r + \eta\log r - \eta c + \frac{\delta}{r} - \frac{\gamma}{r^2}\right]\psi = 0\,. \tag{5}$$

Next setting

$$r = e^z \qquad (-\infty < z < \infty) \tag{6}$$

and

$$\psi = \Phi\, e^{z/2} \tag{7}$$

gives

$$\frac{d^2\Phi}{dz^2} + [-L^2 + v(z)]\,\Phi = 0\,, \tag{8}$$

where

$$\left.\begin{aligned} v(z) &= \alpha e^{2z} - \beta e^{3z} + \eta (z - c) e^{2z} + \delta e^{z} \\ L^2 &= \left(\gamma + \frac{1}{4}\right). \end{aligned}\right\} \tag{9}$$

We now find that value of z say z_0 for which $v(z)$ becomes maximal. In the vicinity of this maximum $(v(z) - L^2)$ can become positive and the solution therefore oscillatory as required for the existence of eigenvalues. Thus setting

$$\left(\frac{dv}{dz}\right)_{z=z_0} = 0$$

and solving for z_0 we get

$$z_0 = \log \frac{2\alpha}{3\beta}\left[1 + \frac{\eta}{2\alpha}(2k + 1) + \frac{3\beta\delta}{4\alpha^2}\right] \tag{10}$$

and

$$v(z_0) = \frac{4\alpha^3}{27\beta^3} + \frac{2\alpha\delta}{3\beta} + \frac{4\alpha^2\eta k}{9\beta^2} + \frac{\delta^2}{4\alpha^2}\,, \tag{11}$$

where

$$k = \log \frac{2\alpha}{3\beta r_0}\,. \tag{12}$$

Expanding $v(z)$ in the neighbourhood of the maximum at z_0 we obtain

$$v(z) = v(z_0) + \sum_{i=2}^{\infty} \frac{(z - z_0)^i}{i!} v^{(i)}(z_0)\,, \tag{13}$$

where $i = 0, 1, 2, 3, \ldots$.

For $i = 0$, this expression is positive, for $i = 1$ it is zero and for $i > 1$ it is negative (as required for a maximum of $v(z)$ at $z = z_0$ for $\alpha > 0$).

Setting

$$h = \{-2\, v^{(2)}(z_0)\}^{1/4} \tag{14}$$

i.e.

$$h^2 = \frac{4\alpha^{3/2}}{3\beta}\left[1 + \frac{3\beta\delta}{4\alpha^2} - \frac{\eta k}{\alpha} - \frac{\eta}{\alpha}\right] + 0(\beta^2) \tag{15}$$

and changing the independent variable in Eq. (8) to $\omega = h(z - z_0)$, one gets

$$\frac{d^2\Phi}{d\omega^2} + \left[\frac{-L^2 + v(z_0)}{h^2} - \frac{\omega^2}{4}\right]\Phi = \sum_{i=3}^{\infty} \frac{v^{(i)}(z_0)\,\omega^i\,\Phi}{2v^{(2)}(z_0)^i/h^{i-2}}\,. \tag{16}$$

In particular for $i = 3, 4, 5, 6$ we get

$$
\begin{aligned}
A &= \frac{v^{(3)}(z_0)}{v^{(2)}(z_0)} = \left[5 - \frac{3}{2}\frac{\beta\delta}{\alpha^2} + \frac{6\eta k}{\alpha} + \frac{4\eta}{\alpha}\right], \\
B &= \frac{v^{(4)}(z_0)}{v^{(2)}(z_0)} = \left[19 - \frac{9\beta\delta}{\alpha^2} + \frac{30\eta k}{\alpha} + \frac{22\eta}{\alpha}\right], \\
C &= \frac{v^{(5)}(z_0)}{v^{(2)}(z_0)} = \left[65 - \frac{75\,\beta\delta}{2\alpha^2} + \frac{114\,\eta k}{\alpha} + \frac{90\eta}{\alpha}\right], \\
D &= \frac{v^{(6)}(z_0)}{v^{(2)}(z_0)} = \left[211 - 135\frac{\beta\delta}{\alpha^2} + 390\frac{\eta k}{\alpha} + \frac{32\,6\eta}{\alpha}\right].
\end{aligned}
\tag{17}
$$

For large values of h, the RHS of Eq. (16) can to a first approximation be neglected. The corresponding behaviour of the "eigenvalues" $\{-L^2 + v(z_0)\}/h^2$ can then be determined by comparing the equation with the equation of parabolic cylinder function. The solutions are square integrable only if

$$
\frac{1}{h^2}\left[-L^2 + v(z_0)\right] = q/2\,, \tag{18}
$$

where q is an odd integer i.e.

$$
q = (2n + 1) \tag{19}
$$

(provided the wavefunction is required to vanish at infinity, otherwise it is only approximately an odd integer).

For complete solution we now set,

$$
\frac{1}{h^2}\left[-L^2 + v(z_0)\right] = \frac{q}{2} + \frac{\Delta}{h}\,, \tag{20}
$$

where the quantity Δ in (20) is yet to be determined. Substituting (20) in (16) we have

$$
\mathfrak{D}_q\,\Phi = \frac{2\Delta}{h}\,\Phi - \sum_{i=3}^{\infty}\frac{v^i(z_0)}{v^{(2)}(z_0)}\cdot\frac{\omega^i\,\Phi}{i\,|\,h^{i-2}}\,, \tag{21}
$$

where

$$
\mathfrak{D}_q = -2\frac{d^2}{d\omega^2} - q - \frac{\omega^2}{2}\,. \tag{22}
$$

Eq. (21) now is suitable for application in our perturbation method. To a first approximation $\varphi = \varphi^{(0)}$ is simply a parabolic cylinder function $D_{\frac{q-1}{2}}(\omega)$ i.e.

$$
\Phi^{(0)} = \Phi_q = D_{\frac{q-1}{2}}(\omega)\,, \quad \mathfrak{D}_q\,\Phi_q = 0\,. \tag{23}
$$

We have

$$D_{\frac{q-1}{2}}(\omega) = 2^{\frac{q-3}{4}} \cdot e^{-\frac{\omega^2}{4}} \Psi\left(\frac{3-q}{4}, \frac{3}{2}; \frac{\omega^2}{2}\right),$$

where Ψ is a confluent hypergeometric function. The function φ_q is well known to obey the recurrence relation

$$\omega \Phi_q = (q, q+2)\, \Phi_{q+2} + (q, q-2)\, \Phi_{q-2}, \tag{24}$$

where

$$(q, q+2) = 1 \quad \text{and} \quad (q, q-2) = \frac{1}{2}(q-1). \tag{25}$$

For higher powers we have

$$\omega^i \Phi_q = \sum_{j=2i}^{-2i} S_i(q, j)\, \Phi_{q+j} \tag{26}$$

and a recurrence relation can be written down for the coefficients S_i. The first approximation $\varphi = \varphi^{(0)}$ then leaves uncompensated terms amounting to

$$R_q^{(0)} = \frac{2\Delta}{h} \Phi_q - \sum_{i=3}^{\infty} \frac{1}{h^{i-2}} \sum_{j=2i}^{-2i} \tilde{S}_i(q, j) \Phi_{q+j}(\omega), \tag{27}$$

where we have set

$$\tilde{S}_i(q, j) = \frac{v^{(i)}(z_0)}{v^{(2)}(z_0)} \cdot \frac{S_i(q, j)}{i!}. \tag{28}$$

We rewrite (27) in the form

$$R_q^{(0)} = \sum_{i=3}^{\infty} \frac{1}{h^{i-2}} \sum_{j=2i}^{-2i} [q, q+j]_i\, \Phi_{q+j}(\omega), \tag{29}$$

where we have set

$$[q, q]_3 = 2\Delta - \tilde{S}_3(q, 0)$$

and for

$$j \neq 0 \quad [q, q+j]_3 = -\tilde{S}_3(q, j).$$

For

$$i > 3, \qquad -2i \leq j \leq 2i$$

$$[q, q+j]_i = -S_i(q, j). \tag{30}$$

Following the procedure adopted by MÜLLER-KIRSTEN et al [6], the next order contribution of φ becomes

$$\Phi^{(1)} = \sum_{i=3}^{\infty} \frac{1}{h^{i-2}} \sum_{j=2i}^{-2i} \frac{[q, q+j]_i}{j} \Phi_{q+j}(\omega). \tag{31}$$

In its turn this contribution leaves uncompensated

$$R^{(1)} = \sum_{i=3}^{\infty} \frac{1}{h^{i-2}} \sum_{\substack{j=2i \\ j\neq 0}}^{-2i} \frac{[q, q+j]_i}{j} R^{(0)}_{q+j} . \tag{32}$$

The higher order corrections to the eigenfunctions i.e. $\varphi^{(2)}$, $\varphi^{(3)}$, ... are now obtained in a manner analogous to the derivation of $\varphi^{(1)}$. Then adding successive contributions we obtain

$$\Phi = \Phi^{(0)} + \Phi^{(1)} + \Phi^{(2)} + \ldots . \tag{33}$$

Eq. (33) represents the solution of (21) which is nothing but an asymptotic expansion in descending powers of h valid for $(z - z_0) = 0\left(\frac{1}{h}\right)$ i.e. around $z = z_0$. For Eq. (33) to be a solution of Eq. (21), the sum of the coefficients of φ_q in $R^{(0)}_q$, $R^{(1)}_q$, $R^{(2)}_q$, ... left uncompensated so far must be set equal to zero i.e.

$$0 = \frac{1}{h}[q, q]_3 + \frac{1}{h^2}\left\{[q, q]_4 + \sum_{\substack{j=6 \\ j\neq 0}}^{-6} \frac{[q, q+j]_3}{j}[q+j, q_3]\right\} + 0\left(\frac{1}{h^3}\right). \tag{34}$$

This is the equation which determines Δ and hence eigenvalues, thus

$$\begin{aligned} 2h\Delta = \Big\{ & \tilde{S}_4(q, 0) - \frac{1}{6}\tilde{S}(q, 6)\,\tilde{S}_3(q+6, -6) + \frac{1}{6}\tilde{S}_3(q, -6)\,\tilde{S}_3(q-6, 6) - \\ & - \frac{1}{2}\tilde{S}_3(q, 2)\,\tilde{S}_3(q+2, -2) + \frac{1}{2}\tilde{S}_3(q, -2)\,\tilde{S}_3(q-2, 2)\Big\} + \\ & + 0\,(1/h^2). \end{aligned} \tag{35}$$

Using Eqs. (4), (17), (19) and (20), we obtain

$$\left(l + \frac{1}{2}\right)^2 = \frac{h^4}{12} - \frac{qh^2}{2} + \frac{(q^2+1)}{2^5} B - \frac{(15\,q^2+7)}{2^5 \cdot 3^2} A^2 + 0\left(\frac{1}{h_2}\right). \tag{36}$$

Solving for l, one gets

$$\begin{aligned} l = & -\frac{1}{2} + \frac{h^2}{2\sqrt{3}} - \frac{\sqrt{3}}{2} q + \frac{\sqrt{3}\,(q^2+1)}{2^5 h^2} B - \frac{(15\,q^2+7)}{2^5 \cdot 3^2 h^2} A^2 + \\ & + \frac{\sqrt{3}\,q}{2^8 h^4}\big[q^2\{3 \cdot 111\,AC - 0.444\,D + 0.944\,B^2 - 8.333\,A^2 B + \\ & + 0.407\,B^2\} + \{8.444\,AC - 2.22\,D + 3.722\,B^2 - 17\,A^2 B + \\ & + 7.129\,A^4\}\big] + 0\,(1/h^3). \end{aligned} \tag{37}$$

It may be of interest to note that for $\eta = 0$ and $\delta = 0$, the expression (37) reduces to the analogous expansion for the pure linear potential. This expansion is found to be in exact agreement with that obtained by MÜLLER-KIRSTEN et al [6] upto $0(1/h^2)$.

Applications

(A) Regge trajectories

We have used Eq. (37) for plotting Regge trajectories. The Regge trajectories for the potential (3) are shown in Fig. 1. The values of quark mass m, δ, β and η chosen for plotting these trajectories are given in Table I. We observe that these trajectories are almost linear over the range of immediate interest. It may, therefore, be concluded that Regge trajectories for the potential considered by us in this paper do not lose their linearity and their behaviour is similar to the ones as obtained for pure logarithmic and linear potentials.

(B) Calculation of bound quark—antiquark mass

Since the quark mass is twice the reduced mass μ, the mass M_q of a bound quark—antiquark pair in the state q is given by

$$M_q = 4\mu + E.$$

In Table I the calculated values of lowest S and P states masses alongwith their experimental values are given. The values of the parameters β, η, δ and ϱ_0 used in the calculation are also given in the Table. It is interesting to note that while making calculations related to Table I — column (a), parameter β was the same as used by MÜLLER-KIRSTEN et al [6] for pure linear

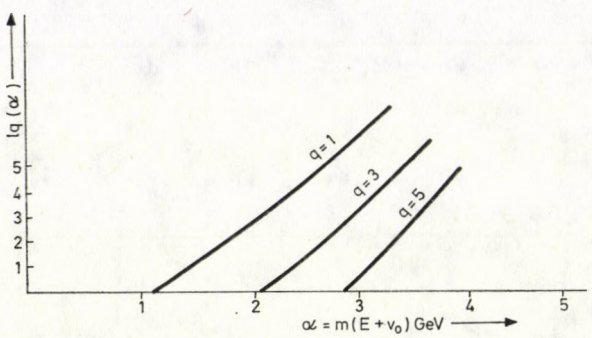

Fig. 1. The first three Regge trajectories for the potential (3) with $m = 1.65$ GeV $\beta = 0.3$ GeV^3, $\eta = 0.001$ GeV^2, $\delta = 0.0001$ and $r_0 = 1$ GeV^{-1}.

potential. For calculations related to column (b) of Table I, the magnitude of parameter η chosen was the same as used by MÜLLER-KIRSTEN et al [9] for pure logarithmic potential. It is, therefore, easy to conclude from Table I that the values of quark mass have improved on account of superposition of linear potential and logarithmic potential alongwith a weak coulombian component. A similar observation for the improvement of quark mass due to superposition of potentials has been made by SHARMA et al [13].

(C) Calculations for leptonic decay widths

Decay width plays an important role in exploring the origin of a newly found hadronic state. The leptonic decay widths of a vector quark-antiquark bound state such as ψ can be expressed in terms of the S wave bound state wave function at the origin. Thus

$$(\psi \to l\bar{l}) = \frac{16\pi \alpha_S^2 e_Q^2}{M_\psi^2} |\psi(0)|^2.$$

Here α_S is the fine structure constant, e_Q is the charge of the constitutent quark of ψ.

In the case of an s-wave bound state, the wave function is related to the potential V via the following expression:

$$|\psi(0)|^2 = \frac{\mu}{2\pi}\left\langle \frac{dV}{dr} \right\rangle = \frac{\mu}{2\pi}\int \psi^*(r)\frac{dV}{dr}\psi(r)\,d\vec{r}.$$

In order to calculate $\left\langle \frac{dV}{dr} \right\rangle$ and hence $|\psi(0)|^2$ the WKB approximation method is used.

Thus for the potential (3)

$$|\psi(0)|^2 = \frac{\mu}{2\pi} \cdot \frac{\int_{r_0}^{\bar{r}} dr \left(E - g_1 r + g_2 \log\frac{r}{r_0} + \frac{g_3}{r} + V_0\right)^{-1/2} \frac{dV}{dr}}{\int_0^{\bar{r}} dr \left(E - g_1 r + g_2 \log\frac{r}{r_0} + \frac{g_3}{r} + V_0\right)^{-1/2}},$$

where $\bar{r}$ is the classical turning point, $r_0 = 1$ and

$$\frac{dV}{dr} = \left[g_1 - \frac{g_2}{r} + \frac{g_3}{r^2}\right].$$

The results obtained for the decay widths for potential (3) are shown in Table II and compared with the experimentally observed values.

Discussion

The investigation made in this paper shows that simple perturbation methods can be formulated for solving the wave equation for the superposition of potentials. In particular, the asymptotic expansions and eigenvalues for the potential (3) have been derived.

In the potential (3) we have superposed the Coulomb potential with linear and logarithmic confining potentials. We have, however, assumed that the Coulombian component is sufficiently weak.

It is observed that our results show improvement over those obtained for either linear potential or for logarithmic potential taken separately. We, therefore, conclude that combination of linear potential with logarithmic potential is more appropriate for the quark confinement.

The main features of the results obtained in this paper may be summarized as follows:

(1) The expansions are invariant under joint interchange $q \to -q$ and $h^2 \to -h^2$ which obviously converts one solution into another.

(2) The values of the s-states predicted agree well with those stated by other authors.

(3) The values for P-states have also shown improvement even without spin-orbit and tensor corrections.

(4) The decay width calculations do not give good results for $2\ ^3S_1$ state while for other states they are satisfactory.

REFERENCES

1. J. J. Aubert et al. Phys. Rev. Lett., **33**, 1404, 1974; J. E. Augustin et al. ibid. **33**, 1406 1974.
2. Abrams et al. Phys. Rev. Lett., **33**, 1453, 1974.
3. T. Appelquist and H. D. Politzer, Phys. Rev. Lett., **34**, 43, 1975; Phys. Rev., **D12**, 1404, 1975.
4. T. Appelquist, A. De Rujula, H. D. Politzer and S. L. Glashow, Phys. Rev. Lett., **34**, 365, 1975.
5. E. Eichten, K. Gottfried, T. Kinoshita, K. D. Lane and T. M. Yan, Phys. Rev., D **17**, 3050, 1978.
6. H. J. W. Müller-Kirsten, G. E. Hite and S. K. Bose, J. Math. Phys., **20**, 1878. 1979.
7. A. De. Rujula and S. L. Glashow, Phys. Rev. Lett., **34**, 46, 1975; C. G. Callan, R. L. Kingsley, S. B. Treiman, F. Wilczek and A. Zee, ibid. **34**, 52, 1975; B. J. Harrington, S. Y. Paik and A. Yildiz, ibid. **34**, 168, 706, 1975; J. S. Kang and H. J. Schnitzer, Phys. Rev., **D12**, 841, 1975; **D12**, 2791, 1975.
8. M. Kramer and H. Krasemann, Nuovo Cim., **32A**, 394, 1976.
9. H. J. W. Müller-Kirsten and S. K. Bose, J. Math. Phys., **20**, 2471, 1979.
10. L. M. Lederman in "Proceedings of International Symposium on Lepton and Photon Interactions at High Energies", edited by F. Gutbrod, DESY Hamburg, p. 567, 1977.
11. C. Quigg and J. L. Rosner, Fermi Lab. 77/82 THY Preprint, unpublished 1977.
12. J. L. Rosner and C. Quigg, Fermi Lab. 77/90 THY, Preprint, 1977.
13. L. K. Sharma, V. P. Iyer, S. Metha, S. V. Kulkarni and J. Choubey, J. Math. Phys., **23**, 780, 1982.
14. H. J. Schnitzer, Phys. Rev., **D13**, 74, 1975.
15. H. J. Schnitzer, Phys. Rev. Lett., **35**, 1540, 1975.

Acta Physica Academiae Scientiarum Hungaricae, 52 (2), pp. 199—209 (1982)

NEGATIVE PARITY LEVELS IN ^{195}Pt VIA COULOMB EXCITATION

R. G. KULKARNI

DEPARTMENT OF PHYSICS, SAURASHTRA UNIVERSITY, RAJKOT—360 005, INDIA

and

K. ANDHRADEV

DEPARTMENT OF PHYSICS, M. U. COLLEGE, UDGIR—413517, INDIA

(Received 20. X. 1981)

Low lying negative parity levels in ^{195}Pt were Coulomb excited with 4.0—5.5 MeV protons to test the weak coupling core-excitation model. A Ge(Li) detector was used to measure gamma ray yields and angular distributions. The levels at 449.6 and 793 keV were Coulomb excited repeatedly. The results of the gamma-ray angular distributions not only confirmed the assignment of 3/2 spin to the 199 keV level but also established 5/2, 5/2, and 3/2 spins for the levels at 389.6, 449.6 and 793 keV, respectively. The E2 and M1 transition probabilities for the 389.6, 449.6 and 793 keV transitions were found for the first time. The 211.2, 239.2, 389.6 and 793 keV states have electromagnetic magnetic properties consistent with the interpretation of coupling of a P1/2 neutron to the 2_1^+ and 2_2^+ core-states.

1. Introduction

Since DE-SHALIT [1] introduced the core excitation model nineteen years ago, a number of levels in odd-A nuclei have been identified as arising from weak coupling of the odd particle to the first excited state of the even core. With the advent of high resolution Ge(Li) detectors many one phonon and a few two phonon states in even-even nuclei have been observed. Consequently the neighbouring odd-A nuclei are being re-examined for levels resulting from the coupling of an odd particle to higher lying core-states.

If the ground state spin of the odd nucleus is 1/2, the description of excited states in the core-excitation model is especially simple, For each core state having spin J_c and energy E_c there are at most two states in odd-A nucleus with spins $J_c \pm 1/2$. The model also predicts the B(E2) of the decay from each member of the multiplet to the ground state to be identical and equal to the B(E2; $2 \rightarrow 0$) for the core state, if the core state is identical to the first excited state of the neighbouring doubly even nucleus. In its simplest form, the model forbids M1 radiation and transitions between members of a multiplet. Some odd-A isotopes of Pt, Hg, and possibly Pb for which the neutron

is in a $p_{1/2}$ orbit are good test cases for the core-excitation model. The present paper describes our measurement of the properties of levels in ^{195}Pt in terms of the core-excitation model.

Coulomb excitation studies of ^{195}Pt have been carried out by a number of investigators [2, 3, 4, 5, 6, 7] and all these have been reported in Nuclear Data Sheets [8]. Coulomb excitation of the levels at 449.6 and 793 keV has not yet been reported. According to Nuclear Data Sheets [8], definite spin assignments are not known for the levels at 389.6 and 449.6 keV. The definite assignment of $3/2^-$ is taken for the 199.3 keV state from the Table of Isotopes (1978). In this paper we report the results of Coulomb excitation experiments with protons on ^{195}Pt. With protons, direct E2 excitation is usually the dominant process, and only $3/2^-$ and $5/2^-$ states are populated when the ground-state spin is $1/2^-$. Then the B(E2) values for ground state transitions can be extracted unambiguously from the gamma-ray yields. By measuring the angular correlation of the gamma-rays with respect to the incident proton beam, information on spins of the excited states and the multipolarity of the decay radiation can be obtained.

2. Experimental

The Coulomb excitation studies of ^{195}Pt were done using protons. Beams of protons from the Bhabha Atomic Research Centre, Trombay, Van de Graaff accelerator, with energies from 4.0 to 5.5 MeV were used to bombard a natural platinum target which was in the form of a self-supporting metallic foil of 55 mg/cm^2 thickness and 99% purity. The target was inclined at an angle of 45° with respect to the incident beam to insure identical geometries for 0° and 90° angular anisotropy measurements. The de-excitation gamma-rays were observed by means of a 30 cm^3 Ge(Li) detector placed at an angle of 55° to the beam direction to minimize the angular distribution effects on the gamma ray yields. The detector resolution was about 3.5 keV for the 1.33 MeV ^{60}Co line. The experimental measurements consisted of gamma-ray yields and angular distributions with protons. Since the target was thick, the target chamber served as a Faraday cup for beam integration. The target current was integrated and recorded with appropriate correction for dead time.

The absolute efficiency of the Ge(Li) detector was measured with a set of standard calibrated gamma sources. These sources were obtained from the International Atomic Energy Agency, Vienna. Absolute efficiency measurements were performed immediately following Coulomb excitation experiments without altering the geometry. For the gamma ray of interest (0.1 to 0.8 MeV) we believe the absolute efficiency of the Ge(Li) detector was known to be $\pm 3\%$.

3. Experimental results

3.1 *Gamma-ray yields*

The thick target gamma-ray yields were observed for excitation of levels in ^{195}Pt with 4.0—5.5 MeV protons in steps of 250 keV. Because the predominant mode of excitation with this projectile is direct E2, accurate B(E2) values can be extracted by means of the first-order perturbation theory of ALDER et al [9]. A typical gamma ray spectrum obtained from the bombardment of ^{195}Pt with 5.0 MeV protons is shown in Fig. 1. Gamma rays at 140.2 shown in Fig. 1 199.3, 211.2, 259.7, 290.9, 319.9, 350.9, and 793 KeV were assigned to de-excitation of levels in ^{195}Pt on the basis of their well-known energies from previous work and because their yields varied in the manner expected from Coulomb excitation process. In addition to these gamma rays, the gamma rays arising from the de-excitation of the first excited states of ^{192}Pt, ^{194}Pt, ^{196}Pt and ^{198}Pt are observed and these are identified in the spectrum (Fig. 1).

The yield per incident proton was obtained from the charge collected and the area under the full energy peak corrected for detector efficiency, the gamma absorption by the target and mount, the internal conversion co-efficient, and cascade transitions from higher levels.

The values of the reduced matrix elements for E2 transitions can be calculated from the measured thick target yields using the formula of ALDER et al [9] provided one is certain that only the Coulomb field is responsible for these upward transitions. To confirm the Coulomb character of these transitions, the thick target yields determined as a function of incident proton energy were compared with the theoretical predictions based on the assumption of Coulomb excitation alone, for the excitation mechanism. Typical theoretical fits (solid-line) to the measured yields of 319.9 and 793 keV gamma rays are shown in Fig. 2. The theoretical fits to measured yields support the view that E2 excitation is the only process responsible for the gamma transition observed. The B(E2) values were extracted from the measured thick target yields and the results are summarized in Table I. The major sources of experimental error for the B(E2) values were due to uncertainties in the peak areas, the Ge(Li) detector efficiency, the beam current measurements, and the stopping power for incident particles. The error is estimated to be as high as 16%.

In deducing these upward transition probabilities B(E2) as listed in Table I, the branching of each gamma transition to intermediate levels was taken into account. An energy level scheme for ^{195}Pt as shown in Fig. 3 was established on the basis of Coulomb excited levels. The deducted B(E2) values from thick target yields were compared with the B(E2) values obtained previously [6, 7]. These results are tabulated in Table II.

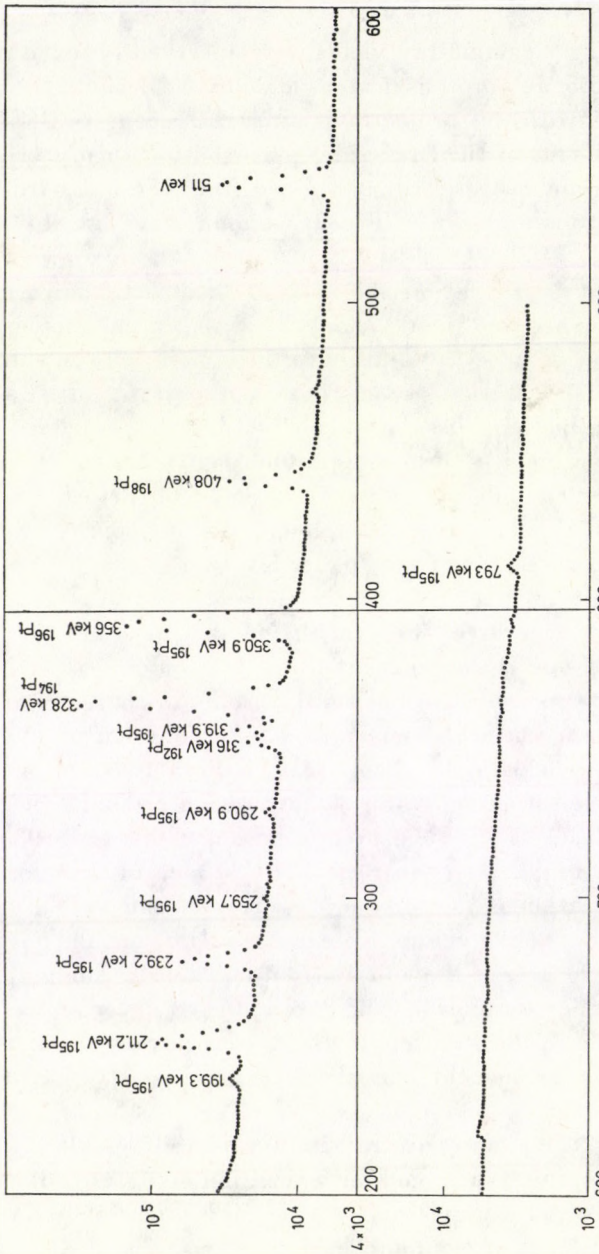

Fig. 1. Spectrum of the gamma rays of ^{195}Pt Coulomb excited by 5.00 MeV protons.

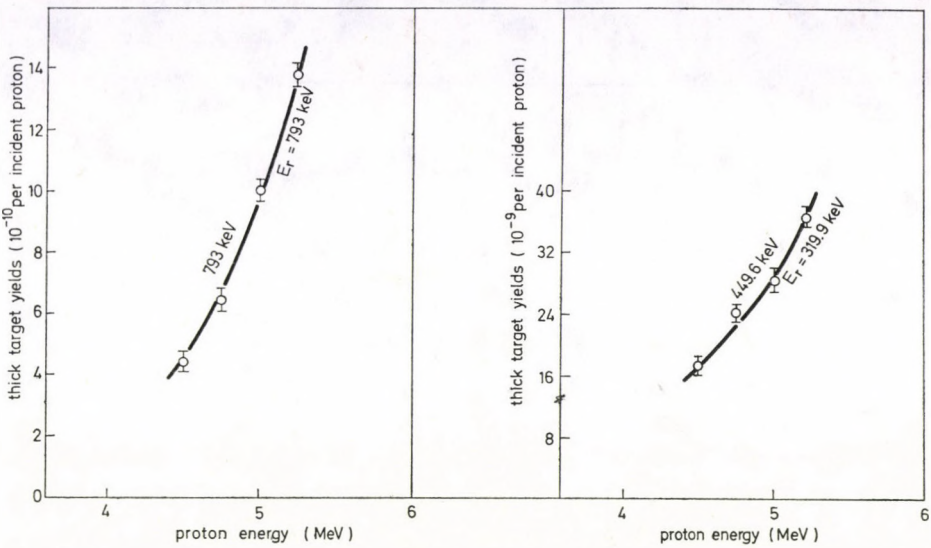

Fig. 2. Thick target gamma-ray yields as a function of the proton energy. The solid curves give the theoretical energy dependence predicted from E2 Coulomb excited states for 449.6 and 793 keV levels.

Table I

Summary of branching ratios and reduced transition probabilities of ^{195}Pt levels

Level energy keV	Transitions	Branching ratios (%)	$\varepsilon B(E2)\uparrow$ ($e^2\,b^2$)	$B(E2)\uparrow$ ($e^2\,b^2$)
199.3	199.3→g.s.	100	0.0150 ±0.0014	0.0245±0.0023
211.2	211.2→g.s.	100	0.251 ±0.015	0.442 ±0.026
239.2	239.2→g.s.	62 (a)	0.165 ±0.008	0.559 ±0.027
	239.2→98.9	38 (a)		
389.6	389.6→98.9	71±1	0.0116 ±0.0008	
				0.218 ±0.0015
	389.6→129.7	29±1	0.00484±0.00033	
449.6	449.6→98.9	9 (b)	0.0126 ±0.0020	
				0.142 ±0.017
	449.6→129.7	88 (b)	0.125 ±0.015	
793	793 →g.s.	100	0.0149 ±0.0024	0.0149±0.0024

(a) Branching ratios from W. T. MILNER, private communication to Nuclear Data Sheets [8].
(b) Branching ratios from JANSEN et al [11].

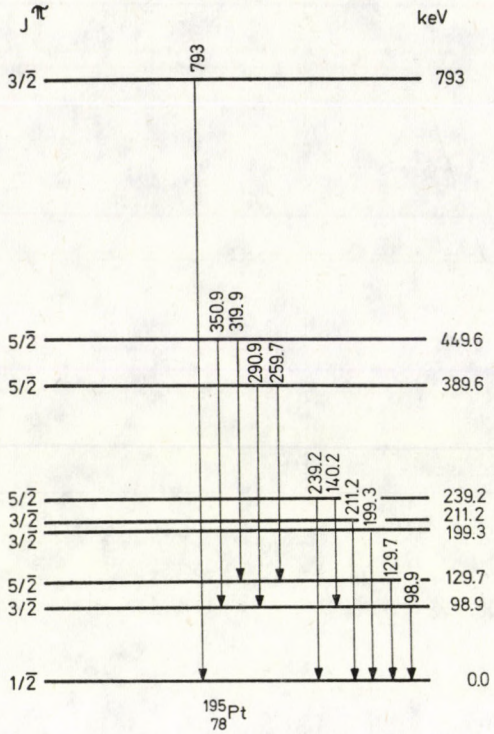

Fig. 3. Energy level scheme of ^{195}Pt.

Table II

Comparison of B(E2) ↑ values of ^{195}Pt with previous Coulomb excitation studies

Level energy (keV)	B(E2) ↑ e^2b^2		
	Present work	BRUTON et al [6]	MILNER et al [7]
199.3	0.0245±0.0023	0.029±0.003	0.022±0.003
311.2	0.442 ±0.026	0.40 ±0.03	0.40 ±0.03
239.2	0.559 ± 0.027	0.58 ±0.03	0.55 ±0.03
389.6	0.0218±0.0015*	—	—
449.6	0.142 ±0.017	—	—
793	0.0149±0.0024	—	—

* W. T. MILNER in a private communication to Nuclear Data Sheets [8] gives εB(E2) of 259.7 keV gamma ray from 389.6 keV level as (0.00474 ± 0.00043) e^2b^2 with 4.5 MeV protons and (0.00363 + 0.00038) e^2b^2 with 43.75 MeV 160 ions and εB(E2) of 290.9 keV gamma ray 389.6 keV level as (0.0123 + 0.006) e^2b^2 with 4.5 MeV protons and (0.0110 ± 0.009) e^2b^2 with 43.75 MeV ^{16}O ions.

3.2 *Angular distributions*

The gamma-ray angular distributions were measured at 5.0 MeV protons. The angular distributions of the gamma rays were obtained from the spectrum taken with the Ge(Li) detector placed at angles of 0° and 90° relative to the beam direction and at a distance of 6.5 cm from the target. The gamma ray angular distribution according to first order theory is expressed as

$$W(\theta) = 1 + g_2 a_2 A_2 P_2 (\cos\theta) + g_4 a_4 A_2 P_2 (\cos\theta),$$

where $P_2(\cos\theta)$, $P_4(\cos\theta)$ are Legendre polynomials and A_2, A_4 are the usual directional correlation coefficients. The quantities a_2, a_4 are the thick target particle parameters and g_2, g_4 are the finite solid angle corrections. For the present experimental geometry, the g_2 and g_4 values are calculated from the tables of CAMP and VANLEHN [10]. The angular distributions of 328, 356 and 408 KeV gamma rays of $(0^+ \rightarrow 2^+)$ first excited states of ^{194}Pt, ^{196}Pt and ^{198}Pt, respectively, were used for the alignment of the axis of rotation of the detector and for location of beam position on the target during collection of data. The A_2 values were extracted by neglecting the P_4 term in the correlation because a_4 is quite small. The a_2 is about 10—12 times greater than a_4 so by neglecting a_4 in correlation function, one may incur an error of 6 to 7%, if one takes into account the solid angle correction.

A summary of the results from the angular distribution measurements is given in Table III for six transitions in ^{195}Pt. The fourth column gives the assumed decay spin sequence and the fifth column $\delta = \left(\frac{E2}{M1}\right)^{1/2}$ values allowed by the A_2 results. The reduced M1 transition probabilities B(M1) were calcul

Table III

Summary of angular distributions of the gamma rays for 5.00 MeV protons on ^{195}Pt (D is Magnetic Dipole (M1) and Q is Electric Quadrupole (E2).)

Level energy (keV)	E_γ (keV)	A_2	Spin sequence	δ
199.3	199.3	$+0.450\pm0.40$	3/2 (D,Q) 1/2	$+1.1$ $+0.2$ or $(+3.3\pm0.6)$
211.2	211.2	$+0.090\pm0.004$	3/2 (D,Q) 1/2	$+0.39\pm0.01$ or (-5.8 ± 0.2)
239.2	239.2	$+0.301\pm0.018$	5/2 (Q) 1/2	∞
389.6	290.9	-0.033 ± 0.022	5/2 (D,Q) 3/2	-0.12 ± 0.02 or 2.2 ± 0.4
449.6	319.9	$+0.319\pm0.032$	5/2 (D,Q) 5/2	$\pm0.20+0.04$ or 1.1 ± 0.2
793	793	$+0.437\pm0.080$	3/2 (D,Q) 1/2	$+1.0+0.4$ or (3.6 ± 1.4)

Table IV

Values of reduced E2 and M1 transition probabilities in units of e^2b^2 and $(nm)^2$ respectively, for ^{195}Pt levels

E_γ (keV)	$J_i \to J_f$	B(E2)↓ (e^2b^2)	δ	B(M1)↓ $(nm)^2$
199.3	3/2→1/2	0.0123±0.0012	1.1 ±0.2	0.00026±0.0006
211.2	3/2→1/2	0.211 ±0.013	0.29±0.01	0.0453 ±0.0023
239.2	5/2→1/2	0.186 ±0.009		—
793	3/2→1/2	0.0075±0.0012	1.0 ±0.4	0.0033 ±0.0013
			3.6 ±1.4	0.00025±0.00010

ated with the knowledge of the B(E2) values and the mixing ratios $\delta = \left(\frac{E2}{M1}\right)^{1/2}$ for each transition. The reduced E2 and M1 transition probabilities found in the present work are listed in Table IV.

4. Discussion

As the Coulomb excitation study of first two excited states at 98.9 and 129.7 keV in ^{195}Pt has been done by a number of investigators thoroughly, the present work aims at the study of higher excited states.

An upward transition from the ground state to the excited state at 199.3 keV was observed and its Coulomb character has been found to be E2. The deduced B(E2)↑ value for this state agrees within experimental errors with the previous measurements [6, 7]. The spin assignment $J^\pi = 3/2^-$ for this state from earlier work [6] is consistent with the present work.

A direct E2 transition from the ground state to the excited state at 211.2 keV was observed in this work with 100% branching. The present B(E2)↑ value agrees with earlier measurements [2, 4, 6, 7]. The angular distribution measurements assign 3/2 spin to this level which is in agreement with the spin value already accepted [8].

In the present investigation, a level at 239.2 keV was Coulomb excited and it was found to be an E2 transition. The B(E2)↑ value found in this work gives reasonable agreement with the previous measurements [2, 6, 7]. The angular distribution measurements uniquely assign 5/2 spin to this level which is in agreement with the value from Nuclear Data Sheets [8].

A level at 389.6 keV decays to the first excited state at 98.9 keV and to the second excited state at 129.7 keV with the branching ratios of 71 ± 1% and 29 ± 1%, respectively. As no gamma radiation was observed at 150 keV in this work, the branching ratios found presently may not agree with Nuclear

Data Sheets [8]. The comparison of the thick target yields with theoretical predictions suggests that 290.9 and 259.7 keV transitions are excited by E2 mechanisms. Using the thick target yields of 290.9 and 259.7 keV transitions, the B(E2) values were extracted for this state. The angular distribution measurements establish 5/2 spin to this level.

A level at 449.6 keV was Coulomb excited for the first time. From a comparison of our gamma ray spectrum to that of BRUTON et al [6], it is apparent that the 319.9 and 350.9 keV gamma rays are seen in the present work but not in the latter. Relative gamma-ray yields seem to be almost the same for most of the other lines. Both of these spectra were taken by the Coulomb excitation experiments on thick natural Pt target although the projectiles used were different. In the present case protons were used as projectiles whereas ^{4}He ions and ^{16}O ions were used in earlier work [6]. With heavy ions, multiple Coulomb excitation is important, and it is possible that these low intensity gamma rays might not have been seen in earlier work [6]. According to the β-decay studies of JANSEN et al [11], in addition to the 319.9 and 350.9 keV gamma rays, gamma rays at 239 and 211 keV are also expected. These two gamma rays occur at energies which coincide with the energy of the levels at 239.2 and 211.2 keV. Hence it is rather difficult to place them in the decay scheme with proper branching. So, the branching ratios given by JANSEN et al. [11] are accepted for the present purpose. The gamma transitions of 319.9 and 350.9 keV follow E2 excitation. The B(E2)$\uparrow$ values have been found using thick target gamma ray yields and the branching ratios of JANSEN et al [11]. The angular distribution measurements have established 5/2 spin to this level.

An upward transition from the ground state to the state at 793 keV was observed recently and it was found to be E2 in character (Fig. 2). A level was seen in (p, d) experiment at 798 keV by BERRIER-RONSIN et al [12] which they identified with the level at 793 ± 2 keV seen in (d, t) reaction by YAMAZAKI and SHELINE [13]. A spin of $13/2^+$ has been proposed for this level by BERRIER-RONSIN et al [12]. As the presently excited 793 keV level is E2 in character, its parity must be negative and its spin cannot be greater than 5/2. B(E2) value has been extracted for this level for the first time. A spin of 3/2 has been assigned on the basis of the present angular distribution measurements for this level. E2 and M1 transition probabilities have also been found.

5. Core-excitation model

A decade ago GAL (Braunstein) [13] has attempted to describe the electromagnetic properties of the low-lying states in ^{195}Pt in terms of core-excitation model and had achieved very little success. This is mainly because very scanty

experimental data abount B(E2) and B(M1) values existed then. The presently found B(E2) and B(M1) value (Table IV) for the low-lying negative parity levels in ^{195}Pt from the Coulomb excitation reaction were used to test the predictions of DE-SHALIT's [1] core-excitation model of the nucleus.

According to the core-excitation model of DE-SHALIT [1] two states in ^{195}Pt with spins 3/2 and 5/2 should arise from coupling of a $3p_{1/2}$ neutron or hole to the 2^+ core state which is identified with the first 2^+ level in the neighbouring even nucleus. The B(E2) values for decay of the 5/2 and 3/2 states should be nearly equal and close to the B(E2; $2 \rightarrow 0$) value for the even core-nucleus. In the present analysis, the doublet in ^{195}Pt was taken to be, in keV, 211.2 ($3/2^-$) and 239.2 (5/2). The existence of the $3/2^-$, $5/2^-$ doublet separated by only 28 keV supports the model although the centre of gravity is only 66.5% of the average of the first 2^+ states in the two core nuclei ^{194}Pt and ^{196}Pt. The B(E2; $3/2 \rightarrow 1/2$) and B(E2; $5/2 \rightarrow 1/2$) values are nearly equal to each other and their average, 203.5 e^2f^4 agrees with the average B(E2; $2 \rightarrow 0$) value of 300 e^2f^4 for ^{194}Pt and ^{196}Pt within 32% error. However, the B(M1; $3/2 \rightarrow 1/2$) value is 0.0453 $(\text{nm})^2$ instead of zero as predicted by the model. A slight admixture of the $p_{3/2}$ single-particle configuration could account for this M1 radiation.

While the core excitation model gives a reasonably good description of the two negative parity excited states of 211.2 and 239.2 keV, the higher levels provide a more sensitive test of the model. If the higher lying core excited states in ^{195}Pt can be identified with the two-phonon triplets in ^{194}Pt and ^{196}Pt, five levels with $J^\pi = 1/2^-$, $3/2^-$, $5/2^-$, $7/2^-$ and $9/2^-$ should be observed at an energy consonant with the two phonon to one phonon energy ratio in the even mass nuclei. Indeed there are three negative parity states (389.6, 449.6 and 793 KeV) which lie near the predicted energy. Averages of the ^{194}Pt and ^{196}Pt[6] for the 2^+ and 4^+ states are 655 and 845 keV, respectively. On the basis of spin values, the 389.6 and 793 keV states are good candidates for the two members of the 2_2^+ core-excitation doublet. Further, rather low B(E2) values of 389.6 and 793 keV levels are in accord with the small B(E2; $2_2^+ \rightarrow 0^+$) value of ^{194}Pt[6]. In addition, the average separation between the 2_1^+ and 2_2^+ states of ^{194}Pt and ^{196}Pt is 311 keV and this value agrees with the separation of 322 keV between the centre of gravity of the 211.2 and 239.2 keV states and 389.6 and 793 keV states of ^{195}Pt. These facts support the view that the four states at 211.2, 239.2, 389.6 and 793 keV in ^{195}Pt can be described in terms of the core-excitation model. The states at 211.2 and 239.2 keV are identified as the two members of the 2_1^+ core-excitation multiplet and the states at 389.6 and 793 keV are identified as the two members of the 2_2^+ core-excitation multiplet.

Acknowledgements

The authors are grateful to Dr. M. K. MEHTA, Head, Nuclear Physics Division, Bhabha Atomic Research Centre, Trombay, for extending Van de Graaff accelerator facilities. One of the authors (K. A.) is thankful to the University Grants Commission, New Delhi, for providing Teacher Fellowship during the course of this work. We are also grateful to the Department of Atomic Energy, Government of India, for financial assistance in the form of research project.

REFERENCES

1. A. DE-SHALIT, Phys. Rev., **122,** 1530, 1961.
2. F. K. MCGOWAN and P. H. STELSON, Phys. Rev., **116,** 154, 1959.
3. R. L. ROBINSON, P. H. STELSON, F. K. MCGOWAN, and M. T. MILNER, Nucl. Phys., **74,** 281, 1965.
4. L. GRODZINS, R. R. BORCHERS and G. B. HAGEMANN, Nucl. Phys., **88,** 474, 1966.
5. H. W. KUGEL, R. R. BORCHERS and R. KALISH, Nucl. Phys., A **137,** 500, 1969.
6. E. J. BRUTON, J. A. CAMERON, A. W. GIBB, D. B. KENYON and L. KESZTHELYI, Nucl. Phys., A $\mathbf{152}_1$ 495, 1970.
7. W. T. MILNER, F. K. MCGOWAN, R. L. ROBINSON, P. H. STELSON, and R. O. SAYER, Nucl. Phys., A **177,** 1, 1971.
8. Nuclear Data Sheets, **23,** 607, 1978.
9. K. ALDER, A. BOHR, T. HUSS, B. MOTTELSON and A. WINTER, Rev. Mod. Phys., **28,** 432, 1956.
10. D. C. CAMP and A. L. VANLEHN, Nucl. Insts. and Methods, **76,** 192, 1969.
11. J. F. N. JANSEN, A. FAOS and W. S. B. WINTER, Z. Phys., **261,** 95, 1973.
12. G. BERRIER-RONSIN, M. VERGNES, G. ROTBARD, J. VERNOTTE, J. KALIFA, R. SELTZ and H. L. SHARMA, Phys. Rev., C **17,** 529, 1978.
13. A. GAL (Braunstein), Phys. Lett., **20,** 414, 1966.

Acta Physica Academiae Scientiarum Hungaricae, 52 (2), pp. 211—219 (1982)

THE NUCLEON FORM FACTORS IN THE GEOMETRODYNAMICAL MODEL

T. MARGARITISZ and K. SZEGŐ

CENTRAL RESEARCH INSTITUTE FOR PHYSICS
1525 BUDAPEST, HUNGARY

(Received 20. X. 1981)

In this paper the G_E and G_M form factors of the proton and neutron are calculated in the geometrodynamical model of hadrons. Asymptotic behaviour and gross features are correctly reproduced, but there are deviations from experiments in fine details.

1. Introduction

The geometrodynamical model is a bag-type model for hadrons, invented and elaborated by PREPARATA and his coworkers [1]. The basic idea, explained in more detail in the next Section, is that simple geometrical approach is enough to determine the wave-functions of hadrons, built from quark degrees of freedom.

The model has been successful in explaining the meson [2] and baryon spectrum [3], as well as certain dynamical properties, too [4]. When describing the baryons, the interesting result was obtained that the three quarks in it are in a quark-diquark formation in the centre-of-mass system. This reduces the inner degrees of freedom.

In this paper we have extended that model to find the current matrix elements of nucleons. Specifying it to the electromagnetic current, the form factors G_E and G_M can be obtained for the nucleons. It is a fairly difficult question how to get conserved current matrix elements in models; for the case of the geometrodynamical model it was discussed in [5]. In our case, using an approximate form of the wave function, the current is conserved. That approximate form is very suitable for calculation, hence we do not treat the question of conservation in general.

The physical picture for current interaction is very simple: the current hits one of the quarks, the other two exchange momentum via exchanging a meson in their t-channel, and get rearranged into quark-diquark formation.

The picture is similar in other form factor calculations, too. FARRAR and JACKSON [6] calculated the pion form factor by solving the light-cone pion Bethe—Salpeter equation to leading-log accuracy, taken the kernel from QCD.

They obtained

$$F_n(q^2) \xrightarrow[q^2 \to \infty]{} \frac{1}{Q^2 \ln (Q^2)} .$$

Similar analysis was done by LEPAGE and BRODSKY [7] for the baryon. Up to logarithmic correction the $(Q^2)^{-2}$ behaviour was reproduced. For the low-energy region the result depended on the assumption what the effective wave function of the 3-quark system looked like. Trying two different Ansätze for that, the curves fall faster than the experimental one. The character of our results is very similar, let alone that in our model there is no room for different assumptions.

To compare our results with experiment, we used the excellent review paper of HÖHLER et al [8].

In Section 2 we summarise briefly what the baryon wave function looks like in the model, in Section 3 the current matrix element is discussed and the results are presented.

2. The model

The baryon wave function is denoted by

$$\Psi_{\alpha a, \beta b, \gamma c}(P ; x_1, x_1, x_3) = e^{iPX} \Psi_{\alpha a, \beta b, \gamma c}(P, x, y), \tag{2.1}$$

where a, b and c are internal flavour indices, α, β and γ are Dirac indices, x_i are the quark coordinates, and

$$X = \frac{1}{3}(x_1 + x_1 + x_3), \quad x = \frac{1}{\sqrt{2}}(x_1 - x_3), \quad y = \sqrt{\frac{2}{3}}\left(x_1 - \frac{x_1 + x_3}{2}\right). \tag{2.2}$$

The principles, on which the geometrodynamical approach is based, are the following:

i) Confinement

$$\Psi_{\alpha a, \beta b, \gamma c}(P ; x, y) = 0 \quad \text{for} \quad x, y \notin R^8(P ; x, p), \tag{2.3}$$

where $R^8(P; x, y)$ is a compact eight-dimensional space-time region with boundary $B^8(P; x, y)$.

ii) Continuity

For $x, y \in B^8(P; x, y)$ $\Psi(P; x, y)$ must be continuous, i.e.

$$\Psi_{\alpha a, \beta b, \gamma c}(P ; x, y) = 0 \quad \text{for} \quad x, y \notin B^8(P ; x, y). \tag{2.4}$$

More precisely, continuity is required only for suitable scalar functions appearing in a Lorentz-covariant decomposition of the wave functions. See [4] for the details.

iii) Wave equation

For $x, y \in R^8(P; x, y)$ Ψ obeys the simple differential equation

$$D_1 D_2 D_3 \Psi = 0, \tag{2.5}$$

where $D_i = (i_i + m_i)$ is the Dirac operator, acting on the i-th coordinate.

iv) Approximate freedom

The "distance" of Ψ from the "free solution" $\Psi^{(0)}(P; x, y)$, determined by the free equations

$$D_i \Psi^{(0)} = 0 \quad i = 1, 2, 3 \tag{2.6}$$

is minimum, the distance is calculated by an appropriate definition of the norm of the wave functions [2].

The solution of (2.3—2.5) was examined in [3]. The wave function factorizes into a scalar part and a spin part:

$$\Psi = \tilde{\Phi} \mid B > . \tag{2.7a}$$

The scalar part has the form

$$\tilde{\Phi}(P; x, y) = \int d\xi \, \tilde{\Phi}(P; y, \xi) \, \delta^4(\xi P - x) . \tag{2.7b}$$

The Fourier transform of $\tilde{\Phi}(P; y, \xi)$ is

$$\Phi(P; q, \eta) = \int d^4 x d\xi e^{-iqx} \, e^{-i\xi\eta} \tilde{\Phi}(P; y, \xi) , \tag{2.8}$$

where

$$\begin{aligned} p_1 &= \frac{1}{3} P + \sqrt{\frac{2}{3}} q , \\ p_1 &= \frac{1}{3} P - \sqrt{\frac{1}{6}} q - \sqrt{\frac{1}{3}} p, \\ p_3 &= \frac{1}{3} P - \sqrt{\frac{1}{6}} q + \sqrt{\frac{1}{2}} p, \end{aligned} \tag{2.9}$$

are the quark momenta. Due to the quark-diquark structure, both x and p are proportional to P, $x = \xi P$, $p = \eta P$. The quantities ξ and η are scalars in the CM system, their values concide with x_0 for ξ, and with p_0 for η. In

the CM,

$$\tilde{\Phi}_{CM}(P;q,p_0)=\frac{\omega^2}{8}\cos\frac{R+C_1}{\frac{\omega^2}{16}-C_1^2}\cos\frac{R+C_1}{\frac{\omega^2}{16}+C_1^2}f(|q|),$$

$$f(|q|)=\frac{J_{1/2}\left(\frac{\pi|q|}{a}\right)}{\frac{\pi}{a}|q|(|q|^2-a^2)},$$

$$C_1=-E_2+\frac{3\omega}{4}+\frac{M}{2}-\frac{1}{\sqrt{6}}q_0-\frac{1}{\sqrt{2}}p_0,$$

$$C_2=-E_3+\frac{3\omega}{4}+\frac{M}{3}-\frac{1}{\sqrt{6}}q_0+\frac{1}{\sqrt{2}}p_0,$$

$$a=\frac{\sqrt{\pi}}{2},\quad m=0.1,\quad E_1=\sqrt{\frac{2}{3}a^2+m^2},$$

$$E_2=E_3=\sqrt{\frac{a^2}{6}+m^2},\ \omega=E_1+E_2+E_3-M,$$

$$R=\frac{2\pi}{\omega}. \tag{2.10}$$

Next we turn to the spin part. In the non-relativistic SU(6) model the baryon has the wave function

$$|B>=\varphi_S^{SU(3)}\chi_S^{SU(2)}+\varphi_A^{SU(3)}\chi_A^{SU(2)}, \tag{2.11}$$

where ψ_S, ψ_A are the symmetric/antisymmetric combinations of the SU(3) part and χ_S, χ_a are the appropriate spin part:

$$\begin{aligned}
\varphi_S&=\frac{1}{\sqrt{6}}(2ppn-pnp-npp),\\
\varphi_A&=\frac{1}{\sqrt{2}}(pnp-npp),\\
\chi_S&=\frac{1}{\sqrt{6}}(2\alpha\alpha\beta-\alpha\beta\alpha-\beta\alpha\alpha)=\frac{1}{\sqrt{6}}(2\uparrow\uparrow\downarrow-\uparrow\downarrow\uparrow-\downarrow\uparrow\uparrow),\\
\chi_A&=\frac{1}{\sqrt{2}}(\alpha\beta\alpha-\beta\alpha\alpha)\qquad\quad=\frac{1}{\sqrt{2}}(\uparrow\downarrow\uparrow-\downarrow\uparrow\uparrow),
\end{aligned} \tag{2.12}$$

where p, n are the proton and neutron quarks, α and β are the spin up and down functions.

In our case the only difference is (in the CM frame) that instead of the static spinors, Dirac spinors are used with the appropriate momentum variables e.g. (for instance χ_A has the following form):

$$\chi_A = \frac{1}{\sqrt{2}} \left[U_\uparrow(p_1)\, U_\downarrow(p_2)\, U_\uparrow(p_3) - \tfrac{1}{2} U_\downarrow(p_1)\, U_\uparrow(p_2)\, U_\uparrow(p_3) \right]. \tag{2.13}$$

The wave function in an arbitrary system can be obtained by a Lorentz transformation Λ, which satisfies the equations:

$$\begin{aligned} \Lambda P &= P', \\ \Lambda P_i &= P_i'. \end{aligned} \tag{2.14}$$

Due to alignment (i.e. quark-diquark structure) in CM, no Wigner rotation appears in (2.13).

3. Calculation of the form factors

As it was mentioned in the Introduction, the physical picture of current-hadron interaction is that the current interacts with one of the quarks, and the other two interact between themselves to get rearranged into quark-diquark formation.

The kinematics is given according to Fig. 1

$$\begin{aligned} P &= (M, 0, 0, 0), \\ Q &= \left(-t/2M, 0, 0 - \frac{1}{2M} \sqrt{t(t + 4M^2)}, \right. \\ P' &= P - Q, \qquad t = Q^2. \end{aligned} \tag{3.1}$$

The incoming hadron is characterised by the set P, q, η, the outgoing one by P', q', η' according to Eqs. (2.9). If the first quark is hit by the current, in the

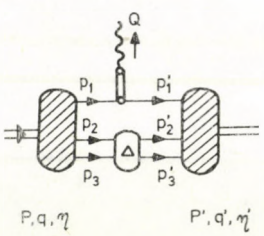

Fig. 1

configuration space one has to evaluate the integral

$$\begin{aligned}\langle \mathbf{P} \mid J_\mu(Z) \mid \mathbf{P}' \rangle_1 = \int \prod_{i=0}^{3} d^4 x_i \, d^4 x_i \, \overline{\Psi}_{\alpha\beta\gamma}(P, x_i) \, \Psi_{\alpha'\beta'\gamma'}(P', x_i') \times \\ \times e_1 [\gamma_\mu]_{\alpha\alpha'} \, \delta^4(z - x_1) \, \delta^4(x_1 - x_1') \times \\ \times \Delta_{\beta\gamma,\beta'\gamma'}(x_2, x_3, x_2', x_3') \, \delta^4(x_2 + x_3 - x_2' - x_3') \,,\end{aligned} \tag{3.2}$$

where e_1 is the charge of the first quark, and $\Delta_{\beta\gamma,\beta'\gamma'}(x_2, x_3, x_2', x_3')$ takes care of the quark interaction. Inserting (2.1) into (3.2) and using Eq. (2.7) we get

$$\begin{aligned}\langle \mathbf{P} \mid J_\mu(Z) \mid \mathbf{P}' \rangle_1 = e^{-iQZ} \int d^4 q \, d\eta \, d\eta' \, \overline{\Psi}_{\alpha\beta\gamma}(q, \eta) \, c_1 [\gamma\mu]_{\alpha\alpha'} \Psi_{\alpha'\beta'\gamma'} \left(q + \sqrt{\frac{2}{3}} Q, \eta' \right) \times \\ \times \Delta_{\beta\gamma,\beta'\gamma'}(\eta P - \eta' P') \,,\end{aligned} \tag{3.3}$$

with $\Psi(q, \eta)$ given by Eqs. (2.7). We have to sum (3.3) for all three configurations. It is not difficult to see that

$$\langle \mathbf{P}\uparrow \mid J_0(t) \mid \mathbf{P}'\uparrow \rangle = \sqrt{\frac{1}{2}(t + 4M^2)} \, G_E(t) \,, \tag{3.4a}$$

$$\langle \mathbf{P}\uparrow \mid J_1(t) \mid \mathbf{P}'\downarrow \rangle = -\sqrt{\frac{t}{2}} G_M(t) \,, \tag{3.4b}$$

where G_E and G_M are the electromagnetic form factors.

Next we have to fix $\Delta(\eta P - \eta' P')$. The first natural guess would be

$$\Delta(\eta P - \eta' P') = \delta^4(\eta P - \eta' P') \,, \tag{3.5a}$$

i.e. that the non-hit quarks propagate freely. However, it is easy to see that it leads to $P = P'$ which is nonsense. So we have to allow meson exchanges, e.g.

$$\Delta_{\beta\gamma,\beta'\gamma'}(\eta P - \eta' P') = \frac{\delta_{\beta\beta'} \delta_{\gamma\gamma'}}{[\eta P - \eta' P']^2 + i\epsilon} \tag{3.5b}$$

for scalar meson exchange. Mass term could have been allowed in the denominator. This propagator has a pole in the variable t, its imaginary part is just $\delta[(\eta P - \eta' P')^2]$. Using Eqs. (3.4) we are going to calculate the imaginary part of G_E, G_M and the form factors will be recovered by using the dispersion

$$G_{E,M} = \frac{1}{\pi} \int \frac{Im G(t')}{t' - t_0} \, dt. \tag{3.6}$$

Here this is just a mathematical trick, it has nothing to do with the analytical properties of the form factors.

Strictly speaking, Eq. (3.3) is valid only if the current hits the single quark, and the diquarks rearrange among themselves. However, it can be pro-

ven that quark-diquark rearrangement (i.e. when the single quark becomes a member of the diquark system after the interaction) is very much suppressed.

The current (3.3) is not conserved as it stands. This can be remedied in the same way as in [5] for the meson current in this model. However, the space part of the wave-function, (2.10) $f(|q|)$ can be approximated by $\delta(q^2 - a^2)$. As can be calculated, in this approximation the current is conserved. This approximation considerably simplifies the calculation, so we use it in this paper.

It is fairly easy to obtain the high t behaviour of (3.3) A t^{-1} factor comes from the propagator (3.5), and another t^{-1} from the space part of the wave function of the outgoing baryon. At first sight the spin part of the outgoing baryons contributes with $\sqrt{t^3}$ as in the kinematical configuration (3.1) each spinor carries $\sqrt{t}$, however, for those two which are coupled to a scalar, this $\sqrt{t^2}$ cancels out, and the net behaviour of the spin part is $\sqrt{t}$. Comparing this to (3.4), we obtain

$$G_E(t) \sim G_M(t) \sim t^{-2} \quad \text{for high } t.$$

This behaviour is confirmed by experiments.

We have started this Chapter with the physical picture of the current-hadron interaction. However, it is quite conceivable that the current interacts via vector-meson dominated term too, as in Fig. 2, and not only the direct term of Fig. 1 is allowed. In the framework of the geometrodynamics, the meson wave function appearing here depends on the variable $Q(p_1 - p_1')$ fixed to a number due to the δ-functions in the wave functions. Thus the t-dependence will not be altered by adding this type of contributions.

The overall normalisation is fixed at $t = 0$ by the requirement of the re-establishment of the total charge which is the sum of quark charges. If the quark masses were not equal, to recover the quark charge additivity would be quite a problem.

The rest of the paper is a numerical calculation. It is fairly tiresome because the integrand is oscillating, and most of the multidimensional integration procedures fail. We have succeeded at last with the routine DIVONNE (D105 in CERNLIB) performing a multidimensional Monte-Carlo integration with intervallum adjustment.

Let alone the propagator (3.5), we tried a pseudoscalar propagator too but that yielded funny small-t behaviour. We have not tried a vector-meson nominator due to technical (i.e. numerical) complication. However, we consider (3.5) as some "effective propagator" for several types of meson exchanges.

The results for the proton in the low-energy region are presented in Table I and Figs. 3, 4. As can be seen, they fall faster than the experimental data.

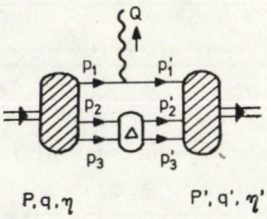

Fig. 2

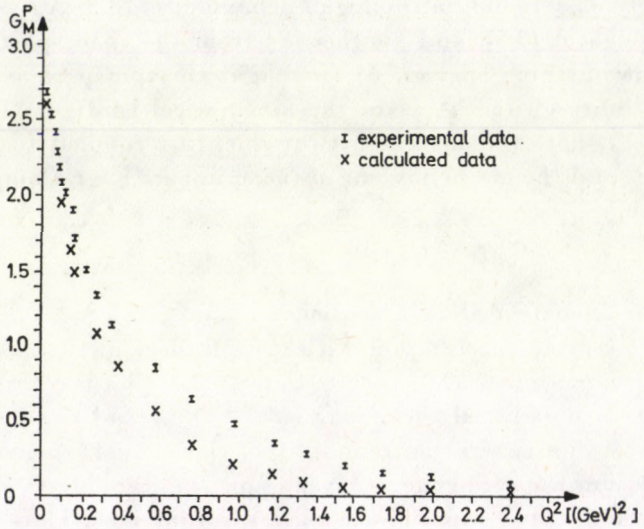

Fig. 3

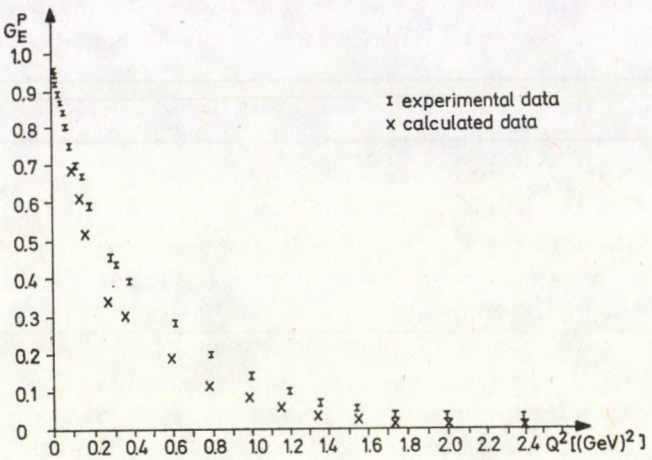

Fig. 4

Table I

Q^2 [GeV]^2	G_E^p	G_M^p
0.017	0.94	2.60
0.120	0.69	1.95
0.146	0.62	1.64
0.195	0.52	1.51
0.311	0.34	1.08
0.393	0.31	0.92
0.584	0.20	0.59
0.780	0.12	0.34
0.990	0.11	0.25
1.170	0.08	0.20
1.360	0.05	0.16
1.560	0.025	0.11
1.750	0.014	0 09
2.00	0.010	0.06
2.40	0.008	0.02

A similar calculation can be repeated also for the neutron. Roughly it is true that

$$G_M^{(n)} = -2/3\, G_M^{(p)},$$

the factor between them varies with q^2. $G_E^{(n)}(q^2)$ is rather flat as a function of q^2, (the high q^2 behaviour is the same) but in the small-q region ($0.1 < q^2 < 0.4$) its value is too big to be accepted.

In our view this shows that the model using the kernel (3.5b) reproduces the gross features, but further improvement would be necessary to get fine details. However, due to enormous technical difficulties, we do not think it possible and feasible.

The authors are indebted to Prof. G. PREPARATA for useful discussions.

REFERENCES

1. G. PREPARATA, Nucl. Phys. **B122**, 29, 1977.
G. PREPARATA and U. S. CRAIGE, Nucl. Phys. **B102**, 478—496, 1976.
2. G. PREPARATA, CERN-TH. 2271.
3. G. PREPARATA and K. SZEGŐ, Phys. Lett., **68B**, 239, 1977.
4. G. PREPARATA and K. SZEGŐ, Nuovo Cim., **47A**, 303, 1978.
5. F. CSIKOR and G. PREPARATA, CERN-TH. 2396.
6. G. R. FARRAR and D. R. JACKSON, Phys. Rev. Lett., **43**, 246, 1979.
7. G. P. LEPAGE and S. J. BRODSKY, Phys. Rev. Lett., **43**, 545, 1979.
8. G. HÖHLER et al., Nucl. Phys., **B114**, 505, 1976.

Acta Physica Academiae Scientiarum Hungaricae, 52 (2), pp. 221—235 (1982)

MODIFICATION OF THE MHD EQUATIONS TO REDUCE NUMERICAL INSTABILITY IN THE SIMULATION OF SLOW PLASMA MOTIONS*

G. ADLER

ADLER MATHEMATICAL LTD.
CALGARY, ALBERTA, CANADA**

(Received 29. XI. 1981)

The stability of explicit finite difference numerical schemes for the solution of equations admitting wave solutions is always limited by a stability condition of the type

$$\frac{\Delta t}{\Delta x} < \frac{\text{constant}}{v},$$

where Δt and Δx are the time- and space steps of the scheme, respectively, and v is the phase velocity of the wave. In certain cases we are interested in slow, non-ondulatory motions described by the equations, while the fast waves superposed on this motion play no essential role and do not influence the slow phenomenon at all, but make the numerical simulation of it quite impossible.

A typical case of the above mentioned situation is that of the tearing mode in Tokamak plasmas, where the Alfvén waves have no essential influence but they take place on a much faster time scale than the tearing mode itself. In order to make the numerical simulation of these slow motions (with realistic parameters) possible, we propose two modifications of the MHD equations. One of them is based on the idea of an artificial "electromagnetic viscosity", the other is obtained by purely algebraic considerations.

The effect of these modifications is a drastic reduction of the phase velocity of the wave solutions without any substantial influence on the slow motion itself.

Introduction

In the following we shall consider the problem of the tearing mode in a Tokamak, which gave rise to the research presented here.

For the tearing mode instability in a Tokamak there are two underlying time scales: the diffusive (also called resistive) time scale $\tau_{\text{res}} = L^2/\eta$ and the magnetohydrodynamic time scale $\tau_{\text{MHD}} = L/(A^2 + a^2)^{1/2}$, where L is the characteristic length in the Tokamak, η is the resistivity of the plasma, A is the Alfvén speed in the plasma (speed of the transverse wave), a is the sound speed in the plasma (in the absence of magnetic field) and $(A^2 + a^2)^{1/2}$ is the speed of the fast MHD wave.

In Tokamak plasmas for the ratio $S = \tau_{\text{res}}/\tau_{\text{MHD}}$ a value as high as $S = 10^8$ is also realistic.

* This work has been prepared in the Laboratory of Ionized Gases of the Italian National Committee for Nuclear Energy (CNEN) in Frascati in 1980 while the author was a consultant to this Laboratory. See references [1] and [2].

** Postal address: #83—1190, Ranchview Rd. N. W. Calgary, Alberta, Canada T3G 1Y2

The waves superposed on the tearing mode can be considered as smal perturbations unimportant from the point of view of the resistive-diffusive phenomenon. Nevertheless, the basic difficulty in the numerical simulation of the tearing mode is caused by the fact that the stability of the explicit numerical schemes for the solution of any differential equations admitting a wave solution with phase velocity v is limited by the condition

$$\frac{\Delta t}{\Delta x} < \frac{\text{constant}}{v},$$

where the value of the constant is usually less than 1. (In some simple cases it is exactly 1.) In the case of the tearing mode this means that a Δt satisfying the stability condition above would be prohibitively small, considering the speed of today's computers. Hence in the numerical simulation of the tearing mode only such physical parameters have been used for which the value of S is essentially smaller than 10^8 (see [3], [4], [5]). (One model eliminates wave solutions altogether by eliminating the terms of inertia from the MHD equations (see [5]), but this method seems to be useful under very restricted circumstances only.)

Our approach to solve the numerical stability problem is completely different and consists in modifying the MHD equations themselves by the addition of such terms which drastically reduce the speed of the otherwise unimportant wave solutions without essentially changing the diffusion process described by the equations. It is important that the effects of the modifying terms can be quantitatively evaluated on the basis of the characteristic time scales alone.

We propose two modifications. One is based on ideas having a "physical" background, the other is based on purely algebraic considerations. In the first case we construct a force term for the MHD equations with the help of the electromagnetic field variables only without involving the kinetic velocity, in order to avoid interfering with the original viscosity properties of the plasma. In particular, if the plasma is non-viscous, the inclusion of the new electromagnetic viscosity does not need the modification of the boundary conditions for the kinetic velocity. In the second case we start by modifying the dispersion relation which defines the phase velocities of the wave solutions, and we work backwards to find the corresponding modifications of the differential equations themselves.

We shall consider the following equations of a compressible plasma:

$$\frac{\partial B}{\partial t} = \eta \Delta B - \operatorname{curl} E, \tag{1}$$

$$\frac{\partial(\varrho V)}{\partial t} + \operatorname{div}(\varrho V V) = \frac{1}{\mu} J \times B - \operatorname{grad} p + \frac{\varkappa}{\mu} \Phi, \tag{2}$$

$$\frac{\partial \varrho}{\partial t} + \operatorname{div}(\varrho V) = 0\,, \tag{3}$$

$$\varrho = \frac{1}{a^2} p\,, \quad J = \operatorname{curl} B\,, \quad E = -V \times B\,. \tag{4}$$

The case of an incompressible plasma is included by assuming ϱ = constant in (2) and (3). The viscosity term Φ will only be used in the first approach and will be dropped in the second one. This system admits two types of infinitesimal wave solutions: transverse (Alfvén) and longitudinal (magneto-acoustic) waves (see [6]). We shall discuss separately the two cases.

1. Modification of the MHD equations by an "electromagnetic viscosity" term

The viscosity term will be defined as

$$\Phi = \Delta E \times B - J \times \operatorname{curl} E \equiv \frac{\partial}{\partial t}(J \times B)\,.$$

In order to see the effects of this force on the wave phenomena, let us study the infinitesimal magnetohydrodynamic waves in the case of zero resistivity: $\eta = 0$. We shall denote by a superscript 0 the unperturbed values. Let us take as unperturbed state

$$B^0 = (B_x^0, B_y^0, 0)\,,$$
$$V^0 = (0, 0, 0)\,,$$

and consider the infinitesimally perturbed state

$$B = B^0 + (b_x, b_y, 0)\,,$$
$$V = (v_x, v_y, 0)\,,$$
$$\varrho = \varrho^0 + \varrho'\,.$$

The linearized equations of these waves can be written in the following way (see [6]), by assuming a space dependence on the x-coordinate only:

$$\frac{\partial b_x}{\partial t} = 0\,, \tag{1x}$$

$$\frac{\partial b_y}{\partial t} = B_x^0 \frac{\partial v_y}{\partial x} - B_y^0 \frac{\partial v_x}{\partial x}\,, \tag{1y}$$

$$\varrho^0 \frac{\partial v_x}{\partial t} = - a^2 \frac{\partial \varrho'}{\partial x} - \frac{1}{\mu} B_y^0 \frac{\partial b_y}{\partial x} + \frac{1}{\mu} \varkappa \Phi_x , \tag{2x}$$

$$\varrho^0 \frac{\partial v_y}{\partial t} = \frac{1}{\mu} B_x^0 \frac{\partial b_y}{\partial x} + \frac{1}{\mu} \varkappa \Phi_y , \tag{2y}$$

$$\frac{\partial \varrho'}{\partial t} = - \varrho^0 \frac{\partial v_x}{\partial x} . \tag{3'}$$

Here the linearized form of the viscosity is the following:

$$\Phi = \frac{\partial}{\partial t} (\mathrm{curl}\, b) \times B^0 = \frac{\partial}{\partial t} \left(- B_y^0 \frac{\partial b_y}{\partial x} , B_x^0 \frac{\partial b_y}{\partial x} , 0 \right) =$$

$$= \left(- B_y^0 \frac{\partial b_y}{\partial x \partial t} , B_x^0 \frac{\partial b_y}{\partial x \partial t} , 0 \right) \equiv (\Phi_x, \Phi_y, 0) .$$

We shall discuss separately the cases of transverse and longitudinal (magnetoacoustic) waves. In all cases we have from Eq. (1x): $b_x = 0$.

Transverse waves

The transverse waves are defined by

$$B_y^0 = 0 ,$$
$$v_x = 0 .$$

Then we have $\varrho' = 0$, and the system of equations is reduced to

$$\frac{\partial b_y}{\partial t} = B_x^0 \frac{\partial v_y}{\partial x} ,$$

$$\varrho^0 \frac{\partial v_y}{\partial t} = \frac{1}{\mu} B_x^0 \frac{\partial b_y}{\partial x} + \frac{\varkappa}{\mu} B_x^0 \frac{\partial^2 b_y}{\partial x \partial t} .$$

By substituting here a harmonic wave solution of the form

$$b_y = \hat{b}_y e^{i(kx - \omega t)} ,$$
$$v_y = \hat{v}_y e^{i(kx - \omega t)} ,$$

we get the following dispersion relation when the determinant of the system for $\hat{b}_y$ and $\hat{v}_y$ is set equal to zero:

$$\begin{vmatrix} \omega & B_x^0 k \\ B_x^0 \left(\frac{k}{\mu} - i \frac{\varkappa}{\mu} \omega k \right) & \omega \varrho^0 \end{vmatrix} = 0 .$$

Hence we have

$$\omega = \frac{1}{2}\left(-\varkappa A^2 k^2 i \pm \sqrt{4A^2k^2 - \varkappa^2 A^4 k^4}\right),$$

where

$$A = \frac{B_x^0}{\sqrt{\mu \varrho^0}}$$

is the Alfvén speed in absence of viscosity. The wave solution will have the form:

$$b_y = \hat{b}_y e^{-\frac{1}{2}\varkappa A^2 k^2 t} e^{i(kx \mp \tilde{\omega} t)},$$

$$\tilde{\omega} = k\sqrt{A^2 - \frac{1}{4}\varkappa^2 A^4 k^2},$$

i.e., the original phase velocity A will be decreased to

$$A_\varkappa = A\sqrt{1 - \frac{1}{4}\varkappa A^2 k^2},$$

and the amplitude of the wave will be damped as

$$e^{-\frac{1}{2}\varkappa A^2 k^2 t}.$$

As one can expect, the phase velocity of the shorter waves will be slowed pown stronger and their amplitude damped faster.

Longitudinal waves

We have to distinguish two types of longitudinal waves, characterized by

1) $B_y^0 = 0$, $b_y = 0$,
$v_y = 0$;

2) $B_x^0 = 0$, $b_x = 0$,
$v_y = 0$.

In case 1) we have

$$\frac{\partial \varrho'}{\partial t} = -\varrho^0 \frac{\partial v_x}{\partial x},$$

$$\varrho^0 \frac{\partial v_x}{\partial t} = -a^2 \frac{\partial \varrho'}{\partial x}.$$

This is the case of a pure sound wave not involving the electromagnetic field and having the speed a. (The viscous force Φ has no effect on this wave, as expected).

In case 2) the system of equations is reduced to

$$\frac{\partial b_y}{\partial t} = - B_y^0 \frac{\partial v_x}{\partial x},$$

$$\frac{\partial \varrho'}{\partial t} = - \varrho^0 \frac{\partial v_x}{\partial x},$$

$$\varrho^0 \frac{\partial v_x}{\partial t} = - a^2 \frac{\partial \varrho'}{\partial x} - \frac{1}{\mu} B_y^0 \frac{\partial b_y}{\partial x} + \frac{\varkappa}{\mu} B_y^0 \frac{\partial^2 b_y}{\partial x \, \partial t}.$$

For a harmonic wave solution

$$b_y = \hat{b}_y \, e^{i(kx - \omega t)},$$

$$v_x = \hat{v}_x \, e^{i(kx - \omega t)},$$

$$\varrho' = \hat{\varrho} \; e^{i(kx - \omega t)}$$

we find the dispersion relation

$$\begin{vmatrix} -i\omega & iB_y^0 k & 0 \\ 0 & i\varrho^0 k & -i\omega \\ \frac{1}{\mu} B_y^0 (ik - \varkappa k \omega) & -i\varrho^0 \omega & ia^2 k \end{vmatrix} = 0 .$$

Hence we have:

$$\omega = \frac{1}{2} \left(\varkappa A^2 k^2 i \pm \sqrt{4 (A^2 + a^2) k^2 - \varkappa^2 A^4 k^4} \right),$$

and for the magnetic field

$$b_y = \hat{b}_y \, e^{-\frac{1}{2} \varkappa A^2 k^2 t} \cdot e^{i(kx \mp \tilde{\omega} t)}$$

$$\tilde{\omega} = k \sqrt{A^2 + a^2 - \frac{1}{4} \varkappa^2 A^4 k^2}.$$

The phase velocity will be the following:

$$A_\varkappa = \sqrt{A^2 + a^2} \sqrt{1 - \frac{1}{4} \varkappa \frac{A^4}{A^2 + a^2} k^2} .$$

The amplitude will decay again exponentially. This result is in complete analogy with the result obtained for the transverse wave.

While, on one hand, the result has the disadvantage that it depends on the wave number k (our second method discussed in the next point will be free of this feature), on the other hand it has the advantage that the position of k in the formulae assures an increasing stabilizing effect for increasing k, exactly where the stability of the numerical schemes is deteriorating.

The order of magnitude of the viscous perturbation

The resistive tearing mode (for $\eta \neq 0$) develops on the resistive time scale

$$\tau_{\text{res}} = \frac{L^2}{\eta}, \quad (L = \text{characteristic length}).$$

The relative order of magnitude of the viscosity term with respect to the Lorentz force on this resistive time scale is

$$\frac{\varkappa}{\tau_{\text{res}}}.$$

By writing $\varkappa = h\tau_{\text{MHD}}$, where τ_{MHD} is the magnetohydrodynamic time scale defined by

$$\tau_{\text{MHD}} = \frac{L}{\sqrt{A^2 + a^2}},$$

the relative error will be

$$h\frac{\tau_{\text{MHD}}}{\tau_{\text{res}}}.$$

2. Modification of the MHD equations by algebraically constructed terms

As in the previous case, let us denote by a superscript 0 values corresponding to the unperturbed state of the plasma. The unperturbed velocity is zero: $V^0 = 0$. We shall denote the perturbation of the magnetic field, velocity and density by $b = (b_x, b_y, b_z)$, $v = (v_x, v_y, v_z)$ and ϱ', respectively, i.e. the perturbed state will be

$$B = B^0 + b,$$

$$V = V^0 + v = v,$$

$$\varrho = \varrho^0 + \varrho'.$$

a) Transverse waves

In the case of transverse waves the pressure (and consequently the density as well) is constant, hence the plasma can be considered incompressible. (In an incompressible plasma the transverse waves are the only possible waves). We take the direction of the x-axis in the direction of the uniform magnetic field, i.e. we take $B^0 = (B_x^0, 0, 0)$. Then the wave propagates in the x-direction. Let us further assume that the field oscillates in the y-direction. Then the system of equations is reduced (for infinitesimal waves) to the following equations (see [6]):

$$\frac{\partial b_y}{\partial t} = B_x^0 \frac{\partial v_y}{\partial x} , \tag{1'}$$

$$\varrho^0 \frac{\partial v_y}{\partial t} = B_x^0 \frac{\partial b_y}{\partial x} . \tag{2'}$$

For simplicity let us write this system in the form

$$\frac{\partial u}{\partial t} = P \frac{\partial v}{\partial x} , \tag{5}$$

$$\frac{\partial v}{\partial t} = Q \frac{\partial u}{\partial x} . \tag{6}$$

In order to determine the dispersion relation for the solutions of this system, we substitute a harmonic wave solution

$$u = \hat{u}\, e^{i(kx-\omega t)} ,$$

$$v = \hat{v}\, e^{i(kx-\omega t)}$$

into these equations, and then we have

$$\begin{vmatrix} \omega & Pk \\ Qk & \omega \end{vmatrix} = 0 .$$

Hence $\omega^2 = PQk^2$, and the phase velocity is

$$\xi = \frac{\omega}{k} = \pm A, \qquad A = \sqrt{PQ}.$$

Our idea for reducing the value of $|\xi|$ is to insert further terms, consisting of ω or k or both, in the determinant. Our choice is the (simplest possible) modified form

$$\begin{vmatrix} \omega & P(k-\alpha\omega) \\ Q(k-\beta\omega) & \omega \end{vmatrix} = 0 .$$

This characteristic equation corresponds to the modified system

$$\frac{\partial u}{\partial t} = P\left(\frac{\partial v}{\partial x} + \alpha \frac{\partial v}{\partial t}\right), \tag{7}$$

$$\frac{\partial v}{\partial t} = Q\left(\frac{\partial u}{\partial x} + \beta \frac{\partial u}{\partial t}\right). \tag{8}$$

The corresponding phase velocity ξ is defined by the equation

$$(1 - \alpha\beta A^2)\,\xi^2 + (\alpha + \beta)\,A^2\,\xi - A^2 = 0.$$

Let us use the following values for α and β:

$$\alpha = -\beta = \frac{h}{A}.$$

Then

$$\xi = \pm \frac{A}{\sqrt{1 + h^2}}. \tag{9}$$

The new phase velocity (for high values of h) is approximately h times smaller than the phase velocity of the original solution. It is also important that the new velocity does not depend on the wave number k.

b) Longitudinal waves

In longitudinal waves the magnetic field component parallel to the direction of propagation does not play any role, hence we can assume that the field is perpendicular to the direction of propagation. We take the direction of the x-axis in the direction of the wave propagation and assume the unperturbed field as $B^0 = (0, B_y^0, 0)$. Then the wave is described by the equations (see [6])

$$\frac{\partial b_y}{\partial t} = -B_y^0 \frac{\partial v_x}{\partial x}. \tag{1''}$$

$$\varrho^0 \frac{\partial v_x}{\partial t} = -B_y^0 \frac{\partial b_y}{\partial x} - a^2 \frac{\partial \varrho'}{\partial x}, \tag{2''}$$

$$\frac{\partial \varrho'}{\partial t} = -\varrho^0 \frac{\partial v_x}{\partial x}. \tag{3''}$$

We write this system in the form

$$\frac{\partial u}{\partial t} = -P \frac{\partial v}{\partial x},$$

$$\frac{\partial v}{\partial t} = -Q \frac{\partial u}{\partial x} - R \frac{\partial w}{\partial x},$$

$$\frac{\partial w}{\partial t} = -S \frac{\partial v}{\partial x}.$$

The characteristic equation of this system is

$$\begin{vmatrix} \omega & -Pk & 0 \\ -Qk & \omega & -Rk \\ 0 & -Sk & \omega \end{vmatrix} = 0 .$$

We modify this equation in the following way:

$$\begin{vmatrix} \omega & -P(k-\alpha\omega) & 0 \\ -Q(k-\beta\omega) & \omega & -R(k-\gamma\omega) \\ 0 & -S(k-\delta\omega) & \omega \end{vmatrix} = 0 . \tag{10}$$

The corresponding system of differential equations is the following:

$$\frac{\partial u}{\partial t} = -P\left(\frac{\partial v}{\partial x} + \alpha\frac{\partial v}{\partial t}\right), \tag{11}$$

$$\frac{\partial v}{\partial t} = -Q\left(\frac{\partial u}{\partial x} + \beta\frac{\partial u}{\partial t}\right) - R\left(\frac{\partial w}{\partial x} + \gamma\frac{\partial w}{\partial t}\right), \tag{12}$$

$$\frac{\partial w}{\partial t} = -S\left(\frac{\partial v}{\partial x} + \delta\frac{\partial v}{\partial t}\right). \tag{13}$$

One root of Eq. (10) for $\xi = \frac{\omega}{k}$ is $\xi = 0$. The other two roots satisfy the equation

$$(1 - \alpha\beta PQ - \gamma\delta RS)\,\xi^2 + [(\alpha+\beta)PQ + (\gamma+\delta)RS]\,\xi - (PQ + RS) = 0 .$$

By selecting the values

$$\alpha = -\beta = \frac{h}{A} \qquad A = \sqrt{PQ},$$

$$\gamma = -\delta = \frac{l}{a} \qquad a = \sqrt{RS},$$

we find for the modified new phase velocity

$$\xi = \pm\frac{\sqrt{A^2 + a^2}}{\sqrt{1 + h^2 + l^2}} .$$

Similarly, the values

$$\alpha = -\beta = \gamma = -\delta = \frac{h}{\sqrt{A^2 + a^2}}$$

give

$$\xi = \pm \frac{\sqrt{A^2 + a^2}}{\sqrt{1 + h^2}}. \tag{14}$$

(Here A and a correspond to the Alfvén speed and the sound speed, respectively, while $\sqrt{A^2 + a^2}$ is the fast Alfvén speed).

Modification of the original MHD equations

The previous modifications for the infinitesimal waves have to be synthetized for the original system (1) + (2) + (3). The form of the modifications to be performed on this system, in order to get the systems (7) + (8) and (11) + (12) + (13) for the infinitesimal waves, is not uniquely defined. We shall present here one (probably the simplest possible) choice.

The modified systems (7) + (8) and (11) + (12) + (13) written in the original field variables are the following:

transverse waves:

$$\frac{\partial b_y}{\partial t} = B_x^0 \left(\frac{\partial}{\partial x} + \alpha \frac{\partial}{\partial t} \right) v_y ,$$

$$\varrho^0 \frac{\partial v_y}{\partial t} = B_x^0 \left(\frac{\partial}{\partial x} + \beta \frac{\partial}{\partial t} \right) b_y ;$$

longitudinal waves:

$$\frac{\partial b_y}{\partial t} = - B_y^0 \left(\frac{\partial}{\partial x} + \alpha \frac{\partial}{\partial t} \right) v_x ,$$

$$\varrho^0 \frac{\partial v_x}{\partial t} = - B_y^0 \left(\frac{\partial}{\partial x} + \beta \frac{\partial}{\partial t} \right) b_y - a^2 \left(\frac{\partial}{\partial x} + \gamma \frac{\partial}{\partial t} \right) \varrho' ,$$

$$\frac{\partial \varrho'}{\partial t} = - \varrho^0 \left(\frac{\partial}{\partial x} + \delta \frac{\partial}{\partial t} \right) v_x .$$

Comparing these equations term by term with the corresponding unmodified ones, we conclude the following:

α) in the terms deriving from curl $(V \times B)$ (where B is the unperturbed field $B = B^0$) space derivatives of the velocity components $\partial v_q / \partial r$ $(q = x, y, z, r = x, y, z)$ are modified by the addition of time derivatives $\partial v_q / \partial t$;

β) in the terms resulting from $J \times B$ (where $B = B^0$ is again the unperturbed field, perturbations appearing in J only) space derivatives of the magnetic field components $\partial b_q / \partial r$ $(q = x, y, z, r = x, y, z)$ in J are modified by the addition of the time derivatives $\partial b_q / \partial t$;

γ) space derivative of ϱ in the longitudinal direction: $\partial\varrho/\partial x$ is modified by the addition of the time derivative $\partial\varrho/\partial t$; (space derivative of ϱ in the transverse direction does not appear in the equations);

δ) in the term deriving from div V (in the equation for ϱ') the space derivative $\partial v_x/\partial x$ of the longitudinal component of the velocity v_x is modified by the time derivative $\partial v_x/\partial t$ of the same component.

Now let us see how these modifications can be generalized for the case of three space variables.

ad α) In the term curl $(V\times B^0)$ the inclusion of the mentioned modifications leads to the form

$$\operatorname{curl}(V\times B^0)\to\begin{vmatrix} e_x & e_y & e_z \\ \frac{\partial}{\partial x}+\alpha\frac{\partial}{\partial t} & \frac{\partial}{\partial y}+\alpha\frac{\partial}{\partial t} & \frac{\partial}{\partial z}+\alpha\frac{\partial}{\partial t} \\ B_z^0V_y-B_y^0V_z & B_x^0V_z-B_z^0V_x & B_y^0V_x-B_x^0V_y \end{vmatrix}=$$

$$=\operatorname{curl}(V\times B^0)+\alpha\left(\hat{B}^0\frac{\partial V}{\partial t}-B^0\frac{\partial\hat{V}}{dt}\right),$$

where $\hat{U}=U_x+U_y+U_z$ for any vector $U=(U_x, U_y, U_z)$.

ad β) What we have said in point β) is tantamount as to substitute $J=\operatorname{curl}B$ by

$$\operatorname{curl}B\to\begin{vmatrix} e_x & e_y & e_z \\ \frac{\partial}{\partial x}+\beta\frac{\partial}{\partial t} & \frac{\partial}{\partial y}+\beta\frac{\partial}{\partial t} & \frac{\partial}{\partial z}+\beta\frac{\partial}{\partial t} \\ B_x & B_y & B_z \end{vmatrix}=$$

$$=\operatorname{curl}B+\beta I\times\frac{\partial B}{\partial t},$$

where

$$I=(1,1,1).$$

Hence the term modifying the Lorentz force $J\times B$ will be

$$\beta\left(I\times\frac{\partial B}{\partial t}\right)\times B.$$

ad γ) The term deriving from grad p will be modified as follows:

$$\operatorname{grad}p\to\operatorname{grad}p+\gamma\frac{\partial p}{\partial t}e_{\|},$$

where $e_{\|}$ is the unit vector in the direction of the field B.

ad δ) The term div V will be modified to

$$\operatorname{div} V \to \operatorname{div} V + \delta \frac{\partial V}{\partial t} e_{||} .$$

In final conclusion, we propose the following modified form of the MHD equations:

$$\frac{\partial B}{\partial t} = \eta \Delta B + \operatorname{curl}(V \times B) + \alpha \left(\hat{B} \frac{\partial V}{\partial t} - B \frac{\partial V}{\partial t} \right), \tag{15}$$

$$\frac{\partial(\varrho V)}{\partial t} + \operatorname{dir}(\varrho V V) = J \times B - \operatorname{grad} p + \beta \left(I \times \frac{\partial B}{\partial t} \right) \times B - \gamma \frac{\partial p}{\partial t} e_{||} , \tag{16}$$

$$\frac{\partial \varrho}{\partial t} + \operatorname{div}(\varrho V) = - \delta \varrho \frac{\partial V}{\partial t} e_{||} . \tag{17}$$

The effect of the modifications on the diffusive process

Let us denote by $\bar{V}$, $\bar{B}$, $\bar{J}$, $\bar{p}$ and $\bar{\varrho}$ the characteristic values of V, B, J, p and ϱ, respectively, in addition to the characteristic length L and characteristic times τ_{res}, τ_{MHD} already introduced. We shall estimate the relative order of magnitude of the modifying terms with respect to other terms originally present in the equations. For the coefficients α, β, γ and δ we take, in accordance with their values in the infinitesimal wave problems, the values

$$\alpha = - \beta = \gamma = - \delta = \frac{h}{\sqrt{A^2 + a^2}} ,$$

where

$$A = \frac{|B|}{\sqrt{\varrho \mu}} , \quad a = \sqrt{\frac{\partial p}{\partial \varrho}} .$$

(A and a are the local Alfvén and sound speeds). We have the following cases:
α) in Eq. (15) we weight

$$\alpha \left(\hat{B} \frac{\partial V}{\partial t} - B \frac{\partial \hat{V}}{\partial t} \right) \quad \text{against} \quad \operatorname{curl}(V \times B) .$$

Their orders of magnitude are:

$$\frac{h}{\sqrt{A^2 + a^2}} \frac{\bar{V} \cdot \bar{B}}{\tau_{\text{res}}} = h \frac{\tau_{\text{MHD}}}{\tau_{\text{res}}} \frac{\bar{V} \cdot \bar{B}}{L} \quad \text{against} \quad \frac{\bar{V} \cdot \bar{B}}{L} .$$

β) In Eq. (16) the term $\beta\left(I\times\frac{\partial B}{\partial t}\right)\times B$ will be compared to $J\times B$, their orders of magnitude being

$$\frac{h}{\sqrt{A^2+a^2}}\,\frac{\bar{B}^2}{\tau_{\rm res}}=h\,\frac{\tau_{\rm MHD}}{\tau_{\rm res}}\,\frac{\bar{B}^2}{L}\ \text{against}\ \bar{J}\cdot\bar{B}=\frac{\bar{B}^2}{L}\,.$$

In the same equation the magnitudes of the other two terms are

$$\frac{h}{\sqrt{A^2+a^2}}\,\frac{p}{\tau_{\rm res}}=h\,\frac{\tau_{\rm MHD}}{\tau_{\rm res}}\,\frac{\bar{p}}{L}\ \text{against}\ \frac{\bar{p}}{L}\,.$$

γ) Finally, in the last Eq. (17) we have

$$\frac{h}{\sqrt{A^2+a^2}}\,\frac{\bar{\varrho}\bar{V}}{\tau_{\rm res}}=h\,\frac{\tau_{\rm MHD}}{\tau_{\rm res}}\,\frac{\bar{\varrho}\bar{V}}{L}\ \text{against}\ \frac{\bar{\varrho}\bar{V}}{L}\,.$$

In all cases we find that the relative error introduced into the equations is of the order of magnitude

$$h\,\frac{\tau_{\rm MHD}}{\tau_{\rm res}}\,.$$

Hence, to keep the introduced perturbation small, h should satisfy the only condition

$$h\,\frac{\tau_{\rm MHD}}{\tau_{\rm res}}\ll 1\,.$$

In order to give an idea of the effects in practice, let us consider the case of an incompressible plasma with $S=\tau_{\rm res}/\tau_{\rm MHD}=10^8$. Accepting a relative error of 1%, we can take $h=10^6$. Then, according to formulae (9) and (14), the speed of the MHD waves will be reduced 10^6 times. Consequently, we can expect a similar reduction in the computer time required for the simulation of the tearing mode.

Acknowledgements

I wish to thank Dr. P. SOMON (C.N.E.N., Frascati) for the numerous discussions on the tearing mode problem.

REFERENCES

1. G. ADLER, An artificial electromagnetic "viscosity" for plasmas. Internal note, C.N.E.N. — EURATOM-CNEN, Frascati, 1980 (CM-80-10, Fusion).
2. G. ADLER, A method for reducing the speed of perturbing MHD waves in the tearing mode problem. Internal note, C.N.E.N. — EURATOM-CNEN, Frascati, 1980 (CM-80-9, Fusion).

3. D. SCHNACK and J. KILLEEN, Linear and Non-Linear Calculations of the Tearing Mode, IAEA-SMR-32/6.
4. H. R. HICKS, B. CARRERAS, J. A. HOLMES and B. V. WADDELL, Interaction of Tearing Modes of Different Pitch in Cylindrical Geometry, Oak Ridge National Laboratory, Fusion Energy Division, December 1977.
5. B. V. WADDELL, M. N. ROSENBLUTH, D. A. MONTICELLO, R. B. WHITE and B. CARRERAS, Non-Linear Numerical Algorithms for Studying Tearing Modes. Theoretical and Computational Plasma Physics, International Centre for Theoretical Physics, Trieste (IAEA, Vienna, 1978), pp. 79—91.
6. G. W. SUTTON and A. SHERMAN, Engineering Magnetohydrodynamics, McGraw-Hill, 1965, pp. 309—315.

Acta Physica Academiae Scientiarum Hungaricae, 52 (2), pp. 237—245 (1982)

NORMAL COORDINATE ANALYSIS OF THE TETRAFLUORO-1,3 DITHIETANE

A. NATARAJAN and S. SOMASUNDARAM

DEPARTMENT OF PHYSICS, MADRAS UNIVERSITY, AUTONOMOUS P. G. CENTRE
TIRUCHIRAPALLI 620 020, INDIA

(Received 10. XII. 1981)

A complete normal coordinate analysis has been performed for the tetra fluoro-1,3 dithietane which is planar belonging to D_{2h} point group. The symmetric. F, and the internal valence force constant, f, matrices were derived in general case by using a GVFF and the results were applied to $C_2S_2F_4$. In addition, mean amplitudes, generalised mean square amplitudes, the Coriolis coupling coefficients, the rotation distortion constants and the thermodynamic properties have also been evaluated.

Introduction

The infrared and Raman spectra of the tetrafluoro-1,3 dithietane molecule has been obtained first by DURIG and LORD [1] in vapour phase and the molecule was recognised to have a planar structure of type $X_2Y_2Z_4$ belonging to symmetry D_{2h}. ZUZANA SMITH [2] has made an electron diffraction study and verified the planarity of the molecule in the vapour phase and the dependence of the low frequency ring puckering motion on the relative magnitude of bond angle strain and torsional strain.

Recently, KLABOE et al [3] have reinvestigated the infrared and Raman spectra of this molecule in vapour phase. They have confirmed the results of DURIG and LORD [1] but made reassignments for four of the eighteen fundamentals. They have carried out the normal coordinate analysis on UBFF and determined the force constants.

The purpose of the present work is to perform a complete normal coordinate analysis of $C_2S_2F_4$ as sufficient infrared and Raman data are available and to evaluate all the molecular constants using GVFF.

The standard F-G matrix formalism of WILSON [4] was used to derive the symmetrical and internal valence force constants in GVFF.

Structure and internal valence coordinates

The geometry of the molecule is given in Fig. 1. The X and Y atoms form a four membered ring and Z atoms are at the terminals. All the atoms are in the YZ plane. The origin of Cartesian axes is the centre of gravity and also the

centre of the molecular model. The Z axis coincides with the principal axis of the molecule. In Fig. 1, the orientation of the Cartesian coordinates and all the valence coordinates are shown.

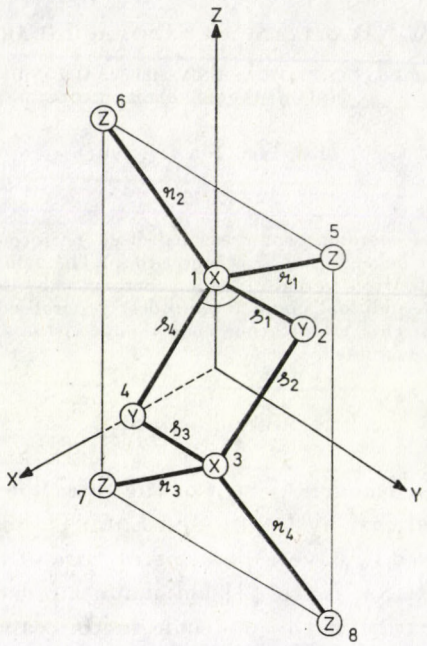

Fig. 1. The numbering of atoms, the internal coordinates and the orientation of Cartesian coordinate axes of $X_2Y_2Z_4$ molecule

The coordinates t and τ are in plane and out of plane ring deformation respectively defined by

$$t = \frac{R}{\sqrt{2}}(\alpha_1 + \alpha_2)$$

and

$$R\tau = X_1 - X_2 + X_3 - X_4 .$$

The structural parameters are taken from the electron diffraction data of ZUZANA SMITH et al [2]. The equilibrium bond lengths of C—F and C—S bonds are $R = 0.1344$ nm and S $= 0.1820$ nm, respectively. The angles are $F\hat{C}F = 106.5°$ and $S\hat{C}S = 97.3°$. According to the results obtained from the cited works [1—3] the frequencies have been adopted (Table I) to compute the force constants.

Symmetry valence coordinates

Group theoretical considerations show that the eighteen fundamental frequencies can be distributed among different species as

$$\Gamma_{\text{vib}} = 4a_g + 2b_{1g} + 2b_{2g} + 1b_{3g} + 1a_u + 3b_{1u} + 2b_{2u} + 3b_{3u}.$$

All gerade modes are infrared active and ungerade modes are Raman active. The a_u mode is inactive in both.

The eighteen independent symmetry coordinates without any redundancies were obtained by appropriate linear combinations of the internal coordinates. The bending symmetry coordinates were scaled with the factors of dimensions of length.

Force constant calculations

The symmetry force constant matrix F was computed from the observed frequencies which determine the matrix Λ_k where $\Lambda_k = \frac{4\pi^2 c^2}{N^2} \nu_k^2 = 0.058915 \times$ $\times 10^{-5} \nu_k^2$ and the G-matrix in the theory of GVFF.

A simple 30 parameter general valence force field was first assumed in terms of valence coordinates. The initial set of approximate force constant matrix was obtained by transforming the force constant values of C—F and C—S bonds in similar molecules. CYVIN's W matrix method [5] has been followed which gave a convenient practical computation of F matrix by means of a T matrix.

The CYVIN's method [5] employing W and T matrices introduces several non-vanishing off-diagonal elements in F. This enabled us to calculate many interaction constants. A refined force field was obtained by adjusting the force constants to reproduce the observed frequencies based on least square fit method. The calculated valence force constants are reported in Table II

Potential energy distribution

In order to describe completely and correctly the normal modes of vibrations, potential energy distribution (P. E. D.) has been computed.

The energy distribution has been computed using the formula [6—9]

$$\text{P. E. D.}: V_{ij}^k = F_{ij} L_{ik} L_{jk} / \lambda_k .$$

The computed energy distributions are presented in Table I. The results show that the diagonal values are predominant. According to the criterion of energy distributions, this confirms the choice of the symmetry coordinates representing the normal vibrations.

Table I

Observed and calculated frequencies (10^2 m^{-1}) and the potential energy (%) distribution of $C_2S_2F_4$ molecule

Species	Observed	Calculated	P.E.D.
a_g	1171	1171.89	$100\,S_1$
	670	670.66	$96.3S_2+2.3S_3+1.4S_4$
	518	517.97	$3.4S_2+92.1S_3+4.5S_4$
	330	330.67	$6.7S_2+3.1S_3+90.2S_4$
b_{1g}	840	839.15	$93.6S_5+6.4S_6$
	420	420.68	$2.6S_5+97.4S_6$
b_{2g}	1092	1091.99	$100S_7$
	378	377.82	$2.1S_7+97.9S_8$
b_{3g}	288	288.05	$100S_9$
a_u	255	254.98	$100S_{10}$
b_{1u}	1118	1117.28	$99.3S_{11}+0.7S_{12}$
	447	447.22	$5.9S_{11}+94.10S_{12}$
	59	58.77	$100S_{13}$
b_{2u}	966	966.00	$100S_{14}$
	323	322.99	$0.1S_{14}+99.9S_{15}$
b_{3u}	1080	1079.69	$93.7S_{16}+3.1S_{17}+3.2S_{18}$
	653	653.21	$7.1S_{16}+90.4S_{17}+2.5S_{18}$
	430	430.32	$2.3S_{16}+4.6S_{17}+92.1S_{18}$

Table II

Valence force constants (Nm^{-1}) of $C_2S_2F_4$ molecule

f_r	465.12	f_{rS}	40.00
f_S	336.95	f'_{rS}	−10.00
f_φ	104.65	f''_{rS}	1.50
f_{rr}	39.62	$f_{r\varphi}$	48.80
f'_{rr}	−47.26	$f'_{r\varphi}$	−5.18
f''_{rr}	−9.99	$f''_{r\varphi}$	24.40
f_{SS}	120.70	$f_{S\varphi}$	−25.10
f'_{SS}	−0.10	$f'_{S\varphi}$	15.03
f''_{SS}	−10.50	$f''_{S\varphi}$	−25.37
$f_{\varphi\varphi}$	65.34	$f_\alpha+f_{\alpha\alpha}$	98.00
$f'_{\varphi\varphi}$	2.18	$f_{S\alpha}+f'_{S\alpha}$	−43.13
$f''_{\varphi\varphi}$	−4.65	$f_{\alpha\varphi}+f'_{\alpha\varphi}$	−27.15
f_τ	45.00	$f_{S\tau}-f'_{S\tau}$	25.00

Mean amplitudes and generalised mean amplitudes of vibration

The mean square amplitude matrix Σ has been evaluated by CYVIN's [10] L matrix method. The Σ matrix elements have been used to compute the stretching, bending and interaction mean square amplitude quantities reported in Table III.

The generalised mean square amplitudes of vibration, both parallel and perpendicular, have been calculated following the method of MORINO and HIROTA [11].

The mean amplitudes of vibration u are of appreciable interest because they characterize the bonding and tightness of structures of the molecules. The mean amplitudes of vibration u for bonded and non-bonded distances for this molecule have been calculated at 300 K and presented in Table IV. The Table also contains experimental values obtained from electron diffraction data [2]. The mean amplitudes of C—S and C—F bonds in similar molecules are also given for comparison.

It is observed that the mean amplitudes of vibration for C—S and C—F bonds are quite characteristic as expected from the fact that the corresponding normal frequencies and force constants also are characteristic.

Coriolis coupling coefficients and centrifugal distortion constants

The Coriolis matrix elements C_{ij}^{α} were obtained by the vector method of MEAL and POLO [12] and the zeta matrix elements were evaluated from the relation,

$$\zeta^{\alpha} = L^{-1} C^{\alpha} (L')^{-1} .$$

Table III

Mean square amplitude quantities (10^{-2}nm^2) at 300 K of $C_2S_2F_4$ molecule

σ_r	0.002264	$\sigma''_{\varphi\varphi}$	0.002276
σ_s	0.002731	σ_{rs}	0.0006221
σ_{φ}	0.006973	σ'_{rs}	0.0002654
σ_{τ}	0.202171	σ''_{rs}	0.000442
σ_{rr}	−0.000138	$\sigma_{r\varphi}$	−0.000861
σ'_{rr}	0.000299	$\sigma'_{r\varphi}$	0.000130
σ''_{rr}	0.000188	$\sigma''_{r\varphi}$	−0.000630
σ_{ss}	−0.000272	$\sigma_{s\varphi}$	−0.000523
σ'_{ss}	0.000711	$\sigma'_{s\varphi}$	0.000611
σ''_{ss}	0,000193		
$\sigma_{\varphi\varphi}$	−0.002853	$\sigma_{\alpha}+\sigma_{\alpha\alpha}$	0.006732
$\sigma'_{\varphi\varphi}$	−0.002399		

Table IV

Mean amplitude of vibration (nm) at 300 K of $C_2S_2F_4$ molecule

	u (calc.)	u (E.D)	Ref.
u_{C-F}	0.00476	0.00490	[2]
u_{C-S}	0.00521	0.00500	[3]
$u_{C\cdots C}$	0.00591	0.00570	[3]
$u_{S\cdots S}$	0.00461	0.00460	[3]
$u_{S\cdots F}$	0.00660	0.00670	[3]
$u_{F_5\cdots F_8}$	0.00570	0.00530	[2]
$u_{F_5\cdots F_7}$	0.00810	0.00820	[2]
$u_{F_5\cdots F_6}$	0.01820	0.01810	[3]

Molecule	u_{C-F}	Ref.	Molecule	u_{C-S}	Ref.
CH_2FCl	0.00464	[17]	CS	0.00389	[17]
CH_2FBr	0.00463	[17]	CS_2	0.00387	[17]
CHFClBr	0.00464	[17]	CSSe	0.00389	[5]
CHF_3	0.00451	[17]	CSTe	0.00391	[5]
C_2F_4	0.00429	[17]			

For the molecule under investigation, the non-vanishing couplings are: $a_g \times b_{1g}$, $b_{2g} \times b_{3g}$, $a_u \times b_{1u}$ and $b_{2u} \times b_{3u}$, all corresponding to ζ^z elements.

CYVIN et al [13] have reformulated the theory of rotation distortion by introducing a set of new elements $\tau_{\alpha\beta\gamma\delta}$ instead of the partial derivatives of inertia tensor components $J_{\alpha\beta\gamma\delta}$ of KIVELSON and WILSON [14, 15]. Using the CYVIN's method, $\tau_{\alpha\beta\gamma\delta}$ quantities and hence the rotation distortion constants have been evaluated.

The thermodynamic properties were calculated using PITZER's [16] table on rigid rotor approximation.

Results and discussion

The stretching force constant for C—F bond (f_r) is greater than that of C—S bond (f_s). This shows the dependence of force constant on electronegativity. (Electronegativity for sulphur is 2.5 and for fluorine 4.0). Further, since the C—S bonds constitute the four membered ring of the molecule form-

Table V

Generalised mean square amplitudes of (10^{-2}nm^2) of $C_2S_2F_4$ molecule

Atom pairs	$\langle(\Delta z)^2\rangle$	$\langle(\Delta y)^2\rangle$	$\langle(\Delta x)^2\rangle$
C—F	0.002264	0.012376	0
C—S	0.002731	0.022430	0
C...C	0.003560	0.008088	0
S...S	0.002196	0.004748	0
S...F_8	0.004405	0.027619	0
F_5...F_6	0.003294	0.044064	0
F_5...F_7	0.006601	0.007349	0
F_5...F_8	0.033240	0.007349	0

ing a bridged structure of tight bonding, the force constant f_S is found to be smaller. The low value of the ring puckering force constant f_τ predicts the low frequency of ring puckering motion which depends upon the relative magnitudes of bond angle strain and torsional strain.

The mean amplitudes of vibration calculated at 300 K (Table IV) agree very well with the values obtained in the electron diffraction study [2]. $u_{C-S} > u_{C-F}$ since $f_s < f_r$. This is in accordance with the theory that the higher the force constant, the smaller will be the mean amplitude. The mean amplitude calculations are useful in the interpretation of electron diffraction studies in molecular structure determination.

Table VI

Coriolis coupling coefficients of $C_2S_2F_4$

$a_g \times b_{1g}$		$a_u \times b_{1u}$	
ζ_{15}	−0.0882	$\zeta_{10,11}$	−0.3662
ζ_{25}	0.8608	$\zeta_{10,12}$	0.6873
ζ_{35}	−0.4423	$\zeta_{10,13}$	0.0000
ζ_{45}	0.2359	$b_{2u} \times b_{3u}$	
ζ_{16}	−0.7578	$\zeta_{14,16}$	0.9538
ζ_{26}	−0.1073	$\zeta_{14,17}$	−0.2576
ζ_{36}	0.2573	$\zeta_{14,18}$	0.1546
ζ_{46}	0.5899	$\zeta_{15,16}$	0.6696
$b_{2g} \times b_{3g}$		$\zeta_{15,17}$	0.6289
ζ_{79}	0.7921	$\zeta_{15,18}$	−0.3958
ζ_{89}	0.6103		

Table VII

Rotation distortion constants of $C_2S_2F_4$ (kHz)

Designation	Value
D_J	0.040636
D_K	0.594086
D_{JK}	−1.491347
R_5	−0.015669
R_6	0.0031564
δ_J	0.0114840

Table VIII

Thermodynamic properties (J mole^{-1}degree^{-1}) of $C_2S_2F_4$ molecule

Temp. (K)	C_p	H	F	S
100	53.2480	41.1948	249.8879	291.0827
200	85.6832	54.3586	281.9861	336.0935
273.16	109.1420	67.9660	301.4740	369.4400
300	114.9501	71.8586	309.1499	381.0085
400	133.8419	85.2483	330.6948	415.9431
500	146.5657	96.2818	351.5537	447.8354
600	155.3739	105.5253	370.1161	475.6414
700	161.4515	113.0823	387.0237	500.1060
800	165.8451	119.4785	402.9218	522.4002
900	169.0520	125.0823	417.0529	541.8003
1000	175.5575	129.5048	431.1053	560.6101

The generalised mean square amplitudes (Table V) along the bond $\langle(\Delta z)^2\rangle$ are equal to the mean square amplitude quantities (u^2). The quantities in bonded and nonbonded directions agree very well with the available literature values [2]. The Coriolis coupling coefficients are presented in Table VI. All the couplings are found to obey the zeta square sum rule. These constants facilitate the analysis of vibration-rotation spectra.

The rotation distortion constant (Table VII) will be of great use to the investigators of microwave spectra of this molecule. Since this is an asymmetric rotor, all the six constants D_J, D_K, D_{JK}, R_5, R_6 and δ_J exist. The positive value of D_J indicates that the centrifugal forces about any given axis will

always tend to increase the moment of inertia about that axis which in turn reduces the rotation distortion constant.

The thermodynamic properties are given in Table VIII.

REFERENCES

1. J. R. Durig and R. C. Lord, Spectrochim. Acta, **19,** 769, 1963.
2. Zuzana Smith and Ragnhild Sheip, Acta Chem. Scand., **30,** 759, 1976.
3. Peter Klaboe and Zuzana Smith, Spectrochim. Acta, **33A,** 489, 1978.
4. E. B. Wilson Jr., J. C. Decius and P. C. Cross, Molecular Vibrations, McGraw Hill Co. Inc. New York, 1955.
5. S. J. Cyvin, Molecular Structures and Vibrations, Chap. 6, Elsevier, Amsterdam, 1972.
6. Y. Marino and K. Kuchitsu, J. Chem. Phys., **20,** 1809, 1952.
7. W. J. Taylor, J. Chem. Phys., **22, 1780,** 1954.
8. E. Rytter, J. Chem. Phys., **60,** 3882, 1974.
9. A. J. P. Alix, D. E. Freeman and A. Muller, Z. Naturforsch., **29**a, 1454, 1974.
10. S. J. Cyvin, Acta Polytechnica Scand., **6,** 279, 1960.
11. Y. Morino and E. Hirota, J. Chem. Phys., **23,** 737, 1955.
12. J. H. Meal and S. R. Polo, J. Chem. Phys., **24,** 1119, 1126, 1956.
13. S. J. Cyvin, B. N. Cyvin and G. Hagen, Z. Naturforsch., **23**a, 1649, 1968.
14. D. Kivelson and E. B. Wilson, Jr., J. Chem. Phys., **20,** 1575, 1952.
15. D. Kivelson and E. B. Wilson, Jr., J. Chem. Phys., **21,** 1229, 1955.
16. K. S. Pitzer, Quantum Chemistry, Prentice Hall, 1954.
17. S. J. Cyvin, Molecular Vibrations and Mean Amplitudes, Universitetstorlaget, Oslo and Elsevier, Amsterdam, 1968.

Acta Physica Academiae Scientiarum Hungaricae, 52 (2), pp. 247—249 (1982)

SHORT COMMUNICATION

CERTAIN CHARACTERISTICS OF COOPER PAIR

S. C. JAIN* and C. M. KACHHAVA

DEPARTMENT OF PHYSICS, UNIVERSITY OF RAJASTHAN, JAIPUR—302004, INDIA

(Received in revised form 17. IX. 1981)

The physical existence of the Cooper pairs in building a reasonably sophisticated theory of superconductivity is a valid proposition which has been amply demonstrated by a variety of experimental measurements. In this communication, we, therefore, attempt to discuss the fundamental pair characteristics like binding energy, size and density. Such considerations would naturally enhance our understanding of the role played by Cooper pairs in the phenomenon of superconductivity.

The simplest possible form of the electron—ion interaction potential is [1]

$$V_{\mathbf{k}\mathbf{k}'} = -V \quad \text{for} \quad E_F > \epsilon_{\mathbf{k}} < E_F + \hbar\omega_D\,, \tag{1}$$

where the potential corresponds to the electron scattering from the state $\mathbf{k}$ to $\mathbf{k}'$, E_F is the Fermi energy and $\omega_D = k_B\theta_D/\hbar$ is the Debye frequency. This assumption leads to the following form for the binding energy of the Cooper pair

$$E_b = \hbar\omega_D\, e^{-1/N_0 V} \approx k_B\,\theta_D\, e^{-1/N_0 V}\,. \tag{2}$$

This form holds good only in the weak-coupling limit ($N_0 V \ll 1$), where N_0 is the density of states for electrons of up spin at the Fermi surface.

Using quantum mechanics and the assumption that the mates of the Cooper pair exist in the vicinity of the Fermi surface (and so they have momenta $\hbar v_F$), it is a straightforward matter to derive the following expression for the size of the Cooper pair:

$$\{\langle r^2\rangle\}^{1/2} = \frac{2}{\sqrt{3}}\,\frac{\hbar v_F}{E_b} \approx 10^{-4}\ \text{cm}. \tag{3}$$

The quantity represented by Eq. (3) is essentially the coherence length and refers to the distance over which superconducting electrons are correlated. It is sometimes called the radius of the bound state or root mean square radius of the Cooper pair.

* UGC Teacher Fellow on leave from Government College, Jhalawar-32600, India.

On the basis of the assumption of the existence of the weak-coupling, the use of the variational principle leads to the following result for the superconducting ground state energy relative to normal state at 0 K:

$$E(0) = -2N_0(\hbar\omega_D)^2 e^{-2/N_0 V} = -\frac{1}{2}\frac{n_c^2}{N_0}, \tag{4}$$

where

$$n_c = 2N_0 k_B \theta_D e^{-1/N_0 V} \tag{5}$$

is the number of pairs virtually excited above the Fermi surface. The quantity $N_0 k_B \theta_D$ occurring in Eq. (5) signifies the number of Cooper pairs in the interaction shell which is centred around the Fermi surface and has the thickness $k_B \theta_D$.

Finally, the condensation energy E_c can be expressed in terms of binding energy as:

$$E_c = 2N_0 E_b^2. \tag{6}$$

The relevant parameters used in the calculation along with the calculated values of the various characteristics of the Cooper pair are displayed in Table I. The values of $N_0 V_{\text{exptl}}$ are taken from MESERVEY and SCHWARTZ [2] while that of k_F, T_c and θ_D from JAIN and KACHHAVA [3—4]. It can be easily observed that the transition temperature is strongly dependent on the binding energy of a Cooper pair, and it increases with the increase in binding energy (except Al). For most of the superconductors the numerical value of binding energy ranges from 0.59×10^{-4} eV for weak coupling superconductor Cd to 6.39×10^{-4} eV for strong coupling superconductor Pb. It is further observed

Table I

Characteristic data and theoretical estimates of various characteristics of the Cooper pair

Element	k_F (au^{-1})	θ_D (K)	T_c (K)	$N_0 V_{\text{exptl}}$	E_b (10^{-4} eV)	$N_0\hbar\omega_D$ (10^{18}cm^{-3})	n_c (10^{18} cm^{-3})	E_c (10^{13} eV/cm^3)	$\langle r^2\rangle^{1/2}$ (10^{-4} cm)
Cd	0.7423	209.0	0.560	0.175	0.59	168	1.11	6.58	20.78
Zn	0.8342	309.0	0.875	0.18	1.03	279	2.16	22.20	13.48
Ga	0.8776	324.7	1.091	0.19	1.45	309	3.20	46.31	10.07
Al	0.9276	420.0	1.196	0.175	1.19	422	2.78	33.24	12.92
Tl	0.7738	87.0	2.390	0.27	1.85	73	3.59	66.35	6.97
In	0.7972	109.0	3.404	0.29	2.99	94	5.98	178.78	4.44
Sn	0.8674	195.0	3.722	0.25	3.08	183	6.71	206.55	4.68
Hg	0.7213	71.9	4.153	0.35	3.56	56	6.45	229.64	3.37
Pb	0.8350	96.3	7.193	0.39	6.39	87	13.41	856.70	2.17

that T_c is also dependent upon n_c, the number of pairs virtually excited over the Fermi sea and on $(\langle r^2 \rangle)^{1/2}$, the size of the Cooper pair. However, n_c increases with the increase in T_c (except Al and Hg) while reverse is the case for the size of the Cooper pair (except Al and Sn). The anomaly in the results of Al for its binding energy, the size of the Cooper pair and the number of pairs excited above the Fermi sea, of Hg for its n_c and of Sn for its $\langle r^2 \rangle^{1/2}$, can be accounted for by the uncertainties involved in the experimental data for θ_D and the approximate nature of the constant potential used in this theory. The uncertainty in the θ_D can be removed for medium and strong coupling superconductors (e.g. In, Tl, Sn, Hg and Pb) on replacing it by another parameter, $\langle \omega \rangle$, namely the average phonon frequency whose reliable experimental values are readily available from tunnelling technique. Since the tunnelling technique is restricted only to medium and strong coupling superconductors, we have, therefore, used θ_D for all the metals under consideration for the sake of consistency.

In conclusion, it may be admitted that the present results may be quantitatively improved by using a realistic k-dependent potential. However, such an attempt would not alter the qualitative features of the conclusions derived from the present investigation.

REFERENCES

1. L. N. Cooper Phys Rev., **104**, 1189, 1956.
2. M. Meservey and B. B. Schwartz, Superconductivity, Marcel Dekker, Inc., New York, 1969
3. S. C. Jain and C. M. Kachhava, Indian J. Pure and Appl. Phys., **18**, 489, 1980.
4. S. C. Jain and C. M. Kachhava, Indian J. of Phys. (in press).

BOOK REVIEWS

Quantum Dynamics of Molecules, The New Experimental Challenge to Theorists

NATO Advanced Study Institute Series, Series B: Physics, Volume 57 (Ed.: R. G. Woolley) Plenum Press, New York, 1980, pp. 557

The Advanced Study Institute on the quantum dynamics of molecules was organized by Professor R. G. WOOLLEY at Trinity Hall, Cambridge University, England, from September 15th to 29th, 1979. The present volume of the Physics Series contains the texts of the twelve lecture courses on the following subjects: The Eckart Hamiltonian for molecules (B. T. SUTCLIFFE), Foundations of theoretical chemistry (H. PRIMAS), Supersonic molecular beams and van der Waals molecules (D. H. LEVY), A general phenomenology for small clusters, however floppy (R. S. BERRY), The Generator Coordinate Method in molecular physics (P. VAN LEUVEN, L. LATHOUVERS), Generator Coordinate theory of diatomic systems (L. LATHOUVERS, P. VAN LEUVEN), Irreversible and non-linear dynamics of open systems (E. B. DAVIES), Quasiperiodic and stochastic intramolecular dynamics: the nature of intramolecular energy transfer (S. A. RICE), Manifestations of parity violations in atomic and molecular systems (R. A. HARRIS), High resolution laser spectroscopy of molecules (W. DEMTRÖDER), Spectral properties of atomic and molecular systems (J. M. COMBES, R. SEILER), Theory of electron—molecule collisions (P. G. BURKE).

The purpose of the Institute with the present volume was to juxtapose new theoretical developments in molecular and atomic physics to new experimental possibilities in the study of isolated small atomic and molecular systems, thus mainly for the gaseous phase. These new experimental approaches, e.g. high resolution laser spectroscopic techniques lead to results that require novel theoretical approaches and tools, and even question long-standing theories — deeply entrenched in chemical thinking — such as the celebrated Born—Oppenheimer approximation. Of course, by a careful examination of such fundamental techniques one is led logically to have a new look at the concept of potential surfaces governing vibrational motions. Any new and valid substitute of the Born—Oppenheimer method — such as perhaps the Generator Coordinate Method — could lead to a fundamentally new view of molecular processes, in addition to the immense pedagogical benefit that would derive for students of molecular physics.

The volume is therefore eminently suitable for advanced level chemistry and physics courses and is warmly recommended to theoretical workers in spectroscopy as well.

From the viewpoint of genuine challenge to traditional ways in molecular physics the courses deserving special mention are those by Professor R. S. BERRY on floppy quantum mechanical systems, by Professors P. VAN LEUVEN and L. LATHOUVERS on the Generator Coordinate Method, and by Professor R. A. HARRIS on parity violations. Very lucid and compact expositions of new experimental methods are found for high resolution laser spectroscopy by Professor W. DEMTRÖDER, for supersonic molecular beams by Professor D. H. LEVY and for electron-molecule collisions by Professor P. G. BURKE. The purely theoretical texts by Professor H. PRIMAS and by Professors J. M. COMBES and R. SEILER are the most abstract contributions to the volume and will probably be assimilated only by the selected few of topmost theoreticians.

The book is produced in a pleasing clean format by photographic techniques and contains only few typographic errors.

LÁSZLÓ NEMES

Pattern Formation by Dynamic Systems and Pattern Recognition

Proceedings of the International Symposium on Synergetics at Schloss Elmau, Bavaria, April 30—May 5, 1979 Ed.: H. Haken

Springer-Verlag, Berlin, Heidelberg, New York, 1979, 156 figs., 16 tab. VIII + 305 pp, DM 68.—

This book contains the papers of a Symposium on Synergetics, held in West Germany in 1979. A general description of pattern formation by dynamic systems and pattern recognition methods are described. The different chapters are devoted to the physics of lasers and quantum optics; the dynamics of fluids; biology; mathematics; ecology, sociology and history; and other subjects of general interest. Some papers are devoted to the theoretical problems of pattern formation while some others deal with recent experimental results in the field. As far as pattern recognition is concerned the fundamental ideas are discussed in detail and possible or realized practical applications are also described. The links between pattern recognition and pattern formation are also revealed.

The state of art of a new and fast developing field of research is described in this volume being of use for scientists involved directly or working in related fields of research. The volume can, however, be recommended to any scientist or university lecturer working or lecturing in physics, chemistry, mathematics, astrophysics and different social sciences.

NORBERT KROÓ

M. D. SCADRON: Advanced Quantum Theory and Its Applications through Feynman Diagrams

Texts and Monographs in Physics Series, Eds.: W. Beiglböck, M. Goldhaber, E. H. Lieb, W. Thirring
Springer-Verlag, Berlin, Heidelberg, New York, 1977, pp. 386

The book treats a comprehensive material containing the elements of covariant Feynman diagrams after a necessary introduction of two parts. In a concise form many important developments of advanced quantum theory are included, but such topics as the quark model, non-abelian gauge theories and their applications are beyond the scope of the book. In this manner the volume forms an introduction to later higher studies and at the same time offers a good survey of the methods and physical results of the early advanced quantum theory for a wider audience. While emphasis is always put on physics, its style and composition are equally enjoyable. A few applications in atomic, solid state and nuclear physics are also included.

Part I provides a description of the transformation theory where rotations in three-space, the inhomogeneous Lorentz group, boson and spin-half wave equations, as well as discrete symmetries are treated.

Part II is devoted to various aspects of the scattering theory: general formal theory, phase shifts, low and high energy scatterings, and nonrelativistic perturbation theory.

In Part III, by introducing covariant Feynman diagrams the four fundamental interactions are surveyed through physical phenomena in lowest order of perturbation theory. A brief outlook on higher-order graphs and phenomena is also included.

The appendices, bibliography, and the long list of problems are very useful.

Summarizing, this book on symmetries, wave equations, scatterings, fundamental forces is an enjoyable reading for those who already know the elements of nonrelativistic quantum mechanics.

G. PÓCSIK

T. D. LEE: Particle Physics and Introduction to Field Theory

Contemporary Concepts in Physics, Volume 1, Ed.: H. Primakoff

Harwood Academic Publishers, Chur — London — New York, 1981, pp. 865,
Cloth US $ 59.50 Paper US $ 19.50

At the start of this new series the Editor has anticipated that "the various volumes in the series will be rigorous and complete in their treatment", and "the subjects to be covered will include those at the forefront of current research". No doubt, T. D. LEE's book fully satisfies these expectations. In particle physics a complete treatment, from the elements to the contemporary results is almost impossible. Nevertheless, T. D. LEE selected his coherent material successfully and provided a fascinating, personal and in-depth presentation of particle physics and field theory.

The subject of Part I (field theory) is traditional: from free fields to the S-matrix. An exciting description of the development of soliton physics is also included.

Part II (particle physics) starts with symmetries; here the usual space — time reflections and internal symmetries (global SU(3) too) are treated. It is quite an experience to read about the P, CP violations, $K-\overline{K}$ system. (T. D. LEE and C. N. YANG were awarded the Nobel Prize in Physics, 1957, for P violation.)

Part IIB contains the newer developments in particle physics such as quark confinement, gauge theories and quantisation (path integrals), quark models, weak interactions and unified electroweak gauge theory, quark — parton model and high-energy processes, chiral symmetry.

These topics are alloyed into a coherent unity making the book an outstanding writing. Derivations are always explicit, therefore the volume is good reading.

The book is recommended for those who are interested or working in particle physics.

G. PÓCSIK

JAN WEILAND — HANS WILHELMSSON: Coherent Nonlinear Interaction of Waves in Plasmas

International Series in Natural Philosophy, Vol. 88 Pergamon Press, Oxford, New York, 1977
US $ 30.25, £ 15.50

The evolution of plasma physics has been deeply motivated by the research aiming at the realization of controlled thermonuclear energy production as well as the investigation of the interaction of laser beams and matter, to mention two of the major fields only. In both fields one encounters theoretical difficulties in relation with the essentially nonlinear character of the explored basic laws. Though we are as yet far from being able to handle the nonlinearities in general, we see that for the treatment of nonlinear effects most fields offer fruitful hints, especially in wave propagation phenomena. The Authors, both of Chalmers University, Gothenburg, attempt here to treat the nonlinear interaction of plasma waves in a way that favours the general aspects rather than the ad hoc ones. The research monograph groups the material into the following chapters: Simple nonlinear examples; Coupled mode theory; The field energy in dispersive media; Formulation of nonlinear wave equations in terms of a nonlinear current; Some examples of three-wave interaction in plasmas; Solutions to the coupled mode equations (stability criteria, explosive instability, damping, interaction of two electromagnetic waves and three plasma waves, stabilization); The influence of dissipation; Beam—plasma systems; Second order dispersive effects; Interaction between waves with finite spread in wave vectors; Nonlinear excitation of collective waves; Parametric excitation of hybrid resonances in plasmas; Nonresonant wave—wave interaction and wave-particle effects; Experiments on nonlinear effects in plasmas; Trends in the development of nonlinear plasma research.

The book contains five appendices to guide the reader in special questions and their literature. Some useful exercises are also given which help mastering and understanding this rather extended field.

The structure and the content of this well written research monograph and its technical presentation will hopefully contribute to the fruitful collaboration of physicists in understanding and taming nonlinear phenomena, not only in plasma physics but also in other fields of research.

I. ABONYI

Manuscript received by Akadémiai Kiadó: 12 March 1982
Manuscript received by the Printers: 19 March 1982
Date of publication: 22 December 1982

PRINTED IN HUNGARY

Akadémiai Nyomda, Budapest

NOTES TO CONTRIBUTORS

I. PAPERS will be considered for publication in Acta Physica Hungarica only if they have not previously been published or submitted for publication elsewhere. They may be written in English, French, German or Russian.

Papers should be submitted to

Prof. I. Kovács, Editor
Department of Atomic Physics, Technical University
1521 Budapest, Budafoki út 8, Hungary

Papers may be either articles with abstracts or short communications. Both should be as concise as possible, articles in general not exceeding 25 typed pages, short communications 8 typed pages.

II. MANUSCRIPTS

1. Papers should be submitted in three copies.

2. The text of papers must be of high stylistic standard, requiring minor corrections only.

3. Manuscripts should be typed in double spacing on good quality paper, with generous margins.

4. The name of the author(s) and of the institutes where the work was carried out should appear on the first page of the manuscript.

5. Particular care should be taken with mathematical expressions. The following should be clearly distinguished, e.g. by underlining in different colours: special founts (italics, script, bold type, Greek, Gothic, etc.); capital and small letters; subscripts and superscripts, e.g. x^2, x_3; small l and 1; zero and capital O; in expressions written by hand: e and l, n and u, v and v, etc.

6. References should be numbered serially and listed at the end of the paper in the following form: J. Ise and W. D. Fretter, Phys. Rev., **76**, 933, 1949.

For books, please give the initials and family name of the author(s), title, name of publisher, place and year of publication, e.g.: J. C. Slater, Quantum Theory of Atomic Structures, I. McGraw-Hill Book Company, Inc., New York, 1960.

References should be given in the text in the following forms: Heisenberg [5] or [5].

7. Captions to illustrations should be listed on a separate sheet, not inserted in the text.

8. In papers submitted to Acta Physica all measures should be expressed in SI units.

III. ILLUSTRATIONS AND TABLES

1. Each paper should be accompanied by three sets of illustrations, one of which must be ready for the blockmaker. The other sets attached to the copies of the manuscript may be rough drawings in pencil or photocopies.

2. Illustrations must not be inserted in the text.

3. All illustrations should be identified in blue pencil by the author's name, abbreviated title of the paper and figure number.

4. Tables should be typed on separate pages and have captions describing their content. Clear wording of column heads is advisable. Tables should be numbered in Roman numerals (I, II, III, etc.).

IV. RETURN OF MATERIAL

Owing to high postage costs, the Editorial Office cannot undertake to return *all* material not accepted for any reason for publication. Of papers to be revised (for not being in conformity with the above Notes or other reasons) only *one* copy will be returned. Material rejected for lack of space or on account of the Referees' opinion will not be returned to authors outside Europe.

Periodicals of the Hungarian Academy of Sciences are obtainable at the following addresses:

AUSTRALIA
C.B.D. LIBRARY AND SUBSCRIPTION SERVICE
Box 4886, G.P.O., *Sydney N.S.W. 2001*
COSMOS BOOKSHOP, 145 Ackland Street
St. Kilda (Melbourne), Victoria 3182

AUSTRIA
GLOBUS, Höchstädtplatz 3, *1206 Wien XX*

BELGIUM
OFFICE INTERNATIONAL DE LIBRAIRIE
30 Avenue Marnix, *1050 Bruxelles*
LIBRAIRIE DU MONDE ENTIER
162 rue du Midi, *1000 Bruxelles*

BULGARIA
HEMUS, Bulvar Ruszki 6, *Sofia*

CANADA
PANNONIA BOOKS, P.O. Box 1017
Postal Station "B", *Toronto, Ontario M5T 2T8*

CHINA
CNPICOR, Periodical Department, P.O. Box 50
Peking

CZECHOSLOVAKIA
MAD'ARSKÁ KULTURA, Národní třida 22
115 66 Praha
PNS DOVOZ TISKU, Vinohradská 46, *Praha 2*
PNS DOVOZ TLAČE, *Bratislava 2*

DENMARK
EJNAR MUNKSGAARD, Norregade 6
1165 Copenhagen K

FEDERAL REPUBLIC OF GERMANY
KUNST UND WISSEN ERICH BIEBER
Postfach 46, *7000 Stuttgart 1*

FINLAND
AKATEEMINEN KIRJAKAUPPA, P.O. Box 128
SF-00101 Helsinki 10

FRANCE
DAWSON-FRANCE S. A., B. P. 40, *91121 Palaiseau*
EUROPÉRIODIQUES S. A., 31 Avenue de Versailles, *78170 La Celle St. Cloud*
OFFICE INTERNATIONAL DE DOCUMENTATION ET LIBRAIRIE, 48 rue Gay-Lussac
75240 Paris Cedex 05

GERMAN DEMOCRATIC REPUBLIC
HAUS DER UNGARISCHEN KULTUR
Karl Liebknecht-Straße 9, *DDR-102 Berlin*
DEUTSCHE POST ZEITUNGSVERTRIEBSAMT
Sraße der Pariser Kommüne 3–4, *DDR-104 Berlin*

GREAT BRITAIN
BLACKWELL'S PERIODICALS DIVISION
Hythe Bridge Street, *Oxford OX1 2ET*
BUMPUS, HALDANE AND MAXWELL LTD.
Cowper Works, *Olney, Bucks MK46 4BN*
COLLET'S HOLDINGS LTD., Denington Estate
Wellingborough, Northants NN8 2QT
WM. DAWSON AND SONS LTD., Cannon House
Folkstone, Kent CT19 5EE
H. K. LEWIS AND CO., 136 Gower Street
London WC1E 6BS

GREECE
KOSTARAKIS BROTHERS INTERNATIONAL BOOKSELLERS, 2 Hippokratous Street, *Athens-143*

HOLLAND
MEULENHOFF-BRUNA B.V., Beulingstraat 2,
Amsterdam
MARTINUS NIJHOFF B.V.
Lange Voorhout 9–11, *Den Haag*
SWETS SUBSCRIPTION SERVICE
347b Heereweg, *Lisse*

INDIA
ALLIED PUBLISHING PRIVATE LTD., 13/14
Asaf Ali Road, *New Delhi 110001*
150 B-6 Mount Road, *Madras 600002*
INTERNATIONAL BOOK HOUSE PVT. LTD.
Madame Cama Road, *Bombay 400039*
THE STATE TRADING CORPORATION OF INDIA LTD., Books Import Division, Chandralok
36 Janpath, *New Delhi 110001*

ITALY
INTERSCIENTIA, Via Mazzé 28, *10149 Torino*
LIBRERIA COMMISSIONARIA SANSONI, Via Lamarmora 45, *50121 Firenze*
SANTO VANASIA, Via M. Macchi 58
20124 Milano
D. E. A., Via Lima 28, *00198 Roma*

JAPAN
KINOKUNIYA BOOK-STORE CO. LTD.
17-7 Shinjuku 3 chome, Shinjuku-ku, *Tokyo 160-91*
MARUZEN COMPANY LTD., Book Department, P.O. Box 5050 Tokyo International, *Tokyo 100-31*
NAUKA LTD. IMPORT DEPARTMENT
2-30-19 Minami Ikebukuro, Toshima-ku, *Tokyo 171*

KOREA
CHULPANMUL, *Phenjan*

NORWAY
TANUM-TIDSKRIFT-SENTRALEN A.S., Karl Johansgatan 41–43, *1000 Oslo*

POLAND
WĘGIERSKI INSTYTUT KULTURY, Marszałkowska 80, *00-517 Warszawa*
CKP I W, ul. Towarowa 28, *00-958 Warszawa*

ROUMANIA
D. E. P., *Bucureşti*
ILEXIM, Calea Grivitei 64–66, *Bucureşti*

SOVIET UNION
SOJUZPECHAT — IMPORT, *Moscow*
and the post offices in each town
MEZHDUNARODNAYA KNIGA, *Moscow G-200*

SPAIN
DIAZ DE SANTOS, Lagasca 95, *Madrid 6*

SWEDEN
ALMQVIST AND WIKSELL, Gamla Brogatan 26
101 20 Stockholm
GUMPERTS UNIVERSITETSBOKHANDEL AB
Box 346, *401 25 Göteborg 1*

SWITZERLAND
KARGER LIBRI AG, Petersgraben 31, *4011 Basel*

USA
EBSCO SUBSCRIPTION SERVICES
P.O. Box 1943, *Birmingham, Alabama 35201*
F. W. FAXON COMPANY, INC.
15 Southwest Park, *Westwood Mass. 02090*
THE MOORE-COTTRELL SUBSCRIPTION AGENCIES, *North Cohocton, N. Y. 14868*
READ-MORE PUBLICATIONS, INC.
140 Cedar Street, *New York, N. Y. 10006*
STECHERT-MACMILLAN, INC.
7250 Westfield Avenue, *Pennsauken N. J. 08110*

YUGOSLAVIA
JUGOSLOVENSKA KNJIGA, Terazije 27, *Beograd*
FORUM, Vojvode Mišića 1, *21000 Novi Sad*

HU-ISSN 0001-6705 **Index: 26.022**

ACTA PHYSICA

ACADEMIAE SCIENTIARUM HUNGARICAE

VOLUME 52 NUMBERS 3–4

AKADÉMIAI KIADÓ, BUDAPEST
1982

ACTA PHYS. HUNG. APAHAQ 52 (3–4) 255–468 (1982)

ACTA PHYSICA

A JOURNAL OF THE HUNGARIAN ACADEMY OF SCIENCES

EDITED BY

I. KOVÁCS

Acta Physica publishes original papers on subjects in physics. Papers are accepted in English, French, German and Russian.

Acta Physica is published in two yearly volumes (4 issues each) by

AKADÉMIAI KIADÓ
Publishing House of the Hungarian Academy of Sciences
H-1054 Budapest, Alkotmány u. 21

Subscription information

Orders should be addressed to

KULTURA Foreign Trading Company
1389 Budapest P.O. Box 149

or to its representatives abroad.

ACTA PHYSICA

ACADEMIAE SCIENTIARUM HUNGARICAE

VOLUME 52 NUMBERS 3–4

AKADÉMIAI KIADÓ, BUDAPEST

1982

ACTA PHYS. HUNG.

CONTENTS

Manuscripts received by the Editorial Office on 12 November 1981.

PROCEEDINGS

of the

HUNGARIAN—AUSTRIAN HEALTH PHYSICISTS' MEETING

Győr, Hungary
28 September—1 October, 1981

organized by

Health Physics Section
Roland Eötvös Physical Society
President: I. Fehér
Secretary: L. Koblinger

Österreichischer Verband für Strahlenschutz
President: E. Tschirf
Secretary: A. Hefner

List of participants

H. AIGINGER
Atominstitut der Österreichischen Universitäten
Schüttelstr. 115, Wien, A-1020

A. ANDRÁSI
Central Research Institute for Physics
P.O.Box 49, Budapest, H-1525

É. BELEZNAY
Central Research Institute for Physics
P.O.Box 49, Budapest, H-1525

H. BINDER
Institut für Radiochemie der Universität Innsbruck
Innrain 67, Innsbruck, A-6020

J. BIRÓ
Central Research Institute for Physics
P.O.Box 49, Budapest, H-1525

T. BIRÓ
Institute of Isotopes
P.O.Box 77, Budapest, H-1525

I. BOJTOR
Frédéric Joliot-Curie National Research Institute for Radiobiology and Radiohygiene
Pentz K. u. 5, Budapest, H-1221

L. BOZÓKY
Central Institute for Oncology
Ráth Gy. u. 7—9, Budapest, H-1122

S. DEME
Central Research Institute for Physics
P.O.Box 49, Budapest, H-1525

Z. DÉZSI
Radiological Clinic of the Medical University of Debrecen
Klinika telep, Debrecen, H-4032

P. DUDOK
Institute for Development of Videoton
Vöröshadsereg u. 54, Budapest, H-1021

K. E. DUFTSCHMID
Österreichisches Forschungszentrum Seibersdorf
Lenaugasse 10, Wien, A-1082

I. ERDÉLYVÁRI
Central Research Institute for Physics
P.O.Box 49, Budapest, H-1525

I. FEHÉR
Central Research Institute for Physics
P.O.Box 49, Budapest, H-1525

E. GERMÁN
Paks Nuclear Power Station
P.O.Box 71, Paks, H-7031

A. GROSSKOPF
Allgemeine Unfallversicherungsanstalt
Adalbert Stifterstr. 65, Wien, A-1200

A. HEFNER
Österreichisches Forschungszentrum Seibersdorf
Lenaugasse 10, Wien, A-1082

W. HELMREICH
Inglomark, Markowitsch Co.
Mariahilfer Str. 133, Wien, A-1150

W. HOFMANN
Abteilung für Biophysik
Universität Salzburg
Erzabt-Klotz-Str. 11, Salzburg, A-5020

J. K. HOHENBERG
Bundesministerium für Soziale Verwaltung
Kundmanngasse 21, Wien, A-1030

É. HOLLAND
Frédéric Joliot-Curie National Research Institute for Radiobiology and Radiohygiene
Pentz K. u. 5, Budapest, H-1221

E. HORVÁTH
Paks Nuclear Power Station
P.O.Box 71, Paks, H-7031

E. HUBER
Arbeitsinspektorat
Fichtegasse 11, Wien, A-1010

L. KOBLINGER
Central Research Institute for Physics
P.O.Box 49, Budapest, H-1525

M. KOVÁCS
PVOP
P.O.Box 25, Budapest, H-1885

K. KOZÁK
Institute of Isotopes
P.O.Box 77, Budapest, H-1525

J. KRISCHAN
Amt der Kärntner Landesregierung
Arnulfpl. 2, Klagenfurt, A-9020

G. KUHM
Inglomark, Markowitsch Co.
Mariahilfer Str. 133, Wien, A-1150

E. KURTÁCS
Frédéric Joliot Curie National Research Institute for Radiobiology and Radiohygiene
Pentz K. u. 5, Budapest, H-1221

GY. LANCSARICS
Central Research Institute for Physics
P.O.Box 49, Budapest, H-1525

E. LÁNG
Central Research Institute for Physics
P.O.Box 49, Budapest, H-1525

K. LUN
Municipal Public Health—Epidemics Institute
Váci út 174., Budapest, H-1138

S. MAKRA
Central Institute for Oncology
Ráth Gy. u. 7—9, Budapest, H-1122

I. MASCHEK
Frédéric Joliot-Curie National Research Institute for Radiobiology and Radiohygiene
Pentz K. u. 5., Budapest, H-1221

L. MEDVECZKY
Institute of Nuclear Research
Bem tér 18/c., Debrecen, H-4026

J. MOLNÁR
Central Research Institute for Physics
P.O.Box 49, Budapest, H-1525

I. NÉMETH
Central Research Institute for Physics
P.O.Box 49, Budapest, H-1525

I. NIKL
Frédéric Joliot-Curie National Research Institute for Radiobiology and Radiohygiene
Pentz K. u. 5, Budapest, H-1221

M. OSVAY
Institute of Isotopes
P.O.Box 77, Budapest, H-1525

R. OUVRARD
International Atomic Energy Agency
P.O.Box 100, Vienna, A-1400

F. PECHACEK
Österreichisches Elektrizitätswirtschafts AG
Am Hof 6A, Wien, A-1010

T. PORUBSZKY
Medicor Works
P.O.Box 90, Budapest, H-1475

T. PREDMERSZKY
Frédéric Joliot-Curie National Research Institute for Radiobiology and Radiohygiene
Pentz K. u. 5., Budapest, H-1221

G. SARINGER
Bundesministerium für Gesundheit und Umweltschutz
Stubenring 1, Wien, A-1010

O. SCHMIEDMAYER
Österreichisches Draukraftwerke AG
Kohldorferstr. 98, Klagenfurt, A-9020

H. SORANTIN
Österreichisches Forschungszentrum Seibersdorf
Lenaugasse 10, Wien, A-1082

F. STEGER
Österreichisches Forschungszentrum Seibersdorf
Lenaugasse 10, Wien, A-1082

P. P. SZABÓ
Central Research Institute for Physics
P.O.Box 49, Budapest, H-1525

Á. SZÖRÉNYI
National Office of Measures
Németvölgyi út 37/39, Budapest, H-1124

GY. THÉK
Frédéric Joliot-Curie National Research Institute for Radiobiology and Radiohygiene
Pentz K. u. 5, Budapest, H-1221

J. TOPERCZER
Central Institute for Oncology
Ráth Gy. u. 7—9, Budapest, H-1122

E. TSCHIRF
Atominstitut der Österreichischen Universitäten
Schüttelstr. 115, Wien, A-1020

M. TSCHURLOVITS
Atominstitut der Österreichischen Universitäten
Schüttelstr. 115, Wien, A-1020

E. UNFRIED
Atominstitut der Österreichischen Universitäten
Schüttelstr. 115, Wien, A-1020

I. URAY
Institute of Nuclear Research
Bem tér 18/c, Debrecen, H-4026

J. URBÁN
Central Research Institute for Physics
P.O.Box 49, Budapest, H-1525

N. VANA
Atominstitut der Österreichischen Universitäten
Schüttelstr. 115, Wien, A-1020

E. VIRÁGH
Training Reactor of the Technical University of Budapest
Műegyetem rakpart 9, Budapest, H-1111

P. ZOMBORI
Central Research Institute for Physics
P.O.Box 49, Budapest, H-1525

K. ZSDÁNSZKY
National Office of Measures
Németvölgyi út 37/39, Budapest, H-1124

Acta Physica Academiae Scientiarum Hungaricae, 52 (3—4), pp. 263—264 (1982)

PROFESSOR LÁSZLÓ BOZÓKY, 70 YEARS OLD

Professor BOZÓKY, Member of the Hungarian Academy of Sciences, was 70 on 4th May 1981. LÁSZLÓ BOZÓKY is widely known for his interest in the physics and dosimetry of radiations, this interest dates from an early age. He completed his academic studies under OTTO HAHN and WALTER FRIEDRICH and began working in the Eötvös Loránd Radium and X-ray Institute in 1937; when this establishment was reorganized to become the National Institute of Oncology he continued to work as leader of its Physics Department.

In addition to his activities in routine clinical radiology, he established in Hungary the basis of investigations concerning dosimetry, radiation protection and associated measuring techniques. As early as in the thirties he introduced the use of personal dosimeters to monitor the radiation burden of physicians and nurses engaged in carrying out treatment by radiotherapy. To minimize exposure of radiotherapists he worked on the development of shielding devices whose use enabled personnel engaged in, for example, gynaecological radiotherapy to be substantially reduced. The reliability of the high precision ionization chambers and of the radioactive contamination

measuring equipment with GM-tubes is confirmed by the fact that to date they are still operating to satisfaction.

In 1951 he was given the additional responsibility of leading the Radiological Department of the Central Research Institute for Physics which post he held for about 10 years. In the latter capacity he did pioneering work in Hungary for the introduction of isotope techniques into research on mineral oil, aluminium metallurgy and on hydrological problems. For many years the pocket ionization chamber personal dosimeter developed by Prof. BOZÓKY was used for radiation protection in every isotope laboratory in the country.

His activities concerning the medical application of radioisotopes led to the building of two types of irradiation facility, the "Gravicert" and the "Rotacert", and development of new therapeutical methods. By the construction of "Gravicert" cobalt therapy became possible in our country. The unique technical features as well as the shielding of these irradiation facilities provide for the maximum radiation protection of the physicians treating the patient.

Noteworthy observations have been made by him on radiation scattering; his findings are of practical use in the design of radiation shieldings.

BOZÓKY's name is indelibly linked with initiating the teaching and education of students on the disciplines of radiation physics, isotope techniques and radiation protection; he is still active in this field. Standard permissible radiation levels established in Hungary for the safe use of ionizing radiations and radioisotopes in the last three decades were worked out under his guidance.

In addition to multifarious scientific and educational activities, he is an active member of the Radiological Section of the Scientific Society of Measurement and Automation and the Biophysical Society. Now the honorary president of the Health Physics Section of the Roland Eötvös Physical Society; he was, from its foundation in 1962 and for many years after, its president. He was an elected member of the Executive Council of the International Radiation Protection Association when it was formed and he has officiated for a decade as a Council member.

The participants of the Hungarian—Austrian Health Physicists' Meeting dedicate this session's Proceedings to Prof. BOZÓKY to commemorate his 70th birthday offering him best wishes for many more years of fruitful scientific achievement from all Hungarian radiologists and health physicists.

I. FEHÉR

Acta Physica Academiae Scientiarum Hungaricae, 52 (3—4), pp. 265—274 (1982)

I. STANDARDIZATION

CHAIRMEN: L. BOZÓKY, E. TSCHIRF

HUNGARIAN—AUSTRIAN CO-OPERATION IN RADIATION DOSIMETRY

K. ZSDÁNSZKY

NATIONAL OFFICE OF MEASURES (OMH)
1124 BUDAPEST, HUNGARY

and

K. E. DUFTSCHMID

AUSTRIAN RESEARCH CENTER SEIBERSDORF (ÖFZS)
SEIBERSDORF, AUSTRIA

Since 1974 a close and fruitful co-operation has been in progress between the Hungarian National Office of Measures (OMH) and the Austrian Research Center Seibersdorf (ÖFZS) in the field of radiation dosimetry. The work began with intercomparison measurements and calibration of dose meters at OMH. The practical experiences gained at OMH have been applied in the design of the new Austrain dosimetry laboratory established between 1975 and 1977.

Since 1976 the cooperation of the two Institutions has been included in the Hungarian—Austrian inter-governmental agreement on technical-scientific co-operation as a joint priority research project. The mutually advantageous results contribute to the improvement of the dosimetry standard and the calibration facilities in both countries.

1. Primary standards

Free-air parallel plate ionization chambers for X-rays of 20—80 kV and 50—400 kV (Fig. 1) and cylindrical, graphite cavity ionization chambers of known, measured volume for gamma radiation of ^{60}Co and ^{137}Cs (Fig. 2) were designed at OMH between 1968 and 1972. Their important data were published in 1975 [1].

Between 1972 and 1974 these OMH standards were compared with the exposure standards of the International Bureau of Weights and Measures (BIPM). The results of these comparisons were published by BIPM in 1975 [2]. The agreement of these direct comparisons was better than 0.3% for 30 and 50 kV X-rays and for ^{60}Co gamma rays. For medium energy X-rays, indirect comparisons were undertaken with BIPM using two OMH transfer-standard ionization chambers. The differences were found to be less than 0.5% for X-rays in the range of 100 to 250 kV.

The Austrian primary standards of exposure had been manufactured at Seibersdorf according to the instruments designed by OMH. For the lowest energy range of 5—30 kV X-rays two free-air chambers have been constructed

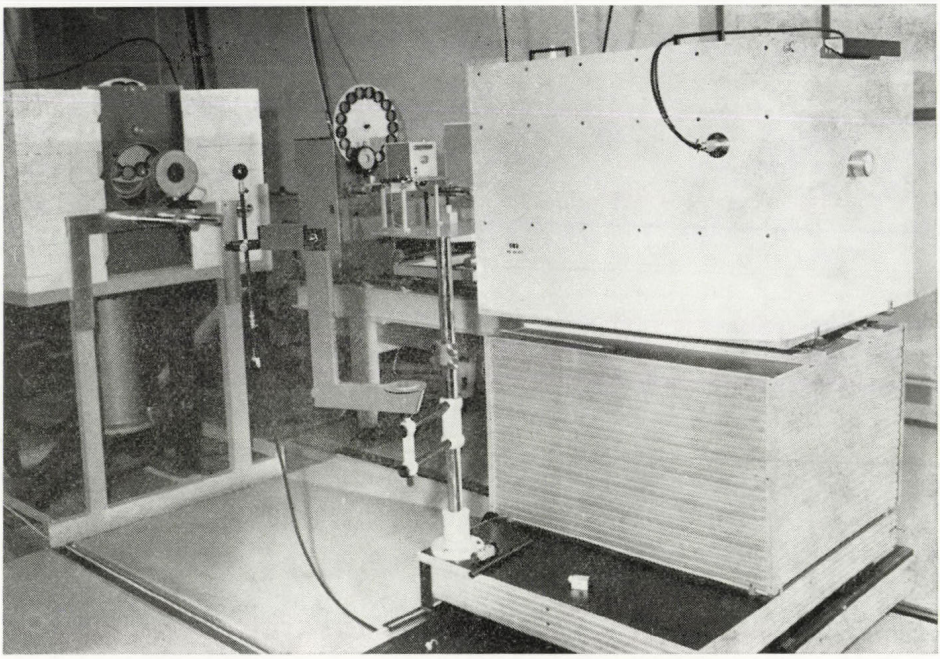

Fig. 1. Primary standard free-air ionization chambers of OMH.

at Seibersdorf which are now used as primary standards in Austria and in Hungary, respectively.

The Austrian and Hungarian national standards of exposure have been compared during the past few years. Fig. 3 shows the results of intercomparison measurements between the Austrian and Hungarian primary standard free-air chambers for 5—30 kV X-rays. Fig. 4 contains the results of similar measurements with the 20—80 kV free-air chambers. In the field of gamma-radiation especially of ^{60}Co absolute determinations of exposure rate have been performed with the primary standards of OMH and ÖFZS, graphite cavity chambers of measured volume as mentioned before. Fig. 5 shows the results of such absolute determinations of ^{60}Co exposure rate — normalized to the mean value of the measurements — in the beam of the teletherapy system at Seibersdorf made with the Hungarian National Standard No. AGO and three identical primary standards of ÖFZS Seibersdorf. It can be seen that the comparison measurements between the Austrian and Hungarian exposure standards for X-rays and ^{60}Co gamma rays showed agreement within a few tenths of a percent.

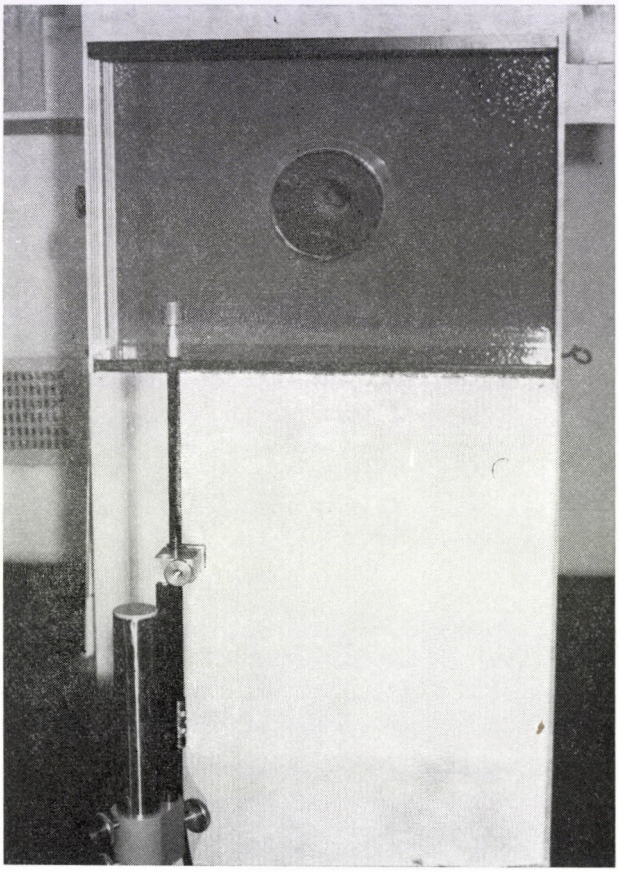

Fig. 2. Primary standard graphite cavity ionization chamber of OMH with the calibration arrangement for gamma radiation.

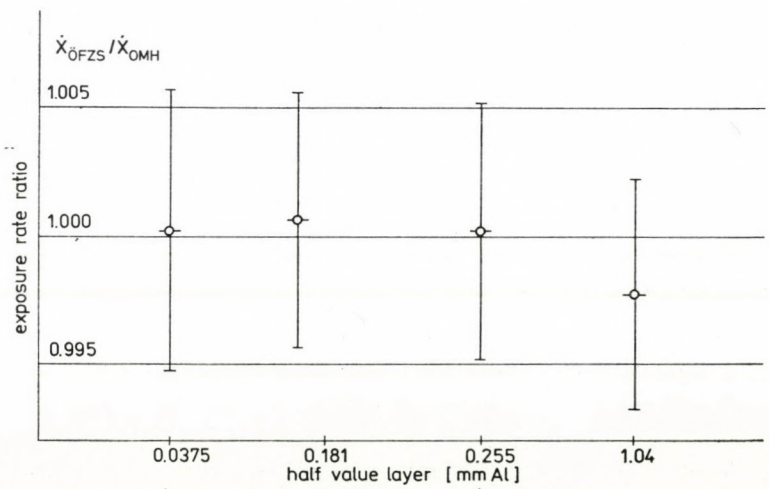

Fig. 3. Results of intercomparison measurements between the Austrian and Hungarian primary standard free-air chambers for 5—30 kV X-rays.

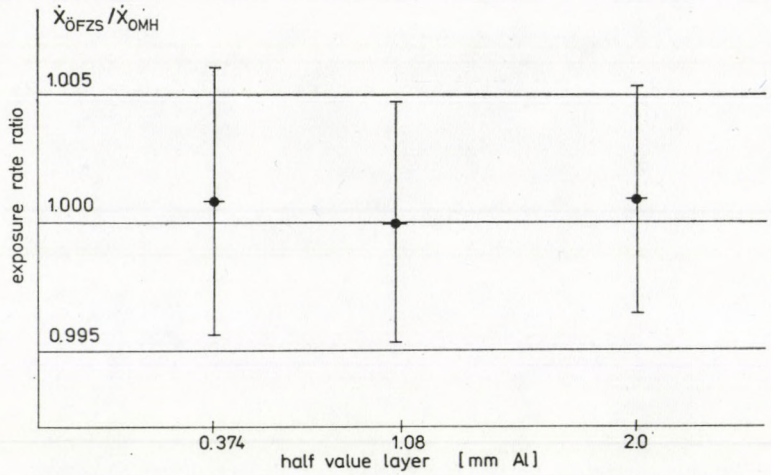

Fig. 4. Results of intercomparison measurements between the Austrian and Hungarian primary standard free-air chambers for 20—80 kV X-rays.

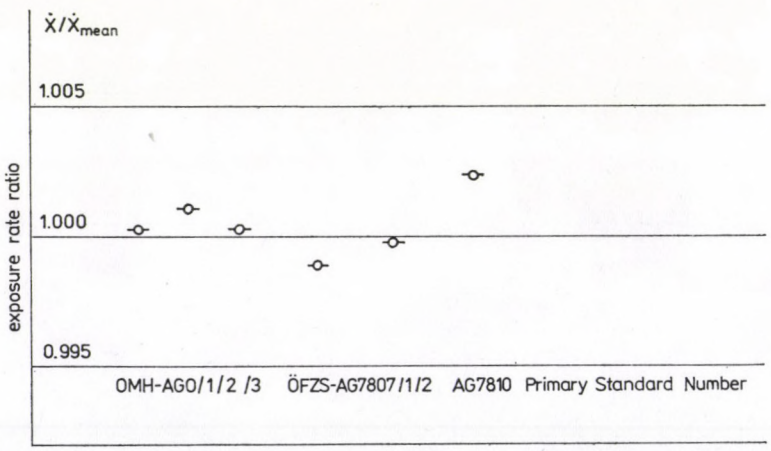

Fig. 5. Results of intercomparison measurements between the Austrian and Hungarian primary standard graphite cavity ionization chambers for ^{60}Co gamma radiation

2. Secondary standards

Three types of secondary-standard ionization chambers (Fig. 6) have been designed at OMH for dissemination of the dosimetry units derived from the primary standard chambers [3]. The smallest one of 1 cm in diameter may be used for therapy level measurements of X-rays. The energy dependence of this chamber is $\pm 1\%$ for X-rays in the range of 50—250 kV. For radiation-protection-level measurements ionization chambers of 40 and 140 mm diameter

have been designed at OMH. Their energy dependence is $\pm 2\%$ in the range of 30 keV to the energy of ^{60}Co gamma radiation ($\sim$1.25 MeV).

Precision digital current integrators (Fig. 7) were developed at OMH in 1970 for the accurate measurement of the currents from the primary as well as the secondary standard ionization chambers [4, 5]. A high-gain operational amplifier with MOS/FET input is used as a feedback type of current integrator, constituting in effect an automatic Townsend balance. Remote control inputs and digital outputs make the automation of the measurement process possible.

A series of OMH secondary standard ionization chambers and digital current integrators are used at the Austrian laboratory. Long-term stability tests with radium sources performed at Seibersdorf over a period of more than three years indicated a variation of well below 1% even with the largest chamber [6].

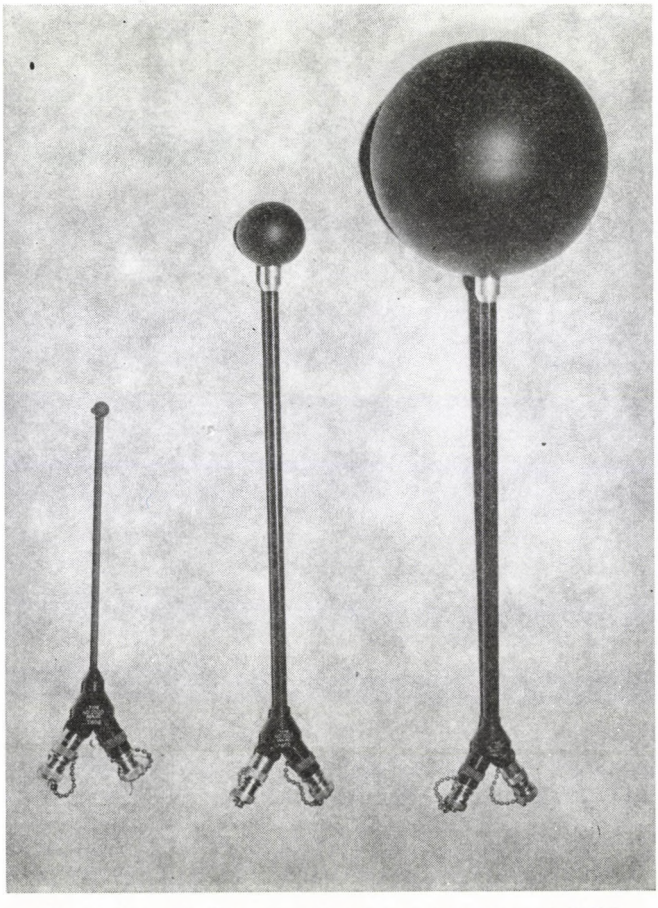

Fig. 6. Secondary standard ionization chambers of OMH.

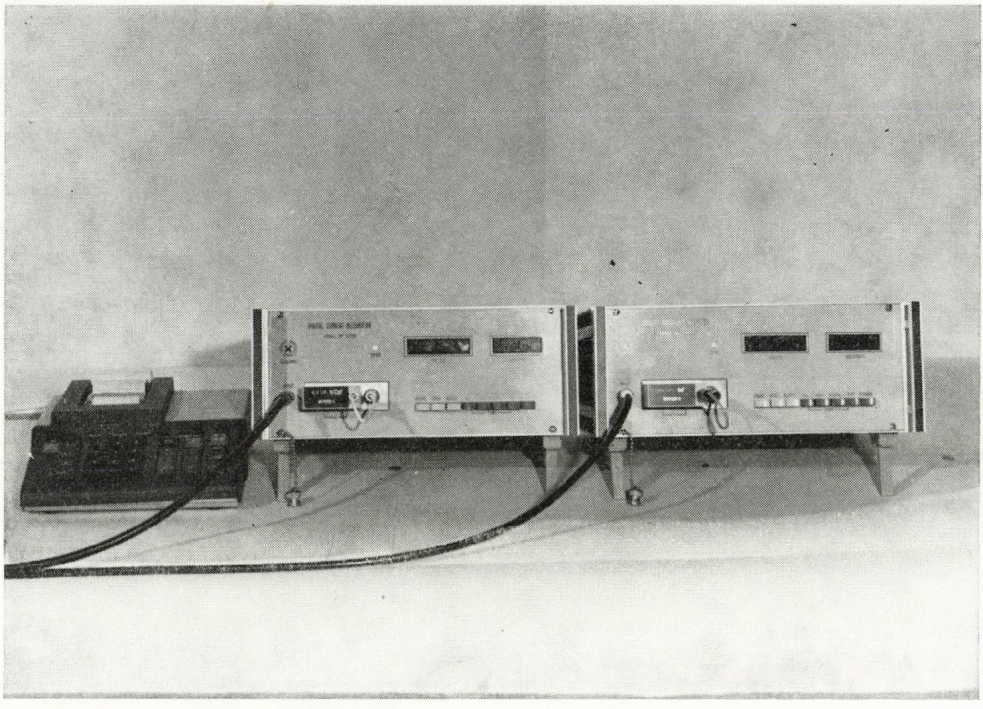

Fig. 7. Two digital current integrators with automatic control and printer equipment for the accurate measurements of the currents from ionization chambers.

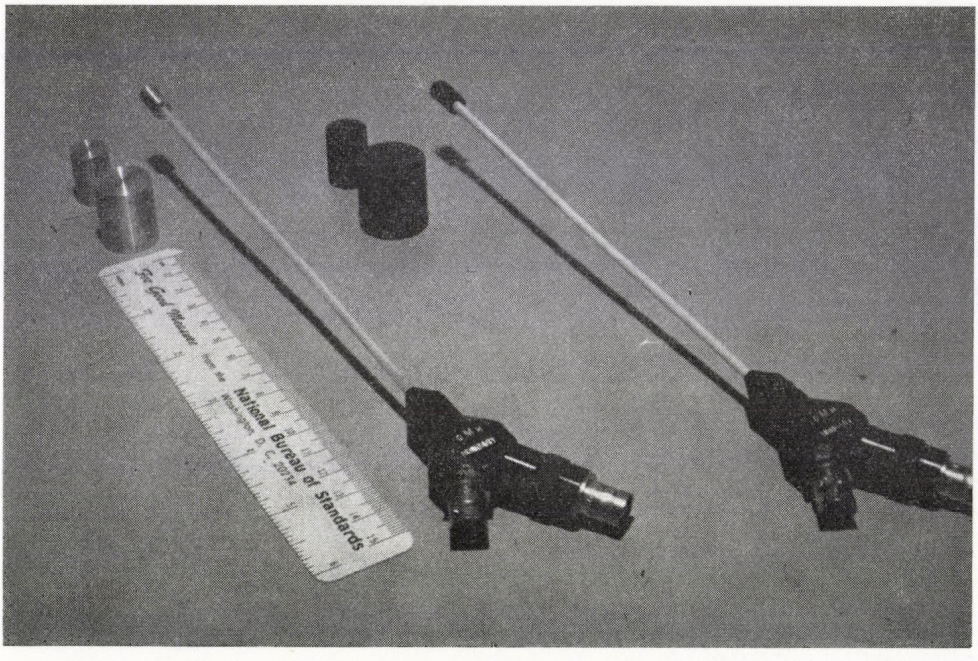

Fig. 8. Two mini-chambers made of aluminium and graphite.

3. Results of joint research projects

A joint research project of this co-operation resulted in the improvement of the secondary standard ionization chambers and the digital current integrator. A novel ionization chamber system with extremely large sensitive

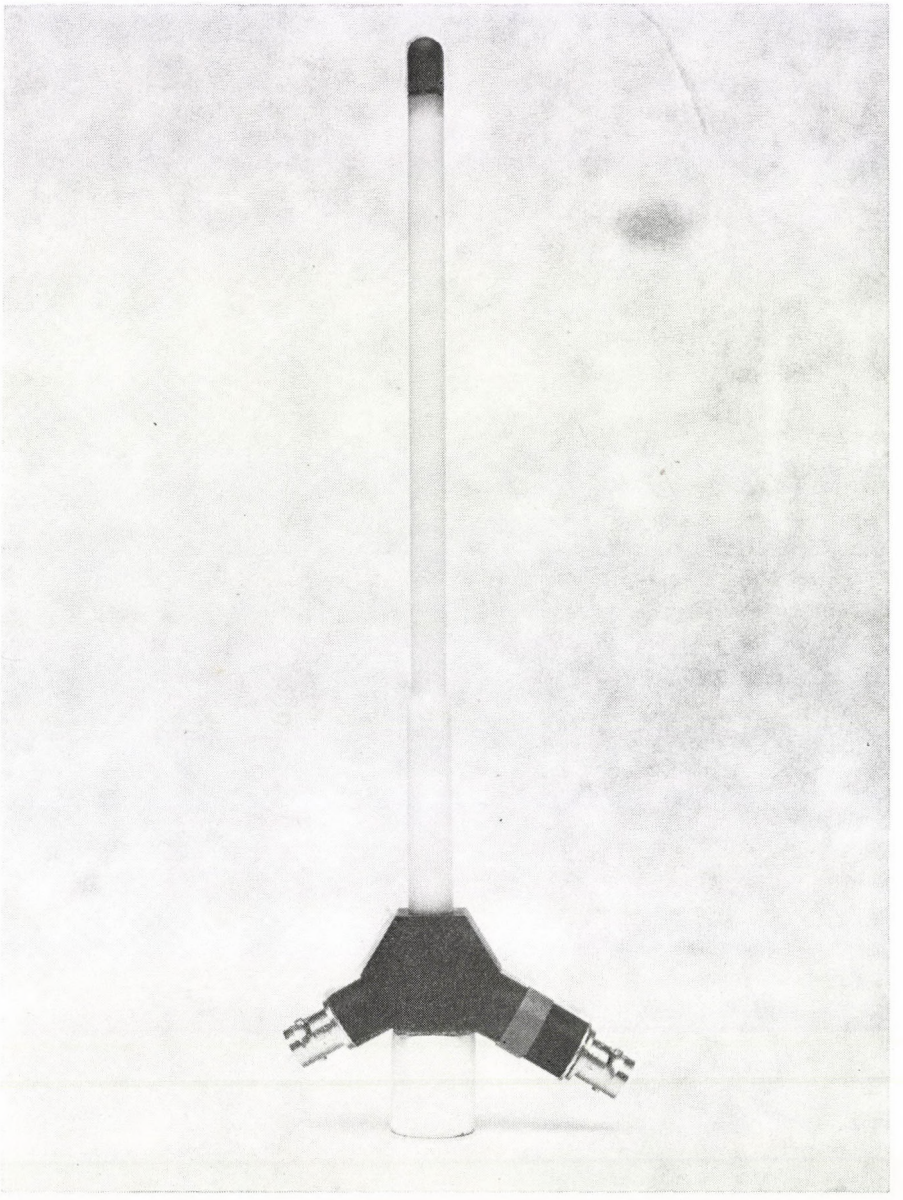

Fig. 9. Secondary standard ionization chamber for calibration of clinical dose meters in water-phantom.

volume of 10 l have been designed. It provides a sensitivy of about 0.1 μSv/h and low energy dependence. In the new model of current integrator a microprocessor unit provides automatic calculation of dose and dose rate based on the calibration factors stored in a PROM memory. This system may be used as Secondary Standard for environmental dosimetry. More details of this system have been published by DUFTSCHMID and HIZÓ [7].

Another joint research project is devoted to the development of an experimental method for the absolute determination of absorbed dose to water by cavity chambers traceable to primary exposure standards. The problem arising from the accurate determination of absorbed dose to water in water-phantom by ionization chamber measurement is the uncertainty in the energy absorption coefficients for water and the chamber material, respectively, caused by the unknown X-ray spectrum in water. The aim of this project is to determine the effective energy of different X-ray qualities in water using special miniaturized ionization chambers of homogeneous materials i.e. aluminium and graphite. From the measurements with both mini-chambers in water with various X-ray beams well defined by exposure standards the ratio of the energy absorption coefficients can be determined for the two materials.

The results can be applied to derive the effective energy in water and finally to calculate the absorbed dose to water.

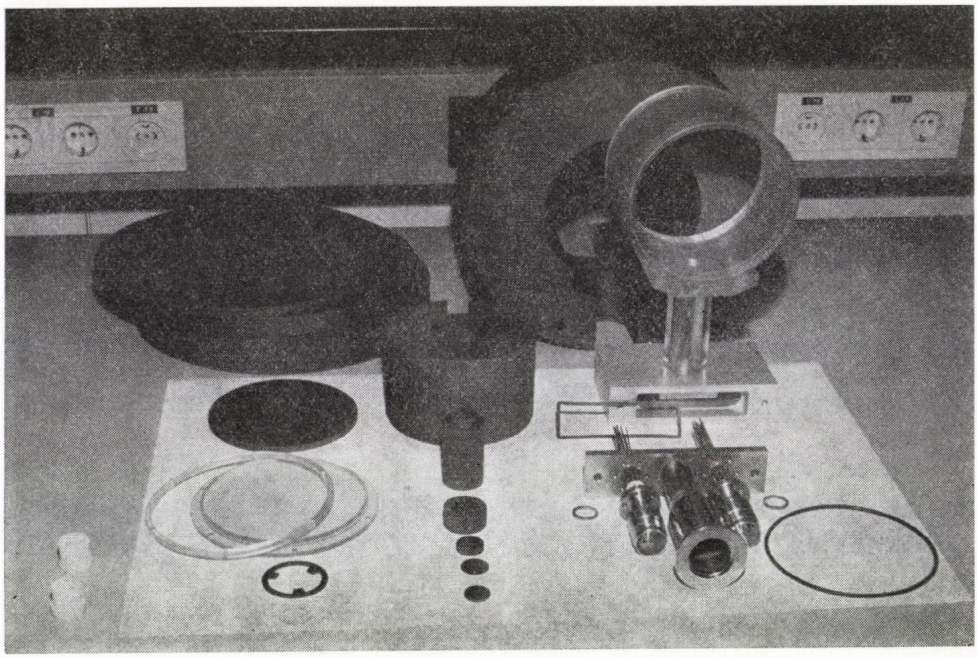

Fig. 10. Mechanical components of the graphite-calorimeter for absolute measurement of absorbed dose.

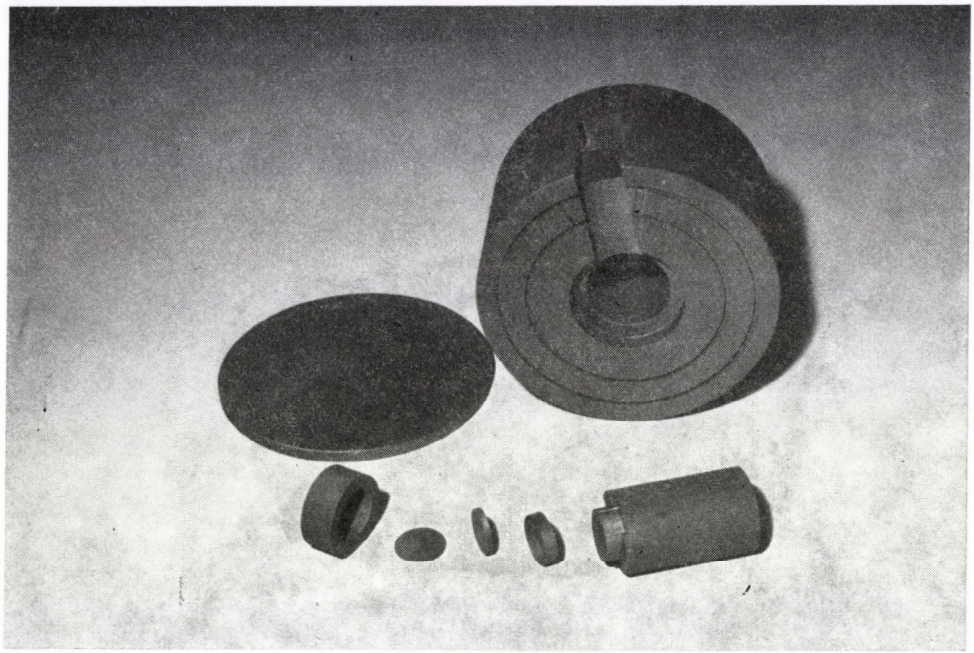

Fig. 11. Graphite components of the calorimeter: core, jacket, shield and medium including cover plate.

As a first step after constructing the two mini-chambers (Fig. 8) the effective collecting volumes have been radiometrically determined by free-air measurements in our well defined cobalt beams. The present results of this project have been discussed in detail with R. LOEVINGER of the US National Bureau of Standards (NBS) (Washington D.C.) and it has been agreed to continue this project also in cooperation with the NBS.

Our third joint project led to the design and construction of a new thimble chamber made from polyacetal resin mixtures (Fig. 9) which can be directly used in a water-phantom without additional protective covering. The sensitive volume of the chamber, approx. 0.3 cm^3 is covered by air-equivalent walls, the stem, however, is made from a water-equivalent material exactly equal in mass to the displaced water to minimize the influence of the chamber stem. This chamber can be used as an advanced secondary standard for therapy level measurements and is particularly useful as a reference instrument of absorbed dose determination in water.

A long-term joint research project is the development of a portable graphite calorimeter as a primary standard for absorbed dose measurement in co-operation with the IAEA Dosimetry Laboratory (Vienna), the US National Bureau of Standards and our Institutions. In co-operation with the inventor of the heat-loss compensated calorimeter, S. DOMEN (NBS), a proto-

type unit is now under development at Seibersdorf and Budapest. Figs. 10 and 11 show the components of the graphite calorimeter before final assembly. After completion and testing of the prototype three complete units will be manufactured by our common project team and each of them will be used as primary standard for absorbed dose at the dosimetry laboratories of IAEA Vienna, OMH Budapest and ÖFZS Seibersdorf.

In conclusion, it can be stated that the co-operation between the Austrian and Hungarian National Dosimetry Laboratories has resulted in significant developments and improvements to the mutual benefit of our countries.

REFERENCES

1. L. BOZÓKY, K. ZSDÁNSZKY and J. HIZÓ, Primary Standard Dosimetry in Hungarian and International Dose Intercomparisons since 1938, in Proc. Vienna Symp. on Biomedical Dosimetry, 1975, IAEA, Vienna, 405. 1975.
2. Le Bureau International des Poids et Mesures 1875—1975, BIPM, Sèvres pp. 187, 192, 1975.
3. K. ZSDÁNSZKY, Primary and Secondary Standards of Dosimetry, Calibration Methods in Hungary in Proc. Atlanta Symp. on National and International Standardization of Radiation Dosimetry, 1977, IAEA, Vienna, 107, 1978.
4. K. ZSDÁNSZKY, The design of High Impedance Measuring Circuit of High Accuracy for Picoampere Measurements, IMEKO V, Versailles, 1970, B-423.
5. K. ZSDÁNSZKY, Nucl. Instr. Meth., **112**, 299, 1973.
6. K. E. DUFTSCHMID, The Austrian Dosimetry Laboratory, a National Standard and Routine Calibration Centre in Proc. Atlanta Symp. on National and International Standardization of Radiation Dosimetry 1977, IAEA, Vienna, 199, 1978.
7. K. E. DUFTSCHMID and J. HIZÓ, Acta Phys. Hung. this issue, p. 275.

Acta Physica Academiae Scientiarum Hungaricae, 52 (3—4), pp. 275—282 (1982)

A SECONDARY STANDARD DOSIMETRY SYSTEM FOR CALIBRATION OF RADIATION PROTECTION INSTRUMENTS

K. E. DUFTSCHMID

AUSTRIAN RESEARCH CENTER SEIBERSDORF (ÖFZS)
SEIBERSDORF, AUSTRIA

and

J. HIZÓ

NATIONAL OFFICE OF MEASURES (OMH)
1124 BUDAPEST, HUNGARY

In view of the increasing need and accuracy requirements for the calibration of radiation protection dosimeters, a novel secondary standard system consisting of a low level ionization chamber with 10^4 cm^3 sensitive volume operating at ambient atmospheric pressure and an automated digital current integrator with dose/dose rate calculation has been designed.

The spherical ionization chamber of 27 cm diameter and 3 mm wall thickness is made from high pressure extruded polyacetal resins $(CH_2O)_x$ providing a rugged structure of excellent long term stability of sensitive volume combined with extremely flat energy response. The wall thickness of the chamber is sufficient for secondary electron equilibrium up to several MeV of photon radiation without additional build-up-caps, etc. For compensation of absorption in the low energy X-ray range a thin layer of higher Z-material is deposited on the inner wall surface. This technique results in an energy response showing a variation less than $\pm 1\%$ in the photon energy range of 0.03—1.3 MeV. Due to the spherical shape of the chamber and collecting electrode the directional sensitivity is highly uniform.

The central collecting electrode contains an axial tubing on guardring potential in order to insert an internal check source of 70 MBq ^{241}Am into the centre of the chamber without interfering with the electric field.

The measurement of the ionization current is performed with our digital current integrator model NP 2100. It basically consists of a MOS/FET electrometer with dual slope integrator working as TOWNSEND balance circuitry. The measurement signal is converted into dose and/or dose rate by a microprocessor unit using calibration factor stored in an exchangeable EPROM memory chip.

Using an intermediate transfer secondary standard chamber of 30 cm^3 volume the low level chamber can be connected to our primary standards, i.e. free-air-parallel-plate-chambers and absolute graphite cavity chambers with measured volume.

The limit of detection, defined by 3 standard deviations of the background reading is in the order of 0.1 μSv/h.

1. Introduction

The accurate measurement of ionizing radiation at low dose rate levels due to natural environmental background has gained increasing importance particularly in view of environmental monitoring around nuclear facilities. Although various radiation monitors based on GM-tubes, scintillators or high-pressure ionization chambers are used for this application, it has been difficult to perform accurate calibration of such instruments in terms of exposure or

dose equivalent rate since no secondary standards have been available for this range.

In order to overcome this problem we have developed a novel low level secondary standard dosimetry system consisting of a large spherical ionization chamber of 10^4 cm^3 sensitive volume operated at atmospheric pressure and a digital current integrator.* The fully automated system can be used for photon radiation of 0.02 MeV up to several MeV and dose rates in the range of 0.1 μSv/h to 1 Sv/h for an integration time of approximately 100 s.

2. Ionization chamber

Existing secondary standard ionization chambers for therapy level radiation are generally made from graphite as the wall material to obtain good long-term stability of volume. A sufficiently flat energy response is provided mostly with a collecting electrode made from Al. Our approach is based on polyacetal resins $(CH_2O)_x$ as the wall material which provides excellent mechanical properties assuring the necessary long-term stability combined with a chemical composition which can be made virtually air, tissue, or water equivalent by small additions of polytetrafluoroethylen (PTEE) and/or traces of higher Z-materials such as CaO or Al. Using a special mould the spheres of the chamber are manufactured by high pressure extrusion, with the dimensions 270 mm internal diameter and 3 mm wall thickness. The central electrode is made from a styrofoam ball of 80 mm diameter coated with graphite.

Fig. 1 shows the basic details of construction.

Due to this spherical shape of chamber and collecting electrode the directional response is highly uniform.

The wall thickness of 3 mm is sufficient to provide secondary electron equilibrium up to several MeV. On the other side the absorption of soft X-rays in the wall is compensated by a thin layer of higher Z-material on the inner surface of the chamber. This electrically conducting coating generates a higher photoelectron yield for soft X-rays compensating for absorption and becomes negligible at higher energies. By this method an energy response of better than $\pm$ 1% between 0.03 MeV—1.2 MeV or $\pm$ 2% down to 0.02 MeV effective energy can be achieved without build-up caps, etc.

Fig. 2 gives the energy response measured between 38 keV_{eff} and ^{60}Co.

In order to verify the constancy of calibration an internal check source of 74 MBq (2 mCi) ^{241}Am can be inserted into the centre of the chamber by an axial tube protruding through the collecting electrode. The tube is kept on guardring potential to avoid interference of the measurement when the check

* International patents

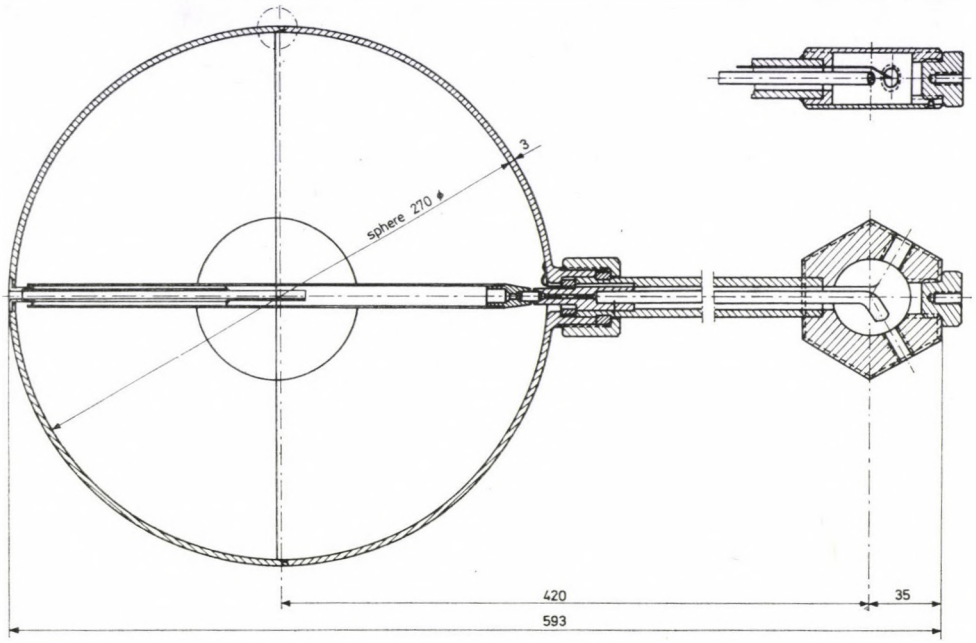

Fig. 1. Assembly drawing of ionization chamber.

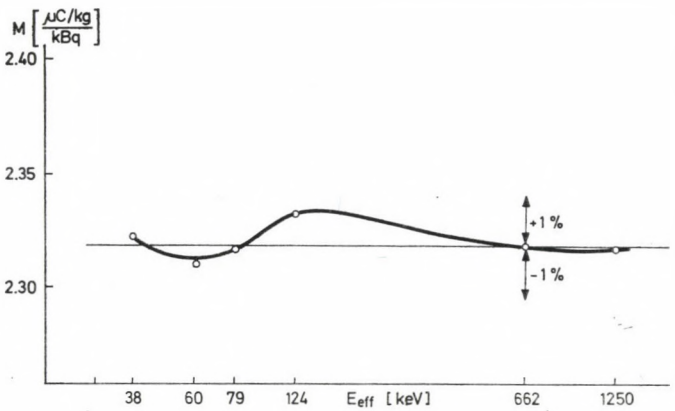

Fig. 2. Energy response of low level secondary standard chamber.

source is inserted. The activity of the source is low enough to avoid any radiation protection precautions, the surface dose rate being only 2 μSv/h but sufficient to generate a signal equivalent to approx. 15 μSv/h with a standard deviation in the order of 0.1%. The chamber is mounted on a stem with a terminal box on the other end containing signal and high voltage connectors and a mounting screw for a tripod.

Fig. 3 is a photograph of the complete chamber assembly.

Fig. 3. Low level chamber on tripod.

3. Digital current integrator

The design of the digital current integrator model NP 2100 is explained in the simplified block diagram Fig. 4.

It basically consists of a MOS/FET electrometer amplifier connected to an automatic TOWNSEND-balance circuitry designed by ZSDÁNSZKY [1, 2]. With an offset current below 10^{-15}A ionization currents in the range of 10^{-12}A to 10^{-7}A can be measured within $\pm$ 1% error. To provide a wide dynamic range exchangeable measurement capacitors (C) are used in the range of 0.1 nF—100 nF.

The output signal of the digital current integrator is fed into a microprocessor circuitry containing a 1 k$\times$8 bit CPU with 64 byte RAM and 6 MHz quartz clock. An additional 320 byte RAM controlled by the CPU operates as a buffer. The calibration factors of up to 8 different chambers and 10 radiation

qualities are stored in an exchangeable memory chip (2 k×8 bit EPROM) together with the accurate capacitance values of C.

With atmospheric pressure, temperature and radiation qualities manually set with BCD thumbwheel switches on the front panel dose or dose rate are calculated from the integrated voltage signal by an arithmetic processing unit in the microprocessor. The LED display includes voltage signal, dose with prefix and unit (Gy) and integrating time. The results are printed by a miniaturized alphanumeric printer including mean-value and standard deviation for repeated measurement cycles. Fig. 5 is a photograph of the digital current integrator.

4. System calibration and performance

In order to qualify as a secondary standard the instrument has to be calibrated by primary standards per definition. The Austrian primary standards for exposure are operated at our Dosimetry Laboratory Seibersdorf [3]. For X-rays in the energy range of 5—400 kV three free-air-parallel-plate-chambers are used. For gamma radiation of ^{137}Cs and ^{60}Co graphite cavity chambers of measured volume are applied.

Because of the large difference in sensitive volume or diameter of entrance diaphragm (approx. 1 cm) resp. of the primary standards compared to the secondary standard chamber (27 cm dia.) direct intercomparison is not feasible in view of the different beam size required. Therefore, the calibration is made through an additional transfer chamber of 30 cm^3 volume which can be directly

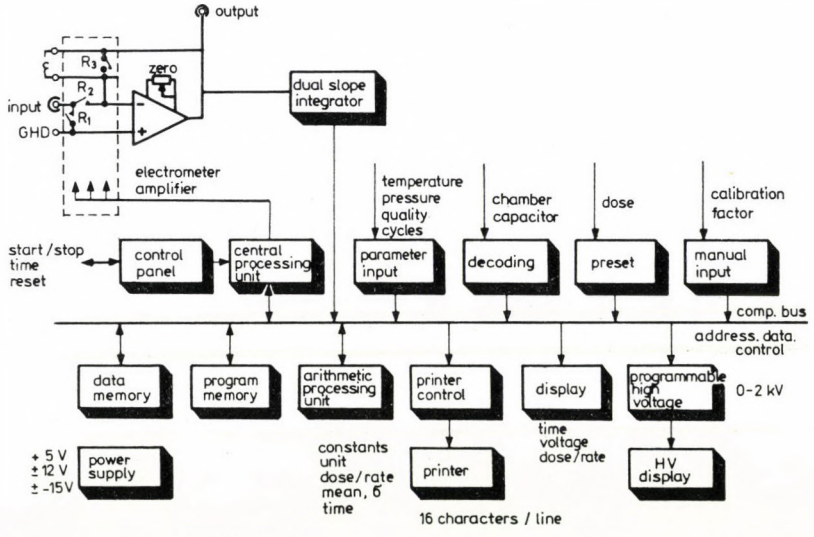

Fig. 4. Simplified block diagram of digital current integrator NP 2100.

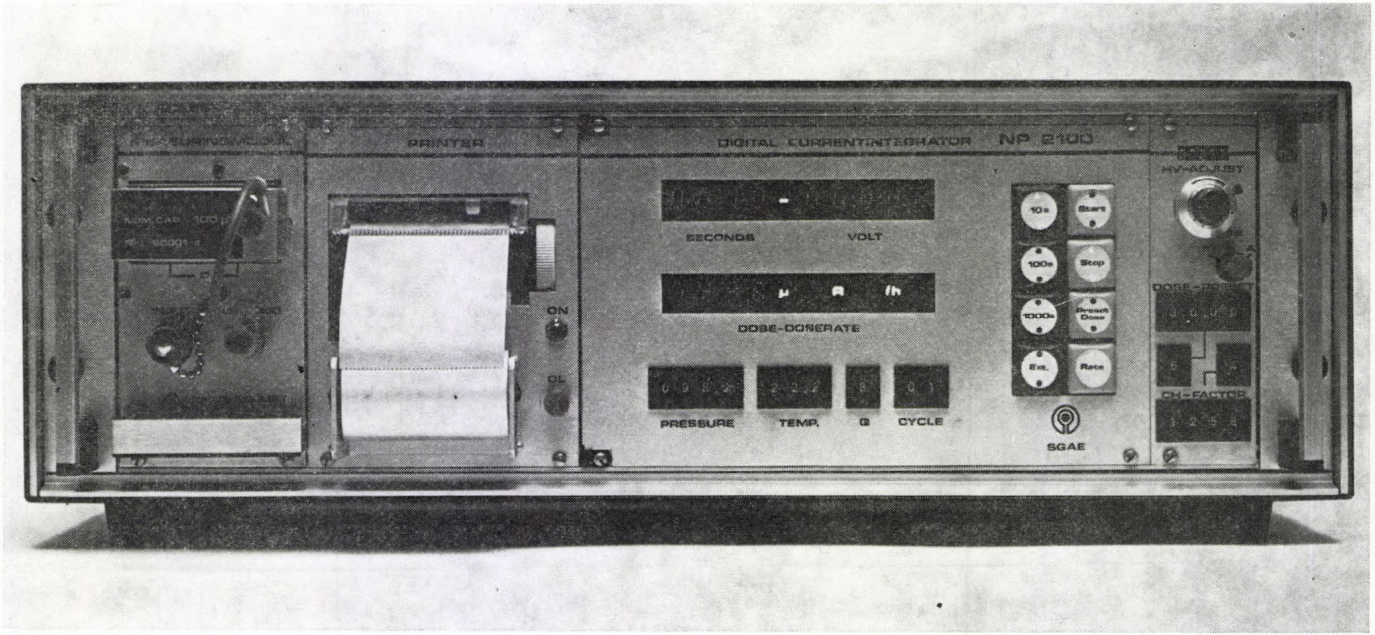

Fig. 5. Digital current integrator NP 2100 — Front panel.

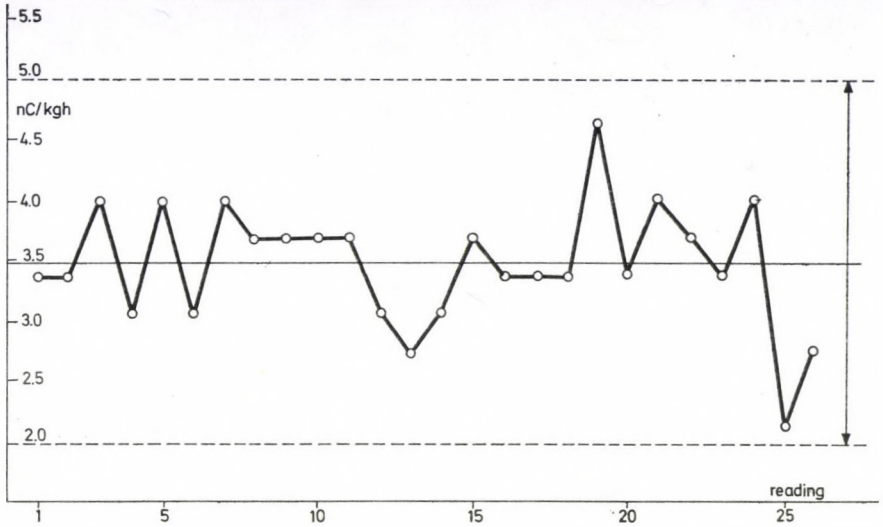

Fig. 6. Variation of background readings — Limit of detection.

compared with both the primary and secondary standard at different distances. After calibration of the chamber in units of exposure the limit of detection has been determined by repeated measurements at environmental background radiation levels. In Fig. 6 a series of 25 consecutive background readings are plotted. With a mean value of 0.136 μSv/h the standard deviation is 0.019 μSv/h. The limit of detection defined by 3 standard deviations of the background reading (99.7% confidence level) is therefore approximately 0.06 μSv/h.

The upper limit of dose rate measured with this chamber is determined by the saturation effect. With a polarizing voltage of 1500 V the saturation loss is 0.5% at 0.1 Sv/h and 5% at 1 Sv/h.

5. Conclusion

The system described is a useful secondary standard for calibration of environmental radiation monitoring instrumentation at dose rates well below 10 μSv/h.

The ionization chamber provides excellent energy response, directional response and long-term stability combined with a low limit of detection in the order of 0.1 μSv/h and a large dynamic range over seven orders of magnitude. The computerized digital current integrator with automated dose/dose rate calculation makes the system a very convenient tool for routine measurement and calibration at low dose rates frequently needed for dosimetry laboratories or calibration facilities.

REFERENCES

1. K. ZSDÁNSZKY, Primary and Secondary Standards of Dosimetry. Calibration Methods in Hungary, in Proc. Atlanta Symp. on National and International Standardization of Radiation Dosimetry, 1977, IAEA, Vienna, 107, 1978.
2. K. ZSDÁNSZKY, Nucl. Instr. Meth., **112**, 299, 1973.
3. K. E. DUFTSCHMID, The Austrian Dosimetry Laboratory, a National Standard and Routine Calibration Centre, in Proc. Atlanta Symp. on National and International Standardization of Radiation Dosimetry, 1977, IAEA, Vienna, 199, 1978.

Acta Physica Academiae Scientiarum Hungaricae, 52 (3—4), pp. 283—289 (1982)

THE ROLE OF RADIOACTIVITY STANDARD REFERENCE MATERIALS IN HUNGARIAN HEALTH PHYSICS PRACTICE

Á. SZÖRÉNYI

NATIONAL OFFICE OF MEASURES (OMH
1124 BUDAPEST, HUNGARY

Radioactivity Standard Reference Materials (RSRMs) have been issued by the National Office of Measures (OMH) for more than ten years. At the present time OMH offers various solutions and solid standards for over 50 radionuclides. The interest in RSRMs has especially increased since 1976 after the issue of the Government Decree on Measures. The paper shows the role of RSRMs by several examples in radiation protection of nuclear power plants and in nuclear medicine. Suitable absolute and relative methods and equipment have been developed for the activity determination of RSRMs of very different forms. The equipment and their most important parameters will be briefly reviewed.

Introduction

After the commencement of measurements in the field of dosimetry in the early 1960s the National Office of Measures (OMH) extended its activities to the metrology of radionuclides, the use of which spread rapidly in the various fields of application in Hungary. In 1965 we succeeded in completing the design of our first coincidence equipment suitable for measuring the activity of a number of radionuclides by absolute method. Some years later we started nuclear spectrometric measurements to determine the radionuclidic impurity in radioactive sources.

This research work was followed in the late 1960s by the preparation of Radioactivity Standard Reference Materials (hereinafter RSRMs) offered for sale by the Institute of Isotopes of the Hungarian Academy of Sciences. Interest in RSRMs has particularly increased since 1976, after the issue of a Government Decree on Measures. According to the Decree measurements involving legal responsibility (for example metrological supervision, measurements in the field of health physics, commercial accounts) can be made by verified measuring instruments only. Part of the measuring instruments used in health physics practice will be verified (or a control being equivalent to verification) by means of RSRMs, which will be illustrated by some examples hereafter.

The application of RSRMs in different fields

As the first Hungarian nuclear power plant to be put into operation in the near future requires a high level of safety, several thousands of measuring instruments, among others instruments for radiation protection, are applied to supply the data necessary for the checking. The instruments for radiation protection include, in addition to those used in dosimetry, surface, liquid and gas activity measuring equipment. These instruments have been tested by type at OMH. Measuring instructions and RSRMs have been worked out to control their operation before and in application (periodical control) and/or after repairs.

The radiation protection system involves a number of surface, body and clothing monitors for the control of which large surface standards are needed. $^{90}Sr(+^{90}Y)$ standards with a 600 cm^2 active surface were prepared for example for the verification of clothing monitors. The standards were designed to provide sufficient sealing and mechanical protection while using a protecting layer of minimum thickness. In the certificate of these standards emission rate was also given in addition to surface activity. (At 99% confidence level the overall uncertainty of surface activity amounted to $\pm$ 2% and that of the emission rate to $\pm$ 3%). Moreover, ^{45}Ca and ^{204}Tl standards of similar sizes were prepared for the study of the energy-dependence of monitors.

To test the instrument measuring the total beta-activity a series of ^{60}Co standard sources was prepared in the activity range of 40 kBq—90 MBq. These standards are point sources on a polystyrene holder in a 17 mm aluminium frame. RSRMs play an important role in health physics, too, to optimize the dose burden of patients to be cured (and/or examined). Recently, radioisotope calibrators (previously called dosis calibrators) have found general application in Hungarian clinics; the activity of radioactive solutions can be easily and reliably checked in the syringe or in the ampoule before dosage. Our early experiences have proved that these calibrators should be submitted to metrological supervision, too, which is currently in progress: The clinics receive RSRMs of an activity unknown to them, they have to measure in the way they generally do and to submit the result in a questionnaire to OMH. OMH will deal with those calibrators only whose measured values are not within the prescribed uncertainty limits. Calibrators measuring satisfactory values are considered to be verified. Control measurements have been made first with ^{125}I and ^{131}I standardized solutions, but we plan to apply gradually other isotopes as well.

This form of metrological supervision is considered to be superior to the present verifications, since in this case not only the correct operation of the measuring instrument but the measuring process as a whole is controlled.

In addition to the RSRMs applied for the above purposes, many other

kinds of RSRMs are permanently supplied by OMH. The assortment of standardized solutions and solid standards made of 53 radionuclides is listed in our Catalogue, including nuclides with different decay schemes such as pure β-emitters (^{35}S, ^{32}P), others with $\alpha-\gamma$, and $\beta-\gamma$ coincidence decay schemes (^{241}Am, ^{131}I, ^{60}Co) and electron capture nuclides (^{125}I, ^{75}Se, ^{57}Co), etc. RSRMs are prepared as shown in Fig. 1. As it appers from the block diagram, high importance is attributed to checking the validity of certified values [1]. Therefore, for example, the activity is determined by means of a calibrated ionization chamber and a calibrated Ge(Li) detector, too. The traceability to previous standardizations can also be provided for nuclides of short half-life.

Standardized solutions are prepared of all types of nuclides listed in our Catalogue, while solid standards are generally made of γ-emitters only. A set of 8 standards, which can be selected of 9 nuclides, deserves special attention. This set is used of the energy and efficiency calibration of Ge(Li) semiconductor γ-spectrometers and is available in three different types.

Other standards satisfying special requirements are also produced: a pair of ^{133}Ba solid standards for blood volume determination, ^{125}I solid standards for sample changer measuring equipment for therapeutic purposes, as well as quartz sand labelled with γ-emitter of various specific activities.

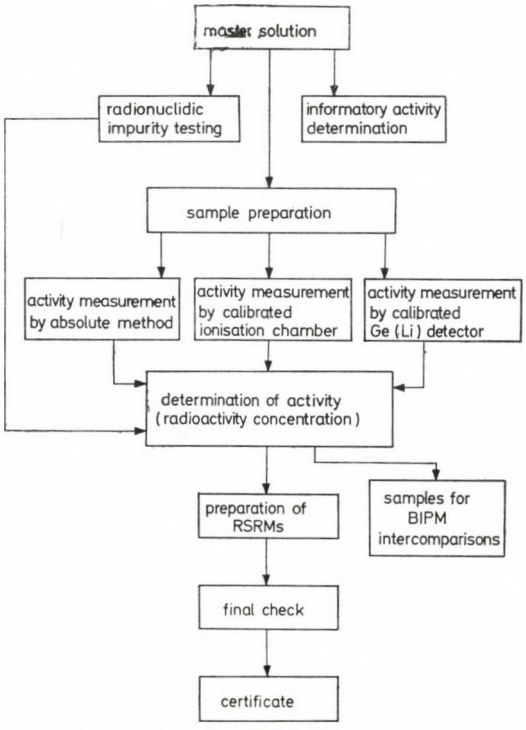

Fig. 1. Block diagram of the production of RSRMs.

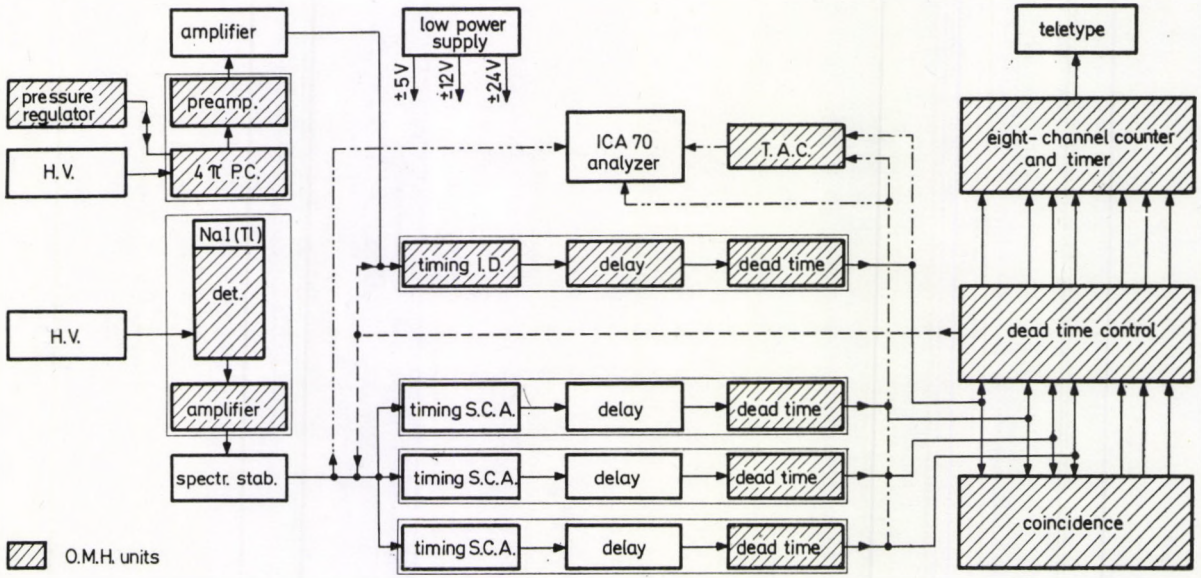

Fig. 2. Block diagram of coincidence equipment with 4π pressurized proportional counter.

Activity determination

In the last 15 years absolute and relative measuring methods and apparatus haven been developed to determine the activity (or the emission rate) of the various types of RSRMs of different forms. We have found that more than two thirds of the nuclides occurring most frequently in practice can be measured with the highest accuracy by one of the coincidence methods (α—γ, β—γ, x—γ, etc.). A coincidence method is used for nuclides where the radioactive decay is followed within a very short time ($\leq \mu$s) by the emission of at least two particles or photons. In this case we need a measuring equipment in which a first detector measures selectively one of the emitted particles, the second detector the other one and the number of coincidence events occurring during the measuring time are determined simultaneously. OMH has several equipment of this type [2], [3]; the block diagram of the coincidence equipment with 4π pressurized proportional counter is shown in Fig. 2.

The 4π pressurized gas-flow proportional counter is placed in common lead shielding and immediately below it there is a NaI(TI) scintillation detector for γ-photon detection. To avoid perturbing effects and to simplify the mechanical construction the 4π proportional counter is built in with a voltage preamplifier designed by OMH. The energy equivalence of the discrimination level is 100 eV. The counter is dimensioned according to the size of the counter operating in the Physikalisch-Technische Bundesanstalt (Braunschweig, GFR), but slightly modified according to our purposes. Since the counter will be operated under a pressure not exceeding 2 MPa and the wall thickness shall be of minimum size, materials of particularly great strength had to be used (AlCuMg alloy). We succeeded in reducing the thickness of counter wall, which is an absorbent layer regarding the detector, to 2 mm. The sensitive volume of the cylindrical counter is $\varnothing$ 40 $\times$ 40 mm and the sample is placed between two anode wires. The anode wire holders strengthened by sticks can be removed easily from the counter together with the teflon insulation and this is convenient when replacing the wires. Stainless steel wire of $\varnothing$ 30 μm is used as anode.

During the measurement constant pressure is provided in the proportional counter by a gas pressure control system and the pressure in the counter is continuously compared to the pressure set in the reference vessel of the gas pressure control system.

The electronic system of the equipment consists of units designed in accordance with the standard specification of Nuclear Instrument Modules. These units are partly designed by OMH and are partly available in commerce. A teletype puncher coupled to the equipment facilitates the computer-aided processing of measuring data. The measuring apparatus is suitable for so-called multigamma measurements, which makes it possible to measure the activity

simultaneously in several settings by using several differential discriminators in the γ-channel, and thus several coincidence circuits as well as counters. In this way we can increase the accuracy while the measuring time remains the same or reduce the time while the same accuracy is maintained. Moreover, the simultaneous measurement facilitates an easier estimation of the effect of possible external disturbances. The multigamma mode is advantageous for measuring the activity of ^{133}Ba, ^{88}Y and ^{152}Eu nuclides.

In the past few years we have designed several other measuring instruments and modernized the older ones (e. g. a liquid scintillation equipment, an α-counter with defined solid angle). The large-surface proportional counter should be especially emphasized [4]. The latter measuring apparatus designed in bilateral cooperation between the Mendelejev Institute (VNIIM), Leningrad, and OMH, consists of three main units (4π proportional counter, gas pressure control system and electronic units). The block diagram is shown in Fig. 3. This apparatus enables us to determine the activity and the emission rate of α- and β-standards of large surfaces, which are of great importance in radiation protection. The counter consists of two halves, each of them is a 2π counter itself. The large-surface source is placed in a framing in the middle between the two halves so that the source holder constitutes one of the walls of the counter. In each half counter there are three constantan anode wires of $\varnothing$ 100 μm separated from each other by shielding electrodes. The wire system of the counter is designed so that both halves can be separated electrically by an external switch. The whole 4π counter is placed in a sealed glass bell. Sources of max. 200 cm^2 can be measured. The most important parameters of the apparatus, such as length and slope of the counter plateau, detectable energy, position dependence of the counter and background were evaluated and found to be satisfactory [4]. The activity range for α-emitters is 0.5 Bq—20 kBq, for β-emitters 20 Bq—25 kBq and thus the apparatus is suitable for measuring directly the activity and the emission rate of large-surface RSRMs necessary to verify surface monitors. The overall uncertainty depends on the radionuclide and the activity, too, but the systematic uncertainty evaluated according to ICRU Report 12 (1968) is not higher than $\pm$ 3%.

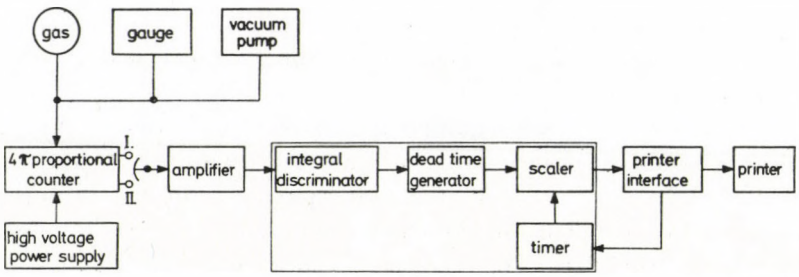

Fig. 3. Block diagram of 4π large surface proportional counter.

Conclusions

To determine the activity (the radioactivity concentration) of RSRMs, OMH applies high-precision absolute measuring methods, therefore it is not necessary to calibrate the measuring apparatus in advance or to use some standard sources.

In spite of all that we are making further efforts to check the correct operation of measuring instruments. Since measuring apparatus of similar type are not used by any other organization in Hungary, they can only be checked by bilateral or multilateral intercomparisons. Such intercomparisons are regularly organized by the International Bureau of Weights and Measures (BIPM, Sèvres), by the Metrological Section of the Standing Committee for Standardization as well as by the Committee for Peaceful Uses of Atomic Energy of COMECON. In the past few years we have participated in several intercomparisons (^{99}Mo, ^{125}I, ^{133}Ba, ^{134}Cs, ^{241}Am, etc.) the results of which have definitely proved the correctness of our measuring methods and apparatus [5], [6].

Finally, it can be stated that by applying methods and apparatus described above we succeeded in developing the most important and widely used RSRMs for radiation protection in Hungary. In the future we wish to enlarge the assortment regarding the type of nuclides and the form of RSRMs in compliance with the users' requirements.

REFERENCES

1. L. Szokolyi, Á. Szörényi and K. Zsdánszky, Mérésügyi Közlemények, **XX**, 82, 1979 (in Hungarian).
2. Á. Szörényi, Mérésügyi Közlemények, **XXI**, 14, 1980 (in Hungarian).
3. Á. Szörényi, Mérésügyi Közlemények, **XXI**, 25, 1980 (in Hungarian).
4. V. J. Aleksejev, Á. Szörényi and M. Csikós, 4π proportional counter for activity measurement of large surface α- and β-standards in Proc. of COMECON Symposium on Production and Checking of Radioactive Standards, Marianske Lazne, ČSSR, 14—19 May 1979, 77.
5. Á. Szörényi, Izotóptechnika, **21**, 186, 1978 (in Hungarian).
6. L. Szokolyi and Á. Szörényi, Results and Experiences of Latest Activity Intercomparisons, Proc. of Second Symposium on Radiochemistry, Debrecen, 3—5 November 1980, 239.

Acta Physica Academiae Scientiarum Hungaricae, 52 (3—4), pp. 291—296 (1982)

II. INTERNAL CONTAMINATION

CHAIRMEN: N. VANA, K. ZSDÁNSZKY

RADIATION EXPOSURE AND ASSOCIATED CANCER RISK DUE TO RADON AND DECAY PRODUCTS

E. POHL, F. STEINHÄUSLER, W. HOFMANN and J. POHL-RÜLING

DIVISION OF BIOPHYSICS, UNIVERSITY OF SALZBURG
A-5020 SALZBURG, AUSTRIA

The atmospheric content of radon and its decay products, especially in buildings, represents a significant contribution to the radiation exposure of man even in a normal environment. A study in Salzburg-City/Austria over several years was carried out in over 1000 working-, living- and bedrooms. Dose calculations were performed for 729 test persons, considering individual differences in age, sex and life-style and atmospheric nuclide concentration at different sites.

Induction of lung cancer caused by inhalation of radon and its decay products was correlated with cumulative exposure based on experience with lung cancer incidence amongst uranium miners. It was shown for Salzburg City that 15 to 35% of the observed number of lung cancer cases may be induced by radon and its decay products, although Salzburg is an area with a "normal" natural radioactive environment.

Introduction

Although the first scientific evidence of the problem of indoor exposure from the natural radiation environment (NRE) dates back to as early as 1956 [1] national and international institutions have long underestimated its significance up to the present days. This lack of interest is signified by a regulatory framework that is inadequate with regard to the setting of practically applicable standards for optimized radiation protection of the public to NRE levels.

The dilemma is added to by restriction of existing recommendations of dose limits, i.e. they are not regarded to apply to "normal" levels of the NRE, unless they result from man-made activities or occur in special environments. The ambiguity of the terms "normal" and "man-made" becomes evident, if either worldwide data on the dose range for members of the public resulting from the "normal" NRE are considered [2], or e. g. the use of natural stone with elevated radionuclide levels by man as contruction material.

Recently potential problems of public health associated with the indoor radiation exposure of large population groups attracted significant exploitation by the media, e.g. in Sweden and Canada. In the future an exposure increase of the general public can be anticipated:

a) energy conservation measures demand the reduction of ventilation rates and the increased use of air-recirculation, causing an increase of radon

levels and dose-determining equilibrium fraction between radon and its decay products.

b) concern about the environmental impact of large amounts of industrial waste products (coal as fuel, tailings from the mining and phosphate industry) stimulates the recycling of these waste materials as construction material. Due to technological enrichment processes some of these new materials show a high content of radium 226.

The basis for a rational assessment of potentially harmful health effects due to indoor exposure is profound scientific and technical data on indoor radiation sources and radionuclide levels as well as the quantitative determination of the radiation burden resulting from the various superimposed locally and temporally varying NRE components. For the assessment of the radiation induced risk of a given population group it is necessary to determine annual mean doses for the respective radiation-sensitive organs and tissues of a representative group of test persons. This way the frequency distribution of organ-specific annual doses can be determined for the population under study and the risk assessed for epidemiological investigations [3].

Radiation burden in a "normal" urban environment

A typical Central European city (Salzburg, Austria) was selected to assess the risk for lung cancer induction associated with "normal" exposure to radon and its daughters. The geological subsoil of Salzburg City (about 130 000 inhabitants) is mainly lime stone and gravel with a generally low content of natural radionuclides. There are no radioactive wells and the mean radon concentration of the drinking water supply is only 1.63 Bq m^{-3} [4]. Gamma spectrometric analysis of building material samples showed low nuclide concentrations for ^{238}U, ^{226}Ra, ^{232}Th, ^{228}Th and ^{40}K [5]. Altogether more than 1000 rooms were investigated by using combined radon grab-sampling methods together with continuous measurements of radon and daughters at selected control stations (over 5000 measurements). The methodology has been described in detail elsewhere [4].

The results of the measurements have shown that about 70% of the rooms have mean values less than or equal to 22 Bq m^{-3} which is low compared to the global average indoor radon concentration of 37 Bq m^{-3} [2]. However, despite this low radon concentration in most cases, in about 15% of the rooms the annual mean radon concentration ranges from 37 to 185 Bq m^{-3}.

From the results of the indoor filter measurements the mean equilibrium factor F was determined as $F = 0.6 \pm 0.1$. In some selected buildings atmospheric concentrations of ^{210}Pb and ^{212}Pb were also measured, the latter contri-

buting significantly to the dose of the respiratory tract. The mean values at the different sites ranged from 1.48×10^{-3} Bq m^{-3} to 7.4×10^{-3} Bq m^{-3} for ^{210}Pb, and from 0.37 Bq m^{-3} to 22.2 Bq m^{-3} for ^{212}Pb.

Individual lung dosimetry

Lung dosimetry is commonly based on the anatomical and physiological data of the so-called Reference Man [6]. These characteristics, however, apply only to a small percentage of a given population. Therefore, for epidemiological investigations, such as lung cancer incidence, the use of Reference Man should be improved by the application of dose modifying factors which account for the variety of personal characteristics. The most important personal parameters of a healthy individual for lung dose assessments are age, sex, body size, weight and physical activity. For the simulation of their influence on deposition, retention and radiation dose, a multiparameter computer model for inhaled alpha-emitting nuclides, called "LUMO", was developed [7]. With the use of this model correction factors were obtained for the deviations of an individual from the characteristics of Reference Man with special emphasis on age.

Dose calculations were carried out for 729 demoscopically selected test persons, considering individual differences in age, sex and life-style and atmospheric nuclide concentration at different sites. In this manner dose frequency distributions rather than only mean or extreme values could be evaluated for the population of Salzburg City. Applying a quality factor of 20 for alpha-radiation, Fig. 1 represents the frequency distribution of the basal cell doses in segmental bronchioles for the 729 test persons. Although the general level of the natural radiation environment in Salzburg is low, it is remarkable that for these cells about 2% of the population, i.e. about 300 people are exposed to levels between 60 and 215 mSv/yr.

This wide range of individual doses is caused only by differences in the radionuclide content of the inhaled air and personal characteristics of the test persons. For the latter, however, this still does not include dose modifications due to biological variabilities. Individual differences in the anatomical structure of the lung, respiration standards as well as clearance half-lives can be observed even for people of the same age, sex, etc. Therefore, biological data in lung dosimetry should be represented in terms of probability distributions. Describing the stochastic nature of the processes we used the Monte Carlo techniques, and as the result of such a simulation not only mean values but also probability distributions for the quantities of interest will be obtained [8]. Using experimental data for the biological parameters involved, log-normal basal cell dose distributions were obtained with a median which differs only slightly from the deterministic mean and a geometrical standard deviation of about 2.5.

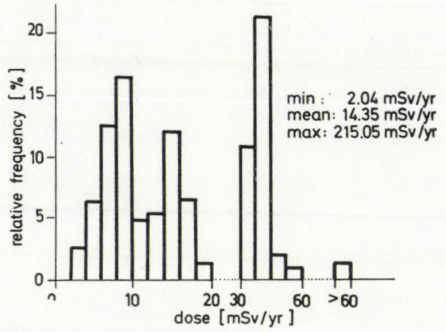

Fig. 1. Dose frequency distribution in the "normal" urban environment of Salzburg City, Austria.

A second source of randomness in lung dosimetry is caused by the stochastic nature of discrete energy-loss events in microscopic regions. Therefore, at the dimensions of single cells or cell organelles the concept of absorbed dose loses its significance and should be replaced by the corresponding microdosimetric quantities, e.g. specific energy [8]. Considering all sources of stochastic effects in the basal cells of the bronchial epithelium, a log-normal specific energy distribution was obtained again. These microdosimetric effects cause an additional dispersion of the basal cell dose distribution in Fig. 1.

Lung cancer risk

The indoor exposure of man at environmental levels of natural radioactivity accounts for the largest of the radiation burden of the general public. Since the dose to the basal cells of the bronchial epithelium from inhaled radon daughters exceeds the dose from external radiation typically by an order of magnitude, the risk for lung cancer induction from radon daughter inhalation is also much higher. At present the only available data for risk assessments from radon daughter exposure are derived from epidemiological studies of occupationally exposed workers in mining environments. Applying information derived from the correlation of past radon daughter exposure and lung cancer induction amongst miners to NRE exposure indoors is a controversial issue. In Table I pro and contra arguments about the validity of this extrapolation are summarized.

Based on the latest UNSCEAR report [2] the life time risk factor (r_t) for lung cancer induction from the inhalation of radon daughters ranges from 20×10^{-5} to 45×10^{-5} per working level month (WLM) exposure of the bronchial epithelium. The exposure of 1 WLM corresponds to a dose of about 40 mSv for a mean respiratory minute volume of 20 l/min. For the population of Salz-

burg City the total number of annual number of lung cancer cases (r_{Rn}) due to radon and radon daughter exposure was assessed for each dose interval of the histogram in Fig. 1 according to the equation:

$$r_{Rn} = \frac{r_t}{t} D_{ind} N(\bar{a} - L),$$

where r_t is the standardized individual probability for radiation induced death per dose unit during a period t ($t = 40$ years), D_{ind} is the absorbed dose due to

Table I

Pro and contra arguments about the validity of applying risk assessments derived from mining environments to indoor conditions

CONTRA	PRO
Respiratory minute volume (rmv) is higher for miners than for inhabitants of dwellings.	This has been taken into account in the dose calculations for inhabitants of Salzburg.
Aerosol characteristics in mining environments are different from those of homes, i.e. AMAD without diesel fumes $\sim$0.17 μm, with diesel fumes $\sim$0.3 μm.	The dose calculations for inhabitants of Salzburg are based on an AMAD of 0.09 μm. Increasing of AMAD results in higher deposition in the segmental bronchioles due to impaction rather than diffusion; it is likely that increase of AMAD due to hygroscopic growth [10] is of more importance than differences in aerosol particle size spectrum.
Mine atmosphere contains other suspected or known carcinogens besides radon daughters (diesel fumes, ore dust, acid fumes) which may act synergistically with radon daughters.	The most important carcinogenic factor, i.e. smoking, is effective in the same way amongst miners as it is for the general public [11]; additional cocarcinogens occur increasingly also in the normal environment due to industry- or traffic-related air pollution; there is no evidence which would justify the assumption that synergism between radon daughters and cocarcinogens is limited to mining environments only.
Only adult men are employed as miners, whilst indoor exposure of the general public comprises women and children also.	The dose frequency distribution takes into account the different rmv-values for women and children; however, it cannot be ruled out that women are at lower risk for lung cancer induction than men even at the same level of exposure to radon daughters and with similar smoking characteristics.
Radon daughter levels in mining are generally 1 to 2 orders of magnitude higher than in the "normal" NRE.	Analysis of miner data indicate that decreasing exposure rates are accompanied by an increasing risk of lung cancer induction per unit of cumulative radiation exposure [12]; consequently even higher risk factors would have to be assumed for exposure in dwellings compared to risk factors for mining environments.

accumulative exposure, N is the population size, $\bar{a}$ is the mean age of all population groups, and L is the mean latency period, assumed to be independent of the age at the onset of exposure.

It was found that 5 to 12 cases per year and 10^5 persons can be attributed to radon daughter exposure. Compared to an actually observed annual lung cancer rate of 34.4 per 10^5 persons in Salzburg Province, this means that about 15% to 35% of the lung cancer incidence of Salzburg City can be related to inhalation of radon daughters.

Conclusions

The major component of the dose from the natural radiation environment (NRE) is represented by the indoor exposure of man. The use of radiologically disadvantageous material in or near the building, radon-rich tap water, specific architectural styles and decreased ventilation rates can cause NRE levels indoors which exceed even the upper limit for occupational exposure. The resulting risk can be of the same order or even higher than risks from other non-radiation risks, e.g. general air pollution [9]. Whilst it is justified that every possible and reasonable effort should be undertaken to reduce the population exposure from the application of nuclear technologies, it appears desirable to follow the same principle in the case of exposure to the NRE, since the biological target "man" cannot discriminate between man-made and natural radiation exposure.

REFERENCES

1. B. HULTQUIST, Kungl. Svenska vetenskapsakademius handligar, **6/3,** Stockholm, 1965.
2. United Nations Scientific Committee on the Effects of Atomic Radiation (UNSCEAR), United Nations Publ., No. E. 77. IX. 1, New York, 1977.
3. S. STEINHÄUSLER, E. POHL and W. HOFMANN, Proc. Int. Radon Specialist Meeting, Rome, RD Press, University of Utah, USA, 259, 1982.
4. F. STEINHÄUSLER, W. HOFMANN, E. POHL and J. POHL-RÜLING, Proc. Symp. on Natural Radiation Environment III, Houston, USA, CONF-780422-Vol. 2, DOE Symp. Ser. **51,** 1145, 1980.
5. W. HOFMANN, F. STEINHÄUSLER, P. PFLIGERSDORFFER and E. POHL, Annual Meeting, Austrian Radiation Protection Association, Vienna, 135, 1979.
6. International Commission on Radiological Protection (ICRP), ICRP Publ. 23, Pergamon Press, Oxford 1975.
7. W. HOFMANN, F. STEINHÄUSLER and E. Pohl, Health Phys., **37,** 517, 1979.
8. W. HOFMANN, Acta Phys. Hung., this issue p. 297.
9. F. STEINHÄUSLER, Berichte der naturwissenschaftlich-medizinischen Vereinigung, Salzburg, **6,** 7, 1982.
10. T. B. MARTONEN and M. PATEL, Am. Ind. Hyg. Assoc. J., **42,** 453, 1981.
11. J. SEVC, E. KUNZ and V. PLACEK, Health Phys., **30,** 433, 1976.
12. V. E. ARCHER, E. P. RADFORD and O. AXELSON, Conf. Workshop Lung Cancer Epidemiology and Individual Application of Sputum Cytology, Col. Schools of Mines Press, 342, 1979.

Acta Physica Academiae Scientiarum Hungaricae, 52 (3—4), pp. 297—302 (1982)

STOCHASTIC ASPECTS OF LUNG DOSIMETRY FOR RADON DECAY PRODUCTS AT LOW DOSE LEVELS

W. HOFMANN

DIVISION OF BIOPHYSICS, UNIVERSITY OF SALZBURG
A-5020 SALZBURG, AUSTRIA

The determination of upper limits for the amount of inhaled radon decay products needs detailed information on the resulting radiation dose in different organs and tissues, particularly in the respiratory tract. The common procedure of theoretical lung dosimetry is characterized by applying simple analytical techniques to a data base consisting of mean values for all anatomical and physiological parameters involved. However, it is well known that great inter- as well as intrasubject variabilities of lung dimensions and clearance processes could be observed, questioning, therefore, the applicability of simplified anatomical and clearance models. Substituting the mean values by probability distributions and applying Monte Carlo techniques a dosimetric method for determining lung doses is presented, taking into consideration these variabilities.

A second source of fluctuations in lung dosimetry is caused by the randomness of nuclide distributions, lung tissue structure and stochastic energy absorption in lung cells. A microdosimetric approach is discussed based on the superposition of computer-generated alpha-particle tracks onto magnified images of randomly selected tissue sections on the monitor of an electronic image analyzer. Including also results of alpha-particle track structure calculations the resulting specific energy distribution in lung cells can be estimated. All these random effects are much more pronounced in the case of low doses and dose rates which are typical for environmental low-level exposure of natural radionuclides than at higher doses.

Introduction

Lung cancer is commonly regarded as the most important somatic risk arising from the inhalation of radon decay products. Originating preferentially in the basal cells of the bronchial epithelium in lobar and segmental bronchioles, the evaluation of basal cell doses is, therefore, the main objective of all lung dose assessments.

In general there are three possible dosimetric approaches:

1) Calculation of the mean absorbed dose in the critical compartment or organ, taking the mean organ or compartmental dose as representatives for basal cell doses;

2) Calculation of the distribution of the mean absorbed dose around single radionuclides at the depth of the basal cell layer;

3) Calculation of the probability density distribution of the stochastic variable "specific energy" in basal cells and cell nuclei.

In the case of the alpha-emitting radon daughters with high energy deposition restricted to a small cylindrical volume around the alpha particle track and with particle ranges over some cellular diameters only concept 3) has been considered as an adequate approach in radiobiology.

In internal dosimetry the detailed knowledge of the microdistribution of radionuclides throughout the respiratory tract is of particular significance. Caused by experimentally observed inter- as well as intra-subject variabilities of anatomical structure, respiration standards and clearance mechanisms, a broad range of surface activities are obtained for the same nuclide concentrations in the inspired air. Regarding these activities as alpha-emitting sources probability distributions for the specific energy in basal cells can be determined. Both steps will be explored in the following sections in more detail.

Stochastic deposition and clearance

The common procedure of theoretical lung dosimetry is characterized by applying simple analytical techniques to a data pool, consisting of mean values for all anatomical and physiological parameters involved. The values of input parameters and transfer coefficients are generally averages over different experimental investigations, e.g. anatomical lung data as provided by the WEIBEL model [1] were obtained from various lung tissue sections of different individuals. However, it is a well known fact that great inter- as well as intra-subject variabilities of lung dimensions could be observed, questioning, therefore, the applicability of simplified anatomical models. Substituting the mean values by probability distributions and applying Monte Carlo techniques, a dosimetric method was developed taking into consideration the above variabilities [2]. Therefore, data on anatomical structure, respiration parameters, clearance rates and basal cell distances were represented in terms of probability distributions derived from experimental results available [3]. On biological as

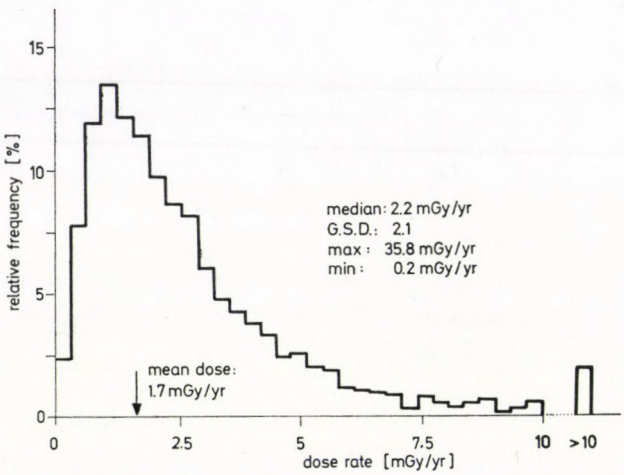

Fig. 1. Relative frequency distribution for the basal cell dose in generation 4.

well as mathematical grounds truncated log-normal distributions were chosen. Fig. 1 represents the basal cell dose distribution in generation 4 of the WEIBEL model A for inhalation of typical values for radon decay product concentrations and respiration standards [3]. This frequency distribution is highly skewed and can be approximated with high statistical significance again by a log-normal distribution with a median dose rate of 2.2 mGy/yr and a geometrical standard deviation of 2.1. About 1.5% of the individuals exposed receive doses higher than 10 mGy/yr with a maximum of about 40 mGy/yr. The corresponding mean dose calculated with the deterministic model amounts to 1.67 mGy/yr.

From these restults it can be concluded that mean values for deposition, retention and dose supply only inadequate information. Personal variabilities exert an essential influence on the resulting dose distribution and in further consequence on the observable biological effects in the individual lung. Log-normal dose probability functions illustrate the fact that a small but non-negligible percentage of individuals can receive considerably higher doses than indicated by a mean value. It could, therefore, be arguable whether lung cancer induction is not better correlated with the percentage of individuals receiving randomly such high doses than with mean radiation doses for inhaling the same amount of radionuclides.

Microdosimetric model

A second source of fluctuations in lung dosimetry is caused by the randomness of nuclide distributions, lung tissue structure and stochastic energy deposition in microscopic sites. Therefore, at the dimensions of single cells or cell organelles the concept of absorbed doses loses its significance and should be replaced by the corresponding microdosimetric quantity, i.e. specific energy. Microdosimetric quantities are stochastic variables taking into consideration the random nature of discrete energy-loss events in microscopic regions.

Specific energy probability distributions of alpha particles in lung cells can be attributed to four sources of stochastic effects:

1) Randomness of nuclide distributions on airway surfaces, ranging from homogeneous radiation sources to hot spot distributions;

2) Biological variability of tissue and cellular structures in various lung regions irradiated by alpha particles;

3) Statistical variations of the number of cells hit and — in the case of a hit — of the path length through a cell;

4) Stochastic nature of energy deposition in radiation-sensitive sites which becomes more effective for small sites and low doses or dose rates.

The basic approach of this microdosimetric model is the superposition of computer-generated alpha particle tracks onto magnified images of randomly

selected lung tissue sections with the aid of an electronic image analyzer [4]. This semi-experimental method allows to account for stochastic variations of nuclide distributions and chord length distributions, and the biological variability of tissue and cellular structure. Adult Sprague—Dawly laboratory rats have been used as model animals providing 1 μm thick lung tissue specimen. Applying image analysis techniques, specific energy distributions in the basal cells hit were calculated on the basis of chord length distributions. Fig. 2 represents the specific energy distribution in basal cells for radon decay products homogeneously distributed on bronchial airway surfaces. This distribution is a so-called conditional probability density distribution, insofar as it is conditional on energy being deposited in cells and does not include cells which are not hit at all. Cellular doses at the upper range of the distribution are caused by multiple cell hits or more frequently by the higher energy deposition at the end of alpha particle tracks. The percentage of cells not hit amounts to about 35%, resulting in a mean cellular dose for all cells of about 200 mGy. This mean value, however, occurs with a relatively small probability, since most of the cells receive doses between 200 and 400 mGy, or are not hit at all.

Investigations with different absorbed doses revealed that the shape of the specific energy distributions remains unchanged up to mean doses of about 1 Gy. Since more lung cells are hit, the area beneath the curves increases gradually. As the dose exceeds about 1 Gy the curves are shifted to higher specific energies due to the greater probability for multiple cell hits. Therefore, in the dose range up to 1 Gy which will be hardly exceeded in environmental exposure for an inhalation period of one year, specific energy (z) distributions can be characterized statistically by the single event density $f(z; 1)$ with a defined median, mode and dispersion factor.

Assuming a D_0 of 1 Gy for cell killing [5] the percentage of lethally and non-lethally demaged cells can be estimated directly from these specific energy distributions. As can be derived from Fig. 2, only a negligible number of cells will be killed by natural radioactive exposure. Hence all cells are candidates for being transformed into malignant cells or being completely repaired.

Statistical fluctuations of ionization events or energy imparted in microscopical sites cause an additional variation of the specific energy in lung cells. Using results of track structure calculations for alpha particles, these stochastic effects were evaluated for radon daughter alpha particles and lung cells. For cells and cell nuclei, these statistical variations do not exceed about 10%. For sites in the nanometer region, however, the stochastic nature of energy imparted determines preferentially the dispersion of the specific energy distribution.

The expectation value of the specific energy does not represent an appropriate quantity at low doses and dose rates. Selecting randomly z-values from the experimentally derived $f(z)$-distribution (Fig. 2) the statistical varia-

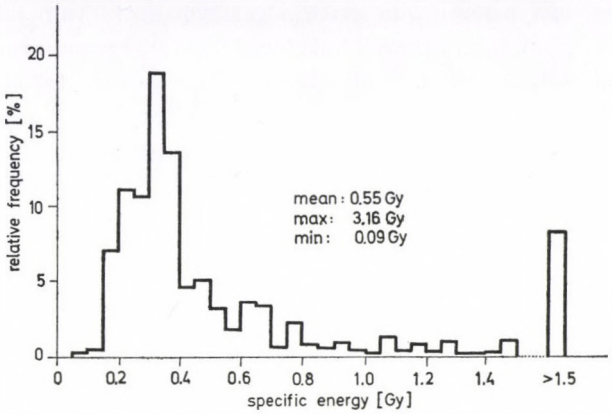

Fig. 2. Cellular specific energy distribution for RaC′ nuclides homogeneously distributed on bronchial airway surfaces.

tion of the mean specific energy $\bar{z}$ with gradually increasing number of intersections, i.e. dose, was studied. About 13 intersections are necessary to reach an actual fractional standard deviation smaller than 20%. Assuming a median specific energy per energy-loss-event of about 300 mGy, about 3.9 Gy have to be deposited in a lung cell in order to get a statistically significant mean value of z. These multiple hit numbers will never be reached in normal radiation protection cases. Moreover, these cells will hardly survive. For single hits, however, the statistical fluctuation of the actual energy absorbed can deviate from the mean up to some hundred per cent according to the probability distribution of the specific energy (Fig. 2).

Conclusions

Lung cancer is commonly regarded as the most important somatic risk due to inhalation of alpha-emitting nuclides. Candidates for cancer induction are cells receiving radiation energy which is sufficient to induce transformation, but insufficient to kill the cell. The specific energy distribution contains information on the chord length distribution of single traversals, multiple hits and increased energy deposition at the end of the particle track. Assuming a D_0 for reproductive cell death of 1 Gy the percentage of potentially-lethally damaged cells can be estimated directly from this distribution. The statistical fluctuation of the activity deposited in individual exposure causes an additional variation of $f(z)$ only in the case of many multiple hits. It influences, however, together with the varying number of cells hit per alpha particle track, the total number of cells hit. For cancer induction it can be reasonably assumed that a defined number of cells must be hit. If multicellular effects are responsible for carcino-

genesis, then the cells hit must lie within certain interaction distances, probably even adjacent to each other. Therefore, the total number of potentially-lethally damaged cells is not the only determining factor, but also the spatial distribution of these cells.

From these considerations it appears that the following three parameters provide a more complete description of radiation carcinogenesis in physical terms than the macroscopical dose:

1) Number of cells hit in a defined tissue volume;

2) Specific energy distribution $f(z)$ of cells hit and the resulting number of potentially-lethally damaged cells;

3) Spatial distribution of the potentially-lethally damaged cells, represented by a distance distribution.

REFERENCES

1. E. R. WEIBEL, Morphometry of the Human Lung, Springer-Verlag, Berlin, 1963.
2. W. HOFMANN and F. DASCHIL, Proc. Int. Symp. Applied Modelling and Simulation, Lyon, Vol. V, 40, 1981.
3. W. HOFMANN, Radiat. Environ. Biophys., **20**, 113, 1982.
4. W. HOFMANN, Proc. 7th Symp. on Microdosimetry Harwood Academic Publishers, Chur, 129, 1980.
5. J. A. SIMMONS and S. R. RICHARDS, Proc. 7th Symp. on Microdosimetry, Harwood Academic Publishers, Chur, 1433, 1980.

Acta Physica Academiae Scientiarum Hungaricae, 52 (3—4), pp. 303—310 (1982)

QUANTITATIVE PROFILE SCANNING, A MEANS FOR INTERNAL DOSE ASSESSMENT

A. ANDRÁSI and É. BELEZNAY

HEALTH PHYSICS DEPARTMENT, CENTRAL RESEARCH INSTITUTE FOR PHYSICS
1525 BUDAPEST, HUNGARY

A combined measuring and computing method is given by means of which the Committed Effective Dose Equivalent can be estimated. A sensitive detector equipped with a suitable collimator moving along the length of a person being investigated, enables the count rate profile to be obtained from which organ activities can be deduced. With repeated measurements the activity time variations and their time integrals can be derived, the latter being proportional to the organ doses. The general description of the methods and its implementation in the radiation protection practice of the Central Research Institute for Physics is given. Test experiments show the method to be suitable for internal dose assessment when the activity exceeds 0.5 kBq per organ.

Introduction

The dose received from internal sources is characterized by the Committed Effective Dose Equivalent, the weighted sum of the Committed Dose Equivalent values concerning the individual tissues specified by the ICRP. The Committed Dose Equivalent $H_{50,T}$ for a given target tissue T, and a given radionuclide can be obtained as follows:

$$H_{50,T} = \sum_S U_S \times SEE\,(T \leftarrow S),$$

where $SEE\,(T \leftarrow S)$ is the specific effective energy absorbed in T per radioactive disintegration in the source organ S, U_s is the number of disintegrations of the radionuclide in each source organ.

In the radiation protection practice the number of disintegrations U_S, or, in other words, the time integral of activity for the source organs over 50 yr, has to be determined in each case when individual dose assessment is needed. The calculated *SEE* values for Reference Man are tabulated in a couple of reports [1, 2]. The influence of individual differences on these values can be considerable, but this is beyond the scope of the present paper. The activity variation in time in different source organs, i.e. the retention functions, can be determined by the method of quantitative profile scanning.

Method

In the last few years an increasing number of whole body counters are being used not only for the activity determination in the human body as a whole, but also for obtaining information about the activity distribution.

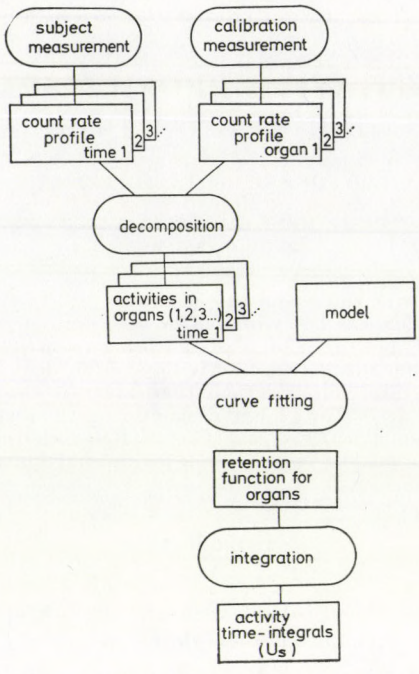

Fig. 1. Scheme of activity time integral determination by quantitative profile scanning.

If a large NaI(Tl) detector equipped with proper collimator is moving along the length of the person to be investigated, the count rate profile in a given energy range can be obtained. After a sophisticated calibration procedure using an anthropomorphic phantom containing the organs in question, the activities in the different organs of the investigated person can be computed from the count rate profile. With repeated measurements the activities at discrete points of time are obtained from which the required time integral can be derived. The best fit can be expected if the function describes the real transport of radionuclides in the body. As a good approximation these functions can advantageously be obtained for instance by means of multi-compartment modelling of the radionuclide transport. If there is no possibility to carry out such sophisticated calculations, a simpler curve fitting procedure can also be satisfactory for obtaining retention functions to be integrated. The different steps for determining the activity time integral can be followed in Fig. 1.

Implementation

The whole body counter of the Central Research Institute for Physics [3] has proved to be suitable for profile scanning measurements. The one or two 150×100 mm NaI(Tl) cylindrical scintillation detectors move along the

subject to be investigated with controllable speed in the range of 0.6—20 mm/s, and with adjustable length up to 1330 mm. The distance between the bed and the detectors can also be varied in a reasonably wide range. The detectors are equipped with changeable collimators like 2 and 8 cm thick simple slit and focusing slit collimators. The spatial resolutions and relative efficiencies of different collimators are shown in Fig. 2 [4]. The pulses coming from the detectors are processed by a multi-channel analyser in externally controlled multi-scaling mode, making it possible to obtain the count-profile in a preselected gamma energy range. The measured data are punched on paper tape for further computer evaluation. The bed-detector arrangement is surrounded by a 200 mm thick iron shielded room covered by 4 mm lead and 1 mm copper with inside dimensions of $1600 \times 2000 \times 2200$ mm. A REMCAL type anthropomorphic phantom containing ten different organs is at our disposal for calibration. By filling the organs of the phantom with a water solution containing the radionuclide in question with known activity the count rate profile due to unit activity in the individual organs can be obtained.

A computer code DECOMP (DAS2) was developed by means of which the most probable activities in the individual organs can be calculated from the measured count profile [5]. This calculation consists of the numerical solution of a linear equation system, where the most probable values of the

No.	collimator	FWHM [cm]	total relative efficiency [%]
1	—	—	100
2	15 cm ø hole	37.5	53.2
3	8 cm slit	20	25.7
4	2 cm slit	7.0	2.66
5	focusing	4.6	4.80

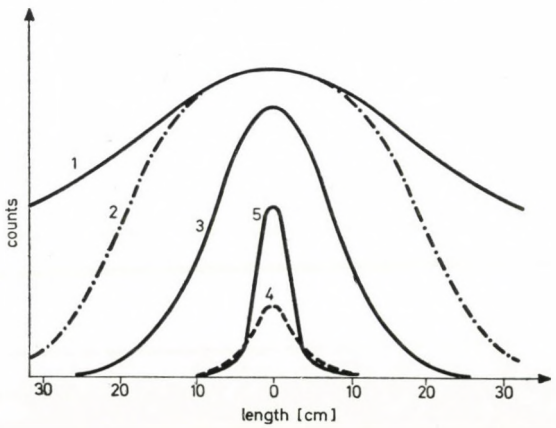

Fig. 2. Spatial resolution and total relative efficiency of different collimators.

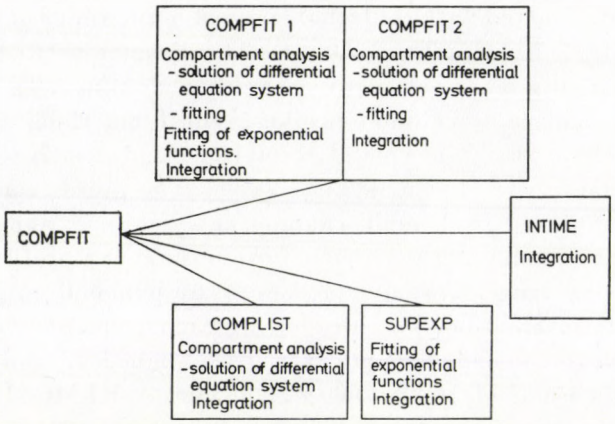

Fig. 3. Functions of the different subprograms of COMPFIT.

organ activities can be determined using the method of weighted least squares by minimizing the expression

$$\sum_i W_i (N_i - \sum_j A_j X_{i,j})^2,$$

where W_i is a weighting factor calculated for the i-th channel, N_i is the number of counts in the i-th channel, A_j is the activity of the j-th organ, $X_{i,j}$ is the number of counts due to unit activity of the j-th organ in the i-th channel.

The DECOMP program can be run on ES 1020 and 1040 as well as on IBM/360 and 370 machines. A computer program with similar capability was also developed for a PDP 11/34 under RT-11 operating system.

If the activities of the radionuclides in the different organs or tissues have already been obtained at discrete points of time the retention function and the activity time integral can be calculated by the COMPFIT computer program developed in our laboratory [6]. The program consists of the five subprograms seen in Fig. 3, these make it possible to solve the task in a large variety of cases, i.e. the program can handle the task of multicompartment analysis, can fit the sum of exponential functions and can calculate the time integral, separately or simultaneously in various reasonable combinations.

The subprogram COMPFIT1 and its variant COMPFIT2 perform the numerical solution of the differential equation system defined by an arbitrarily chosen compartment model which describes the radionuclide transport in the living organism and estimates the transport coefficients and the values of the time integral by fitting the solution to the organ activity data calculated by the DECOMP code. COMPFIT1 and COMPFIT2 have a number of very useful features, e.g. they can handle measured activities relating not only to one compartment but to some of their combinations (in the case of poor spatial

resolution or overlapping organs), they can also calculate activity data for those compartments that take part in the process without any measured data, they can extend the validity of the calculated data beyond the time range of observations, etc.

The subprogram COMPLIST in turn, computes the activities at discrete points of time of the individual compartments and the time integrals for the arbitrarily chosen values of transport coefficients. In this way, the most different models and the values of their transport coefficients can be tested. It can also help in the selection of the most appropriate model describing the real kinetic situation in the case investigated.

When insufficient information is available to carry out compartment analysis, it is expedient to fit a sum of exponential functions to the measured activity data and calculate the exponential parameters together with the values of the time integral. These calculations can be performed by the subprogram SUPEXP.

The simple subprogram INTIME is suitable for the calculation of the time integral in a given period of time from an arbitrary series of data. This subprogram is generally used as a part of other subprograms but it can also be applied separately.

Testing

The suitability of the applied method has been tested by phantom measurements and by in vivo experiments as well.

Known activities of ^{131}I nuclide were put into different organs of the REMCAL phantom and the count profiles were measured separately and together with different combinations. Then the profiles measured on the phantom having a radioactive source in two organs were decomposed by the DECOMP program. The results can be seen in Table I, where the calculated activities

Table I

Comparison of calculated phantom organ activities with actual values

Organs	Relative differences from actual values [%]	
	(1)	(2)
Bladder (1) + liver (2)	−5.8	−1.5
Liver (1) + stomach (2)	−14.0	+5.0
Stomach (1) + thyroid (2)	− 2.5	0
Thyroid (1) "whole body" (2)	− 2.6	0

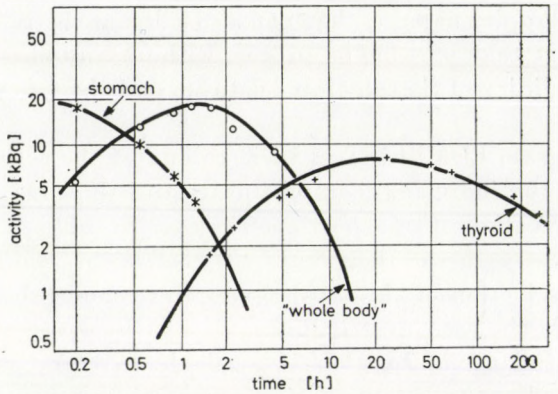

Fig. 4. Time variation of measured and calculated activities after a single ingestion of ^{131}I.

of the single organs are compared with the actual values. The measurements were carried out using an 8 cm wide slit collimator and 45 cm bed-detector distance. The decomposition can be considered as successful especially in cases where the count profiles belonging to the organs in question are quite different but it is even acceptable for the liver and stomach combination where the organs have a partly overlapping position in the phantom and consequently the count profiles are very similar.

In an experiment on a human being an amount of 20 kBq ^{131}I in iodide form was orally administered to a volunteer. The count profile was then measured at different times after the intake enabling the redistribution of the radioactive substance to be followed [7]. The activities of organs having the most important role in iodine metabolism were computed by the DECOMP code using calibration profiles obtained on the REMCAL phantom. Assuming a simple compartment model for iodine metabolism the COMPFIT program calculated the fitted values of the individual organ activities in time, the time integrals and the most probable values of transport coefficients involved in the model. The activities obtained by the DECOMP code and their time variation computed by the COMPFIT program can be seen in Fig. 4. The sum of the calculated organ activities is quite constant up to the first excretion and it

Table II

Time integrals and dose equivalents from ^{131}I for two organs

Organ	Time integral (kBq × day]	Dose equivalent [mSv]
Stomach	0.49	0.0031
Thyroid	102	14

differs by less than 10% of the activity actually present. The fitted curves, which are also determined by the model, lie quite close to the values evaluated by the DECOMP code. The computed activity time integrals to infinite time and the corresponding dose equivalents for two organs are shown in Table II. For dose equivalent calculations the *SEE* values were taken from the work of SNYDER et al [1]. The dose equivalent for thyroid per unit ingested activity, i.e. 0.7 mSv/Bq, is in the range of other published data [8].

Conclusion

The applied DECOMP program is suitable for count profile decomposition even with poor spatial resolution. This allows the use of a wider slit collimator with a higher counting efficiency which is one of the most important requirements in radiation protection practice. The method applied makes it possible to determine organ activities exceeding 0.5 kBq per organ in a reasonable measuring time. Another advantage of the method is that the whole body without the organs investigated can also be considered as a separate body region. The problem due to the differences in the shape and size of human individuals and the anthropomorphic phantom can be reduced by using two detector systems and different data handling programs.

A complete analysis of repeated profile measurements can be performed advantageously by a computer program like COMPFIT, which was specially worked out for the task discussed here and is capable of handling the problem in a large variety of cases. The special advantages of the compartment analysis by COMPFIT can be summarized as follows. The time integral of organ activity can be calculated also for organs not being measured or for organs being measured but together with others and also for times exceeding the range of observation.

Individual assessment of the committed effective dose equivalent is necessary especially in the range of the annual limit specified by the ICRP. The method of quantitative profile scanning seems to be promising in individual dose estimation due to internal contamination.

REFERENCES

1. W. S. SNYDER, MARY R. FORD, G. G. WARNER and SARAH B. WATSON, A Tabulation of Dose Equivalent per Microcurie-Day for Source and Target Organs of an Adult for Various Radionuclides, Report, Oak Ridge National Laboratory, ORNL-5000/2, 1972.
2. D. E. DUNNING, Jr. J. C. PLEASANT and G. G. KILLOUGH, SFACTOR: A Computer Code for Calculating Dose Equivalent to a Target Organ per Microcurie-Day Residence of a Radionuclide in a Source Organ, Report, Oak Ridge National Laboratory, ORNL/NUREG/TM-85, 1977.
3. Directory of Whole Body Radioactivity Monitors, IAEA, Vienna, 1970.

4. G. INGRAO, A. ANDRÁSI and G. F. CLEMENTE, The Characteristics of the Scanning System of the CSN Casaccia Whole Body Counter, Report, National Commission of Nuclear Energy, Casaccia, CNEN-RT/PROT/80/9, 1980.
5. A. ANDRÁSI and Gy. KÖTÉL, Computerized Spectrum Decomposition (in Hungarian), Report, Central Research Institute for Physics, Budapest, KFKI-71-16, 1971.
6. A. ANDRÁSI, ÉVA BELEZNAY and GY. KÖTÉL, COMPFIT: a Computer Program for Internal Tissue Dose Calculation, in Proc. Int. Symp. on Biomedical Dosimetry: Physical Aspects, Instrumentation, Calibration IAEA, Vienna, 1981.
7. A. ANDRÁSI and ÉVA BELEZNAY, Activity Distribution Measurement in the Human Body by Quantitative Profile Scanning, in Condensed Papers, Third European Congress of the International Radiation Protection Association, Amsterdam, 1975.
8. D. E. DUNNING, Jr. and G. SCHWARZ, Health Phys., **40**, 661, 1981.

Acta Physica Academiae Scientiarum Hungaricae, 52 (3—4), pp. 311—316 (1982)

III. OCCUPATIONAL RADIATION BURDEN

CHAIRMEN: T. PREDMERSZKY, H. SORANTIN

RETROSPECTIVE EVALUATION OF OCCUPATIONAL ANNUAL DOSES RECEIVED BY WORKERS PRODUCING RADIOACTIVE SOURCES

I. BOJTOR

"FRÉDÉRIC JOLIOT-CURIE" NATIONAL RESEARCH INSTITUTE FOR RADIOBIOLOGY AND RADIOHYGIENE
1775 BUDAPEST, HUNGARY

F. GOLDER and M. OSVAY

INSTITUTE OF ISOTOPES
1525 BUDAPEST, HUNGARY

É. BOBOK

COMPUTER AND ORGANIZATION ENTERPRISE, MINISTRY OF LIGHT INDUSTRY
1076 BUDAPEST, HUNGARY

Personal dosimetric data from external radiation recorded during a 19-year period at the Institute of Isotopes were subjected to extensive computer analysis to examine the applications of the relevant ICRP dose limitation system by following the trend of radiation exposures and estimating the risk levels for various occupational fields.

Based on the values of the average annual dose equivalents and Ω obtained from the whole observation period, even the most exposed group of maintenance, packaging and transportation workers can be classified as belonging to working category "B" of UNSCEAR, thereby permitting the conclusion that working conditions at the Institute are satisfactory.

The average annual dose equivalents in time intervals of employment were found to decrease with increased time spent doing the same work.

The risk levels were estimated from 25-year-lifetime doses by using "time-related" average annual doses. The risk for the highest exposed group (workers in maintenance, packaging and transportation) was assessed to be 1.2 10^{-3} fatalities per working lifetime. It may be concluded that in each occupational group of the Institute the mortality risk of radiation-induced cancer is lower than the hazards in non-radiation occupations having high standards of safety.

Introduction

A correct way to maintain the efficiency of radiation protection and to monitor the practical compliance with regulations is to evaluate the trends in occupational radiation exposures. In general, trends may be followed by assessing, as a function of time, relevant quantities which reflect possible changes in radiation doses associated with various occupational fields. Such parameters are: the mean of the distribution of annual dose equivalents, the relative proportion Ω of the annual collective dose equivalent due to annual dose equivalents above 15 mSv [1], and the total collective dose equivalent to the practice in question.

In the ICRP dose limitation system for radiation workers one of the basic concepts is that the average mortality risk from low level radiation exposure be comparable with that in other occupations accepted to be of a high standard of safety [2]. This means that in radiation occupational fields where the dose limitation system has been applied, the average risk factor for death from cancer is about $10^{-2}Sv^{-1}$ [2]. However, ABRAHAM et al [3] have reported that estimates of risk factors may contain uncertainties of a half to one order of magnitude.

It thus seems to be reasonable to check the proper application of dose limitation principles by quantifying the risks in various fields and identifying groups with higher or lower risk level [1]. When doing so, occupational subgroups in which workers are continuously exposed to near or over the annual dose equivalent limit should be distinguished from subgroups receiving high doses occasionally — either during a year or their whole period of employment [4]. For this reason the ICRP has suggested the expected occupational life time dose to be used for indicating the total individual risk [2].

In this paper the trends of radiation exposures are evaluated and the risks associated with various job categories are estimated on the basis of a 19-year period of observation of workers at the Institute of Isotopes.

The analysis of the annual doses was made by computer program utilizing a data file containing records of external radiation doses since 1960.

Record keeping system

A data file exists to record individual annual doses and to indicates the efficiency of radiation protection. The program was designed for current data processing and for following the trends of radiation exposures. The file structure and program device are illustrated in Fig. 1.

Specification of occupational groups

The ICRP states that in circumstances where the recommendations have been applied, the distribution of the annual dose equivalents has been shown very commonly to fit a log-normal function with an arithmetic mean of about 5 mSv [2]. As a consequence of introducing the reference distribution into the dose limitation system, UNSCEAR offered a possibility to distinguish various occupational groups. The classification can be made by the average annual dose $\bar{D}_a$ and Ω, defined as $\Omega = 3.25\ S_{15}/S$, where S stands for the annual collective dose.

In the UNSCEAR Report [1] reference was made to the variation of Ω with years, therefore personnel involved in producing radioactive sources were

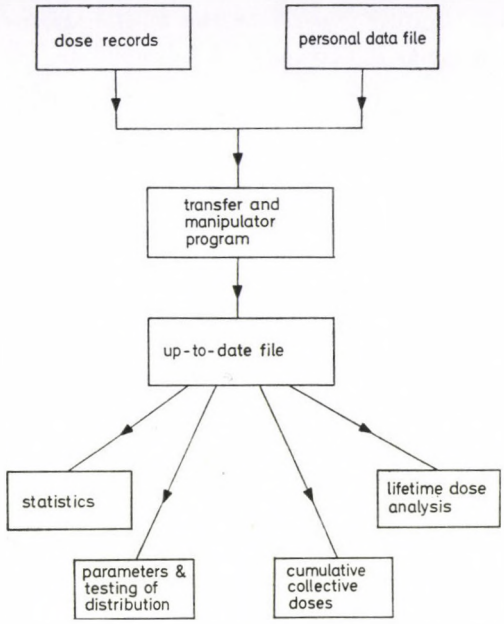

Fig. 1. Program device for trend analysis and data processing.

classified by parameters calculated from the records of covering 19 years of observation (1960—1978).

Statistical analysis and the parameters of the annual dose distribution for various groups are summarized in Table I. The values obtained for $\overline{D}_a$ and Ω_{19} indicate that workers engaged in the maintenance, packaging and trans-

Table I

Statistical analysis and parameters of the annual dose distribution obtained from 19 years of observation

Occupation	Number of workers	Total number of records in the period of 19 years*	Number of records above the registration level during 19 years**	Average annual dose requivalent $\overline{D}_a$ (19) [mSv]	Ω_{19}
Production of radioactive sources incl. research	36	343	245	2.73	0.33
Maintenance, packaging, transportation***	83	529	447	5.91	1.17
Radiation chemistry	63	489	182	1.58	0.99
Others****	111	819	335	1.06	0.74
Total	293	2180	1209	2.37	0.92

* 1 record = annual dose equivalent of one individual
** 0.4 mSv per month
*** Unskilled workers
**** Radiation physics, installation of irradiation facilities, radiography

porting of radioactive sources constitute the most exposed group of persons. Even so, each group belongs to category "B" defined as

$$1 \text{ mSv} \leq \bar{D}_a < 10 \text{ mSv and } 0.1 < \Omega < 2.0 .$$

Workplaces in this category are considered as where radiation protection is satisfactory.

Risk estimates

The risk for a random individual radiation worker (R) is proportional to the average dose $\bar{D}$, that is, $R = r\bar{D}$, where r is the risk factor [5].

For the extrapolated lifetime doses the average annual doses were calculated from the whole of the 19-year period of observation and are given in Table II. It was expected that the risk level would be indicated more reliably if the annual doses were to be averaged over the periods of time the workers have been employed [6, 7] instead of other possible methods available [1]. (The differences between the methods of calculating the mean annual dose are due to be discussed elsewhere.) The "time-related" average annual dose $\bar{D}_t$ was then obtained using the formula

$$\bar{D}_t = \frac{1}{N} \sum_{j=1}^{N} \frac{\sum_{i=1}^{k} D_{ij}}{k} ,$$

where N is the total number of employees during the time of observation, k indicates the period of employment of individual j in years and D_{ij} is the dose of individual j in year i.

The formula was applied to the total number of workers instead of considering a single group with a relatively long period of employment. Thus $\bar{D}_t$ was obtained from many more records than otherwise. In comparison, $\bar{D}_t$

Table II

"Time-related" average annual dose equivalents from 19 years of observation

Occupation	Number of workers	Average annual dose equivalent $\bar{D}_t$ [mSv]
Production of radioactive sources incl. research	36	2.92
Maintenance, packaging, transportation	83	3.79
Radiation chemistry	63	0.10
Others	111	1.51
Total	293	2.22

Table III

Average annual dose equivalent of auxiliary workers in time intervals of employment

Time interval (year)	Number of workers	Average annual dose equivalent $\overline{D_t}$ [mSv]
1— 4	46	2.35
5— 9	13	6.52
10—14	11	5.70
15—19	13	4.52
Total	83	3.79

Table IV

Risks associated with lifetime dose equivalents for various occupational groups

Occupation	Lifetime dose equivalent [mSv]	Fatalities Lifetime
Production of radioactive sources incl. research	72.99	$9.1 \cdot 10^{-4}$
Maintenance, packaging, transportation	94.61	$1.2 \cdot 10^{-3}$
Radiation chemistry	24.95	$2.6 \cdot 10^{-4}$
Others	37.57	$4.8 \cdot 10^{-4}$
Total	55.36	$7.0 \cdot 10^{-4}$

values in various time intervals of employment are presented in Table III for unskilled workers. It can be seen from the figures that the average annual dose equivalent slightly decreased after the initial period of employment. This finding seems to support the assumption reported by WILSON [6]. This "tendency" is probably due to experience or skill acquired by workers having remained for a long period in the same job.

In accordance with the recommendations of the ICRP [8] it was presumed that the mean interval from the relevant exposure to death from an induced malignancy lies between 20 and 25 years. Consequently, the average "working" lifetime doses were extrapolated for 25 years. It is not likely, however, that the cumulative risk would grow in the 25-to-35-year interval of being employed as a radiation worker [9, 10].

Two factors are accepted as reasonable to indicate the mortality risk for radiation-induced cancers. The ICRP applies the factor of $1.25\,10^{-2}\,Sv^{-1}$ under the condition of being the average annual dose equivalent of about 5 mSv [2], and the BEIR Committee estimates it as $1.5\ 10^{-2}Sv^{-1}$ for 25 years [10]. In our estimates the factor given by the ICRP was applied.

The extrapolated lifetime dose equivalents and risks of fatalities per working lifetime are summarized in Table IV in various fields. Among the

occupations considered, unskilled workers have a higher level of risk than the average. If one compares the figures with those obtainable from data published by WILSON [6] and IYER and DHOND [9] one can see that the risk for auxiliary workers of the Institute of Isotopes is equal in order of magnitude to that for mechanical maintenance workers in Ontario Hydro Nuclear Station in Canada. The risk in other occupations is approximately the same as that for workers in fuel fabrication facilities in India.

The mortality per working lifetime corresponds to an annual rate of $8.2 \cdot 10^{-3} y^{-1}$ for 293 persons employed as radiation workers in the Institute. It means that one of the 293 individuals would have the chance to die from radiation-induced cancer in every 100 years.

In an attempt to interpret the risk levels, let an extreme situation be supposed. One estimate reports [8] that if every worker happened to be continuously exposed to the annual dose equivalent limit of 50 mSv instead of the average [11], it would be equivalent to an occupation with a fatality rate of $3.4 \cdot 10^{-4} y^{-1}$. Our results permit us to state that the risk level of an individual working in the most exposed situation is equivalent to that in a nonradiation occupation with a mortality rate of $2.57 \cdot 10^{-5} y^{-1}$. It must be stressed, however, that occupations in which the average annual mortality due to occupational hazards does not exceed 10^{-4} are recognized as having high standards of safety [2].

Acknowledgements

Thanks are due to Dr. Á. VERES, Director-in-Chief, Institute of Isotopes, and Dr. I. BIRÓ, Department Head, for supporting the work.

REFERENCES

1. United Nations Scientific Committee on the Effects of Atomic Radiation, (UNSCEAR) Sources and Effects on Ionizing Radiation, Report to the General Assemby, U.N., New York, 1977.
2. International Commission on Radiological Protection, Recommendations of the ICRP, ICRP Publ. 26, Pergamon Press, Oxford, 1977.
3. P. ABRAHAM, V. K. GUPTA and A. K. GANGULY, in: Proc. Sem. Application of the Dose Limitation System for Radiation Protection: Practical Implications, Vienna, 1979, IAEA, Vienna, p. 337, 1979.
4. I. BOJTOR and L. B. SZTANYIK, in: Proc. Symp. Advances in Radiation Protection Monitoring, Stockholm, 1978, IAEA, Vienna, p. 745, 1979.
5. D. BENINSON, in: Current Problems and Concerns of the Health Physicist, I., Boris Kidric Institute of Nuclear Sciences, Belgrade, p. 191, 1977.
6. R. WILSON, Health Physics, **33**, 177, 1977.
7. R. WILSON and K. DONNELLY, in: Proc. Symp. Occupational Radiation Exposures in Nuclear Fuel Cycle Facilities, Los Angeles, 1979, IAEA, Vienna, p. 3., 1980.
8. International Commission on Radiological Protection, Problems Involved in Developing an Index of Harm, ICRP Publ. 27, Pergamon Press, Oxford, 1977.
9. P. S. IYER and R. V. DHOND, in: Proc. Symp. Occupational Radiation Exposure in Nuclear Fuel Cycle Facilities, Los Angeles, 1979, IAEA, Vienna, p. 113, 1980.
10. United States National Research Council, The Effects on Populations of Exposure at Low Levels of Ionizing Radiation, Report of the Advisory Committee on the Biological Effects of Ionizing Radiations, Washington, DC, 1974.
11. L. B. SZTANYIK, personal communication.

Acta Physica Academiae Scientiarum Hungaricae, 52 (3—4), pp. 317—321 (1982)

DIE ENTWICKLUNG DES STRAHLENSCHUTZES IN ÖSTERREICH IN DEN LETZTEN ZEHN JAHREN

J. K. HOHENBERG

BUNDESMINISTERIUM FÜR SOZIALE VERWALTUNG
A-1030 WIEN, ÖSTERREICH

In Österreich sind die ionisierenden Strahlen seit dem Ende des 19. Jahrhunderts benutzt, aber die ersten gesetzlichen Vorschriften wurden im Jahr 1971 inkraftgesetzt. Es wird die Tätigkeit der österreichischen Strahlenschutzbehörden vorgezeigt. Die Einrichtungen und Anlagen zum Umgang mit ionisierenden Strahlen sind mindestens jährlich einmal bewilligt. Für die Personendosisüberwachung werden Film und TL-Dosimeter verwendet. Die beruflich strahlenexponierten Personen sind jährlich kontrolliert. Die Kosten für die ärztlichen Untersuchungen beliefen sich zuletzt auf etwa 8 000 000 ÖS. Infolge der Tätigkeit der österreichischen Strahlenschutzbehörden ist die schädigende Einwirkung ionisierender Strahlung viele Jahre zurückliegt.

Obwohl ionisierende Strahlen in Österreich seit dem Ende des 19. Jahrhunderts zur Anwendung gelangten, traten mit 1. Jänner 1971 erstmals umfassende gesetzliche Vorschriften zum Schutz des Lebens und der Gesundheit von Menschen einschliesslich ihrer Nachkommenschaft vor Schäden durch ionisierende Strahlen in Kraft. Mit Inkrafttreten der Strahlenschutzverordnung im Feber 1972 wurden diese Bestimmungen dann endgültig vollziehbar.

Die Anwendung von Röntgenstrahlen und radioaktiven Stoffen in nichtmedizinischen Betrieben wurde erstmals durch eine Verordnung des Jahres 1941 geregelt. Verschiedene Bestimmungen dieser Verordnung standen später auf Grund einer Verordnung des Bundesministeriums für soziale Verwaltung aus dem Jahre 1956 weiter in Kraft. Ausserdem enthält die Allgemeine Dienstnehmerschutzverordnung einige sehr allgemein gehaltenen Bestimmungen zum Schutz vor Strahleneinwirkung. Auch bestand im Einzelfall die Möglichkeit, anlässlich der Bewilligung von industriellen und gewerblichen Einrichtungen Massnahmen zum Schutz der Dienstnehmer vor ionisierender Strahlung vorzuschreiben. Bemerkenswert ist jedoch, dass vor dem Jahre 1971 für den Bereich der medizinischen Anwendung der ionisierenden Strahlen keine gesetzlichen Vorschriften erlassen wurden.

Diese Unterschiede der gesetzlichen Regelung des Schutzes vor ionisierender Strahlung sollten auch nach dem Inkrafttreten umfassender gesetzlicher Bestimmungen auf dem Gebiete des Strahlenschutzes Anlass für Schwierigkeiten bei deren Vollziehung bringen, da den Betriebsinhabern im nichtmedizinischen Bereich der Kontakt mit Bewilligungsbehörden geläufig war, im medizinischen Betrieb die Tätigkeit behördlicher Organe und die damit verbundene Vorschreibung von Schutzmassnahmen, die teilweise auch beträchtliche Kosten verursachte, oftmals völlig neu war.

Auch darf nicht unberücksichtigt bleiben, dass mit Inkrafttreten der gesetzlichen Strahlenschutzbestimmungen, die mit der Vollziehung dieser Bestimmungen befassten Behörden in personeller und messtechnischer Hinsicht überfordert waren und zunächst auch hier die organisatorischen Voraussetzungen zur Bewältigung der bestehenden Aufgaben geschaffen werden mussten.

Diese Problematik war vor allem im Bereich der medizinischen Anwendung gegeben, da doch die zum Zeitpunkt des Inkrafttretens der Strahlenschutzverordnung im Betrieb befindlichen Anlagen möglichst rasch einem Bewilligungsverfahren zu unterwerfen waren und mangels geltender Bestimmungen zum Zeitpunkt ihrer Errichtung, die schon viele Jahre zurückliegen konnte, auch erwartet werden musste, dass zum Teil gröbere Misstände zu beseitigen wären. Hiezu trat noch die schon erwähnte Tatsache, dass in Krankenanstalten und ärztlichen Praxen erstmals Behörden tätig wurden, die zum Teil sehr kostenintensive Schutzmassnahmen vorschrieben. Auch der Verpflichtung, dass beruflich strahlenexponierte Personen einer physikalischen und ärztlichen Kontrolle unterliegen, wurde von den Betroffenen anfangs zum Teil grosser Widerstand entgegen gesetzt.

Den an Ort und Stelle tätigen behördlichen Organen, aber auch den auf dem Gebiete des Strahlenschutzes tätigen Sachverständigen autorisierter Anstalten ist es zu danken, dass doch in verhältnismässig kurzer Zeit ein entsprechender Prozess des Umdenkens beobachtet werden konnte.

Die auf Grund der wirksam gewordenen Strahlenschutzgesetzgebung einsetzende Behördentätigkeit lässt im medizinischen Bereich in den Jahren 1975 bis 1978 einen sehr starken Anstieg von strahlenschutzrechtliche Bewilligungen erkennen. In den genannten Jahren wurden etwa 1.200 Bewilligungen erteilt. Der grösste Teil betraf Röntgeneinrichtungen, die schon zum Zeitpunkt des Inkrafttretens der gesetzlichen Bestimmungen in Betrieb standen. In den folgenden Jahren nahm die Zahl der Bewilligungen im Durchschnitt wieder ab, wobei eine stärkere Zunahme von neuerrichteten Einrichtungen zu beobachten ist. Heute kann gesagt werden, dass nahezu alle Einrichtungen, die zum Zeitpunkt des Inkrafttretens der strahlenschutzrechtlichen Bestimmungen in Betrieb standen einer Bewilligung unterzogen wurden und somit aus der Sicht des Strahlenschutzes die anlagebedingten Mängel zum grössten Teil bereinigt sein müssten. Bei der Neuerrichtung von Anlagen, muss im Hinblick auf die Teilung des Verfahrens in eine Errichtungsbewilligung und eine nach Erprobung der Anlage und Überprüfung der baulichen Strahlenschutzmassnahmen zu erteilende Betriebsbewilligung angenommen werden, dass zumindest die wesentlichen baulichen oder anlagebedingten Schutzmassnahmen getroffen sind. Der Gesetzgeber verlangt um einen sicheren Betrieb bewilligter Einrichtungen und Anlagen zum Umgang mit ionisierenden Strahlen auch nach erteilter Bewilligung zu garantieren eine mindestens jährlich einmal durch-

zuführende Überprüfung durch die Bewilligungsbehörde. Eine Aufgabe, der infolge der Überlastung der zuständingen Behörden erst in den letzten Jahren die notwendige Aufmerksamkeit gewidmet werden konnte, wobei jedoch auch hier im Falle einer Novellierung der strahlenschutzrechtlichen Vorschriften zu prüfen sein wird, ob auch in ferner Zukunft mindestens einmal jährlich alle bewilligten Einrichtungen und Anlagen geprüft werden müssen. Neben dem baulichen Strahlenschutz ist von den Bewilligungsbehörden auch den begleitenden organisatorischen dem Strahlenschutz dienenden Massnahmen Beachtung zu schenken. So fordert der Gesetzgeber beispielsweise als eine der Voraussetzungen für die Erteilung einer Betriebsbewilligung die Bestellung eines Strahlenschutzbeauftragten. Es handelt sich dabei um eine beruflich strahlenexponierte Person, die nachweislich hinreichende Kenntnisse im Strahlenschutz besitzen muss und vom Betreiber der Anlage mit der Wahrnehmung des Strahlenschutzes betraut wurde. Der Umfang der erforderlichen Ausbildung dieser Personen ist gesetzlich geregelt und umfasst in der Regel neben der bereits erworbenen Berufsausbildung auch eine spezielle Strahlenschutzausbildung, die vorwiegend durch zusätzliche Kursbesuche erworben werden muss. Auch hiezu waren grosse organisatorische Aufgaben zu bewältigen um den erforderlichen Personenkreis möglichst rasch auszubilden, wobei teilweise grosser Widerstand vor allem aus dem medizinischen Anwendungsbereich gegen die Notwendigkeit dieser Ausbildung vorgebracht wurde.

Die beruflich strahlenexponierten Personen sind auf Grund gesetzlicher Bestimmungen einer physikalischen und ärztlichen Kontrolle zu unterziehen. Die physikalische Kontrolle erfolgt mittels Personendosimetern, welche in mindestens monatlichen Abständen durch staatlich autorisierte Anstalten auszuwerten sind.

Als Personendosimeter werden derzeit neben Filmen vorwiegend Thermolumineszenzdosimeter verwendet.

In Österreich stehen für die Auswertung derzeit vier Anstalten zur Verfügung. Die Entwicklung der Zahl der ausgewerteten Dosimeter ist der Tabelle I zu entnehmen. Aus dieser Tabelle ist auch deutlich das Wirksamwerden der Behörden auf dem Gebiete des Strahlenschutzes nach Inkrafttreten der gesetzlichen Bestimmungen erkennbar.

Neben der physikalischen Kontrolle unterliegen die beruflich strahlenexponierten Personen auch der ärztlichen Kontrolle, die eine Einstellungsunter-

Tabelle I

Ausgewertete Personendosimeter pro Monat

Jahr	1970	1971	1972	1973	1974	1975	1976	1977	1978	1979	1980
Anzahl	2400	2900	4000	5400	6300	7700	8700	13 600	16 900	20 000	21 000

suchung vor Aufnahme der Tätigkeit, jährlich wiederkehrende Untersuchungen und eine Enduntersuchung nach Abschluss der Tätigkeit im Kontrollbereich, umfasst. Diese Untersuchungen dürfen nur von eigens hiezu ermächtigten

Tabelle II

Vom Bundesministerium für soziale Verwaltung nach den Bestimmungen des Strahlenschutzgesetzes ermächtigte Ärzte

Bundesland	1973	1974	1975	1976	1977	1978	1979	1980	1981*	Summe
Burgenland	—	1	—	—	—	2	—	2	—	5
Niederösterreich	—	13	10	3	1	—	—	2	—	29
Oberösterreich	—	7	9	1	1	3	4	6	—	31
Kärnten	—	—	—	—	—	—	1	—	—	1
Salzburg	—	3	1	—	5	—	—	—	—	9
Tirol	—	5	4	2	3	3	—	1	1	19
Vorarlberg	—	—	—	—	—	1	—	1	—	2
Steiermark	—	2	14	15	—	6	5	4	—	46
Wien	1	12	6	9	4	6	1	2	—	41
Summe	1	43	44	30	14	21	11	18	1	183

* Incl. September 1981

Tabelle III

Anzahl der ärztlich untersuchten und der davon für eine Tätigkeit als beruflich strahlenexponierte Person nicht geeigneten Arbeitnehmer

Jahr	Medizinische Anwendung		Nicht med. Anwendung		Summe	
	untersuchte	ungeeignet	untersuchte	ungeeignet	untersuchte	ungeeignet
1975	1382	4	1033	—	2415	4
1976	3154	14	1400	5	4554	19
1977	4222	12	1672	—	5894	12
1978	4375	4	2080	5	6450	9
1979	5306	23	1836	5	7142	28

Tabelle IV

Anzahl der gemeldeten Berufserkrankungen durch Einwirkung ionisierender Strahlen

Jahr	1975	1976	1977	1978	1979
Anzahl	1	2	2	2	2

Ärzten bzw. Krankenanstalten durchgeführt werden. Die Zahl der vom Bundesministerium für soziale Verwaltung ermächtigten Ärzte ist der Tabelle II zu entnehmen.

Die Anzahl der untersuchten Arbeitnehmer, die den überwiegenden Anteil der nach den Bestimmungen des Strahlenschutzgesetzes untersuchten Personen stellt, ist der Tabelle III zu entnehmen. Auch kann dieser Tabelle entnommen werden, wieviele Personen hievon zur Tätigkeit als beruflich strahlenexponierte Personen nicht geeignet waren. Die Differenz zwischen den Zahlenwerten in den Tabellen I und III erklärt sich zum Teil auch aus der Tatsache, dass viele Betreiber einer Strahlenquelle auch Personen physikalisch kontrollieren lassen, die eigentlich nicht zum Kreis der beruflich strahlenexponierten Personen gehören.

Die Kosten für die ärztlichen Untersuchungen beliefen sich zuletzt auf etwa 8 000 000 Schilling, die zum Teil von der Unfallversicherung und zum Teil vom Bund aufgebracht wurden.

Abschliessend ist aus der Tabelle IV die Zahl der jährlich gemeldeten Berufserkrankungen auf Grund der Einwirkung ionisierender Strahlen ersichtlich. Es handelt sich hiebei durchwegs um Personen, bei denen die schädigende Einwirkung ionisierender Strahlung viele Jahre zurückliegt.

Acta Physica Academiae Scientiarum Hungaricae, 52 (3—4), pp. 323—331 (1982)

IV. DOSIMETRY

CHAIRMEN: T. BIRÓ, K. E. DUFTSCHMID

TLD MEASUREMENTS WITH LiF AND $CaSO_4$: Tm

P. P. SZABÓ

CENTRAL RESEARCH INSTITUTE FOR PHYSICS
1525 BUDAPEST, HUNGARY

LiF chips of Polish origin used for personnel monitoring at our Institute are planned to be used at the Paks Nuclear Power Station (Hungary). The thermal and intermediary neutron sensitivities of the LiF chips were established.

In environmental monitoring, Hungarian $CaSO_4$: Tm TLDs are used in tandem: one being heavily, the other being slightly filtered. In this way not only the dose but also the low energy contribution of terrestrial radiation can be established. The system was tested in International Intercomparisons.

Certain other dose rate dependence measurements of $CaSO_4$: Tm in the literature are questionable, leading to the conclusion of TLD reader instability.

Introduction

Details are given here of measurements performed with Polish LiF chips for personnel monitoring and with Hungarian $CaSO_4$:Tm powder for environmental monitoring. TL mesurements were carried out on a TLD-04B reader [1—3] developed at our Institute and on its modified version, the NHZ-204 TLD reader. The TLD readers have an EMI 9844B photomultiplier tube with a bi-alkali cathode whose temperature is stabilized by thermoelectronic cooling. The glow curves can be recorded through linear or logarithmic outputs on an X-Y recorder. The light integration period, and preheating and postannealing can be varied as can the heating time, maximum heating temperature and high voltage. The TL data were written via an interface onto a Teletype writer and were evaluated on a PDP-11 computer.

To eliminate fading the light integration period was started when the temperature of the heating tray was higher than 140 °C.

Measurements with LiF chips

LiF chips (diameter 4.8 mm, thickness 0.8 mm), produced in Poland under the trade name of MTS-N, are used with Kodak radiation monitoring film for personnel monitoring at our Institute.

The low dose detection ability of the LiF chips was investigated. The spread of the TL outputs of LiF chips at different absorbed dose levels in air is illustrated in Figs. 1 and 2. The standard deviation of 20 chips irradiated

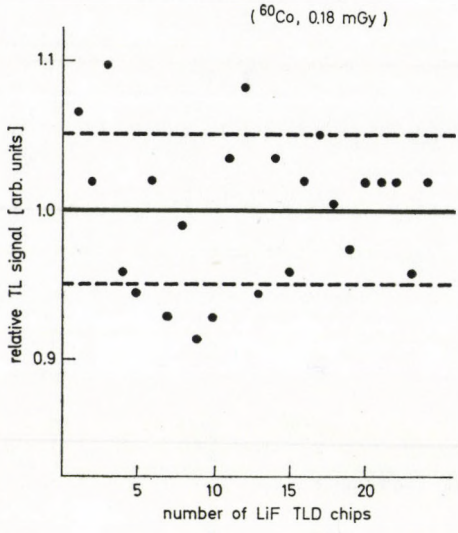

Fig. 1. Spread of the TL signals of the LiF chips, after ^{60}Co gamma irradiation to an absorbed dose in air of 0.18 mGy. The standard deviation of 5% of the TL readings is indicated.

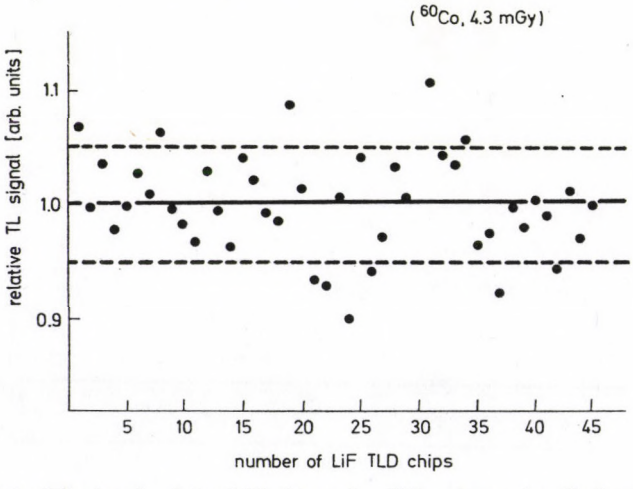

Fig. 2. Spread of the TL signals of the LiF chips after ^{60}Co gamma irradiation to an absorbed dose in air of 4.3 mGy. The standard deviation of the TL readings is 5%.

with the same dose was found to be 4—5% above 0.2 mGy in air. The linearity of the LiF chips in the low dose region is shown in Fig. 3.

LiF chips are to be used also at the Hungarian nuclear power station at Paks, where the personnel may be irradiated by neutrons in an accidental situation. The chips are made from LiF of natural isotopic abundance, the thermal neutron sensitivity of which can be high. This is the reason why the actual neutron sensitivity of the LiF chips was studied.

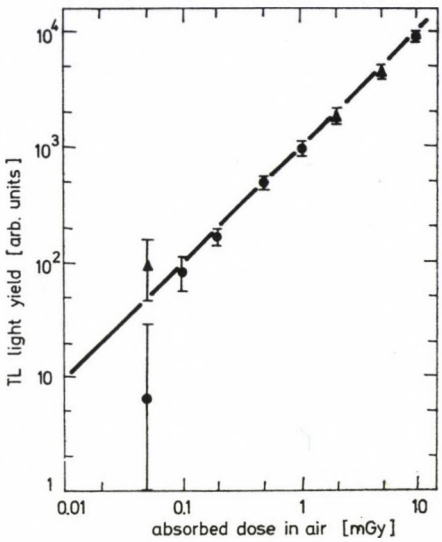

Fig. 3. TL response of the LiF chips vs the dose absorbed in air.

Table I

Thermal neutron sensitivities of different LiF TLDs of natural isotopic abundance

Type of LiF TLD	TL response for 10^{10} n.cm^{-2} / TL response of 1 Gy (^{60}Co) absorbed in air	References
TLD 100 (Harshaw)	2.87	AYYANGAR [5]
	1.39	TOCHILIN [6]
	2.17	TOCHILIN [6]
	4.26	DUA [7]
	3.13	MAJBORN [8]
	1.74	WOODLEY [9]
	1.74	WINGATE [10]
	1.91	SIMPSON [11]
	4.65	REDDY [12]
	2.69	WALLACE [13]
	0.56	SCARPA [14]
	3.22	HENAISH [15]
LiF	3.22	CAMERON [16]
LiF in Teflon	2.09 ± 0.07	SPURNY [17]
LiF : Mg PTL710	3.91 ± 0.35	SPURNY [17]
MTS-N LiF chips	2.3 ± 0.4	SZABÓ [18]

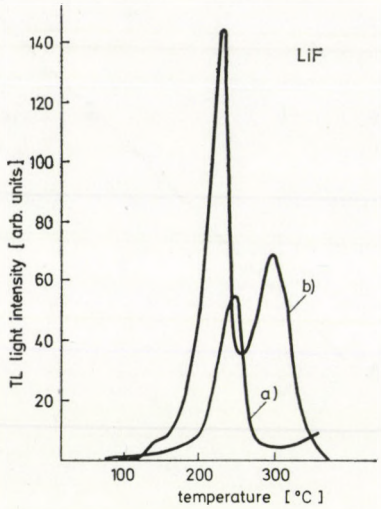

Fig. 4. Glow curves of LiF chips after ^{60}Co gamma (a), and neutron irradiation (b). After neutron irradiation a second peak appears around 300 °C.

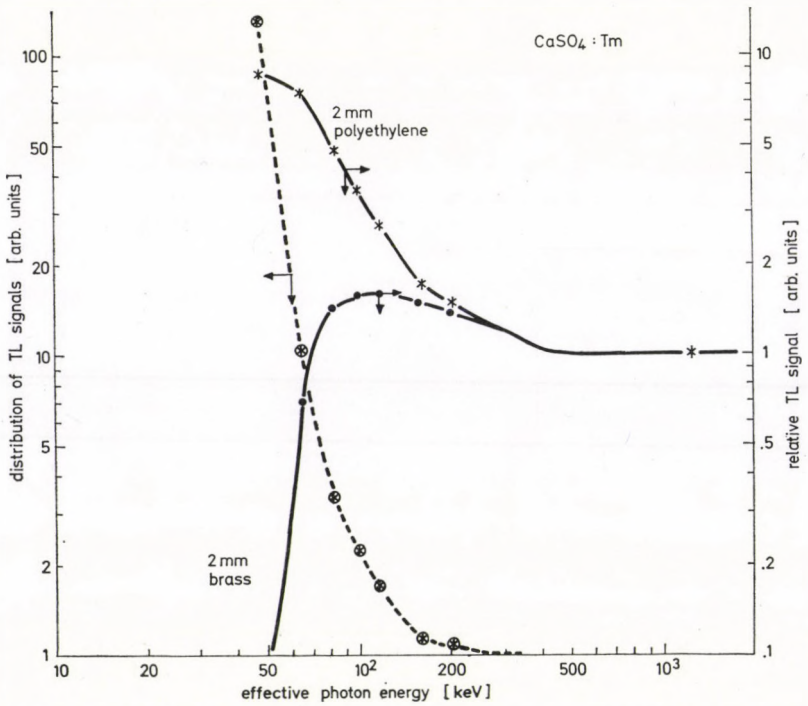

Fig. 5. Energy response of the $CaSO_2$: Tm TLD powder in 2 mm thick brass or 2 mm thick polyethylene capsules used in environmental monitoring at our Institute and in the environment of the Paks Nuclear Power Station. The dotted line is the distribution of relative TL signals in polyethylene and in brass capsules.

The LiF chips were put into the thermal column of the ZR-4 zero power reactor of our Institute, where the neutron fluence was monitored by activation gold foils and sandwiched track detectors [4].

The preliminary results show that the thermal neutron sensitivity of the LiF chips was of the same order as for other natural LiF (see Table I). For intermedier neutrons of 1/E spectrum with an energy range of $0.5-10^4$ eV, the sensitivity of the LiF chips was found to be equal to 1.5 $Gy/10^{10}$ n · cm^{-2} [18]. The glow curves of the LiF chips are shown in Fig. 4, after ^{60}Co gamma and neutron irradiation. After neutron irradiation the glow curve of the LiF chips differs from the glow curves of gamma irradiation [19, 20], which makes it possible to differentiate between gamma and neutron irradiation. During these TL measurements the LiF chips were heated to 370 °C and the evaluation was based on each of the two glow peaks.

TL measurements with $CaSO_4$: Tm

Hungarian $CaSO_4$:Tm [21] is used for environmental monitoring at our Institute and in the environment of the Paks Nuclear Power Station. Two capsules are used at every environmental station. One is made of brass, the other of polyethylene, both with a wall thickness of 2 mm [22]. The energy dependence of the two capsules is shown in Fig. 5 which also shows the distribution of the relative TL signals. These parameters enable not only the dose but also the low photon energy contribution of the terrestrial radiation to be established. The accuracy of our environmental system was tested in the International Intercomparison of Environmental Dosimeters held in the USA, 1980 (see

Table II

Results of $CaSO_4$: Tm TLDs at the Fifth International Intercomparison of Environmental Dosimeters, USA, 1980

	Our values [mGy]	True values [mGy]	Mean of all dosimeters [mGy]
field	0.263 ±0.034	0.261 ±0.026	0.262 ±0.063
beginning lab. exposure	0.703 ±0.066	0.653 ±0.033	0.659 ±0.176
end lab. exposure	0.841 ±0.076	0.768 ±0.038	0.788 ±0.136
estimated transit exposure	0.119 ±0.016		

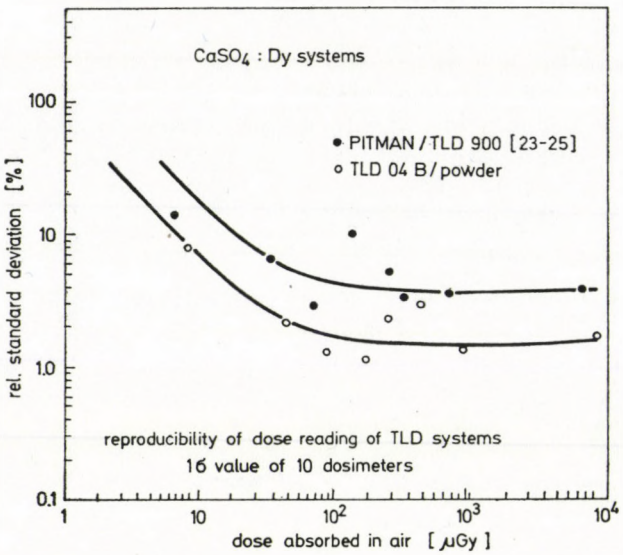

Fig. 6. Reproducibility of the Pitman TLD 900 $CaSO_4$: Dy [23—25], and our TLD-04 B $CaSO_4$: Dy powder [26] environmental TLD systems.

Table II). We also took part in the European Intercomparison of the Environmental TLD Systems organized by Kernforschungszentrum Karlsruhe, FRG [23—25]. Our results are shown in Fig. 6 [26].

The $CaSO_4$:Tm TLDs were exposed to cosmic radiation on board the spacecraft "Salyut-6". The measured dose rates were between 100—300 μGy · · day^{-1} [27, 28].

Dose rate independence of $CaSO_4$:Dy (or $CaSO_4$:Tm)

The question of dose rate dependence in the low dose rate region of highly stable TLD materials like Dy or Tm activated $CaSO_4$ was raised recently [29]. The low dose rate independence is important from the viewpoint of calibration because the calibration of environmental TLDs is carried out at a dose rate level some magnitudes higher than the actual dose rate at the environment. In this way the dose rate dependence, if it proved to be true, would mean an error of 10—15% in the environmental TLD measurements.

All data available on this subject indicate that dose rate dependence (Fig. 7) was found only when the $CaSO_4$:Dy TLDs were measured on a TLD reader (Teledyne 7100) which has no thermoelectric cooling around its photomultiplier tube [29—33]. BECKER and his co-workers found that a Teledyne TLD reader was unstable in a subtropical environment (Fig. 8), even if a high voltage stabilizer was applied [34]. When the $CaSO_4$:Dy TLDs were measured on TLD readers which have a thermoelectrically cooled photomultiplier tube on

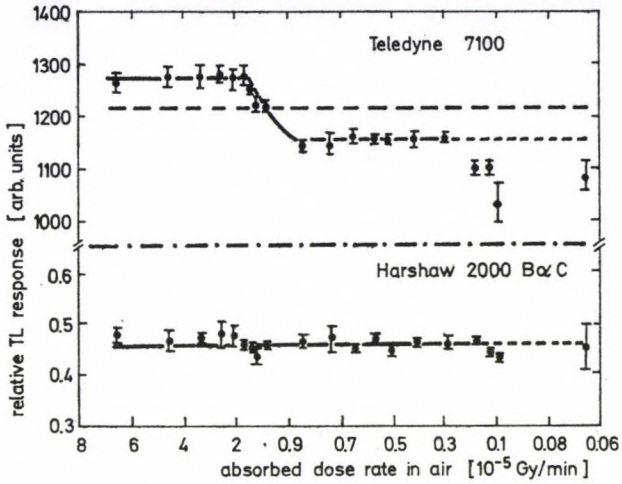

Fig. 7. Dose rate dependence on the Teledyne 7100 reader, and the dose rate independence on a Harshaw 2000 B+C TLD reader found by HSU and WENG [32].

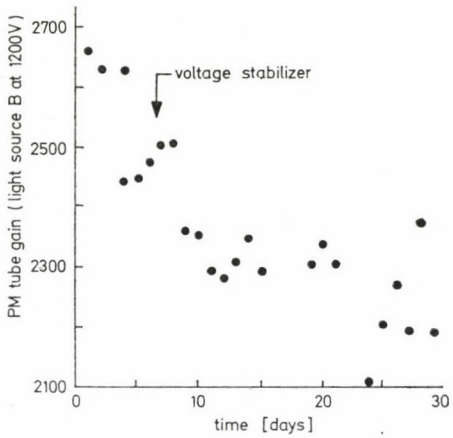

Fig. 8. Instability of a Teledyne TLD reader in a subtropical country found by BECKER et al [34].

the TLD-04B reader (Fig. 9) [31], or on the Harshaw 2000B + C reader (see Fig. 7) [32], *no* dose rate dependence was found.

Work is now in progress to measure $CaSO_4$:Dy TLDs on different TLD readers and to show that there is no dose rate dependence in the low dose rate region.

Conclusions

The Polish LiF chips used at our Institute for personnel monitoring can measure doses higher than 0.2 mGy with a standard deviation of 5%. The shape of the glow curve of LiF chips differs after gamma or neutron irradiation, so

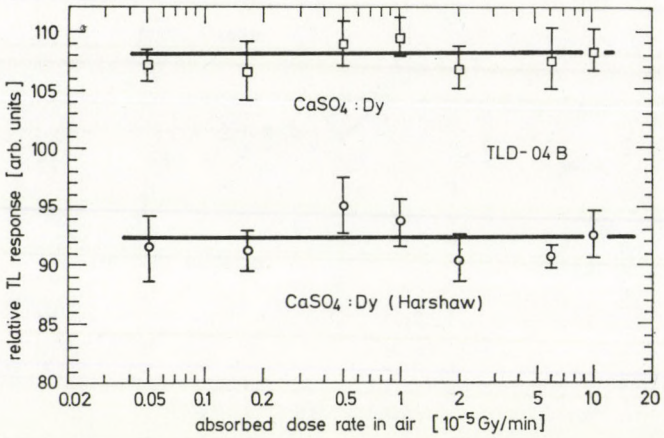

Fig. 9. Dose rate independence on a TLD-04B reader found by SZABÓ [31].

that gamma or neutron irradiations can be distinguished. The thermal and intermedier neutron sensitivities of LiF chips were found to be in agreement with other results.

Hungarian $CaSO_4$:Tm powder is used for environmental monitoring in two different capsules. In this way the low photon energy contribution of terrestrial radiation can also be estimated. Our environmental monitoring TLD system has been satisfactorily tested in international intercomparisons.

The low dose rate dependence of $CaSO_4$:Dy reaffirmed by HSU and WENG [29] is questionable, and may be due to the instability of their TLD reader.

The author is indebted to Dr. E. PIESCH for permission to publish Fig. 6.

REFERENCES

1. B. SZABÓ, P. P. SZABÓ, S. MAKRA, J. VÁGVÖLGYI and J. SOÓS, The TLD-04B Thermoluminescent Reader for Research and Routine Dosimetry Applications, Report, Central Research Institute for Physics, Budapest, KFKI-77-33, 1977.
2. B. SZABÓ, Finommechanika-Mikrotechnika, **20,** 24, 1981 (Fine Mechanics-Microtechnics, in Hungarian).
3. J. VÁGVÖLGYI and P. P. SZABÓ, Finommechanika-Mikrotechnika, **20,** 55, 1981 (Fine Mechanics-Microtechnics, in Hungarian).
4. J. PÁLFALVI, Thermal and Intermedier Neutron Flux Density Determination for Accident Dosimetry Purposes Using Thick Gold Foils, Report, Central Research Institute for Physics, Budapest, KFKI-78-42, 1978.
5. K. AYYANGAR, A. R. LAKSHMANAN, B. CHANDRA and K. RAMADAS, Phys. Med. Biol., **19,** 665, 1974.
6. E. TOCHILIN, N. GOLDSTEIN and W. G. MILLER, Health Phys., **16,** 1, 1969.
7. S. K. DUA, R. BOULENGER, L. GHOOS and E. MERTENS, Proc. 3rd. Int. Conf. Luminescence Dosimetry, Risö, Risö Report **249,** 1074, 1971.
8. B. MAJBORN, P. BOTTER-JENSEN and P. CHRISTENSEN, Dosimetry in Agriculture, Industry, Biology and Medicine, STI/PUB/311, IAEA, Vienna, 1972.
9. R. G. WOODLEY and N. M. JOHNSON, Proc. Int. Conf. Luminescence Dosimetry, CONF-650637, USAEC, 502, 1967.

10. C. L. WINGATE, E. TOCHILIN and N. GOLDSTEIN, Proc. Int. Conf. Luminescence Dosimetry, CONF-650637, USAEC, 421, 1967.
11. R. E. SIMPSON, Proc. Int. Conf. Luminescence Dosimetry, CONF-650637, USAEC, 444, 1967.
12. A. R. REDDY, K. AYYANGAR and G. L. BROWNELL, Rad. Res., **40,** 552, 1969.
13. R. H. WALLACE and P. L. ZIEMER, Proc. 2nd Int. Conf. Luminescence Dosimetry, CONF-680920, 140, 1968.
14. G. SCARPA, Health Phys., **19,** 91, 1970.
15. B. A. HENAISH, A. M. SAYED and S. M. MORSY, Nucl. Instr. Meth., **178,** 395, 1980.
16. J. R. CAMERON, N. SUNTHARALINGHAM and G. N. KENNEY, Thermoluminescence Dosimetry, University of Wisconsin Press, Wisconsin, USA, 1968.
17. F. SPURNY and G. PORTAL, Proc. 4th Int. Conf. Luminescence Dosimetry, Krakow, 1105, 1974.
18. P. P. SZABÓ and J. PÁLFALVI, to be published.
19. E. PIESCH, in Applied Thermoluminescence Dosimetry, Eds. M. Oberhofer and A. Scharmann, Adam Hilger, Oxford, 1981.
20. E. PIESCH, B. BURGKHARDT and S. KABADJOVA, Nucl. Instr. Meth., **126,** 563, 1975.
21. J. FÉLSZERFALVI, P. P. SZABÓ, J. BACSÓ and P. KOVÁCS, PACT, **3,** 311, 1979.
22. P. P. SZABÓ, J. FÉLSZERFALVI and A. LÉNÁRT, Nucl. Instr. Meth., **175,** 45, 1980.
23. B. BURGKHARDT and E. PIESCH, Nucl. Instr. Meth., **175,** 159, 1980.
24. E. PIESCH and B. BURGKHARDT, Report KfK 2626, 1978.
25. B. BURGKHARDT, E. PIESCH and H. SEGUIN, Proc. 5th Int. Cong. Rad. Prot., Jerusalem, 141, 1980.
26. P. P. SZABÓ and E. HORVÁTH, '80 Hungarian Health Phys. Meeting, Tihany, 1980.
27. YU. A. AKATOV, T. V. BATENCHUK, A. M. BORODIN, V. E. DUDKIN, A. M. MARENNY, V. A. SAKOVICH, G. G. VASILEV, A. G. KARADJOV, P. P. SZABÓ, I. FEHÉR, W. MALZ, G. VOIGTMAN and D. HASHEGANU, Adv. Space Res., **1,** 67, 1981.
28. I. FEHÉR, S. DEME, B. SZABÓ, J. VÁGVÖLGYI, P. P. SZABÓ, A. CSŐKE, M. RÁNKY and YU. A. AKATOV, Adv. Space Res., **1,** 61, 1981.
29. P. C. HSU and P. S. WENG, Nucl. Instr. Meth., **174,** 73, 1980.
30. P. C. HSU and P. S. WENG, Nucl. Instr. Meth., **138,** 307, 1976.
31. P. P. SZABÓ, Nucl. Instr. Meth., **147,** 451, 1977.
32. P. C. HSU and P. S. WENG, Nucl. Instr. Meth., **147,** 453 1977.
33. P. P. SZABÓ, Izotóptechnika **21,** 1, 1978 (in Hungarian).
34. K. BECKER, R. H. W. LU and P. S. WENG, Proc. 3rd Int. Conf. Luminescence Dosimetry, Risö, Risö Report **249,** 960, 1971.

Acta Physica Academiae Scientiarum Hungaricae, 52 (3—4), pp. 333—339 (1982)

DETERMINATION OF THE ENERGY RESPONSE OF DOSIMETERS WITH A BRAGG-MONOCHROMATIZED BEAM

N. VANA and H. AIGINGER

ATOMIC INSTITUTE OF THE AUSTRIAN UNIVERSITIES
A-1020 VIENNA, AUSTRIA

In the energy region below 50 keV the energy response of dosimeters is usually determined by means of filtered Bremsstrahlung radiation. The "monochromatic" radiation produced by filtering the continuous X-ray spectrum of an X-ray tube shows a broad energy distribution for the maximum of the intensity and a considerable "tailing" to low energies.

To avoid this disadvantage we used a Bragg monochromator for the energy region between 10 keV and 50 keV. The Bragg monochromator, a commercially available X-ray spectrometer, reflects selectively monochromatic X-rays from a continuous bremsspectrum of a tungsten X-ray tube. The angle of reflection and the energy are determined by the Bragg condition. The energy resolution obtained was 2%. The photon flux density at the place of the dosimeter was measured with an efficiency calibrated Ge(Li) semiconductor detector. From this photon flux density the actual exposure of the dosimeter under examination can be calculated.

1. Introduction

The determination of the energy response of all kinds of dosimeters is one of the most important mesurements in experimental dosimetry [1]. Most of these determinations are usually done by means of filtered bremsstrahlung radiation. X-ray bremsstrahlung spectra are commonly characterized by the kilovoltage across the X-ray tube, the filtration and the half-value layer. Some laboratories also specify other quantities, such as the homogeneity coefficient (the ratio of the first and second HVL's), the mean energy, or an "effective energy" (commonly defined as the photon energy of a monochromatic beam with the identical HVL) [2].

The photoeffect as the dominating process in the low energy region < 50 keV causes a strong effective atomic number dependence in the response function dosimeter material. The "monochromatic" radiation produced by filtering the continuous X-ray spectrum of an X-ray tube shows a broad energy distribution for the maximum of the intensity and a considerable "tailing" to low energies. A few examples are given in Figs. 1 to 3 [2].

Fig. 1 (C 4 from [2]) shows a filtered spectrum (12 kV tube, 0.4 mm Al filter, homogeneity coefficient 95) with good homogeneity. Fig. 2 (C 5 from [2]) shows a filtered spectrum (14 kV, 0.11 mm Al, h. c. 87). Fig. 3 (C 69 from [2]) shows a filtered spectrum (100 kV, 3 mm Al, h.c. 59), which can no longer be called a homogeneous spectrum. Fig. 3a (C 43 from [2]) shows a filtered spectrum (50 kV, "mean energy" 24.4 keV for exposure, 29.4 keV for photon flux density, homogeneity coefficient 80), which has its "mean energy" near the

25 keV, used later on in our example. The inhomogeneity of the spectra also calls for a distinction between a "mean energy" for the photon flux density and a "mean energy" for the exposure rate.

Both properties are a clear disadvantage in the above mentioned energy region with its steep changes of dosimetric response with energy.

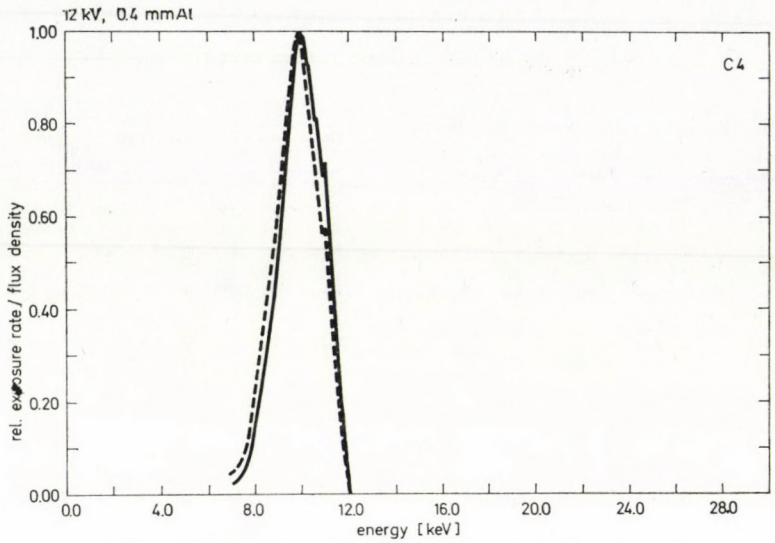

Fig. 1. Filtered spectrum: 12 kV tube, 0.4 mm Al, homogeneity coefficient (h.c.) 95 [2]. Dotted line: exposure rate, solid line: flux density.

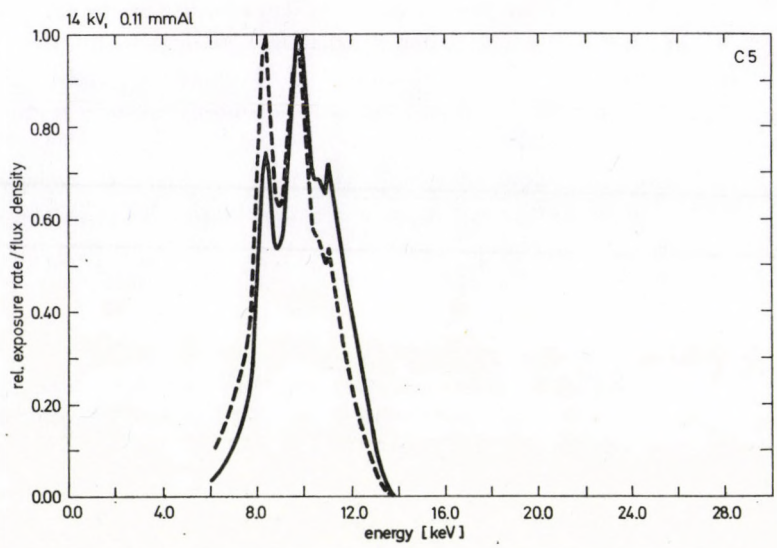

Fig. 2. Filtered spectrum: 14 kV, 0.11 mm Al, h. c. 87 [2]. Dotted line: exposure rate, solid line: flux density.

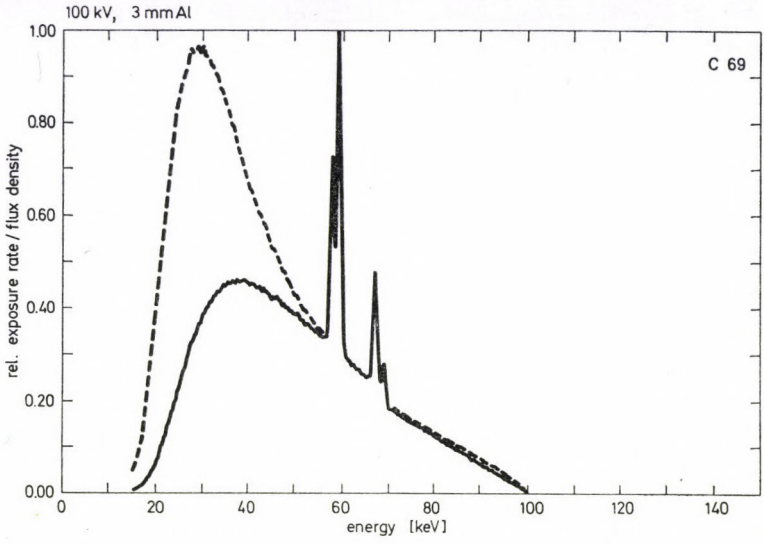

Fig. 3a. Filtered spectrum: 100 kV, 3 mm Al, h. c. 59 [2]. Dotted line: exposure rate, solid line: flux density.

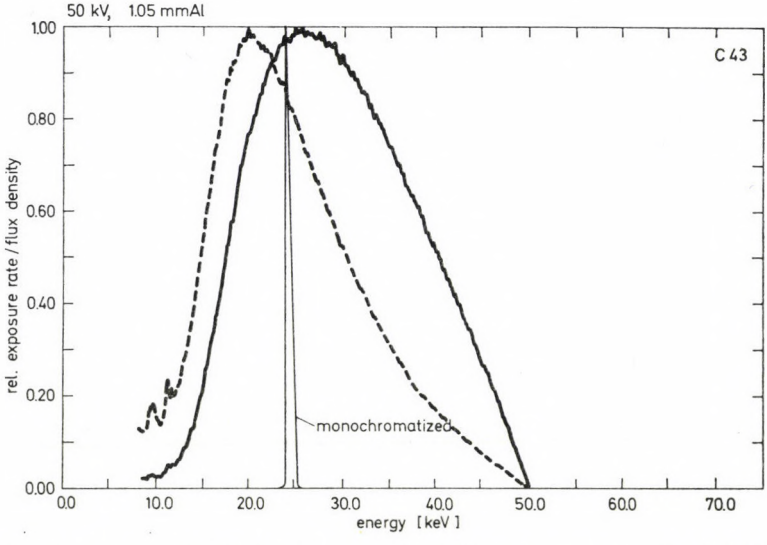

Fig. 3b. Filtered spectrum: 50 kV, "mean energy" 24.4 keV for exposure, 29.4 keV for photon flux density, h. c. 80 [2] and the Bragg-monochromatized beam. Dotted line: exposure rate, solid line: flux density.

2. The Bragg-monochromator facility for dosimeter calibration in the energy range of 10 keV to 50 keV [3]

Fig. 4 shows the details of this facility. The X-ray beam from X-ray tube (W-anode, 10—60 kV) is geometrically defined by an aperture and Bragg-reflected at an angle ϑ. After the reflection the X-rays are monochromatic

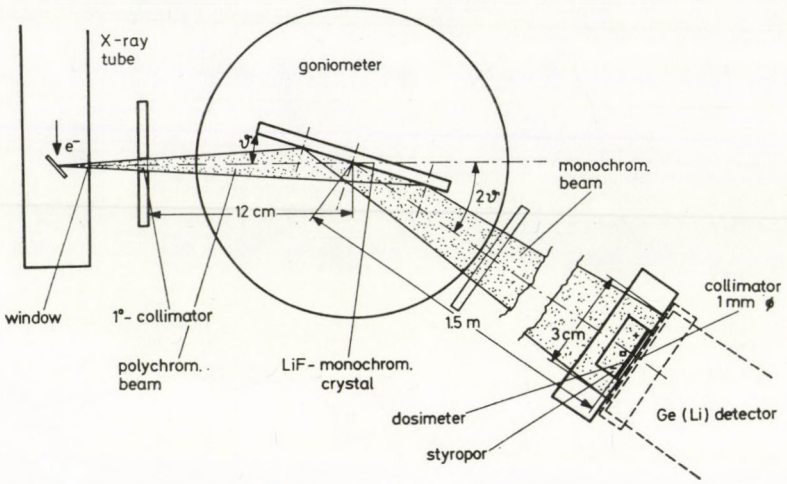

Fig. 4. Bragg-monochromator facility for dosimeter calibration in the energy range of 10 keV to 50 keV.

with a half-width of ~ 0.5 keV for the energy distribution. Energy E and angle ϑ are related by

$$\vartheta = \arcsin \frac{n\,h\,c}{2\,d\,E}$$

or with the wavelength

$$\lambda = \frac{hc}{E}, \qquad n\lambda = 2\,d \sin \vartheta,$$

which is the well-known Bragg condition, where n is the order of diffraction ($n = 1, 2, 3, \ldots$) and d is the spacing between lattice planes of atoms in the monochromator crystal. To avoid higher order diffraction ($n = 2, 3, \ldots$) the condition $eU < 2E$ must be fulfilled. Fig. 4 shows the defined place for the dosimeter calibration and the arrangement for the determination of energy and flux density of the radiator at the dosimeter's place.

3. Determination of the photon flux density and the energy distribution and flux density exposure rate relation

An efficient calibrated Ge(Li)-detector with an 1 mm ∅ aperture was used for the determination of the energy distribution and the flux density. Fig. 5a gives the energy distribution and the calculation of the average flux density at the dosimeneter's place (5b) calculated by the method of equal areas from the measured flux densities at various points with a deviation of ± 3 mm (the dosimeter actually calibrated was 6 mm$\times$6 mm$\times$1) from the origin. As can be gathered from Fig. 5b the counts/1 mm ∅ and 1 min counting interval were $\bar{I} = 23.64 \times 10^4$ in the peak area. The exposure can be obtained with

$$D = \bar{I} f z \frac{k}{\varepsilon}.$$

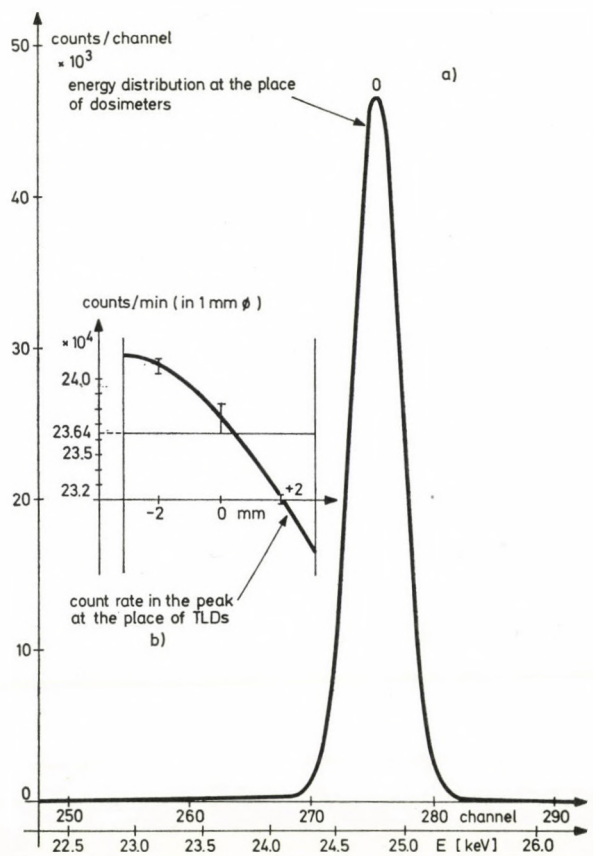

Fig. 5. a) Energy distribution at the dosimeters' place. b) Average flux at the dosimeter's place.

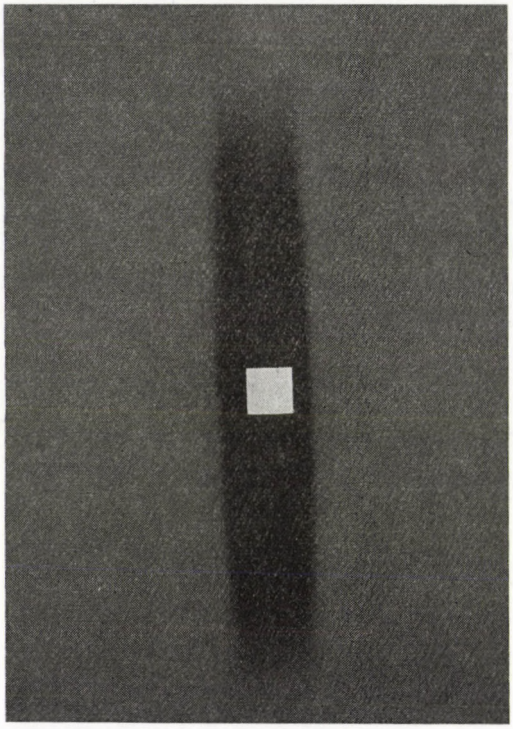

Fig. 6. Intensity distribution of the monochromatized X-ray beam obtained with a film at the dosimeter.

A numerical example for 25 keV $\pm$ 0.5 keV gives: k is the exposure rate/flux density conversion factor from STORM—LIER [4] (1R = 258 μC/kg)

$$k = 3.109 \frac{\mu\text{C/kg}}{10^8\text{Ph/cm}^2} \text{ (at } 25 \pm 0.5 \text{ keV)};$$

ε is the counting efficiency

$$\varepsilon > 0.937 \qquad \text{at} \qquad 25 \pm 0.5 \text{ keV};$$

f is the correction for the respective areas

$$f = \frac{1\text{cm}^2 \times 4}{(0.1\text{cm})^2 \pi} = 127.3;$$

z is the correction time of detector exposure/counting time

$$z = 60.$$

The exposure in the place of the flux density determining detectors

$$D = 59.9 \pm 3.9\ \mu\text{C/kg}\ (232 \pm 15\ \text{mR}).$$

Fig. 6 gives a visual impression of the spatial intensity distribution obtained with an X-ray film. The dosimeter appears as a white square.

4. Irradiation of a calibrated TL-dosimeter

The dosimeter (TLD-100, 60 min, 25 keV) was exposed and calibrated in a different way (^{60}Co irradiation, correction of the different sensitivity for 25 keV radiation and ^{60}Co radiation). According to this calibration the following exposure was obtained

$$D = 60.9 \pm 3.9\ \mu\text{C/kg} \qquad (236 \pm 15\ \text{mR}).$$

The result proves the proper accuracy obtainable at a very well defined photon energy.

REFERENCES

1. K. Becker, Solid State Dosimetry, CRC Press, Cleveland, 1960.
2. W. W. Seelentag, W. Panzer, G. Drexler, L. Platz and F. Santner, A Catalogue of Spectra for the Calibration of Dosimeters, GSF-Bericht 560/1979.
3. N. Vana, H. Aiginger and W. Erath, Measurements of Doses in the 1 mrad-Range by Means of LiF, CaF_2 and $CaSO_3$ Dosimeters and Determination of the Energy Response of LiF and CaF_2 in Proc. IVth IRPA Congress, Paris, Vol. 4, 1253, 1977.
4. E. Storm and D. W. Lier, Health Phys., **23**, 73, 1972.

Acta Physica Academiae Scientiarum Hungaricae, 52 (3—4), pp. 341—345 (1982)

MEASUREMENT OF THE ENERGY RESPONSE OF LiF—, CaF_2— AND $CaSO_4$ — TL-DOSIMETERS

N. VANA, H. AIGINGER, W. ERATH and T. MICHEV

ATOMIC INSTITUTE OF THE AUSTRIAN UNIVERSITIES
A-1020 VIENNA, AUSTRIA

The most important materials used in thermoluminescence dosimetry (TLD) are LiF, CaF_2 and $CaSO_4$ with various dopants. LiF : Mg, Ti is almost tissue equivalent and therefore the most applied TLD-material in personnel and medical dosimetry. CaF_2 : Dy offers the highest sensitivity of the above mentioned materials and is used in environmental and low-dose dosimetry. $CaSO_4$: Dy can easily be labor made and is the cheapest phosphor. As the effective atomic numbers of CaF_2 and $CaSO_4$ differ markedly from that of tissue material the response curve of both materials must be carefully determined in the energy range dominated by the photoeffect. The energy responses of these three listed phosphors were determined by means of a Bragg monochromator, filtered radiation from a gold target bombarded by electrons from a Van de Graaff accelerator, the radiation of a ^{137}Cs-source (662 keV) and a ^{60}Co-source (1.17, 1.33 MeV). The response-energy dependence of the three dosimeters shows maxima at 35 keV (LiF and CaF_2) and 40 keV ($CaSO_4$).

1. Introduction

The most important materials used in thermoluminescence dosimetry (TLD) are LiF, CaF_2 and $CaSO_4$ matrix systems with various dopants. LiF:Mg,Ti is almost tissue equivalent and therefore the most widely applied TLD material in personnel and medical dosimetry.

CaF_2:Dy offers the highest sensitivity of the above listed materials and is used in environmental and low-dose dosimetry.

$CaSO_4$:Dy can easily be labor made and is the cheapest phosphor.

As the effective atomic numbers of CaF_2 and $CaSO_4$ differ markedly from that of tissue material, the photon energy response curve of both materials must be carefully determined, especially in the photoeffect dominated low energy range [1, 2, 3].

2. The methods of sample irradiation used

2.1. Irradiation with Bragg-monochromatized X-ray bremsstrahlung

As already mentioned a Bragg monochromator can be used for the selection of a certain energy in the energy range from 10 to 50 keV [4]. The well defined energy and the straightforward determination of the spectral shape and intensity are advantageous in this energy region with fast changes of sensitivity vs photon energy. The extension of the method up to 80 keV is possible if topas and quartz (SiO_2) are used as monochromator materials.

2.2. *Irradiation with filtered bremsstrahlung from a gold target bombarded with electrons from a Van de Graaff accelerator (energy range 60—260 keV)*

Fig. 1 shows the experimental arrangement used in this energy range. The electrons accelerated in the Van de Graaff (130 keV, 140 keV, 275 keV) are stopped in a water cooled Au-target. The produced bremsstrahlung is filtered.

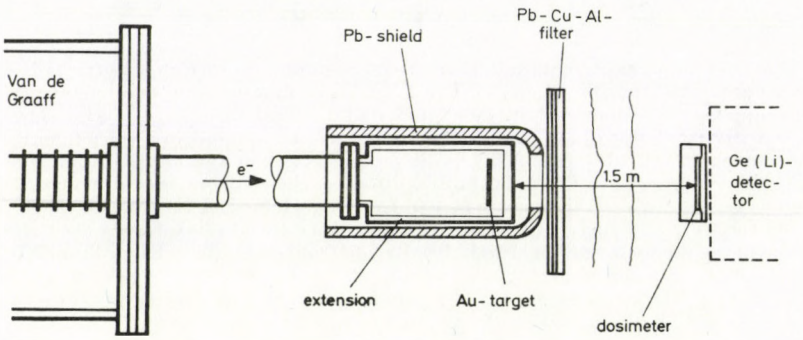

Fig. 1. Irradiation of the dosimeters with filtered bremsstrahlung produced with a Van de Graaff accelerator.

The shape of the filtered bremsstrahlung spectrum and the intensity of the radiation at the place of the dosimeter is determined with a Ge(Li)-spectrometer. A calibrated dose ratemeter was used additionally for the determination of the dose rate. Table I gives the electron energy, the filter combinations, the effective energy of the filtered radiation and the full width of half maximum (FWHM) as the parameter which defines the "homogeneity" of the radiation.

2.3. *Irradiation with 662 keV photons from a ^{137}Cs source*

A collimated beam was used. The source — dosimeter distance was 2 m to provide secondary electron equilibrium (e. equ.) in air at the dosimeter place. Dose rate determination was obtained with a calibrated dose-ratemeter.

Table I

Electron energy (keV)	Filter combination	"Mean energy" photon flux density [keV]	Full width of half maximum [keV]
130	2 mm Cu	72	12
140	1.2 mm Sn	106	30
	5 mm Cu		
275	2 mm Pb	255	43
	2.4 mm Sn		

2.4 Irradiation with 1.17 and 1.3 MeV photons (1.25 MeV) from a ^{60}Co source

In determining the dosimeter response for ^{60}Co radiation the following conditions must be used for all mesurements:

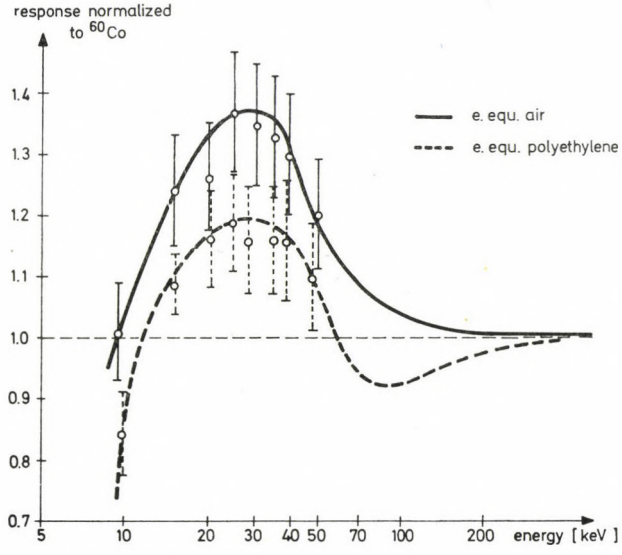

Fig. 2. Response vs energy of TLD-100 (LiF : Mg, Ti) for secondary electron equilibrium (e.equ.) in air and in a polyethylene wrapping.

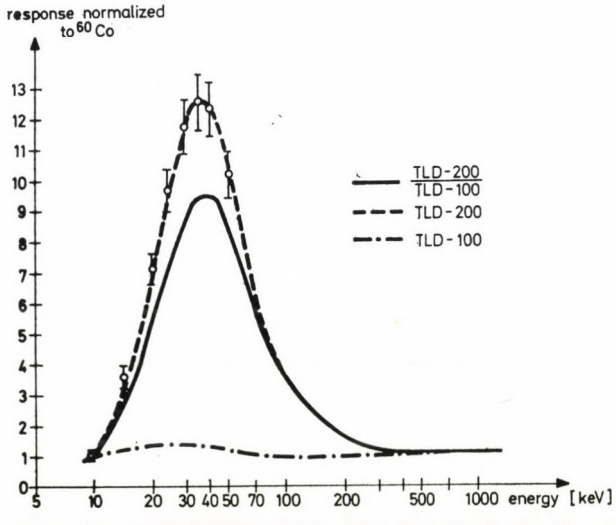

Fig. 3. Response vs energy for TLD-200 (CaF_2 : Dy), TLD-100 and the relation of TLD-200/TLD-100-response for e.equ. in air.

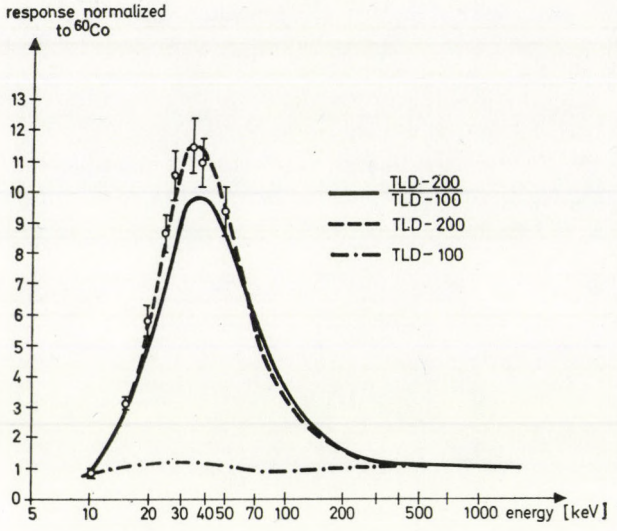

Fig. 4. Response vs energy for TLD-200, TLD-100 and the relation of TLD-200/TLD-100-response for e.equ. in a polyethylene wrapping.

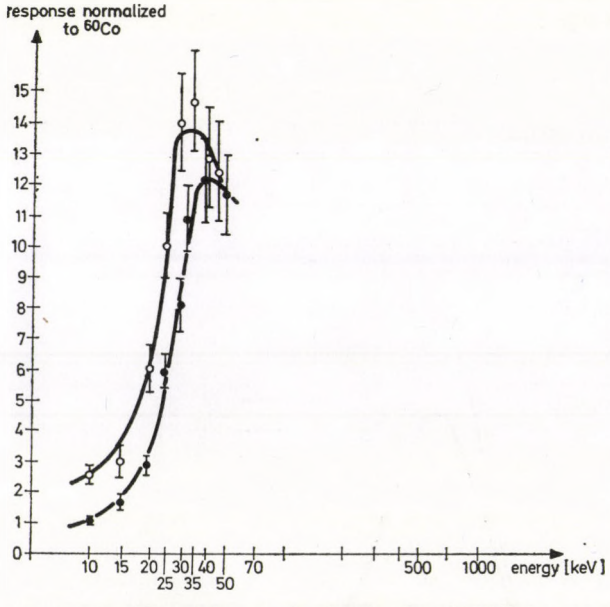

Fig. 5. Response vs energy for a labor made $CaSO_4$: Dy (0.1%) in a small "plexiglass"-box (open circle) and in a gelatine capsule.

— the distance from the ^{60}Co source must be large enough to obtain e. equ.
— same material and thickness for the dosimeter wrapping to obtain e. equ. in the material.

3. Results

3.1. Results for TLD-100 (LiF) and TLD-200 (CaF_2)

Fig. 2 shows the energy dependence of the response of TLD-100 in the case of secondary electron equilibrium in air and in a polyethylene wrapping. The response is normalized to ^{60}Co response.

Figs. 3 and 4 show the response vs energy for TLD-100 and TLD-200 and the relation of TLD-200/TLD-100-response.

3.2. Results for labor made $CaSO_4$:Dy (0.1%)

Fig. 5 shows the energy dependence of $CaSO_4$ obtained with Bragg-monochromatized radiation for $CaSO_4$ powder in a small "plexiglass" box and in a gelatine capsule.

REFERENCES

1. P. KREPLER, C. HAVRANEK and N. VANA, Röntgenpraxis, **29,** (12) 271, 1976.
2. P. KREPLER, N. VANA and C. HAVRANEK, Pediat. Radiol., **5,** 231, 1977.
3. N. VANA, R. WANECK, G. LECHNER, Strahlenbelastung des Patienten bei angiographischen Untersuchungen unter Verwendung Seltener-Erden-Folien (SEF), in O. Messerschmidt und F. Olbert "Strahlenschutz in Forschung und Praxis", Band XX, 98, 1980.
4. N. VANA and H. AIGINGER, Acta Phys. Hung., this issue, p. 333.

Acta Physica Academiae Scientiarum Hungaricae, 52 (3—4), pp. 347—352 (1982)

DOSISMESSUNGEN IM UNTERRICHTSREAKTOR DER TU — BUDAPEST NACH DER REKONSTRUKTION

E. VIRÁGH

UNTERRICHTSREAKTOR DER TECHNISCHEN UNIVERSITÄT
1521 BUDAPEST, UNGARN

Der Unterrichtsreaktor der TU — Budapest wurde zwischen 1979—81 rekonstruiert und die Reaktorleistung auf 100 kW erhöht. Diese Arbeit enthält die wichtigsten Messergebnisse des gemischten Reaktor-Strahlenfeldes.

Einleitung

Der Unterrichtsreaktor der TU—Budapest ist seit Juni 1971 in Betrieb. Die Maximalleistung des Reaktors betrug anfangs 10 kW. Zwischen 1979—81 wurde der Reaktor rekonstruiert und auch die Reaktorleistung auf 100 kW erhöht. Auf Grund dieser erhöhten Leistungsfähigkeit werden in dieser Arbeit einige Messergebnisse vorgelegt.

Der Unterrichtsreaktor in Budapest

Der Unterrichtsreaktor der TU—Budapest liegt in der Stadtmitte neben der Donau, unweit der Freiheitsbrücke. Das Reaktorgebäude ist ein halbkugelförmiger Bau (Abb. 1) in dessen Mitte der Reaktor mit biologischer Abschirmung untergebracht ist. Abb. 2 zeigt den Grundriss des Reaktors. In der Spaltzone befinden sich die Brennstoffkassetten, EK-10 Brennstoffelemente aus der UdSSR enthaltend, die mit 10% ^{235}U angereichert wurden. Das Moderatormaterial im Reaktor besteht aus Graphit und Wasser. Der Reaktor hat 5 horizontale Kanäle, 1 sog. Bestrahlungstunnel und 23 senkrechte Kanäle (Abb. 3). Zur senkrechten Abschirmung befindet sich über der Spaltzone eine Wasserschicht von 4.80 m. Tabelle I zeigt die wichtigsten Angaben des Reaktors.

Strahlungsmessgeräte und ihre Kalibrierung

Bei den Dosismessungen wurden verschiedene Strahlungsmessgeräte verwendet:

— VA-J-18 Gammadosisleistungsmessgerät (DDR) mit der VA-K-253 Ionisationskammer;
— VA-J-15 Gammadosisleistungsmessgerät (DDR);

Acta Physica Academiae Scientiarum Hungaricae 52, 1982

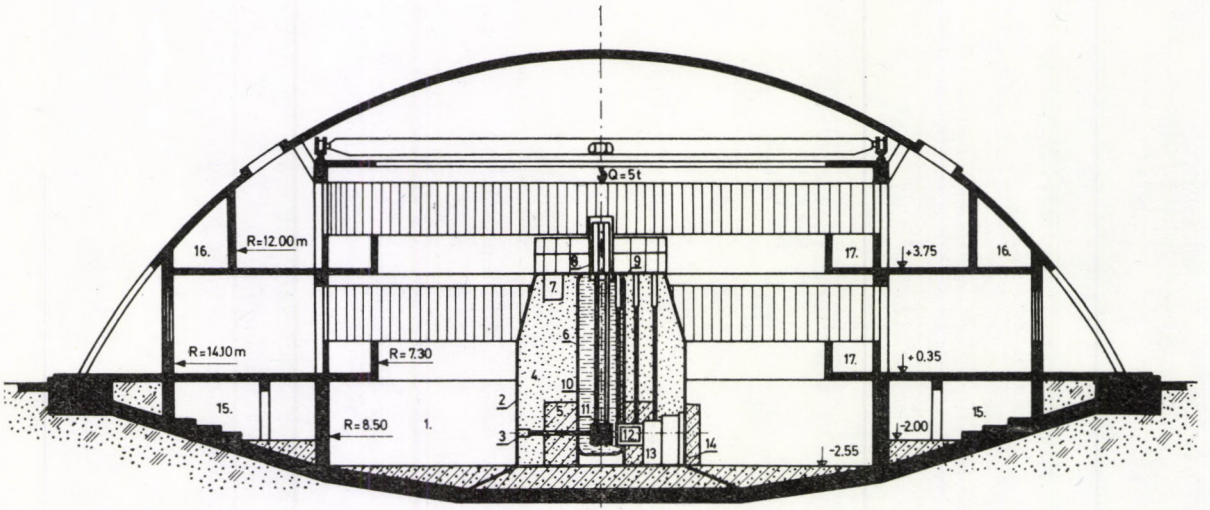

Abb. 1. Das Reaktorgebäude. 1 — Reaktorhalle; 2 — Reaktorblock; 3 — Horizontalkanal; 4 — Normalbetonabschirmung; 5 — Schwerbetonabschirmung; 6 — Reaktortank; 7 — Versuchsschacht; 8 — Plexiglasschutz; 9 — Vertikalkanäle; 10 — Sicherheits- und Regelungstäube; 11 — Aktive Zone; 12 — Wassertank; 13 — Bestrahlungstunnel; 14 — Schwerbetonblock für Zusatzabschirmung; 15 — Kellerräume; 16 — Technologische Räume; 17 — Innerer Rundkorridor.

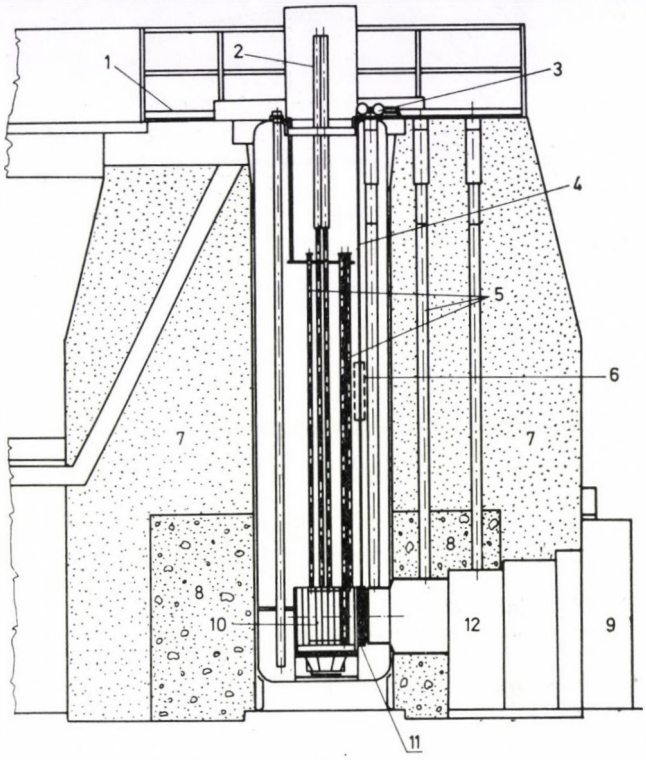

Abb. 2. Der Grundriss des Reaktors. 1 — Reaktorbrücke; 2 — Sicherheits- und Regelungsstäube; 2 — Motor; 4 — Aufhängung der Bleiabschirmung; 5 — Vertikalkanäle; 6 — Bleiabschirmung während des Reaktorbetriebs; 7 — Normalbeton; 8 — Schwerbeton; 9 — Schwerbetonblock für Zusatzabschirmung; 10 — Aktive Zone; 11 — 7 cm Bleiabschirmung bei der Öffnung des Tunnels; 12 — Bestrahlungstunnel.

— RUP-I. Universalradiometer mit einer GM-Sonde für die Gammadosisleistungsmessung;
— RUST Strahlungsmessgerät (Polen) mit einer SSNT-2 Sonde, die ein Bonnerzähler für Neutronendosisleistungsmessungen ist;
— LiF und CaF_2TL-Detektoren und das TL-Auswertegerät VICTOREEN 2800 (USA).

Bei den Messungen wurden die Messergebnisse in Äquivalentdosis (Sv) angegeben, wobei in den Rechnungen der Zusammenhang

$$100\ \mathrm{R} \sim 1\ \mathrm{Gy} = 1\ \mathrm{Sv}$$

berücksichtigt ist.

Bei der Kalibrierung der Dosismessgeräte wurden folgende Strahlungsquellen verwendet:

— ^{137}Cs Gammastrahlungsquelle mit 954 MBq (25,8 mCi) Aktivität;
— Pu-Be Neutronenquelle mit $2.25 \cdot 10^6\ \mathrm{s}^{-1}$ Quellstärke.

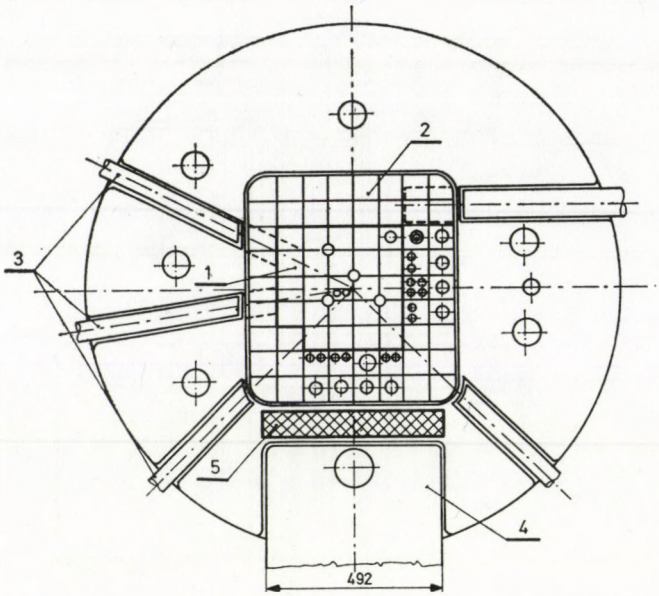

Abb. 3. Die aktive Zone (nach der Rekonstruktion). 1 — Brennstoffelemente; 2 — Graphit; 3 — Horizontalkanäle; 4 — Bestrahlungstunnel; 5 — 7 cm Bleischutz.

Tabelle I

Die wichtigsten Daten des Unterrichtsreaktors nach der Rekonstruktion

Reaktorleistung (thermisch)	100 kW
Typ der Brennstoffelemente	VVRS-EK-10
Kritische Masse in der Spaltzone (min.)	2470 g ^{235}U
Eingebauter Brennstoff	2952 g ^{235}U
Reaktivitätsmaximum	170 C
Neutronenfluss (thermisch bei 100 kW)	max. $2.7 \cdot 10^{12}$ cm^{-2} s^{-1}
Horizontale Kanäle	5
Senkrechte Kanäle	23
Bestrahlungstunnel	1
Abschirmung des Reaktors:	2 m Beton
in seitlicher Richtung	(1,1 m Schwerbeton + 0,9 m Normalbeton)
in senkrechter Richtung	4,8 m Leichtwasser

Dosismessungen

Es werden die wichtigsten Messergebnisse der Neutronen- und Gammadosismessungen an verschiedenen Stellen des Reaktors zusammengefasst.

Viele Messungen wurden bei geöffneten Horizontalkanälen durchgeführt. Bei den Messungen wurde die VA-J-18, VA-K-253 Kombination angewendet. Die Gammadosisleistungen bei geöffneten Horizontalkanälen sind in Tabelle II zusammengefasst. Tabelle III zeigt den Zusammenhang zwischen Reaktorleistung und Gammadosisleistung bei Horizontalkanal II.

Der Bestrahlungstunnel ist potenziell die gefährlichste Stelle der Reaktorhalle, weil die äussere Strahlenbelastungsmöglichkeit *nach* dem Reaktorbetrieb

Tabelle II

Gammadosisleistung bei 100 kW im Primärbündel der Horizontalkanäle (VA-J-18)

Horizontalkanal	I.	II.	III.*	IV.	V.
Gammadosisleistung [Sv/h]	16,6	18,6	1,4	3,8	14,8

* In diesem Kanal befindet sich eine Bi-Abschirmung.

Tabelle III

Zusammenhang Reaktorleistung—Gammadosisleistung im Primärbündel des Horizontalkanals II

Reaktorleistung [kW]	1	10	20	40	100
Gammadosisleistung [Sv/h]	0,18	1,86	3,78	6,72	18,6

Tabelle IV

Dosisleistungswerte in der Nähe des Bestrahlungstunnels bei 50 kW

Messstelle	A	B	C	D	E
$\dot{D}_n + \dot{D}_\gamma$ [μSv/h]	99	8	10	3	8

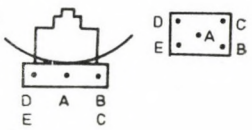

Tabelle V

Dosisleistungswerte auf dem oberen Teil des Reaktors bei 100 kW

Messstelle	A	B	C	D	E	F
$\dot{D}_n + \dot{D}_\gamma$ [μSv/h]	129	141	136	133	151	8,5

an der Öffnung des Bestrahlungstunnels relativ hoch ist, wenn Personen in der Umgebung des Tunnels nicht vorsichtig sind. Aus Sicherheitsgründen wurde eine bewegliche Abschirmungswand aus 7 cm Blei in den Reaktortank eingebaut, die bei der Tunnelöffnung zwischen der Spaltzone und dem Bestrahlungstunnel herunterlassbar ist. Die 7 cm Bleiabschirmung reduziert die Gammadosisleistung nach unseren Messungen mit einem Faktor 20—25.

Der Bestrahlungstunnel ist zur Zeit mit Graphit als thermische Säule ausgekleidet. Vor dem Bestrahlungstunnel befindet sich ein 70 cm starker Betonschutz. Die Gamma- und Neutronendosisleistungen vor der biologischen Abschirmung sind in Tabelle IV zusammengefasst.

Abschliessend werden die Messergebnisse über dem 4.80 m hohen Wasserschutz der Spaltzone ausführlich dargelegt (siehe Tabelle V).

Viele Messungen wurden noch in verschiedenen Stellen des Reaktorgebäudes, z.B. in Laboratorien, bei den techischen Anlagen, u.s.w. durchgeführt, deren Ergebnisse hier jedoch nicht spezifiziert werden.

Diskussion

Die gefährlichsten Stellen im Reaktorgebäude während des Reaktorbetriebs sind die Reaktorhalle mit den Horizontalkanälen und dem Bestrahlungstunnel, die Reaktorbrücke und die technischen Räume im Keller. Nach Ermittlung dieser Messergebnisse wurden im Interesse des Personals und der Studenten neue Vorschriften für den 100 kW Reaktorbetrieb herausgegeben. Einige wichtigere Punkte der neuen Strahlenschutzvorschrift sind:

1. Während des Reaktorbetriebes muss unter dem Betriebpersonal auch ein Strahlenschutzfachmann (Messtechniker) anwesend sein.

2. Der Versuchsleiter hat eine sogenannte "Versuchserlaubnis" auszufüllen und sie vom technischen Vizedirektor und dem Leiter der Strahlenschutzgruppe genehmigen zu lassen. Auf der Versuchserlaubnis ist auch der Abschirmungsplan angegeben.

3. Bei den Versuchen auf der Reaktorbrücke, in der Reaktorhalle und bei der Arbeit in den technischen Räumen ist die Anwesenheit des Messtechnikers notwendig. Von diesem ist vor Beginn des Versuches die Dosisleistung an allen Arbeitsplätzen zu ermitteln.

LITERATUR

E. VIRÁGH, Dosismessungen bei erhöhter Leistung (100 kW). Beilage 1 der Genehmigungsdokumentation, Unterrichtsreaktor der TU Budapest, März 1981 (ungarisch).

Acta Physica Academiae Scientiarum Hungaricae, 52 (3—4), pp. 353—356 (1982)

LITHIUM DRIFTED BERYLLIUM OXIDE HIGH SENSITIVITY THERMOLUMINESCENT DOSIMETER

S. MAKRA

NATIONAL ONCOLOGICAL INSTITUTE
1122 BUDAPEST, HUNGARY

A new BeO : Li detector sensitized by a novel method is described. The glow curve of the detectors shows two peaks, the ratio of peak heights depends on dose. The light output per unit dose slightly exceeds that of lithium fluorides. Reproducibility is $\pm 2\%$ for doses higher than 3 mGy, detection limit is 50 μGy, exceeding by two — three orders of magnitude the values obtained for commercial BeO detectors. Response shows less than $\pm 15\%$ change with photon energy. Fading is lower than 2% per month.

Beryllium oxide (BeO) TL dosimeters were used by the author and his co-workers in the past for gamma and mixed neutron-gamma radiation dosimetry [1], [2]. In spite of several advantages (precision, low neutron response, etc.) por sensitivity restricted their field of application to nuclear accident and radiobiological dosimetry [3], [4].

The present paper deals with a new BeO:Li detector, sensitized by a novel lithium diffusion technique, developed by BOROS for TSEE detectors [5], [6]. The 8 mm dia $\times$ 0.25 mm thick BeO disks, produced by Consolidated Beryllium Co. (Milfordhaven, England) and sensitized by the BOROS method have the following TL properties.

The glow curve shows two peaks, at temperatures of approximately 250 °C and 380 °C, respectively. The ratio of peak heights depends on dose, as it can be seen from the set of glow curves of Fig. 1. The detection limit is of the order of 50 μGy (5 mrad).

The light output per unit tissue dose slightly exceeds that of a lithium fluoride chip of 4.6 mm dia, when the dosimeters are read by a TLD-04B reader [7].

The triboluminescence of the dosimeters in question is a major effect which determines the minimum detectable dose. The reproducibility of readings of an unirradiated detector is $\sigma_0 = 2—3$ μGy equivalent if the detector is not removed from the heater planchet between consecutive readings. Removing the detector from the heating planchet after read-out with a metal tweezer and putting it back again for the next reading, σ_0 reaches 20 μGy equivalent, clearly showing the effect of triboluminescence. Scratching the detector surface with a steel laboratory tweezer increases the σ_0 of the triboluminescent signal to 40—80 μGy equivalent (Table I).

Values for triboluminescent effect were obtained by measuring the TL signal between temperatures of 160 °C and 400 °C. Comparing the tribolumines-

Table I

Triboluminescent signal induced by handling

Handling method	Triboluminescent signal μGy equivalent	Standard deviation of triboluminescent signal, μGy equivalent
untouched	$\sim$ 60	2— 3
grasped with steel tweezer	$\sim$100	15—20
scratched 5 times with a steel tweezer	$\sim$160	40—80

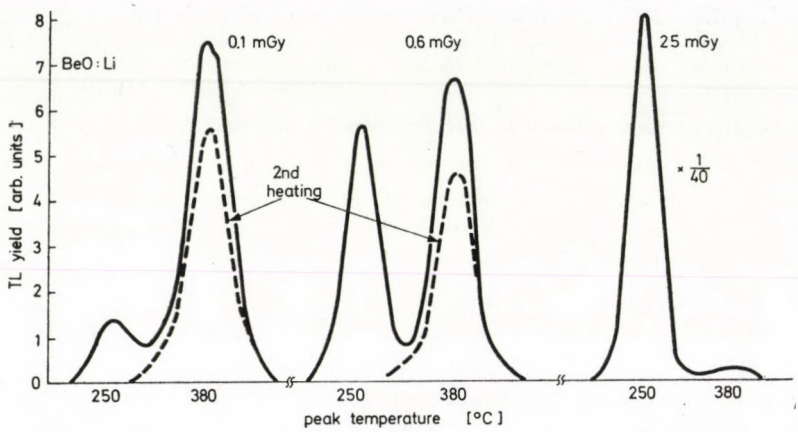

Fig. 1. Glow curves of BeO : Li detectors, irradiated with different doses. Heating parameters of read-out: 12 °C/s heating rate, 420 °C maximum temperature. The right hand glow curve was divided by 40.

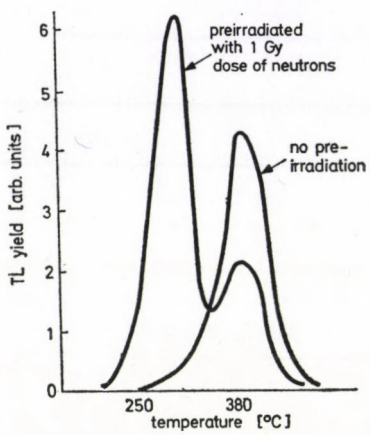

Fig. 2. Triboluminescent glow-curve of a virgin detector and that of a detector previously irradiated with 1 Gy tissue dose of thermal neutrons and read out several times. Triboluminescent signal was induced in both cases by tweezer handling.

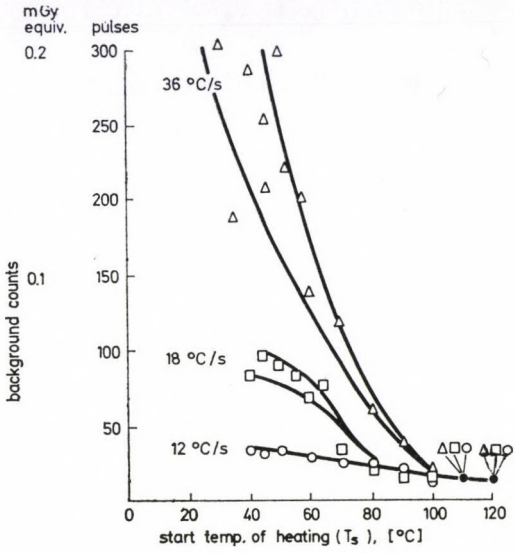

Fig. 3. Thermal effects on background counts of unirradiated detectors. Parameter is the heating rate. Counts were accumulated between 120 °C and 300 °C temperature.

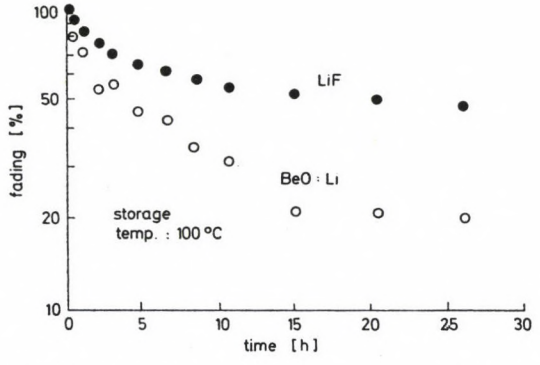

Fig. 4. Fading of BaO : Li detectors at elevated temperature. For comparison the fading of LiF hot pressed chips (produced at Nuclear Research Inst. Cracow, Poland) is also plotted.

cent glow-curves of no preirradiation (Fig. 2) with those of induced by gamma radiation it is evident that a large part of the triboluminescent signal can be excluded by proper detection window setting. The two-peaked glow curve in Fig. 2 shows that neutron irradiation increases triboluminescent sensitivity. Increased triboluminescent sensitivity is not reduced by repeated read-out cycles.

In order to investigate possible heating rate effects the following measurement was carried out: 1) Unirradiated detectors were read with a linearly increasing heating profile followed by constant heating at a temperature of

380 °C for 5 s, 2) a second reading cycle was started before the detector cooled down to room temperature.

Counts obtained during the 2nd read-out are plotted against start temperature of that read-out in Fig. 3. Results indicate that background counts increase, if a longer cooling time is allowed. With the increase of heating rate the background also increases. These heating rate effects are probably due to the thermal stress of the ceramic disk.

Fading of the irradiated detectors stored in darkness at room temperature was found to be less than 2% per month. Results of fading mesurements at an elevated temperature are shown in Fig. 4.

The gamma-energy dependence of the detectors is very favourable, response below 80 keV slightly decreases to a value of 0.85 at 30 keV if the response 1.25 MeV is taken to be unity [8].

Summarizing our findings it can be stated that BeO:Li detectors can be used as virtually energy-independent detectors for X and gamma radiation. The detection limit is ~ 50 μGy, if some precautions are taken: a heating rate not exceeding 10 °C/s and the use of plastic coated tweezer.

Reproducibility is excellent, $\pm$ 2% s.d. for doses higher than 3 mGy.

The author is indebted to Dr. L. Boros for delivering the detectors and for discussions.

REFERENCES

1. L. Lakosi, P. P. Szabó and S. Makra, BeO as a Thermoluminescent Dosimeter, Report Central Research Institute for Physics, Budapest, KFKI-75-10, 1975.
2. S. Makra, Izotóptechnika, **21**, 96, 1978 (in Hungarian).
3. S. Makra and P. Zaránd, Nuclear Accident Dosimetry Measurements at the 2nd IAEA Intercomparison at Oak Ridge, USA, May 1971, Report, Central Research Institute for Physics, Budapest, KFKI-71-82, 1971.
4. S. Makra and P. Zaránd, Proc. Conf. Radiobiol. Appl. Neutron Irrad., IAEA, Vienna, 41, 1972.
5. L. Boros, Acta Phys. Hung., **24**, 255, 1973.
6. L. Boros, Izotóptechnika, **17**, 15, 1974 (in Hungarian)
7. B. Szabó, P. P. Szabó, S. Makra, J. Vágvölgyi and J. Soós, The TLD-04B Thermoluminescent Reader for Research and Routine Dosimetry Applications, Report, Central Research Institute for Physics, Budapest, KFKI-77-33, 1977.
8. K. Becker, Solid State Dosimetry, CRC Press, Cleveland, 1973.

Acta Physica Academiae Scientiarum Hungaricae, 52 (3—4), pp. 357—362 (1982)

NEUTRON SENSITIVITY OF SSNTD

L. MEDVECZKY

INSTITUTE OF NUCLEAR RESEARCH OF THE HUNGARIAN ACADEMY OF SCIENCES
4001 DEBRECEN, HUNGARY

Various types of solid state nuclear track detectors (SSNTDs) with and without converter radiators were irradiated with neutrons of different energy spectra in order to obtain information on their neutron sensitivity in beam dosimetry. Track revealing was performed by chemical etching. A manual track counting technique was chosen except for the case of thin plastic foils, where also automatic spark counting was used.

1. Introduction

The growing number of neutron producing facilities increases the importance of neutron dosimetry. Various methods are known for the measurement of neutrons, but only few of them are suitable for radiation-protection purposes. Among these are the solid state nuclear track detectors (SSNTDs), which are also commonly used as personnel neutron dosimeters [1]. The SSNTDs are characterized by a number of advantageous features. They are small in volume and generally inexpensive. SSNTDs have the same sensitivity to many orders of magnitude of neutron intensity and offer long periods of integration, practically without fading. They are practically insensitive to electromagnetic radiation and lightly ionizing charged particles. At the same time SSNTDs do also have disadvantages, similarly to the other types of neutron dosimeters. The sensitivity of SSNTDs depends on the energy of the neutrons; the dose values from dosimeters using SSNTD cannot be obtained directly; the track evaluation can be automated only within restricted limits.

For the determination of neutron doses one has to know the neutron flux density, the energy spectrum of neutrons and the neutron sensitivity of the detector. In the present study various types of solid state nuclear track detectors with and without converter radiators have been irradiated with neutrons of known energy spectra and known neutron flux densities, and data of the neutron sensitivities of several chemically etched detectors are compiled.

2. Experimental conditions

The detection of neutrons with SSNTDs can be realized with or without external converter radiators. The radiators can be fissile materials or elements which produce charged particles through nuclear reactions. If no external radiator is applied, charged particles are produced from nuclear reactions and recoil processes originating in the detector or in materials in its immediate vicinity [2]. All these possibilities were studied by the author.

Table I

Types of SSNTDs studied and their etching conditions

Detector	Thickness (l_0) [μm]	Etching conditions
Cellulose nitrate KODAK LR115 I (Kodak-Pathé, France)	6	2.5 N NaOH, 60 °C, 90—140 min
Cellulose nitrate KODAK LR115 II (Kodak-Pathé, France)	12	
Cellulose nitrate KODAK LR115 IB (Kodak-Pathé, France)	6	
Cellulose nitrate KODAK LR115 IIB (Kodak-Pathé, France)	12	
Cellulose nitrate KODAK LR115 II stripable (Kodak-Pathé, France)	12	2.5 N NaOH, 60 °C, 120 min
Cellulose nitrate KODAK CA 80-15 (Kodak-Pathé, France)	100	2.5 N NaOH, 60 °C, 15 min
Cellulose nitrate KODAK CA 80-15 IB (Kodak-Pathé, France)	100	2.5 N NaOH, 60 °C, 15 min
Polycarbonate LEXAN (General Electric, USA)	250	4.24 N KOH, 60 °C, 45 min
Polycarbonate MAKROFOL E (Bayer, FRG)	200	If irradiated without radiator: PEW (15 g KOH + 40 g C_2H_5OH + 45 g H_2O), 70 °C, 20 min
Polycarbonate MAKROFOL KG (Bayer, FRG)	14	6.9 N KOH, 60 °C, 90 min
Polyethylene terephthalate MELINEX O (ICI, UK)	100	6.9 N KOH, 60 °C, 45 min
Muscovite mica	100—300	40% HF, 22 °C, 150—600 min

The types of SSNTDs used, and the chemical etching conditions adopted are presented in Table I. (Notable results were obtained also by electrochemical etching for neutron detection at this Institute, e.g. [3, 4].) The LR 115 type cellulose nitrate detectors were etched stepwise. Before and after each phase of etching the thickness of the foils was measured with a 352/403 type TESA made instrument. The accuracy of thickness measurements was better than $\pm$ 0.1 μm.

The tracks revealed were counted manually using a projection microscope with a magnification of 500 $\times$ for all detectors except Makrofol KG and LR 115 stripping film, where automatic spark counting was used. In the LR type detectors in visual evaluation only the etched through tracks (holes) with diameters of $\geq$ 2 μm were accepted for counting.

The irradiation of the detectors was performed, in every case, perpendicularly to their surface. The detectors were irradiated in free air at the neutron generator of Institute of Nuclear Research, Debrecen, and also in the biological irradiation facility [5], built into a horizontal channel of a WWR-SM type reactor at the Central Research Institute for Physics, Budapest. The neutron beam of the reactor was filtered by 1 cm B_4C and 70 or 145 mm Bi [6]. In case of 145 Bi a 165 mm polyethylene filter was also used in part of the irradiation.

LR 115 type cellulose nitrate detectors were irradiated also in the water tank of the APSARA swimming pool reactor at Bhabha Atomic Research Centre, Bombay in different positions with and without an aluminium filter in order to obtain four different neutron energy spectra [7].

Reference neutron flux densities at the irradiation positions were measured with activation detectors (gold, sulphur), calibrated fission track detectors. In the reactor experiments also Bonner spheres were simultaneously irradiated [6, 8].

As fissile converter radiators, thick uranium metal and thick Th-232, as alfa producing radiators natural boron converter (Kodak BN1) or B type Kodak cellulose nitrate were applied. These types of detectors have on one side a removable lithium tetraborate converter screen. In all experiments also unirradiated detectors were revealed and the background track densities were evaluated under identical conditions. (Further data of experimental conditions can be found in the papers referred to, except data of experiments with B and $Li_2B_4O_7$ radiators, which will be published elsewhere at a later date.)

3. Experimental results

The neutron sensitivity in case of SSNTDs means the track density produced by one neutron. If SSNTDs covered with thick fissile external radiators are used the neutron flux densities (Φ, cm^{-2} s^{-1}) can be calculated [9] from

$$\Phi = \frac{T_f}{1.16 \times 10^{-5} . \sigma . t},$$

Table II

Neutron sensitivities of detectors with fissile radiators.
(Data obtained from spark couting evaluation are marked with asterisk)

Type of detector	Neutron sensitivities				
	Average energy of the neutron spectrum [MeV]			Neutron energy [MeV]	
	1.44	1.45	1.7	2.4	14
Mica + U				8.6×10^{-6}	3.5×10^{-5}
MELINEX O + U				8.6×10^{-6}	3.5×10^{-5}
MELINEX O + U					$*1.7 \times 10^{-5}$
MAKROFOL E + U					2.6×10^{-5}
MAKROFOL KG + U			3.3×10^{-6}		$*1.2 \times 10^{-5}$
Mica + Th	6.3×10^{-7}				5.8×10^{-6}
MELINEX O + Th					4.7×10^{-6}
MELINEX O + Th					$*3 \times 10^{-6}$
MAKROFOL E + Th	5.3×10^{-7}	4.9×10^{-7}			5.1×10^{-6}
MAKROFOL KG+Th	$*4.2 \times 10^{-7}$	$*3.3 \times 10^{-7}$			$*2.3 \times 10^{-6}$

Table III

Neutron sensitivities of detectors with non-fissile radiators

Type of detector	Neutron sensitivities		
	Average energy of the neutron spectrum [MeV]		Neutron energy [MeV]
	1.44	1.7	14
LR 115 IB	1.5×10^{-5}		2.8×10^{-5}
LR 115 IIB	2.8×10^{-5}		8×10^{-5}
CA 80—15 IB	2.4×10^{-4}		5.2×10^{-5}
LR115 II + $Li_2B_4O_7$		2×10^{-5}	3.4×10^{-5}
LR115 II + B		2×10^{-4}	2.5×10^{-5}
MAKROFOL E + $Li_2B_4O_7$		4.4×10^{-4}	
MAKROFOL E + B		1.3×10^{-3}	

where T_f is the fission track density (track cm^{-2}) on the SSNTD, σ is the average fission cross section (cm^{-24}) [10] calculated in reactor experiments on the basis of the neutron spectra [8], t is the time of irradiation (s). If Φ, σ, t are known, one can calculate neutron sensitivity from the measured track density. The results of our measurements are presented in Table II. The neutron sensitivities of detectors with non-fissile radiators are measurable in a similar way. The results can be found in Table III.

The sensitivity of LR 115 type recoil detectors depends on neutron energy (E_n, MeV) and the measured thickness of the foil before (l_0, μm) and after (l, μm) etching and it can be given [11, 12] by the expression

$$S(E) = (ml + cl_0)\left(\frac{E_n}{E_0}\right)^k,$$

where $m = -1.7 \cdot 10^{-8}$ and $c = 8.115 \cdot 10^{-9}$, k was found to be 2.25, but it was modified later [13] to $k = 2.2$, $E_0 = 1$ MeV.

Table

Neutron sensitivities of LR115 type cellulose nitrate

Type of detector		Neutron			
		Average energy of the			
		0.832	0.835	0.909	1.42
LR115 I	min				
	max				
LR115 II	min	1.9×10^{-7}	2.1×10^{-7}	1.5×10^{-7}	3.2×10^{-7}
	max	2.1×10^{-7}	2.2×10^{-7}	2.1×10^{-7}	4.7×10^{-7}

Then, for a given neutron spectrum $\Phi(E)$:

$$S = \frac{\int_{E_1}^{E_2} S(E)\,\Phi(E)\,dE}{\int_{E_1}^{E_2} \Phi(E)\,dE},$$

where E_1 and E_2 are the limits of the neutron energy range where flux density is to be determined. The neutron flux densities for a given residual layer thickness (l) can be obtained from the averaged sensitivity ($\bar{S}$) and from the measured hole densities (T_l, holes $\cdot$ cm^{-2}) by the formula

$$\Phi_{CN} = T_l \cdot \bar{S}^{-1} \cdot t^{-1}.$$

The sensitivity values measured at various neutron energy spectra can be seen in Table IV.

The sensitivities of detectors without radiator can be calculated from the measured track and flux density values. These values are valid only for a well defined track revealing process (Table I). The measured sensitivities can be seen in Table V.

Table V

Neutron sensitivities of detectors without radiator

Type of detector	Neutron sensitivities				
	Average energy of the neutron spectrum			Neutron energy MeV	
	1.44	1.45	1.7	2.4	14
CA 80—15	2.3×10^{-5}	1.4×10^{-5}		2.6×10^{-5}	4.5×10^{-5}
LEXAN					8.6×10^{-5}
MAKROFOL E	4.1×10^{-6}		5×10^{-5}	4.9×10^{-5}	8.4×10^{-5}
MELINEX O					0.9×10^{-5}

IV

detectors without external radiator

sensitivities				
neutron spectrum [MeV]			Neutron energy [MeV]	
1.44	1.45	1.7	2.4	14
	2.3×10^{-7}		1.4×10^{-7}	0.5×10^{-5}
	6.9×10^{-7}		2×10^{-7}	1×10^{-5}
1.8×10^{-7}	1.3×10^{-7}	$1.6+10^{-7}$	2×10^{-7}	0.5×10^{-5}
6.9×10^{-7}	4.1×10^{-7}	6.9×10^{-7}	7×10^{-7}	3×10^{-5}

Acknowledgements

The author is indebted to Mr. J. PÁLFALVI for his invaluable help in making the irradiations with reactor spectra and to Dr. G. SOMOGYI for critically reading the manuscript.

REFERENCES

1. R. V. GRIFFITH, D. E. HANKINS, R. B. GAMMAGE, L. TOMMASINO and R. V. WHEELER, Health Phys., **36,** 235, 1979.
2. L. MEDVECZKY and G. SOMOGYI, ATOMKI Közl., **8,** 226, 1966 and Proc. VIth Intl. Conf. on Corpuscular Photogr. (Florence, July 19—23, 1966) CEPI Roma, 461.
3. G. SOMOGYI, G. DAJKÓ, K. TUREK and F. SPURNY, Nucl. Tracks, **3,** 125, 1979.
4. K. TUREK, F. SPURNY, G. DAJKÓ and GY. SOMOGYI, Jaderná Energie, **27,** 174, 1981.
5. S. MAKRA and P. ZARÁND, Construction and dosimetry of biological radiation facilities at light-water-moderated reactions, Central Research Institute for Physics, Budapest, KFKI-71-74, 1971.
6. L. MEDVECZKY and J. PÁLFALVI, ATOMKI Közl., **21,** 347, 1979.
7. J. PÁLFALVI, A. M. BHAGWAT and L. MEDVECZKY, Health Phys. **41,** 505, 1981.
8. J. PÁLFALVI, Nuclear accident dosimetry measurements, Czechoslovak-Hungarian intercomparison, Budapest, Hungary, 1977, Central Research Institute for Physics, Budapest, KFKI-78-65, 1978.
9. S. PRÊTRE, E. TOCHILIN and N. GOLDSTEIN, U.S. Naval Radiological Defense Laboratory, USNRDL-TR-1089, 1968.
10. A. SCHETT, K. OKAMOTO, L. LESCA, F. H. FRÖHNER, H. LISKIEN and A. PAULSEN, European—American Nuclear Data Committee, EANDC-95-U (1974).
11. L. MEDVECZKY, Proc. II. Symp. on Neutron Dosimetry in Biology and Medicine, ed. by G. Burger and H. G. Ebert (EUR 5848, Brussels—Luxembourg, 1978) p. 759.
12. L. MEDVECZKY, J. PÁLFALVI, Izotóptechnika, **21,** 464, 1978 (in Hungarian).
13. J. PÁLFALVI, Nucl. Instr. Meth., **180,** 511, 1981.

Acta Physica Academiae Scientiarum Hungaricae, 52 (3—4), pp. 363—372 (1982)

V. ENVIRONMENTAL MONITORING

CHAIRMEN: H. AIGINGER, L. MEDVECZKY

UMGEBUNGSÜBERWACHUNG BEZÜGLICH ÄUSSERER STRAHLUNG — GERÄTE UND MESSRESULTATE

E. TSCHIRF und N. VANA

ATOMINSTITUT DER ÖSTERREICHISCHEN UNIVERSITÄTEN
A-1020 WIEN, ÖSTERREICH

Zwei verschiedene Methoden werden für die Messung des Strahlungsfeldes in der Umgebung des TRIGA-Reaktors des Atominstituts der Österreichischen Universitäten abgeschrieben. Die Dosismessungen wurden mit GM-Zählröhren (Typ BZ-120) bzw. mit TL-Detektoren (CaF_2 : Dy und LiF : Mg,Ti) durchgeführt. Die Messergebnisse sind für den Zeitabschnitt 1979 April — 1981 August zusammengefasst.

1. Anforderungen an die Messeinrichtungen

In der Umgebung des Forschungsreaktors TRIGA Mark II besteht die Möglichkeit, dass bei Strahlrohrversuchen eine Erhöhung des Pegels der Umweltstrahlung auch ausserhalb der Reaktorhalle auftritt. Es ist daher für die Sicherheit von Personen, die sich am Rand des Institutsgeländes aufhalten, wichtig, die auftretende Strahlung dauernd zu registrieren. In dieser Arbeit sollen die Methoden und Resultate bei der Kontrolle von Photonenstrahlung auf dem Gelände des Atominstituts beschrieben werden.

Die einzelnen, an den Messtellen auftretenden Strahlungskomponenten sind in der Abb. 1 schematisch dargestellt. Zu berücksichtigen sind dabei:

1.1. Die natürliche Umweltstrahlung

Diese wird üblicherweise in zwei Komponenten unterteilt:

1.1.1. Die terrestrische Strahlung. Sie besteht in der Hauptsache aus der Gammastrahlung von Nukliden der ^{238}U und ^{232}Th Serie sowie von ^{40}K. Ihre Dosisleistung schwankt in Österreich entsprechend dem geologischen Aufbau des Untergrundes zwischen weniger als 20 nSv/h und 0,4 μSv/h [1]. Im Bereich des Atominstituts ist mit einem mittleren Wert von etwa 50 nSv/h zu rechnen.

Das Energiespektrum der terrestrischen Strahlung reicht von etwa 80 keV bis über 2.0 MeV; besondere Bedeutung haben Energien über 0.1 MeV. Die terrestrische Komponente zeigt nur geringe zeitliche Schwankungen, die von meteorologischen Einflüssen abhängig sind. So ist bei Einsetzen von Regen meist ein deutliches Ansteigen des Strahlenpegels zu beobachten. Andererseits

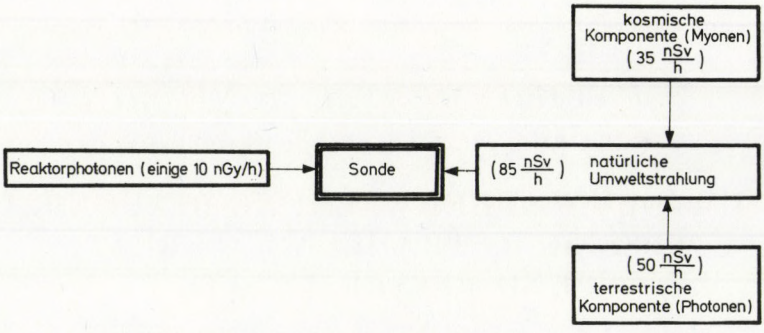

Abb. 1. An der Sonde der Messstelle auftretende Strahlungskomponenten und ihre Dosisleistung in der Umgebung des Atominstitutes.

wird durch die Anwesenheit einer Schneedecke die terrestrische Strahlung merklich geschwächt. Die verschiedenen meteorologischen Einflüsse bedingen einen kleinen, aber signifikanten Jahresgang, wobei im Sommer die Maxima und im Winter die Minima der Dosisleistung gemessen werden.

In den Jahren 1959 bis 1962 konnten lange andauernde Erhöhungen der terrestrischen Strahlenkomponente festgestellt werden, die durch den fall-out der Kernwaffenversuche hervorgerufen worden waren. Seit einigen Jahren ist diese zusätzliche Strahlung wieder soweit abgeklungen, dass praktisch normale Verhältnisse herrschen.

1.1.2. Kosmische Strahlung. Die biologisch relevante Wirkung der die Erdoberfläche treffenden kosmischen Strahlung beruht hauptsächlich auf hochenergetischen Myonen ($E > 10$ MeV), zu einem kleineren Teil auch auf Neutronen- und Photonenstrahlung.

Das Dosisleistungsäquivalent hängt von der Seehöhe und der geographischen Breite ab; es beträgt im Bereich des Atominstituts (160 m SH) etwa 35 nSv/h [2]. Schwankungen, zum Beispiel durch die Sonnenfleckenperiode, verbleiben in diesen tiefen Luftschichten unter $\pm$ 10% [2].

1.2. Zusätzliche Strahlung durch Einwirkung des Reaktors

Der in der Reaktorhalle installierte TRIGA Mark II-Reaktor mit einer Höchstleistung von 250 kW verursacht bei der Durchführung von Strahlrohrversuchen auch ausserhalb des Gebäudes geringe Veränderungen der Umgebungsstrahlung. Die aus dem Reaktor austretende Photonenstrahlung besteht hauptsächlich aus der beim Spaltprozess entstehenden prompten Gammastrahlung, deren Spektrum beim Durchgang durch Abschirmmaterialien verändert wird. Die mittlere Energie dieser Strahlung liegt im Bereich von 1 bis 2 MeV. Ein gewisser Beitrag wird ausserdem von (n, γ)-Einfangreaktionen geliefert, wobei einige hochenergetische Linien (E bis über 10 MeV) zu berücksichtigen sind.

1.3. Anforderungen an das Messystem

Die Messeinrichtung soll imstande sein, die kleinen Schwankungen der natürlichen Strahlung im Bereich von $\pm$ 10 nSv/h noch nachzuweisen. Sie soll auf Photonen mit Energien von etwa 0.1 MeV an möglichst energieunabhängig ansprechen und entweder die Dosisleistung in bestimmten Intervallen registrieren oder die akkumulierte Dosis anzeigen.

2. Detektoren für die Umgebungsstrahlung

Aus den zahlreichen für diesen Messzweck geeigneten Möglichkeiten haben die Autoren zwei Systeme ausgewählt, die für Dauermessungen im Freien tauglich sind und neben ausreichenden radiometrischen Eigenschaften auch relativ einfach realisierbar sind:

Zur Messung der Dosisleistung wurde ein hochempfindliches Geiger—Müller-Zählrohr mit automatischer Registriereinrichtung vorgesehen; zur Ermittlung der akkumulierten Dosis an bestimmten Messtellen wurden Thermolumineszenz-Dosimeter verwendet.

2.1. Messung der Umweltstrahlung mit einem GM-Zählrohr

Die von einem Zählrohr abgegebene Impulsrate setzt sich aus drei Komponenten zusammen:

$$I_{\text{ges}} = I_e + I_\gamma + I_{\text{kosm}},$$

wo I_{ges} die Gesamtimpulsrate (s^{-1}), I_e die Eigenimpulsrate des Zählrohres (s^{-1}), I_γ die Impulsrate durch terrestrische und künstliche Gammastrahlung (s^{-1}) und I_{kosm} die Impulsrate durch die kosmische Strahlung (s^{-1}) bezeichnet.

Bei der Kalibrierung von Zählrohren, mit denen sehr kleine Dosisleistungen gemessen werden sollen, besteht die Schwierigkeit, dass die Eigenimpulsrate I_e und das Ansprechvermögen auf die kosmische Strahlung zunächst nicht bekannt sind, während das Ansprechvermögen auf Gammastrahlung relativ einfach ermittelt werden kann. Durch Messungen mit dem Zählrohr über Wasserflächen in unterschiedlicher Seehöhe, über denen die terrestrische Komponente vernachlässigt werden kann, ist I_e und I_{kosm} bestimmbar, da die Höhenabhängigkeit der kosmischen Strahlungsdosisleistung gut bekannt ist.

Eine weitere Möglichkeit zur Kalibrierung von Zählrohren für die Umweltstrahlung sind Vergleichsmessungen mit einer als Quasi-Sekundärstandard dienenden Ionisationskammer in Gebieten mit verschiedenen Pegeln für die Umweltstrahlung, wobei auch möglichst unterschiedliche Höhenlagen einbezogen werden sollten. Abb. 2 zeigt Vergleichsmessungen des hier verwendeten Zählrohres BZ 120 mit einer Hochdruck-Ionisationskammer der Type RSS 111

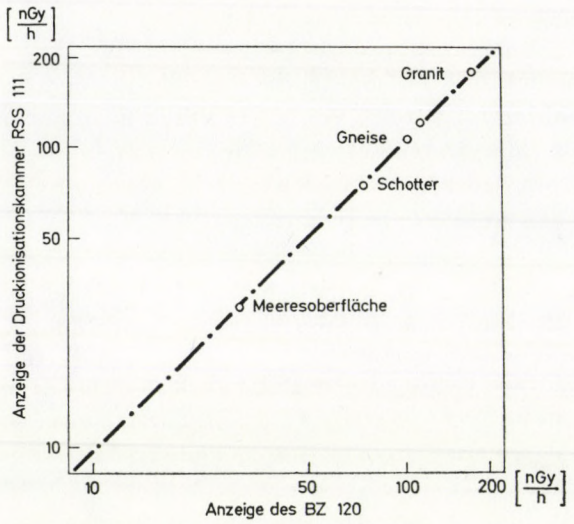

Abb. 2. Vergleichsmessungen zwischen der Hochdruckionisationskammer RSS 111 und einem Zählrohr BZ 120 bei unterschiedlichen Pegeln natürlicher Strahlung.

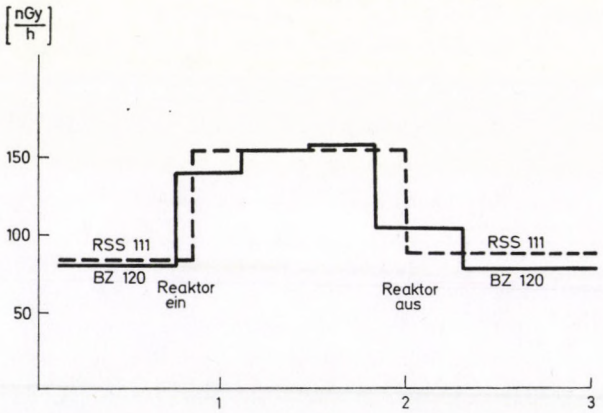

Abb. 3. Messung der Gammadosisleistung in der Umgebung der Reaktorhalle bei Betrieb des TRIGA mit einer Druckionisationskammer RSS 111 und einem Zählrohr BZ 120.

bei natürlicher Strahlung, Abb. 3 im Bereich der Strahlung des TRIGA-Reaktors.

Das Messverfahren beruht auf der Registrierung der jeweils bis zur Aufsummierung von 10^4 Impulsen vergangenen Zeit. Dieses Verfahren sichert eine von der Impulsrate unabhängige statistische Schwankung des Messwertes.

Weitere Daten für das Zählrohr BZ 120 sind: Eigenzählrate = 100 Imp/min; Empfindlichkeit für die natürliche Umweltstrahlung (terrestrische und kosmische Komponente) $= \dfrac{2760 \text{ Imp/min}}{\mu\text{Gy/h}} \cdot \left[\dfrac{24 \text{ Imp/min}}{\mu\text{R/h}}\right]$.

2.2. Thermolumineszenz-Dosimeter zur Messung der Dosis der Umweltstrahlung

Bestimmte Festkörper können nach Anregung mit ionisierender Strahlung einen Teil der Anregungsenergie speichern. Durch Zufuhr weiterer Energie kann nach der Anregung diese gespeicherte Energie als Licht freigesetzt werden. Erfolgt diese nochmalige Anregung durch Wärmezufuhr, so spricht man von Thermolumineszenz. Bei den in der Thermolumineszenz-Dosimetrie verwendeten Phosphoren ist die emittierte Lichtintensität proportional der bei der Anregung absorbierten Dosis. Thermolumineszenz-Dosimeter (TLD) werden heute in der Personendosimetrie, in der medizinischen und in der Umweltdosimetrie eingesetzt.

2.2.1. TLD-System. Zur Messung der Umweltdosis wurden zwei Phosphore, nämlich LiF:Mg,Ti (TLD-100, Firma Harshaw) und CaF_2:Dy (TLD-200, Firma Harshaw) verwendet. Die Auswertung der TLD's erfolgte mit einer modifizierten, programmierbaren EG & G-Anlage, bestehend aus 2025A Readout, 2020A Universal Read Head und 1020A Programmer. Die Kalibrierung der Dosimeter (chips $\frac{1}{4}$" $\times$ $\frac{1}{4}$" $\times$ 0.35) erfolgte im Strahlungsfeld einer 3.11 GBq ^{60}Co-Quelle. Die mit dem verwendeten TLD-System erreichte untere Nachweisgrenze lag für TLD-100 bei 8.7 nGy und für TLD-200 bei 0.6 μGy.

2.2.2. Durchführung der Messungen. Vor dem Beginn der eigentlichen Messung — dem Anbringen der Dosimeter an den entsprechenden Messtellen (TL-A, TL-B), Abb. 4, im Gelände des Atominstituts — wurde ein Teil der gereinigten und ausgeheizten Dosimeter mit einer definierten Dosis bestrahlt. Die Bestrahlung erfolgte in verschraubten, lichtdichten Kunststoffbehältern, die auch für die Messungen im Gelände verwendet wurden. In diesen Kapseln (Höhe 92 mm, Durchmesser 35 mm, Wandstärke 1.8 mm) wurden 10 Dosimeter in 2 Reihen zu 5 Stück in Schaumstoff gebettet eingebracht.

Nach der Bestrahlung wurden 5 der bestrahlten Dosimeter aus der Kapsel entnommen und durch 5 ausgeheizte, unbestrahlte ersetzt, wobei die Anordnung so war, dass immer neben einem unbestrahlten ein bestrahltes Dosimeter lag. Anschliessend wurden die Kapseln an die Messtellen gebracht und an einem Bambusstab 1 m über dem Erdboden beziehungsweise an dem GM-Zählrohr (TL-A) befestigt.

Nun wurde sofort der Leerwert (LW) der unbestrahlten Dosimeter bestimmt und die bestrahlten Dosimeter ausgewertet. Daraus konnte für jede Kapsel ein Kalibrierungsfaktor K_f bestimmt werden:

$$K_f = \frac{I_0 - LW}{D_0} \left[\frac{\text{Imp}}{\text{mGy}}\right],$$

wo I_0 die Impulse der TL der mit der definierten Dosis D_0 bestrahlten Dosimeter bezeichnet.

3. Messergebnisse

Die Skizze in Abb. 4 zeigt die Anordnung der einzelnen Messtellen auf dem Gelände des Atominstituts. Das GM-Zählrohr und die Sonde TL-A wurden an der Stelle der höchsten Strahlenbelastung in der Umgebung der Reaktorhalle installiert, während die Sonde TL-B in einem Gebiet mit nur natürlicher Strahlung zur Aufstellung kam.

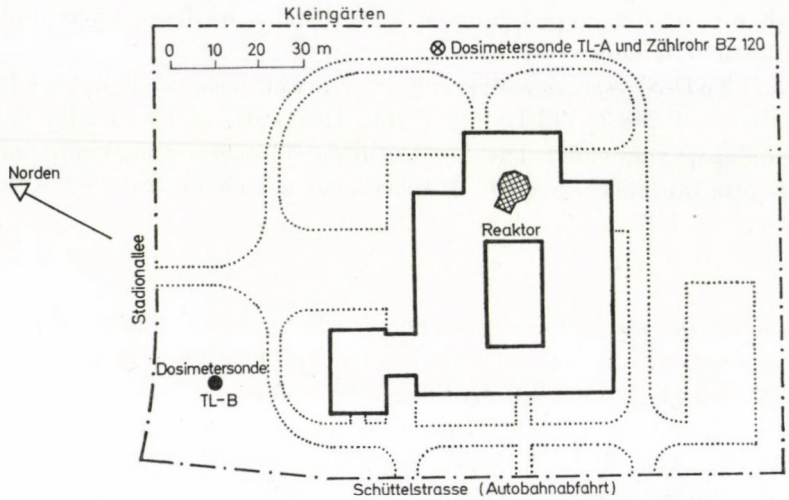

Abb. 4. Gelände des Atominstitutes und Lage der Sonden.

Abb. 5. Monatsmittelwerte für die natürliche Umweltstrahlung (bei abgeschaltetem Reaktor) auf dem Gelände des Atominstitutes der Österr. Universitäten.

3.1. Messresultate mit dem Zählrohr

Zu Studien über zeitabhängige Veränderungen der natürlichen Umweltstrahlung wurden mittlere Messwerte von Tagen herangezogen, an denen der Reaktor nicht in Betrieb stand. In Abb. 5 ist deutlich der jährliche Gang für die Dosisleistung zu erkennen, die im Sommer ein Maximum und im Winter ein Minimum aufweist. Dieser Effekt ist bei Messungen, die in Gebieten mit lang andauernden Schneelagen (Alpen, Skandinavien) durchgeführt wurden, noch wesentlich deutlicher ausgeprägt. Er dürfte einerseits auf die häufigen Regenfälle im Sommer zurückzuführen sein, bei denen durch Auswaschungseffekte immer wieder radioaktive Folgeprodukte des Radon auf die Erdoberfläche transportiert werden. Im Winter wirkt die Schneedecke abschirmend, ausserdem könnte die Diffusion von Radon in den obersten Erdschichten durch Frosteinwirkung behindert werden. Bei einem Jahresmittel von 70.64 beziehungsweise 70.56 nGy/h für 1979 betrug 1980 die Sommerspitze 73.17 (+ 3,6%) beziehungsweise 73.34 nGy/h (+ 3.9%). Das winterliche Minimum betrug 1979/1980 67.6 nGy/h (— 4.2%) und 1980/81 67.86 nGy/h (— 3.7%).

Abb. 6 zeigt den typischen Verlauf der Dosisleistung bei Einsetzen von Regen. Nach einer langen Schönwetterperiode setzte am 19. Juli 1981 zunächst leichter Regen ein, der ein geringfügiges Ansteigen des Strahlungspegels um etwa 10.4 nGy/h bewirkte. Der um den Mittag dieses Tages auftretende starke Regenfall erhöhte die Dosisleistung innerhalb von etwas mehr als 4 Stunden um 40.9 nGy/h (+ 45%). Nach dem Auswaschen der Atmosphäre klingt jedoch die auf der Erdoberfläche abgelagerte Radioaktivtät wegen der kurzen Halbwertszeiten der Radonfolgeprodukte relativ rasch wieder ab; nach einigen Stunden ist der ursprüngliche Wert wieder erreicht.

Bei der Auswertung von Messungen der Umgebungsstrahlung ist daher die Korrelation zu meteorologischen Daten überaus wichtig, um natürliche

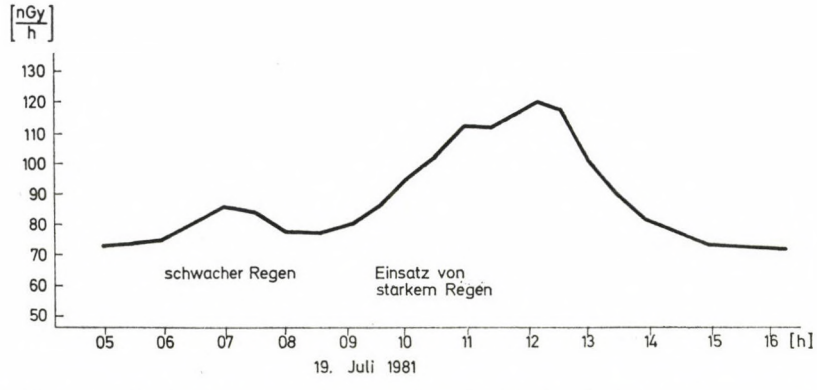

Abb. 6. Typischer Verlauf der Dosisleistung der natürlichen Umweltstrahlung an einem Tag mit starken Niederschlägen.

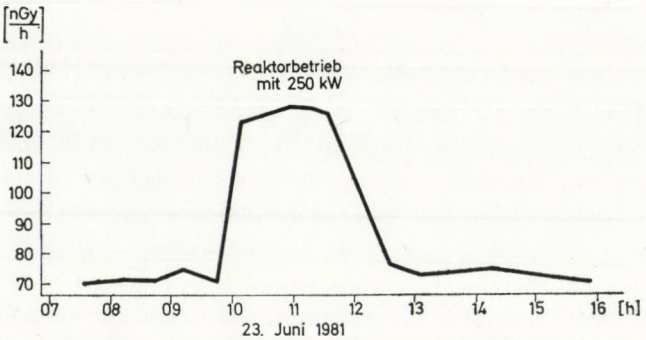

Abb. 7. Dosisleistung an der Zählrohrmesstelle an einem Tag mit Reaktorbetrieb.

Tabelle I

Natürliche Strahlungdosis und Beitrag von Reaktorphotonen (1μ R = 8,7nGy)

Jahr	Mittlere Dosisleistung (gesamt)	Mittlere Dosisleistung (nat. Strahlg.)	Beitrag des Reaktors	
	nGy/h	nGy/h	nGy/h	μGy/a
1979	80.0	71.3	8.7	76.2
1980	78.3	70.5	7.8	68.6

Vorgänge von den Effekten künstlicher Strahlenquellen unterscheiden zu können.

Abb. 7 zeigt den Verlauf der Dosisleistung an der Zählrohrsonde bei Betrieb des Reaktors. Die Höhe der zusätzlichen Strahlenbelastung hängt natürlich von der Reaktorleistung und den experimentellen Bedingungen ab. Die Tabelle gibt einen Überlick über die durch den Reaktor bewirkten jährlichen Dosiserhöhungen an der Messtelle.

3.2. Messresultate mit den TL-Dosimetern

Nach Beendigung der Messperiode wurden die Dosimeter ausgewertet. Da während der Messperiode die Kapseln und damit auch die Dosimeter unterschiedlicher Sonnenbestrahlung und verschieden hohen Temperaturen ausgesetzt waren, musste eine Fadingkorrektur durchgeführt werden. Der Fadingfaktor ergab sich zu:

$$F = \frac{I_0 - LW}{I - I_u} ,$$

wo I_0 die TL-Impulse der mit D_0 bestrahlten Dosimeter, I die TL-Impulse der bestrahlten Dosimeter nach der Messperiode, I_u die TL-Impulse der unbestrahlten Dosimeter nach der Messperiode, und LW den Leerwert der Dosimeter bezeichnet.

Tabelle II

Messergebnisse der TL-Dosimeter und Vergleich mit dem Zählrohr in nGy/h ($1\mu R = 8{,}7$ nGy)

Periode	TLD-200		TLD-100		Zählrohr BZ 120 (am Ort TL-A)
	TL-A	TL-B	TL-A	TL-B	
81-05-15	78.8 ± 13%	83.5 ± 12%	78.3 ± 50%	—	76.6
81-05-25					
81-06-02	82.1 ± 21%	78.7 ± 23%	101.8 ± 40%	69.2 ± 40%	79.2
81-06-15		80.7 ± 27×			
81-06-19	88.9 ± 30%	89.6 ± 25%	—	—	74.8
81-07-06	1.5 mmCu	1.5 mmCu			
	75.3 ± 25%	61.8 ± 23%			

Die mittlere Dosisleistung ergibt sich nun zu:

$$\dot{D} = \frac{L_u - LW}{K_f T} F.$$

T bedeutet die Dauer der Messperiode in Stunden. Mittlere Dosisleistung in nGy/h $= \dot{D}$.

Die Dauer der Bestrahlungsperioden lag zwischen 240 h und 410 h, die Gesamtdosis zwischen 17 μGy und 3,5 μGy. Da die untere Nachweisgrenze von TLD-100 bei 1,7 μGy liegt, treten bei der Bestimmung der Umweltdosis in so kurzen Zeiträumen grosse Fehler auf. Eine Verwendung dieses Dosimetertypes bei Expositionszeiten von unter drei Monaten erscheint daher nicht sinnvoll.

4. Diskussion der Ergebnisse

Die Ergebnisse mit den TLD's zeigen zunächst einen etwas höheren Wert als bei den Messungen mit dem Zählrohr. Dies wurde teilweise auf die starke Energieabhängigkeit der TLD-200 zurückgeführt. So zeigten Messungen, bei denen die Kapsel mit einer 1.5 mm starken Cu-Folie abgeschirmt waren, einen bis zu 30% geringeren Wert. Da die Empfindlichkeit von TLD-200 für Quanten $<$ 100 keV bis zu einem Faktor 12 grösser wird als für Quanten der Energie von 1.2 MeV [3] (mit dieser Photonenenergie erfolgte die Kalibrierung), kann bereits ein Anteil von 2.5% an niederenergetischen Quanten eine Erhöhung der mit TLD-200 gemessenen Dosis bis zu 30% zur Folge haben. Das Verhältnis der Dosiswerte mit und ohne Cu-Abschirmung lässt ausserdem erkennen, dass am Ort TL-A ein Spektrum mit weniger niederenergetischem Anteil (Gammastrahlung des Reaktors) herrscht.

Es kann gezeigt werden, dass im Rahmen der für die Messaufgabe geforderten Genauigkeit die beiden Verfahren übereinstimmen.

LITERATUR

1. E. TSCHIRF, W. BAUMANN, R. NIESNER and P. VYCHYTIL, Strahlenkarte Österreich, Bundesministerium für Gesundheit und Umweltschutz, 1975.
2. Natural Background Radiation in the U.S., NCRP-Report No. 45, November, 1975.
3. N. VANA, H. AIGINGER and W. ERATH, Measurements of Doses in the 1 mrad-Range by Means of LiF, CaF_2 and $CaSO_4$ Dosimeters and Determination of the Energy Response of LiF and CaF_2, in Proc. IVth IRPA Congress, Paris, Vol. 4, 1253, 1977.

Acta Physica Academiae Scientiarum Hungaricae, 52 (3—4), pp. 373—379 (1982)

ENVIRONMENTAL MONITORING SYSTEM AT THE PAKS NUCLEAR POWER STATION

I. FEHÉR, S. DEME and A. ANDRÁSI

HEALTH PHYSICS DEPARTMENT, CENTRAL RESEARCH INSTITUTE FOR PHYSICS
1525 BUDAPEST, HUNGARY

The environmental monitoring system of the Paks Nuclear Power Station (Hungary) has been designed with a dual aim:

in normal operation: to check that the population's burden does not exceed the prescribed dose limit;

under accidental conditions: to provide rapid information on the expected radiation burden of the population so that necessary steps can be taken.

For assessing environmental doses the following parts of the monitoring system are used

— telemetric stations to determine the time integral of ^{131}I concentration in air and the gamma dose rate;
— sampling stations and devices for sample measurement;
— mobile laboratories;
— a meteorological tower.

The main principles and structure of the environmental monitoring system are discussed.

Introduction

In the next future nuclear power is due to contribute in a substantial measure to the supply of electrical energy in Hungary; the first 440 MW_e block of the Paks Nuclear Power Station is near completion, three others are to follow. Environmental monitoring is one of the prerequisites of the safe operation of a nuclear power plant. The Central Research Institute for Physics has been commissioned to develop and to implement the environmental monitoring system of the Paks Nuclear Power Station. The conception and main elements of the monitoring system will be reviewed in the following.

Aim and basic methods of environmental monitoring

The environmental monitoring system of the Paks Nuclear Power Station has been designed with a twofold aim:

in the case of normal operation to keep the radiation burden of the population due to the power station below the dose limit prescribed by the competent authority;

under accidental conditions to provide rapid information on the expected radiation burden of the population in order that the competent authority should be able to take the necessary measures.

To achieve this dual aim two parallel basic methods are used:

— the external radiation burden and the radioactive contamination are computed by use of a normal operation diffusion model utilizing measured values of radioisotope release and local meteorological data,

— the external radiation dose and the radioactive contamination of the environment are evaluated partly from telemetric data, partly by the laboratory analysis of environmental samples.

The first method is suitable for the determination of the environmental burden due to activity release during normal operation when the expected value of the field dose and of the environmental contamination is near or below the detection limit of direct measurements. The results of measurements by the second method either directly confirm the correctness of the values measured by the first method, or they furnish direct data on the population burden to be expected in the case of any accident.

The second method is of special importance in the case of accidental activity release when the activity of the radioisotopes released into the environment cannot be measured. In this case the accidental diffusion model has to be fitted to the data of telemetric environmental measurements in order to determine the expected radiation burden of the population in the concerned area. Under accidental conditions quick results are obtained from sample measurements by mobile laboratories.

The environmental monitoring system is schematically shown in Fig 1.

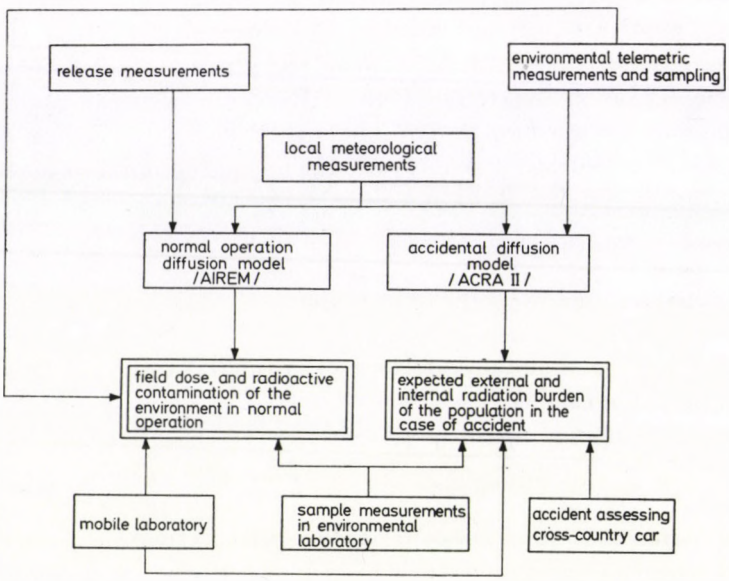

Fig. 1. Scheme of the environmental monitoring system.

Main modules of the environmental monitoring system

Measurements of activity release

In the case of normal operation as well as under accidental conditions activity from the Paks Nuclear Power Station can be released practically only into the atmosphere. For this reason primarily the environmental atmosphere is covered by activity release measurements. The release of radioactive noble gas, radioiodine, radioaerosols including ^{89}Sr, ^{90}Sr is continuously measured by the use of the Soviet KALINA apparatus which is completed by the high sensitivity noble gas concentration meter (Budapest Technical University product) and by the continuous ^{131}I monitor (Central Research Institute for Physics product).

The radioactive contamination of cooling water is due to be prevented by a multiple safety system. To ensure the quality of the water of the Danube, a water monitor system is being built. The system is composed of a continuous gross-gamma concentration meter, a continuous water sampler and of remote controlled automatic water sampler units. Cold water, hot water and sewage are monitored by the system.

Meteorological tower

The most important local meteorological data for diffusion calculation are obtained from wind direction, wind speed and thermometer probes on the 20, 50 and 120 meter levels of the 120 m high meteorological tower as well as on the 2 m high field station. At the field station complementing meteorological data are furnished by radiation equilibrium, atmospheric humidity measuring instruments and a precipitation meter. The meteorological station is incorporated in the national network of wireless and telex communication.

Diffusion models

For the normal operation diffusion model the AIREM [1] while for the accidental diffusion model the ACRA II [2] computer codes have been adapted. The external effective dose-equivalent is calculated by use of the POKER-CAMP program [3] developed at our Institute.

Measuring and sampling stations

The so-called "A"-type stations are built on a circle of 1.5 km radius around the nuclear power plant in the direction of settlements. The gamma dose rate and time integral of ^{131}I concentration are continuously measured by the

7 "A" stations, which are connected by cable to the radiation protection control room of the nuclear power plant. The telemetric and data acquisition system installed in the control room is connected to the "A" stations, the release meters and to the sensors of relevant meteorological data. The telemetric and data acquisition system is described in more detail in another paper of this issue [4].

Continuous aerosol, large volume aerosol and radioiodine samplers are operating on the "A" stations and on a "B"-type station mounted at 26 km distance from the nuclear plant. Fall-out, tacky cloth sampling and thermoluminescent gamma dose measurements are also carried out.

The 14 "C"-type sampling stations built in the environment of the nuclear plant within a circle of a radius of about 30 km, are suitable for fall-out tacky-cloth sampling and thermoluminescence gamma dose measurements.

Soil and plant (grass) samples are taken in the environment of the "A",

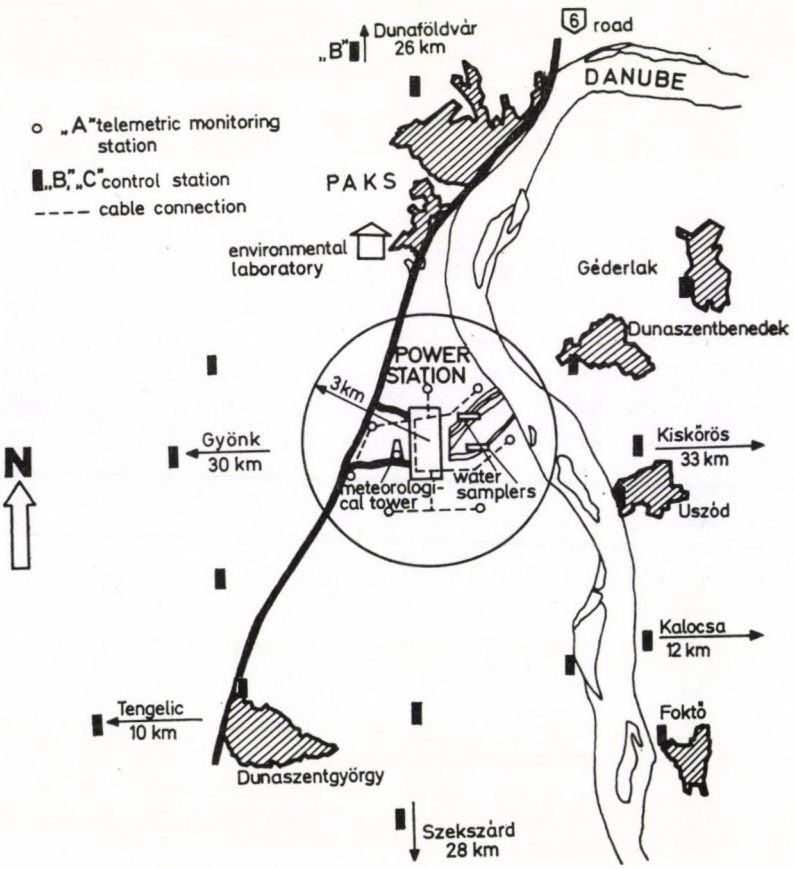

Fig. 2. Location of the environmental monitoring stations around the nuclear power plant.

and "B"-type stations. Milk samples are taken from dairy-farms which pasture cattle in fields near the "C" stations within the 30 km radius circle.

Radioactive contamination of ground water is measured on samples taken from wells intended for this purpose. Periodically mud and fish samples are taken from the Danube for the detection of possible radioactive contamination.

The geographical positions of the measuring and sample stations are mapped in Fig. 2.

Environmental laboratory

In Paks Town at about 5 km from the nuclear plant an environmental laboratory has been built for the measurement of environmental samples. The laboratory comprises three main units:

Sample preparation unit, where the physical processing of samples, e.g. evaporation of water samples, comminution and drying of soil and plant samples, takes place.

Radiochemistry unit, where the samples are chemically and physicochemically enriched. Procedures of this type are the concentration of fall-out and milk by ion exchange, elimination of radon from iodine adsorbents. Laborious radiochemical procedures are used only in the above specified cases. External institutes will be commissioned by the nuclear plant to perform long-lived radioisotope concentration measurements and tritium determination by high sensitivity isotopic enrichment procedure on environmental samples.

Radiometry unit equipped with

— low background beta counters,
— low background scintillation and Ge(Li) gamma-spectrometers, and
— a thermoluminescence reader.

The gamma spectrometer is dealt with in more detail in another paper of this issue [5]. The program of environmental sample measurements is specified in Table I.

Mobile laboratory

The mobile laboratory is equipped with a gamma spectrometer and with a G—M counter dose rate meter similar to that mounted in the "A" stations. The mobile laboratories have their own power supply and a wireless connection to the environmental laboratory.

Preoperational measurements by the mobile laboratory have already been in progress for two years at the sites of the "A", "B" and "C"-type stations. After the start of the nuclear power plant's operation systematical monitoring is to take place at the "A" and "B" stations and in the environment of the expected maximum radioactive deposition.

Table I

The program of environmental sample measurements

Media	Measured samples	Sampling station	Sampling			Measured components
			number	duration (days)	frequency (sample/year)	
	TLD	A + B + C	22	30	4	gamma doses
	aerosols	A + B	8	3.5	104	gross-beta conc.
			8	4×7	12	gross-gamma conc. + individual nuclides in certain samples
Air	radioiodine	A + B	8	7	52	^{131}I conc.
	fall-out tacky cloth coll.	A + B	8	7	52	gross-gamma conc. + individual nuclides
		A + B + C	22	30	12	
Milk			5		12	^{131}I conc.
Plants	grass	A + B	8		2	individual nuclides conc.
Soil		A + B	8		1	
Monitor well	ground water		5		12	gross-beta, tritium, individual nuclides in certain samples
	water		1	1	365	gross-beta, tritium
Danube	mud		4		2	individual nuclides
	fish		4		2	

In another paper a comparison of the results of in situ field dose rate measurements in the environment of the Paks Nuclear Power Station with values computed by use of the POKER-CAMP program is reported [6].

Accident assessing cross-country car

The cross-country car which can take samples will be equipped with recording gamma dose rate and beta surface contamination measuring instruments operated from a battery and with a "Pille"-type [7] small thermoluminescence reader operated from the car battery. The Pille-type reader will permit the thermoluminescent dosimeters on the spot to be rapidly evaluated without the contribution from the transport dose. Similarly to the mobile laboratory, the cross-country car has a wireless connection to the low background laboratory.

A substantial part of the environmental monitoring system installed at Paks Nuclear Power Station is already in operation and performs systematical preoperational measurements. The mounting of the telemetric and data acquisition system is still in progress.

REFERENCES

1. J. A. Martin, C. B. Nelson and P. A. Cuny, A Computer Code for Calculating Doses, Population Doses, and Ground Depositions due to Atmospheric Emissions of Radionuclides. Environmental Protection Agency Report EPA-520, 1974.

2. F. W. STALLMANN and F. B. K. KAM, ACRA—A Computer Program for the Estimation of Radiation Doses Caused by a Hypothetical Reactor Accident, Report, Oak Ridge National Laboratory, ORNL-TM-4082, 1973.
3. L. KOBLINGER, POKER-CAMP: A Program for Calculating Detector Responses and Phantom Organ Doses in Environmental Gamma Fields, Report, Central Research Institute for Physics, Budapest, KFKI-1981-79, 1981.
4. S. DEME, I. FEHÉR and M. RÖVID, Acta Phys. Hung., this issue, p. 381.
5. A. ANDRÁSI and P. ZOMBORI, Acta Phys. Hung., this issue, p. 389.
6. L. KOBLINGER, I. NÉMETH and P. ZOMBORI, Acta Phys. Hung., this issue, p. 397.
7. I. FEHÉR, S. DEME, B. SZABÓ, J. VÁGVÖLGYI, P. P. SZABÓ, A. CSŐKE and M. RÁNKY, Adv. Space Res., **1**, 61, 1981.

Acta Physica Academiae Scientiarum Hungaricae, 52 (3—4), pp. 381—387 (1982)

TELEMETRIC AND DATA ACQUISITION SYSTEM FOR ENVIRONMENTAL MONITORING AT THE PAKS NUCLEAR POWER STATION

S. DEME, I. FEHÉR and M. RÖVID

HEALTH PHYSICS DEPARTMENT, CENTRAL RESEARCH INSTITUTE FOR PHYSICS
1525 BUDAPEST, HUNGARY

The telemetric and data acquisition system is an inherent part of the total environmental monitoring system of the Paks Nuclear Power Station (Hungary). The detectors of the telemetric system measure the following parameters: the gamma dose rates, the time integral of the ^{131}I activity concentration, the water temperature, and the meteorological data needed for dispersion calculations.

In the 48 channels of the central acquisition system the data mentioned above are stored in the form of pulses, with the exception of the wind direction, which is characterized by the most frequent direction during the measuring period (one hour or 6 minutes). The results are printed on a telex writer and punched on tape for further computer analysis.

The paper deals with the characteristic features of the system and with the possible uses of the data obtained, both for normal operation and emergency cases.

Introduction

At the Paks Nuclear Power Station a telemetric and data acquisition system has been constructed for environmental radiation monitoring [1].

The aims of this system are:

— to give all activity and meteorological data needed for environmental dose calculations for normal releases into the atmosphere and water;

— to verify or correct the data used for diffusion calculations for higher atmospheric releases;

— to provide the real radiation data for measuring points type "A" in accidental situations — especially in cases of uncontrolled releases into the atmosphere.

All of these data together with parameters measured by the sensors of a meteorological tower and by other meteorological stations in neighbouring towns form the basis for deciding on the optimal counter-measures.

Telemetric system

To control the radiation situation in the environment of the power station (Fig. 1), there are 7 so called "A" type stations ("B" and "C" type measuring stations are not connected to the telemetric system). Every "A" type station is built in a thermally isolated container. The temperature inside the container is regulated by ventilation and heating, the internal temperature range is 10—45 °C for external temperatures from —20 °C to 35 °C.

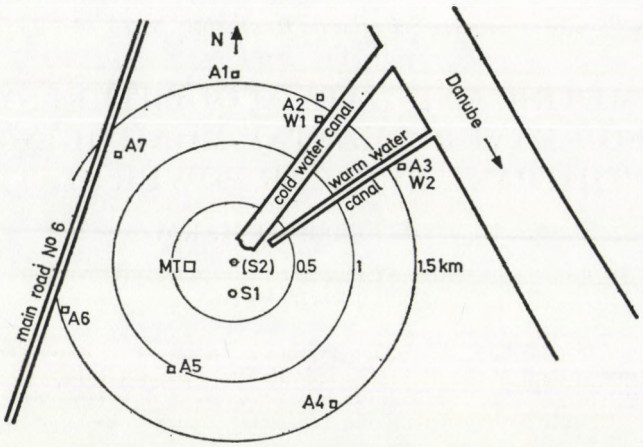

Fig. 1. Layout of the detector locations at Paks Nuclear Power Station. A1—A7 measuring points of gamma-dose rate and time integral of ^{131}I-concentration; W1, W2 water gross gamma concentration control; S1, S2 (planned) stack monitors; MT-meteorological tower.

Gamma-radiation measurements

The G—M tubes are located in measuring probes outside the container; every probe contains three G—M tubes (type SBM-19, made in USSR). The probes are in pairs: one pair has an energy compensation filter (tin 1 mm, lead 0.3 mm) and serves for dose rate measurement; the second probe is without a filter and therefore it gives about 20 times higher sensitivity for gamma energies of ^{133}Xe.

Iodine monitors

The air inlet for iodine measurements has a glass fibre filter. The temperature of the measured air is stabilized at 45 $\pm$ 2 °C. The adsorber material (AC6120, Herfurt, FRG) used at this temperature has low adsorption coefficient for noble gases (e.g. xenon). The adsorber is located around the heat resistant scintillation crystal. If the counting rate is high there is a possibility to enlarge, by remote control the adsorber — crystal distance to obtain a large enough measuring range for the iodine monitor.

The stack iodine monitor is similar to the device described above. The noble gas spectrometric analyser was constructed at the Technical University (Budapest).

Water control

The water activity concentration measurement is based on the gamma-radiation counting by a $\varnothing$ 76$\times$76 mm NaI(Tl) crystal from a water volume of about 8 m^3. The one metre water layer serves as the sample and also as the shielding for the detector.

Meteorological tower

For the meteorological measurements we use several different devices. On the basis of these measurements the parameters needed for diffusion calculations are given. For our calculations we need the wind direction, wind speed and Pasquill category. To determine the category we use the vertical temperature gradient and wind speed. Moreover, for correlation studies we determine the Pasquill category also from the radiation balance, or the wind speed dependence on height, or the standard deviation of the wind direction.

The air temperature and the relative humidity are not directly used for diffusion calculations. In the future we plan to record precipitation automatically by a rate of rainfall gauge.

The main characteristics of the detectors are given in Table I.

Data acquisition system

All data mentioned above are registered by the data acquisition system (Fig. 2) in the form of counts by a 48 (max. 64) channel 10^6-1 capacity scaler. This type of registration is suitable for all data except wind direction. To specify this, we average the wind direction every 20 seconds and find the corresponding 22.5 degrees sector. At the end of the measuring period (normally every hour; in an emergency every 6 minutes) the most frequent direction sector is given by the system.

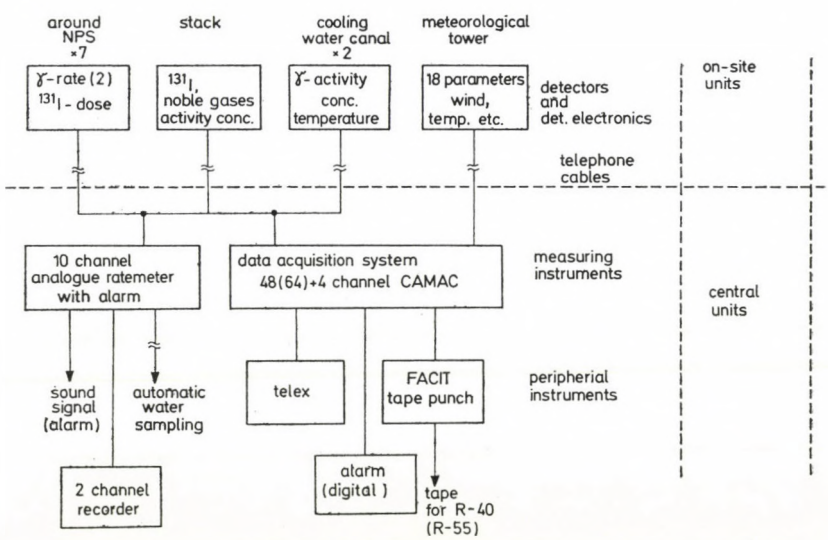

Fig. 2. Schematic diagram of the telemetric and data acquisition system.

Table 1

Main characteristics of the detectors

Location of detector	Number of channels	Measured parameter	Type of detector	Signal processing unit	Converter unit	Measuring range
Measuring points A1—A7	7	gamma radiation dose rate	G—M tube with filter	integral discriminator	frequency divider (1 : 10)	10nGy/h—100μGy/h
	7	gamma radiation intensity	G—M tube without filter	integral discriminator	frequency divider (1 : 10)	1 nGy/h—10 μGy/h (for ^{133}Xe)
	7	^{131}I concentration	NaI(Tl) detector	amplifier, diff. discriminator	frequency divider (1 : 100)	$1-7 \cdot 10^6$ Bq · h/m^3
	1	^{121}I concentration	NaI(Tl) detector	amplifier, diff. discriminator	frequency divider (1 : 100)	$1-7 \cdot 10^6$ Bq · h/m^3
Stack	(4) not connected to scalers	activity concentrations of noble gases	Ga(Li) spectrometer	other CAMAC system	CAMAC interface	1—1000 MPC for ^{85}Kr, ^{88}Kr, ^{133}Xe, ^{135}Xe
Cooling water canal	2	activity concentration of water	NaI(Tl) detector	amplifier, int. discriminator	frequency divider (1 : 100)	$5 \cdot 10^{-4}$—0.5 Bq/cm^3 (for ^{137}Cs)
		water temperature	platinum resistance bulb sensor	measuring bridge	voltage-frequency	0—40 °C ($\pm$0.3 °C)
	1	radiation balance	thermopiles	DC-amplifier	voltage-frequency	—0.7 — (+6.6) J/cm^2 · min
	4	wind speed	cup anemometer	high frequency tachometer	frequency divider (1 : 3)	1—160 km/h
	4	wind direction	lightweight vane	potentiometer 540° system	voltage-frequency	0—540° (1.2 km/h min. speed)

Meteorological tower	2	wind direction standard deviation	the same as for wind direction	analogous computer	voltage-frequency	45°
	2	air temperature difference	platinum resistance bulb sensor	measuring bridge	voltage-frequency	−5 °C−(+5) °C (±0.2 °C)
	2	air temperature	platinum resistance bulb sensor	measuring bridge	voltage-frequency	−20 °C−(+40) °C (±0.5 °C)
	3	relative humidity	solid state probe	high frequency oscillator	voltage-frequency	0−100%

For radiation data there are lower and higher signalling levels (given in numerical form). The lower limit indicates the detection failure, the higher means that radiation is increased above the normal range. When determining the levels we have to take into account the variations of radiation level due to natural sources. The alarm level is controlled digitally at the end of the measuring period. To overcome this disadvantage there is a built-in ten channel analogous ratemeter with an alarm. These channels are connected to gamma-radiation intensity measuring detectors (7 channels), to water activity concentration measuring detectors (2 channels) and to a stack iodine monitor. If there is an emergency the measuring period of the acquisition system is automatically changed from one hour to 6 minutes. When a signal comes from the water channel the automatic system extracts a water sample of several litres.

The outputs of the data collecting system are printed by teletype and an ASCII code tape is punched. The latter is used for calculations on an R-40 and/or R-55 computer.

For nornal releases or slightly increased releases into the atmosphere through the stack a modified version of the AIREM program [2] is used to calculate doses, population doses, and ground depositions. The time period for one run may be equal to one month. In the case of significant release we plan to run the program separately and compare the measured and calculated environmental radiation data. The most sensitive method for environmental control in our system is the G—M counter pack without compensation filter. With this detector it is possible to indicate 1—3 per cent of gamma-dose intensity increase due to ^{133}Xe. As a result of this comparison we hope to find the best calculation method for the Paks nuclear power station site.

For accidental release we are not able to determine directly the environmental radiation burden because of the lack of emission data. In this case we intend to use the previously calculated relative distribution curves for ground concentration and gamma-dose at unit release [3]. To choose the right distribution curves we have to determine the actual diffusion category from the meteorological tower measurements. The real release may be calculated from the wind direction and radiation data determined by the tower and the "A" type measuring points. The latter are representative points for a considerable part of the population.

The way in which this data acquisition is constructed ensures the possibility of directly (on-line) linking the system to a high capacity computer of the station. This linking is very important for accidents having widespread environmental consequences.

REFERENCES

1. I. Fehér, S. Deme and A. Andrási, Acta Phys. Hung., this issue, p. 373.
2. J. A. Martin, C. B. Nelson and P. A. Cuny, A Computer Code for Calculating Doses, Population Doses, and Ground Depositions due to Atmospheric Emissions of Radionuclides. Environmental Protection Agency Report EPA-520, 1974.
3. F. W. Stallmann and F. B. K. Kam, ACRA — A Computer Program for the Estimation of Radiation Doses Caused by a Hypothetical Reactor Accident, Report, Oak Ridge National Laboratory, ORNL-TM-4082, 1973; ACRA-II: Kernel Integration Code. RSIC Computer Code Collection CCC-213, Oak Ridge National Laboratory, 1974.

Acta Physica Academiae Scientiarum Hungaricae, 52 (3—4), pp. 389—395 (1982)

GAMMA SPECTROMETRIC MEASURING SYSTEM FOR ENVIRONMENTAL SAMPLE ANALYSIS

A. ANDRÁSI and P. ZOMBORI

HEALTH PHYSICS DEPARTMENT, CENTRAL RESEARCH INSTITUTE FOR PHYSICS
1525 BUDAPEST, HUNGARY

A desk calculator controlled gamma spectrometer was installed and calibrated for routine sample analysis in the environment of the first Hungarian nuclear power plant. A combined application of high efficiency Na(Tl) and high resolution Ge(Li) spectrometry was elaborated to process the great number of measurements. Measurement is controlled and spectrum evaluation is performed by an on line program (MEASSYS1) developed for the EMG-71666 desk calculator. The multi-step testing procedure proved the applicability and reliability of the system.

Introduction

The Health Physics Department of the Central Research Institute for Physics was commissioned to elaborate the environmental monitoring system of the first Hungarian nuclear power plant at Paks. As an important part of the system a sampling and sample measuring program was elaborated. During the planning and realization the following requirements and conditions had to be taken into consideration.

- All or most of the environmental media (air, water, soil, vegetation, etc.) must be monitored to check the extent of radioactive pollution.
- The methods of measurement must be sensitive and accurate to provide reliable data for important decisions; redundant information should be avoided.
- Activity determination should be as automatic and easy-to-use as possible.
- The cost of the system must be reasonably low (with priority being given to Hungarian produced hardware).

In Table I detailed information is given on the number, kind, and preparation method of various samples measured by gamma spectrometry. The most frequently used method is direct gamma spectrometric measurement of the samples collected regularly in the environment of the power plant. The spectrometer is situated in the Environmental Laboratory of the power plant.

Instrumentation

The instrumental set-up of the gamma-spectrometric system is shown in Fig. 1. An 8% relative efficiency Ge(Li) detector (produced in Czechoslovakia) and a 3"×3" NaI(Tl) scintillation detector (made in Hungary) are placed in

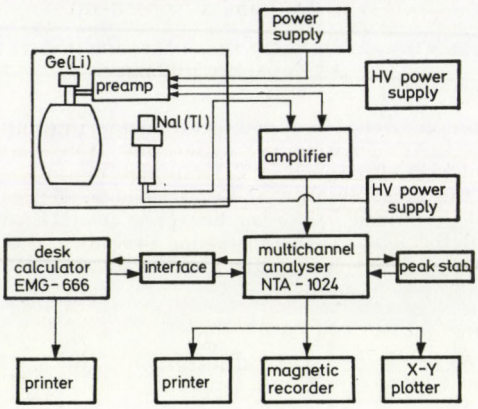

Fig. 1. Gamma spectrometric measuring and evaluating system.

a 15 cm thick old iron shield. The two detectors can be operated alternately. The detector signals are analysed by an NTA-1024 multichannel analyser and the mesurement is controlled and evaluated by an 8 kbyte memory capacity

Table I

Some characteristic data on the gamma-spectrometric sampling program of the environmental monitoring system at Paks Nuclear Power Plant

Sample		Sampling		Total number of samples/year	Preparation
		number of places	frequency (sample/year)		
air	aerosol	8	12	96	none
	fall-out	8	52	416	ion exchange
	tacky cloth coll.	22	12	264	none
vegetation		8	2	16	none
soil		8	1	8	drying
ground water		1	12	12	none
Danube	water	1	12	12	none
	mud	4	2	8	drying
	fish	4	2	8	grinding
release water	water from hot canal	1	12	12	none
	sewage water	1	12	12	none

EMG-71666 type desk calculator. The spectrometer is equipped with the necessary peripherals. All parts of the signal and data processing electronics are of Hungarian make.

Basic concepts and organization of measurements

Because of the great number of samples (see Table I) the following philosophy of measurement organization was accepted:

— All the samples are measured by a short (typically 2000 s) scintillation spectrometric measurement.

— The spectra obtained are reduced by a stripping method to eliminate the contribution of natural radionuclides (^{40}K, ^{226}Ra, ^{232}Th).

— The integral values of the reduced spectra over the energy range of 100—1350 keV are checked to see whether they exceed a predetermined limit.

— After screening the samples exceeding the limit are measured by Ge(Li) spectrometry with longer (typically overnight) measurements.

— As a "background" program representatives of each type of sample are monitored by Ge(Li) spectrometry in accordance with a certain rule of selection.

The measurement of screened samples has a higher priority and gives detailed information on the activity concentrations of the individual radionuclides in a relatively short time after the sampling. The "background" program having lower priority helps to reveal long-term low extent pollution of the environment by radioisotopes of artificial origin. The combination of different spectrometric methods in the way described is efficient and time saving.

Structure and functioning of MEASSYS1

For controlling and evaluating Ge(Li)-spectrometric measurements a program system, named MEASSYS1, was developed on the EMG-71666 desk calculator. The structure and functioning of MEASSYS1 is illustrated in Fig. 2. The aim of program development was to provide optimum automation while retaining the option for further detailed manual investigation if necessary. In a simple case only some preliminary information (date, type and size of sample, number of isotope library to be used, preset time, etc.) are needed as input, the whole further process (starting and stopping the measurement, evaluating the spectra, etc.) is performed automatically. The printed output contains the list of data belonging to each peak found. In a complete set of data the position and area of the peak, its energy and activity are given together with the corresponding errors. Using the option of isotope identification the lines of the spectrum are assigned to certain radioisotopes. Five different libra-

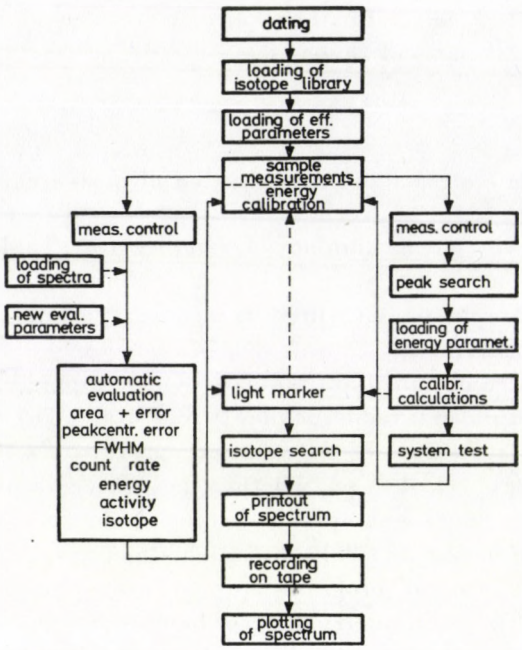

Fig. 2. Structure and functioning of MEASSYS1.

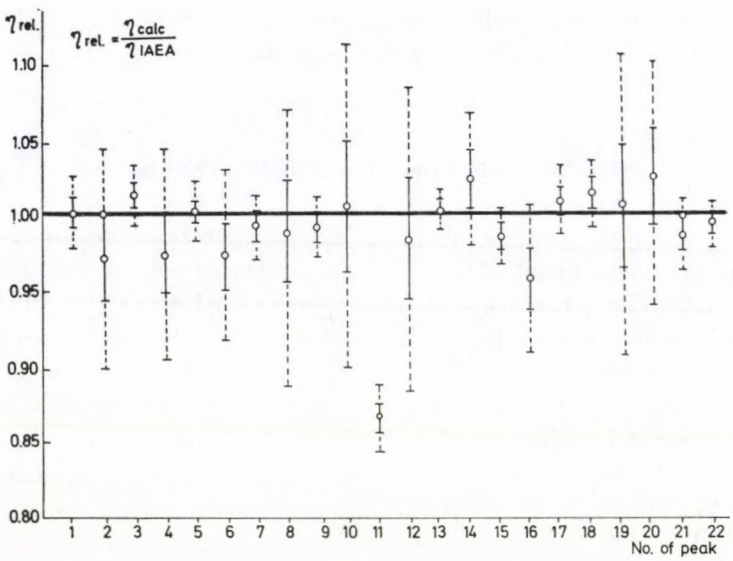

Fig. 3. Results of peak area determination test on spectra Nos. 300—305 of the G-1 intercomparison program. Values determined by MEASSYS1 are related to those reported by IAEA for 22 different peaks. Broken lines represent standard deviation of peak areas; continuous lines correspond to the uncertainty of mean values.

ries each containing 50 lines of the most frequently occurring radionuclides can be loaded into the memory.

The determination of activity requires an accurate knowledge of the mesuring efficiency as a function of energy, sample size and density. On the basis of a thorough calibration procedure the following analytic expression was obtained for efficiency calculations:

$$\eta(E, \varrho, h) = AE^{-\alpha} e^{-BE^{-\beta}} e^{-\varrho h C E^{-\gamma}},$$

where E is the energy, ϱ is the density of the sample, h is the effective thickness of the sample and A, α, B, β, C, γ are mathematical parameters.

Efficiency parameters were determined for three different source-detector geometries:

1. point source at a fixed distance from the detector with an absorbent of varying thickness and density between them;
2. extended source of smaller quantity (up to 100 cm^3) in a cylindrical holder for samples with higher activity concentration;
3. extended source of larger quantity (1500 cm^3) in a Marinelli beaker for voluminous samples with low activity concentration.

Testing

A multi-step thorough testing procedure was performed to check the capability, accuracy and reliability of the system.

— The G-1 synthesized spectra distributed by the IAEA for laboratory intercalibration was used to test the goodness of the mathematical algorithms (peak search and peak area determination). Fig. 3 shows a comparison of the results of peak area determination obtained by MEASSYSI and reported by the IAEA.

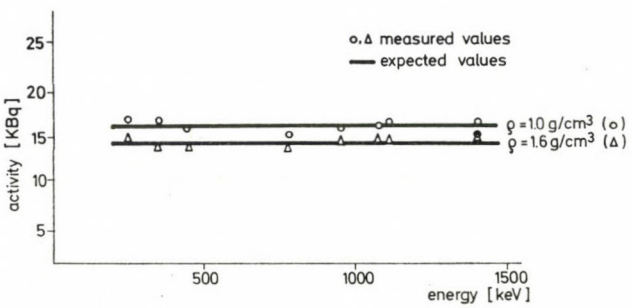

Fig. 4. Determination of ^{152}Eu extended source activity by its different energy lines for two different matrix densities.

Table II

Results of the SD-B-2 marine sediment sample measurement

Isotope	Measured values [Bq/g]	Reference values [Bq/g]
^{134}Cs	0.444 ± 0.019	0.422 ± 0.019
^{137}Cs	3.286 ± 0.033	3.367 ± 0.111
^{60}Co	10.80 ± 0.06	10.36 ± 0.37

— The accuracy of efficiency calculation was tested by standard point (^{232}Th) and extended (^{152}Eu) sources. The results obtained for extended sources are shown in Fig. 4.

— As a typical environmental material marine sediment of known activity concentration (SD-B-2 intercomparison of the IAEA) was measured and analysed. The results are summarized in Table II in comparison with the average values of 43 laboratories.

— Grass, mud and soil samples from the environment of nuclear installations were analysed simultaneously by MEASSYSl and by an independent data acquisition and evaluation system using sophisticated software (SAMPO80) on a PDP-11/34 minicomputer.

The different testing procedures gave good arguments for the applicability of the MEASSYSl program system.

Conclusion

As the fulfilment of the main objectives of this work an easy to handle and desk calculator controlled gamma spectrometric system has been developed for routine use which allows measurement and evaluation to be carried out

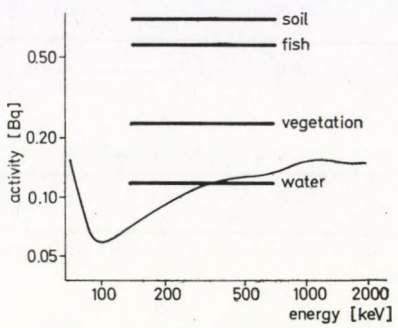

Fig. 5. Minimum detectable activities in Marinelli-beaker geometry for $6 \cdot 10^4$ s measuring time. The predetermined limits for some typical environmental samples are indicated by horizontal lines.

with optimum level of automation. It means that a complete analysis needs only a few starting instructions and data at the beginning and this results in the activities of individual radionuclides contained in environmental samples of different origin being given at the end. It has been proved by the different test investigations that the method elaborated is suitable to determine sample activities higher than 0.1 Bq of individual radionuclides with an accuracy of 3—8% in the energy range from 100 to 2000 keV and for density ranging from 0.1 to 1.6 g/cm^3. The indicated 0.1 Bq detection limit attainable with $6 \cdot 10^4$s measuring time proved to be low enough for the activity determination of radionuclides at the prescribed level to be measured [1] as shown in Fig. 5.

REFERENCES

1. M. Winter, J. Narroy, M. Friedriech, Empfehlungen zur Überwachung der Umweltradioaktivität, Loseblattsammlung Arbeitskreis Umweltüberwachung (AKU), FS-78-15-AKU, Karlsruhe, 1979.

Acta Physica Academiae Scientiarum Hungaricae, 52 (3—4), pp. 397—404 (1982)

COMPARISON OF FIELD DOSE RATE MEASUREMENTS AND MONTE CARLO CALCULATIONS

L. KOBLINGER, I. NÉMETH, P. ZOMBORI and A. ANDRÁSI

HEALTH PHYSICS DEPARTMENT, CENTRAL RESEARCH INSTITUTE FOR PHYSICS
1525 BUDAPEST, HUNGARY

Dose rates from natural terrestrial gamma sources calculated by a Monte Carlo program and derived from NaI(Tl) scintillation measurements as well as calculated and measured count rates of G—M detectors are compared and show satisfactory agreement.

Introduction

The installation of the first Hungarian nuclear power station, due to be put into operation in the near future at Paks (110 km south of Budapest), gave our Department the task of designing the environmental monitoring system. There are several types of detectors used in this system and the readings of these detectors are further analysed and interpreted on the basis of theoretical considerations and on the results of computer model calculations.

The fulfilment of the first task: the determination of the natural background, the so-called pre-operational-level, gave us a good opportunity for checking our measuring and calculational methods. Several such comparisons are described in this paper.

Calculations

For computing the field parameters and detector responses a general environmental gamma flux and dose calculating program, the POKER-CAMP [1], was used. With this adjoint Monte Carlo code flux, air kerma and spectra of photons at any point in the environment; responses of point-like, cylindrical, or spherical detectors; or doses absorbed in organs of anthropomorphic phantoms can be calculated.

The geometrical model is the following: the soil and the air are two semi-infinite bulks and an intermediate layer of arbitrary thickness can be placed between them (for modelling grass, snow, etc.). Three types of geometrical source distributions can be specified in each region:

— uniform source;
— plane source on the surface of the solid regions or at any height in the air;

— source decreasing exponentially with depth in the soil or with height in the air.

Calculations can be carried out also for any combination of these elemental distributions.

This wide range of input specification possibilities enables the code to be applied for studying a great variety of environmental problems.

In the investigations presented here no intermediate layer is specified, the natural radioactive sources are assumed to be uniformly distributed in the soil. Air dose rates and responses of point-like detectors are calculated. The dose rates are actually replaced by the kerma rates — a very reasonable approximation for the gammas of the natural sources.

Soil samples

Soil samples were collected from 24 locations in the Paks area. The activity concentrations of the samples were determined by TÓTH and LAKATOS—NOVOTNY [2] and are given in Table I. The estimated over-all error lies in the range of 5—10 per cent for all activities. The activity concentrations listed in Table I were used as input data for the Monte Carlo calculations. There was no soil composition analysis, we used the typical soil composition given by BECK [3]: Al_2O_3 13.5 weight per cent, Fe_2O_3 4.5 per cent, SiO_2 67.5 per cent, CO_2 4.5 per cent and H_2O 10.0 per cent, with a density of 1.6 g/cm^3. Computations carried out with significantly deviating compositions have shown that the soil composition hardly influences the dose rates.

The statistical uncertainties of the Monte Carlo calculated results are 1—2 per cent.

Dose rate measurements with NaI(Tl) scintillation detector

Dose rates were measured four times during two years on the same sites from which the soil samples were taken [4]. The centre of the $\varnothing 7.6\,\text{cm} \times 7.6\,\text{cm}$ NaI(Tl) detector was placed at 1 m above ground level.

Full-energy peaks of the 1460 keV line of the ^{40}K isotope and two characteristic lines of the U(Ra)-series and the Th-series (1760 and 2615 keV, respectively) were determined. The factors that convert the directly measured peak area data of the characteristic lines to the dose rates caused by the individual radioactive chains were derived from theoretical considerations [5, 6] and calibrations. The overall uncertainty of the dose rates obtained by this method is estimated to be about 8, 30, and 12 per cent for the ^{40}K, U(Ra) and Th sources, respectively.

Table I

Activity concentrations in the soil samples

Sample No.	Activity concentration [Bq/kg]		
	^{40}K	U(Ra)-chain	Th-cain
1	258	9.2	12.2
2	305	13.7	18.1
3	460	30.3	36.6
4	515	31.4	39.6
5	272	14.4	17.4
6	267	12.2	15.5
7	246	9.6	11.5
8	289	18.8	23.7
9	389	30.0	26.6
10	456	30.3	34.0
11	295	15.9	22.9
12	343	23.3	30.0
13	249	12.2	15.2
14	411	32.9	38.1
15	477	35.9	48.8
16	406	28.1	31.1
17	418	30.7	32.6
18	306	15.5	25.2
19	437	32.9	32.2
20	302	14.8	18.5
21	407	38.5	43.3
22	409	33.3	42.2
23	389	32.9	40.7
24	256	11.8	15.5

Measurements with G—M detectors

Measurements were also carried out four times in two years by detectors containing three CTC-6 type Soviet G—M tubes placed at 1 m above the ground.

Two coverings were used:

— G—M detector No. 1 was covered by 2 mm Al;

— G—M detector No. 2 was covered (from internal to external layers) by 1 mm Sn + 0.3 mm Pb + 2 mm Al.

Both detectors have an internal layer of 2 mm plastic to absorb the beta radiation of structural materials.

Table II

Sensitivity of G—M detector No. 1

Angles	0°	30°	60°	90°	120°	150°	180°
Energies [keV]	Sensitivities in [cps/(μGy/h)]						
60	9.8	42.6	60.6	65.8	62.7	42.0	7.9
81	12.5	33.2	51.8	57.2	51.8	32.6	9.0
140	20.3	37.0	44.1	46.0	44.7	39.3	15.2
379	10.2	16.9	19.2	19.6	19.0	17.6	7.9
662	13.4	18.8	21.7	22.6	21.5	18.8	11.1
1252	19.0	21.3	24.6	26.1	25.5	24.2	15.7

Table III

Sensitivity of G—M detector No. 2

Angles	0°	30°	60°	90°	120°	150°	180°
Energies [keV]	Sensitivities in [cps/(μGy/h)]						
60	7.7	2.3	0.23	0.21	0.23	1.3	5.9
81	8.1	0.92	0.38	0.63	0.5	2.1	6.1
140	14.4	4.0	4.2	6.9	4.6	3.5	12.5
379	10.5	10.9	15.0	15.5	14.8	12.1	8.6
662	12.9	15.7	19.0	19.4	19.0	15.9	11.5
1252	19.4	20.9	25.1	25.9	25.1	21.5	17.1

The axes of the tubes were horizontal and their sensitivities were determined at several energies and for several angles of incidence with point sources. The dose rates for these calibrations were measured by an ion chamber. Tables II and III contain the elements of the sensitivity matrices that were used by POKER-CAMP to calculate the responses of these detectors. Linear interpolation was used for intermediate energies and angles. Zero sensitivity was given to all angles at 5 keV energies and the values measured at 1252 keV were used for all higher energies.

The contribution of cosmic rays is always subtracted from the counts. The values of 1.80 and 1.74 cps for the two detectors, respectively, were determined by measurements on Lake Balaton.

The overall uncertainty of the G—M measurements is 6—8 per cent.

Results

All the measured values are averages of the 4 separate measurement series.

The free-in-air kerma rates obtained by Monte Carlo calculations and measured by the NaI(Tl) detector are given in Figs. 1—3 for the 24 test sites.

Figs. 4 and 5 show the relationship between the calculated and measured responses of the two G—M detectors.

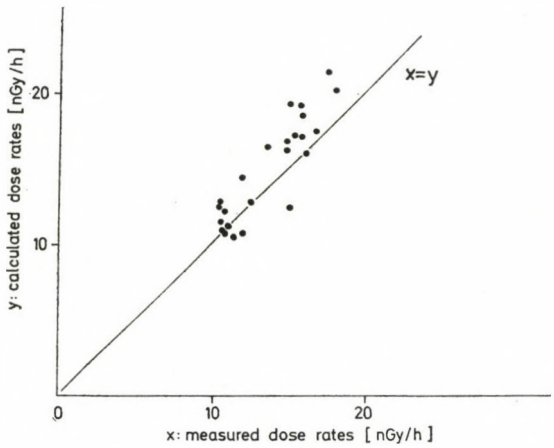

Fig. 1. Dose rates from the ^{40}K isotope. Values calculated by POKER-CAMP code and measured by NaI(Tl) detector.

The correlation between the measured and calculated data seems to be quite acceptable for all cases, especially if all the sources of errors are taken into account, viz.

- the question of representativeness of the soil samples analysed;
- uncertainties of activity concentration measurements;
- the lack of knowledge of actual soil compositions and densities;
- approximations of the calculational model (homogeneous soil and source distributions, omission of vegetation layer, the neglecting of radon and thoron emanation);
- uncertainties in the determination of the cosmic ray contribution;
- the poor resolution of the G—M detector sensitivity matrix;
- possible systematic error of the peak area determination in NaI(Tl) spectrometry;
- the uncertainty of the peak area to dose rate conversion factors applied in scintillation spectrometry.

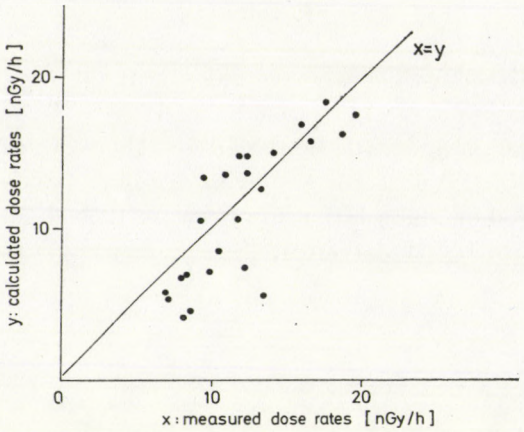

Fig. 2. Dose rates from the U(Ra)-series. Values calculated by POKER-CAMP code and measured by NaI(Tl) detector.

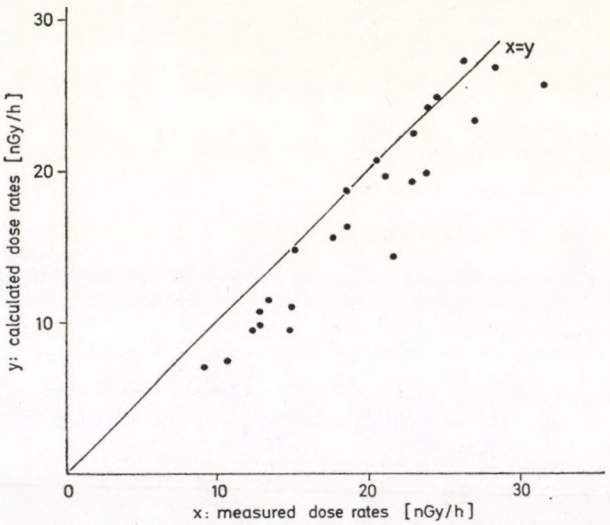

Fig. 3. Dose rates from the Th-series. Values calculated by POKER-CAMP code and measured by NaI(Tl) detector.

Remarks on further applications

These comparisons, based on pre-operation level measurements, have proved the applicability of the calculational and experimental methods developed in our Department. In view of this, we can safely extend these techniques to other source distributions in different environmental media both for normal and accidental situations in the vicinity of power stations. Moreover, the method is suitable for calculations of such hardly measurable quantities as organ doses.

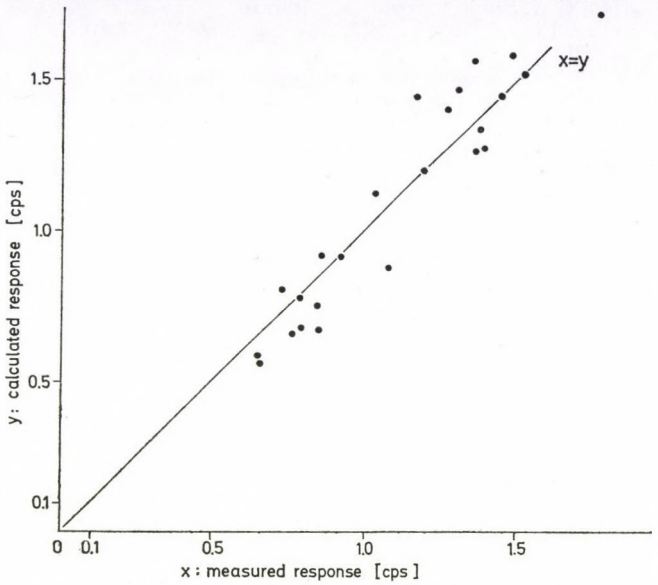

Fig. 4. Calculated and measured responses of G—M detector No. 1.

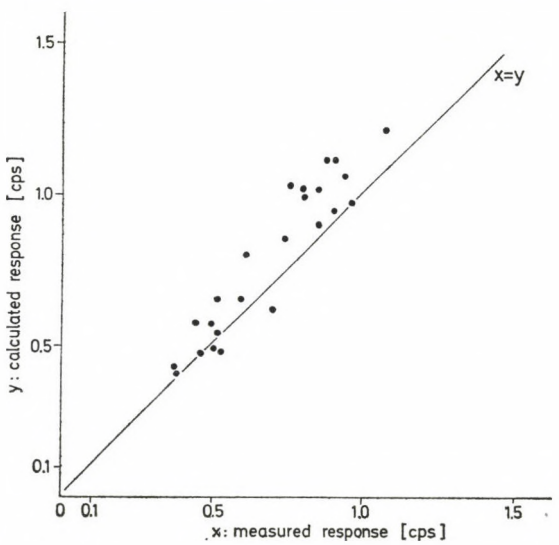

Fig. 5. Calculated and measured responses of G—M detector No. 2.

REFERENCES

1. L. Koblinger, POKER-CAMP: A Program for Calculating Detector Responses and Phantom Organ Doses in Environmental Gamma Fields, Report, Central Research Institute for Physics, Budapest, KFKI 1981—79, 1981.
2. Á. Tóth and S. Lakatos-Novotny, ^{226}Ra, ^{232}Th and ^{40}K Concentrations as well as Emanation Coefficients in Soil Samples from the Vicinity of the Paks Nuclear Power Station

(in Hungarian). In: Environmental Monitoring of the Paks Nuclear Power Station — Pre-operational Level Survey, Vol. 2: Central Research Institute for Physics edition, Budapest, 1979.

3. H. L. BECK, The Physics of Environmental Gamma Radiation Fields. In: Proc. 2nd Int. Symp. on the Natural Radiation Environment. USERDA Rep. CONF-720805-P1, 1974.
4. A. ANDRÁSI, I. NÉMETH and P. ZOMBORI, In-situ Measurements of the Pre-operational Background Radiation in the Vicinity of the Paks Nuclear Power Station (in Hungarian). In: Environmental Monitoring of the Paks Nuclear Power Station — Pre-operational Level Survey, Vol. 5: Central Research Institute for Physics edition, Budapest, 1979.
5. H. L. BECK, J. DECAMPO and C. GOGOLAK, In-situ Ge(Li) and NaI(Tl) gamma-ray spectrometry. Report of the Health and Safety Laboratory, New York, 1972.
6. P. ZOMBORI, Gamma Spectrometric Methods for Determining the Environmental Background Radiation (in Hungarian). In: Environmental Monitoring of the Paks Nuclear Power Station — Pre-operational Level Survey, Vol. 1: Central Research Institute for Physics edition, Budapest, 1978.

Acta Physica Academiae Scientiarum Hungaricae, 52 (3—4), pp. 405—411 (1982)

EXAMINATION OF A HOT PARTICLE FROM A RECENT ATMOSPHERIC TEST

I. MASCHEK and T. CSEPREGI

"FRÉDÉRIC JOLIOT-CURIE" NATIONAL RESEARCH INSTITUTE FOR RADIOBIOLOGY AND RADIOHYGIENE
1775 BUDAPEST, HUNGARY

Changes in airborne activity concentration can usually be observed by determining the activity of collected aerosol. The present work is considered as an exception: a hot particle was found on an aerosol sample and it offered the occasion of this contribution.

The report follows observations and radiological methods regarding particle study and it provides the following results. The hot particle contained fission nuclides like ^{95}Zr and ^{95}Nb, it was solely present on the sample, it originated in the atmospheric nuclear test of 16 October 1981, it was captured a few days before reaching the maximum activity of ^{95}Nb induced directly by ^{95}Zr, and finally its size was about one micrometer.

Introduction

A continuous check on the radiological state of air at a certain site is maintained by systematic monitoring of airborne activity. The changes of activity concentration in air can usually be followed by the activity of collected aerosol. When, however, the aerosol activity is found too high, the following questions arise: Is the increase due to a higher radioactive concentration or rather to some individual hot particles? What nuclides are involved? What is the possible source? These questions are important from the viewpoint of radiation protection and radiation hygiene. In the latter case further information on particle size is also required.

Before putting the first Hungarian nuclear reactor into operation, assessment and analysis of background airborne activity are being carried out. The background activity related to natural background can be increased to a great extent by atmospheric nuclear tests producing active particles. They should be distinguished from radioaerosols released by the reactor.

This paper reports on examinations of the radiological character of a hot particle sampled in Budapest, in December 1980. This particle gave us the opportunity of more detailed study as we had already analysed a hot particle by gamma spectrometry in 1976. Examinations here were carried out by gamma spectrometry, autoradiography and energy dispersive X-ray spectrometry whereby the time of origin of the particle, the included fission nuclides, activity, and approximate particle size are discussed. The particle is rightly supposed to be a tropospheric aerosol. We have no facilities for characterizing stratospheric aerosols at low altitudes.

Fluctuation of environmental airborne activity

The particle was captured with the help of an environmental radioaerosol sampling system which was put into operation for monitoring the airborne activity concentration. Beta activity is generally measured three days after sampling [1]. The histogram on the upper part of Fig. 1 shows the daily activity concentration during the period of October 1980—July 1981. On the horizontal

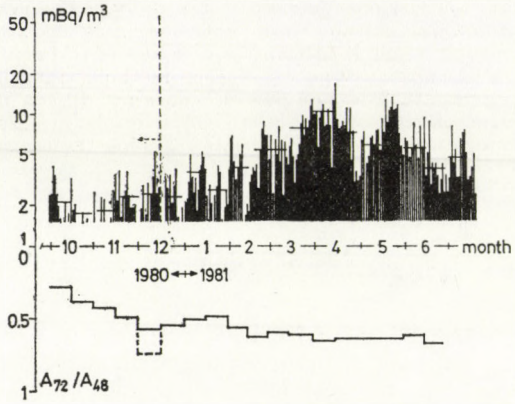

Fig. 1. Top : Daily radioaerosol concentration in mBq/m³ outside air. Activity is measured three days after end of sampling and is related to natural uranium. Bottom: Ratio of activities measured at the 72nd and 48th hour after sampling, drawn in averages of each half-month. Ratios exceeding 0.5 depend on half-life of fission products.

axis no data are indicated below the limit accepted for evaluating concentration. Horizontal lines represent average data over half months. The concentration which exceeds the average background of about 2 mBq/m³ on this historgam is assumed to be caused by some artificial source. From the beginning of 1981 an increased level of more peaks was observed attributable to stratospheric aerosol originating from an atmospheric nuclear test.

However, before the longer-staying increase a sample of high activity was found one day in December. The activity marked by the broken line in Fig. 1 was about thirty times higher than the activity measured days before and after. It is to be mentioned that no similar anomaly was observed in samples collected by other aerosol samplers and separators in use at the same time. Hence, this aerosol sample of high activity could plausibly be no part of a radioactive cloud. Therefore, it is unrealistic to quote concentration from that.

The bottom part of Fig. 1 gives the ratio of activities measured in the 72nd (A_{72}) and 48th (A_{48}) hour after sampling, i.e. the decrease of activity on the third day. The ratio is drawn in averages over half months. If fission products are present the ratio exceeds 0.5 depending on the half lives of the fission

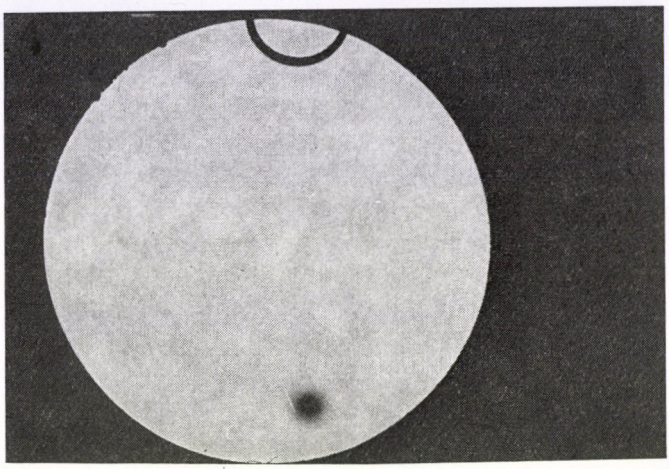

Fig. 2. Autoradiograph with KODAK RM film on sample containing beta and gamma active particle. The black spot represents the hot particle.

products [1]. The increase in both concentration and ratio characterizes the relationship between natural and artificial activity in air.

Further discussion relates to the extremely active sample of December 1980.

Hot particle recorded on autoradiograph

Kodak RM film was used for autoradiographs exposed for one month. Photos of both sides of the filter were very similar. That presented in Fig. 2 shows the sole presence of a hot particle localized in a 2 mm ∅ spot. The black spot represents exposure from beta and gamma radiation, too, as is to be expected from film sensitivity [2]. Intensity and energy of radiation were not estimated on the record.

Origin of the particle and included fission nuclides

The time of origin of the particle, i.e. the date of the explosion, can be deduced from the disintegration of characteristic fission nuclides [3]. For this purpose the sample was analysed by a Ge(Li) gamma spectrometer. Spectra were taken in an 8×10^4 s long analysis twice after the sampling. One of the spectra is given at the upper part of Fig. 3. Among others ^{95}Zr and ^{95}Nb as fission products were identified by energy. Their activity was also determined. The lower part of Fig. 3 shows the intensity of ^{95}Zr and ^{95}Nb in an extended scale of channel number. The continuous line stands for the first analysis on 13 January 1981, the broken line is for the second mesurement on 4 March 1981.

The relevant nuclides for time recalculation are ^{95}Zr and ^{95}Nb. Assuming that ^{95}Nb is the progeny only of ^{95}Zr disintegrating from the origin of the particle, and ^{95}Nb does not exist alone or from other precursors, the elapsed time from the origin of the particle can be expressed by the equation [3]

$$t - t_0 = -1.443 \frac{T_1 T_2}{T_1 - T_2} \ln \left(1 - \frac{A_{2t}}{A_{1t}} \frac{T_1 - T_2}{T_1}\right), \tag{1}$$

where A_{1t} and A_{2t} are the activities of ^{95}Zr and ^{95}Nb at time t, T_1 and T_2 represent the respective half lives of ^{95}Zr and ^{95}Nb, that is, 65 and 35 days.

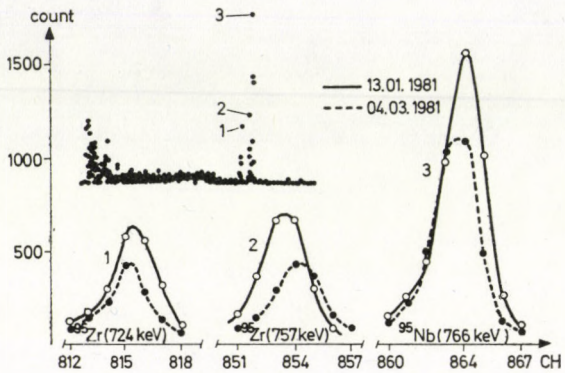

Fig. 3. Ge(Li) gamma spectra performed on sample including hot particle. Scale of channel number is extended in regard to ^{95}Zr and ^{95}Nb. The upper and lower curves result from analyses on 13.01.1981 and 04.03.1981, respectively. One complete spectrum is to the left above the curves.

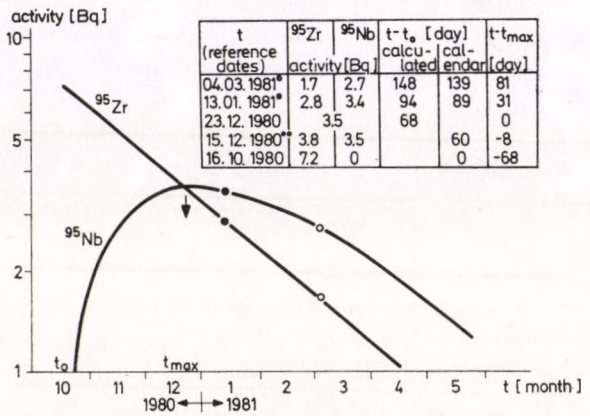

t (reference dates)	^{95}Zr activity [Bq]	^{95}Nb activity [Bq]	t-t$_0$ [day] calculated	t-t$_0$ [day] calendar	t-t$_{max}$ [day]
04.03.1981*	1.7	2.7	148	139	81
13.01.1981*	2.8	3.4	94	89	31
23.12.1980	3.5		68		0
15.12.1980**	3.8	3.5		60	-8
16.10.1980	7.2	0		0	-68

Fig. 4. Activity of ^{95}Zr, ^{95}Nb vs calendar time. Table correlating the diagram shows measured and calculated ^{95}Zr, ^{95}Nb activity and elapsed time from the origin of particle (t_0) and from maximum ^{95}Nb activity (t_{max}) up to the dates as follows: analyses (○ , ●), maximum daughter element activity, sampling (○ ○), origin of the particle. Relative statistical error of the measured activities (○ , ●) are 10%, the estimated relative error of the complete method is less than 18%.

Otherwise, the time elapsing from the maximum activity of the induced nuclide can be given by

$$t - t_{\max} = 1.443 \frac{T_1 T_2}{T_1 - T_2} \ln \frac{T_1}{T_2}. \tag{2}$$

At '$t_{\max}$' the activity of mother and daughter nuclides can be justified as being the same.

The diagram in Fig. 4 illustrates the ^{95}Zr and ^{95}Nb activities vs calendar time. The measured and calculated figures of time and activity relating to a few reference dates are also summarized in the Table above the diagram. It can be seen that the date of origin of the hot particle was obtained with a good approximation to the date of a recent atmospheric nuclear test (16 October 1981) known from the press. The capture date of 15 December 1980 was a few days before the ^{95}Nb maximum activity, in view of which the long measuring process was carried out along the descending branch of the Nb curve.

Consideration on particle size

The size of a particle injected from an explosion into the atmosphere depends on the characteristics of the test and is modified during the long atmospheric transport [4]. Micron sized particles are able to descend from the

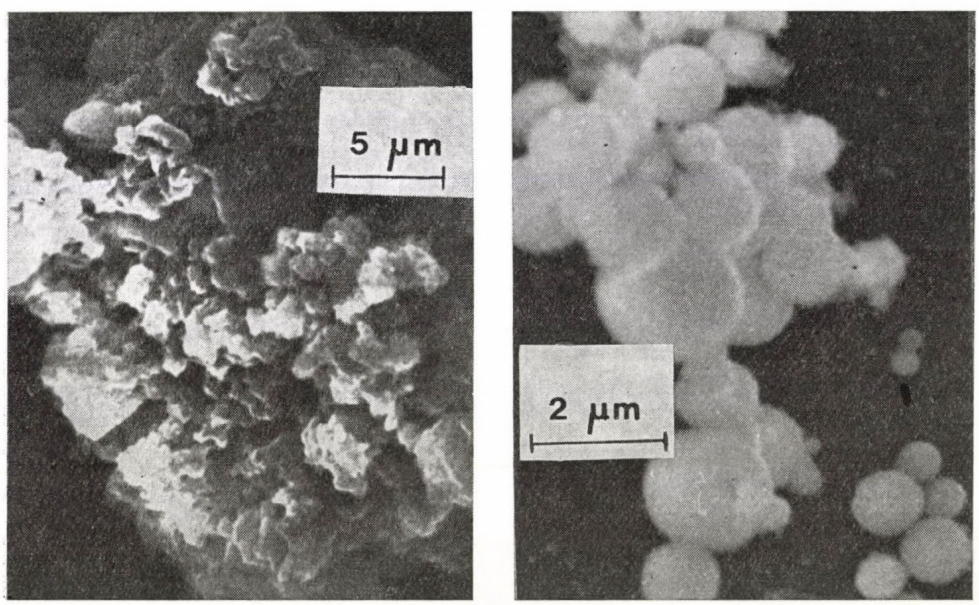

Fig. 5. a) Electronmicrograph of cluster around the hot particle. b) Particle collection in a closed region of the hot particle.

troposphere within a few months after the explosion, whereas submicron ones settle from the stratosphere mainly in spring time because of the tropopause opening late winter. It is likely that the examined particle belongs to the first case.

Identification and size measurement of the particle required electron-microscopic localization. Even though the whole filter and also its autoradiographically localized part has deposited aerosol in a thickness of 100—200 μm, the finding of the particle can be hopeless even with a scanning electron microscope. However, data available from gamma spectra suggest that one characterizes the particle from the included element. For the purpose an energy dispersive X-ray spectrometer with an automatic stepping device was utilized.

From a preliminary calculation — substituting the physical parameters and original activity of ^{95}Zr — the size of the active kernel within the particle was found to be about 0.15 μm in diameter. Although, as the particle can include a series of other elements from earth and stone at the detonation place and temper material of the bomb, the size would be much larger. Because of this the initial information for X-ray spectrometry was the calculated mass of the fission elements.

Regarding the multilayer aerosol deposition a mechanical detaching process had to be utilized to obtain a small and thin sample for microanalysis. The electronmicrograph (Fig. 5a) shows the cluster of the hot particle removed from the filter; Fig. 5b informs us about the possible particle size in the cluster of the hot particle of Fig. 5a. Hence, the geometrical size was found in the range 0.8—2 μm. An additional justification would have exceeded the reasonable limit.

Summary

A discussion is presented on the examination of a hot particle captured on an aerosol filter. ^{95}Zr and ^{95}Nb fission nuclides were identified in the particle by gamma spectrometry. On the basis of their activity it was found that the time of origin of the particle corresponded to the date of a recent atmospheric nuclear test (16 October 1980) and that the capture was a few days before the maximum activity of ^{95}Nb induced directly by ^{95}Zr. The individual presence of the hot particle was registered with autoradiographs. In addition, by means of microanalysis, the size of the hot particle was found to be about one micrometer in diameter.

The applied methods are also suitable for distinguishing between radioaerosols released by nuclear reactors or produced by explosion.

REFERENCES

1. I. MASCHEK, V. PRODI and Á. MÉSZÁROS, 7th Conf. Assoc. Aerosol Res., 1979 Düsseldorf, Proc. 96; J. Aerosol Sci., **11**, 241, 1980.
2. I. BOJTOR, personal communication.
3. T. LENGYEL, Á. JÁSZ, Izotóplaboratóriumi zsebkönyv (Isotope Laboratory Pocketbook, in Hungarian), Műszaki Könyvkiadó, Budapest, 1966.
4. United Nations Scientific Committee on the Effects of Atomic Radiation (UNSCEAR) Sources and Effects of Ionizing Radiation, Report to the General Assembly, U.N., New York, 1977.

Acta Physica Academiae Scientiarum Hungaricae, 52 (3—4), pp. 413—417 (1982)

ESTIMATION OF PER CAPUT DOSE AND COLLECTIVE DOSE FROM THE USE OF DANUBE WATER*

M. TSCHURLOVITS

ATOMIC INSTITUTE OF THE AUSTRIAN UNIVERSITIES
A-1020 VIENNA, AUSTRIA

The paper deals with methods for assessment of both per caput and collective dose resulting from the use of the water of the Danube river, where drinking water and fish consumption pathway are considered. Results of previous measurements are used as basis for the estimation. It was found that the dose from natural radionuclides is by far exceeding the dose from artificial radionuclides.

1. Introduction

The terms "collective dose" or "collective dose commitment" are frequently used today in assessing the impact of a source of ionizing radiation, where the term source can be used in the widest sense. As a few examples, the natural background, the global inventory of a given radionuclide, but also the use of a sector of the environment can be considered as a source, depending on the purpose of the assessment.

In the present case, the exposure resulting from use of the water of the Danube river is discussed, and therefore the water of the Danube river is the source. The basic definition of the collective dose commitment is discussed below very briefly only in order to provide a suitable basis for further discussion.

2. Definition

The collective dose is used in assessment of the relative detriment from different radioactive sources, and finally the number of harmful effects in a given population due to the source under consideration can be estimated. Considering internal exposure, the collective dose can be written as [1]

$$S_C = \bar{k} \int_0^\infty Q\, N(Q)\, dQ, \tag{1}$$

where $N(Q)\, dQ$ is the number of persons ingesting an activity in the range Q to $Q + dQ$, and $\bar{k}$ is the population weighted conversion factor committed dose per unit intake. The following quantities have therefore to be discussed:

— Conversion factor committed dose per unit intake. Just recently,

* This work was carried out partly within IAEA Coordinated Research Program on Radioecology of the Danube river with Research Contract 1825/RB.

ICRP published an almost complete set of these factors [2], which are applicable, by definition, only for workers. To apply these factors for population, additional considerations not only dealing with a different age distribution, but also with other chemical forms have to be carried out. In a first approach, it seems that ICRP values can be taken for artificial radionuclides, but are not applicable for natural radioactive substances [3, 4]. This quantity is independent of the type of assessment and integration time, etc. and therefore applicable in all cases.

— Distribution of activity intake in population and time. Regarding this distribution, two different cases have to be distinguished for practical reasons:

i) assessment based upon actual release data;

ii) assessment based upon data from environmental monitoring.

The main difference is that in the first case the origin of the radioactivity is well known and that both release rate and future release (lifetime of the source) are known or can be predicted. In lieu of release data, the total activity inventory can also be used as information, e.g. in the nuclear fuel cycle. Since the time dependence of Q is known, the collective dose commitment can be estimated.

This consideration is particularly useful to estimate the total consequences of a given source or practice, where per MWa, per year of operation, etc. are useful units. The prediction of future exposure is an important point of the assessment. When data of environmental monitoring are serving as basic information, as in the case under discussion, no simple relation between activity detected in material to be ingested (water, diet, etc.) and the originating source can be established, even employing selective measurements. This leads to the fact that no dose commitment can be derived from environmental monitoring, but only a dose (rather a committed dose) for the time period actually monitored (e.g. conveniently one year in routine monitoring). This case is considered in the following. One has to be aware, however, that no prediction of future exposure is possible from environmental monitoring. The quantity actually derived from measurements of environmental monitoring includes, however, the contribution of all sources without further discrimination.

If the dose is expressed in effective committed dose by appropriate weighting of organ doses, a direct relation between these pathways and other exposures, e.g. external annual dose from natural radionuclides can be easily obtained.

3. Monitoring of river water

When drinking water and fish consumption pathway are assumed as to contribute significantly to the exposure, the annual per caput dose of radionuclide i [5] can be described as

$$D = \bar{k}_i I = \bar{k}_i (m_w c_{wi} + f_i c_{wi} m_f) \qquad [\mathrm{Sv} \cdot \mathrm{a}^{-1}] \tag{2}$$

where m_w is the average annual consumption of water [kg · a^{-1}], f_i is the concentration factor by fish for the radionuclide i [1], m_f is the average annual consumption of fish [kg · a^{-1}], c_{wi} is the concentration of the radionuclide i in water [Bq/kg], I is the annual intake [Bq · a^{-1}].

The consumption of the whole population is the expressed value multiplied by the number N of concerned people. Since N is usually not available directly, it can be derived from the total produced amount and the per caput consumption, conveniently both per year.

The annual collective dose due to the radionuclide i is then given by:

$$S_{c,i} = c_{wi} \bar{k}_i (W + f_i F), \tag{3}$$

where $S_{c,i}$ is the annual collective dose due to the radionuclide i, k_i is the conversion factor (as discussed in Section 2) [Sv · Bq^{-1}], W is the total extracted annual amount of water used for drinking, F is the total amount of fish obtained from the river and assumed to be consumed.

Usually, a treatment process is carried out in extracting water from a river system for drinking purposes, and hence a treatment factor result. Nominal values for this quantity are given in [1].

Concentration of radionuclides in fish

For the given purpose, only the concentration of a given radionuclide in the edible fraction of fish is required, whereas other organs, even with higher concentration factors, are of little interest for that purpose. Concentration factors are frequently used to describe the concentration in fish. However, one must be aware that a large number of influencing factors, both technical and conceptual, are leading to rather large uncertainties in that quantity. The factors used in the following Tables are extracted from a number of references, mainly from the Danube river. The question of the actual distribution of this factor, which is mainly following a lognormal distribution, cannot be raised here.

4. Results

4.1. Per caput dose

Tables I and II show results of calculations for per caput dose. The calculations are based on measurements [6, 7] carried out since 1977, and the 1977 values were chosen because the highest activity concentration appeared in that year.

Table I

Annual per caput dose for some radionuclides — drinking water pathway

Radionuclide	Concentration in water [mBq/kg]	Annual intake [Bq]*	Conversion factor [Sv/Bq]	Annual per caput dose (direct ingestion) [nSv]	Drinking water treatment factor	Drinking water per caput dose [nSv]
^{3}H	13 600	6000	1.7×10^{-11}	100	1	100
^{90}Sr	5.6	2.5	2.4×10^{-8}	60	0.5	30
^{137}Cs	1.9	0.84	1.4×10^{-8}	12	0.2	2.4
^{89}Sr	1.9	0.84	2.4×10^{-9}	2	0.5	1
^{95}Nb	3.3	1.5	6×10^{-10}	0.9	0.1	0.1
^{226}Ra	3	1.3	7×10^{-7}	900	0.5	450
U_{nat}	6	2.6	1.3×10^{-6}	3400	0.5	1700
^{40}K	56	25		under homeostatical control of the body		

* Annual consumption 440 l/a

Table II

Annual per caput dose — fish consumption pathway

Radionuclide	Average activity concentration in water [mBq/kg]	Concentration factor	Conversion factor [Sv/Bq]	Per caput dose [nSv]
^{90}Sr	5.6	5	2.4×10^{-8}	7
^{137}Cs	1.9	500	1.4×10^{-8}	13
^{226}Ra	3.0	5	7×10^{-7}	10
U_{nat}	6.0	5	1.3×10^{-6}	40
^{95}Nb	3.3	1000	6×10^{-10}	2

This methodology is applicable in assessing the exposure of persons belonging to one or more critical groups, because usually limits are established for these persons.

4.2. Collective dose (Estimation of the number of exposed people)

Drinking water pathway. Water works are keeping records on production rate, and the average per caput dose consumption is also well known. The ratio of these figures is then the number of exposed people. In the Vienna region, two plants can be considered as to be related to the Danube river, and the relevant figures are leading to an involved number of people of about 0.3×10^{6}, corresponding to about one fifth of the population of Vienna.

A similar estimation leads to a total of about 10^6 people drinking water from the Danube river in Austria.

Fish pathway

A total fish catch of about 2×10^5 kg per year in Austria is reported, where about one half can be assumed as to be edible [4].

These figures lead to a total collective dose in Austria of about 2.3 manSv.a^{-1} in the drinking water and 0.01 manSv.a^{-1} in the fish consumption pathway, respectively. It can be seen from Tables I and II that about 90% of the dose are from natural radionuclides, which in turn is a small fraction of activity ingested by foodstuffs [1]. Regarding the artificial radionuclides, the by far greatest fraction is still from ^{90}Sr. It may be worth stating that the total activity found in water samples since 1977 was identified as to be from nuclear fallout, the contributions of other sources being much smaller and unidentifiable.

REFERENCES

1. United Nations Scientific Committee on the Effects of Atomic Radiation (UNSCEAR), Sources and Effects of Ionizing Radiation, Vienna, 1977.
2. International Commission on Radiological Protection (ICRP), Publ. 30 Pergamon Press, Oxford, 1979 ff.
3. W. JACOBI, Internal Dosimetry and Radiotoxicity of Long Lived Uranium Isotopes, Report of the Gesellschaft für Strahlen- und Umweltforschung, Munich, p. 686, 1980.
4. M. TSCHURLOVITS, Assessment of Per Caput and Collective Dose Resulting from the Use of Danube Water from Drinking Water and Fish Consumption Pathways, Atominstitut der Österr. Universitäten, Vienna, AIAU-Report 80605, 1980.
5. M. TSCHURLOVITS, On the Application of the Concept of Collective Dose Commitment in Environmental Monitoring, IAEA, TECDOC-229, 35, 1980.
6. M. TSCHURLOVITS, K. BUCHTELA, J. SAS-HUBICKI and E. UNFRIED, Determination of Cs-137, Sr-89 and Sr-90 and Gamma Spectroscopy of Water Samples from the Danube River, IAEA, TECDOC-229, 9, 1980.
7. D. RANK, Ergebnisse von Tritiumanalysen an Wasserproben aus dem österreichischen Bundesgebiet, Frühjahrs- (ÖSRAD)-Tagung 1979 des Österreichischen Verbandes für Strahlenschutz, Wien, 23, 1980.

Acta Physica Academiae Scientiarum Hungaricae, 52 (3—4), pp. 419—423 (1982)

RADIOACTIVE CONTAMINATION OF FILAMENTOUS GREEN ALGAE IN THE HUNGARIAN REACH OF THE RIVER DANUBE

É. HOLLAND, L. B. SZTANYIK and L. VANICSEK

"FRÉDÉRIC JOLIOT-CURIE" NATIONAL RESEARCH INSTITUTE FOR RADIOBIOLOGY AND RADIOHYGIENE
1775 BUDAPEST, HUNGARY

In connection with the national nuclear power station programme a series of measurements was initiated to detect radionuclides in the River Danube. Examinations started in Spring 1978 at six sampling points along the Hungarian reach of the Danube. From among algae of various species of the Danube the localized and well-propagating filamentous green algae (Cladophora sp., Vaucheria sp.) were investigated. The activity concentration of gamma-radiating nuclides absorbed by algae was determined with a Canberra 8100 type Ga(Li)-spectrometer. This apparatus facilitated radioactivity measurements on wet samples or samples subjected to simple physical preparation.

The metabolic character and accumulative abilities of filamentous green algae showed them to be suitable indicators of radionuclide contamination of the water ecosystem. Results are ^{131}I nuclide at min. 72.5 mBq/g to max. 5440.0 mBq/g and other fission products from 55 mBq/g to 929 mBq/g.

The nuclear power programmes of the countries located along the River Danube and the construction of power plants called for the monitoring of radiation safety of the river and its environment. A coordinated research programme was initiated by the International Atomic Energy Agency [1]. In the framework of this activity, this Institute has performed extensive studies for six years [2]. The investigations aim at detecting radionuclides entering the hydrosphere as well as at the assessment of radiological hazards due to the utilization of the river water.

As the various aquatic micro- and macro-organisms live in "contaminated" water, possible pollutants like radioactive materials may be incorporated into them, thereby accumulating in these organisms and proceeding further by entering the aquatic food chain. The first components of this chain are mostly phyto-organisms, the last are carnivorous animals.

Two types of phytoorganisms and molluscs living in fresh water are suitable for radionuclide monitoring programmes [3]. One of the indicator types is the so called "actual-level monitor" having prompt concentration and discharging abilities. In such kinds of phytoorganisms the metabolism of radioactive elements depends on the species, the quality of the nuclides, the type of compound and on many ecological factors. The other kind of indicator is the "integrating monitor" which continuously accumulates its nuclide content. Aquatic phytoorganisms of such a kind may give information even after the termination of the environmental contamination due to their slow discharging speed. Within both types distinction can be made between floating-streaming

and localized phytoorganisms which form a living coating on the sides of the pontoons of landing stages, on piers, buoys, and other similarly located structures. The only higher aquatic plant observed in the Danube bed is Ricciocorpus natans which is to be found on riverside stones [4]. The most frequqent species of aquatic plants in the Hungarian reach of the Danube are lower species of algae: protophytes (planktonic) and filamentous algae (localized).

With regard to quantitative conditions, the number of algae in the vegetation period is very high. Their number is doubled in summer and autumn compared with the yearly average. It is known that algae easily bind some trace elements (iodine, metallic salt) and some radioactive nuclides primarily because of their polysaccharidas, i.e. alginates and other complex-forming compounds like derivatives of hydroxamic acid [5]. Accordingly, some radioactive contaminants are enriched in these plants and the values of the measured radioactivities contain important information on the contamination of waters. Various indicators of radioactive contamination can be selected on the basis of whether they are to be used for investigating certain local conditions at a certain spot, or for model experiments in the laboratory, e.g. for the assessment of concentration factors.

In connection with the national nuclear power programme, large series of measurements were initiated in an attempt to detect the migration of radionuclides entering the Danube [6]. Investigations were started in May 1978 at six sites of the Hungarian reach of the Danube.

The sampling points were: Győr, Gyönyű, north Budapest, south Budapest, north Paks, and Mohács near the southern frontier. Mainly filamentous green algae were selected for measurement as they are localized and form a coating on stones and artificial objects, which facilitates sampling in a suitable quantity. We report on our methodological approach and measurement data concerning the radioactivity content of the filamentous green algae.

Procedure for sampling, preparation and measurements

The collected plants were cleaned from macroscopic contamination, washed in flowing tap water and filtered. Taxonomic determination was performed with a stereo-microscope at 200 × magnification. While washing algae with flowing tap water, unicellular phyto- and zooplanktons also get into the wash water together with smaller contaminants. Those species forming bark-like settlements and filaments, i.e. Cladophora and Vaucheria species canbeseparated by centrifuging. After weighing, the wet samples are dried at 105 °C for 12h and then milled. To get approximately 100—150 g of dry powder, 800—1000 g of wet algae is required. The detection of gamma-emitting nuclides absorbed bythe algae is performed by a Ge-Li nuclear detector joined to a Canberra 8100 type 4096 channel analyser. This high capacity apparatus permitted the mea-

Table I

Radionuclide content of filamentous green algae samples mBq/g dry weight

Sampling site	^{40}K		^{137}Cs		^{131}I	
	1979	1980	1979	1980	1979	1980
Győr	363	134	5.9	4.8	4.4	3.3
	± 0.014	± 0.028	±0.9	±0.9	±6.4	±0.4
Gönyü	142	145	8.2	3.8	—	—
	± 0.014	± 0.015	±0.7	±0.9	—	—
Bp. North	729	+	5.9	+	56.9	+
	± 0.011		±0.9		±1.6	
Bp. South	441	679	10.7	6.2	181.3	8.2
	± 0.014	± 0.015	±1.2	±0.7	±6.4	±1.2
Paks	1012	227	5.3	3.9	9.8	8.8
	± 0.010	± 0.028	±0.7	±0.4	±1.2	±0.9
Mohács	857	856	3.4	3.3	8.2	5.7
	± 0.011	± 0.028	±0.2	±0.6	±1.2	±0.6

* N. Budapest landing place terminated (1980).

suring of the samples without any chemical separation [7]. Due to the very low activity concentrations, long-time measurements are performed, i.e. 60 000s per sample. The identification of nuclides and the evaluation of spectra was made by a built-in microprocessor. Measurement data on the different radioisotopes in samples collected during 1979—1980 are summarized in Table I. It is obvious that the natural radionuclide ^{40}K occurs everywhere. Trace amounts of ^{141}Ce and ^{144}Ca were measured only in some cases. ^{137}Cs, a derivative of the earlier atomic bomb tests, appeared in a concentration lower than ^{40}K. ^{131}I was detectable at almost every sampling point but to a varying extent. No ^{131}I could be detected in water samples collected from the same spots and at the same time. ^{131}I content of algae is assumed to originate from wastes of isotope applications. No other short half-life radioisotopes such as ^{140}La or ^{140}Ba appeared. For a better selection of the most suitable biological monitor the capacities of various algae for radionuclide incorporations are to be determined. In view of this various methods have been elaborated.

Unicellular green algae

Chlorella vulgaris and Scenedesmus obtusiusculus were cultivated under laboratory conditions on inactive medium. The cultures were placed in glass cylinders with semipermeable membranes at both ends and fastened to a buoy in the main stream of the river.

Filamentous green algae

Chladophora glomerata and Enteromorpha intestinalis species were collected from the artificial lake system of Százhalombatta. One part of the sample served for radiometric determination, the other part — approximately 600—900 g — was immersed for one month in the Danube in a water permeable system as mentioned above.

Radioactivity measurement showed that the unicellular algae culture (Chlorella vulgaris, Scenedesmus obtusiusculus) did not take up gamma emitting nuclides from the river. The filamentous green algae, however, (Chladophora glomerata and Enteromorpha intestinalis) seemed to accumulate measurable quantities during a period of one month, but it should be mentioned that incorporation depends on various factors.

Monitoring with the help of a biological raft

Recently, comparative examinations have been initiated on the radionuclide contamination of algae-coenosis developed on the "biological raft" settled at south Budapest and north Paks as a function of time and environmental factors. The "biological raft" is an artificial biotope (Fig. 1) providing a place for periphyton algae to settle. They are thus provided with an imitation of their normal living conditions since under such circumstances they develop the special composition of litoral bentos.

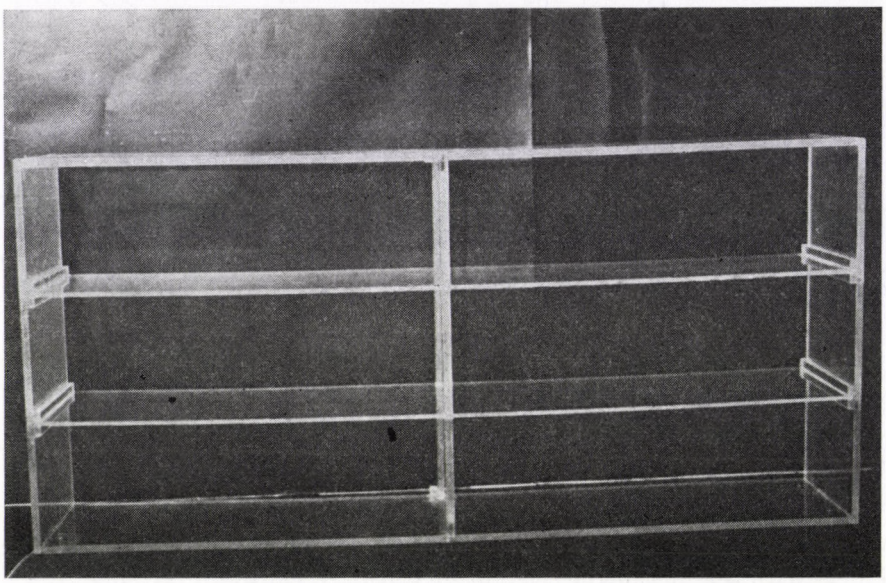

Fig. 1. Monitoring with the help of a biological raft.

It is hoped that the monitoring by means of this facility indicates the real conditions of radioactive pollution.

Finally, it can be stated that according to their accumulative and complex forming abilities filamentous green algae are suitable for detecting the radionuclide contamination of aquatic ecosystems. These species permit the biological monitoring of the stream at a certain site. The measurements on algae, the low level parts of the aquatic food chain, may well indicate the level of radionuclide contamination of the aquatic ecosystem of the River Danube.

However, more investigations are needed on the applicability of these biological indicators under varying conditions (season, temperature, other pollutants, etc.).

REFERENCES

1. G. Köteles, IAEA Bull., **22,** 46, 1975.
2. L. B. Sztanyik et al., IAEA TECDOC- **229,** 95, 1980.
3. E. F. Gloyna, Y. Yousef and C. Shih, Transport of radionuclides in a model river, Proc. Symp. May, IAEA **72/2**.
4. G. Szemes, in R. Liepolt, Limnologie der Donau, Springer Verlag, Stuttgart, 170, 1965.
5. G. E. Fogg, The Algae, Methuen Co. Ltd. London 1953, p. 240.
6. L. B. Sztanyik et al., IAEA TECDOC-219, 37, 1979.
7. É. Holland and L. Vanicsek, Botanikai Közlem., 109, 1980 (in Hungarian).

Acta Physica Academiae Scientiarum Hungaricae, 52 (3—4), pp. 425—427 (1982)

RADIOACTIVITY OF FISH IN THE HUNGARIAN REACH OF THE RIVER DANUBE

E. KURTÁCS

"FRÉDÉRIC JOLIOT-CURIE" NATIONAL RESEARCH INSTITUTE FOR RADIOBIOLOGY AND RADIOHYGIENE
1775 BUDAPEST, HUNGARY

In connection with the national nuclear power programme a series of measurements was initiated to detect radionuclides in fish of the Danube river. Since spring 1978 a number of species of fish have been investigated at two sampling points near the nuclear station region. The beta activity of samples was counted with anticoincidence shielded low background Tesla NZ-602 type apparatus. The radioactivity of samples was measured after simple physical or radiochemical preparation.

The results show no significant difference according either to sampling place or season. Activity concentrations of ^{90}Sr and ^{137}Cs of natural or global fallout origin are low and hardly differ from values obtained earlier by other researchers.

The complexity of the aquatic environment, which is obviously influenced by the operation of existing or projected hydroelectric power stations in the Danube valley, will be increased by the development of the nuclear industry; ware quality will also be affected. The total installed nuclear capacity, which is approximately 2.5 GWe at present, in this region, will increase four-fold in 6 years and approximately six-fold by the end of the century. This growth rate is approximately three times higher than the European or the world average. Data cited by KÖTELES [1] indicate that radioactive releases from nuclear power stations with a total capacity of approximately 13 400 MWe will enter the river.

Data are reported here on the radioactive contamination of Danube fish. The investigations are justified by the important role of fish as the main element of the aquatic food chain and in the food consumption of a number of countries. Although the per caput fish consumption (including tinned fish) in Hungary in 1980 amounted to 2.5 kg, in settlements along the River Danube consumption is much higher (5—20 kg per caput/annum).

In connection with the national nuclear power programme, radioecological investigations started in the Hungarian reach of the Danube in 1978. Various species of fish are obtained from the Fishermen's Cooperative in the vicinity of Mohács and of Paks twice a year, (2—3 kg per species). Initially, the activity concentration of radionuclides in the various tissues was found to be around or below the detectable level in the course of direct gamma spectrometric measurements of variously prepared fish samples (scute, head, skeleton, musculature, internal organs).

In 1979 radiochemical separation of ^{90}Sr and ^{137}Cs from the ash of fish samples was initiated.

Preparation of samples:

— physical preparation;
— incineration of musculature at 450 °C, of bones at 750 °C. The ash is homogenized mechanically;
— chemical processing.

Determination of ^{137}Cs: after acidic destruction, ammonium-phosphomolybdenate (AMP) is added to the material which binds Cs in a selective manner. After AMP dissolution Cs can be separated by precipitation with hydrogenchloroplatinum. Chemical yield is determinable by gravimetric measurement of caesiumchloroplatinum.

Determination of ^{90}Sr: After acidic treatment, yttrium is extracted by tributylphosphate and, following aqueous reextraction, oxalate precipitate is separated [2].

The chemical yield of the yttrium is determined by flame emission photometry.

Radioactivity measurement

The beta activity of samples was counted with anticoincidence shielded, low background TESLA NZ-602 type apparatus and a TESLA NKR-213 gas-flowing end-window GM tube.

The background intensity of the instrument was 1.5—2.0 cpm.

Efficiency for	^{90}Y	0.418
	^{137}Cs	0.315
	^{40}K	0.210
Detectable limit of	^{137}Cs	50—60 mBq
	^{90}Sr	30—35 mBq

The measurement time was 50 min.

The results of total beta activity measurements are related to the ^{40}K content of 1 g of ash.

From the practical point of view, fish components were separated into two groups: edible and non-edible, and these were measured separately.

In Table I the total beta activity and the activity concentration of ^{90}Sr and ^{137}Cs measured in the musculature and non-edible parts of some Danube fish species are given in mBq/g ash value.

It is to be noted that some other species were also included in the measurements (Blicca bjoerkna L., Silver bream, Carassius auratus gibelio Bloch, Esox lucius L., Pike, Silurus glanis L., Sheat Fish, Tinca tinca L., Tench, Aspius aspius L., Barbus barbus L., Ctenopharingodon idella Valenciennes) but they have been omitted from the Table, because they were not obtained regularly. The results of the measurement of these species do not differ essenti-

Table I

Total beta activity and activity concentration of ^{90}Sr and ^{137}Cs in Danube fish [mBq/g ash]

Species	Activity	1979	1980	1981
Abramis brama L. (bream)	Total beta*	3750 ± 260	7200 ± 250	5616 ± 184
	**	1416 ± 148	1265 ± 154	495 ± 53
	^{90}Sr	32.82 ± 5.2	38.54 ± 5.7	22.40 ± 4.1
	^{137}Cs	13.76 ± 4.7	12.63 ± 4.1	48.70 ± 9.10
Cyprinus carpio L. (carp)	Total beta*	7520 ± 237	8405 ± 257	7749 ± 148
	**	644 ± 65	1402 ± 76	686 ± 65
	^{90}Sr	35.74 ± 5.8	34.50 ± 4.2	13.42 ± 3.48
	^{137}Cs	19.32 ± 5.12	11.57 ± 3.8	28.05 ± 45.9
Stizosteidon lucioperca L.	Total beta*	8537 ± 235	7607 ± 210	7465 ± 220
(perch pike)	**	694 ± 83	741 ± 70	816 ± 78
	^{90}Sr	19.31 ± 4.4	18.48 ± 3.4	19.20 ± 4.3
	^{137}Cs	16.83 ± 4.72	33.72 ± 5.52	31.14 ± 8.60
Chondrostoma nasus L.	Total beta*	7645 ± 240	8276 ± 228	8129 ± 211
(nose carp)	**	820 ± 84	886 ± 72	932 ± 79
	^{90}Sr	22.00 ± 4.2	22.64 ± 4.5	34.04 ± 4.4
	^{137}Cs	24.20 ± 4.9	34.16 ± 5.2	25.40 ± 4.84

* muscle
** non-edible parts

ally from the results obtained with those shown in Table I. No significant difference is apparent concerning sampling site, season and species of fish. 98% of the total beta activity comes from ^{40}K.

The activity concentrations of ^{90}Sr and ^{137}Cs range within the limit measured earlier by other researchers in Danube fish. These radionuclides originate mainly from global fallout. Bearing in mind the national fish consumption per caput, the radioactivity levels measured in the Danube fish are negligible in the radiation burden of the population.

REFERENCES

1. G. Köteles, IAEA Bull., **22**, 46, 1980.
2. HASL-300. "Radiochemical strontium (rapid)", E-Sr-05, Ed. John H. Harley, Health and Safety Laboratory, U.S. Energy Research and Development Administration, New York, 1972.

Acta Physica Academiae Scientiarum Hungaricae, 52 (3—4), pp. 429—434 (1982)

ANALYSIS OF TRITIUM IN TREE RINGS

K. KOZÁK

INSTITUTE OF ISOTOPES
1525 BUDAPEST, HUNGARY

Tritium in the cellulose content of the growth rings of two trees was analysed. The two trees were separated by a distance of 5 km; one of them grew just beside the building of the Institute of Isotopes, Budapest. The distribution of tritium concentration in the sequence of the rings of the latter tree showed good agreement with the environmental background concentrations for the years 1957—63. Excess tritium was found in the rings of subsequent years. This was due to the activity of the Institute and indicated the elevated level of the local environment. The tritium content of a few rings of the other tree reflected the environmental background level of the past years and showed no contamination due to the Institute.

Introduction

The sequence of growth rings of a tree presents a well-dated series of samples characteristic of a given area. The isotope content of the organic matter of an individual tree ring reflects the environmental level of the year of growth, thereby enabling sampling to be achieved at a later date. For isotope studies such as ^{14}C and the ratios of $^{13}C/^{12}C$, $^{18}O/^{16}O$ and D/H, the analysis of the cellulose of growth rings is a preferred method. The cellulose content of an annual ring is synthesized and bound just in the year of ring growth; this means that the problem of contamination from subsequent years and that of chemical heterogeneity can be avoided. In the case of hydrogen isotopes attention must be paid to the problem of isotopic exchange [1]. Carbon-bound hydrogen in cellulose is non-exchangeable whereas the hydroxyl hydrogens exchange readily [2].

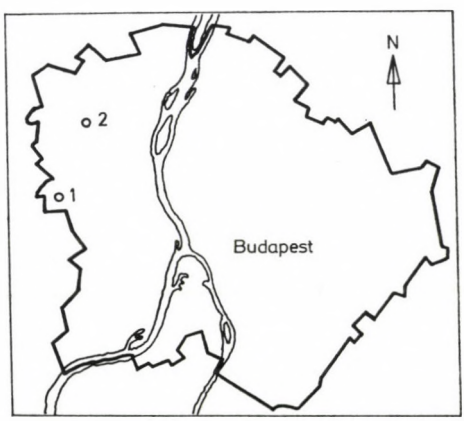

Fig. 1. Sampling sites in Budapest. 1. Csillebérc; 2. Vadaskert.

Studies on tritium in tree rings are few in number. Recently BROWN [3] reported a study in this field. He found that this technique is suitable as a means of determining past concentrations of HTO in the environment as a whole and in locally contaminated areas.

We have investigated the tritium concentrations of the cellulose content in two trees. Both of them grew in Budapest (Fig. 1): one grew beside the Institute of Isotopes (Csillebérc tree) the other 5 km NW of the Institute (Vadaskert tree).

The HTO level of atmospheric moisture in the environs of the Institute is known to be somewhat elevated though it is emphasized that this level is not a health hazard since it is much lower than the derived concentration limit for population exposure.

Methods

For ring separation 4 cm thick sectors of the stump were cut and polished. Individual tree rings were separated manually with a chisel. The method of cellulose separation and OH equilibration was different in the two cases. The chips of the Csillebérc tree (Aesculus hippocastanum L.) were ground to 0.5—3 mm and the fine powder was sifted.

Cellulose was extracted by the Kürschner and Hoffer method: 70 g of wood was boiled for 90 minutes in a mixture of 800 ml 96% ethanol and 200 ml 65% nitric acid. The pulp was filtered through a glass filter, rinsed with absolute alcohol and dried. To enable tritium exchange between the OH groups cellulose was boiled in tritium-free, 0.4 N HCl solution.

The cellulose of the Vadaskert tree (Pinus nigra Arn.) was extracted in the Research Institute of the Pulp and Paper Industry. Chips were placed in nets made from stainless steel mesh and six samples were cooked in each batch. Extractions were carried out in a Weverk type autoclave. 1000 g of wood needed 5 l solute with 275 g NaOH and 125 g Na_2S content. The so-called sulphate process was performed at 165 °C ($\sim$ 760 kPa) and lasted 120 min. The pulp was rinsed with water and dried. The yield was 51%, the lignin content of the product was $\sim$3%. To equilibrate the OH tritiums the pulp was treated for two hours in tritium-free water in the same vessel at 165 °C.

Combustion

The combustion apparatus consisted of two electrically heated quartz tubes. One of them served as a sample holder, the other was filled with Pd coated porcelain rings and its temperature was kept at 400 °C.

The cellulose sample still damp from tritium-free water, was placed into the tube and dried at 120 °C with 300 l/h flow of dried air. The dried

cellulose was ingnited and incinerated in 50 l/h flow of dried oxygen. The water formed was condensed in a vessel maintained at 0 °C in an ice—water mixture. The rate of water loss did not exceed that of a normal distillation step. The condensed water contained acidic contaminants so it was re-distilled after neutralization with Na_2O_2.

Water extraction from soil

The tritium content of soil samples taken from the Institute of Isotopes was also analysed. The moisture content of these samples was extracted by azeotropic distillation with benzene [4].

Tritium measurement

All the samples were analysed in a Berthold BF 8000 type liquid scintillation spectrometer. The background of 9 ml water—11 ml Instagel cocktails in plastic vials was 4—5 cpm at 21% efficiency. We measured single samples of the Csillebérc tree and double samples of the Vadaskert tree. All measurements of tritium concentration reported here are expressed in tritium units (TU). One tritium unit corresponds to an activity concentration of 0.12 Bq/l (in water).

Results and discussion

The concentrations of HTO in the cellulose of the Csillebérc tree are shown in Table I. On the basis of the number of annual growth rings, this tree was 63 years old when it was felled in November 1978. The outer six rings were so narrow that the rings of 1973—74, 1975—76 and 1977—78 were prepared simultaneously. Data obtained from the Vadaskert tree are shown in Table II. Based on the number of annual growth rings, this tree was 87 years old when it was felled in June 1981. Similarly to BROWN [3] we also found tritium in the rings of the pre-thermonuclear era of the trees. For the Csillebérc tree it was 130 TU; for the Vadaskert tree 61 TU. We considered these values as background and subtracted them from the data of each year. Differences were divided by a factor of 0.7 as an adjustment for OH equilibration (70% of the hydrogen of the cellulose is unexchangeable and 30% is in hydroxyl groups). These values were corrected for radioactive decay ($T_{1/2} = 12.43$ years) to count the tritium concentrations back to the original levels. These data are shown in Fig. 2 together with the HTO concentrations of the general environment. Yearly averages of the general environment are represented by HTO concentrations in precipitation. For the years 1957—59 a set of Ottawa records [5] was used. Data for 1977—80 were obtained from Budapest records and for the

Table I

Tritium concentration of cellulose of Csillebérc tree

Ring year	Tritium concentration (corrected) TU ± SD
1957	250 170
1958	360 180
1959	580 170
1960	80 140
1961	180 140
1962	1 170 190
1963	2 070 190
1964	2 820 180
1965	2 400 170
1966	4.340 170
1967	8 500 260
1968	18 700 530
1969	17 000 480
1970	12 600 360
1971	8 500 240
1972	13 100 370
1973—74	35.200 990
1975—76	24 400 700
1977—78	17 100 480

Table II

Tritium concentration of cellulose of Vadaskert tree

Ring year	Tritium concentration (corrected) TU ± SD
1965	1100* 100
1970	200 70
1975	140 50
1980	60 40

* Sample supposed as being contaminated by ~200 TU in excess

years 1960—76 data were reconstructed from measurements on Hungarian wines [6].

Tritium concentrations of the pre-1964 rings of the Csillebérc tree agree well with that of the general environment. Concentration started to rise in 1964 and reached a peak in 1968. This elevated level resulted from the activity

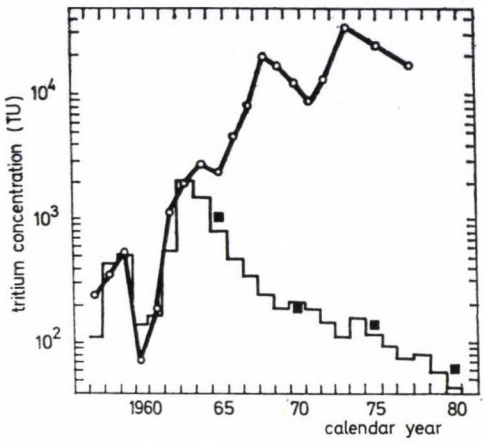

Fig. 2. Comparison of tritium concentration of two Budapest trees with that of the general environment.
○ — ○ — ○ Csillebérc tree; ■ Vadaskert tree; _|‾|_ Yearly average concentration of tritium in precipitation

of the Institute. The production of tritiated compounds has been a matter of routine since 1965 and leads to a release of excess tritium into the environment on a local scale.

At present we cannot explain the zigzag shape of the tritium concentration of the subsequent years.

Trees take up tritium from the soil and directly from the surrounding atmospheric moisture. Experiments [7] show that the tritium content of tissue water of the leaves originates from the air rather than from the soil.

We have measured the tritium concentration profile of the soil at the spot where the Csillebérc tree was felled. Data are shown in Table III. Concen-

Table III

Tritium concentration of the soil profile at Csillebérc, November 1978

Depth cm	Tritium concentration TU ± SD
0—5	6200 250
15—20	3400 140
35—40	2800 110
60—65	3100 120
100	2700 110
150	2800 110
200	3300 130
300	1970 80

trations are in the order of 10^3 TU. Sporadic measurements of atmospheric moisture in the environs of our Institute indicate that the tritium concentration of the ambient moisture varied between 10^3 and 10^5 TU both in 1974 and 1978.

In contrast with the Csillebérc tree, the concentration of the Vadaskert tree followed the environmental level faithfully in the mid-60's and in the 70's. Despite the relatively short distance the Vadaskert tree is not affected by the release of HTO from our Institute.

Conclusions

Analysis of the tritium content of cellulose extracted from tree rings presents a means of investigating tritium release from industrial sources. A dated record of past concentrations of tritium is preserved in the trees so these serve as documents.

For dating underground waters the input function for a given catchment area can be reconstructed by this technique.

Anomalies in tritium fallout can be investigated on a regional scale. For example, BAYER et al [8] reported high activity in the May 1974 precipitation at many stations in Austria. Doubtless, this anomaly occurred in the precipitations in Hungary as well but at that time collection was performed at only a few stations. We intend to examine this question by analysing the rings from the exposed area and period around 1974.

Acknowledgements

The author acknowledges the help of Mr. D. STUR and his Colleagues in the preparation of samples.

He wishes to extend his thanks to Dr. S. ANNUS, Director of the Research Institute of the Pulp and Paper Industry, for his kind permission for cooperation and to Mr. A. RAB for fitting the pulping process to our wishes.

REFERENCES

1. S. EPSTEIN, C. J. YAPP and J. H. HALL, Earth Planet. Sci. Lett., **30,** 241, 1976.
2. J. MANN, Deuteration and Tritiation, in: Cellulose and Cellulose Derivatives, V, Part IV, Bikales and Segal, eds. Wiley Interscience, New York, 89, 1971.
3. R. M. BROWN, Environmental Tritium in Trees, in: Proc. Symp. Behaviour of Tritium in the Environment, San Francisco, 1978. IAEA 1979, 405—417.
4. A. A. MOGHISSI, E. W. BRETTHAUER and E. H. COMPTON, Anal. Chem., **45,** 1565, 1973.
5. Environmental Isotope Data No. I: World Survey of Isotope Concentrations in Precipitation (1953—63). Technical report series No. 96. IAEA, 1969.
6. K. KOZÁK and T. BIRÓ, Reconstruction of Environmental Tritium Levels from Hungarian Wines, in preparation.
7. Y. BELOT, D. GAUTHIER, H. CAMUS and C. CAPUT, Health Phys., **37,** 575, 1979.
8. F. BAUER, V. RAJNER and D. RANK, Naturwiss., **62,** 526, 1975.

Acta Physica Academiae Scientiarum Hungaricae, 52 (3—4), pp. 435—441 (1982)

DER AKTUELLE ^{3}H-GEHALT DER HYDROSPHÄRE IN MITTELEUROPA (1980)

D. RANK und V. RAJNER

GEOTECHNISCHES INSTITUT DER BUNDESVERSUCHS- UND FORSCHUNGSANSTALT ARSENAL, WIEN, ÖSTERREICH

Der ^{3}H-Gehalt der Hydrosphäre wird noch immer von den bei den Kernwaffenversuchen freigesetzten ^{3}H-Mengen bestimmt. Die ^{3}H-Konzentration der Niederschläge in Mitteleuropa beträgt derzeit noch das Fünf- bis Zehnfache des natürlichen — durch die Höhenstrahlung bedingten — Wertes. Seit 1978 ist ein verstärkter Rückgang des ^{3}H-Gehaltes der Niederschläge — und damit in der Folge auch der Oberflächenwässer — zu beobachten, von ungefähr 10 Bq/kg auf 4.8 Bq/kg im Jahr 1980 (Abb. 1). Der jahreszeitliche und langfristige Verlauf der ^{3}H-Konzentration in den Oberflächenwässern wird ausser vom ^{3}H-Gehalt des Niederschlags als Eingangsgrösse entscheidend von den hydrologischen Bedingungen in den Einzugsgebieten mitbestimmt. Die Pro-Kopf-Dosis durch ^{3}H im Trinkwasser in Wien betrug 1980 ungefähr 70 nSv/a.

1. ^{3}H-Gehalt der Niederschläge[1]

Nach wie vor gelangt ^{3}H fast ausschliesslich über den atmosphärischen Niederschlag in die Hydrosphäre. Die umittelbare Freisetzung von ^{3}H in Oberflächen- und Grundwässer durch die Industrie (Kernkraftwerke, Wiederaufbereitungsanlagen, Uhren- und Leuchtfarbenindustrie) hat zur Zeit nur lokale Bedeutung. Der ^{3}H-Gehalt der Niederschläge zeigt seit 1978 einen verstärkten Rückgang (Abb. 1), der bestimmende Anteil ist aber noch immer das Kernwaffentritium. Die mittlere ^{3}H-Konzentration ist noch um einen Faktor 5—10 grösser als es der natürlichen ^{3}H-Produktion in der Atmosphäre entspräche. Ein Überblick über die ^{3}H-Verteilung im Jahre 1980 (Abb. 1) weist für die Niederschlags-Monatsproben Werte um 5 Bq/kg aus. Die Werte der Einzelniederschläge streuen dabei fast um den Faktor 10, wobei kein eindeutiger Zusammenhang zwischen Niederschlagsmenge und ^{3}H-Konzentration zu erkennen ist [2]. Betrachtet man die gewichteten Monatsmittel, so erhält man im allgemeinen einen Jahresgang mit einem Maximum im späten Frühjahr und einem Minimum im Spätherbst. Die örtlichen Variationen der ^{3}H-Gehalte der Monatsniederschläge zwischen verschiedenen Niederschlagssammelstationen können in Gebieten mit ausgeprägtem Relief 30—50% betragen. Dies ist vor allem auf die unterschiedliche Niederschlagstätigkeit verbunden mit der starken Variation des ^{3}H-Gehaltes der Einzelniederschläge zurückzuführen. Auch die unterschiedliche Herkunft der feuchten Luftmassen wirkt sich dabei aus; beispielsweise spielt im Süden und Osten Österreichs der Einfluss ^{3}H-armer mediterraner

[1] Messmethodik: Elektrolytische Anreicherung und Aktivitätsmessung im Flüssigkeitsszintillationsspektrometer [1]; die Nachweisgrenze der Messanordnung beträgt 0.15 Bq/kg.

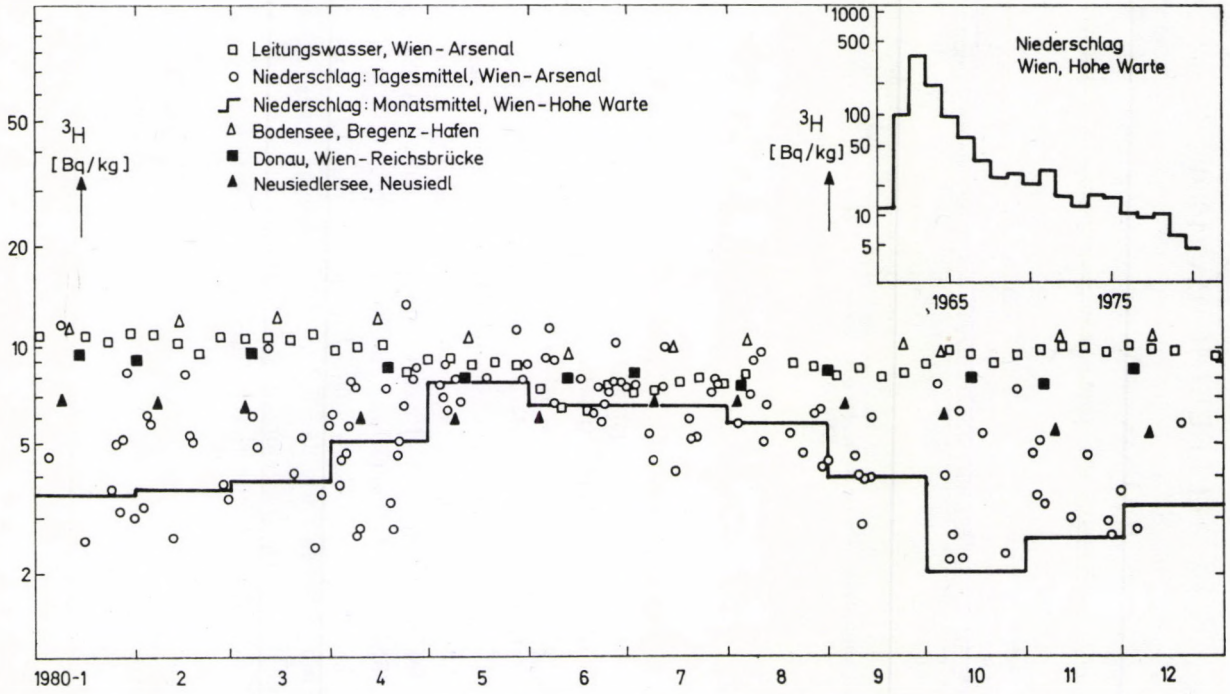

Abb. 1. ^{3}H-Gehalte von Niederschlag und Oberflächenwasser in Mitteleuropa im Jahr 1980 sowie Verlauf des ^{3}H-Jahresmittels des Niederschlags zwischen 1961 und 1980.

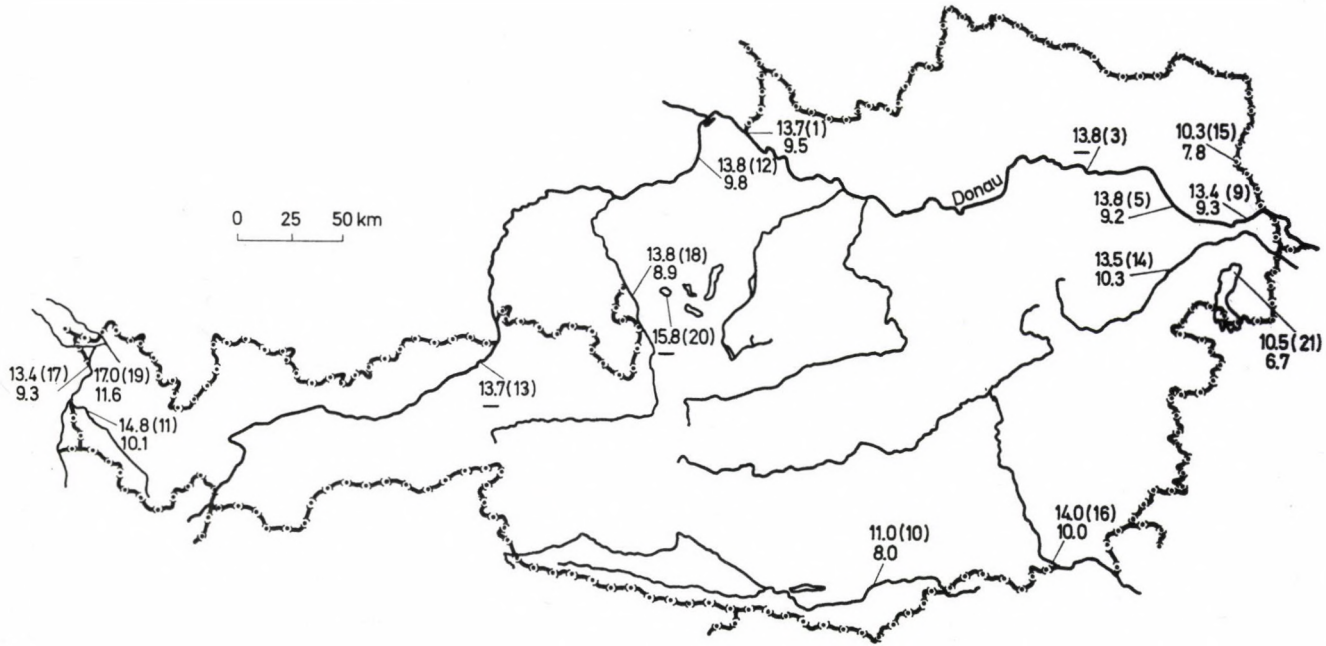

Abb. 2. ^{3}H-Jahresmittel 1977 und 1980 von Oberflächenwässern in Österreich in Bq/kg (Mittel aus 12 Momentanwerten; in Klammern Nummer der Probenahmestelle).

Luftmassen eine gewisse Rolle, sodass etwa der Niederschlag auf der Villacher Alpe 30—50% weniger ^3H enthält als in Wien [3]. Besondere Ereignisse, wie Maxima infolge von Kernwaffenversuchen oder erhöhten ^3H-Abgaben der Kernindustrie bzw. ungewöhnliche Verteilungen, wie sie beispielsweise im Zeitraum Mai/Juni 1974 im Ostalpenbereich aufgetreten waren [4], konnten in letzter Zeit nicht beobachtet werden.

2. ^3H-Gehalt der Oberflächen- und Grundwässer

Die Oberflächen- und Grundwässer zeigen einen im Vergleich zum Niederschlag stark gedämpften ^3H-Jahresgang (Abb. 1 und 3), bei Alpenflüssen — z.B. Salzach — tritt im späten Frühjahr häufig ein ausgeprägtes ^3H-Minimum als Folge der Schneeschmelze auf. Die Jahresmittel des ^3H-Gehaltes der wichtigeren Fliessgewässer Österreichs unterscheiden sich im allgemeinen nur geringfügig (Abb. 2). Niedrigere Werte treten bei der Drau (Messstelle 10) — in deren Einzugsgebiet sich der früher erwähnte Einfluss mediterraner Luftmassen auswirkt — und der March (15) auf. Bei der March hat wegen der geringen Niederschlagssumme im Osten Österreichs auch der Anteil an abfliessendem alten Grundwasser einen mitbestimmenden Einfluss [3]. Die gleiche Ursache dürfte neben der geringen Seetiefe — die eine rasche Erneuerung des Wassers ermöglicht — für den niedrigen ^3H-Gehalt des Neusiedlersees (Messstelle 21) verantwortlich sein. Die höheren Werte des Bodensees (19) und des Fuschlsees (20) sind auf die Speicherwirkung dieser Gewässer zurückzuführen, als deren Folge sich noch der höhere ^3H-Gehalt des Niederschlags früherer Jahre aus-

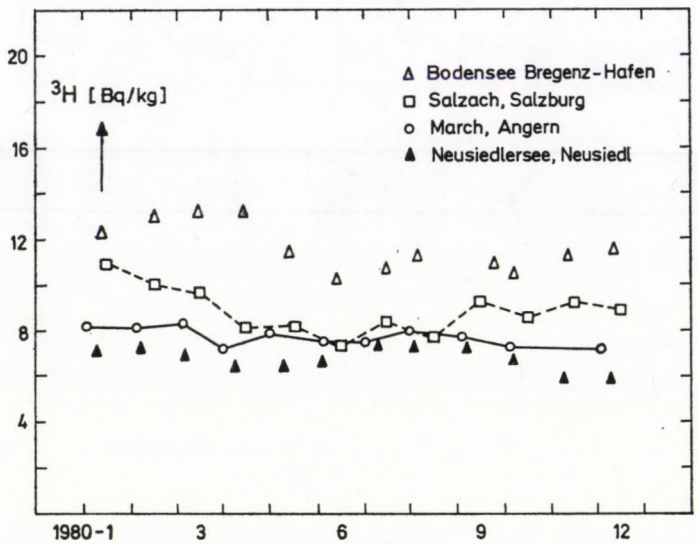

Abb. 3. ^3H-Jahresgänge einiger Oberflächenwässer.

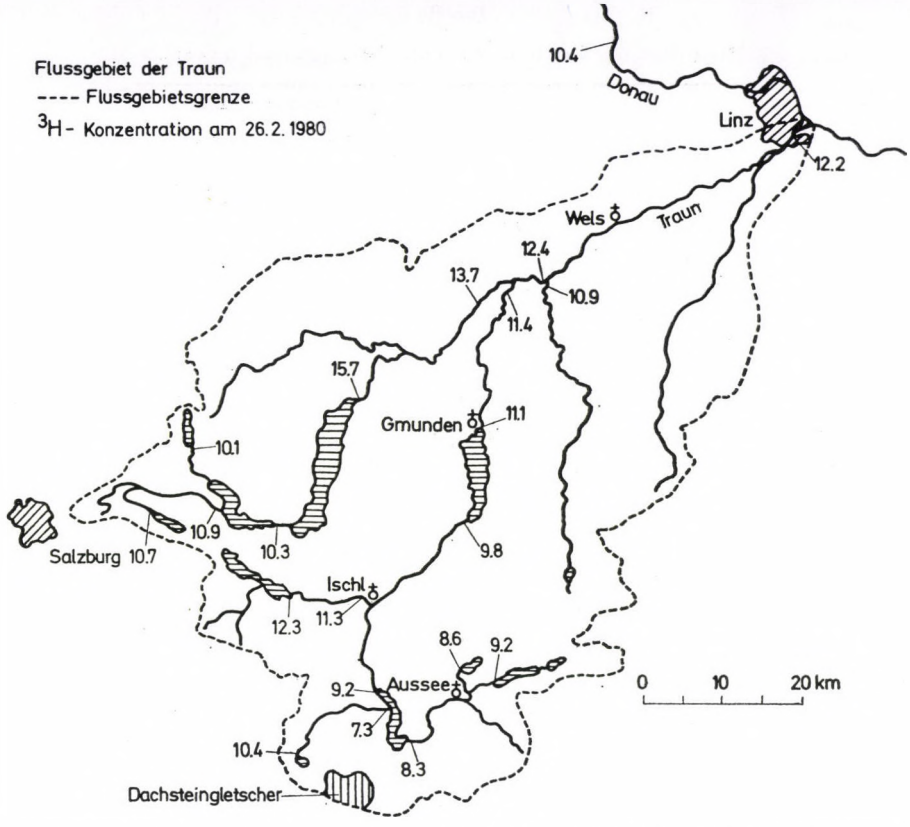

Abb. 4. Der Einfluss von Speichern (Seen, Gletscher) auf den Verlauf des ^{3}H-Gehaltes in einem Flussystem.

wirkt. Ebenso dürfte der höhere Wert der I11 (11) seine Ursache im Abschmelzen von Niederschlägen früherer Jahre haben. Auch beim Grundwasser kommt es zu ähnlichen Speichereffekten [3].

Natürliche oder künstliche Speicher — Seen, Staubecken, Gletscher, grosse Grundwasserspeicher — im Einzugsgebiet eines Flusses und die damit verbundene grössere Verweilzeit des Wassers können zu grossen Unterschieden im ^{3}H-Gehalt innerhalb des Flusssystems führen. Beispielsweise bewegten sich die ^{3}H-Konzentrationen im Flussgebiet der Traun am 26.2. 1980 zwischen 7.3 und 15.7 Bq/kg (Abb. 4). Naturgemäss treten die höchsten Werte bei den Abflüssen aus den grösseren Seen auf, während die niedrigen Werte im Oberlauf auf grössere Anteile von rasch abfliessendem Niederschlagswasser hindeuten. Der ^{3}H-Gehalt der Traun bei ihrer Mündung liegt noch ungefähr 20% über dem der Donau, der als Gebietsmittelwert aufgefasst werden kann.

Der ^{3}H-Gehalt der Donau verändert sich flussabwärts nicht wesentlich. Ein Vergleich des österreichischen mit dem bulgarisch-rumänischen Donauab-

Tabelle I

^{3}H-Gehalt der Donau in Wien und bei Sagraschden/Corabia

Ort	^{3}H-Gehalt [Bq/kg]	
	1979	1980
Wien-Reichsbrücke	10,8[1]	9,2[1]
Sagraschden/Corabia	9,6[2]	8,1[3]

[1] Mittel aus 12 Werten
[2] Mittel aus 5 Werten
[3] Mittel aus 2 Werten

schnitt zeigt, dass der ^{3}H-Gehalt um ungefähr 10% abnimmt (Tab. I). Die Gründe hierfür dürften sowohl der Einfluss ^{3}H-armer maritimer Luftmassen — wie im Einzugsgebiet der Drau — als auch der relativ höhere Grundwasseranteil — wie im Einzugsgebiet der March — im Unterlauf der Donau sein.

Die ^{3}H-Jahresgänge verschiedener Oberflächenwässer unterscheiden sich charakteristisch (Abb. 3). Während der zeitliche Verlauf der ^{3}H-Konzentration der March (Flachlandfluss) mit entsprechender Dämpfung ungefähr dem des Niederschlags gleicht (Minimum zu Jahresbeginn, Maximum im Sommer), weist die Salzach wegen des verzögerten Abschmelzens der Winterniederschläge im Gebirge ein ausgeprägtes Minimum zur Jahresmitte auf. Bei der Traun wird dieses Minimum durch die Speicherwirkung der Seen in den Herbst hinein verschoben [3]. Der Neusiedlersee mit seiner geringen Wassertiefe folgt verhältnismässig rasch dem Jahresgang und dem ^{3}H-Gehalt des Niederschlags. Im Jahr 1980 sind die Jahresgänge wegen der allgemein stärkeren Abnahme des ^{3}H-Gehaltes der Niederschläge allerdings etwas verfälscht, jahreszeitlich bedingte Konzentrationsrückgänge erscheinen verstärkt, während Anstiege und Maxima stark gedämpft werden. Der fast stufenartige Konzentrationsrückgang beim Bodensee (Hafengelände) im Frühjahr 1980 ist durch den gleichzeitigen Einfluss der ^{3}H-armen Schmelzwässer und der infolge des starken Rückganges des ^{3}H-Gehaltes der Atmosphäre im Vergleich zu 1979 ebenfalls ^{3}H-armen Frühjahrsniederschläge zu erklären. Der Verlauf der ^{3}H-Konzentration im Donauwasser (Abb. 1) beschreibt am besten den allgemeinen Rückgang des ^{3}H-Gehaltes in der Umwelt im betrachteten Zeitraum. Der Einfluss der Alpenflüsse führt aber auch bei der Donau zu einem ^{3}H-Minimum im späten Frühjahr.

3. Pro-Kopf-Dosis der Bevölkerung durch ^{3}H im Trinkwasser

Der ^{3}H-Gehalt des Wiener Trinkwassers — vorwiegend verhältnismässig rasch abfliessendes Karstwasser aus den nördlichen Kalkalpen — entspricht ungefähr dem der Oberflächenwässer (Abb. 1). Die Pro-Kopf-Dosis betrug 1980

Tabelle II

Jährliche Pro-Kopf-Dosis durch ^{3}H im Trinkwasser (Wien-Arsenal)

Jahr	mittlere Konzentration [Bq/kg]	jährliche Aktivitätsaufnahme[1] [Bq]	Konversionsfaktor[2] [Sv/Bq]	Pro-Kopf-Dosis pro Jahr [nSv/a]
1966	60	26 400	$1.7 \cdot 10^{-11}$	450
1977	13.6	6 000	$1.7 \cdot 10^{-11}$	102
1980	9.8	4 300	$1.7 \cdot 10^{-11}$	73
Anteil aus natürlicher ^{3}H-Produktion ca.	0.7	300	$1.7 \cdot 10^{-11}$	5

[1] Bei einem Pro-Kopf-Wasserverbrauch von 440 l/a
[2] Nach [5]

etwa 70 nSv (Tab. II). Der Maximalwert nach dem Höhepunkt der Wasserstoffbombenversuche dürfte bei 1500—2000 nSv/a gelegen haben (1963/64). Vergleichsweise dazu beträgt die natürliche äussere Strahlenbelastung ungefähr 1 mSv/a.

LITERATUR

1. D. Rank, Tagungsbericht der 2. Informationstagung der ÖSRAD, Geotechnisches Institut der BVFA-Arsenal, Wien, 22, 1976.
2. D. Rank, Tagungsbericht der 3. Informationstagung der ÖSRAD, Geotechnisches Institut der BVFA-Arsenal, Wien, 85, 1977.
3. D. Rank, Tagungsbericht der 5. and 6. Jahrestagung der ÖSRAD, Österreichischer Verband für Strahlenschutz, Wien, 23, 1980.
4. F. Bauer, V. Rajner und D. Rank, Die Naturwiss., **62**, 526, 1975.
5. United Nations Scientific Committee on the Effects of Atomic Radiation (UNSCEAR), Report 1977.

Acta Physica Academiae Scientiarum Hungaricae, 52 (3—4), pp. 443—454 (1982)

VI. MISCELLANEOUS

CHAIRMEN: A. HEFNER, E. VIRÁGH

DIE COBALT 60 BESTRAHLUNGSANLAGE IM FORSCHUNGSZENTRUM SEIBERSDORF

K. MAYR, G. NEZAVDAL und K. SPALEK

ÖSTERREICHISCHES FORSCHUNGSZENTRUM SEIBERSDORF GesmbH, SEIBERSDORF, ÖSTERREICH

Der Bericht beinhaltet die Beschreibung der ^{60}Co-Bestrahlungsanlage mit den dazugehörigen strahlenschutztechnischen Einrichtungen sowie den erforderlichen Sicherheitskriterien.

Eine bereits bestehende ^{60}Co-Bestrahlungsanlage mit einem Aktivitätsinventar von 1.4 Peta-Becquerel wurde auf 4.1 Peta-Becquerel erweitert. Diese Aufstockung erforderte aus strahlenschutztechnischen Gründen zusätzliche Abschirmungen, eine Neuinstallierung des Quellentransportsystems sowie der Steuerungs- und brandschutztechnischen Anlagen.

Einleitung

Die ^{60}Co-Bestrahlungsanlage im Forschungszentrum Seibersdorf ist für folgende Anwendungsbereiche vorgesehen:

— Bestrahlungen für industrielle Anwendungen und

— Bestrahlungen für wissenschaftliche Zwecke.

Für diese Anforderungen sind zwei Bestrahlungsräume, die sich in ihrer Bauweise und im Aktivitätsinventar unterscheiden, vorgesehen.

Der Bestrahlungsraum für industrielle Anwendungen hat ein Aktivitätsinventar von ca. 3.7 Peta-Becquerel ^{60}Co. Die für diese Produkte erforderlichen Dosiswerte liegen in der Grössenordnung von 10^4 Gy. Folgende Bestrahlungen sind vorgesehen:

— Radiosterilisation von Tierfutter und Artikeln der medizinischen Industrie, wie Einwegspritzen, chirurgische Handschuhe, künstliche Nieren, Verbandsstoffe, etc..

— Strahlenpolymerisation von mit monomeren Verbindungen Imprägnierten Materialien wie Holz, etc.

— Haltbarkeits- und Funktionsprüfungen von elektrotechnischen und elektronischen Bauelementen in hohen Strahlenfeldern, wie sie z.B. in Kernkraftwerken und Strahleneinrichtungen vorkommen.

Der Bestrahlungsraum für wissenschaftliche Zwecke mit einem Aktivitätsinventar von 0.44 Peta-Becquerel ^{60}Co wird zu Bestrahlungsversuchen auf den Gebieten der Biologie und Strahlenchemie verwendet. Hier können neben hohen Bestrahlungsdosen auch biologische und strahlenchemische Bestrahlun-

gen mit geringen Dosisleistungen in der Grössenordnung von 0.01 Sv/h vorgenommen werden.

Eine bereits bestehende ^{60}Co-Bestrahlungsanlage mit einem Aktivitätsinventar von 1.4 Peta-Becquerel wurde auf 4.1 Peta-Becquerel erweitert. Dies erforderte aus strahlenschutztechnischen Gründen bauliche Veränderungen und eine Neuinstallierung des Quellentransportsystems sowie einer Steuerungsanlage und brandschutztechnischer Einrichtungen. Durch diese Voraussetzungen ergab sich folgendes

Planungsbild

Strahlenschutztechnische Massnahmen gliedern sich in:
- bautechnische
- maschinenbauliche
- elektrotechnische
- Lüftung und brandschutztechnische
- strahlenmesstechnische
- steuerungstechnische

Organisatorische Strahlenschutzmassnahmen gliedern sich in:
- Einteilung der Strahlenbereiche
- Personenüberwachung
- Betriebspersonal

Grundlegende Sicherheitskriterien der ^{60}Co-Bestrahlungsanlage sind, dass die Anlage weder durch betriebsbedingte Abläufe noch durch Störfälle in einen strahlenschutztechnisch unsicheren Zustand versetzt werden kann.

Der Aufbau der systematischen Planung zur Modernisierung der Bestrahlungsanlage war von dem Umstand begleitet, dass das Bauwerk einschliesslich der Raumaufteilung vorgegeben war.

Bautechnische Massnahmen

Die ^{60}Co-Bestrahlungsanlage ist als ein eigener Baukörper zweigeschossig ausgeführt und in einen Gebäudeverband eingebunden. Im Erdgeschoss befinden sich:

- Vorbereitungsraum — 113 m^2
- Lagerraum — 14 m^2
- Bedienungsraum — 9 m^2
- Bestrahlungsraum für industrielle Produkte — 9 m^2
- Bestrahlungsraum für wissenschaftliche Zwecke — 13 m^2
- dazugehöriger Labyrinthgang — 18 m^2.

Im Obergeschoss befinden sich:

— Werkstätte — 13 m²
— zwei Nebenräume — je 7 m²
— Maschinenraum — 66 m²
— Batterieraum — 5 m².

Das die Bestrahlungsräume umgebende Mauerwerk mit Decken besteht aus Stahlbeton. Auf den 130—150 cm starken Umfassungsmauern liegt eine 150 cm starke Massivbetondecke mit einer Dichte von 2.4 t/m³. Der Bestrahlungsraum für industrielle Anwendungen ist durch ein fahrbares, nach innen dreistufig abgesetztes Betontor, jener für wissenschaftliche Zwecke durch eine Stahlblech-Schiebetüre durch den Labyrinthgang erreichbar.

Da die ^{60}Co-Bestrahlungsanlage vor dem Umbau mit 1.4 Peta-Becquerel ^{60}Co beladen war, wurden die nunmehr erforderlichen Schutzstärken neu berechnet und durch Messungen überprüft.

Die Aussenmauern der Bestrahlungsräume benötigten eine Verstärkung um 30 cm mit einer Betondichte von 2.4 t/m³. Dadurch ergab sich nach Neubeladung eine mittlere Dosisleistung von 0.75 μSv/h. In den angrenzenden Räumen hat sich bei 40 Stunden Aufenthalt pro Woche eine Dosis von durchschnittlich 20 μSv ergeben.

Zusätzlich erfolgte im Maschinenraum eine Verstärkung der Abschirmung oberhalb der Quellenführungsrohre, sodass sich dort eine Dosisleistung von durchschnittlich 1 μSv/h ergeben hat. Befinden sich die Quellen in Bestrahlungsposition, ergeben sich im Maschinenraum Dosisleistungen unter 1 μSv/h, wobei die geringste bei 0,6 μSv/h und die höchste an einer schwer zugänglichen Stelle bei 0,9 mSv/h liegt.

Maschinenbauliche Massnahmen

Strahlenquelleneinheiten des Bestrahlungsraumes für industrielle Anwendung

Eine Strahlenquelleneinheit besteht aus je zwei umschlossenen Strahlenquellen von je 0.15 Peta-Becquerel ^{60}Co in besonderer Form, die in rostfreien Stahlrohren beweglich miteinander verbunden sind. Sie sind mit dem zugehörigen Kabelzug über eine formschlüssig gesicherte Kupplung verbunden. Insgesamt werden 12 derartige Quelleneinheiten verwendet.

Strahlenquelleneinheiten des Bestrahlungsraumes für wissenschaftliche Zwecke

Diese sechs Quelleneinheiten haben eine Aktivität von je 7.4 Tera-Bequerel. Die maximale Gesamtaktivität beträgt daher 0.44 Peta-Becquerel. Die Einheiten bestehen ebenfalls aus einer aus rostfreiem Stahl gefertigten Umhüllung, die verschraubt gesichert und mit einem Kabelzug über eine formschlüssig gesicherte Kupplung verbunden ist.

Quellenführungssystem

Das Quellenführungssystem besteht aus:

— dem Quellenführungseinsatz im zylindrischen Bleibehälter;
— den Quellenführungsrohren vom zylindrischen Bleibehälter in die Bestrahlungsräume;
— der Bestrahlungskonfiguration.

Der *Quellenführungseinsatz* enthält 18 Rohre, deren Zwischenräume mit Blei ausgegossen sind. Die durch die Lagerung der Strahlenquelleneinheiten entstehende Wärme wird durch Wasserkühlung im zylindrischen Bleibehälter abgeführt.

Die *Quellenführungsrohre* führen vom zylindrischen Bleibehälter in einem horizontalen und vertikalen Bogen in die Bestrahlungsräume. Sie münden jeweils an der Deckenmitte und setzen sich zur Bestrahlungskonfiguration fort.

Jede *Bestrahlungskonfiguration* besteht aus nahtlos gezogenen rostfreien Stahlrohren, die in der Deckenmitte des Bestrahlungsraumes an die jeweiligen Quellenführungsrohre angeschraubt werden.

Transport der Strahlenquelleneinheiten

Der Transport der Strahlenquelleneinheiten erfolgt mit in Rohren geführten Kabelzügen von der Ruheposition zur Bestrahlungsposition und umgekehrt. In deren Mitte befindet sich ein Antriebsmechanismus, bestehend aus polumschaltbaren Gleichstrom-Getriebemotoren (24 V) mit elektrischen Bremsen und Kabelzuggeberdosen. In jeder Geberdose bewirkt ein Antriebsrad den Transport der Strahlenquelleneinheiten. Die Getriebemotoren besitzen eine elektronische Drehmomentüberwachung, die bei einem mechanischen Widerstand von 180 N abschaltet.

Rohrpostsystem des Bestrahlungsraumes für wissenschaftliche Zwecke

Die Rohrpostleitung besteht aus einem Aluminiumrohr und führt vom Bedienungsraum in den Bestrahlungsraum. Durch einen Dreiweghahn kann die Luftzufuhr wahlweise vom Bedienungsraum in den Bestrahlungsraum und umgekehrt gesteuert werden. Das Rohrpostsystem dient zur exakten Bestrahlung kleinerer Proben (sog. Rabbits) in einer Zentralposition der Bestrahlungskonfiguration.

Elektrotechnische Massnahmen

Netzversorgung

Beleuchtungskörper, Steckdosen, Batterieladegerät, Lüftung, Kompressor für die Druckluftversorgung der Rohrpost, werden mit $3 \times 220/380$ V Wechselstrom mit einem Anschlusswert von 82 kVA versorgt.

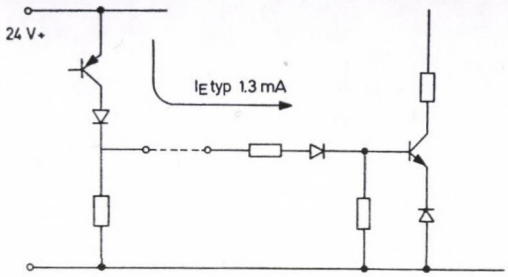

Abb. 1. Elektrische Schaltung.

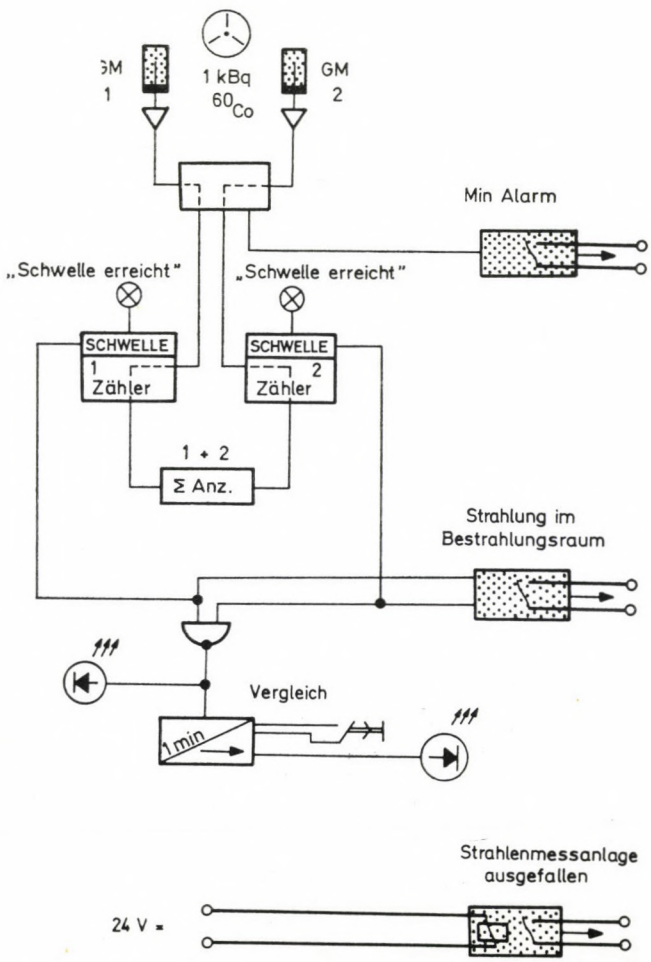

Abb. 2. Strahlenmesseinrichtung innerhalb der Bestrahlungsräume.

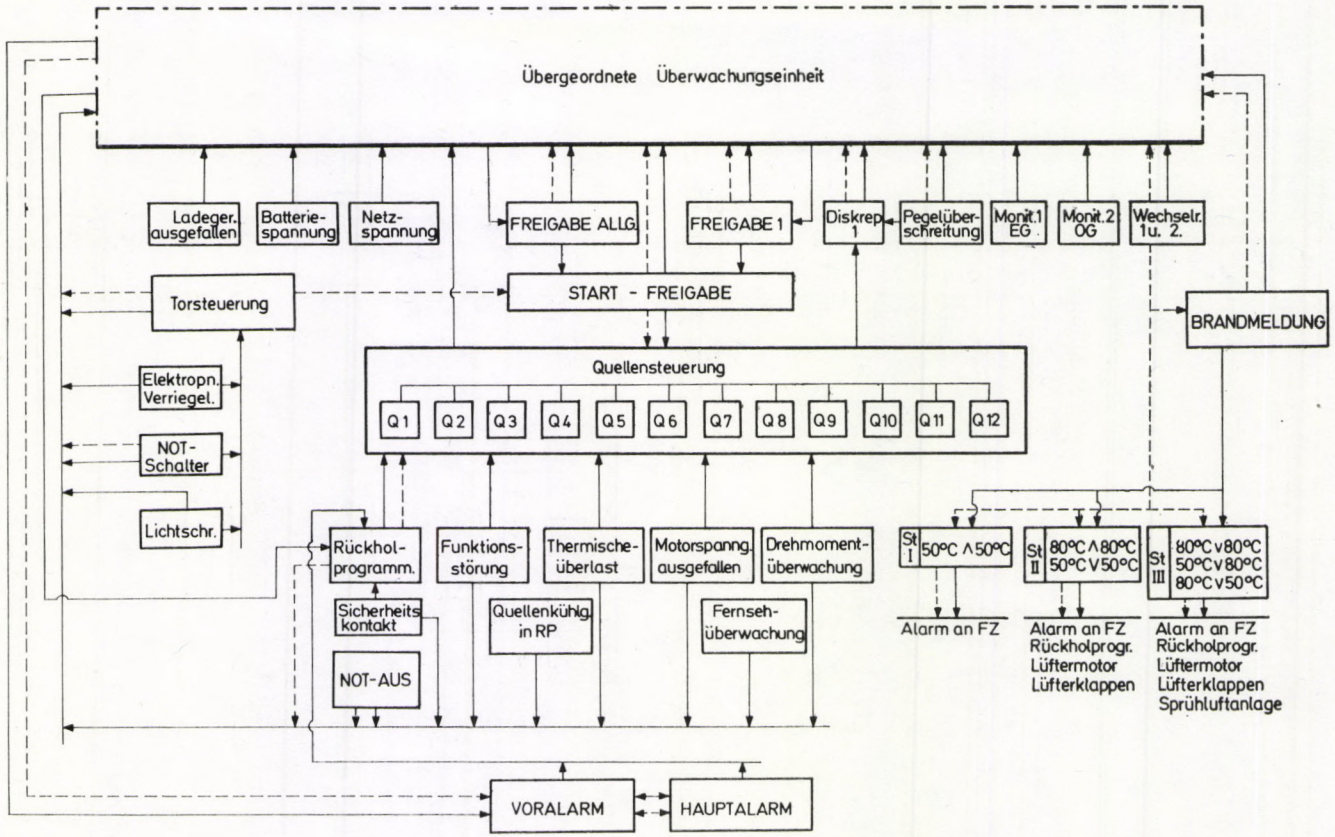

Abb. 3. Blockschaltbild.

Notstromversorgung

Not- und Warnleuchten werden mit einer Gleichspannung von 220 V von einer nahegelegenen Trafostation aus versorgt.

Pufferbatterie mit Lade- und Kontrolleinrichtung

Für die Spannungsversorgung der Steuerungsanlage sorgt eine Pufferbatterie mit Ladegleichrichter und Kontrolleinrichtung. Die Batterie hat eine Spannung von 24 V, eine Nennkapazität von 1000 Ah und 10 Stunden Entladezeit. Bei Netzausfall ist bei einer Betriebsfrequenz von drei Transportwegen pro Stunde mit allen 18 Strahlenquelleneinheiten der Betrieb für 10 Stunden gewährleistet.

Lüftungstechnische und brandschutztechnische Massnahmen

Bestrahlungsräume

Beide Bestrahlungsräume werden mit Zuluft versorgt, die Luftaustrittsöffnungen befinden sich in Bodennähe. Die Abluft wird nahe der Decke durch einen Lüfter abgesaugt. In der Abluftleitung jedes Bestrahlungsraumes befindet sich eine Klappe. Lüftermotor und Klappen werden im Brandfall geschlossen. Mit dieser Massnahme wird erreicht, dass der im Bestrahlungsraum vorhandene Luftsauerstoff durch den Verbrennungsvorgang weitgehendst verbraucht wird und die entstehenden Brand- und Stickgase den Löschvorgang noch zusätzlich beschleunigen. Die Auslösung dieses Steuervorganges wird mit einer Temperaturmeldeanlage, deren Fühler an der Decke der Bestrahlungsräume angebracht sind, ausgelöst. Die Temperaturmeldeanlage ist mit zwei Grenzwerten ausgestattet. Bei Überschreiten des 2. Grenzwertes wird eine Sprühflutanlage in Funktion gesetzt, die so lange in Betrieb ist, bis die Raumtemperatur entsprechend absinkt. Die Massnahme bewirkt zusätzlich eine ausreichende Kühlung der Bestrahlungskonfiguration, damit diese durch einen Brandfall keinen Schaden erleiden kann. Diese Massnahmen — Abschalten dees Lüftermotors und Schliessen der Klappen sowie Auslösen der Sprühflutanlage — werden durch die Steuerungsanlage hierarchisch bewirkt.

Steuerschränke

Die Schaltschränke der Steuerungsanlage werden mit Differentialmaximaltemperaturmeldern überwacht. Bei Ansprechen dieser Melder wird die Spannungsversorgung der Steuerungsanlage abgeschaltet und damit auch das Öffnen der Tore der Bestrahlungsräume verhindert. Auch diese Meldung ist in der Steuerungsanlage hierarchisch eingeordnet.

Übrige Räume

Alle weiteren Räume der Bestrahlungsanlage sind mit Brandmeldern, wie sie im Forschungszentrum Seibersdorf allgemein üblich sind, ausgestattet. Im Vorbereitungsraum sind gekennzeichnete Lagerflächen vorgesehen, die eine Brandlastbegrenzung für feste brennbare Stoffe darstellen.

Strahlenmesstechnische Massnahmen

Strahlenmesseinrichtungen innerhalb der Bestrahlungsräume (siehe Abb. 2)

Als Detektoren werden zwei Auslösezählrohre, die als getrennte Messkanäle ausgeführt sind, verwendet. Sind die Strahlenquelleneinheiten in Bestrahlungsposition, herrscht im Bestrahlungsraum hohe Dosisleistung. Deshalb befinden sich die Zählrohre in einer abgeschirmten Position innerhalb der Umfassungsmauern. Sind die Strahlenquelleneinheiten in Ruheposition, ist der Leerwert gering. Um diesen anzuheben, ist nahe der Zählrohre eine Strahlenquelle geringer Aktivität (37 kBq ^{60}Co) angebracht. Die von den Zählrohren ausgehenden Impulse werden überprüft, ob zwischen zwei aufeinanderfolgenden Impulsen ein nicht zu grosser zeitlicher Abstand besteht. Dies bedeutet: "Minimumalarm" für die Steuerungsanlage.

Die Impulsraten der beiden Zählrohre werden getrennten Zählern zugeführt, den Zählern ist je ein Schwellwert zugeordnet. Der Schwellwert kann so gesetzt werden, dass bereits eine halbe Strahlenquelleneinheit im Bestrahlungsraum erkannt werden kann.

Das Erreichen beider Schwellwerte wird in einem Äquivalenzgatter überprüft. Der Ausgang des Äquivalenzgatters wird einem Zeitglied zugeführt. Ungleichheit der Schwellwerte wird sofort angezeigt. Dies kann aber auch kurzzeitig während des Quellentransportes auftreten. Im Zeitglied wird das Bestehen einer Ungleichheit der Schwellwerte ca. 1 min lang zur Kenntnis genommen, besteht diese länger, liegt eine Störung eines Messkanals vor. Das Bedienungspersonal wird durch ein Blinksignal auf diesen Umstand hingewiesen.

Ortsfeste Strahlenmesseinrichtungen ausserhalb der Bestrahlungsräume

Als Detektoren werden Auslösezählrohre, die mit einem Pegelwächter verbunden sind, verwendet. Bei Erreichen einer am Pegelwächter eingestellten Schwelle wirkt das abgehende Signal auf die Steuerungsanlage.

Ortsfeste Pegelwächter sind an mehreren Stellen der ^{60}Co-Bestrahlungsanlage vorgesehen.

Steuerungsanlage

Anforderungen

Aufgrund folgender Überlegungen wurde das Grundkonzept für die Steuerungsanlage entworfen:

- Kombinierbarkeit mit elektromechanischen Bauelementen
- Grosse Schalthäufigkeit der Bauelemente
- Toleranzgrenze des Systems (Grenztemperatur, Spannungstoleranz, Erschütterungsfestigkeit)
- Platzerfordernis in Schaltschränken bei vorgegebener Raumgrösse
- Einfache Erweiterungs- und Anpassungsmöglichkeit
- Schaltsicherheit
- Gute Übersichtlichkeit redundant ausgeführter Steuerkreise mit einfacher Kontrollmöglichkeit
- Wartungsfreundlichkeit
- Modulare Ausführung der Überwachungssteuerkreise für Meldungen und Drehmomentüberwachung
- Einfacher Umbau bei Funktionsveränderungen
- Konfektionierte Verbindungsleitungen mit Steckhülsen
- Leitungsführung in handelsüblichen Kanälen und systemgerechte Montage
- Speisespannung von 24 V Gleichstrom
- Reichhaltige Möglichkeiten zur logischen Verkupplung und Verriegelung bei Vorhandensein einer grösseren Anzahl von Eingangssignalen und einer geringeren Anzahl von Ausgangssignalen.

Den genannten Anforderungen hat das verdrahtungsprogrammierte System "Sigmatronic" der Österreichischen Brown Boveri AG voll entsprochen. (Beschreibung des Systems "Sigmatronic" und Aufbau der Steuerungsanlage: A. Polasek). Es hat folgende *elektrische Eigenschaften:*

Speisespannung 24 V
Spannungstoleranz $\pm$ 30%
Welligkeit 4 V (Scheitelwert)
Eingangsspannung bis 50 V = dauernd zulässig
Hohe Belastbarkeit der Ausgänge — Anschluss von 100 Eingängen, leichte Prüfung mit Prüfbausteinen
Grosse Signalbereiche, hoher statischer Störabstand
Verzögerung der speichernden Geräte, hoher dynamischer Störabstand
Mischtechnik mit elektromechanischen Geräten problemlos.

Strukturelle Eigenschaften (siehe Abb. 1)

Aktiv-L-Technik, Geradeaus-Logik, Sicherheit gegen Fehler, übersichtliche Projektierung. Im Falle eines L-Signals liegt an einem Geräteausgang positive Spannung. Es fliesst ein Strom in den nachgeschalteten Geräteeingang. Im Falle eines 0-Signals liegt am Geräteausgang keine Spannung. Es fliesst kein Strom in den Geräteeingang. Dieser Fall ist gleichbedeutend mit einem offenen Eingang. Der L-Zustand wird also aktiv durch Spannung und Strom dargestellt: Aktiv-L-Technik. Da im System "Sigmatronic" auf signalumkehrende Elemente weitgehend verzichtet wird, bedeutet L-Signal durch die ganze Steuerung hindurch den EIN-Zustand, also auch ein eingeschaltetes Stellglied.

Neben der Übersichtlichkeit der Projektierung, Inbetriebnahme, Wartung und Fehlersuche hat diese Methode den Vorteil hoher Sicherheit. Im Falle der häufigsten Fehler — Drahtbruch und Erdschluss von Leitungen — wird nämlich automatisch 0-Signal erzeugt, also kein Stellglied eingeschaltet und so ein gefährlicher Zustand vermieden. Einfache Erweiterungs- und Anpassungsmöglichkeiten werden durch anwendungsgerechte Funktionseinheiten in Aktiv-L-Technik erreicht.

Mechanische Eigenschaften

Kunststoffgehäuse um jede Funktionseinheit
Montage durch Aufschnappen auf Tragschienen
Kombinierter Aufbau mit elektromechanischen Bauelementen
Elektrische Verbindung durch Steckhülsen
Dreiteilige Flachstecker von vorn zugänglich, ermöglichen den Anschluss von Leitungen und einfache Kontrollmöglichkeiten des Bauelementes.
Konfektionierte Verbindungsleitungen mit Steckhülsen
Leitungsführung in handelsüblichen Kanälen
Systemgerechte Montage der Kanäle

Aufbau (siehe Abb. 3)

Die Aufbauorganisation der elektronischen Steuerung stellt eine Einzelantriebssteuerung mit hierarchischer Struktur dar. Durch die "übergeordnete Überwachungseinheit" wird die Gruppensteuerebene "Torsteuerung — Startfreigabe — Brandmeldung" gesteuert und diese ist wieder den Einzelantrieben "Transport der Strahlenquelleneinheiten" übergeordnet. Durch diese Anordnung werden sämtliche Störfälle hierarchisch überwacht, der strukturelle Aufbau aller Programme ist mindestens zweifach abgesichert. Um die höchstmögliche ökonomisch vertretbare Sicherheit zu erreichen, sind alle Vor- und Hauptalarmkriterien redundant ausgeführt.

Die Anlage steuert den Transport der Strahlenquelleneinheiten und die Zugänglichkeit zu den Bestrahlungsräumen. Der Transport der Strahlenquelleneinheiten von der Ruhe- in die Bestrahlungsposition und zurück kann wahlweise automatisch oder manuell vom Steuerpult ausgelöst werden.

Die Laufrichtung der Gleichstrom-Getriebemotore wird durch die Vorwahl beim Strahlenquelleneinheitentransport bestimmt. Durch das Signal von der Strahlenüberwachungsanlage "Strahlung im Raum" sowie die Stellung der Kontrollkontakte der Kabelzüge ist die Position der Strahlenquelleneinheiten bestimmt. Alle Strahlenquelleneinheiten können wahlweise einzeln oder gemeinsam transportiert werden.

Es wird sichergestellt, dass der Operator auch bei grösster Nachlässigkeit keine Person im Bestrahlungsraum irrtümlich einschliessen kann. Der Steuerungsvorgang zum Schliessen des Tores beginnt mit der Betätigung der Tortaste im Bestrahlungsraum. Dieser Vorgang wird vom Operator persönlich durchgeführt und ist mit einer Besichtigung des Raumes unmittelbar vor dem Schliessen des Tores verbunden. Durch die Tortaste bedingt, ertönt 10 sec ein Summton. Innerhalb dieser Zeit muss der Bestrahlungsraum verlassen und die Schlüsseltaste "Tor zu" betätigt werden.

Verstummt der Summton vor dem Drücken der Schlüsseltaste, muss der Vorgang wiederholt werden. Die Schlüsseltaste muss gedrückt bleiben, bis das Tor geschlossen ist. Vorzeitiges Loslassen bewirkt eine automatische Öffnung des Tores.

Ein nichteinschaubarer Bereich während des Schliessens wird durch eine Lichtschranke abgesichert. Die Zugänglichkeit zu den Bestrahlungsräumen wird durch die Torsteuerung geregelt.

In den Bestrahlungsräumen befindet sich ausserdem eine Taste, die es ermöglicht, das bereits geschlossene Tor von innen her zu öffnen. Wenn die übergeordnete Überwachungseinheit den Zugang zum Bestrahlungsraum freigibt, kann das Tor vom Bedienungspult aus geöffnet werden. Um den Bereich vom Bedienungsraum aus überblicken zu können, ist die Anlage mit einer Fernsehüberwachung ausgestattet. Zusätzlich wird das geschlossene Tor von der Steuerungsanlage elektropneumatisch verriegelt. —

Zur Brandbekämpfung sind die Bestrahlungsräume mit je einer Sprühflutanlage, die auf Temperaturerhöhung anspricht, ausgestattet. In jedem Bestrahlungsraum sind jeweils zwei Temperaturfühler mit 50 °C und 80 °C vorgesehen. Die Grenzwertsignale bewirken in der Steuerungsanlage:

- Meldung an die zentrale Überwachungsanlage des Forschungszentrums
- Start des Rückholprogrammes für den Strahlenquelleneinheitentransport
- Abschalten des Lüftermotors
- Schliessen der Lüftungsklappen
- Auslösen der Sprühflutanlage.

Organisatorische Strahlenschutzmassnahmen

Einteilung der Strahlenbereiche

Alle Räume der ^{60}Co-Bestrahlungsanlage sind Überwachungsbereiche, wenn sich die Strahlenquelleneinheiten in Ruheposition befinden.

Sind die Strahlenquelleneinheiten in Bestrahlungsposition, ergeben sich folgende temporäre Kontrollbereiche:

— Vorraum vor dem fahrbaren Betontor
— Maschinenraum.

Personenüberwachung

Das Betriebspersonal ist mit Thermolumineszenzdosimetern, Durchsichtdosimetern und Warndosimetern ausgestattet. Vor Betreten der Bestrahlungsräume hat das Betriebspersonal mit einem Dosisleistungsmessgerät die Bestrahlungsräume zu überprüfen. Lieferanten können die gekennzeichneten Lagerflächen ohne Dosimeter betreten.

Betriebspersonal

Es besteht aus dem Betriebsleiter und dessen Stellvertreter, die als weitere mit der Wahrnehmung des Strahlenschutzes betraute Personen gelten. Ausserdem ist der Betriebsleiter für den Betrieb, Wartung und Instandhaltung verantwortlich. Für das Ein- und Ausbringen des Bestrahlungsgutes sowie zum Aufbau von Experimenten kann Hilfspersonal herangezogen werden.

Die Verfasser danken der Österreichischen Brown Boveri AG, insbesondere Herrn Dipl. Ing. A. POLASEK, für die Unterstützung bei der Ausarbeitung dieses Berichtes.

Acta Physica Academiae Scientiarum Hungaricae, 52 (3—4), pp. 455—467 (1982)

NOMOGRAMM ZUR ERMITTLUNG DER ENDAKTIVITÄT UND NOTWENDIGEN ABKLINGZEIT NACH PERIODISCHER BEFÜLLUNG EINES BEHÄLTERS MIT KURZLEBIGEN RADIOAKTIVEN STOFFEN

J. KRISCHAN und H. BINDER

AMT DER KÄRNTNER LANDESREGIERUNG
A-9020 KLAGENFURT, ÖSTERREICH

INSTITUT FÜR RADIOCHEMIE, UNIVERSITÄT INNSBRUCK
A-6020 INNSBRUCK, ÖSTERREICH

Das beschriebene Nomogramm dient zur Ermittlung der Endaktivität bei der Sammlung kurzlebiger radioaktiver Abfälle in einem Abfallbehälter und der Abklingzeit, die notwendig ist, um diese Abfälle unter die gesetzlich vorgeschriebenen Freigrenzen abklingen zu lassen, sodass sie wie inaktives Abwasser behandelt werden können.

Einleitung

Bei der Lagerung von kurzlebigen radioaktiven Abfällen stellt sich die Frage, welche Gesamtaktivität zu einem bestimmten Zeitpunkt in einem Container bzw. in einem Tank bekannter Volumenskapazität erreicht wird, wenn dieser in periodischen Abständen mit flüssigen radioaktiven Abfällen eines Nuklids bekannter, konstanter Volums- und Aktivitätsmenge befüllt wird. Die erreichte Aktivität ist schliesslich wesentlich für eine Dimensionierung hinsichtlich der Grösse und Abschirmung eines Lagers oder Abklingtanks mitverantwortlich. Da in der Literatur diese Thematik kaum behandelt wird [1—4], wird in dieser Arbeit eine Möglichkeit präsentiert, für radioaktive Abfälle mittels eines Nomogramms* die nach einer gewissen Zeit erreichte Aktivität sowie die entsprechende Abklingzeit, nach der eine Abgabe an die Umwelt möglich ist, zu ermitteln.

Das Nomogramm sollte eine Hilfe zur Dimensionierung von Abklingräumen im medizinischen wie auch nichtmedizinischen Bereich darstellen. Durch

*Da die Umarbeitung des an der Konferenz in nicht-SI-Einheiten präsentierten Nomogramms die Veröffentlichung des gesamten Konferenzmateriale auf eine längere Zeit verzögert hätte, sind die originalen Einheiten hier beibehalten. Die Umrechnungsfaktoren auf SI-Einheiten sind die folgenden:

$$1\ \mu\text{Ci} = 37\ \text{kBq} \quad \text{bzw.} \quad 1\ \frac{\mu\text{Ci}}{\text{ml}} = 37\ \frac{\text{kBq}}{\text{cm}^3}$$

und

$$1\ \text{kBq} = 0{,}027\mu\text{Ci} \quad \text{bzw.} \quad 1\ \frac{\text{kBq}}{\text{cm}^3} = 0{,}027\ \frac{\mu\text{Ci}}{\text{ml}}\ .$$

die gewonnenen Daten kann die Zahl und Grösse der notwendigen Tanks ermittelt werden, sodass ein sicherer Betrieb im Rahmen der jeweils geltenden Gesetze möglich ist.

Berechnung der Gesamtaktivität bzw. der notwendigen Abklingzeit

Die periodische Zugabe einer bestimmten Aktivitätsmenge eines radioaktiven Stoffes in ein Sammelgefäss bewirkt ein Anwachsen der Gesamtaktivität. Die im Behälter nach einer bestimmten Zeit erreichte Aktivität strebt einem Sättigungswert zu, wobei der gesamte Verlauf der Aktivität von der Halbwertszeit sowie der Aktivität der einzelnen Zugaben und den zwischen den einzelnen Zugaben liegenden Zeitintervallen abhängig ist.

Unter der Annahme, dass während einer Periode (z.B. ein Tag) einmalig oder auch mehrmals eine gleichbleibende Aktivität in konstanten Zeitabschnitten in einen Abfallbehälter gegeben wird und nach einer grösseren Ruhepause (Nachtstunden) dieser Zyklus von neuem beginnt, lässt sich der Anstieg der Aktivität im Sammelgefäss durch die aus den Gleichungen (1) und (2) abgeleitete Formel (3) beschreiben. In (1) ist die aktivität je Periode, in (2) die erreichte Aktivität nach einer Gesamtzeit t_{ges} von k Perioden gemäss Abb. 1 dargestellt.

$$A_{\text{per}} = (((A_0 \cdot e^{-tx} + A_0)\, e^{-tx} + A_0)\, e^{-tx} + \ldots + A_0 = A_0 \cdot \sum_{n=0}^{n-1} e^{-ntx}. \qquad (1)$$

Dabei ist $x = \ln 2/\tau$ und $t_{\text{per}} = t_p + (n-1) \cdot t$

$$A_e = A_{\text{per}} \cdot \sum_{k=0}^{k-1} e^{-kt_{\text{per}}x}. \qquad (2)$$

Aus (1) und (2) und mit $t_{\text{ges}} = k \cdot t_{\text{per}}$ ergibt sich

$$A_e = A_0 \cdot \sum e^{-kt_{\text{per}}x} \cdot \sum e^{-ntx} =$$

$$= \frac{A}{n} \cdot \frac{e^{-t_{\text{ges}}x} - 1}{e^{-t_{\text{per}}x} - 1} \cdot \frac{e^{-ntx} - 1}{e^{-tx} - 1}. \qquad (3)$$

Für $t_{\text{ges}} \to \infty$ ergibt sich die Sättigungsaktivität zu

$$A_{\max} = \frac{A}{n} \cdot \frac{1}{1 - 2^{-t_{\text{per}}/\tau}} \cdot \frac{e^{-ntx} - 1}{e^{-tx} - 1}. \qquad (4)$$

Aus der Gesamtaktivität und aus dem Volumen der einzelnen Aktivitätszugaben kann die notwendige Abklingzeit errechnet werden, nach der die

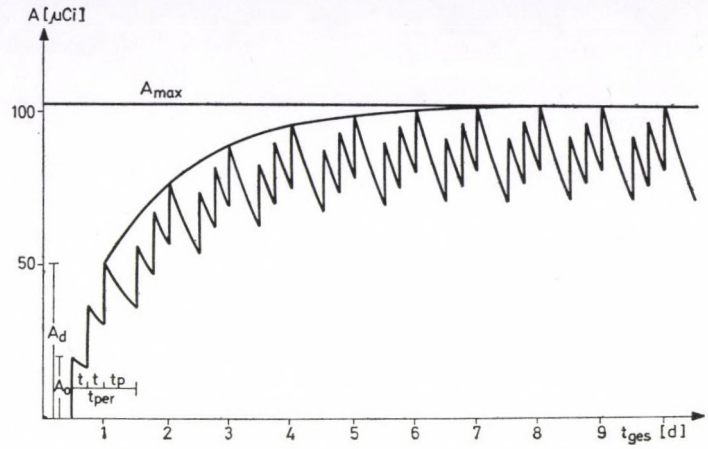

Abb. 1. Verlauf der Gesamtaktivität in einem Sammelbehälter bei dreimaliger Aktivitätszugabe pro Tag ($A_0 = 20$ µCi) in sechsstündigen Intervallen (t) und einer 12-stündigen Abklingphase während der Nacht (t_p). Die Halbwertszeit des Nuklids beträgt 1 Tag.

spezifische Aktivität im Behälter unter den in Anlage 5 der Österreichischen Strahlenschutzverordnung [5] angegebenen Wert gesunken ist.

$$t_a = \frac{\tau}{\ln 2} \cdot \ln \frac{A_e}{F \cdot V_e} . \tag{5}$$

Dabei bedeuten:

A_e Endaktivität nach der Zeit t_{ges}; Betrachtung nach der letzten Zugabe einer Periode

A_{max} Sättigungsaktivität; Maximalwert von A_e

A Summe der Aktivitäten einer Periode

A_0 Aktivität einer Zugabe

n Zahl der Zugaben pro Periode

t Zeitintervall zwischen den Zugaben einer Periode

t_p Zeit zwischen der letzten Zugabe der vorhergehenden und der ersten Zugabe der nächsten Periode

t_{ges} Gesamtdauer der Aktivitätszugaben inklusive der dazwischenliegenden Pausen

t_{per} Periodendauer; beinhaltet eine Pausenlänge (t_p) sowie bei mehreren Zugaben die Zeitintervalle t zwischen diesen.

t_a Abklingzeit, die notwendig ist, die erreichte Endaktivität im Abklingtank zu lagern, ehe eine Beseitigung mit dem Betriebsabwasser erfolgen kann.

V Volumen einer Zugabe

V_e erreichtes Endvolumen aller Zugaben

Tabelle

Aktivität im Sammelgefäss in Abhängigkeit von der Akkumulierungsdauer
A_e in mCi, t_{ges}

τ	t_{ges}					
	1	2	4	8	16	32
1.5	50.0000	50.0000	50.0000	50.0000	50.0000	50.0000
3	50.0000	50.1953	50.1961	50.1961	50.1961	50.1961
6	50.0000	53.1250	53.3325	53.3333	53.3333	53.3333
12	50.0000	62.5000	66.4063	66.6656	66.6667	66.6667
24	50.0000	75.0000	93.7500	99.6094	99.9985	100.0000
48	50.0000	85.3553	128.0330	160.0413	170.0438	170.7081
96	50.0000	92.0448	157.1303	235.6955	294.6194	313.0331
192	50.0000	95.8502	176.4503	301.2195	451.8292	564.7865
384	50.0000	97.8802	187.6367	345.4197	589.6683	884.5024
768	50.0000	98.9286	193.6630	371.2527	683.4377	1166.7012
1536	50.0000	99.4614	196.7915	385.2398	738.5062	1359.5135
3072	50.0000	99.7300	198.3857	392.5203	768.3990	1473.0241

V_{max} Volumen eines Behälters

F höchstzulässige Konzentration im Betriebsabwasser nach den jeweils geltenden gesetzlichen Bestimmungen

Die derart berechnete Aktivität innerhalb einer Periode bzw. über mehrere Perioden wird zum Zeitpunkt nach der letzten Zugabe betrachtet. Verbindet man die Endaktivität je Periode, so ergibt sich der Anstieg der Gesamtaktivität gemäss Abb. 1 bzw. Tab. I bis zur Erreichung der Sättigungsaktivität. Diese Kurve wird in dem beschriebenen Nomogramm (Abb. 2) in Kurvenschar B verwendet. Wird die Aktivität auf mehrere Zugaben je Tag bzw. je Periode aufgeteilt, muss zur exakten Ermittlung der Endaktivität zusätzlich ein entsprechender Korrekturfaktor gemäss Tab. II (Periodendauer 1 Tag) bzw. Tab. III (beliebige Periodendauer) verwendet werden. Tab. IV enthält die Korrekturfaktoren für die Endaktivität bei beliebiger Periodenlänge bezogen auf eine Periodendauer von einem Tag.

Das Nomogramm

In dem in sechs Diagramme (A—F) unterteilten Nomogramm wird aus den Kurvenscharen A, B und C die Endaktivität A_e ermittelt. Die Kurven in D, E und F dienen zur Bestimmung der Abklingzeit, die erfordlich ist, um die Abfälle mit dem Betriebsabwasser beseitigen zu können.

Aus A ergibt sich aus dem vorgegebenen Behältervolumen (V_{max}) und

I

bzw. von der Halbwertszeit wenn täglich eine Zugabe von 50 mCi erfolgt.
in d, τ in h

64	128	256	512	1024	2048	4096
50.0000	50.0000	50.0008	50.0008	50.0008	50.0008	50.0008
50.1961	50.1961	50.1961	50.1961	50.1961	50.1961	50.1961
53.3333	53.3333	53.3333	53.3333	53.3333	53.3333	53.3333
66.6667	66.6667	66.6667	66.6667	66.6667	66.6667	66.6667
100.0000	100.0000	100.0000	100.0000	100.0000	100.0000	100.0000
170.7107	170.7107	170.7107	170.7107	170.7107	170.7107	170.7107
314.2559	314.2607	314.2607	314.2607	314.2607	314.2607	314.2607
600.0857	602.4298	602.4390	602.4390	602.4390	602.4390	602.4390
1105.6280	1174.7298	1179.3185	1179.3365	1179.3365	1179.3365	1179.3365
1750·0517	2187.5647	2324.2875	2333.3667	2333.4023	2333.4023	2333.4023
2320.8346	3481.2519	4351.5649	4623.5377	4641.5984	4641.6693	4641.6693
2711.6848	4629.1354	6943.7031	8679.6289	9222.1057	9258.1296	9258.2709

dem zugegebenen Tagesvolumen (V_d) die maximal mögliche Befüllzeit (t_{ges}) bzw. unter Berücksichtigung der Halbwertszeit (τ) der Faktor t_{ges}/τ.

B gibt den Anstieg der Aktivität im Sammelbehälter mit der Befüllzeit für verschiedene Halbwertszeiten wieder, wobei diese Kurvenschar (τ/t_{per}) eine zugegebene Tagesaktivität von 1,85 MBq (50 μCi) zugrunde gelegt wurde. Von diesem Wert abweichende Tagesaktivitäten werden — wie unten beschrieben — in C berücksichtigt. Die Auftragung relativer Parameter in B gestattet einerseits das Ablesen der Aktivität auch bei kurzen Sammelzeiten und andererseits die Berücksichtigung verschiedener Periodenlängen. Im Falle einer von 24 Stunden abweichenden Periodenlänge (t_{per}) ändern sich das Tagesvolumen und die Gesamtzeit gegenläufig, wobei das Verhältnis t_{ges}/t_{per} konstant bleibt (2. Kurvenschar in B). Aus dem Aktivitätswert für $t_{per} = 1$ Tag kann der sich durch die Änderung von t_{per} ergebende neue Aktivitätswert direkt erhalten werden, indem man entlang den Kurven t_{ges}/t_{per} bis zum entsprechenden Wert für τ/t_{per} fährt. Falls es erforderlich ist, kann ausgehend von dem so erhaltenen Aktivitätswert in A die neue Befüllzeit ermittelt werden.

C stellt eine Kurvenschar zur Multiplikation der im Sammelbehälter erreichten Aktivität (rechte Skala in C) dar und dient zur Berücksichtigung von Tagesaktivitäten, die von 50 μCi abweichen, sowie der in den Tabellen II und III angegebenen Korrekturfaktoren für mehrmalige Zugaben pro Tag und verschiedene Periodenlängen. In der linken Skala in C erhält man daraus die tatsächliche Endaktivität (A_e).

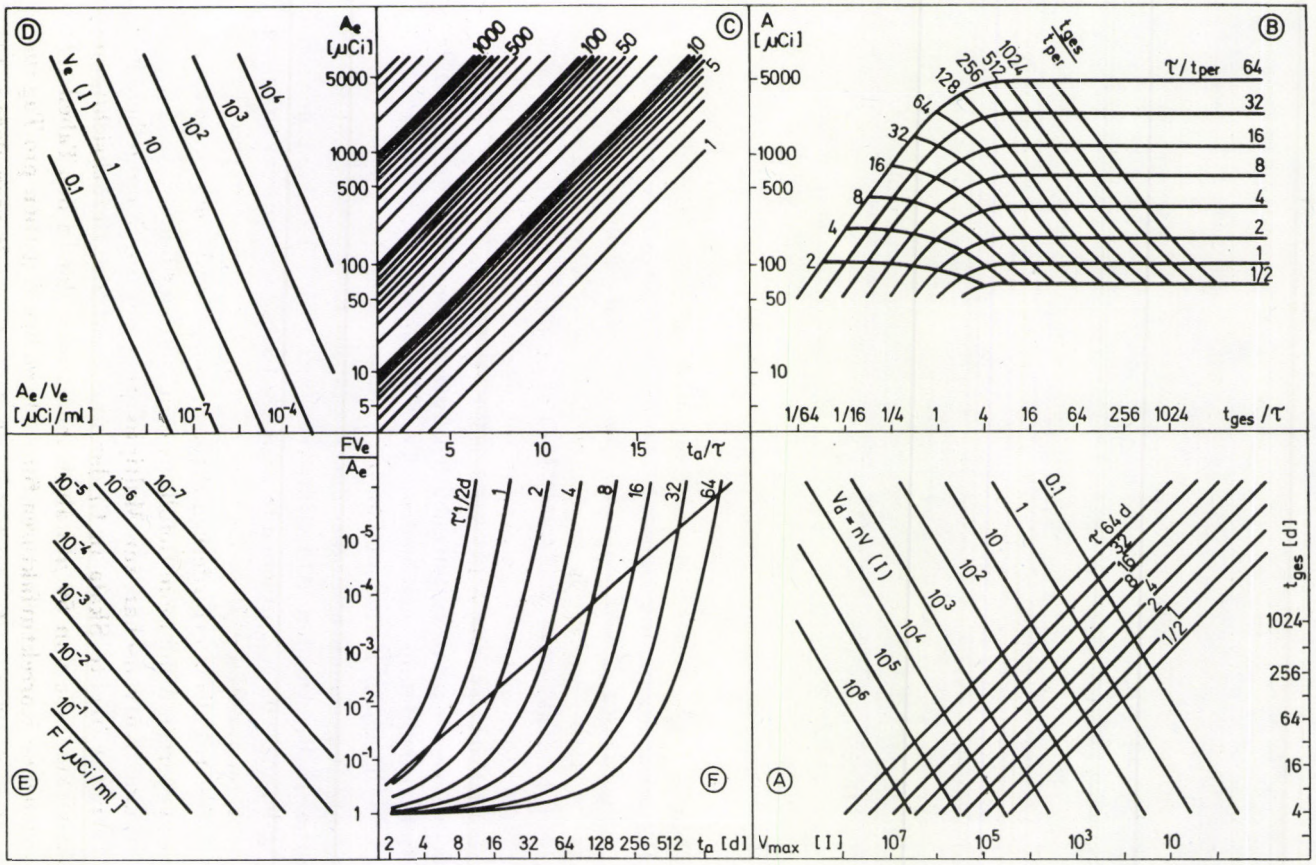

Abb. 2. Nomogramm zur Ermittlung der Endaktivität und der notwendigen Abklingzeit nach periodischer Befüllung eines Behälters mit flüssigen radioaktiven Stoffen. A — Ermittlung der Befüllzeit (t_{ges}) unter Berücksichtigung des Behältervolumens (V_{max}), des Tagesvolumens (V_d) und der Halbwertszeit. B — Anstieg der Aktivität im Behälter bei einer Tagesaktivität von 50 µCi. C — Multiplikationskurven zur Ermittlung der Endaktivität. D — Bestimmung der spezifischen Aktivität im Abklingbehälter. E — Ermittlung des Abklingfaktors unter Berücksichtigung der gesetzlich vorgeschriebenen Freigrenzen. F — Notwendige Abklingzeit in Tagen oder als Verhältnis t_a/τ.

Tabelle II

Korrekturfaktoren, mit denen die ermittelte Aktivität multipliziert werden muss, wenn die Aktivitätszugaben je Tag fraktioniert erfolgen, d.h. die Einzelaktivitäten 50 mCi : n betragen (Periode: 1 Tag)

t_p	n	$\tau = 3$	6	12	24	48	96	192	1420,8 [h]
	2	0.5039	0.5442	0.6487	0.7726	0.8692	0.9297	0.9635	0.9949
	5	0.2840	0.4186	0.5967	0.7555	0.8643	0.9283	0.9631	0.9949
	8	0.2490	0.4001	0.5892	0.7530	0.8635	0.9281	0.9631	0.9949
3	11	0.2353	0.3928	0.5863	0.7521	0.8633	0.9281	0.9631	0.9949
	14	0.2281	0.3888	0.4846	0.7515	0.8631	0.9280	0.9631	0.9949
	17	0.2236	0.3863	0.5836	0.7512	0.8630	0.9280	0.9631	0.9949
	20	0.2205	0.3847	0.5830	0.7510	0.8630	0.9280	0.9631	0.9949
	2	0.5078	0.5625	0.6768	0.7973	0.8856	0.9391	0.9685	0.9956
	5	0.3077	0.4567	0.6356	0.7842	0.8818	0.9381	0.9683	0.9956
	8	0.2766	0.4412	0.6296	0.7823	0.8813	0.9379	0.9682	0.9956
6	11	0.2644	0.4350	0.6273	0.7816	0.8811	0.9379	0.9682	0.9956
	14	0.2579	0.4317	0.6260	0.7812	0.8810	0.9378	0.9682	0.9956
	17	0.2539	0.4297	0.6252	0.7809	0.8809	0.9378	0.9682	0.9956
	20	0.2511	0.4283	0.6246	0.7807	0.8809	0.9378	0.9682	0.9956
	2	0.5156	0.5884	0.7102	0.8242	0.9026	0.9487	0.9736	0.9964
	5	0.3406	0.5037	0.6793	0.8147	0.9000	0.9480	0.9735	0.9964
	8	0.3140	0.4914	0.6748	0.8134	0.8996	0.9479	0.9734	0.9964
9	11	0.3035	0.4864	0.6730	0.8128	0.8995	0.9478	0.9734	0.9964
	14	0.2979	0.4838	0.6721	0.8125	0.8994	0.9478	0.9734	0.9964
	17	0.2944	0.4822	0.6715	0.8123	0.8993	0.9478	0.9734	0.9964
	20	0.2921	0.4810	0.6711	0.8122	0.8993	0.9478	0.9734	0.9964
	2	0.5313	0.6250	0.7500	0.8536	0.9204	0.9585	0.9788	0.9971
	5	0.3875	0.5621	0.7285	0.8472	0.9187	0.9581	0.9787	0.9971
	8	0.3661	0.5531	0.7254	0.8463	0.9185	0.9580	0.9787	0.9971
12	11	0.3577	0.5494	0.7242	0.8460	0.9184	0.9580	0.9787	0.9971
	14	0.3531	0.5475	0.7236	0.8458	0.9183	0.9579	0.9787	0.9971
	17	0.3503	0.5463	0.7231	0.8456	0.9183	0.9579	0.9787	0.9971
	20	0.3484	0.5454	0.7229	0.8456	0.9183	0.9579	0.9787	0.9971
	2	0.5625	0.6768	0.7973	0.8856	0.9391	0.9685	0.9840	0.9978
	5	0.4567	0.6356	0.7842	0.8818	0.9381	0.9683	0.9840	0.9978
	8	0.4412	0.6296	0.7823	0.8813	0.9379	0.9682	0.9839	0.9978
15	11	0.4350	0.6273	0.7816	0.8811	0.9379	0.9682	0.9839	0.9978
	14	0.4317	0.6260	0.7812	0.8810	0.9378	0.9682	0.9839	0.9978
	17	0.4297	0.6252	0.7809	0.8809	0.9378	0.9682	0.9839	0.9978
	20	0.4283	0.6246	0.7807	0.8809	0.9378	0.9682	0.9839	0.9978
	2	0.6250	0.7500	0.8536	0.9204	0.9585	0.9788	0.9893	0.9985
	5	0.5621	0.7285	0.8472	0.9187	0.9581	0.9787	0.9893	0.9985
	8	0.5531	0.7254	0.8463	0.9185	0.9580	0.9787	0.9893	0.9985
18	11	0.5494	0.7242	0.8460	0.9184	0.9580	0.9787	0.9893	0.9985
	14	0.5475	0.7236	0.8458	0.9183	0.9579	0.9787	0.9893	0.9985
	17	0.5463	0.7231	0.8456	0.9183	0.9579	0.9787	0.9892	0.9985
	20	0.5454	0.7229	0.8456	0.9183	0.9579	0.9787	0.9892	0.9985
	2	0.7500	0.8536	0.9204	0.9585	0.9788	0.9893	0.9946	0.9993
	5	0.7285	0.8472	0.9187	0.9581	0.9787	0.9893	0.9946	0.9993
	8	0.7254	0.8463	0.9185	0.9580	0.9787	0.9893	0.9946	0.9993
21	11	0.7242	0.8460	0.9184	0.9580	0.9787	0.9893	0.9946	0.9993
	14	0.7236	0.8458	0.9183	0.9579	0.9787	0.9893	0.9946	0.9993
	17	0.7231	0.8456	0.9183	0.9579	0.9787	0.9892	0.9946	0.9993
[h]	20	0.7229	0.8456	0.9183	0.9579	0.9787	0.9892	0.9946	0.9993

Aus dieser resultiert über die in D aufgetragenen Endvolumina (V_e), die bei vollständiger Ausnützung des Behälters V_{max} entsprechen, die spezifische Aktivität. Über die höchstzulässigen Konzentrationswerte zur Beseitigung flüssiger radioaktiver Abfälle gemäss den gesetzlichen Bestimmungen wird in

Tabelle III

Korrekturfaktoren, mit denen die in Tabelle I ermittelten Aktivitätswerte multipliziert werden müssen, wenn die Aktivitätszugaben je Periode fraktioniert erfolgen, d. h. die Einzelaktivitäten 50 mCi : n betragen; Periodenlänge beliebig ($h = t_p/\tau$, $l = t_{per}/\tau$)

h		n						
		2	3	4	5	8	11	14
	0.1250	0.9788	0.9787	0.9787	0.9787	0.9787	0.9787	0.9787
	0.2500	0.9391	0.9384	0.9382	0.9381	0.9379	0.9379	0.9378
	0.5000	0.8692	0.8659	0.8648	0.8643	0.8635	0.8633	0.8631
	1.0000	0.7611	0.7482	0.7440	0.7418	0.7390	0.7379	0.7373
0,0625	2.0000	0.6305	0.5907	0.5772	0.5704	0.5617	0.5583	0.5564
	4.0000	0.5326	0.4402	0.4075	0.3911	0.3700	0.3617	0.3572
	8.0000	0.5020	0.3560	0.2973	0.2674	0.2292	0.2143	0.2064
	16.0000	0.5000	0.3347	0.2565	0.2135	0.1575	0.1360	0.1248
	0.2500	0.9585	0.9582	0.9581	0.9581	0.9580	0.9580	0.9579
	0.5000	0.8856	0.8831	0.8823	0.8818	0.8813	0.8811	0.8810
	1.0000	0.7726	0.7612	0.7574	0.7555	0.7530	0.7521	0.7515
0,1250	2.0000	0.6363	0.5983	0.5854	0.5789	0.5707	0.5674	0.5656
	4.0000	0.5341	0.4431	0.4109	0.3947	0.3740	0.3653	0.3614
	8.0000	0.5021	0.3565	0.2982	0.2683	0.2304	0.2156	0.2077
	16.0000	0.5000	0.3347	0.2565	0.2136	0.1578	0.1362	0.1251
	0.5000	0.9204	0.9193	0.9189	0.9187	0.9185	0.9184	0.9183
	1.0000	0.7973	0.7886	0.7857	0.7842	0.7823	0.7816	0.7812
	2.0000	0.6487	0.6142	0.6025	0.5967	0.5892	0.5863	0.5846
0,2500	4.0000	0.5372	0.4490	0.4179	0.4023	0.3823	0.3744	0.3702
	8.0000	0.5023	0.3576	0.2998	0.2703	0.2328	0.2181	0.2104
	16.0000	0.5000	0.3348	0.2567	0.2140	0.1583	0.1368	0.1257
	1.0000	0.8536	0.8493	0.8479	0.8472	0.8463	0.8460	0.8458
0,5000	2.0000	0.6768	0.6494	0.6402	0.6356	0.6296	0.6273	0.6260
	4.0000	0.5442	0.4619	0.4331	0.4186	0.4001	0.3928	0.3888
	8.0000	0.5028	0.3599	0.3034	0.2745	0.2379	0.2235	0.2159
	16.0000	0.5000	0.3349	0.2572	0.2146	0.1593	0.1381	0.1270
	2.0000	0.7500	0.7357	0.7309	0.7285	0.7254	0.7242	0.7236
1,0000	4.0000	0.5625	0.4929	0.4688	0.4567	0.4412	0.4350	0.4317
	8.0000	0.5039	0.3654	0.3114	0.2840	0.2490	0.2353	0.2281
	16.0000	0.5000	0.3352	0.2581	0.2161	0.1616	0.1406	0.1297
	4.0000	0.6250	0.5833	0.5692	0.5621	0.5531	0.5494	0.5475
2,0000	8.0000	0.5078	0.3802	0.3320	0.3077	0.2766	0.2644	0.2579
	16.0000	0.5000	0.3360	0.2602	0.2194	0.1667	0.1464	0.1358
	8.0000	0.5313	0.4375	0.4042	0.3875	0.3661	0.3577	0.3531
4,0000	16.0000	0.5001	0.3386	0.2667	0.2286	0.1798	0.1610	0.1511
8,0000	16.0000	0.5020	0.3555	0.2965	0.2664	0.2281	0.2131	0.2052

Tabelle IV

Relative Veränderung der Endaktivität bei verschiedenen Periodenlängen t_{per} bezogen auf $t_{per} = 24$ h (τ als Parameter)

t_{ges}	τ [h]	t_{per} [h]									
		3	6	12	24	48	96	192	384	768	
	1.5	1.3333	1.0667	1.0039	1.0000	1.0000	1.0000	1.0000	1.0000	1.0000	
	3.0	1.9922	1.3281	1.0625	1.0000	0.9961	0.9961	0.9961	0.9961	0.9961	für
	6.8	3.2008	1.8750	1.2500	1.0000	0.9412	0.9375	0.9375	0.9375	0.9375	t_{ges} =
	12.0	4.7139	2.5607	1.5000	1.0000	0.8000	0.7529	0.7500	0.7500	0.7500	const.
	24.0	6.0244	3.1426	1.7071	1.0000	0.6667	0.5333	0.5020	0.5000	0.5000	
	48.0	6.9084	3.5290	1.8409	1.0000	0.5858	0.3905	0.3124	0.2940	0.2929	
	96.0	7.4251	3.7527	1.9170	1.0000	0.5432	0.3182	0.2121	0.1697	0.1597	
	192.0	7.7048	3.8733	1.9576	1.0000	0.5126	0.2834	0.1660	0.1107	0.0885	
	384.0	7.8504	3.9358	1.9786	1.0000	0.5108	0.2665	0.1448	0.0848	0.0565	
	768.0	7.9247	3.9677	1.9892	1.0000	0.5054	0.2582	0.1347	0.0732	0.0429	
	1536.0	7.9622	3.9838	1.9946	1.0000	0.5027	0.2541	0.1298	0.0677	0.0368	
	3072.0	7.9811	3.9919	1.9973	1.0000	0.5014	0.2520	0.1274	0.0651	0.0339	
	6	1.6067	1.4118	1.1765	1.0000	0.9449	0.9412	0.9412	0.9412	0.9412	
	12	1.4727	1.3657	1.2000	1.0000	0.8500	0.8031	0.8000	0.8000	0.8000	
2	24	1.2780	1.2273	1.1381	1.0000	0.8333	0.7083	0.6693	0.6667	0.6667	
	48	1.1467	1.1230	1.0784	1.0000	0.8787	0.7322	0.6224	0.5881	0.5858	
	96	1.0748	1.0634	1.0413	1.0000	0.9273	0.8143	0.6790	0.5772	0.5453	
	192	1.0377	1.0321	1.0212	1.0000	0.9603	0.8905	0.7825	0.6521	0.5543	für
	6	2.4007	1.7578	1.2451	1.0000	0.9412	0.9375	0.9375	0.9375	0.9375	$\frac{t_{ges}}{t_{per}}$ =
	12	2.3662	1.9280	1.4118	1.0000	0.8031	0.7559	0.7530	0.7529	0.7529	
	24	1.8821	1.6761	1.3657	1.0000	0.7083	0.5689	0.5354	0.5333	0.5333	const.
4	48	1.4655	1.3782	1.2273	1.0000	0.7322	0.5187	0.4166	0.3921	0.3905	
	96	1.2325	1.1941	1.1230	1.0000	0.8148	0.5966	0.4226	0.3394	0.3195	
	192	1.1153	1.0975	0.0634	1.0000	0.8905	0.7256	0.5313	0.3763	0.3023	
	6	3.0008	1.8677	1.2500	1.0000	0.9412	0.9375	0.9375	0.9375	0.9375	
	12	3.5355	2.4007	1.4942	1.0000	0.0000	0.7530	0.7500	0.7500	0.7500	
	24	3.0240	2.3662	1.6867	1.0000	0.6693	0.5354	0.5039	0.5020	0.5020	
8	48	2.1583	1.8821	1.4727	1.0000	0.6224	0.4166	0.3332	0.3136	0.3124	
	96	1.5751	-1.4655	1.2780	1.0000	0.6790	0.4226	0.2828	0.2263	0.2130	
	192	1.2789	1.2325	1.1467	1.0000	0.7825	0.5313	0.3307	0.2213	0.1771	
	6	3.1883	1.8750	1.2500	1.0000	0.9412	0.9375	0.9375	0.9375	0.9375	
	12	4.4193	2.5507	1.5000	1.0000	0.8000	0.7529	0.7500	0.7500	0.7500	
	24	4.5184	2.9462	1.7005	1.0000	0.6667	0.5333	0.5020	0.5000	0.5000	
16	48	3.4677	2.6571	1.7326	1.0000	0,5881	0.3921	0.3136	0.2952	0.2940	
	96	2.3197	2.0015	1.5336	1.0000	0.5772	0.3394	0.2263	0.1810	0.1704	
	192	1.6345	1.5126	1.3051	1.0000	0.6521	0.3763	0.2213	0.1475	0.1180	
	6	3.2008	1.8750	1.2500	1.0000	0.9412	0.9375	0.9375	0.9375	0.9375	
	12	4.6955	2.5606	1.5000	1.0000	0.0000	0.7529	0.7500	0.7500	0.7500	
32	24	5.6479	3.1303	1.7071	1.0000	0.6667	0.5333	0.5020	0.5000	0.5000	
	48	5.1811	3.3085	1.8337	1.0000	0.5858	0.3905	0.3124	0.2940	0.2929	
	96	3.7274	2.8256	1.8042	1.0000	0.5453	0.3195	0.2130	0.1704	0.1604	
[d]	192	2.4071	2.0657	1.5661	1.0000	0.5543	0.3023	0.1771	0.1180	0.0944	

E der notwendige Abklingfaktor bestimmt. Daraus ergibt sich in F die erforderliche Abklingzeit entweder direkt in Tagen bei Verwendung der Kurven für verschiedene Halbwertszeiten oder als Verhältnis t_a/τ über die ebenfalls eingezeichnete Abkling-Gerade.

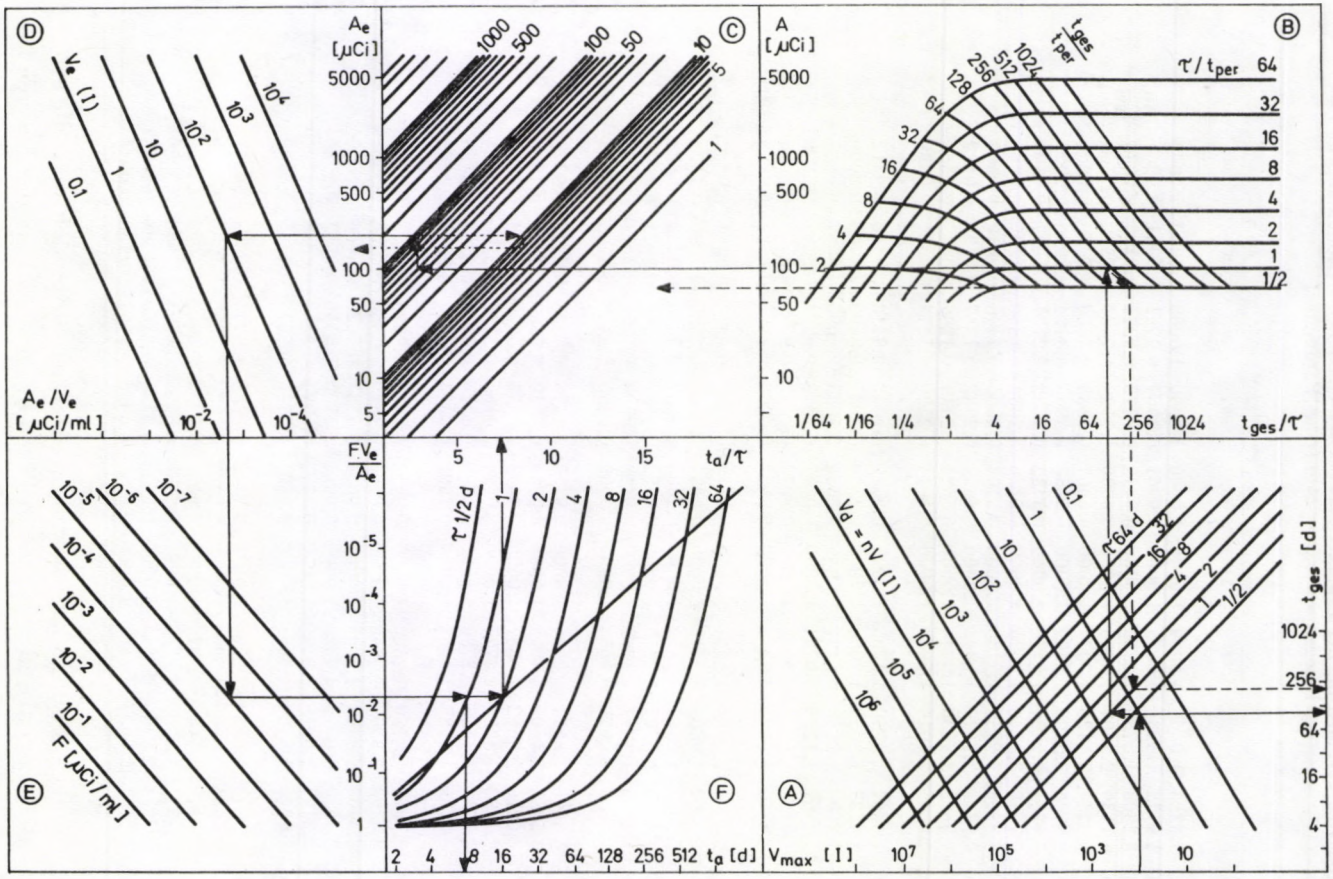

Abb. 3. Beispiel zur Handhabung des Nomogramms: Behältervolumen $V_{max} = 100$ l, Tagesvolumen $V_d = 1$ l, Tagesaktivität = 100 μCi, Periodendauer $t_{per} = 1$d, einmalige Zugabe pro Tag ($n = 1$), Halbwertszeit $\tau = 1$ d, Freigrenze $= 10^{-5}$ μCi/ml. Angedeutete Änderungen von t_{per} bzw. mehrmalige Zugaben pro Tag: t_{per} auf 48 Stunden vergrössert (——), 5-malige Zugabe pro Tag, $t_p = 6$ h, $A_0 = 20$ μCi (. . . . .).

Bei Kenntis der erforderlichen Grössen kann prinzipiell an jeder Stelle des Nomogramms begonnen werden.

Anhand eines Beispiels (Abb. 3) soll die Verwendung des Nomogramms veranschaulicht werden. Dazu wurden folgende Daten verwendet: $V_{max} = 100$ l, $V_d = 1$ l, A = 100 μCi, $t_{per} = 1$ d, $n = 1$, $\tau = 1$ d, $R = 10^{-5}$ μCi/ml. Daraus ergibt sich: $t_{ges} = 100$ d, $A_e = 200$ μCi und $t_a = 7{,}5$ d.

Die folgenden Fälle skizzieren, ausgehend von obigem Fall (durchgehende Linie), die Änderung verschiedener Parameter und sind zu Wahrung der Übersichtlichkeit nur in ihren wesentlichen Punkten angedeutet und müssten analog dem beschriebenen Beispiel vollendet werden:

a) Änderung von t_{per} auf 48 Stunden (strichlierte Linie) ergibt $t_{ges} = 200$ d

b) fünfmalige Zugabe pro Tag, $t_p = 6$ h, $t_{per} = 1$ d, $A_0 = 20$ μCi, $A = 100$ μCi (punktierte Linie) ergibt mittels des Korrekturfaktors aus Tab. III (= 0.7842) $A_e = 157$ μCi.

Diskussion

Wenn t_{per} ungleich einem Tag ist, dann kann bei einmaliger Zugabe pro Periode sowohl — wie im angeführten Beispiel gezeigt — die rein graphische Methode als auch ein Korrekturfaktor aus Tabelle IV in Kombination mit dem zeichnerischen Verfahren verwendet werden. Um bei mehrmaliger Zugabe pro Tag die Multiplikation mit den Faktoren gemäss Tabelle II und III zu umgehen, kann als eine für den Strahlenschutz ausreichende Näherung die Summe der Aktivitäten der Einzelzugaben als Tagesaktivität verwendet werden. Der dabei erhaltene Wert für A und A_e sowie t_a ist etwas höher als bei Verwendung der Korrekturfaktoren, da das Abklingen der Aktivität zwischen den einzelnen Zugaben nicht berücksichtigt wird (in Abb. 1 ist erkennbar, dass die Tagesaktivität kleiner als die Summe der Einzelzugaben ist).

Aus der Kurvenschar B des Nomogramms ist ersichtlich, dass bei Vergrösserung der Periodendauer und gleichbleibender Befüllzeit die erreichte Endaktivität abnimmt, wobei das Volumen des Behälters nicht voll ausgenützt wird. Weiters zeigt sich aus dieser Kurve, dass die Sättigungsaktivität nach jeweils 10 Halbwertszeiten erreicht wird.

Einen Sonderfall stellt die Unterteilung einer Periode in viele Zugaben dar, sodass schliesslich ein kontinuierlicher Zufluss von Abwässern, der nur durch eine nächtliche Pause unterbrochen ist, erreicht wird. Dabei strebt n gegen ∞ und t gegen 0. In Tab. V sind die Korrekturfaktoren, mit denen die Aktivitätswerte in C multipliziert werden müssen, für den Fall einer quasi-kontinuierlichen Zugabe und einer Periodendauer von 24 Stunden bei verschieden langen Pausen angeführt. Dabei wurde n mit 20 000 und t mit 3.24 Sekunden angenommen.

Tabelle V

Korrekturfaktoren für die Endaktivität bei kontinuierlichem Zufluss von radioaktiver Flüssigkeit in den Tank, der je Periode nur durch eine Pausenzeit t_p unterbrochen wird ($n = 20{,}000$, $t = 3{,}24$ s, $t_{per} = 24$ h)

t_p [h]	τ [h]						
	3	6	12	24	48	96	192
1	0.1873	0.3500	0.5533	0.7307	0.8509	0.9214	0.9596
3	0.2045	0.3758	0.5793	0.7498	0.8626	0.9279	0.9630
5	0.2250	0.4049	0.6071	0.7696	0.8745	0.9344	0.9665
7	0.2496	0.4378	0.6369	0.7902	0.8867	0.9411	0.9698
9	0.2795	0.4751	0.6689	0.8116	0.8991	0.9477	0.9734
11	0.3164	0.5176	0.7032	0.8337	0.9117	0.9545	0.9769
13	0.3625	0.5661	0.7401	0.8567	0.9246	0.9613	0.9804
15	0.4208	0.6218	0.7798	0.8806	0.9377	0.9682	0.9840
17	0.4956	0.6858	0.8225	0.9054	0.9511	0.9752	0.9875
19	0.5930	0.7596	0.8685	0.9312	0.9648	0.9821	0.9910
21	0.7213	0.8451	0.9182	0.9579	0.9786	0.9892	0.9947
23	0.8929	0.9444	0.9717	0.9857	0.9928	0.9965	0.9983

Es ist klar, dass ein graphisches Verfahren dieser Art schon allein aus zeichen- und drucktechnischen Gründen hinsichtlich seiner Genauigkeit limitiert ist. Wenngleich auch darauf geachtet wurde, durch die Wahl der einzelnen Parameter eng beieinanderliegende Kurven zu vermeiden oder wie in Kurvenschar F noch eine zweite Möglichkeit zur Ermittlung der Abklingzeit anzubieten, können schliesslich auch Masstab und Kurvendichte einerseits sowie auch obere und untere Grenzen der verschiedenen Parameter andererseits nicht beliebig geändert werden. Eine Interpolation wird daher immer wieder vonnöten sein. Im allgemeinen sollte aber eine recht gute Abschätzung der Werte möglich sein. Zur Verbesserung der Genauigkeit bei Verwendung des Nomogramms, insbesondere zur Wahrung der Achsenparallelität der Hilfslinien, sollte mit einem auf das Nomogramm aufgehefteten, transparenten Millimeterpapiers gearbeitet werden.

Dank

Für die Anregung zu dieser Arbeit wird dem Vorsitzenden der Arbeitsgruppe "Radioaktiver Abfall" des Österr. Normungsinstituts (Univ. Prof. Dr. K. BUCHTELA) gedankt. Hofrat Dr. H. OLEXINSKI vom Amt der Kärntner Landesregierung und Univ. Prof. Dr. O. BOBLETER vom Institut für Radiochemie wird für die Ermöglichung der Durchführung und für Ihr Interesse an dieser Arbeit ebenfalls gedankt.

LITERATUR

1. E. TSCHIRF, Radionuklide in Technik und Medizin, Daten zum Strahlenschutz, Atominstitut der Österr. Hochschulen, Wien, AIAU—77602, 1977.
2. International Commission on Radiological Protection (ICRP) Publ. 5, Report of Committee V, Handling and Disposal of Radioactive Materials in Hospitals and Medical Research Establishments, Pergamon Press, Oxford, 1964.
3. J. B. KRAWCZINSKI, Radioaktive Abfälle, Thiemig Taschenbuch, Band 27, München 1967.
4. IAEA, Basic Factors for the Treatment and Disposal of Radioactive Wastes, Safety Series No. 24, Wien, 1967.
5. B. MOSER, Österreichische Strahlenschutzverordnung, BGBl. Nr. 47/1972.

Acta Physica Academiae Scientiarum Hungaricae, Tomus 52 (3—4), pp. 469—473 (1982)

ACTIVITY DETERMINATION IN SAMPLES OF ISOTOPE MIXTURES BY USING SUM PEAKS IN Ge (Li) SPECTRA

I. URAY, I. TÖRÖK and E. GYARMATI

INSTITUTE OF NUCLEAR RESEARCH OF THE HUNGARIAN ACADEMY OF SCIENCES
4001 DEBRECEN, HUNGARY

The basic concepts of the absolute activity determination based on sum peaks are briefly discussed. A possible extension of the method to measure the absolute activities of monoenergetic gamma sources is also given.

Introduction

The energies of coinciding gamma rays absorbed in a detector giving energy proportional signals are added up. Besides photopeaks, the spectrum also contains sum peaks as a result of coincidence. These sum peaks facilitate absolute activity measurements.

The basic formula for the absolute activity of a sample giving gamma rays in coincidence (derived by BRINKMAN et al [1]) is:

$$N = R + T = \frac{A_1 A_2}{A_{12}} + T\,, \tag{1}$$

where N is the absolute activity of the source, A_1 and A_2 are the measured count rates in the coinciding gamma peaks, A_{12} is the measured count rate in the sum peak, T is the area under the whole spectrum divided by the measuring time, and R is defined by Eq. (1). In the scintillation era the measurements were done in the well of well-type scintillators, so the dominant term in (1) was T. The poor resolution of the scintillation detectors made the determination of the peak area uncertain while these detectors have high efficiency by approximately 4π geometry. This technique was applicable only for the measurement of single isotopes. Using semiconductor detectors it is possible to perform the mesurements far from the detector, when the dominant term is R, which is completely derived from the measured peaks, and the T term is only a minor correction [2]. This fact makes it possible to use the method for multiisotopic sources.

Let us briefly enumerate some advantages of this absolute activity measurement method, using modern detectors [3]: a) The measurable range covers several orders of magnitude, from about 10 Bq upwards. b) The formula

uses directly the raw measured quantities (A_1, A_2, A_{12}, T). c) No standard preparates are required. d) One saves instrumentation and time by getting the coincidence in a single detector, using a simple spectrometer instead of a complicated multiparameter system. e) No efficiency and absorption data are required. f) For pointlike sources the method is rather insensitive to the geometry (distance and angle between source and detector) [4]. g) The method can be used even for extended sources with distributed activity supposing that the source can be arranged approximately on the surface of a sphere, concentric with the detector. h) Due to the good resolution of semiconductor detectors, it is possible to determine the simultaneous absolute activity for several different isotopes in the same sample, provided that all the isotopes give distinct sum peaks. i) The calculation is simple.

Some drawbacks of the method are as follows. a) Unless at least one of the coinciding gamma ray lines is of 100 percent abundance, the basic formula needs correction for branching. b) Angular correlation effect should be considered. c) Clear sum peaks should be available. It is necessary to take the cross-over transition into account and, in any case, a proper dead time and pile up correction are needed against counting losses. d) A fundamental limitation is that the sum peak itself is necessary. This problem emerges with every isotope where the second, third etc. gamma transitions are very weak, or do not exist at all!

The combined sum peak method

In many practical cases the activity of isotopes having only a single gamma-ray should be measured. These isotopes have, of course, no sum peak, consequently, the sum peak method is not directly applicable [2].

In this paper we should like to show that in such cases the activity can be determined on the basis of the sum peak method.

1.) If the sample to be measured has at least one component with coinciding gamma rays, the absolute activity can be determined for this component which may appear further as an internal standard. This procedure compares the intensities of photopeaks, therefore the efficiency and the absorption effects should also be taken into account.

Such a combined absolute-relative method was applicable in the case of the G-2 activity intercomparison mesurement organized by the International Atomic Energy Agency. The task was to measure the activity components of five mixed sources, each composed of ^{57}Co, ^{133}Ba, ^{54}Mn and ^{65}Zn, having different activities. While the ^{133}Ba isotope has more gamma rays in coincidence, its absolute activity was easy to determine by the help of the sum peak method. As a second step this activity was used for the relative activity determination by the comparison of photopeak intensities. The relative efficiency of the

Table I

Measured and nominal activities of the G-2 activity intercomparison standards

Source	^{133}Ba		^{57}Co		^{54}Mn		^{65}Zn	
	A_{sum} [kBq]	A_0 [kBq]	A_{meas} [kBq]	A_0 [kBq]	A_{meas} [kBq]	A_0 [kBq]	A_{meas} [kBq]	A_0 [kBq]
MIXO8-1	20.5	21.2	15.6	16.8	22.0	23.4	44.6	46.5
MIXO8-2	60.2	63.0	44.1	48.5	62.4	63.0	126	132
MIXO8-3	132	129	96.2	99.3	130	129	264	258
MIXO8-4	198	210	144	162	206	222	427	451
MIXO8-5	270	298	194	226	274	312	562	627

detector, and the probabilities of gamma-ray emission were to be taken into consideration (Table I). As it is seen all measured values are in good agreement with the nominal activities.

2.) If the sample to be measured has no component with coinciding gammas, the task is somewhat more complicated. An external source should be placed close to the sample for standardization. Using the photopeak efficiency calibration curve of the detector, the other activities can be determined relative to that of the standard. This part of the procedure is of course very sensitive to the measuring geometry. If they are significant, absorption corrections also must be made.

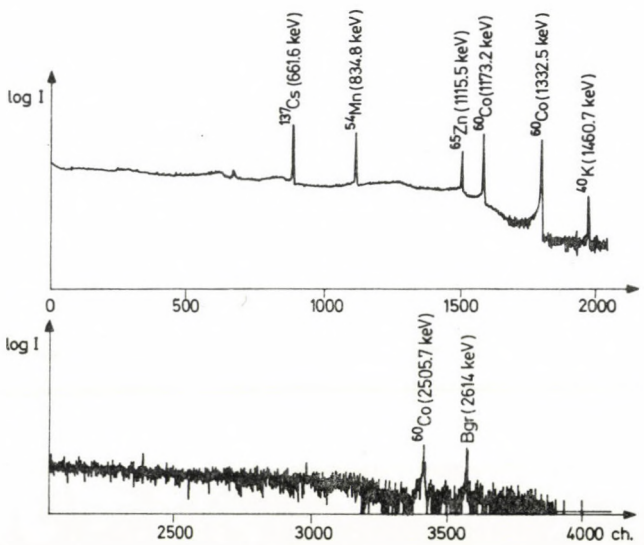

Fig. 1. The complex spectrum of ^{60}Co, ^{54}Mn, ^{137}Cs and ^{65}Zn standard sources.

Table II

Measured and nominal absolute activities using the parallel and the serial method

Isotopes	Nominal activity [kBq]	Measured activity [kBq]		Calculation method
		"Parallel" method	"Serial" method	
^{60}Co	8.89	8.95	9.15	from sum peak
^{137}Cs	9.83	9.31	9.55	relative
^{54}Mn	8.11	7.61	7.47	to ^{60}Co
^{65}Zn	5.22	5.55	5.24	

To test this method we took a collection of standard gamma ray sources* of small volume and put them tightly together, so approximating a point like mixed isotope source, which was measured by a Ge(Li) detector of 12% efficiency. To measure the absolute activity the ^{60}Co spectrum was measured in "parallel" with the spectra to be measured. Fig. 1 shows the spectrum obtained in this way. Table II gives the nominal and mesured absolute activities of the sources.

Table II shows that the measured activity values are approaching the nominal activities quite well. At the same time, the influence of the geometrical uncertainty can be seen in the larger deviation of the value pairs.

In one respect the combined absolute-relative sum peak method explained above needs a relative photopeak efficiency curve (Fig. 2) for the applied geometry. On the other hand, to assess the absolute activity we have to know the T area as a part of the whole spectrum, belonging to the standardising isotope. While it is impossible to determine it from a complex spectrum having more components, it is useful to measure the peak-to-total ratio separately,

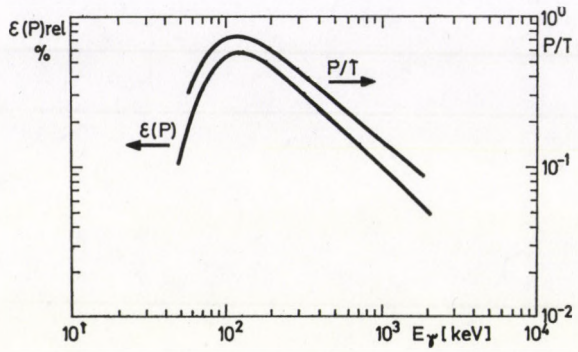

Fig. 2. Peak-to-total and relative efficiency curve of the detector.

* The sources were made available and certified by the National Office of Measures (OMH)

using isotopes emitting monoenergetic gamma rays at different energies. This curve in Fig. 2 may help us to calculate Eq. (1). Otherwise the T term may be measurable, if we have the different isotopes in separated sources, and measure all of their spectra successively in the same, strictly known measuring geometry ("serial method", see last column in Table II).

The estimated error of the measured activity values is generally 5—10%, due to some statistical errors in the evaluation of spectra, positioning errors, the uncertainty of efficiency and peak-to-total curves, angular correlation ambiguities, etc.

Conclusions

The sum-peak coincidence method, using a simple spectrometer consisting of a high resolution, large volume (high efficency) Ge(Li) detector and a multichannel analyser, is suitable to measure absolute activity in a flexible way. Coincidence events without any coincidence circuit can be measured by this method by using a single detector only. As an absolute method, it gives the activity of the measured isotopes without any intensity standard sources. It seems to fit well into health physics laboratories, where it is often necessary to measure many kinds of isotopes over a very large range of intensity.

While the original method can only be used for isotopes having two coinciding gamma rays, the combined absolute-relative method discussed in this paper can also be applied to monoenergetic gamma-ray sources. Activity determination is possible in many cases with an uncertainty less than 10%. In health physics practice such accuracy is sufficient in most cases. The method measures absolute activity in a very simple way, relatively quickly and very cheaply.

REFERENCES

1. G. A. Brinkman, A. H. W. Aten, Jr. and J. Th. Veenboer, Int. J. Appl. Rad. Isotopes **14,** 153, 1963
2. I. Török and I. Uray, The Second International Conference on Low-Level Counting, The High Tatras, Strbske Pleso, Czechoslovakia, 24—28 November 1980, p. 55 (to be published in the Proceedings).
3. I. Török, I. Uray, P. Bornemisza-Pauspertl and P. Kovács, ATOMKI Bull., **22,** 301, 1980.
4. I. Török and I. Uray, Nucl. Instr. Meth. **189,** 635, 1981.

Acta Physica Academiae Scientiarum Hungaricae, 52 (3—4), pp. 475—477 (1982)

DIE ZULASSUNG VON BAUARTEN NACH DEM ÖSTERREICHISCHEN STRAHLENSCHUTZGESETZ

J. K. HOHENBERG

BUNDESMINISTERIUM FÜR SOZIALE VERWALTUNG
1030 WIEN, ÖSTERREICH

In Österreich sind die mit den umschlossenen radioaktiven Stoffen arbeitenden Geräte und die Strahleneinrichtungen von der Strahlenschutzbehörde genehmigt. Bei diesen Geräten ist die Dosisleistung in 10 cm Abstand von der Oberfläche in Wert 10^{-6} Sv/h maximiert. Es werden die Erfahrungen in Zusammenhang mit der Zulassung von Bauarten von Geräten zum Umgang mit ionisierenden Strahlen vorgezeigt.

Die gesetzlichen Bestimmungen auf dem Gebiete des Strahlenschutzes sehen die Zulassung von Bauarten von Geräten, die umschlossene radioaktive Stoffe enthalten, oder von Strahleneinrichtungen vor. Der Gesetzgeber berücksichtigt zum Teil auch ein von diesen Geräten ausgehendes Gefährdungspotential und unterscheidet zwischen Geräten, deren Dosisleistung in 10 cm Entfernung von der Oberfläche 10^{-6} Sv/h unterschreitet oder überschreitet.

Überschreitet bei Geräten die Dosisleistung in 10 cm Abstand von der Oberfläche 10^{-6} Sv/h nicht, ist deren Bauart von der Behörde zuzulassen, wenn die in den Geräten enthaltenen radioaktiven Stoffe ständig von einer Hülle derart umschlossen sind, dass bei üblicher betriebsmässiger Beanspruchung ein Austritt radioaktiver Stoffe mit Sicherheit verhindert wird. Diese Formulierung brachte bei der Zulassung von Ionisationsrauchmeldern, insbesondere solchen mit Radium-226 als radioaktive Strahlenquelle naturgemäss Probleme mit sich. Weiters wird für Geräte, die radioaktive Stoffe enthalten, die nicht von der Bewilligungspflicht ausgenommen sind, bestimmt, dass derartige Geräte nur nach Zulassung ihrer Bauart in den inländischen Verkehr gebracht und im Inland verwendet werden dürfen. Diese Bestimmungen zeigen den Wunsch des Gesetzgebers auf, Geräten die radioaktive Stoffe enthalten, auch dann, wenn deren Dosisleistung an der zugänglichen Oberfläche relativ gering ist, wesentlich grössere Beachtung zu schenken, als Geräten, die als Strahlenquelle z.B. eine Röntgenröhre besitzen. Für die Zulassung von Strahleneinrichtungen ist nur die Dosisleistungsgrenze massgebend.

Für die Zulassung der Bauart von Geräten, deren Dosisleistung den Grenzwert von 10^{-6} Sv/h in 10 cm Entfernung von der Oberfläche überschreitet, wird gefordert, dass diese entsprechend den geltenden Strahlenschutzbestimmungen ausgeführt sind, hinsichtlich ihrer betriebssicheren Ausführung den anerkannten Regeln der Technik entsprechen und eine sichere Bedienung ermöglichen. Weiters wird für Geräte, die radioaktive Stoffe enthalten gefordert, dass nur umschlossene radioaktive Stoffe eingebaut werden dürfen.

Auf Grund gesetzlicher Bestimmungen sind bauartzugelassene Geräte deren Dosisleistung den Grenzwert von 10^{-6} Sv/h nicht überschreitet von der Bewilligungspflicht ausgenommen. Wird der angegebene Grenzwert überschritten, unterliegen die Geräte der Bewilligungspflicht, jedoch kann anlässlich der Zulassung der Bauart eine Ausnahme von der Bewilligungspflicht ausgesprochen werden. Alle Geräte deren Bauart zugelassen wurde, unterliegen einer Meldepflicht.

Die praktische Bedeutung der Zulassung von Bauarten liegt darin, dass die Verwendung von Geräten, die radioaktive Stoffe enthalten, oder von Strahleneinrichtungen durch die beim üblichen betriebsmässigen Umgang eine Gefährdung von Menschen nicht zu erwarten ist, erleichtert werden soll. Dies trifft sicher für die Zulassungen von Geräten zu, deren Dosisleistung den Grenzwert von 10^{-6} Sv/h nicht überschreitet, obwohl hier bei einer Novellierung der gesetzlichen Bestimmungen sicher auch noch andere Gefährdungsmomente, als nur der Grenzwert einer Dosisleistung und die ausschliessliche Berücksichtigung des betriebsmässigen Umganges heranzuziehen wären. Ergaben sich in der Praxis bei einem typischen Vertreter dieser Geräteart, dem Ionisationsrauchmelder, Schwierigkeiten nicht so sehr bei betriebsmässigem Gebrauch als vielmehr bei der erforderlichen Wartung und eventuell notwendigen Reinigung der Strahlenquellen sowie bei Zwischenfällen, wie Bränden. Die erwähnten Ionisationsrauchmelder stellen sowohl im Hinblick auf die Zahl der bisherigen Bauartzulassungen als auch hinsichtlich der Zahl der in Verkehr gebrachten Geräte die bedeutendste Gruppe dar. Es wurden bisher 19 verschiedene Geräte zugelassen, wobei die Aktivität der verwendeten Strahlenquellen zwischen 18.5 kBq und 2.7 MBq bei Americium-241 schwankt. Der einzige zugelassene Melder mit einer Radium-226 Strahlenquelle weist eine Aktivität von 2.2 kBq auf. Zu der relativ hohen Aktivität von 2.7 MBq wird bemerkt, dass es sich bei diesen Geräten um den ersten zugelassenen Ionisationsrauchmelder handelt, der heute für die Errichtung neuer Anlagen nicht mehr eingesetzt wird, sondern nur mehr als Austauschmelder für bestehende Brandmeldeanlagen zur Verfügung steht. Für die Zukunft wird sicher angestrebt werden, Aktivitäten von mehr als einigen zig kBq nicht mehr zuzulassen. Auch wird genau beobachtet werden, wie international die Verwendung von Radium-226 beurteilt wird. Von diesen 19 zugelassenen Ionisationsrauchmeldern sind 15 Geräte für den Einbau in geschlossene Brandmeldeanlagen vorgesehen, 4 Geräte als sogenannte Einzel- oder Heimmelder für die Verwendung in Wohnungen, Einfamilienhäusern, Booten, Wohnwagen etc. vorgesehen. Während von der erstgenannten Kategorie bisher etwa 300 000 Stück in Verkehr gebracht wurden, sind es von den sogenannten Heimmeldern wahrscheinlich derzeit kaum mehr als einige hundert Stück.

Auch wurden fünf weitere Gerätetypen, wie Dicken- und Dichtemessgeräte, Röntgenfluoreszenzeinrichtungen sowie radioaktive Static-Eliminatoren

zugelassen; bei diesen Geräten wird der Dosisleistungsgrenzwert von 10^{-6} Sv/h ebenfalls nicht überschritten. Hievon wurden jeweils nur geringe Stückzahlen in den Verkehr gebracht.

Die Zulassung der Bauart von Geräten, deren Dosisleistung in 10 cm Entfernung von der Oberfläche mehr als 10^{-6} Sv/h beträgt, hat in Verbindung mit einer jeweils ausgesprochenen Ausnahme von der Bewilligungspflicht grosse Bedeutung für zahnmedizinische Röntgeneinrichtungen. So wurden bisher 13 verschiedene Gerätetypen zugelassen. Die Zahl der auf Grund dieser Zulassung in Verkehr gebrachten Geräte beträgt etwa 1500.

Neben zahnmedizinischen Geräten wurden auch für drei Isotopenarbeitsgeräte zur zerstörungsfreien Werkstoffprüfung Bauartzulassungen erteilt. Hievon sind etwa 50 Stück in Verkehr gebracht worden. Darüber hinaus wurden für acht weitere Mess- und Prüfeinrichtungen, wie Flächengewichtsmesseinrichtungen, Feuchte-Dichte-Messeinrichtungen Zulassungen mit einer Ausnahme von der Bewilligungspflicht erteilt. Die in Verkehr gebrachten Stückzahlen sind vergleichsweise gering.

Auch wurden fünf verschiedene Strahlenschutzbehälter für Füllstandskontrolleinrichtungen zugelassen, wobei jedoch im Hinblick auf die Vielfalt der Anwendungsmöglichkeiten in diesen Fällen keine Ausnahme von der Bewilligungspflicht erteilt wurde.

Auf Grund der bisherigen Erfahrung kann zusammenfassend gesagt werden, dass die Zulassung von Bauarten eine geeignete Möglichkeit darstellt, Geräte, die in grösseren Stückzahlen in Verkehr gebracht werden und einer weitgehend gleichartigen Verwendung unterliegen, einem einfachen und kostensparenden Verwaltungsverfahren zu unterwerfen, wobei als Beispiele vor allem die Ionisationsrauchmelder und die zahnmedizinischen Röntgeneinrichtungen dienen sollen.

Abschliessend soll auf eine weitere Besonderheit bauartzugelassener Geräte hingewiesen werden. Geräte oder Anlagen zum Umgang mit ionisierenden Strahlen, die auf Grund einer Bewilligung der örtlich zuständigen Behörde betrieben werden, unterliegen einer jährlichen Überprüfung durch die Bewilligungsbehörde. Für bauartzugelassene Geräte ist eine derartige Überprüfung nicht vorgesehen. Dieser Punkt wird aus Anlass einer eventuellen Novellierung der strahlenschutzrechtlichen Vorschriften neu zu überdenken sein, da zum Teil doch Mängel festgestellt werden mussten, die anlässlich einer zumindest einmaligen Überprüfung der Geräte nach ihrer Inbetriebnahme leicht abgestellt werden könnten.

Acta Physica Academiae Scientiarum Hungaricae, 52 (3—4), pp. 479—486 (1982)

INVESTIGATIONS ON MICROWAVE RADIATION EXPOSURE

T. PREDMERSZKY, L. BALLAY, E. BÖLÖNI, L. D. SZABÓ and L. VÁMOS

"FRÉDÉRIC JOLIOT-CURIE" NATIONAL RESEARCH INSTITUTE FOR RADIOBIOLOGY AND RADIOHYGIENE
1775 BUDAPEST, HUNGARY

The extensive use of microwave devices calls for the radiation control of equipment, work places and environment also in Hungary. Because of the lack of comprehensive knowledge about the biological effects of microwaves there exist no internationally accepted safety standards. The power density values measured at work places seldom exceed the level of $100\,\mu W/cm^2$ recommended in Hungary. Investigations were made with humans and animals. Several persons working in telecommunication for more than five years complained of headache, fatigue, irritability and some vegetative symptoms, but no expressed health damage was observed. Experiments on animals supplied new data about the thermal effects of microwaves on embryos, including effects on liver and brain. To solve the problems of microwave radiation protection Hungarian researchers have started interdisciplinary cooperation.

Introduction

The wide-spread use of equipment generating microwave radiation began during the 2nd World War. At the beginning, these procedures were thought to be harmless to the health and it was only in the early 50s that several papers were published about the biological effects of microwaves on man.

Man is exposed to electromagnetic radiation from both natural and man-made sources. The exposure from man-made sources is permanently increasing.

The term microwaves means that portion of the electromagnetic radiation spectrum which lies between the frequencies of 300 MHz and 300 GHz. In this range the quantum energy of the photon is not sufficient to cause ionization in the irradiated living system.

The effects of microwave radiation on a biological system can be divided into two major sections; thermal and non-thermal. Thermal effects in the living organism occur when the microwave energy is converted into heat causing hyperthermia and other biological responses at high exposure levels and the heat regulatory mechanism of the organism is not effective enough to eliminate them. Non-thermal effects occur when the molecular bonds are stressed or the biopolymers are enhanced or destroyed.

A detailed knowledge about the biological effects is needed to set an appropriate protection standard for working conditions.

The organs of the body most susceptible to thermal effects are the testicles and the eyes (Table I). The reduction in testicular function due to

Table I

Thermal-biological effects of microwaves

Frequency [MHz]	Wavelength [cm]	Site of major tissue effects	Major biological effects
10 000	3	Skin	Skin surface acts as reflector absorber with heating effects
10 000	3	Skin	Skin heating with sensation of warmth
10 000 to 3 300	3 to 10	Top layers of skin, lens of eye	Lens of eye and testicles particularly susceptible
10 000 to 1 000	3 to 30	Lens of eye	Critical wavelength band for eye cataracts and testicular damage
1 200 to 150	25 to 200	Internal body organs	Damage to internal organs from overheating
150	Above 200		Body is transparent to waves above 200 cm

Table II

Neurological effects

Clinical manifestation of chronic occupational exposure of humans to microwave radiation [25]

1. Bradycardia
2. Disruption of the endocrine-humoral process
3. Hypotension
4. Intensification of the activity of thyroid gland
5. Exhausting influences on the central nervous system
6. Decrease in sensitivity to smell
7. Increase in histamine content of the blood

Subjective complaints

1. Increased fatigability
2. Periodic or constant headaches
3. Extreme irritability
4. Sleepiness during work

the thermal effects at 10 mW/cm^2 appears to be temporary and probably reversible [1].

The possibility of damage to the eye is a very serious aspects of microwave radiation. The cataractogenic effect at 100 mW/cm^2 incident power density is well established in experimental animals. Because of the lack of blood vessels the crystalline lens of the eye is easily overheated, the lens becomes non-transparent with subsequent development of a subcapsular cataract and loss of vision.

Continuous and pulse modulated microwave exposures affect hemoglobin synthesis and red cell production. Several authors reported genetic effects and chromosome aberrations, too. Changes in the development of chick embryos and mammalian fetuses were also obtained by microwave exposure.

Many papers deal with the effects on the nervous system and behaviour (Table II). In experimental animals chronic and repeated exposures lead to disturbances in conditioned reflexes and to behavioural changes at incident power densities of 0.1—1 mW/cm^2.

Some authors reported on clinical evidence of the effect of chronic low-power-density microwave radiation. Their chief characteristics lie in their influence on the central and the vegetative nervous system [2].

Epidemiological studies report on subjective complaints e.g.: increased fatigability, periodical or constant headaches, extreme irritability and sleepiness [1].

The main difficulty lies in the complexity of the working environment — temperature and humidity variations in the working area, noise, disturbances in the normal rhythm of sleep and waking periods caused by work shifts.

The X-ray exposure originating from microwave generating tubes presents a small but unavoidable hazard. The shielding of the equipment makes no difficulties though it must not be removed.

In spite of the results of many experiments there is a serious disagreement about the application of the appropriate risk analysis.

Protection standards

In the USA, the United Kingdom and Canada the officially adopted threshold limit value is 10 mW/cm^2 for occupational exposures for workers and for people in the vicinity of microwave emitters. This value is based on the fact that the high power density of microwave can result in pathophysiological manifestations of thermal nature (Table III) [3].

The protection standards in the Soviet Union, Poland and Czechoslovakia are based not only on the thermal effects of microwaves but on the non-thermal effects and on the effects on the nervous system, too. According to the Soviet standard the intensity of microwave radiation at work places should not exceed 10 μW/(cm^2)/working day. The values of the Polish and Czechoslovakian standards lie in the same range.

Reports on the effects made on humans were issued in Hungary in the late 50s. The wide use of microwave devices actually started about 10 years ago. The safety regulations for telecommunication apparatuses issued in 1971 cover the radioprotection of microwave devices as well.

Table III

Radiofrequency standards for occupational exposure to continuous wave fields (working day)

Country	Radiation frequency [GHz]	RFR intensity [mW/cm²]
United States		
ANSI*	0.01—100	10
OSHA**	0.01—100	10
ACGIH***	0.1 —100	10
Great Britain	0.3 — 30	10
Canada	0.1 —100	10
		(1 proposed)
Sweden	0.3 — 3	1
Poland	0.03—300	0.2
Czechoslovakia	0.3 —300	0.025
U.S.S.R.	0.3 —300	0.01

* American National Standards Institute
** Occupational Safety and Health Administration
*** American Congress of Governmental Industrial Hygienists
Note: Some countries have more permissive intensities for shorter exposure times and more restrictive intensities for exposure of the general population.

The number of persons exposed to microwave radiation at the work places or in their vicinity amounts to a few thousand. In view of this, the competent Hungarian Health Authorities have made preparations for an adequate program to control equipment, work places and the environment and to draft the Hungarian Safety Standards on Microwave Radiation.

Investigations at work places

The first task was to control the radiation at work places in connection with broadcasting and television and to monitor the energy pollution in their environment. We had to supervise the manufacture of microwave apparatuses, the different industrial uses with special regard to drying processes and to plastic-curing and welding. Both in the catering industry and private kitchens the utilization of microwave ovens is spreading. We had to control ground-based radar equipment necessary for air traffic. A special use of radar apparatuses is the forecasting of hailstorms. Microwave diathermic devices are used in many Hungarian institutions of physicotherapy.

Table IV

Epidemiological tests on 450 persons working in telecommunication

Group	Subjective complaints		Irritability	Vegetative symptoms
	Headache	Fatigability		
1—2 year	44%	69%	13%	20%
5 year	70%	75%	22%	31%

The measured power density values at work places rarely surpass the levels of 100 μW/cm^2 recommended in Hungary. In a few cases we have measured higher values, but they have never reached the levels recommended in the USA. Actually no health hazards have been observed.

The proper formulation of safety standards is of great importance in Hungary, because some microwave devices originate from countries where the permissible level is 100-times higher. Until now we have had no difficulties with respect to radiation safety; these apparatuses also correspond to the higher requirements of our standards.

We carried out epidemiological investigations (Table IV) on 450 persons working in telecommunication, including extensive medical and psychological tests as well as a detailed interrogation on subjective complaints. We did not find any objective health damage due to microwave radiation but persons employed for more than 5 years complained more often of headache, fatigability, irritability and some vegetative symptoms.

Nevertheless, at work places exposed to microwave radiation, there are many other factors which may affect the health of staff members, so some of the complaints may have been due to causes other than microwave radiation.

Experiments on animals

To investigate whether microwaves had any effect on pregnancy and the development of the embryos, we carried out experiments on chick embryos [4].

The incubation temperature of eggs was 38 $\pm$ 0.5 °C, the relative humidity was 65 $\pm$ 5%.

The microwave source was a continuous cavity irradiator (Siemens model Electronic), at a frequency of 2.45 GHz $\pm$ 50 MHz. Ten eggs were exposed at one time to the cavity irradiation system. The amount of energy absorbed by the eggs and the resulting temperature increase were measured in the eggs by a small thermistor after the microwave field was switched off. Field inhomogeneity, microwave reflections from adjacent eggs, differences

in egg size cause the amount of absorbed power and the temperature of eggs to differ.

Power absorbed by the eggs was determined using a cooling curve [5]. The cooling curve was obtained from the monitored eggs by measuring their final temperatures. They were exposed to continuous irradiation until they reached their final temperatures, so the energy absorbed was equal to the energy lost.

Therefore,

$$(\Delta Q/\Delta t)_{\text{in}} = (\Delta Q/\Delta t)_{\text{loss}} = m \cdot c(\Delta T/\Delta t)_{\text{loss}},$$

where m is the mass of the egg; c is the specific heat; $(\Delta T/\Delta t)_{\text{loss}}$ is the temperature loss per unit time.

Measuring the maximum and the minimum temperatures on the eggs, the $(\Delta T/\Delta t)_{\text{loss}}$ can be determined from the slope of the cooling curve (Fig. 1) between these temperatures, which are 2.2 °C/min and 0.95 °C/min.

The average weight of the eggs was 50 g of which 46% was yolk and 54% was albumin.

Assuming that the temperature loss is the same for the yolk and the albumin the energy absorbed in unit time can be evaluated from:

$$(\Delta Q/\Delta t)_{\text{in}} = m_y C_y(\Delta T/\Delta t)_{\text{loss}} + m_a C_a(\Delta T/\Delta t)_{\text{loss}},$$

where the subscripts "y" and "a" represent yolk and albumin values [5], respectively.

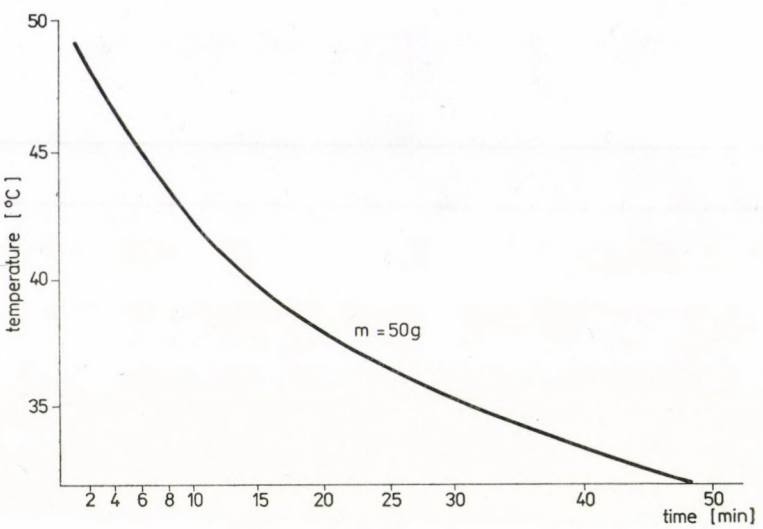

Fig. 1. Cooling curve in 24 °C room air.

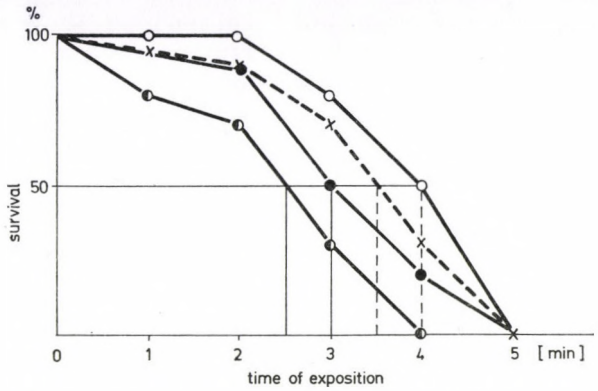

Fig. 2. Irradiation of chick embryos. o——o 2nd day of incubation; ●——○ 5th day of incubation; x----x 7th day of incubation; ○——○ 16th day of incubation.

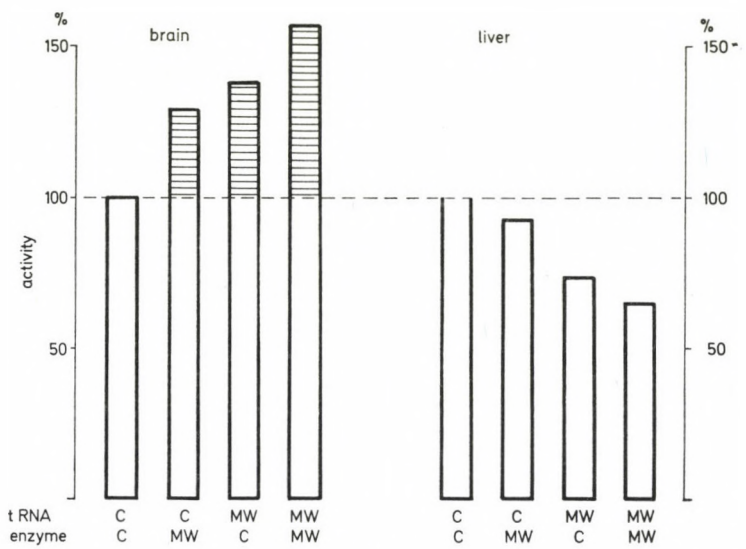

Fig. 3. Changes of activity of the aminoacyl-tRNA synthetase-tRNA system. tRNA — transfer ribonucleic acid; enzyme — aminoacyl-tRNA synthetase; C — control; MW — irradiated by microwave.

By this equation, absorption rates of the power/mass unit were calculated to be minimum 51 mW/g and maximum 115 mW/g.

In the biological experiments we compared the survival of chick embryos using the above mentioned microwave source. The irradiation was performed on the 15th day of incubation.

In the experiments (Fig. 2) we compared the survival curves of chick embryos, when the irradiation was carried out at different ages of embryos: on the 2nd, 5th, 7th and 16th day. It is to be seen that the LD_{50} value is

shifted, presumably due to the growing capacity of the heat regulatory mechanism of embryos.

In close relation to these biological effects of microwave radiation we studied the effects on certain components of protein synthesis.

It is generally accepted that the first events in protein synthesis, the activation of amino acids and their binding to transfer ribonucleic acid (tRNA) are catalysed by specific aminoacyl tRNA synthetases. The growing chick embryo shows a very rapid development for 21 days of its incubation, thus a high rate of protein synthesis can be observed in all of its organs.

In our experiments we chose two organs for a short time irradiation: the brain and the liver (Fig. 3). The changes in the protein synthesis were measured by suitable tracer technique. The combination of two components (enzyme and tRNA) from control and microwave irradiated embryos shows a significant increase of the protein synthetic activity in the brain and at the same time a slight decrease in the liver.

The results of the present biological study at the specific absorption rate used show mainly the thermal effect of microwave radiations. In the biochemical experiments where we used the same specific absorption rate, but shorter time of exposure, the thermal and non-thermal effects cannot be separated.

Differences between the rate of protein synthesis in the brain and in the liver are in good correlation with literature data concerning the effect of microwaves on the brain function [6].

REFERENCES

1. D. I. McRee, Environmental Aspects of Microwave Radiation, Environmental Health Perspectives, October 1972, pp. 41—43.
2. A. A. Letavet, Z. V. Gordon (Eds.): O biologitcheskom vozdeistvii sverchvysokich tchastot. Izd. Akad. Med. Nauk. USSR). Moscow, 1960.
3. D. I. McRee, Bull. N. Y. Acad. Med., **55,** 1133, 1979.
4. L. D. Szabó, L. Ballay, E. B. Bölöni and T. Predmerszky, Biological Effects and Dosimetry of Microwaves: Irradiation of Chick Embryo. XVIth Ann. Meeting of ESRB, Krakow, Poland, 1981. Book of Abstracts, p. 150.
5. P. E. Hamrick and D. I. McRee, J. Microwave Power, **10,** 211, 1975.
6. A. S. Presman, Electromagnetic Fields and Life, Plenum Press, New York and London, 1970.

Manuscript received by Akadémiai Kiadó: 22 March 1982
Manuscript received by the Printers: 24 March 1982
Date of publication: 22 March 1983

PRINTED IN HUNGARY

Akadémiai Nyomda, Budapest

NOTES TO CONTRIBUTORS

I. PAPERS will be considered for publication in Acta Physica Hungarica only if they have not previously been published or submitted for publication elsewhere. They may be written in English, French, German or Russian.

Papers should be submitted to

Prof. I. Kovács, Editor
Department of Atomic Physics, Technical University
1521 Budapest, Budafoki út 8, Hungary

Papers may be either articles with abstracts or short communications. Both should be as concise as possible, articles in general not exceeding 25 typed pages, short communications 8 typed pages.

II. MANUSCRIPTS

1. Papers should be submitted in three copies.

2. The text of papers must be of high stylistic standard, requiring minor corrections only.

3. Manuscripts should be typed in double spacing on good quality paper, with generous margins.

4. The name of the author(s) and of the institutes where the work was carried out should appear on the first page of the manuscript.

5. Particular care should be taken with mathematical expressions. The following should be clearly distinguished, e.g. by underlining in different colours: special founts (italics, script, bold type, Greek, Gothic, etc.); capital and small letters; subscripts and superscripts, e.g. x^2, x_3; small *l* and 1; zero and capital O; in expressions written by hand: *e* and *l*, *n* and *u*, *v* and *v*, etc.

6. References should be numbered serially and listed at the end of the paper in the following form: J. Ise and W. D. Fretter, Phys. Rev., **76**, 933, 1949.

For books, please give the initials and family name of the author(s), title, name of publisher, place and year of publication, e.g.: J. C. Slater, Quantum Theory of Atomic Structures, I. McGraw-Hill Book Company, Inc., New York, 1960.

References should be given in the text in the following forms: Heisenberg [5] or [5].

7. Captions to illustrations should be listed on a separate sheet, not inserted in the text.

8. In papers submitteed to Acta Physica all measures should be expressed in SI units.

III. ILLUSTRATIONS AND TABLES

1. Each paper should be accompanied by three sets of illustrations, one of which must be ready for the blockmaker. The other sets attached to the copies of the manuscript may be rough drawings in pencil or photocopies.

2. Illustrations must not be inserted in the text.

3. All illustrations should be identified in blue pencil by the author's name, abbreviated title of the paper and figure number.

4. Tables should be typed on separate pages and have captions describing their content. Clear wording of column heads is advisable. Tables should be numbered in Roman numerals (I, II, III, etc.).

IV. RETURN OF MATERIAL

Owing to high postage costs, the Editorial Office cannot undertake to return *all* material not accepted for any reason for publication. Of papers to be revised (for not being in conformity with the above Notes or other reasons) only *one* copy will be returned. Material rejected for lack of space or on account of the Referees' opinion will not be returned to authors outside Europe.

Periodicals of the Hungarian Academy of Sciences are obtainable at the following addresses:

AUSTRALIA
C.B.D. LIBRARY AND SUBSCRIPTION SERVICE
Box 4886, G.P.O., *Sydney N.S.W. 2001*
COSMOS BOOKSHOP, 145 Ackland Street
St. Kilda (Melbourne), Victoria 3182

AUSTRIA
GLOBUS, Höchstädtplatz 3, *1206 Wien XX*

BELGIUM
OFFICE INTERNATIONAL DE LIBRAIRIE
30 Avenue Marnix, *1050 Bruxelles*
LIBRAIRIE DU MONDE ENTIER
162 rue du Midi, *1000 Bruxelles*

BULGARIA
HEMUS, Bulvar Ruszki 6, *Sofia*

CANADA
PANNONIA BOOKS, P.O. Box 1017
Postal Station "B", *Toronto, Ontario M5T 2T8*

CHINA
CNPICOR, Periodical Department, P.O. Box 50
Peking

CZECHOSLOVAKIA
MAD'ARSKÁ KULTURA, Národní třida 22
115 66 Praha
PNS DOVOZ TISKU, Vinohradská 46, *Praha 2*
PNS DOVOZ TLAČE, *Bratislava 2*

DENMARK
EJNAR MUNKSGAARD, Norregade 6
1165 Copenhagen K

FEDERAL REPUBLIC OF GERMANY
KUNST UND WISSEN ERICH BIEBER
Postfach 46, *7000 Stuttgart 1*

FINLAND
AKATEEMINEN KIRJAKAUPPA, P.O. Box 128
SF-00101 Helsinki 10

FRANCE
DAWSON-FRANCE S. A., B. P. 40, *91121 Palaiseau*
EUROPÉRIODIQUES S. A., 31 Avenue de Versailles, *78170 La Celle St. Cloud*
OFFICE INTERNATIONAL DE DOCUMENTATION ET LIBRAIRIE, 48 rue Gay-Lussac
75240 Paris Cedex 05

GERMAN DEMOCRATIC REPUBLIC
HAUS DER UNGARISCHEN KULTUR
Karl Liebknecht-Straße 9, *DDR-102 Berlin*
DEUTSCHE POST ZEITUNGSVERTRIEBSAMT
Sraße der Pariser Kommüne 3–4, *DDR-104 Berlin*

GREAT BRITAIN
BLACKWELL'S PERIODICALS DIVISION
Hythe Bridge Street, *Oxford OX1 2ET*
BUMPUS, HALDANE AND MAXWELL LTD.
Cowper Works, *Olney, Bucks MK46 4BN*
COLLET'S HOLDINGS LTD., Denington Estate
Wellingborough, Northants NN8 2QT
WM. DAWSON AND SONS LTD., Cannon House
Folkstone, Kent CT19 5EE
H. K. LEWIS AND CO., 136 Gower Street
London WC1E 6BS

GREECE
KOSTARAKIS BROTHERS INTERNATIONAL BOOKSELLERS, 2 Hippokratous Street, *Athens-143*

HOLLAND
MEULENHOFF-BRUNA B.V., Beulingstraat 2,
Amsterdam
MARTINUS NIJHOFF B.V.
Lange Voorhout 9–11, *Den Haag*

SWETS SUBSCRIPTION SERVICE
347b Heereweg, *Lisse*

INDIA
ALLIED PUBLISHING PRIVATE LTD., 13/14
Asaf Ali Road, *New Delhi 110001*
150 B-6 Mount Road, *Madras 600002*
INTERNATIONAL BOOK HOUSE PVT. LTD.
Madame Cama Road, *Bombay 400039*
THE STATE TRADING CORPORATION OF INDIA LTD., Books Import Division, Chandralok
36 Janpath, *New Delhi 110001*

ITALY
INTERSCIENTIA, Via Mazzé 28, *10149 Torino*
LIBRERIA COMMISSIONARIA SANSONI, Via Lamarmora 45, *50121 Firenze*
SANTO VANASIA, Via M. Macchi 58
20124 Milano
D. E. A., Via Lima 28, *00198 Roma*

JAPAN
KINOKUNIYA BOOK-STORE CO. LTD.
17-7 Shinjuku 3 chome, Shinjuku-ku, *Tokyo 160-91*
MARUZEN COMPANY LTD., Book Department,
P.O. Box 5050 Tokyo International, *Tokyo 100-31*
NAUKA LTD. IMPORT DEPARTMENT
2-30-19 Minami Ikebukuro, Toshima-ku, *Tokyo 171*

KOREA
CHULPANMUL, *Phenjan*

NORWAY
TANUM-TIDSKRIFT-SENTRALEN A.S., Karl Johansgatan 41–43, *1000 Oslo*

POLAND
WĘGIERSKI INSTYTUT KULTURY, Marszałkowska 80, *00-517 Warszawa*
CKP I W, ul. Towarowa 28, *00-958 Warszawa*

ROUMANIA
D. E. P., *Bucureşti*
ILEXIM, Calea Grivitei 64–66, *Bucureşti*

SOVIET UNION
SOJUZPECHAT — IMPORT, *Moscow*
and the post offices in each town
MEZHDUNARODNAYA KNIGA, *Moscow G-200*

SPAIN
DIAZ DE SANTOS, Lagasca 95, *Madrid 6*

SWEDEN
ALMQVIST AND WIKSELL, Gamla Brogatan 26
101 20 Stockholm
GUMPERTS UNIVERSITETSBOKHANDEL AB
Box 346, *401 25 Göteborg 1*

SWITZERLAND
KARGER LIBRI AG, Petersgraben 31, *4011 Basel*

USA
EBSCO SUBSCRIPTION SERVICES
P.O. Box 1943, *Birmingham, Alabama 35201*
F. W. FAXON COMPANY, INC.
15 Southwest Park, *Westwood Mass. 02090*
THE MOORE-COTTRELL SUBSCRIPTION AGENCIES, *North Cohocton, N. Y. 14868*
READ-MORE PUBLICATIONS, INC.
140 Cedar Street, *New York, N. Y. 10006*
STECHERT-MACMILLAN, INC.
7250 Westfield Avenue, *Pennsauken N. J. 08110*

YUGOSLAVIA
JUGOSLOVENSKA KNJIGA, Terazije 27, *Beograd*
FORUM, Vojvode Mišića 1, *21000 Novi Sad*

HU-ISSN 0001-6705 **Index: 26.022**